

Vol. 137, Nos. 1-4 (1995)

REDSEI 137(1-4) 1-354 (1995)  
ISSN 1042-0150  
ISBN 2-919875-16-7

== and ==

EDITOR IN CHIEF

Jochen P. Biersack

REGIONAL EDITORS

N. Itoh/H. Kronmüller/M. A. Kumakhov/N. Tolk

**CLASSIFICATION STATEMENT A**

Approved for public release  
Distribution Unlimited

Proceedings of the  
Seventh Europhysical Conference on  
Defects in Insulating Materials Eurodim 94  
Lyon 1 - University  
July 5-8, 1994

Part IV

Guest Editors:

M. G. Blanchin, J. Davenas, B. Moine,  
C. Pédrini and M. Treilleux

GORDON AND BREACH PUBLISHERS

19970516 055

DTIC QUALITY INSPECTED 3

# Radiation Effects and Defects in Solids

## EDITOR IN CHIEF

Jochen P. Biersack      Hahn-Meitner-Institut, Glienickerstrabe 100,  
14109 Berlin, Germany

## REGIONAL EDITORS

N. Itoh      Department of Physics, Faculty of Science, Nagoya  
University, Furo-cho, Chikusa-ku, Nagoya 464, Japan

H. Kronmüller      Max-Planck-Institut für Metallforschung, Institut für  
Physik, Heisenbergstrabe 1, 70569 Stuttgart 80, Germany

M. A. Kumakhov      Russian Research Center, "I. V. Kurchatov Institute",  
Kurchatov Sq, Moscow 123182 Russia

N. Tolk      Department of Physics and Astronomy, Vanderbilt University,  
P.O. Box 1807-B, Nashville, Tennessee 37325, USA

## FOUNDING EDITORS

L. T. Chadderton (Radiation Effects)      R. R. Hasiguti (CLDAM)

## EDITORIAL BOARD

V. V. Beloshitsky, I. V. Kurchatov Research Center, Russia	J. W. Rabalais, University of Houston, USA
S. Datz, Oak Ridge National Laboratory, USA	S. Radhakrishna, Indian Institute of Technology, India
L. C. Feldman, AT & T Bell Laboratories, USA	E. Rimini, Università di Catania, Italy
A. Gras-Marti, Universitat d'Alacant, Spain	W. A. Sibley, National Science Foundation, USA
E. Kaufmann, Argonne National Laboratory, USA	P. D. Townsend, University of Sussex, UK
M. Kiritani, Nagoya University, Japan	J. C. Tully, AT & T Bell Laboratories, USA
F. F. Komarov, Shevchenko NIIPF, Minsk, Belarus	Z.-L. Wang, Shandong University, China
A. I. Kupchishin, Kirov University, Alma Ata, Kazakhstan	G. Watkins, Lehigh University, USA
G. Margaritondo, Institut de Physique Appliquee, Switzerland	J. Williams, The Australian National University, Australia
W. Möller, Forschungszentrum Rossendorf, Germany	

## AIMS AND SCOPE

*Radiation Effects and Defects in Solids* publishes experimental and theoretical papers of both a fundamental and applied nature that contribute to the understanding of either phenomena induced by the interaction of radiation with condensed matter or defects in solids introduced not only by radiation but also by other processes. Papers are categorised in three groups.

**Section A: Radiation Effects** — Suitable topics include, but are limited to, atomic collisions, radiation induced atomic and molecular processes in solids, the stopping and range of ions and radiation damage, sputtering and mixing in solids, radiation-induced transport phenomena and the role of defects and impurities introduced by radiation. Papers in ion implantation in metals and semiconductors as well as on radiation effects in insulators and superconductors, in fusion and fission devices and in space research are considered. Studies on fission tracks, isotope dating and ion beam analytic techniques are also welcome.

**Section B: Crystal Lattice Defects and Amorphous Materials** — Topics covered include atomic and electronic properties of defects, influence of defects on lattice properties and processes, the lattice-defect approach to solid state reactions such as clustering, precipitation, laser annealing and the role of impurities, the defects dynamics in a non-steady state such as under particle or electromagnetic irradiation or during a rapid temperature change and problems associated with the metastable nature of amorphous materials.

**Section C: Radiation Effects and Defects in Solids Express** — This section is available separately on subscription and presents significant short notes and communications in camera-ready form from the above fields for the fastest possible publication.

Proceedings of the  
Seventh Europhysical Conference on  
Defects in Insulating Materials Eurodim 94

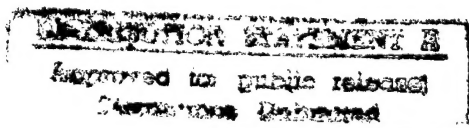
Lyon 1 – University

July 5–8, 1994

Part IV

Guest Editors:

M. G. Blanchin, J. Davenas, B. Moine,  
C. Pédrini and M. Treilleux



## CONTENTS - PART I

### Note on Pagination, Author Index and Table of Contents

*The Proceedings of the EURODIM 94 Conference is being published in four volumes of Radiation Effects and Defects in Solids (Volume 134, Part I, Volume 135, Part II, Volume 136, Part III and Volume 137, Part IV). To facilitate indexing and referring to this Proceedings, the page numbers of Volume 135, Volume 136 and Volume 137 will run continuously from the end of Volume 134. An author index will appear at the end of Volume 137. A complete table of contents will appear in Volume 134, Part I and Volume 137, Part IV.*

<b>Preface</b>	xxiii
<b>Computer Simulation of the Thermodynamics and Diffusion in Nonstoichiometric Materials</b> G. E. MURCH	1
<b>Defects in Glasses</b> A. R. SILINS	7
<b>Optical Properties of Oxide Glasses Doped by Semiconductor Nanocrystals</b> A. I. EKIMOV	11
<b>Scintillators and Applications: Cerium-Doped Materials</b> M. J. WEBER, M. BLISS, R. A. CRAIG, and D. S. SUNBERG	23
<b>The Sol-Gel Method for the Synthesis of Glasses, Ceramics and Hybrid Materials</b> M. GUGLIEMI and P. BARBOUX	31
<b>Ultrafast Spectroscopy of Defects</b> M. LEBLANS	39
<b>1 Calculations and Theory</b>	
<b>Static Simulations of Cu<sup>+</sup> Centers in Alkali Halides</b> V. LUNAÑA, M. A. BLANCO, M. FLÓREZ, A. MARTÍN PENDÁS and L. PUEYO	47
<b>Investigation of the Electronic Structure of Point Defects in Ionic Crystals by the Cluster Scattered Wave Method with the Self-Consistent Calculation of the Lattice Distortion and Long-Range Polarization</b> A. B. SOBOLEV	51
<b>Protons in Oxides</b> C. R. A. CATLOW, P. S. BARAM, S. C. PARKER, J. PURTON and K. V. WRIGHT	57
<b>Electronic Structure of Intrinsic and Impurity Mn-Centres in A<sub>2</sub>BX<sub>4</sub> Crystals with <math>\beta</math>-K<sub>2</sub>SO<sub>4</sub> Type Structure</b> I. BOLESTA, I. KITIKY, Y. FURGALA and S. VELGOSH	65
<b>Electronic Structure of a LiB<sub>3</sub>O<sub>5</sub> Nonlinear Optical Crystal</b> A. Yu. KUZNETSOV, A. B. SOBOLEV, I. N. OGORODNIKOV and A. V. KRUSHALOV	69
<b>Oxygen Vacancy in Perovskite Oxides: Electron Structure Calculation by the SCF X<math>\alpha</math> SW Technique</b> M. A. BUNIN, S. A. PROSANDEYEV, I. I. GEGUSIN and I. M. TENNENBOUM	75
<b>Radiative and Nonradiative Tunneling Processes in Silicon</b> A. J. ZAKRZEWSKI, A. M. FRENS, M. T. BENNEBROEK and J. SCHMIDT	79
<b>Theoretical Simulations of I-Center Annealing in KCl Crystals</b> A. I. POPOV, E. A. KOTOMIN and R. I. EGLITIS	83



<b>Modelling of Point Defects in <math>\alpha</math>-AL2O3</b>	<b>87</b>
E. A. KOTOMIN, A. STASHANS and P. W. M. JACOBS	
<b>A Combined Computer Simulation and EXAFS Study of Dopant Clustering in Lanthanum Oxide</b>	<b>91</b>
A. V. CHADWICK, G. MORRISON and R. RAFIUDDIN	
<b>Cluster Calculation of Impurity-Induced Core-Valence Transitions</b>	<b>95</b>
A. S. VOLOSHINOVSKII, V. B. MIKHAILIK and P. A. RODNYI	
<b>Calculation of the Mollwo-Ivey Parameters in the Point-Ion Approximation</b>	<b>101</b>
M. S. MALGHANI and D. Y. SMITH	
<b>Dynamics of Lithium Ions in Lithium Oxide</b>	<b>107</b>
J. L. GAVARTIN, C. R. A. CATLOW, A. L. SHLUGER, P. W. M. JACOBS and Z. A. RYCERZ	
<b>Computer Modelling and Brillouin Scattering Studies of High Temperature Disorder in CdF<sub>2</sub></b>	<b>111</b>
T. T. NETSHISAULU, P. E. NGOEPE, J. D. COMINS and C. R. A. CATLOW	
<b>Mixed Dimers in Rare-Earth-Doped Fluorides</b>	<b>117</b>
S. S. DE SOUZA and A. R. BLAK	
<b>Theoretical Study of the Coordination of the Cr<sup>3+</sup> Ion in <math>\alpha</math>-Al<sub>2</sub>O<sub>3</sub></b>	<b>123</b>
R. FRANCO, J. M. RECIO, A. MARTÍN PENDAS, E. FRANCISCO, V. LUNA and L. PUEYO	
<b>Local Relaxations and Optical Properties of Cr<sup>3+</sup> in MgO</b>	<b>127</b>
D. J. GROH, R. PANDEY and J. M. RECIO	
<b>Anomalous Charge Screening in the Radiation-Induced Recombination of Charged Defects in Ionic Solids</b>	<b>133</b>
V. N. KUZOVKOV	
<b>The Kinetics of Defect Aggregation: A Novel Lattice Formalism</b>	<b>137</b>
V. N. KUZOVKOV	
<b>Electric Field Induced Energy Shift in F-Centre Emission</b>	<b>141</b>
M. J. PONNAMBALAM	
<b>Semi-Empirical Analysis of the Quantum Yield of the Three Center Auger Effect</b>	<b>145</b>
A. J. ZAKRZEWSKI	
<b>On the Error in the Activation Energy Obtained by the Initial Rise Method for Thermally Stimulated Processes in Dielectrics</b>	<b>147</b>
ANTÔNIO E. DO NASCIMENTO, PIOTR TRZESNIAK, MÁRIO E. G. VALERIO and JOSÉ F. DE LIMA	
<b><i>ab initio</i> Molecular-Cluster Modelling of a Paramagnetic Excess-Electron Vacancy Center in Paratellurite</b>	<b>153</b>
D. P. MADACSI and K. RAKSÁNY	
<b>Point Defect Modelling and Transport Processes in AgBr</b>	<b>157</b>
RADHA D. BANHATTI and Y. V. G. S. MURTI	
<b>Computer Simulation of Uranium Oxide Phases</b>	<b>161</b>
R. A. JACKSON, J. E. HUNTINGTON and R. G. J. BALL	
<b>Shell Model and Embedded Cluster Calculations of Hole Bipolarons in BaTiO<sub>3</sub></b>	<b>165</b>
H. DONNERBERG and A. BIRKHOLZ	
<b>Atomistic Lattice Simulations of Dopant Migration in Planar and Helical-Chain Conductive Polymers</b>	<b>171</b>
J. CORISH, D. A. MORTON-BLAKE, KALYANI VELURI and F. BÉNIÈRE	
<b>Optical Properties of Cr<sup>3+</sup> and Ni<sup>2+</sup> Ions in MgO, LiNbO<sub>3</sub> and LMA</b>	<b>175</b>
F. MICHEL-CALENDINI	

# CONTENTS

v

<b>Simulation of Oxygen Vacancies at the Si-SiO<sub>2</sub> Interface</b> S. CARNIATO, G. BOUREAU and J. HARDING	<b>179</b>
<b>Why is 10Dq so useful for Measuring Changes of the Impurity-Ligand Distance?</b> M. T. BARRIUSO, J. A. ARAMBURU and M. MORENO	<b>185</b>
<b>The Jahn-Teller Effect in the Excited States of MnF<sub>6</sub><sup>4-</sup> and CrF<sub>6</sub><sup>3-</sup> Complexes</b> J. A. ARAMBURU, M. T. BARRIUSO and M. MORENO	<b>189</b>
<b>Energetics of the RbF + CaF<sub>2</sub> → RbCaF<sub>3</sub> Solid State Reaction: A First-Principle Study</b> M. FLÓREZ, J. M. RECIO, A. M. PENDÁS, E. FRANCISCO and V. LUAÑA	<b>193</b>
<b>Effects of a Quantum Crystal Potential on the Derivation of Electron Gas Interionic Energies</b> E. FRANCISCO, J. M. RECIO, M. A. BLANCO, A. M. PENDÁS and L. PUEYO	<b>197</b>
<b>Stability of B1 and B2 Phases from Electronic Density Topology Considerations</b> A. M. PENDÁS, J. M. RECIO, M. FLÓREZ, M. A. BLANCO and E. FRANCISCO	<b>201</b>
<b>Physical Properties of the Ground State of a Tunnelling Particle in a Phonon Field in the Intermediate Coupling Regime</b> G. BENIVEGNA, A. MESSINA and E. PALADINO	<b>205</b>
<b>2 Defects in Oxides</b>	
<b>Microstructure of Single-Crystal Sillenite Fibers</b> V. V. PROKOFIEV, J. P. ANDREETA, C. J. DE LIMA, M. R. B. ANDREETA, A. C. HERNANDES, J. F. CARVALHO, A. A. KAMSHILIN and T. JÄÄSKELÄINEN	<b>209</b>
<b>OH Vibrational Modes in Sillenites</b> P. BENEVENTI, R. CAPELLETTI, L. KOVÁCS, Á. PÉTER and F. UGOZZOLI	<b>213</b>
<b>On the Substitution Site of Cr and Fe in LiNbO<sub>3</sub>: An EXAFS Study</b> G. CORRADI, A. V. CHADWICK, A. R. WEST, K. CRUICKSHANK and M. PAUL	<b>219</b>
<b>Magnetic Bistability and Memory of Conduction Electrons Released from Oxygen Vacancies in Gallium Oxide</b> D. GOURIER, L. BINET and E. AUBAY	<b>223</b>
<b>Second Harmonic Generation and Thermally Stimulated Depolarization Current Investigation of K<sub>1-x</sub>Li<sub>x</sub>TaO<sub>3</sub></b> P. VOIGT, S. KAPPAN, L. OLIVEIRA and M. S. LI	<b>229</b>
<b>Influence of Yttrium and of the Oxygen Pressure on <math>\alpha</math>-Alumina Microstructure. Relation with Mechanical Properties</b> M. K. LOUDJANI, C. HAUT and S. PARISOT	<b>233</b>
<b>The Gigantic Ions of Chromium in Ruby</b> V. I. FLEROV and A. V. FLEROV	<b>239</b>
<b>The Short Life-Time Defect Formation in <math>\alpha</math>-Al<sub>2</sub>O<sub>3</sub> Under the Synchrotron Radiation</b> V. V. HARUTUNYAN, A. N. BELSKY, V. A. GEVORKYON, V. V. MIKHAILIN and G. N. YERITSIAN	<b>243</b>
<b>Thermal Depolarization Spectroscopy for Probing the Contribution of CaCO<sub>3</sub> to the Dielectric Relaxation of Dolomite (CaMg(CO<sub>3</sub>)<sub>2</sub>)</b> A. N. PAPATHANASSIOU, J. GRAMMATIKAKIS, V. KATSIKA and A. B. VASSILIKOU-DOVA	<b>247</b>
<b>Defects and Features of Ion-Electron Processes in Garnets</b> A. E. NOSENKO and V. N. SHEVCHUK	<b>251</b>
<b>Dielectric Response of Natural Zeolite (Stilbite) Single Crystals</b> J. M. KALOGERAS and A. VASSILIKOU-DOVA	<b>257</b>

<b>EPR Spectra of <math>\text{Cr}^{3+}</math> Ions in <math>\text{LiNbO}_3\text{:ZnO}</math> and <math>\text{LiNbO}_3\text{:CaO}</math></b>	<b>261</b>
D. BRAVO, A. MARTÍN, M. VODA and F. J. LÓPEZ	
<b>Tunneling Afterglow and Point Defects in Feldspars</b>	<b>265</b>
R. VISOCEKAS and A. ZINK	
<b>Evidence for Schottky Barrier Formation Due to Hole Centers in <math>\text{Al}_2\text{O}_3\text{:}</math> and <math>\text{MgO:Li}</math> with Metal Contacts</b>	<b>273</b>
R. VILA and M. JIMÉNEZ DE CASTRO	
<b>Nuclear Magnetic Resonance and Electrical Conductivity in Single-Crystalline Paratellurite</b>	<b>277</b>
J. WEGENER, O. KANERT, R. KÜCHLER and A. WATTERICH	
<b>Vibration + Libration Absorption Bands of OH Centres in <math>\text{LiNbO}_3</math></b>	<b>283</b>
A. GRÖNE and S. KAPPAN	
<b><math>\text{OH}^-</math> Absorption in <math>\text{Bi}_4\text{Si}_3\text{O}_{12}</math> Single Crystals</b>	<b>287</b>
L. KOVÁCS, P. BENEVENTI and R. CAPELLETTI	
<b>Anharmonic Effects on Lattice Vibration Modes of Sillenites</b>	<b>293</b>
P. BENEVENTI, R. CAPELLETTI and L. KOVÁCS	
<b>On the Dielectric Relaxations in Crystalline Insulators and Amorphous Systems</b>	<b>299</b>
E. LAREDO, M. ALDANA and A. BELLO	
<b>Lattice Defects in Beryllium Oxide</b>	<b>303</b>
I. N. ANTSGIN and A. V. KRIZHALOV	
<b>Effects of the Microindentation, X-Irradiation and Annealing on the F-Centre-Like Defects Production in MgO</b>	<b>307</b>
T. A. NAZAROVA and M. V. NAZAROV	
<b>Optically Stimulated Luminescence in Anion-Defective Carbon Doped <math>\alpha\text{-Al}_2\text{O}_3</math> Crystals</b>	<b>311</b>
N. KRISTIANPOLLER and L. OSTER	
<b>Thermally Stimulated Depolarization Currents in Natural Beryl</b>	<b>315</b>
C. VIANNA and A. R. BLAK	
<b>Crystal Structure Perfection and Domain Structure Revealing in Epitaxial Ferroelectric Thin Films</b>	<b>321</b>
V. A. ALYOSHIN, E. V. SVIRIDOV, I. N. ZAKHARCHENKO and V. P. DUDKEVICH	
<b>The Effect of Local Ordering in a System of Defects in Weakly Doped <math>\text{KTaO}_3\text{:}</math> Dielectric Anomalies and Their Origin</b>	<b>325</b>
V. TREPAKOV, F. SMUTNÝ, V. VIKHNIN, V. BURSIA, L. SOCHAVA, L. JASTRABÍK and P. SYRNIKOV	
<b>A Cation Vacancy Center in Crystalline <math>\text{Al}_2\text{O}_3</math></b>	<b>329</b>
B. D. EVANS and L. S. CAIN	
<b>3 Colour Centers</b>	
<b>Optical Spectra of <math>\text{Cu}^{2+}</math> Ions in LiF Crystals</b>	<b>333</b>
A. SCACCO, C. MARASCA, U. M. GRASSANO and N. ZEMA	
<b>Nature of Uncommon Nuclear Spin Relaxation in NaCl with High Concentration of Reorienting OH-Impurities at Low Temperatures</b>	<b>337</b>
O. KANERT, M. BACKENS, M. FRICKE, S. KAPPAN, R. KÜCHLER and V. S. VIKHNIN	
<b>Relaxation and IR Spectroscopic Properties of the <math>\text{CN}^-</math> Stretching Mode in Silver Halides</b>	<b>341</b>
C. E. MUNGAN, U. HAPPEK, W. VON DER OSTEN and A. J. SIEVERS	
<b>Time-resolved Picosecond Spectroscopy of the Resonant Secondary Radiation of F Centers in KCl</b>	<b>345</b>
N. AKIYAMA, F. NAKAHARA and H. OHKURA	

# CONTENTS

vii

<b>Four-wave Phase Conjugation with <math>F_3^+</math> Color Centers in LiF</b>	<b>349</b>
T. TSUBOI and H. E. GU	
<b><math>Cu^+</math> and <math>OH^-</math> Pairs Defects Interaction in NaF Crystals</b>	<b>353</b>
J. L. FABRIS, M. MÜLLER, A. C. HERNANDES, M. SIU-LI and S. KAPPAN	
<b><math>Cu^+</math> High Doping Effects in KCl and KBr Films</b>	<b>357</b>
L. OLIVEIRA, C. M. G. S. CRUZ, M. A. P. SILVA and M. SIU-LI	
<b>Radiation Induced Colour Centres in Cerium Fluoride</b>	<b>361</b>
E. APOSTOL, I. DAFINEI, GH. MITROAICA, T. TANASE and V. TOPA	
<b>Up-Conversion and Relaxation Kinetics among <math>CN^-</math> Vibrational States After Single Pulse <math>0 \rightarrow 1</math> Excitation in Rubidium-Halide-Cyanide Crystals</b>	<b>367</b>
H. NAKAGAWA and F. LÜTY	
<b>The Estimation of Size of Gigantic Ions of Chromium in Corundum Lattice</b>	<b>371</b>
V. I. FLEROV, A. V. FLEROV and S. I. FLEROV	
<b>Off-Centre Effects in the Triplet Relaxed Excited State of Impurity <math>ns^2</math> Ions in Alkali Halides</b>	<b>375</b>
V. HIZHNYAKOV, K. KALDER, V. KORROVITS, V. NAGIRNYI, A. STOLOVICH and S. ZAZUBOVICH	
<b>Anharmonicity Effects and Phonon Coupling of OH-Divalent Impurity Complexes in Alkali Halides</b>	<b>379</b>
P. BENEVENTI, R. CAPELLETTI, M. DARRA, R. FIESCHI, W. B. FOWLER and A. GAINOTTI	
<b>Structure and Thermodynamic Behavior of <math>In^{3+}-2V_{Ag}</math> DEFECTS IN AgBr</b>	<b>385</b>
J. C. AUSTIN, K. J. PRICE, B. K. PATNAIK and M. L. SWANSON	
<b>Color Centers in Mixed Crystals of Alkali Silver Halides and Ammonium Silver Halides</b>	<b>389</b>
T. AWANO and T. MATSUYAMA	
<b>On F-Aggregate Centre Formation in KCl Crystals Containing <math>O^{2-}</math>-Vacancy Complexes</b>	<b>395</b>
P. RAERINNE and P. KETOLAINEN	
<b>A Light Induced Configurational Change of <math>F_A</math> Centres in Li Doped KCl-KBr Crystals</b>	<b>401</b>
P. KETOLAINEN and P. SILFSTEN	
<b>E-V Energy Transfer in the <math>F_H(CN)</math> Center in KCl and CsCl</b>	<b>405</b>
L. F. CHEN and K. S. SONG	
<b>Point Defect Interaction in Alkali Halide Crystals</b>	<b>411</b>
A. V. GEKTI, V. YA. SEREBRYANNY and N. V. SHIRAN	
<b>Ultrafast Relaxation of <math>F_H</math>-Centre in <math>KBr:OH^-</math></b>	<b>417</b>
P. PROSPITO, M. CASALBONI, F. IGNOZZA and U. M. GRASSANO	
<b>Configuration of <math>F_A</math> (Na) Defects in KF Crystals</b>	<b>421</b>
A. SCACCO, C. GILIBERTI, U. M. GRASSANO, G. BALDACCHINI, M. CREMONA, R. M. MONTEREALI and A. SHPAK	
<b>Triplet State of <math>F_3^+</math> in LiF</b>	<b>425</b>
G. BALDACCHINI, M. CREMONA, G. D'AURIA, V. KALINOV and R. M. MONTEREALI	
<b>Optical Properties of F and <math>F^+</math> Type Centers in Barium <math>\beta</math>-Alumina</b>	<b>431</b>
D. GOURIER, B. VIANA, P. BELLENOUE, J. THERY and D. VIVIEN	
<b>Identification of <math>I_3^-</math> AND <math>I_5^-</math> Clusters in Irradiated KI by X-Ray Photoelectron, Raman and Optical Absorption Spectroscopies</b>	<b>437</b>
J. D. COMINS, T. P. NGUYEN, M-A. PARISELLE, S. LEFRANT and A. M. T. ALLEN	
<b>Vibronic Scheme of the Franck-Condon State of F Centers that Consistently Elucidates MCD and Resonance Raman Scattering</b>	<b>443</b>
S. MURAMATSU, Y. MORI and H. OHKURA	

<b>Luminescence of Defect Centres in <math>\text{Hg}_2\text{Cl}_2</math></b>	<b>447</b>
Z. BRYKNAR, P. PEKA, A. KOŇÁKOVÁ, J. KRÁL and H.-J. SCHULZ	
<b>Autler-Townes Splittings of Photo-Excited Point Defects</b>	<b>453</b>
M. GLASBEEK, C. J. M. TAVARES, M. A. COSTA NETO and R. SITTERS	
<b>Photoinduced Color Centers Creation in Superionic Crystals <math>\text{RbAg}_4\text{I}_5</math></b>	<b>457</b>
N. KOVALEVA, A. BORIS, S. BREDIKHIN and T. AWANO	
<b>M-Centre Luminescence in NaF and LiF: Towards a Comprehensive Interpretation of the M-centre Emission Properties in Alkali Halides</b>	<b>461</b>
L. BOSI and D. GALLO	
<b>Investigation of the Dynamical Behaviour of the <math>\text{F}_\text{H}(\text{CN}^-)</math> Centre in KCl with Temperature Dependent ENDOR Spectroscopy</b>	<b>465</b>
TH. PAWLIK, R. BUNGENSTOCK, J. M. SPAETH and F. LÜTY	
<b>ODEPR of Indium Colour Centres in the X-Irradiated Storage Phosphor KBr:In</b>	<b>471</b>
U. ROGULIS, J. -M. SPAETH, I. TALE and E. RUZA	
<b>Thermoactivated Spectroscopy of Heterovalent Impurity Traps in <math>\text{CdWO}_4</math></b>	<b>477</b>
V. TÁLE, I. TÁLE and L. L. NAGORNAYA	
<b>Point Defects Related to 260 K Thermostimulated Luminescence in <math>\alpha\text{-Al}_2\text{O}_3</math></b>	<b>481</b>
M. SPRINGIS, P. KULIS and I. TALE	
<b>A Defect Model for the Optical and EPR Activity of the T-Center in Yttrium-Stabilized Zirconia</b>	<b>485</b>
G. B. AZZONI, L. BOLIS, P. CAMAGNI, G. C. CAMPAGNOLI and M. DE SIMONE	
<b>Influence of <math>\text{OH}^-</math> Impurities on the Relaxation of <math>F</math> Centers Studied with Picosecond Optical Pulses</b>	<b>489</b>
E. GUSTIN, W. WENSELEERS, M. LEBLANS, A. BOUWEN and D. SCHOEMAKER	
<b>Stabilization of H Centres in Irradiated <math>\text{LiF:Mg}</math> Crystals</b>	<b>493</b>
S. MYSOVSKY, B. ROGALEV and V. CHERNOV	

## CONTENTS - PART II

### Note on Pagination, Author Index and Table of Contents

*The Proceedings of the EURODIM 94 Conference is being published in four volumes of Radiation Effects and Defects in Solids (Volume 134, Part I, Volume 135, Part II, Volume 136, Part III and Volume 137, Part IV). To facilitate indexing and referring to this Proceedings, the page numbers of Volume 135, Volume 136 and Volume 137 will run continuously from the end of Volume 134. An author index will appear at the end of Volume 137. A complete table of contents will appear in Volume 134, Part I and Volume 137, Part IV.*

### 4 Spectroscopy luminescence

<b>X-Ray Storage Phosphors</b>	1/[499]
J. M. SPAETH, TH. HANGLEITER, F. K. KOSCHNICK and TH. PAWLIK	
<b>Fluorescence Line Narrowing in Mn<sup>4+</sup> Doped Gadolinium Gallium Garnet<sup>1</sup></b>	11/[509]
A. SUCHOCKI, M. POTEMSKI, A. BRENIER, C. PEDRINI and G. BOULON	
<b>Fine Structure of the Absorption and Emission Spectra of Ni<sup>2+</sup>-Ions in BaLiF<sub>3</sub></b>	15/[513]
E. MARTINS, S. L. BALDOCHI, S. P. MORATO, N. D. VIEIRA JR., A. LUCI, M. CASALBONI, U. M. GRASSANO, G. BALDACCHINI, M. CREMONA, R. M. MONTEREALI, E. KRAUSZ and M. RILEY	
<b>Spectroscopic Study of Cr<sup>3+</sup> in New Elpasolites</b>	19/[517]
M. C. MARCO DE LUCAS, J. M. DANCE, F. RODRÍGUEZ, A. TRESSAUD, M. MORENO and J. GRANNEC	
<b>Time Resolved Spectroscopy of Ni<sup>2+</sup> Doped Fluoroclorozirconate Glasses</b>	23/[521]
M. A. BUÑUEL, R. ALCALA and R. CASES	
<b>Charge Exchange Processes between Impurity Ions and the Host Crystal in Wide Band-Gap Crystals</b>	27/[525]
DONALD S. McCLURE, WING C. WONG and SERGEI A. BASUN	
<b>The Role of Different Charge States of Impurity Ions in Photoconductivity of Insulators</b>	37/[535]
S. A. BASUN	
<b>Two-Photon Laser Spectroscopy of Ce<sup>3+</sup> in LiYF<sub>4</sub></b>	41/[539]
J. C. GÂCON, J. BAUDRY, C. GARAPON and G. W. BURDICK	
<b>Optical Spectroscopy of Yb<sup>3+</sup> Ions in Ca<sub>x</sub>Cd<sub>1-x</sub>F<sub>2</sub></b>	45/[543]
K. ŚWIATEK	
<b>ENDOR-Investigations of Rare Earth and Transition Metal Ions in the Cubic Elpasolite Crystal Cs<sub>2</sub>NaYF<sub>6</sub></b>	49/[547]
TH. PAWLIK, J.-M. SPAETH, M. OTTE and H. OVERHOF	
<b>Optical and EPR Spectroscopy of Impurity Manganese Ions in Disordered Ca<sub>3</sub>Ga<sub>2</sub>Ge<sub>4</sub>O<sub>14</sub> Single Crystals</b>	55/[553]
A. E. NOSENKO, R. YE. LESHCHUK and B. V. PADLYAK	
<b>Interaction of Impurity Centres in Cs<sub>2</sub>CdI<sub>4</sub>-Mn Crystals</b>	61/[559]
I. BOLESTA and Y. FURGALA	
<b>Blue Avalanche Upconversion in YAG:Ti</b>	65/[563]
S. GUY, M. F. JOUBERT, B. JACQUIER and C. LINARÉS	
<b>New Spectroscopic Effects of Ferroelectric Phase Transition in Li<sub>2</sub>Ge<sub>7</sub>O<sub>15</sub> Crystals Doped with 3d<sup>3</sup>-Ions</b>	69/[567]
A. A. KAPLYANSKII, S. A. BASUN and S. P. FEOFILOV	
<b>Excited State Absorption in Holmium Doped Gd<sub>3</sub>Ga<sub>5</sub>O<sub>12</sub> Garnet</b>	73/[571]
A. BRENIER, C. MADEJ, C. PÉDRINI and G. BOULON	

<b>Luminescence of Ytterbium Doped <math>\text{LiNbO}_3:\text{MgO}</math> under UV Excitation</b> A. BRENIER, C. MADEJ, C. PÉDRINI and G. BOULON	<b>77/[575]</b>
<b>Optical Detection of <math>\text{Eu}^{3+}</math> Sites in <math>\text{Gd}_3\text{Ga}_5\text{O}_{12}:\text{Eu}^{3+}</math></b> L. C. COURROL, L. GOMES, A. BRENIER, C. PÉDRINI, C. MADEJ and G. BOULON	<b>81/[579]</b>
<b>Study of Bistable (Shallow-Deep) Defect Systems in <math>\text{CdF}_2:\text{M}^{3+}</math> (M: In, Ga)</b> YANG CAI and K. S. SONG	<b>85/[583]</b>
<b>Polarized Charge Transfer Spectra of <math>\text{Cu}^{2+}</math> Doped Perovskite Layers <math>(\text{RNH}_3)_2\text{Cd}_x\text{Mn}_{1-x}\text{Cl}_4</math> (<math>x = 0-1</math>)</b> B. BATICLE, F. RODRÍGUEZ and R. VALIENTE	<b>89/[587]</b>
<b>Optical Properties and Local Structure of <math>\text{MnCl}_6^{4-}</math> in <math>\text{ABCl}_3:\text{Mn}^{2+}</math></b> M. C. MARCO DE LUCAS, F. RODRÍGUEZ, C. PRIETO, M. VERDAGUER, M. MORENO and H. U. GÜDEL	<b>95/[593]</b>
<b>Photo-EPR Studies of Electron and Hole Trapping by <math>[\text{Fe}(\text{CN})_6]^{4-}</math> Complexes in Silver Chloride</b> M. T. OLM and R. S. EACHUS	<b>101/[599]</b>
<b>Site Selective Spectroscopy of <math>\text{Eu}^{3+}</math> and <math>\text{Eu}^{3+}-\text{Ho}^{3+}</math> Doped Glasses</b> V. D. RODRÍGUEZ, V. LAVÍN, U. R. RODRÍGUEZ-MENDOZA, I. R. MARTÍN and P. NUÑEZ	<b>105/[603]</b>
<b>Thermoluminescence of Brazilian Topaz</b> DIVANÍZIA DO N. SOUZA, JOSÉ F. DE LIMA and MÁRIO ERNESTO G. VALERIO	<b>109/[607]</b>
<b>Point Defects Produced by Grinding of CaS Phosphors: An Electron Spin Resonance Study</b> D. CAURANT, D. GOURIER, N. DEMONCY and M. PHAM-THI	<b>115/[613]</b>
<b>Thermally Stimulated Depolarization Current of Monovalent Copper Ions in Calcium Fluoride</b> L. OLIVEIRA, Q. R. NASCIMENTO, M. SIU LI, C. PÉDRINI and H. BILL	<b>121/[619]</b>
<b>Photostimulated Luminescence of KBr-In Crystals</b> I. PLAVINA, A. I. POPOV and A. TALE	<b>125/[623]</b>
<b>Energy Transfer and Up-Conversion in Yb-Tm Codoped Fluorindate Glasses</b> V. D. RODRÍGUEZ, I. R. MARTÍN, R. ALCALÁ and R. CASES	<b>129/[627]</b>
<b>Spectrally Resolved Thermoluminescence of Cu and Eu Doped <math>\text{Li}_2\text{B}_4\text{O}_7</math></b> M. MARTINI, C. FURETTA, C. SANIPOLI, A. SCACCO and K. SOMAIAH	<b>133/[631]</b>
<b>Reversible Photoionization Process in Luminescent <math>\text{Ce}^{3+}</math> Doped Elpasolite-Type Fluoroindates</b> J. P. CHAMINADE, A. GARCIA, T. GAUWANG, M. POUCHARD, J. GRANNEC and B. JACQUIER	<b>137/[635]</b>
<b>Excited Levels of the 2.56 eV Emission in Synthetic Diamond</b> E. PEREIRA, L. PEREIRA, D. M. HOFMANN, W. STADLER and B. K. MEYER	<b>143/[641]</b>
<b><math>\text{Er}^{3+}</math> Ion Concentration and Annealing Temperature Effect on the Fluorescence of <math>\text{Er}^{3+}:\text{TiO}_2</math> Planar Waveguides Prepared by the Sol-Gel Process</b> A. BAHTAT, M. BOUAZAQUI, M. C. MARCO DE LUCAS, M. BAHTAT, B. JACQUIER and J. MUGNIER	<b>149/[647]</b>
<b>EPR and Photoluminescence of <math>\text{Cr}^{3+}</math> Ions in <math>\text{CsCdF}_3</math> and <math>\text{CsCaF}_3</math></b> B. VILLACAMPA, R. CASES and R. ALCALÁ	<b>157/[655]</b>
<b>Spectroscopic Properties of <math>\text{Mn}^{2+}</math> Ions in Mixed Fluoroperovskites</b> F. LAHOZ, P. J. ALONSO, B. VILLACAMPA and R. ALCALÁ	<b>163/[661]</b>
<b>EPR Study of Concentration Dependence in Ce, Ce:La and Ce:Y Doped <math>\text{SrF}_2</math></b> O. DANKERT, D. VAINSHTEIN, H. C. DATEMA and H. W. DEN HARTOG	<b>169/[667]</b>
<b>Differential Spectroscopic Properties of <math>\text{Nd}^{3+}</math> in <math>\text{NdGaO}_3</math> and <math>\text{LaGaO}_3</math></b> V. M. ORERA, L. E. TRINKLER and R. I. MERINO	<b>173/[671]</b>

<b>EPR of Jahn-Teller <math>\text{Cr}^{2+}</math> in <math>\text{CaF}_2</math>, <math>\text{BaF}_2</math> and <math>\text{SrCl}_2</math></b> P. B. OLJETE, V. M. ORERA and P. J. ALONSO	<b>179/[677]</b>
<b><math>\text{Nd}^{3+}</math> Centres in Highly Neodymium Doped <math>\text{LaBGeO}_5</math> Crystals</b> L. BITAR, J. CAPMANY, L. E. BAUSÁ, J. GARCÍA-SOLÉ, R. MONCORGÉ and A. A. KAMINSKII	<b>183/[681]</b>
<b>Energy Levels of the <math>\text{Eu}^{3+}</math> Centers in <math>\text{LiNbO}_3</math></b> J. E. MUÑOZ SANTIUSTE, I. VERGARA and J. GARCÍA SOLÉ	<b>187/[685]</b>
<b>EPR Study of <math>\text{Nd}^{3+}</math> Ions in <math>\text{Bi}_4\text{Ge}_3\text{O}_{12}</math> Single Crystals</b> D. BRAVO, A. MARTÍN, A. A. KAMINSKII and F. J. LÓPEZ	<b>191/[689]</b>
<b>Light-Induced NIR-Absorption in <math>\text{Sr}_{0.61}\text{Ba}_{0.39}\text{Nb}_2\text{O}_6</math> : Ce at Low Temperatures</b> G. GRETEN, S. KAPPAN and R. PANKRATH	<b>195/[693]</b>
<b>Sharp R-Lines in Absorption and Emission of <math>\text{Cr}^{3+}</math> in Stoichiometric (VTE) <math>\text{LiNbO}_3</math></b> C. FISCHER, S. KAPPAN, XI-QI FENG and NING CHENG	<b>199/[697]</b>
<b>Clustering Processes in <math>\text{CaF}_2</math> : Gd + Lu and <math>\text{CaF}_2</math> : Gd + Sm</b> N. SUÁREZ	<b>203/[701]</b>
<b>New Symmetry Properties of the Cubic Rare-Earth Centers in Crystals</b> V. LUPEI	<b>207/[705]</b>
<b>Nonradiative Recombination Processes in Wide Band Gap II-VI Phosphor Materials</b> M. SURMA and M. GODLEWSKI	<b>213/[711]</b>
<b>Upconversion Luminescence Properties of <math>\text{Er}^{3+}</math> Ions Doped in Lithium Niobate Single Crystals</b> H. J. SEO, T. P. J. HAN, G. D. McCURE and B. HENDERSON	<b>217/[715]</b>
<b>EPR and Optical Spectroscopy of <math>\text{Cr}^{3+}</math> Doped <math>\text{CaYAlO}_4</math></b> M. YAMAGA, H. TAKEUCHI, K. HOLLIDAY, P. MACFARLANE, B. HENDERSON, Y. INOUE and N. KODAMA	<b>223/[721]</b>
<b>Optical Properties of <math>\text{Cr}^{3+}</math>-Ions in <math>\text{LaSr}_2\text{Ga}_{11}\text{O}_{20}</math></b> A. LUCI, M. CASALBONI, T. CASTRIGNANÒ, U. M. GRASSANO and A. A. KAMINSKII	<b>227/[725]</b>
<b>Nonlinear Transmission in <math>\text{Cr}^{4+}</math>-Doped Silicates</b> V. P. MIKHAILOV, N. I. ZHAVORONKOV, N. V. KULESHOV, A. S. AVTUKH, V. G. SHCHERBITSKY and B. I. MINKOV	<b>231/[729]</b>
<b>Photo-Stimulated X-Ray Luminescence in <math>\text{LiTaO}_3</math> : <math>\text{Tb}^{3+}</math> Based Green Emitting Phosphors</b> R. BRACCO, C. MAGRO and R. MORLOTTI	<b>237/[735]</b>
<b>Absorption and Luminescence Spectroscopy of Zinc Borate Glasses Doped with Trivalent Lanthanide Ions</b> LUIGI AMBROSI, MARCO BETTINELLI, GUY CORMIER and MAURIZIO FERRARI	<b>243/[741]</b>
<b>Optical Energy Transfer in Rare Earth Doped Silica Gels</b> A. BOUJAJAJ, A. MONTEIL, M. FERRARI and M. MONTAGNA	<b>247/[745]</b>
<b>Samarium Doped Alkaline Earth Halide Thin Films as Spectrally Selective Materials for Hole Burning?</b> A. MONNIER, M. SCHNIEPER, R. JAANISO and H. BILL	<b>253/[751]</b>
<b>5 Excited States</b>	
<b>Upconversion in <math>\text{CsCdBr}_3</math> : <math>\text{Pr}^{3+}</math></b> J. NEUKUM, N. BODENSCHATZ and J. HEBER	<b>257/[755]</b>
<b>Metastable One-Halide Self-Trapped Excitons in Alkali Halides</b> A. LUSHCHIK, CH. LUSHCHIK, F. SAVIKHIN and E. VASIL'CHENKO	<b>263/[761]</b>



<b>Optical Studies of Self-Trapped Holes and Excitons in Beryllium Oxide</b> S. V. GORBUNOV, S. V. KUDYAKOV, B. V. SHULGIN and V. YU. YAKOVLEV	<b>269/[767]</b>
<b>The Experimental Observation of the Potential Barrier for Self-Trapped Exciton Decay into F-H Pair in KCl-Na in Crystals</b> S. A. CHERNOV and V. V. GAVRILOV	<b>275/[773]</b>
<b>Luminescence of ON- And OFF-Center STE in ABX<sub>3</sub> Crystals</b> A. S. VOLOSHINOVSKII, V. B. MIKHAILIK and P. A. RODNYI	<b>281/[779]</b>
<b>Phonon Assisted Excitonic Luminescence in CsPbCl<sub>3</sub></b> I. BALTOG, S. LEFRANT, C. DIMOFTE, and L. MIHUT	<b>285/[783]</b>
<b>Optical Properties Of Pb<sup>2+</sup>-Based Aggregated Phase In NaCl And CsCl Alkali Halide Hosts</b> M. NIKL, K. POLAK, K. NITSCH, G. P. PAZZI, P. FABENI and M. GURIOLI	<b>289/[787]</b>
<b>Dynamical Processes of Ortho- and Para-Excitons in Alkali Iodides</b> KOICHI TOYODA, TORU TSUJIBAYASHI and TETSUSUKE HAYASHI	<b>295/[793]</b>
<b>Defects and Luminescence in Pure and I-Doped AgBr Crystals</b> L. NAGLI, A. SHMILEVICH, A. KATZIR and N. KRISTIANPOLLER	<b>301/[799]</b>
<b>6 Scintillators</b>	
<b>Scintillation Mechanisms in Rare Earth Orthophosphates</b> A. J. WOJCIOWICZ, D. WISNIEWSKI, A. LEMPICKI, and L. A. BOATNER	<b>305/[803]</b>
<b>Scintillation Properties of Lu<sub>3</sub>Al<sub>5-x</sub>Sc<sub>x</sub>O<sub>12</sub> Crystals<sup>1</sup></b> N. N. RYSKIN, P. DORENBOS, C. W. E. VAN EIJK and S. KH. BATYGOV	<b>311/[809]</b>
<b>Monte-Carlo Simulation of the Creation of Excited Regions in Insulators by a Photon</b> R. A. GLUKHOV and A. N. VASILEV	<b>315/[813]</b>
<b>Scintillation Properties of GdAlO<sub>3</sub>:Ce Crystals<sup>1</sup></b> P. DORENBOS, E. BOUGRINE, J. T. M. DE HAAS, C. W. E. VAN EIJK and M. V. KORZHIK	<b>321/[819]</b>
<b>Scintillation Properties of Y<sub>2</sub>SiO<sub>5</sub>:Pr Crystals<sup>1</sup></b> P. DORENBOS, M. MARSMAN, C. W. E. VAN EIJK, M. V. KORZHIK and B. I. MINKOV	<b>325/[823]</b>
<b>Scintillation Mechanism in CsGd<sub>2</sub>F<sub>7</sub>:Ce<sup>3+</sup> and CsY<sub>2</sub>F<sub>7</sub>:Ce<sup>3+</sup> Crystals<sup>†</sup></b> D. R. SCHAART, P. DORENBOS, C. W. E. VAN EIJK, R. VISSER, C. PEDRINI, B. MOINE and N. M. KHAIDUKOV	<b>329/[827]</b>
<b>Nanosecond UV-Scintillation in Cesium Iodide Crystals</b> S. CHERNOV and V. GAVRILOV	<b>333/[831]</b>
<b>Defects Induced by Irradiation at Room Temperature in Cerium Fluoride</b> E. AUFRAY, I. DAFINEI, P. LECOQ and M. SCHNEEGANS	<b>337/[835]</b>
<b>Local Trap Centres in PbWO<sub>4</sub> Crystals</b> E. AUFRAY, I. DAFINEI, P. LECOQ and M. SCHNEEGANS	<b>343/[841]</b>
<b>Temperature Dependence of Crossluminescence Characteristics in CsCl and CsBr in the 20–300 K Range</b> V. MAKHOV, J. BECKER, L. FRANKENSTEIN, I. KUUSMANN, M. RUNNE, A. SCHRÖDER and G. ZIMMERER	<b>349/[847]</b>
<b>Time-Resolved Studies Of Fast Scintillating Crystals Under VUV And X-Ray Synchrotron Radiation Excitation</b> E. G. DEVITSIN, N. M. KHAIDUKOV, N. YU. KIRIKOVA, V. E. KLIMENKO, V. A. KOZLOV, V. N. MAKHOV and T. V. UVAROVA	<b>355/[853]</b>
<b>ODMR of CD Impurity Centers in GG Irradiated BaF<sub>2</sub> Crystals</b> U. ROGULIS, J. TROKŠS, Ā. VEISPĀLS, I. TĀLE, P. KŪLIS and M. SPRINĢIS	<b>361/[859]</b>

<b>Colour Cathodoluminescence from <math>\text{Bi}_4[\text{GeO}_4]_3</math> Crystals</b>	<b>367/[865]</b>
T. A. NAZAROVA, M. V. NAZAROV, G. V. SAPARIN and S. K. OBYDEN	
<b>Further Results on <math>\text{GdAlO}_3:\text{Ce}</math> Scintillator</b>	<b>369/[867]</b>
J. A. MAREŠ, M. NIKL, C. PEDRINI, D. BOUTTET, C. DUJARDIN, B. MOINE, J. W. M. VERWEIJ and J. KVAPIL	
<b>Multiplication of Anion and Cation Electronic Excitations in Alkali Halides</b>	<b>375/[873]</b>
M. KIRM, A. FRORIP, R. KINK, A. LUSHCHIK, CH. LUSHCHIK and I. MARTINSON	
<b>Peculiarities of the Triplet Relaxed Excited State Structure in Thallium-Doped Cesium Halide Crystals</b>	<b>379/[877]</b>
V. NAGIRNYI, A. STOLOVICH, S. ZAZUBOVICH, V. ZEPELIN, M. NIKL, E. MIHOKOVA and G. P. PAZZI	
<b>The Role of Cation Vacancies in Excitation Mechanism of Re-ions in Alkaline-Earth Sulphides</b>	<b>383/[881]</b>
A. N. BELSKY, V. V. MIKHAILIN and A. N. VASIL'EV	
<b>LSO-Ce Fluorescence Spectra and Kinetics for UV, VUV and X-Ray Excitation</b>	<b>391/[889]</b>
I. A. KAMENSKIKH, V. V. MIKHAILIN, I. H. MUNRO, D. Y. PETROVYKH, D. A. SHAW, P. A. STUDENIKIN, A. N. VASIL'EV, I. A. ZAGUMENNYI and YU. D. ZAVARTSEV	
<b>Luminescence and Scintillation Properties of <math>\text{In}_2\text{Si}_2\text{O}_7</math></b>	<b>397/[895]</b>
A. GARCIA, T. GAUWANG, J. P. CHAMINADE, C. FOUASSIER, B. VARREL, B. JACQUIER, M. MESSOUS, B. CHAMBON and D. DRAIN	
<b>Thermoluminescence of Doped <math>\text{Gd}_3\text{Ga}_5\text{O}_{12}</math> Garnet Ceramics</b>	<b>401/[899]</b>
A. JAHNKE, M. OSTERTAG, M. ILMER and B. C. GRABMAIER	
<b>Luminescence Decay of Rare Earth Ions in an Orthophosphate Matrix</b>	<b>407/[905]</b>
B. FINKE and L. SCHWARZ	

## CONTENTS – PART III

### Note on Pagination, Author Index and Table of Contents

*The Proceedings of the EURODIM 94 Conference is being published in four volumes of Radiation Effects and Defects in Solids (Volume 134, Part I, Volume 135, Part II, Volume 136, Part III and Volume 137, Part IV). To facilitate indexing and referring to this Proceedings, the page numbers of Volume 135, Volume 136 and Volume 137 will run continuously from the end of Volume 134. An author index will appear at the end of Volume 137. A complete table of contents will appear in Volume 134, Part I and Volume 137, Part IV.*

## 7 Laser Materials

<b>On The Temperature Dependence of the Rate of Energy Transfer between Rare Earth Ions in Solids</b>	<b>1/[911]</b>
B. DI BARTOLO, G. ARMAGAN and M. BUONCRISTIANI	
<b>Progress in Ultrafast Color Center Lasers</b>	<b>7/[917]</b>
K. MÖLLMANN and W. GELLERMANN	
<b>The Release of Stored Energy in Heavily Irradiated NaCl Explosive Reactions.</b>	<b>11/[921]</b>
D. VAINSHTEIN, M. VAN DEN BEMT, J. SEINEN, H. C. DATEMA and H. W. DEN HARTOG	
<b>On the Mechanism of Contrast in the Cathodoluminescence Imaging of Laser Crystals</b>	<b>15/[925]</b>
V. LUPEI	
<b>Excited State Absorption Of Fe<sup>3+</sup> In Garnet Crystals</b>	<b>19/[929]</b>
V. LUPEI, S. HARTUNG and G. HUBER	
<b>Thermal Effects on the Quantum Efficiency of 3 <math>\mu</math>m Erbium Lasers</b>	<b>23/[933]</b>
S. GEORGESCU, V. LUPEI, T. J. GLYNN and R. SHERLOCK	
<b>Mn<sup>2+</sup> Luminescence in Mg-Al Spinel</b>	<b>29/[939]</b>
U. R. RODRÍGUEZ-MENDOZA, V. D. RODRÍGUEZ and A. IBARRA	
<b>Inhomogeneous Broadening Of The V<sup>4+</sup> Luminescence In CaYAlO<sub>4</sub></b>	<b>33/[943]</b>
M. YAMAGA, T. YOSIDA, Y. INOUE, N. KODAMA and B. HENDERSON	
<b>Multisite Structure of Nd<sup>3+</sup> in YAG</b>	<b>37/[947]</b>
A. LUPEI, C. TISEANU and V. LUPEI	
<b>Cr<sup>3+</sup>-Doped Borates—Potential Tunable Laser Crystals?</b>	<b>43/[953]</b>
G. WANG, H. G. GALLAGHER, T. P. J. HAN and B. HENDERSON	
<b>Nd<sup>3+</sup> Strontium Fluorovandate (SVAP) – A Promising Crystal for Diode Pumped Lasers at 1.06 <math>\mu</math>m and 1.34 <math>\mu</math>m</b>	<b>47/[957]</b>
M. A. SCOTT, H. G. GALLAGHER, T. P. J. HAN and B. HENDERSON	
<b>Charge Compensation and The Spectroscopy of Cr<sup>3+</sup> in KMgF<sub>3</sub></b>	<b>51/[961]</b>
D. R. LEE, T. P. J. HAN and B. HENDERSON	
<b>Perspective Laser Infrared Optics Material Cesium Iodide</b>	<b>57/[967]</b>
I. ANTONIV, I. GARAPYN and R. DIDYK	
<b>Laser Diode Pumping of a Colour Centre Laser with Emission in the 1.5 <math>\mu</math>m Wavelength Domain</b>	<b>61/[971]</b>
A. KONATÉ, J. L. DOULAN and J. MARGERIE	
<b>Ni<sup>2+</sup>:BaLiF<sub>3</sub>: A Promising R. T. Tunable Solid State Laser Material</b>	<b>65/[975]</b>
M. MORTIER, J. Y. GESLAND, M. ROUSSEAU, F. AUZEL, and D. MEICHENIN	
<b>Ag<sup>+</sup> Center in Alkaline-Earth Fluorides: New UV Solid State Lasers?</b>	<b>69/[979]</b>
P. BOUTINAUD, A. MONNIER and H. BILL	

## 8 Photorefractive and non linear materials

- Photorefractive Crystals—The Role of Defects** 73/[983]  
ECKHARD KRÄTZIG

- Hydrogen Defects in LiNbO<sub>3</sub> and Applications** 79/[989]  
J. M. CABRERA

- Luminiscence and Optical Second Harmonic Generation by Dipolar Microregions in KTaO<sub>3</sub>** 85/[995]  
C. FISCHER, C. AUF DER HORST, P. VOIGT, S. KAPPHAN and J. ZHAO

- Non-Linear and Fractal Dynamic Processes in Superionics** 91/[1001]  
A. E. UKSHE and N. G. BUKUN

- Magnetic Circular Dichroism and Absorption Study of Photochromism in Mn-Doped Bi<sub>12</sub>GeO<sub>20</sub>** 99/[1009]  
F. RAMAZ, A. HAMRI, B. BRIAT, V. TOPA and G. MITROAICA

- RBS Study of Defect Profiles in Proton Implanted LiNbO<sub>3</sub>** 103/[1013]  
S. OULD SALEM, B. CANUT, P. MORETTI, J. MEDDEB, S. M. M. RAMOS, and P. THEVENARD

- XPS Studies of Europium Implanted LiIO<sub>3</sub>** 107/[1017]  
S. M. M. RAMOS, C. ROSSO, P. MORETTI, C. GALEZ, B. CANUT and P. THEVENARD

- Characterisation of Planar Waveguides Formed by Proton Implantation in Lithium Iodate** 111/[1021]  
C. ROSSO, P. MORETTI, J. MUGNIER and J. BOUILLLOT

- Structural and Optical Characteristics of Crystallized PbTiO<sub>3</sub> Waveguides Prepared by Sol-Gel Process** 115/[1025]  
C. URLACHER, E. BERNSTEIN, J. SERUGHETTI and J. MUGNIER

- SHG Phase Matching Conditions For Undoped and Doped Lithium Niobate** 119/[1029]  
U. SCHLARB, A. REICHERT, K. BETZLER, M. WÖHLECKE, B. GATHER, T. VOLK and N. RUBININA

- Phase-Conjugate Waves Generated by Anisotropic Four-Wave Mixing in LiNbO<sub>3</sub> and LiTaO<sub>3</sub> Optical Waveguides** 123/[1033]  
D. KIP and E. KRÄTZIG

- Photoinduced Linear Dichroism in Sillenite Crystals and in Diamond** 129/[1039]  
H.-J. REYHER, J. RUSCHKE, and F. MERSCH

- Absorption Spectral Changes with Ultraviolet-Illumination in GeO<sub>2</sub>-SiO<sub>2</sub> Glass Films Prepared by Sputtering Deposition** 133/[1043]  
JUNJI NISHII, HIROSHI YAMANAKA, HIDEO HOSONO and HIROSHI KAWAZOE

- Ion-Beam/Channeling Characterization of LiNbO<sub>3</sub>: Interaction between Impurity Sites** 137/[1047]  
L. REBOUTA, M. F. DA SILVA, J. C. SOARES, M. T. SANTOS, E. DIÉGUEZ and F. AGULLÓ LÓPEZ

- Manifestation of a Confinement-Type Lattice Anharmonicity in the Emission Spectra of Niobate Glass** 141/[1051]  
M. GRINBERG, W. JASKÓSKI, CZ. KOEPKE, J. PLANELLES, and M. JANOWICZ

## 9 Radiation Defects

- The Effect of the Relaxation of 4d I<sup>-</sup> Hole on the Formation of Emission Centers in Alkali Halides** 145/[1055]  
A. N. BELSKY, S. KLIMOV, E. I. ZININ, P. MARTIN, C. PEDRINI and A. V. GEKTIN

- SEM-Analysis of Fracture Features Formed in Excimer-Laser Induced Surface Damage of CaF<sub>2</sub>** 151/[1061]  
H. JOHANSEN, S. GOGOLL, E. STENZEL, M. REICHLING, and E. MATTHIAS

<b>Electron Self-Trapping and Photolysis in PbCl<sub>2</sub> Crystals</b> S. V. NISTOR, E. GOOVAERTS and D. SCHOEMAKER	<b>157/[1067]</b>
<b>NaF Films: Growth Properties and Electron Beam Induced Defects</b> M. CREMONA, A. P. SOTERO, R. A. NUNES, M. H. DO PINHO MAURICIO, L. C. SCAVARDA DO CARMO, R. M. MONTEREALI, S. MARTELLI, and F. SOMMA	<b>163/[1073]</b>
<b>Defects in Ion Implanted and Electron Irradiated MgO and Al<sub>2</sub>O<sub>3</sub></b> R. S. AVERBACK, P. EHRHART, A. I. POPOV and A. v. SAMBEEK	<b>169/[1079]</b>
<b>EPR-Study of Electron-Radiation Induced Ca Colloids in CaF<sub>2</sub> Crystals</b> F. BEUNEU, C. FLOREA and P. VAJDA	<b>175/[1085]</b>
<b>Defect Mechanisms in the Thermoluminescence of LiF:Mg, Cu, P</b> S. MAHAJNA, D. YOSSIAN and Y. S. HOROWITZ	<b>181/[1091]</b>
<b>Photoinduced Phenomena in RbAg<sub>4</sub>I<sub>3</sub> Superionic Crystals</b> S. BREDIKHIN, N. KOVALEVA, T. HATTORI and M. ISHIGAME	<b>187/[1097]</b>
<b>EPR vs. Temperature of Fe<sup>3+</sup> Ions Produced by Radiolysis in CdCl<sub>2</sub>:Fe Crystals</b> S. V. NISTOR, E. GOOVAERTS and D. SCHOEMAKER	<b>191/[1101]</b>
<b>Radiation Effects in Pure and Re Doped KMgF<sub>3</sub></b> N. V. SHIRAN, V. K. KOMAR, V. V. SHLYAKHTUROV, A. V. GEKTI, N. P. IVANOV, V. A. KORNIENKO, I. M. KRASOVITSKAYA and Y. A. NESTERENKO	<b>197/[1107]</b>
<b>Simulation of the Build-Up Radiation Damage in NaCl: Initial Stages of Colloid Formation</b> W. J. SOPPE and J. PRIJ	<b>201/[1111]</b>
<b>Theory of Diffusion-Controlled Defect Aggregation under Irradiation: A Comparative Study of Three Basic Approaches</b> E. A. KOTOMIN, V. N. KUZOVKOV, M. ZAISER and W. SOPPE	<b>209/[1119]</b>
<b>Thermoluminescence of Pure and Eu-Doped NaZnF<sub>3</sub></b> C. FURETTA, M. GRAZIANI, C. SANIPOLI, and A. SCACCO	<b>217/[1127]</b>
<b>Peculiarities of a Radiation Defect Creation in Beryllium Oxide Crystals</b> S. V. KUDYAKOV, I. N. ANTSGIN, S. V. GORBUNOV and A. V. KRIZHALOV	<b>221/[1131]</b>
<b>Interpretation of the Extralarge Inhomogeneous Broadening in the Optical Spectra of Heavily Neutron-Irradiated IaB-Type Diamond</b> A. OSVET and I. SILDOS	<b>227/[1137]</b>
<b>Point Defects and Short-Wavelength Luminescence of LiB<sub>3</sub>O<sub>5</sub> Single Crystals</b> I. N. OGORODNIKOV, A. Yu. KUZNETSOV, A. V. KRIZHALOV and V. A. MASLOV	<b>233/[1143]</b>
<b>Some Specific Features of TL-Output Storage in MgO:Fe Crystals</b> V. S. KORTOV and A. V. MONAKHOV	<b>239/[1149]</b>
<b>Optical Damage of W-Doped KTiOPO<sub>4</sub> Non Linear Single Crystals</b> M. J. MARTÍN, C. ZALDO, F. DÍAZ, R. SOLÉ, D. BRAVO and F. J. LÓPEZ	<b>243/[1153]</b>
<b>Low Temperature Photostimulated Luminescence of KBr - In Crystal After UV Irradiation</b> L. E. TRINKLER and M. F. TRINKLER	<b>249/[1159]</b>
<b>Peculiarities of Interstitials in a Simple Cubic CsCl Crystal</b> A. LUSHCHIK, K. IBRAGIMOV, I. KUDRJAVTSEVA and L. PUNG	<b>253/[1163]</b>
<b>Radiation Processes on the Surface of Irradiated Corundum Monocrystals</b> V. V. HARUTUNYAN, A. K. BABAYAN, V. A. GEVORKYAN and V. N. MAKHOV	<b>257/[1167]</b>

<b>Influence of the Crystallographic Orientation of the Surface on Damage and Chemical Effects in Ion-Implanted MgO</b>	<b>261/[1171]</b>
L. GEA, P. THEVENARD, R. BRENIER, B. CANUT, S. M. M. RAMOS and M. BERANGER	
<b>ESR Study of the Insulator-Conductor Transition in Polyimide Kapton Induced by Swift Heavy Ion Irradiations</b>	<b>267/[1177]</b>
J.-P. SALVETAT, A. BERTHAULT, F. BRISARD, J.-M. COSTANTINI, and J. DAVENAS	
<b>The Exfoliation of LiF Implanted with Alkali Ions at Low Temperature</b>	<b>273/[1183]</b>
J. DAVENAS and B. V. THIEN	
<b>Europium Diffusion in Y- and Z-Cut LiNbO<sub>3</sub> Pre-Irradiated by GeV Uranium Ions</b>	<b>279/[1189]</b>
S. M. M. RAMOS, R. BRENIER, B. CANUT, G. FUCHS, A. MEFTAH, P. MORETTI, S. OULD SALEM, P. THEVENARD, M. TOULEMONDE and M. TREILLEUX	
<b>Optical Study of Defects in RbI and KI Bombarded With High Energy Argon Ions at Temperatures between 20 K and 300 K</b>	<b>283/[1193]</b>
M. A. PARISELLE, E. HOURDEQUIN, J. D. COMINS, E. BALANZAT, S. LEFRANT and B. RAMSTEIN	
<b>Self-Trapped Exciton Luminescence Under Dense Electronic Excitations: Ion-Induced Transient Thermal Effects</b>	<b>287/[1197]</b>
L. PROTIN, E. BALANZAT, S. BOUFFARD, A. CASSIMI, E. DOORYHEE, J.-L. DOULAN, C. DUFOUR, J. P. GRANDIN, J. MARGERIE, E. PAUMIER, and M. TOULEMONDE	
<b>Raman and Optical Absorption Studies of the Annealing of <math>\gamma</math>-Irradiated KI and KI (Sr)</b>	<b>295/[1205]</b>
J. D. COMINS, A. M. T. ALLEN, E. RZEPKA and S. LEFRANT	
<b>A Comparative Study of Glow Curves in Photo-Transferred and Pre-Dose Sensitized Thermoluminescence (PTTL and TL) in LiF:Mg, Ti</b>	<b>301/[1211]</b>
T. M. PETERS, E. M. YOSHIMURA, C. M. SUNTA, E. OKUNO, N. K. UMISED0 and M. P. DIAZ	
<b>Latent Track Formation in LiNbO<sub>3</sub> Single Crystals Irradiated by GeV Uranium Ions</b>	<b>307/[1217]</b>
B. CANUT, R. BRENIER, A. MEFTAH, P. MORETTI, S. OULD SALEM, M. PITAVAL, S. M. M. RAMOS, P. THEVENARD and M. TOULEMONDE	
<b>Modification of Magnesium Phosphate Glass by H<sup>+</sup> Irradiation: Formation of OH-Bond and Phosphorus-Colloid</b>	<b>311/[1221]</b>
N. MATSUNAMI, K. KAWAMURA and H. HOSONO	

## CONTENTS - PART IV

### Note on Pagination, Author Index and Table of Contents

*The Proceedings of the EURODIM 94 Conference is being published in four volumes of Radiation Effects and Defects in Solids (Volume 134, Part I, Volume 135, Part II, Volume 136, Part III and Volume 137, Part IV). To facilitate indexing and referring to this Proceedings, the page numbers of Volume 135, Volume 136 and Volume 137 will run continuously from the end of Volume 134. An author index will appear at the end of Volume 137. A complete table of contents will appear in Volume 134, Part I and Volume 137, Part IV.*

### 10 Surface Defects

- Topography and Dynamics of Surface Defects on Ionic Crystals** 1/[1227]  
R. T. WILLIAMS, R. MARK WILSON, and A. L. SHLUGER
- Influence of the Mismatch Dislocations on the Elastic Properties of the Insulating Fluoride Films Deposited on Si(111)** 11/[1237]  
V. V. ALEKSANDROV and N. L. YAKOVLEV
- Analysis of the Propagation of Strongly Attenuated Leaky Acoustic Modes as Method of the Detection of the Low Scale Interface Defects in the Layered Structures** 15/[1241]  
V. V. ALEKSANDROV, V. R. VELASCO, and N. L. YAKOVLEV
- Bulk and Surface Metallization of  $\text{CaF}_2$  under Low Energy Electron Irradiation** 19/[1245]  
R. BENNEWITZ, C. GÜNTHER, M. REICHLING, E. MATTHIAS, R. M. WILSON and R. T. WILLIAMS
- Surface Modification of Polymers Induced by Ion Implantation** 25/[1251]  
RENÉ ENDRŠT, VÁCLAV ŠVORČÍK, VLADIMÍR RYBKA and VLADIMÍR HNATOWICZ
- The Behaviour of Pure and  $\text{K}^+$  Implanted LiF Surfaces under Electron Bombardment** 29/[1255]  
C. JARDIN, P. DURUPT and J. DAVENAS
- Investigation of ZnSe Films Grown on GGG, YIG** 35/[1261]  
P. KOSOBOUTSKI and P. VODOLAZSKI
- Investigation of the Thermochemical Reaction in ZnSe Crystals from Action by Infrared Light** 39/[1265]  
P. KOSOBOUTSKI, R. KIJAK and R. BIBIKOV

### 11 Nanomaterials

- Effects of Resonance on Low-Frequency Raman Scattering from Semiconductor Nanocrystals** 45/[1271]  
L. SAVIOT, B. CHAMPAGNON, E. DUVAL and A. I. EKIMOV
- Nanocrystalline Copper Doped Zinc Oxide Gas Sensors** 51/[1277]  
A. V. CHADWICK, A. HARSCH, N. V. RUSSELL, K. F. TSE, A. R. WHITHAM and A. WILSON
- Clustering in  $\text{NaCl:Pb}$**  57/[1283]  
K. POLAK, M. NIKL and K. NITSCH
- Optical Study of the Phase Separation in Alkali Halide Solid Solutions** 63/[1289]  
M. INABA and S. HASHIMOTO
- Metallic Na Formation in NaCl Crystals by Electron and VUV Photon Irradiation** 69/[1295]  
S. OWAKI, S. KOYAMA, M. TAKAHASHI, T. OKADA, R. SUZUKI and M. KAMADA
- Nano-Structures and Quantum Size Effects in Heavily Irradiated NaCl** 73/[1299]  
D. VAINSHTEIN, H. P. DEN HARTOG, H. C. DATEMA, J. SEINEN and H. W. DEN HARTOG
- Stacking Fault Excitons in AgBr Microcrystals with Twin Planes** 77/[1303]  
A. MARCHETTI

<b>Optical Properties of Metallic Nanoparticles Synthesized by Implantation of Alkali Ions in LiF</b> J. DAVENAS and C. JARDIN	81/[1307]
<b>Nanometric Metallic Particles in Insulating Materials: Bi-SiO<sub>x</sub></b> C. MARTET, J. F. ROUX, M. TREILLEUX, B. CABAUD, J. C. PLENET and G. FUCHS	89/[1315]
<b>Electronic Structure and Optical Spectra of Overstoichiometric Cadmium Atoms in CdI<sub>2</sub> Crystals</b> I. BOLESTA, I. KITTYK, V. KOVALISKO and R. TURCHAK	95/[1321]
<b>Enhanced Raman Scattering of Phonons in CaF<sub>2</sub> and MgO Containing Ca and Li Colloids</b> P. B. OLLETE, M. L. SANJUÁN and V. M. ORERA	99/[1325]
<b>TEM Study of Fe-Co Oxides System of Ammonia Catalyst</b> V. S. TEODORESCU and L. C. NISTOR	105/[1331]
<b>Optical Non Linear Measurements in CdS Doped Silica Films</b> A. OTHMANI, J. C. PLENET, E. BERNSTEIN, F. PAILLE, C. BOVIER, J. DUMAS, P. RIBLET, J. B. GRÜN, P. GILLIOT and R. LEVY	109/[1335]
<b>12 Carbon and Polymers</b>	
<b>EPR Study of the Hole Paramagnetic Center in C<sub>70</sub> Fullerite</b> L. S. SOCHAVA, V. S. VIKHNIN, YU. S. GRUSHKO, S. N. KOLESNIK and M. V. KORNENKO	115/[1341]
<b>Carbon Nanostructures in Implanted Nonconjugated Polymers</b> O. YU. POSUDIEVSKY	119/[1345]
<b>Compensation Effects in C<sub>60</sub> Doped by Ion Implantation</b> P. TROUILLAS, B. RATIER and A. MOLITON	123/[1349]
<b>High Temperature Behaviour of Thermoelectric Power of Implanted Polymer Films</b> C. MOREAU, B. RATIER, A. MOLITON and B. FRANÇOIS	129/[1355]
<b>Optical Properties Induced by the Formation of Carbon Nanoparticles in Irradiated Polyimide</b> J. DAVENAS and J. P. SALVETAT	135/[1361]
<b>13 Disordered Systems</b>	
<b>Low-Frequency Excitations in Fluoride Glass Studied by Nuclear Spin Relaxation and Electrical Conductivity</b> J. DIECKHÖFER, O. KANERT, R. KÜCHLER and H. JAIN	141/[1367]
<b>Conductivity and Structure Relations in Polycrystalline <math>\alpha/\beta</math>-Lead Fluoride Doped with Scandium Fluoride</b> A. MEYER, J. TEN EICKEN, O. V. GLUMOV, W. GUNSSER, M. KARUS, and I. V. MURIN	147/[1373]
<b>Photovoltaic Effect and Electronic Transitions in RbAg<sub>4</sub>I<sub>5</sub></b> A. BORIS, T. HATTORI and M. ISHIGAME	153/[1379]
<b>EXAFS Studies of Disorder in CdF<sub>2</sub>-PbF<sub>2</sub> Systems</b> T. T. NETSHISAULU, C. R. A. CATLOW, A. V. CHADWICK, G. N. GREAVES and P. E. NGOEPE	159/[1385]
<b>Amorphous Sol-Gel Derived Lead Titanate Thin Films used as Passive Waveguides</b> C. URLACHER, A. BAHTAT, J. MUGNIER, C. BOVIER and J. SERUGHETTI	165/[1391]
<b>Ultrasonic Attenuation Measurements in Neutron-Irradiated Quartz: The Influence of Heat Treatment for a Dose of <math>4.7 \times 10^{19}</math> N/CM<sup>2</sup></b> V. KEPPENS and C. LAERMANS	169/[1395]



<b>Study of the <math>K_{4.2}Ti_{1.2}(PO_4)_3</math> Glass by Dielectric and Raman Spectroscopy</b> C. Z. TAN, O. KANERT and R. KÜCHLER	<b>173/[1399]</b>
<b>Laser Irradiation Induced Structural Relaxation in the Densified <math>SiO_2</math> Glass and <math>SiO_2</math> Thin Film</b> C. Z. TAN, Z. L. WU, and J. ARNDT	<b>179/[1405]</b>
<b>Optical Band-Gap and Activation Energy of Thin Films from the Se-Ag-I and Te-Ag-I Systems</b> T. PETKOVA and M. MITKOVA	<b>183/[1409]</b>
<b>Effect of Ionic Exchange upon the Behaviour of Soda Lime Silicate Glass</b> R. CAPELLETTI, P. GRAU, P. VAN HOI, and M. SUSZYNSKA	<b>187/[1413]</b>
<b>Polarization and Depolarization in Silica by Migration of Electric Charge Carriers</b> M. BARLAND, E. DUVAL, T. ACHIBAT and A. BOUKENTER	<b>191/[1417]</b>
<b>The Polar Transition Of Li-Doped and Nb-Doped <math>KTaO_3</math>: Comparative Analysis from Hard-Phonon Raman Spectra</b> P. CALVI, P. CAMAGNI, E. GIULOTTO and L. ROLLANDI	<b>199/[1425]</b>
<b>14 Dislocation, Plasticity</b>	
<b>Plastic Deformation and Dislocations in Ceramic Materials</b> J. RABIER	<b>205/[1431]</b>
<b>Plastic Deformation of <math>CaF_2</math> Single Crystals</b> A. MUÑOZ, A. DOMÍNGUEZ RODRÍGUEZ and J. CASTAING	<b>213/[1439]</b>
<b>A Material Science Approach for the Evaluation of the Rheological State into the Earth's Lower Mantle</b> F. VALLIANATOS, K. EFTAXIAS and A. VASSILIKOU-DOVA	<b>217/[1443]</b>
<b>Diffusion-Controlled Transitory Creep in Binary Oxides</b> M. JIMÉNEZ-MELENDO, A. DOMÍNGUEZ-RODRÍGUEZ and J. CASTAING	<b>223/[1449]</b>
<b>Creep Behaviour of 21 Mole% <math>Y_2O_3</math>-Fully Stabilized Zirconia Single Crystals</b> D. GÓMEZ-GARCÍA, J. MARTÍNEZ-FERNÁNDEZ, A. DOMÍNGUEZ-RODRÍGUEZ, P. EVENO and J. CASTAING	<b>227/[1453]</b>
<b>Microscopical Studies of Dislocations and Plasticity in Deformed Ionic Crystals</b> M. V. NAZAROV and T. A. NAZAROVA	<b>231/[1457]</b>
<b>15 Transport Phenomena</b>	
<b>Atomic Transport of Oxygen in Nonstoichiometric Oxides</b> J. L. ROUTBORT and G. W. TOMLINS	<b>233/[1459]</b>
<b>Defect Interactions, Statistical Thermodynamic and Electronic Transport in Ionic Nonstoichiometric Oxides</b> R. TETOT and G. BOUREAU	<b>239/[1465]</b>
<b>Defect Parameters for Rubidium Chloride from Ionic Conductivity Measurements</b> PATRICK W. M. JACOBS and MARCIA L. VERNON	<b>247/[1473]</b>
<b>Transport Processes in Fluoride Crystals under High Pressure</b> I. V. MURIN, O. V. GLUMOV, W. GUNSSER and M. KARUS	<b>251/[1477]</b>
<b>Transport Phenomena in Alkali Halide Mixed Crystals</b> F. BÉNIÈRE, V. H. BABU, M. BÉNIÈRE and K. V. REDDY	<b>255/[1481]</b>
<b>Local Structure and Oxygen Transport in Transition Metal Doped YSZ</b> N. NICOLOSO, J. MAIER, F. K. KOSCHNICK and J. M. SPAETH	<b>259/[1485]</b>

<b>Anomalous Point Defect Formation and Phase Transitions: The Significance of a Cube Root Law</b> N. HAINOVSKY and J. MAIER	267/[1493]
<b>Intrinsic Electron Traps and Electronic Conduction in YSZ</b> R. I. MERINO and V. M. ORERA	273/[1499]
<b>High Temperature Annealing Effects on the A.C. Conductivity of Swept Synthetic Quartz</b> P. CAMPONE, M. MAGLIOCCO, G. SPINOLO and A. VEDDA	277/[1503]
<b>Diffusion of <math>^{18}\text{O}</math> in <math>\text{Cr}_2\text{O}_3</math>: Bulk and Scales and Relation with Oxidation Kinetics</b> S. C. TSAI, A. M. HUNTZ, C. DOLIN and C. MONTY	285/[1511]
<b>Influence of Yttrium on Transport Properties of <math>\alpha</math> Alumina Scales Developed on Yttrium Implanted <math>\beta</math> NiAl</b> J. BALMAIN, M. K. LOUDJANI and A. M. HUNTZ	291/[1517]
<b>Effective Diffusion Coefficient and Diffusion-Controlled Reactions in Insulating Solids with Defects</b> YU. H. KALNIN and P. ZAPOL	295/[1521]
<b>Fast Diffusion of the Off-Center Impurities <math>\text{Cu}^+</math> and <math>\text{Li}^+</math> in the KCl Lattice</b> F. DESPA and V. TOPA	299/[1525]
<b>Internal Reduction of Polycrystalline Cr-Doped Alumina</b> M. BACKHAUS-RICOULT and A. PEYROT	305/[1531]
<b>The Second-Order Elastic Constants of AgBr from 20°C to 400°C</b> L. S. CAIN and GANG HU	309/[1535]
<b>Schottky Barriers in Superionic Crystals</b> S. BREDIKHIN, T. HATTORI and M. ISHIGAME	313/[1539]
<b>Electrical Conductivity of a <math>\alpha</math>-<math>\text{LiIO}_3\text{:Cr}^{3+}</math> Single Crystal</b> R. L. MOREIRA, P. BOURSON, C. ROSSO, C. GALEZ, A. RIGHI and J. M. CRETTEZ	319/[1545]
<b>A Renewed Approach of Hopping Conduction in Amorphous Materials</b> R. ONGARO and M. GAROUM	323/[1549]
<b>16 Superconductivity</b>	
<b>Transport Properties and Defect Chemistry of High-Tc-Superconductors</b> M. QUILITZ and J. MAIER	327/[1553]
<b>Laser-Heating and Phonon Modes in <math>\text{YBa}_2\text{Cu}_3\text{O}_x</math></b> L. GASPAROV	331/[1557]
<b>The <math>\text{YBa}_2\text{Cu}_3\text{O}_x</math> Phase Diagram</b> C. PICARD, P. GERDANIAN, A. H. MOUDDEN and M. G. BLANCHIN	337/[1563]
<b>Density of Electron States near Surfaces of Layered Copper Oxides</b> S. A. PROSANDEYEV and I. M. TENNENBOUM	343/[1569]
<b>Increasing of <math>T_c</math> in the New HTSC <math>\text{HgBa}_2\text{CuO}_{4+\delta}</math> PROMOTED BY DEFECTS</b> YU. N. MYASOEDOV, R. V. LUTCIV, I. V. KITIK, V. N. DAVYDOV, and YA. V. BOYKO	347/[1573]
<b>Large Local Distortions Introduced by Defects in <math>\text{YBa}_2\text{Cu}_3\text{O}_7</math> Superconductors: An X-Ray-Absorption Study</b> FRANK BRIDGES, G. G. LI, C. H. BOOTH, J. B. BOYCE and T. CLAESON	351/[1577]
<b>Author Index</b>	i

---

## **10 SURFACE DEFECTS**

## TOPOGRAPHY AND DYNAMICS OF SURFACE DEFECTS ON IONIC CRYSTALS

R. T. WILLIAMS, R. MARK WILSON, AND A. L. SHLUGER\*

*Wake Forest University, Department of Physics, Winston-Salem, NC 27109 USA; \*The Royal Institution of Great Britain, 21 Albemarle Street, London W1X 4BS, UK*

Scanning Force Microscopy (SFM) offers new possibilities for surface studies on insulators, but still needs work on interpretation of the images and on the limits of what may or may not be measured. Experimental and theoretical investigations of tip-sample interactions and interpretation of images at the atomic length scale are discussed. Observations have been made on pure crystals, samples doped with charged defects, and mixed crystal alloys. The SFM has proved useful in investigations of radiation damage on insulators at mesoscopic scales, using both *ex situ* and *in situ* irradiation.

Dynamical processes involving surface defects are an increasingly active area of investigation. Topics include energy transfer from self-trapped excitons to adsorbates or surface constituents and desorption mediated by surface defects.

*Key words:* surface defects, ionic crystals, scanning force microscopy, desorption.

### 1 INTRODUCTION

One of the most fundamental attributes of any solid phase is that it interacts with the outside world through a relatively fixed boundary, the surface. In many cases, the chemical and electronic properties of the surface are strongly influenced by the exceptional sites, i.e. surface defects. This axiom of surface science is easy to illustrate with examples drawn from the vast array of works on surface spectroscopy of semiconductors and metals, including oxidized or other reacted thin layers on their surfaces. However, because so many of the surface-sensitive spectroscopies necessarily involve charged particles coming in or going out, the surfaces of bulk insulators have been more difficult to study in the same detail. Both charging and ionizing radiation damage are more severe in insulators. It should not be surprising that the study of surface defects on some insulators is still a young field.

Recent investigations of surface defects on  $\text{MgO}$ <sup>1</sup> and transition metal oxides,<sup>2</sup> as well as earlier works concentrating on the powder phase in the 1970s, have been motivated partly by their utility as catalysts, and partly by interest in epitaxial growth mechanisms. Interface states on  $\text{SiO}_2$  are of interest for electronic applications. Experimental and theoretical study of nanoscale clusters can address an insulator on a scale where the surface comprises a substantial fraction of all atomic sites,<sup>3</sup> and relates to technological interest in nanophase materials.

The topics of this review are the recent advances and possibilities attendant to scanning force microscopy (SFM), and dynamical processes involving surface defects on insulators.

### 2 SCANNING FORCE MICROSCOPY—ATOMIC SCALE PHENOMENA

Scanning force microscopy (SFM) yields images in which excursions of a cantilever in the near force field of a raster-scanned surface record mesoscopic topographies with unprecedented vertical resolution, and can reproduce a regular lattice with the symmetry and atomic periodicity characteristic of the sample's crystal structure.<sup>4,5,6</sup> Because the SFM

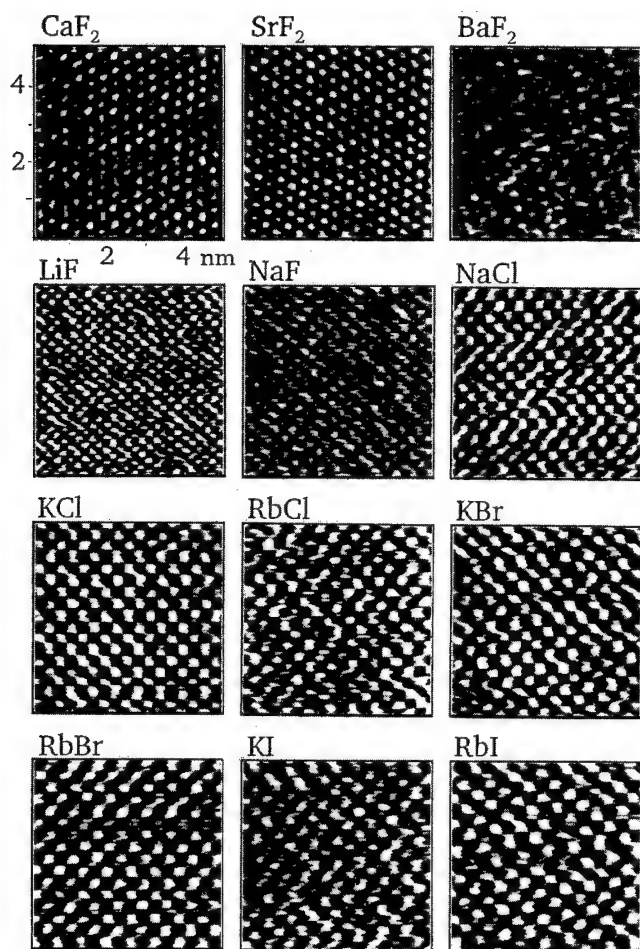


FIGURE 1 Constant-deflection SFM images of 9 alkali halides and 3 alkaline earth fluorides on a  $5 \text{ nm} \times 5 \text{ nm}$  scale. Samples were cleaved and imaged in air at  $\sim 45\%$  relative humidity. (from Ref. 6).

tip-sample contact involves multiple ions or atoms in strong and potentially disruptive interaction, detailed analysis of the tip-sample system is needed as one approaches atomic resolution.

### 2.1 Atomic Periodicity and Contrast

SFM images of  $\text{CaF}_2$ ,  $\text{SrF}_2$ ,  $\text{BaF}_2$ ,  $\text{LiF}$ ,  $\text{NaF}$ ,  $\text{NaCl}$ ,  $\text{KCl}$ ,  $\text{RbCl}$ ,  $\text{KBr}$ ,  $\text{RbBr}$ ,  $\text{KI}$ , and  $\text{RbI}$  are shown in Figure 1. Ten of these twelve images (excepting  $\text{NaF}$  and  $\text{CaF}_2$ ) were obtained with the same cantilever, and all were acquired on cleaved surfaces in air at about 45% relative humidity.<sup>6</sup> Two-dimensional Fourier transforms of the data yield average periodicities which are plotted against the bulk lattice constant from x-ray diffraction in Figure 2. Lattice constants ranging from 2.46 Å (graphite) to 7.34 Å ( $\text{RbI}$ ) in 14 different materials differing substantially in hardness, structure, solubility, and likelihood of yielding

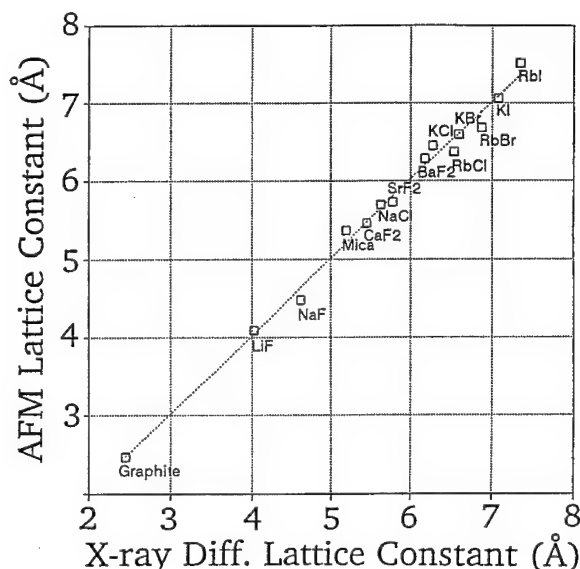


FIGURE 2 Lattice constant measured by SFM versus bulk lattice constant for 14 different crystals.

transportable flakes were reliably reproduced by the SFM. The corrugation is evidently derived from the sample's repeating unit cell without requiring registry of a specific tip and a specific sample. Whether it is a *local* image has to be considered on a case-by-case basis.

On a microscopic scale, changing crystal orientation relative to the cantilever changes the molecular-level interaction between the tip and the structure of the sample. On a macroscopic scale, it determines the alignment of the long axis of the cantilever with particular crystallographic rows. Lateral forces (friction) in the direction of the long axis produce a bowing of the cantilever and consequent optical beam deflection indistinguishable from a height excursion. Friction forces associated with sample translation perpendicular to the long axis of the cantilever produce torsional deflection of the cantilever, which is not detected in the SFM used for Figure 3, but can be detected and is now widely used for 'lateral force microscopy'. Images of LiF for sample orientations rotated from  $-15^\circ$  to  $90^\circ$  (clockwise) in  $15^\circ$  increments relative to the cantilever are summarized in Figure 3. The fast scan direction remained parallel to the cantilever long axis (displayed as horizontal). The quality of the image is best when a  $\langle 100 \rangle$  axis is parallel to the long cantilever axis ( $0^\circ$  or  $90^\circ$ ) so that cations and anions are alternately scanned. When the crystal is rotated  $45^\circ$  to place a  $\langle 110 \rangle$  row parallel to the cantilever axis, the spots appear to merge into rows running along  $\langle 1-10 \rangle$ , perpendicular to the cantilever axis. Because friction along  $\langle 1-10 \rangle$  produces an undetected torsional bend in this case, the loss of contrast confirms that lateral forces are an important contributor to the atomic-scale image contrast.

## 2.2 Theory

Shluger *et al* have performed calculations for molecular cluster models representing the end of the tip and its interaction with the (100) surfaces of NaCl, LiF, and CaO, with and

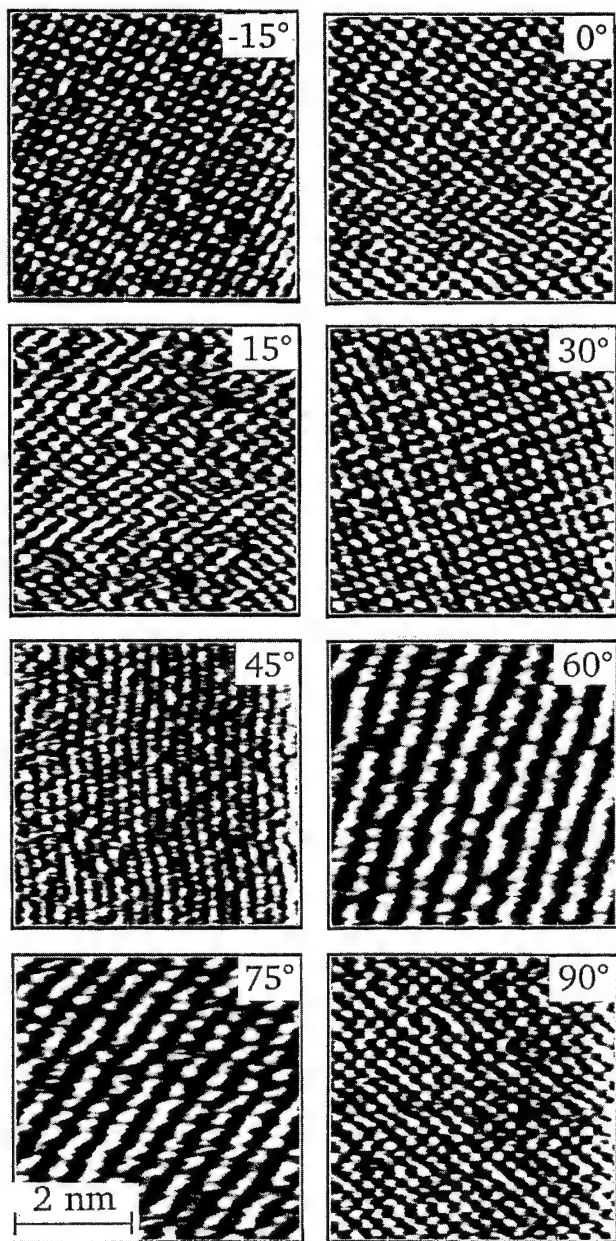


FIGURE 3 Images of LiF on a  $5\text{ nm} \times 5\text{ nm}$  scale are shown as a function of clockwise rotation of the sample under the tip. The cantilever long axis and the rapid raster scan are horizontal relative to all frames. The angle  $0^\circ$  corresponds to alignment of the  $\langle 100 \rangle$  crystal axis with the cantilever axis.

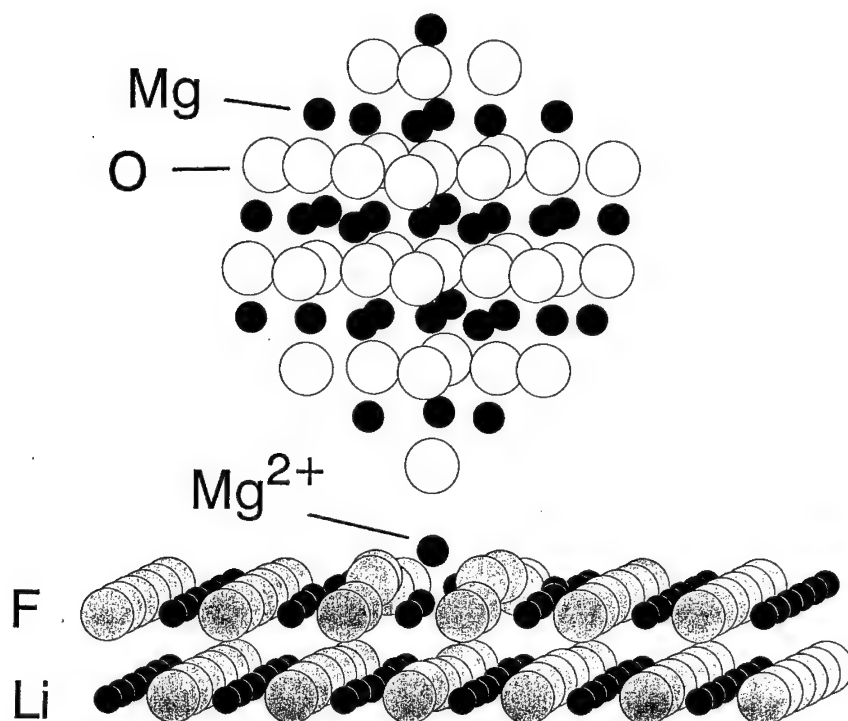


FIGURE 4 MgO tip above a  $\text{Mg}^{2+}$  ion substituting for  $\text{Li}^+$  on the (100) surface of LiF. (from Ref. 7).

without defects.<sup>6,7</sup> The model tips included a  $\text{Si}_4\text{O}_{10}\text{H}_{10}$  cluster with protruding SiOH group<sup>6</sup> and a  $\text{Mg}_{32}\text{O}_{32}$  cube with its corner pointing toward the sample.<sup>7</sup> The latter case is illustrated in Figure 4 above the surface of LiF containing a  $\text{Mg}^{2+}$  impurity ion. The new surface code MARVIN<sup>8</sup> was used to perform the atomistic simulations.<sup>7</sup> Both tip and sample were divided into regions 1, where ion positions are allowed to relax to minimize energy during the calculation, and regions 2, where the ions are frozen. Region 1 of the sample contained two to four planes of 72 ions, while region 2 contained 5 planes of frozen ions. Region 1 of the tip contained the 44 ions nearest the sample. The minimized energy of the total system was calculated as a function of tip-sample distance, where at zero distance the most protruding ion of the unrelaxed tip would cross the surface plane of the perfect sample. The simulation was repeated for lines of approach above various sites on the sample, such as anion site, cation site, vacancy, midpoint between ions, or impurity ion. Force curves for an  $\text{Mg}_{32}\text{O}_{32}$  tip above several sites on LiF containing a  $\text{Mg}^{2+}$  impurity are shown in Figure 5 for tip-sample distances greater than 4 Å. At closer approach, the tip and the sample interact strongly and become distorted or damaged, as shown in Refs. 6 and 7. If the tip can be maintained about 4 Å above the sample, Figure 5 exhibits a good theoretical basis for atomic resolution of a charged defect.



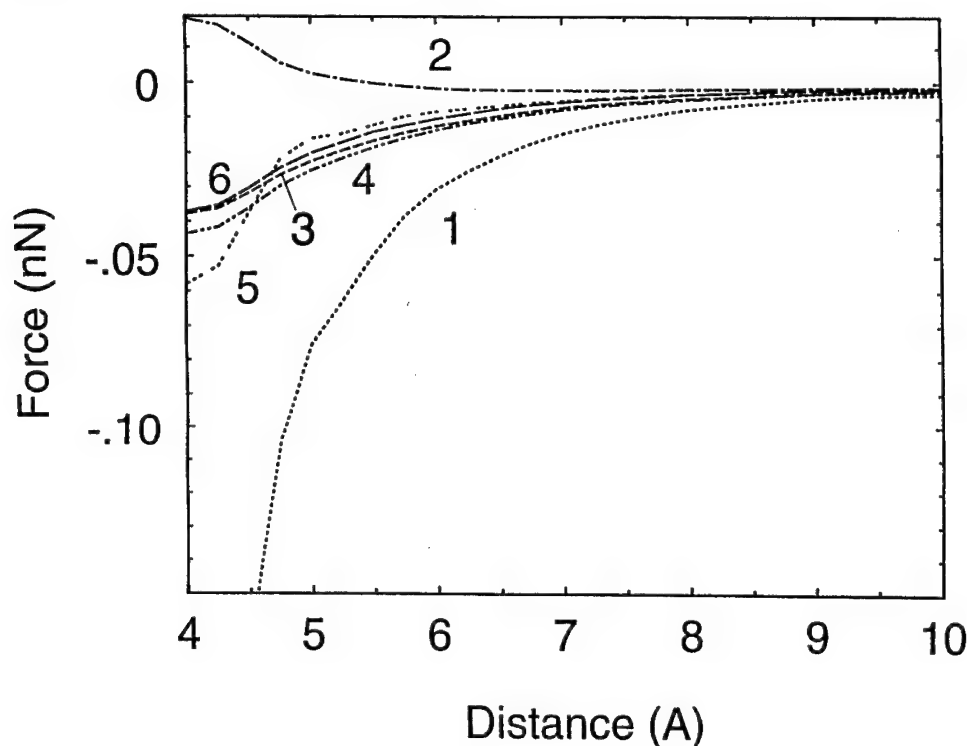


FIGURE 5 Force versus distance curves for a MgO tip above the perfect and defective (100) surfaces of LiF: (1) above the  $\text{Mg}^{2+}$  ion substituting for a  $\text{Li}^+$  ion on the surface; (2) above the cation vacancy; (3) above the regular site position of one of the anions nearest to the vacancy; (4) above the real displaced position of that anion; (5) above the intermediate position between the displaced anion and the cation vacancy; (6) above an anion on the perfect (100) surface. (from Ref. 7).

### 2.3 Defects

Ohnesorge and Binnig have reported the operation of a SFM in a mode where the usual jump to hard contact was avoided while imaging in water.<sup>9</sup> They report nearly point-like lateral resolution of the topmost oxygen sites on calcite, measureable only for tip-sample distance  $4 \text{ \AA} < z < 10 \text{ \AA}$ . Furthermore, they reported resolution of point defects—kinks on monatomic steps. This is an important direction for further work to be compared with theory. The technique is challenging but at least one other group has reported corresponding results.<sup>10</sup> We have observed point defect candidates under close contact of the tip and sample in air, where an interposed water film is believed to play a crucial role of spreading the large tip load over a non-imaged area.<sup>6</sup> Several groups<sup>5,11,12</sup> have now reported atomic periodicity while imaging alkali halides in UHV, usually displaying lateral force. Ohta *et al.*<sup>12</sup> report point defect candidates observed on LiF in UHV.

We have recently recorded SFM images on cleaved surfaces of the doped crystals  $\text{LiF:MgF}_2$  and  $\text{LiF:TiO}_2$  in air with a  $\text{Si}_3\text{N}_4$  tip. In these measurements, however, there is a jump to hard contact, so that the tip-sample distance is considerably smaller than shown in the simulated force curves for  $\text{LiF:MgF}_2$  in Figure 5. Simulations of the  $\text{Si}_4\text{O}_{10}\text{H}_{10}$  tip above NaCl showed cation-anion contrast even at small separations, but also showed the

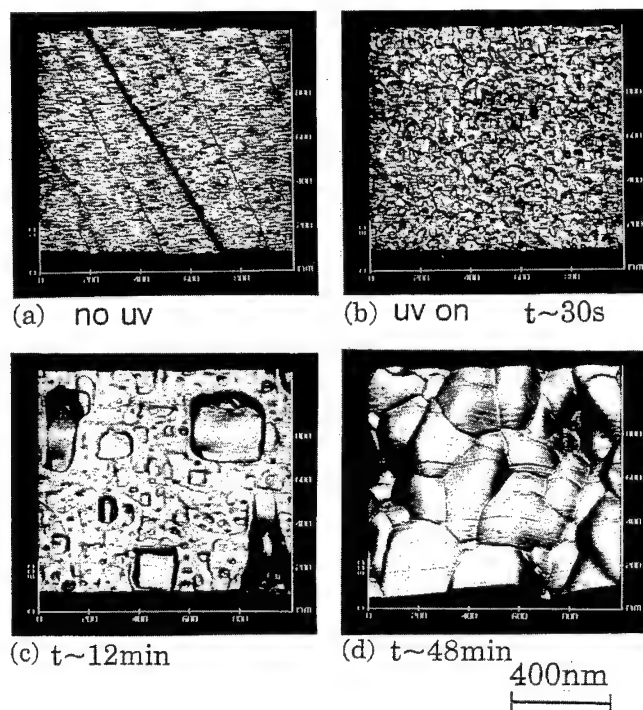


FIGURE 6 Progressive development of radiation damage induced by 5.85-eV light on KI in air at 15% relative humidity, imaged by SFM at  $1000\text{ nm} \times 1000\text{ nm}$  frame size.

existence of multiple constant-force surfaces due to different ions interacting.<sup>6</sup> The experimental images on  $\text{LiF:MgF}_2$  display good atomic periodicity, with occasional defect candidates similar to those reported earlier.<sup>6</sup> We have not yet found persistent defects from scan to scan, which we hoped to find in an impurity-doped sample. One prediction of Ref. 7 suggests a reason: The  $\text{Mg}^{2+}$  ion on LiF is so strongly attracted to the MgO tip, that at close approach it is pulled out of the surface and adheres to the tip.

### 3 MESOSCOPIC DEFECT PHENOMENA IN SFM IMAGES

Scanning electron and transmission electron microscopies have previously been used to study the morphology of near-surface radiation damage on alkali halides, such as erosion, metallization, and subsurface clusters.<sup>13</sup> The SFM offers several advantages over the electron-based techniques, while bringing perhaps a different set of disadvantages. In any case, it affords a fresh perspective and a possibility for ultimate high resolution. We have introduced an ultraviolet laser beam onto the SFM stage to study progressive effects of uv-induced radiation damage on KI and RbI surfaces. Measurements have been made both by alternate disengagement and re-engagement at the same location between exposures, and by *in situ* irradiation during scanning.<sup>14</sup> Figure 6 shows successive stages of radiation damage on KI at 15% humidity.

Electron beam irradiation of  $\text{CaF}_2$  in UHV produces calcium metal islands with a wide variety of morphologies whose dependence on beam energy, current density, exposure time, temperature, and surface treatment has been investigated by SFM.<sup>15</sup> Pits of  $\sim 30$  nm diameter in the  $\text{CaF}_2$  were attributed to the shells of bulk calcium colloids excavated by surface erosion. Ostwald ripening of the surface metal islands has been observed directly by SFM.

#### 4 DYNAMICS OF SURFACE DEFECTS

One of the most evident products of dynamical processes involving surface defects or their creation is the energetic desorption of constituent atoms and ions, or of adsorbates. In the last few years Szymonski *et al* reported startling new data on the direction of emission of energetic halogen atoms from the surfaces of irradiated alkali halides,<sup>16</sup> which prompted new hypotheses and theoretical treatments yielding the adiabatic potential surfaces which govern the dynamics of decomposition of certain near-surface defects and excited states.<sup>16,17</sup>

In parallel work concerning ion emission from the cation sublattice, the critical role of near-surface F centers has been indicated for both halide<sup>18</sup> and oxide<sup>19</sup> crystals. That is, the lattice relaxation following electronic excitation of a near-surface F center can impart significant kinetic energy to a cation located above or possibly adjacent to the defect, causing its desorption. Aspects of this process have been simulated theoretically in recent work.<sup>20</sup> The extensive investigations by the group of Itoh *et al.*<sup>21</sup> on laser-induced Ga desorption from GaP illustrates the contribution of several specific defect sites. The transfer of energy from self-trapped excitons to  $\text{C}_2\text{H}_2$  physisorbed on alkali-halide surfaces has been studied by luminescence spectroscopy.<sup>22</sup>

Two-pulse (sub)picosecond delayed laser-induced desorption and surface damage on insulators introduces time resolution to the study of near-surface defects, whose population is generally too small for conventional absorption and luminescence probes. Two-pulse laser ablation probed by ion emission provides information on processes responsible for near surface laser damage.<sup>23</sup> Spectroscopic experiments based on similar two-pulse techniques for study of near-surface defects and desorption are underway.

#### ACKNOWLEDGMENTS

RTW and RMW acknowledge support by NSF grant DMR-9206745. ALS acknowledges support by SERC grant GR/J31933 and LRC grant 675. We wish to thank D. H. Gay and A. L. Rohl for help with MARVIN calculations, and S. Mysovsky and S. Mironenko for providing  $\text{LiF:MgF}_2$  samples.

#### REFERENCES

1. M. C. Wu, C. M. Truong, K. Coulter, and D. W. Goodman, *J. Vac. Sci. Technol.* **A11**, 2174 (1993); A. L. Shluger, J. Gale, and C. R. A. Catlow, *J. Phys. Chem.* **96** 10389 (1992); and references therein.
2. X. Li and V. E. Henrich, *Phys. Rev.* **B48**, 17486 (1993); G. S. Rohrer, V. E. Henrich, and D. A. Bonnell, *Surf. Sci.* **278**, 146 (1992).
3. E. C. Honea, M. L. Homer, and R. L. Whetten, *Phys. Rev.* **B47**, 7480 (1993); R. Pandey, M. Seel, and A. B. Kunz, *Phys. Rev.* **B41**, 7955 (1990); R. Pandey, X. Yang, J. M. Vail, and J. Zuo, *Solid State Commun.* **81**, 549 (1992).
4. E. Meyer, H. Heinzelmann, D. Brodbeck, G. Overney, R. Overney, L. Howald, H. Hug, T. Jung, H. -R. Hidber, and H. -J. Guntherodt, *J. Vac. Sci. Technol.* **B9**, 1329 (1991).
5. G. Meyer and N. M. Amer, *Appl. Phys. Lett.* **56**, 2100 (1990).

6. A. L. Shluger, R. M. Wilson, and R. T. Williams, *Phys. Rev.* **B49**, 4915 (1994).
7. A. L. Shluger, A. L. Rohl, D. H. Gay, and R. T. Williams, *J. Phys.: Condens. Matter* **6**, 1825 (1994).
8. D. H. Gay and A. L. Rohl, *J. Chem. Soc. Faraday Trans.* (submitted).
9. F. Ohnesorge and G. Binnig, *Science* **260**, 1451 (1993).
10. J. P. Cleveland, M. Radmacher, and P. K. Hansma, NATO *Advanced Study Institute on 'Forces in Scanning Probe Methods'*, Schluchsee, Germany, March 7-18, 1994 (unpublished).
11. F. J. Giessibl and G. Binnig, *Ultramicroscopy* **42-44**, 281 (1992).
12. M. Ohta, T. Konishi, Y. Sugawara, S. Morita, M. Suzuki, and Y. Enomoto, *Jpn. J. Appl. Phys.* **32**, 2980 (1993).
13. D. J. Elliott and P. D. Townsend, *Philos. Mag.* **23**, 249 (1971); L. W. Hobbs, A. E. Hughes, and D. Pooley, *Proc. R. Soc. London* **A332**, 167 (1973).
14. R. M. Wilson, W. E. Pendleton, and R. T. Williams, *Rad. Eff. and Def. in Solids* **128**, 79 (1994); R. M. Wilson, R. K. R. Thoma, W. E. Pendleton, and R. T. Williams, *Nucl. Instrum. and Methods in Phys. Res.* **B91**, 12 (1994).
15. R. Bennewitz, M. Reichling, R. M. Wilson, R. T. Williams, K. Holldack, M. Grunze, and E. Matthias, *Nucl. Instrum. and Methods in Phys. Res.* **B91**, 623 (1994); M. Reichling, R. Bennewitz, R. M. Wilson, R. T. Williams, and E. Matthias, (to be published).
16. M. Szymonski, J. Kolodziej, P. Czuba, P. Piatkowski, A. Poradzisz, N. H. Tolk, and J. Fine, *Phys. Rev. Lett.* **67**, 1906 (1991).
17. V. E. Puchin, A. L. Shluger, and N. Itoh, *Phys. Rev.* **B47**, 10760 (1993); K. S. Song and L. F. Chen, *Rad. Eff. and Def. in Solids*, **128**, 35 (1994).
18. T. Kubo, A. Okano, J. Kanasaki, K. Ishikawa, Y. Nakai, and N. Itoh, *Phys. Rev.* **B49**, 4931 (1994).
19. J. T. Dickinson, S. C. Langford, J. J. Shin, and D. L. Doering (to be published).
20. V. Puchin, A. L. Shluger, Y. Nakai, and N. Itoh, *Phys. Rev.* **B49**, 11364 (1994).
21. J. Kanasaki, A. Okano, K. Ishikawa, Y. Nakai, and N. Itoh, *J. Phys.: Condens. Matter* **5**, 6497 (1993).
22. S. K. Dunn and G. E. Ewing, *Chem. Phys.* **177**, 571 (1993).
23. L. L. Chase, H. W. H. Lee, and R. S. Hughes, *Appl. Phys. Lett.* **57**, 443 (1990); L. L. Chase, *Nucl. Instrum. and Methods in Phys. Res.* **B91**, 597 (1994).

## INFLUENCE OF THE MISMATCH DISLOCATIONS ON THE ELASTIC PROPERTIES OF THE INSULATING FLUORIDE FILMS DEPOSITED ON Si(111)

V. V. ALEKSANDROV and N. L. YAKOVLEV\*

*Chair for Crystallophysics, Physics Department, Moscow State University, 117234 Russia; \*Ioffe Physico-Technical Institute, RAS, St. Petersburg 193144 Russia*

CaF<sub>2</sub> and SrF<sub>2</sub> films grown on Si(111) by molecular beam epitaxy were studied by Brillouin spectroscopy method. The measured velocities of surface acoustic waves are in close agreement with those calculated within simple model of a layered structure. The only discrepancy was a decrease of the velocity in CaF<sub>2</sub> films of about 100 nm thick and was attributed to the different distribution of the defects arising at the early stages of the growth modes at the beginning of CaF<sub>2</sub> and SrF<sub>2</sub> epitaxy on Si(111).

*Key words:* SAW, epitaxial, films, mismatch dislocations.

### 1 INTRODUCTION

Epitaxial films of alkaline earth metal fluorides, such as CaF<sub>2</sub>, SrF<sub>2</sub>, are of great importance both because of the promising applications in microelectronics, being potential candidates for lattice matching of cheap silicon substrates with films of other semi- and superconductors. It is a reason why a thorough study of crystal structure of the film becomes very important.<sup>1,2</sup>

Brillouin scattering could be regarded as a useful additional method that enables one to study hypersonic properties of these structures. Several systematic investigations already conducted reveal Brillouin scattering as a productive tool for the detection of the homogeneity of thin solid films as well as the examination of the structural peculiarities of the interface region.<sup>3</sup>

Here we report on the comparative Brillouin scattering study of films CaF<sub>2</sub>/Si(111) and SrF<sub>2</sub>/Si(111) heterostructures and finding of the correlation between the mismatch dislocations distributions in both films and their elastic properties.

### 2 EXPERIMENTAL

The fluoride films were grown by molecular beam epitaxy in a research chamber. Silicon substrates were chemically etched and thermally cleaned at 1250°C in the chamber. Reflection high energy electron diffraction pattern proves atomically smoothness of their surface. The interface as well as the rest part of the film was at 700°C–770°C during the deposition. During the growth the films were doped with Eu or Sm ions which were impurity luminescent probes sensitive to the homogeneous planar strain, and to random strains produced by dislocations and defects.<sup>4</sup>

In the present work the structures CaF<sub>2</sub>/Si(111) with fluoride thickness  $h = 0 \div 400$  nm and those of SrF<sub>2</sub>/Si(111) with  $h = 0 \div 200$  nm have been investigated.

Brillouin scattering experiments were performed using a five-pass Fabry-Perot piezoscanned interferometer of Burleigh supported by DAS 1 stabilizing and data acquisition system (for the details, see <sup>5</sup>). Starting from the frequency shifts of Brillouin satellites the velocities of corresponding surface modes has been determined. Theoretical

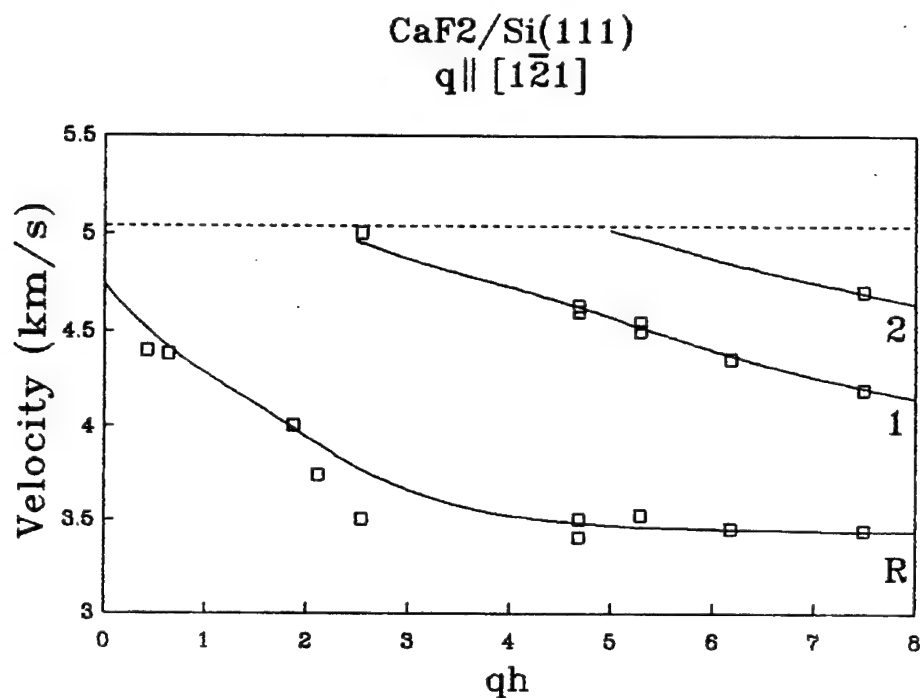


FIGURE 1a Experimental and calculated data for the SAW velocities in CaF<sub>2</sub>/Si(111) structures versus  $qh$  parameter;  $q \parallel [1\bar{2}1]$ . Squares are experimental SAW values. Theoretical dispersion curves were calculated using elastic constants of bulk CaF<sub>2</sub>, Si of .<sup>7</sup>

values of SAW velocities were calculated following simple elastic continuum model of ref.<sup>6</sup> using the material parameters taken from.<sup>7</sup>

Values of SAW velocity versus the normalized thickness,  $qh$ , in CaF<sub>2</sub>/Si(111) system are shown in Figure 1a.  $q$  is the wave vector of SAW parallel to the crystallographic direction<sup>121</sup> in the (111) plane. Continuous lines of Figure 1a are for **R**, **1**, **2**, are calculated velocities of Rayleigh, and higher order Sezawa modes, respectively. Dashed line in the Figure corresponds to the bulk threshold velocity value. One can see from the Figure that except  $qh = 1.8 \div 2.2$  the measured velocity values fit the calculated ones rather well. At  $qh \approx 2$  ( $h \approx 100$  nm) experimental values of the Rayleigh wave are  $5 \div 7\%$  lower than calculated ones.

The results of similar measurements for SrF<sub>2</sub>/Si(111) heterostructure are presented in Figure 1b. In this case, however, experimental values fit rather well the calculated ones in the whole span of  $qh$ .

### 3 DISCUSSION

Reasonable agreement between measured and calculated SAW velocity values is observed for both, CaF<sub>2</sub>/Si(111), SrF<sub>2</sub>/Si(111) heterostructures. This fact approves their high structural quality. Meanwhile noticeable deviation of the measured SAW velocity values from theory has been detected for CaF<sub>2</sub> films about 100 nm thick.

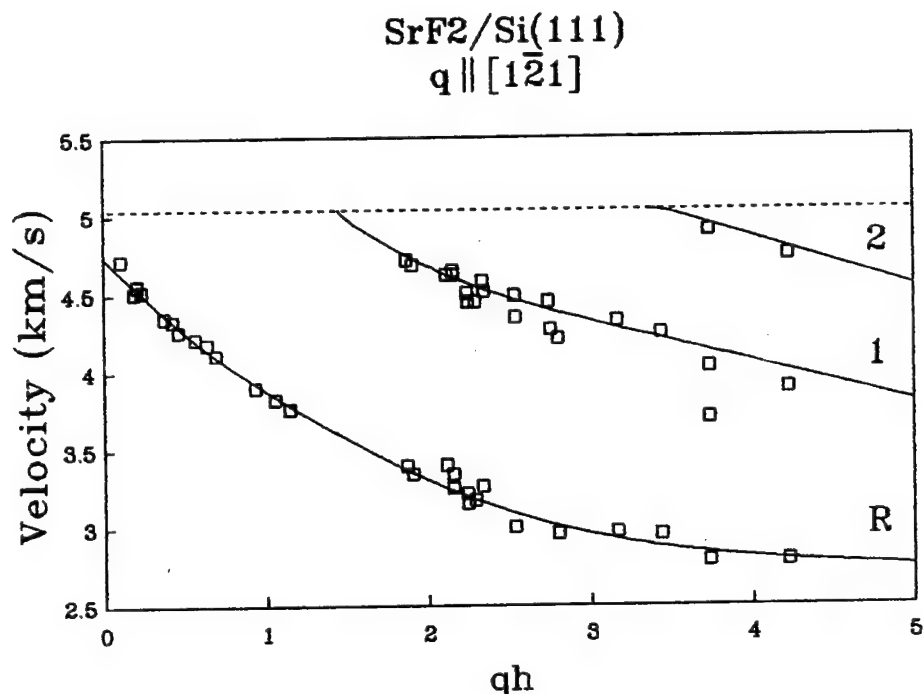


FIGURE 1b Experimental and calculated data for the SAW velocities in SrF<sub>2</sub>/Si(111) structures versus  $qh$  parameter;  $q \parallel [1\bar{2}1]$ .<sup>121</sup> The same conventions as in Figure 1a.

In order to clear up the nature of this phenomenon one should consider different behavior of the dislocations in CaF<sub>2</sub> and SrF<sub>2</sub> films originated during their growth. We believe this difference is connected with the peculiarities of the initial stages of the growth mode which is the coherent one in case of CaF<sub>2</sub>, whereas it is not coherent in case of SrF<sub>2</sub>.

SrF<sub>2</sub>/Si(111) is characterized by 8% lattice mismatch at growth temperature 770°C. High resolution transmission electron microscopy analysis proved that the lattice mismatch of this scale produces the misfit dislocations already at the initial monolayer growth stage.<sup>8</sup> That means that these dislocations are highly concentrated in a thin (< 1 nm) interface layer region. The defective layer is small as compared both, with total film thickness, and with acoustic wave length ( $2\pi/q \approx 300$  nm), its effect upon the elastic properties of the heterostructure becomes negligible.

Situation is changed dramatically in case of CaF<sub>2</sub>/Si(111). Here the lattice mismatch is 1.8% at the growth temperature of 700°C. At the early stages the growth proceeds coherently,<sup>9</sup> the layer lattice accurately following the planar parameter of the substrate. At small film thickness ( $\leq 30$  nm) partial relaxation of mismatch stress takes place. Dislocation concentration is low but it grows with total film thickness increase. In the films thicker than 100 nm defective region remains of approximately constant thickness, and the contribution of this region appears to be relatively less. In CaF<sub>2</sub> films the thickness of  $\approx 100$  nm is somewhat critical because the contribution of the defective layer becomes maximal (approx. 1/3 of the total film thickness) and its influence is found to be significant for the elastic properties of the film in GHz range and for the velocity of SAW.

## REFERENCES

1. T. Minemura, J. Asano, K. Tsutsui, S. Furukawa, *J. Cryst. Growth*, **99**, 287 (1990).
2. N.S. Sokolov, J. C. Alvarez, N. L. Yakovlev, *Appl. Surf. Sci.*, **60/61**, 421 (1992).
3. F. Nizzoli, J. R. Sandercock, in: *Dynamical Properties of Solids* (North-Holland, Amsterdam, 1990) eds. G. K. Horton, and A. A. Maradudin, vol. 6, 1990, p. 281.
4. S. V. Gastev, S. V. Novikov, N. S. Sokolov, N. L. Yakovlev, *Pis'ma Zh. Tech. Fiz.* **13**, 961 (1987) [Sov. Tech. Phys. Lett. **13**, 401 (1987)].
5. V. V. Aleksandrov, Ju. B. Potapova, A. M. Diakonov, N. L. Yakovlev, N. S. Sokolov, *J. Phys.: Condens. Matter* **6**, 1213 (1994).
6. G. W. Farnell, E. L. Adler, in: *Physical Acoustics* (NY, Academic Press, 1972) eds. W. P. Mason, R. N. Thurston, vol. IX, p. 35; E. Sanz-Velasco, O. Hardin-Duparc, V. R. Velasco, *Surf. Sci.*, **126**, 202 (1983).
7. Landolt-Bornstein. *Numerical data and Funct. Relationships in Sci. and Technol. New Series* (Springer, Berlin, 1966, 1983) Group III, V. 1, 17/f.
8. S. Blunier, H. Zogg, C. Maisseu, A. N. Tiwari, R. H. Overney, H. Hoefke, G. Kosterz. *Phys. Rev. Lett.*, **68**, 3599 (1992).
9. N. S. Sokolov, N. L. Yakovlev, J. Almeida, *Sol. St. Commun.* **76**, 883 (1988).



# ANALYSIS OF THE PROPAGATION OF STRONGLY ATTENUATED LEAKY ACOUSTIC MODES AS METHOD OF THE DETECTION OF THE LOW SCALE INTERFACE DEFECTS IN THE LAYERED STRUCTURES

V. V. ALEKSANDROV,\* V. R. VELASCO,\*\* and N. L. YAKOVLEV\*\*\*

*\*Chair for Crystallophysics, Physics Department, Moscow State University, 117234 Russia; \*\*Instituto de Ciencia de Materiales, CSIC, Serrano 123, 28006 Madrid, Spain; \*\*\*Ioffe Physico-Technical Institute, RAS, St. Petersburg 193144 Russia*

Propagation of pseudo surface modes, PSMs, propagating on  $\text{SrF}_2$  epitaxial layers deposited on GaAs(111) was studied by means of Brillouin spectroscopy. A lowering of  $3 \div 77\%$  of the velocity values of the PSMs was detected in case of leaky modes of a relatively strong leakage. The observed deviations of the velocity of the PSMs are connected with the presence of a roughness region of fluoride/GaAs(111) interface extending on several nm.

*Key words:* SAW, epitaxial films, mismatch dislocations.

## 1 INTRODUCTION

Brillouin spectroscopy is known to be a useful additional method for characterization of thin layered systems and their structure description, giving the dynamical data in the GHz frequency range.<sup>1</sup> Namely, in refs.<sup>2,3</sup> it was found that in case of  $\text{CaF}_2/\text{Si}(111)$  MBE grown systems exhibiting good single crystalline structure of the deposited layer, experimentally determined Rayleigh Mode (RM) velocity values agree quite well with those calculated using simple elastic continuum approach of ref.<sup>4</sup> The only velocity deviations were detected with the samples having film thickness  $h = 65 \div 100$  nm were experimental values were  $3 \div 5\%$  lower. The latter was explained by the presence of pre-interface distorted region of approximately 30 nm thick specific for the mentioned total thickness values and originated during initial stages of the growth mode.<sup>5</sup>

However, higher sensitivity of the detection of the film distortions might be achieved if one examines propagation of leaky, or so-called pseudo surface modes (PSMs). Contrary to the normal surface waves, PSMs have only two of three partial waves which are evanescent when leaving the surface, whereas the third partial wave is an increasing one.<sup>6</sup>

Heterostructures of  $\text{SrF}_2/\text{GaAs}(111)$  type are proved to be a more suitable object for the investigation of how the presence of the interface defects would influence the PSM propagation. PSMs have been detected successfully in the substrate material, in a wide range of azimuthal directions close to  $[1\bar{1}0]$ .<sup>7,8</sup> Additionally, the existence of the PSM in a sufficiently wide range of the  $h$  parameter was predicted.<sup>9</sup>

## 2 MATERIALS, INSTRUMENTS, AND METHODS

The  $\text{SrF}_2/\text{GaAs}(111)$  films were deposited on GaAs(111) wafers by molecular epitaxy in a research chamber. The substrate temperature was  $530^\circ \div 600^\circ\text{C}$ , and the fluoride deposition rate was 3 to 5 nm per min. The quality of the lattice, as well as its surface

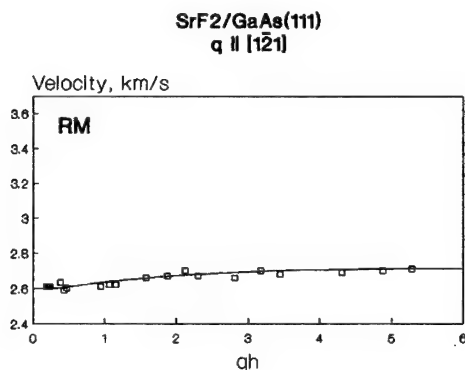


FIGURE 1a Experimental and calculated data for RM velocities versus  $qh$  in  $\text{SrF}_2/\text{GaAs}(111)$ ,  $q \parallel [1\bar{2}1]$ . Solid line is the theoretical dispersion curve, experimental values are shown by Dots.

morphology, was properly monitored during the growth using high energy electron diffraction techniques.<sup>5</sup> Fluoride layer thickness  $h$  was determined using both ellipsometry data. For the present work the structures  $\text{SrF}_2/\text{GaAs}(111)$  with  $h = 10, 20, 50, 150, 230$  nm have been chosen.

Light scattering experiments were conducted by means of five pass piezoscanned Fabry-Perot interferometer of Burleigh in backscattering geometry. For the detailed descriptions of the observation conditions see.<sup>3</sup>

Experimentally determined velocities and PSM attenuation were compared with those calculated using surface Green function matching (SFGM) method.<sup>10</sup>

### 3 EXPERIMENTAL RESULTS AND THE DISCUSSION

The results of surface acoustic wave velocities measured in  $\text{SrF}_2/\text{GaAs}(111)$  heterostructure vs normalized thickness  $qh$  are shown in Figure 1a. Here  $q$  is acoustic wave vector parallel to  $[1\bar{2}1]$  crystallographic direction in (111) plane. Solid curve corresponds to the calculated results of RM velocities ( $V_{\text{RMS}}$ ), and dots are the measured values. Figure 1a shows smooth increase of  $V_{\text{RM}}$  value with  $qh$  variation between the asymptotes describing by  $V_{\text{RM}}$  of the substrate (2.62 km/s,  $qh = 0$ ), and that of the layer material (2.65,  $qh = 6$ ), experimental data being fitted by the theory quite well. This fact approves good structural quality of the films investigated. However,  $3 \div 5\%$  deviations of the measured PSM velocity values ( $V_{\text{PSMS}}$ ) from those predicted were detected for  $q \parallel [1\bar{1}0]$ , in cases when PSM attenuation is strong enough, see Figure 1b,  $qh = 2 \div 4$ . Here dotted curve presents PSM attenuation.

With variation of  $qh$  from zero to six  $V_{\text{PSM}}$  reduces monotonously from 3.2 to 2.67 km/s, and at large  $qh$  values the PSM is found to be a precursor of a new RM of the structure. When the attenuation is far from the resonance,  $qh = 0 \div 1$ ,  $qh \geq 4.5$ , experimental velocity values satisfactorily correlate with the theoretical curve. The results of the measurements of the PSM attenuation are also presented. The measured values (crosses) agree with the dotted curve.

The systematic  $3 \div 5\%$  discrepancy in velocities in the case of PSM modes with a more pronounced attenuation detected is connected with the interface roughness. After removing

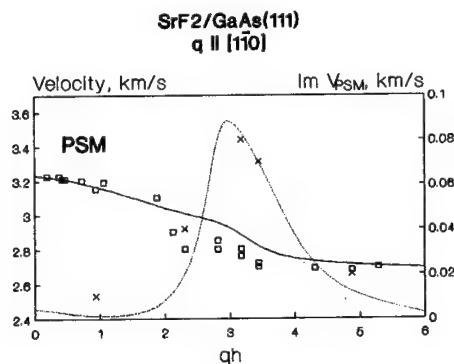


FIGURE 1b Experimental and calculated data for PSM velocity and its attenuation versus  $qh$  in  $\text{SrF}_2/\text{GaAs}(111)$ ,  $q \parallel [110]$ . Same conventions as in Figure 1a. Dotted curve—calculated attenuation values, crosses experimental data (see right ordinate axis).

oxides from GaAs wafer under As flux its (111) surface becomes rough, as it was seen by 3-D spots on reflection high energy diffraction pattern, the dimension of the hillocks being of about several nanometers. During the fluoride film growth the surface becomes flatter giving streaky diffraction patterns, but the buried interface roughness remains. It exists in all the films ( $qh = 0 \div 6$ ). However, it manifests itself in those structures, where the propagating modes are significantly leaky:  $qh = 2 \div 4$  Figure 1b.

This fact shows that the local elastic properties of the fluoride/semiconductor heterostructures may considerably differ from those of the bulk material, and from continuum integrated estimations. Therefore, for the adequate characterization of the elastic properties of even rather fainter epitaxial systems theoretical models including flexible depth depending elasticity variation should be developed. These models could be in the spirit of the planar defect approach,<sup>11</sup> or the effective medium approximation,<sup>12</sup> employed in the case of superlattices.

#### ACKNOWLEDGEMENTS.

The contribution of V.V.A., and V.R.V. was partially supported by NATO under Collaborative Research Grant No. 930164.

#### REFERENCES

1. F. Nizzoli, J. R. Sandercock, in: *Dynamical properties of Solids* (Amsterdam, North-Holland, 1990) eds. H. K. Horton, and A. A. Maradudin, vol. 6, 281.
2. J. M. Karanikas, R. Sooryakumar, J. M. Phillips. *J. Appl. Phys.* **65**, 3407 (1989).
3. V. V. Aleksandrov, Ju. B. Potapova, A. M. Diakonov, N. L. Yakovlev, *Thin Solid Films* **237**, 25 (1993).
4. G. W. Farnell, E. L. Adler, in: *Physical Acoustics* (NY, Academic Press, 1972) eds. W. P. Mason, R. N. Thurston vol. IX, 35.
5. V. V. Afanas ev, S. V. Novikov, N. S. Sokolov, N. L. Yakovlev, *Microelectronics Engineering* **15**, 139 (1991).
6. G. W. Farnell, in: *Physical acoustics*(NY, Academic Press, 1970) eds. W. P. Mason, and R. N. Thurston, vol. VI, 109.

7. G. Carlotti, D. Fioretto, D. Giovannini, F. Nizzoli, G. Socino, L. Verdini, *J. Phys.: Condens. Matter* **4** 257 (1992).
8. V. V. Aleksandrov, T. S. Velichkina, Ju. B. Potapova, I. A. Yakovlev, *Sov. Phys.-JETP* **102** 1019 (1992).
9. V. V. Aleksandrov, C. E. Bottani, G. Caglioti, G. Ghislotti, C. Marinoni, P. Mutti N. L. Yakovlev, and N. S. Sokolov, *J. Phys.: Condens. Matter* **6** 1947 (1994).
10. F. Garcia-Moliner and V. R. Velasco, '*Theory of single and multiple interfaces*,' (World Scientific, Singapore, 1992).
11. V. R. Velasco and F. Garcia-Moliner, *Physica Scripta*, **20** 111 (1979); V. R. Velasco and B. Djafari-Rouhani, *Phys. Rev.* **B26** 1929 (1982).
12. M. Grimsditch and F. Nizzoli, *Phys. Rev.* **B33** 5821 (1986); B. Djafari-Rouhani, J. Sapiel, *Phys. Rev.* **B34** 7114 (1986).

## BULK AND SURFACE METALLIZATION OF $\text{CaF}_2$ UNDER LOW ENERGY ELECTRON IRRADIATION

R. BENNEWITZ, C. GÜNTHER, M. REICHLING, E. MATTHIAS, R. M. WILSON\*  
and R. T. WILLIAMS

*Fachbereich Physik, Freie Universität Berlin, Arnimallee 14, 14195 Berlin, Germany;*

*\*Dept. of Physics, Wake Forest University, Winston-Salem NC 27109, USA\**

Electron irradiation of  $\text{CaF}_2$  with 2 keV electrons causes metallization of the surface and near surface layers by the formation of colloids. Colloids on the surface are significantly larger than those in the bulk indicating a higher mobility of defects on the surface. Optical spectroscopy on extinction bands of bulk colloids reveals Ostwald ripening as the driving force for aggregation, while scanning force microscopy results suggest that similar processes dominate the early stages of surface colloid formation.

**Key words:** electron irradiation,  $\text{CaF}_2$ , defect diffusion, metallization.

The development of metal clusters in the bulk of metal halide crystals after irradiation with high energetic ionizing irradiation has been studied theoretically<sup>1</sup> as well as experimentally<sup>2,3</sup>. Metallization has also been observed at the surface of these materials during electron stimulated desorption experiments.<sup>4,5</sup> The study of these processes is not only of general scientific interest but may also be important for certain applications in semiconductor industry.  $\text{CaF}_2$  is a promising candidate for insulating layers in three dimensional structures of silicon based microcircuits due to the small lattice constant mismatch between these materials. In order to explore the possibilities of creating structures in  $\text{CaF}_2$  films, low energy electron beam processing of  $\text{CaF}_2$  has been studied recently by a process including metallization patterns and subsequent removal of the metal by water.<sup>6</sup> In our contribution, we compare metal aggregation at the surface and metal colloid formation in the bulk of  $\text{CaF}_2$  resulting from 1.5–2.5 keV electron irradiation with regard to the size of aggregates and the aggregation processes.

Electron irradiation and optical absorption experiments have been performed in an UHV chamber with a pressure below  $10^{-9}$  mbar. The specimens were  $\text{CaF}_2$  single crystals of UV grade window material (Karl Korth company) and the (111) surfaces have been studied. For extinction experiments we used monochromatic light from a xenon high pressure lamp modulated with a mechanical chopper in combination with a grating monochromator. Photodiode signals from incident and transmitted intensity were processed by a lock in amplifier. The surfaces were studied ex situ with a commercial Scanning Force Microscope (SFM). Several series of measurements made sure that the surface topography did not change essentially as a function of time after irradiation and during scans with the SFM.

The penetration depth of primary electrons with energies used in these experiments is not well known. However, we assume a relation between the maximum penetration depth  $D$  and the electron energy  $E$  ( $E$  in keV) of the form  $D \text{ (nm)} = 40 E^{1.3}$  i.e. 65 to 130 nm for energies ranging from 1.5 keV to 2.5 keV.<sup>7</sup> The depth of maximum defect creation probability is about 1/5 of the maximum penetration depth.<sup>8</sup> It can be anticipated that the ratio between bulk and surface metallization is determined by both, the depth profile for defect creation as well as diffusion of defects.

To study the influence of the sample temperature *during* irradiation on the metallization process we irradiated one crystal at 150 K and another at 450 K. Spectra of both taken at 450 K are presented in Figure 1. The pronounced extinction band for irradiation at 150 K

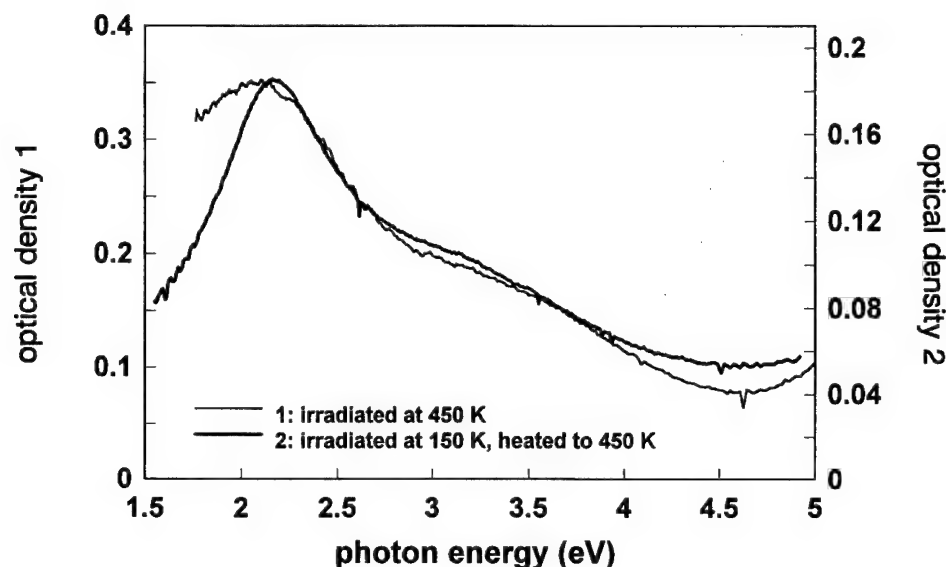


FIGURE 1 Extinction spectra of  $\text{CaF}_2$  taken at 450 K after irradiation with 2.5 keV electrons. Different dosages have been chosen to obtain similar metallization for both irradiation temperatures.

with a maximum around 2.3 eV is in good agreement with calculations of light extinction by Ca colloids in the  $\text{CaF}_2$  matrix based on a model of Orera *et al.*<sup>9</sup> These calculations yield a monotonic relation between colloid size and peak position and a Lorentzian band shape of 0.9 eV width for colloids smaller than 40 nm. From Figure 1 we can extract a mean colloid radius of  $23 \pm 2$  nm for the sample irradiated at 150 K and mean radius of  $32 \pm 3$  nm for that irradiated at 450 K. The extinction band shape and width of the sample with low irradiation temperature represents a narrow size distribution while the one for high temperature exhibits a width much larger than predicted by the theory and, therefore, represents a colloid size distribution that is broadened toward larger colloid sizes. The weak shoulder at about 3.3 eV present in both spectra is due to absorption in F-centers.

Two samples have been irradiated at 150 K using 1.5 keV and 2.5 keV electrons. The development of the colloid extinction band has been studied during slow heating. At 150 K the samples exhibit a broad absorption between 1.5 eV and 4.5 eV photon energy after irradiation. We believe that this absorption is caused by a variety of F-center aggregates, like single F-centers (absorption peak at 3.3 eV), M-centers (2.38 eV), and R-centers (1.86 eV)<sup>10</sup> up to small metallic clusters that are expected to absorb at about 2.5 eV. Heating the sample leads to the development of the Ca colloid absorption band starting at a temperature of about 230 K. The smallest colloid radius of 1 nm deduced from the spectrum is in agreement with the expectation for a F-center aggregate that develops a metallic band structure.<sup>11</sup> Further growth of the colloids during heating to 450 K is displayed in Figure 2. We find a sharp increase of the mean colloid radius from 1 nm to 25 nm in the narrow temperature range between 260 K and 300 K.

It should be noted that the integral amount of metallic calcium determined from the height and width of the absorption band does not change during the growth of the colloids below 350 K and that the number of F-centers, although it may change, is always very low

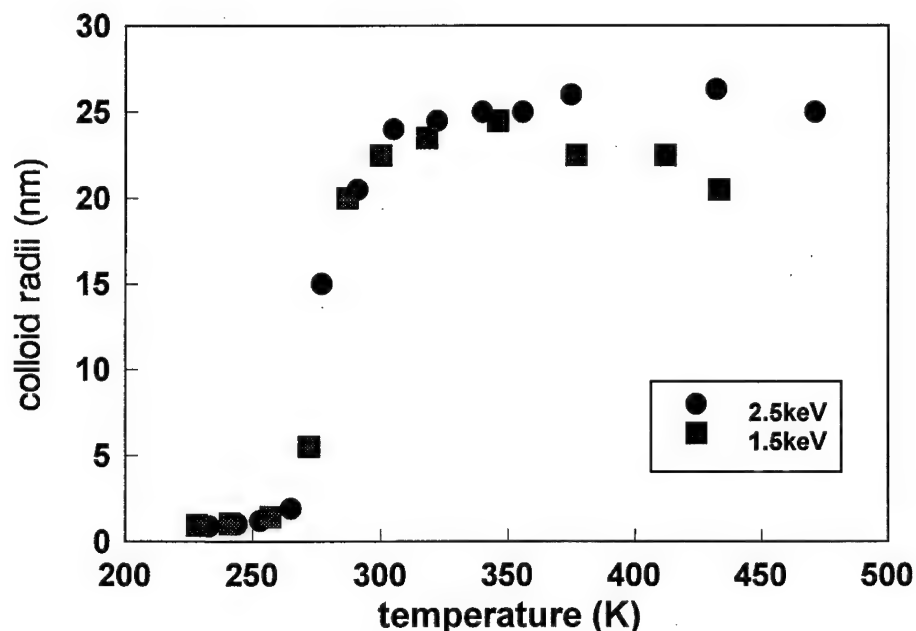


FIGURE 2 The development of Ca colloid size during heating after electron irradiation at 150 K.

compared to those aggregated in colloids. This indicates a colloid growth by a ripening process<sup>1</sup>: the metal colloids and single F-centers are in an equilibrium that depends on the size of the colloids. The equilibrium concentration of F-centers exponentially approaches a minimum value for large colloids. In this way larger colloids will grow at the cost of smaller colloids when the concentration of F-centers is lower than the equilibrium for the small colloids but still higher than the equilibrium for larger colloids. Heating starts this process by increasing both the concentration and mobility of F-centers. The sharp increase of colloid size at 270 K may be due to the activation of F-centers from colloids or diffusion of F-centers.

For the irradiation at 150 K and subsequent heating, the assumption of a ripening process is supported by an analysis of the shape of the resulting absorption band which is similar to a Lorentzian curve with a band width of approximately 1.0 eV (Figure 1). This indicates a narrow distribution of colloid size in good agreement with predictions for the size distribution during a ripening process.<sup>1</sup>

Above 350 K the amount of metal aggregated in bulk colloids decreases. This can be deduced from a lowering of the extinction observed in the original spectra. The enhanced mobility of F-centers causes diffusion of metal from the bulk to the surface, since the colloids are located in a layer close to the surface. The decrease of F-center concentration disturbs also the ripening process, i.e. the F-centers do not necessarily contribute to colloid growth but may alternatively be trapped by the surface. Consequently, colloid size decreases for temperatures above 350 K (Figure 2). This loss by diffusion is more



FIGURE 3 Scanning Force Microscopy image of the  $\text{CaF}_2$  surface irradiated with 0.9 keV electrons (1 mm beam diameter),  $12 \times 12 \mu\text{m}^2$ , irradiated with less than  $1 \mu\text{A}$  for 20 sec.

pronounced for the 1.5 keV irradiation because the effect depends on the mean distance of the colloids to the surface and, therefore, on the energy of the primary electrons.

The surface of  $\text{CaF}_2$  is metallized by low energy irradiation not only by diffusion of F-centers, as mentioned above, but also by fluorine depletion. During the irradiation experiments we always find a strong fluorine desorption while calcium desorption is observed only for temperatures above 450 K. Scanning Force Microscopy was used to study the topography of surface metal aggregation. Figure 3 shows the SFM image of a cleaved surface irradiated with a low electron dose. The colloids on the surface are oblates with a typical relation of height to radius of 1 to 10. The smallest distinctable colloids on the surface are about the size of the largest ones in the bulk determined by optical spectroscopy, but many are significantly larger. This is a hint to a colloid mobility on the surface.





FIGURE 4 Scanning Force Microscopy image of the  $\text{CaF}_2$  surface irradiated with 0.9 keV electrons,  $3.3 \times 3.3 \mu\text{m}^2$ , irradiated with  $1.5 \mu\text{A}$  for 200 sec.

The structure of the size distribution in Figure 3 suggests a model of diffusion of metal colloids on the surface, where smaller colloids which come into contact with large colloids will be swallowed by the latter. Bigger colloids grow at the costs of smaller similar to the process in the bulk what could be regarded as a ripening process at a larger scale. It is presently not clear whether the diffusion is driven by the higher temperature during the irradiation experiment or by the beam of primary electrons.

The result of longer irradiation is presented in Figure 4. The larger colloids tend to form torn up aggregates, which are circularly shaped but still show some reminiscent structure of their constituents. For a possible explanation of this feature we recall that even in UHV the developing metal on the surface can oxidize.<sup>12</sup> This might yield a passivation of the surface of the colloids that prevents the amalgamation of a crude aggregate into one smooth colloid.

In summary, bulk and surface of  $\text{CaF}_2$  are metallized under low energy electron irradiation in a similar process of defect production, aggregation and ripening yielding a narrow distribution of metal colloids. The different crystal structure and the lower dimensionality of the diffusion at the surface is manifested in the oblate shape of the colloids and their bigger size which is due to a higher mobility of defects. Additionally, on the surface complete metal colloids may move while in the bulk material transport is only due to diffusion of point defects. It is obvious from Figure 1 that the electron beam interferes with the developing colloids at higher temperatures. At 450 K the electron beam increases the concentration of F-centers which are already mobile and causes a broadening of the colloid size distribution towards larger colloids compared to the distribution after irradiation at 150 K and subsequent heating to 450 K. Also, on the surface the mobility of defects and, possibly, the mobility of metal colloids is enhanced by the electron beam as shown by the fact that the SFM images of the early metallization stage (Figure 3) represent a frozen state of ripening.

#### REFERENCES

1. A. E. Hughes and S. C. Jain, *Adv. in Phys.* **28** 6, 717 (1979).
2. R. Alcalá and V. M. Orera, *Jou. de Phys.*, **C7** (supp. au 12) (37), 520 (1976).
3. J. M. Calleja and F. Agulló-López, *phys. stat. sol.* **25**, 463 (1974).
4. M. Reichling, R. Wiebel, R. M. Wilson, R. T. Williams, and E. Matthias, *Symposium on Surface Science*. Kaprun 1993, conference digest.
5. P. Wurz and C. H. Becker, *Surf. Sci.* **224**, 559 (1989).
6. P. M. Mankiewich, H. G. Craighead, T. R. Harrison, and A. H. Dayem, *Appl. Phys. Lett.* **44**, 468 (1984).
7. T. A. Green, private communication based on results for LiF in: I. M. Bronshteyn and A. N. Protsenko, *Rad. Eng. Electr. Phys.* (USSR) **15**, 677 (1970).
8. Y. Al Jammal, D. Pooley, and P. D. Townsend, *J. Phys. C: Solid State Phys.* **6**, 247 (1973).
9. V. M. Orera and R. Alcalá, *phys. stat. sol.* **A44**, 717 (1977).
10. W. Hayes (ed.), *Crystals with the Fluorite Structure*, Oxford University Press, London 1974.
11. W. P. Halperin, *Rev. Mod. Phys.* **58**, 533 (1986).
12. C. L. Strecker, W. E. Moddemann, and J. T. Grant, *J. Appl. Phys.* **52** 6921 (1981).

## SURFACE MODIFICATION OF POLYMERS INDUCED BY ION IMPLANTATION

RENÈ ENDRŠT,<sup>1</sup> VÁCLAV ŠVORČÍK,<sup>1</sup> VLADIMÍR RYBKA<sup>1</sup> and VLADIMÍR HNATOWICZ<sup>2</sup>

<sup>1</sup>*Department of Solid State Engineering, Institute of Chemical Technology, Technická 5, 166 28, Prague, Czech Republic,* <sup>2</sup>*Institute of Nuclear Physics, Czech Academy of Science, 250 68 Řež, Czech Republic*

It was found from the IR and UV-visible spectra, that the ion implantation into polymers results in the breakage of molecular chain, creation of double bonds and oxidation, which is connected with formation of carbonyl groups. The considerable increase of the electrical conductivity after the ion implantation was observed in all studied polymers. This increase of the conductivity was essentially caused by the increase of conjugated double bonds. In unpolar polymers, the increase of surface free energy resulting in enhancement of polarity of unpolar polymer was found.

*Key words:* implantation, polymer, oxidation, carbonization.

### 1 INTRODUCTION

Ion implantation is one of the methods frequently used for the modification of surface properties of materials. As a result of ion bombardment, the polymer is degraded and relative carbon content increases in surface layer.<sup>1,2</sup> Another process taking place in ion exposed polymers is oxidation and creation of carbonyl groups and conjugated double bonds.<sup>2–4</sup> Creation of so organized unsaturated double bonds in polymer chain is considered to be responsible for dramatical increase of electrical conductivity in ion beam modified polymers.<sup>2,3</sup> Another property which can be changed by ion implantation is polymer surface polarity. It has been found that for unpolar polymers, i.s. polyethylene, polypropylene,<sup>4</sup> the surface polarity becomes higher as a result of ion implantation.<sup>2–4</sup>

### 2 EXPERIMENTAL

The experiments were performed on thick foils of oriented polyethylene (PE). The samples of PE were implanted with F<sup>+</sup> ions of energy 150 keV to the doses of 10<sup>11</sup>–10<sup>15</sup> cm<sup>-2</sup>.

The structural changes in ion implanted samples were examined using IR and UV-visible<sup>2</sup> spectroscopy. The polar component of surface free energy ( $\gamma_{sp}$ ) was determined from measured contact angles for polar (water) and unpolar (hexane) liquids. A Keithley instrument was used for determination of sheet conductivity.

### 3 RESULTS AND DISCUSSION

The IR spectra of polyethylene prior and after ion implantation were measured and the results shown in Figure 1. One can see that with the increasing F<sup>+</sup> ion dose the absorption maximum at 1720 cm<sup>-1</sup> characteristic for carbonyl group on the chain becomes stronger. This fact indicates oxidation processes related directly to the ion implantation. Another maximum at 1650 cm<sup>-1</sup> which also becomes stronger with increasing ion dose, is related

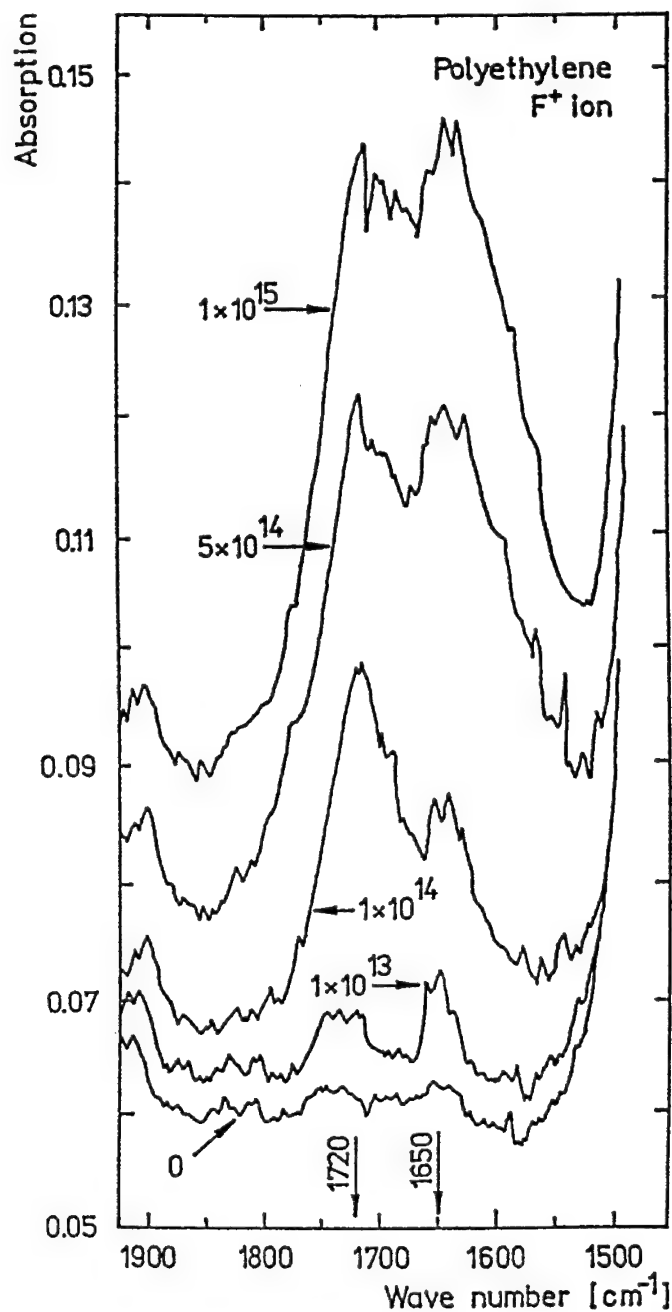


FIGURE 1 IR spectra for the PE samples implanted with 150 keV  $F^+$  ions to different ion doses. The first absorption maximum at 1720  $cm^{-1}$  is characteristic for carbonyl group (C=O), the second 1650  $cm^{-1}$  belongs to double bonds on polyolephins. The numbers are the ion doses in  $cm^{-2}$ .

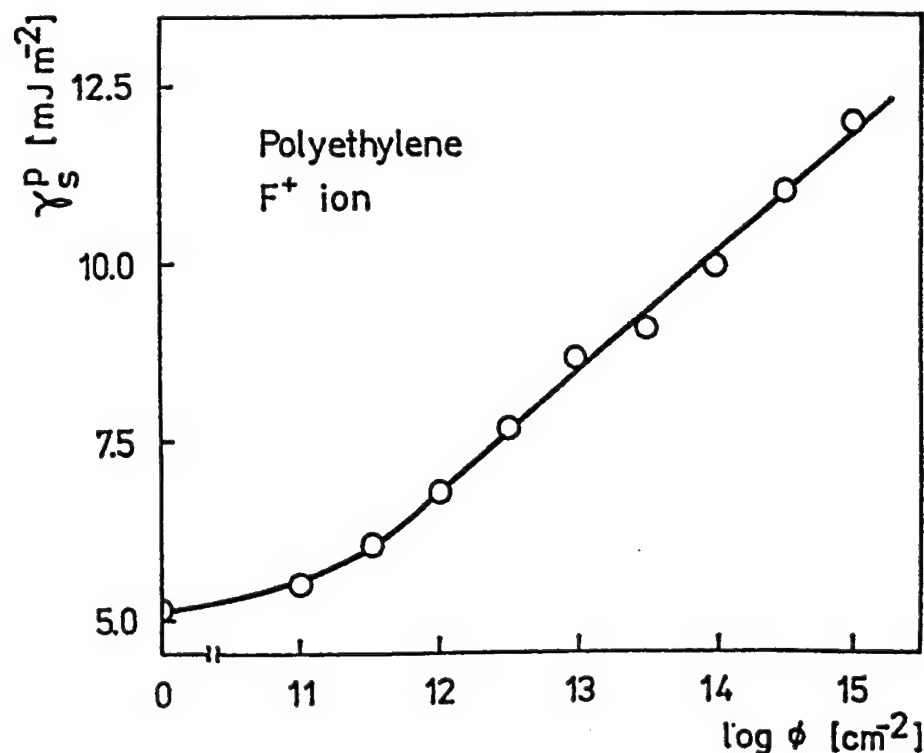


FIGURE 2 The dependence of the polar component of the PE surface free energy on the dose of 150 keV  $F^+$  ions.

to double bonds on polyolephins.<sup>5</sup> The observed phenomena leads to the conclusion that during the implantation of PE with  $F^+$  ions the polymer surfaces is dehydrogenated and free radicals appear from which double bonds or, after oxygen penetration, the carbonyls groups are created.

The measured polar component of free surface energy  $\gamma_{sp}$  as a function of the dose of implanted  $F^+$  ions is shown in Figure 2. One can see that the free energy polar component is relatively high for the unexposed PE samples examined. Polar component  $\gamma_{sp}$  increases linearly with increasing ion dose, that is the PE surface polarity is proportional to the dose of implanted  $F^+$  ions.

The sheet conductivity was measured on pristine and ion implanted PE samples. While the conductivity of pristine undegradated PE varies from  $10^{-17} - 10^{-19}$  S, the polyethylene samples implanted with  $F^+$  ions exhibit the conductivities of  $2 \times 10^{-11}$  S for the ion dose of  $10^{15} \text{ cm}^{-2}$  and  $< 10^{-12}$  S for lower doses. This increase of the conductivity was essentially caused by the increase of conjugated double bonds shown by IR spectroscopy (Figure 1) and UV-visible spectroscopy.<sup>2</sup>

#### REFERENCES

1. K. Yohida and M. Ywaki, *Nucl. Instr. & Meth.* **B19**, 878 (1987).
2. V. Švorčík V. Rybka, R. Endršt, V. Hnatowicz, and J. Kvítek J. Electrochem. Soc., **140**, 549 (1993).

3. V. Švorčík V. Rybka, K. Volka, V. Hnatowicz, and J. Kvítek, *Appl. Phys. Lett.*, **61**, 1168 (1992).
4. V. Švorčík V. Rybka, K. Volka, V. Hnatowicz, J. Kvítek and P. Seidl, *Jpn. J. Appl. Phys. B*, **31**, L287 (1992).
5. B. Wasserman, *Phys. Rev.* **B34**, 1926 (1986).
6. V. Švorčík R. Endršt, V. Rybka, V. Hnatowicz, F. Černý, *J. Electrochem. Soc.*, **141** 582 (1994).

## THE BEHAVIOUR OF PURE AND $K^+$ IMPLANTED LiF SURFACES UNDER ELECTRON BOMBARDMENT

C. JARDIN,\* P. DURUPT\*\* and J. DAVENAS\*

*\*Département de Physique des Matériaux, UA CNRS N° 172; \*\*Laboratoire d'Electronique des Solides, Université Claude Bernard de Lyon, 43 Bvd du 11 Novembre 1918, 69622 Villeurbanne Cedex, France*

As detected by Auger electron spectroscopy (AES), the interaction of a pure (100) LiF surface with an electron beam induces a loss of fluorine. Lithium atoms are oxidized in the vacuum ambient and the formation of lithium oxide  $Li_2O$  has been characterized using electron energy loss spectroscopy (EELS) by typical structures at 18.6 and 10 eV. The loss of fluorine is associated with a decrease of the positive surface potential. The cathodoluminescence (CL) emissions detected in the 250–900 nm wavelength range at 3.8, 3.1, 2.3 and 1.9 eV have been attributed to  $F$ ,  $F_3^+$  and  $F_2$  centers.

A quite different behaviour, without loss of fluorine, is observed for a LiF sample implanted with potassium  $K^+$  ions. This implanted sample appears to be more stable under electron irradiation than pure LiF. Such a different behaviour may be explained by a decrease in the efficiency of energy transfer mechanisms connected to different space-charge effects.

*Key words:* LiF, ESD, F center, space-charge, surface, cathodoluminescence.

### 1 INTRODUCTION

The aim of this study is to compare the behaviour under electron bombardment of a pure LiF insulating substrate and a LiF sample implanted with potassium ions  $K^+$  ( $5 \cdot 10^{16}$  ions/cm<sup>2</sup>; 170 keV). Owing to the insulating nature and the ionic character of the material (bandgap  $E_g = 11.6$  eV; ionicity = 92% for LiF), space-charge effects need to be considered within the framework of usual ESD processes involving known excitations, defects and energy transfer mechanism (1–3).

Different models have been developed in order to explain electron stimulated dissociation (ESD) of alkali halides, and a critical review on the subject has been recently published by Fine and Szymonski.<sup>1</sup> Surprisingly, the characteristic distribution of charges<sup>4–6</sup> inside the insulating material subjected to electron irradiation is often neglected in data related to ESD. The charge distribution leads to the presence of an electric field in the subsurface region between the positively charged surface layers due to the secondary electron emission, (which is very large for alkali halides), and the negatively charged region resulting from the injection of primary electrons inside the sample. This induced electric field may be an important parameter in transport phenomena of charged species.

### 2 THE CHANGE IN THE SURFACE COMPOSITION OF PURE LiF

As detected by Auger electron spectroscopy (Figure 1) from the decrease of the intensity of the F-KLL Auger emission, the interaction of a pure (100) LiF surface with an electron beam induces a loss of fluorine. The simultaneous increase of the O-KLL Auger signal suggests that the excess of lithium atoms resulting from the loss of halogen are oxidized in the vacuum ambient containing residual gases  $O_2$ ,  $CO_2$ ,  $H_2O$  at partial pressures in the  $10^{-10}$  Torr range. Such a situation, i.e. electron-stimulated loss of halogen and subsequent oxidation of alkali atoms, closely corresponds to the observations of Knapp<sup>7</sup> on evaporated

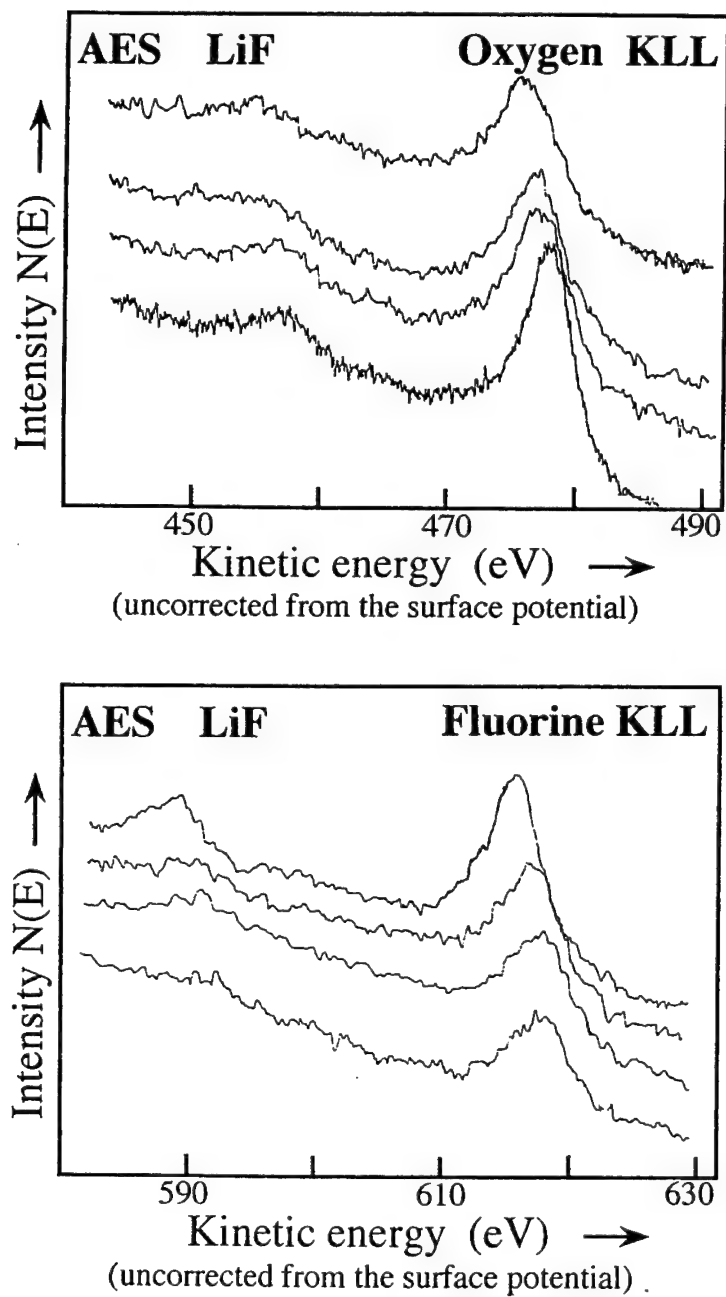


FIGURE 1 The change of the fluorine F-KLL and oxygen O-KLL Auger spectra during the exposure of the LiF surface to the electron beam (energy: 2 keV, intensity: 10  $\mu$ A).



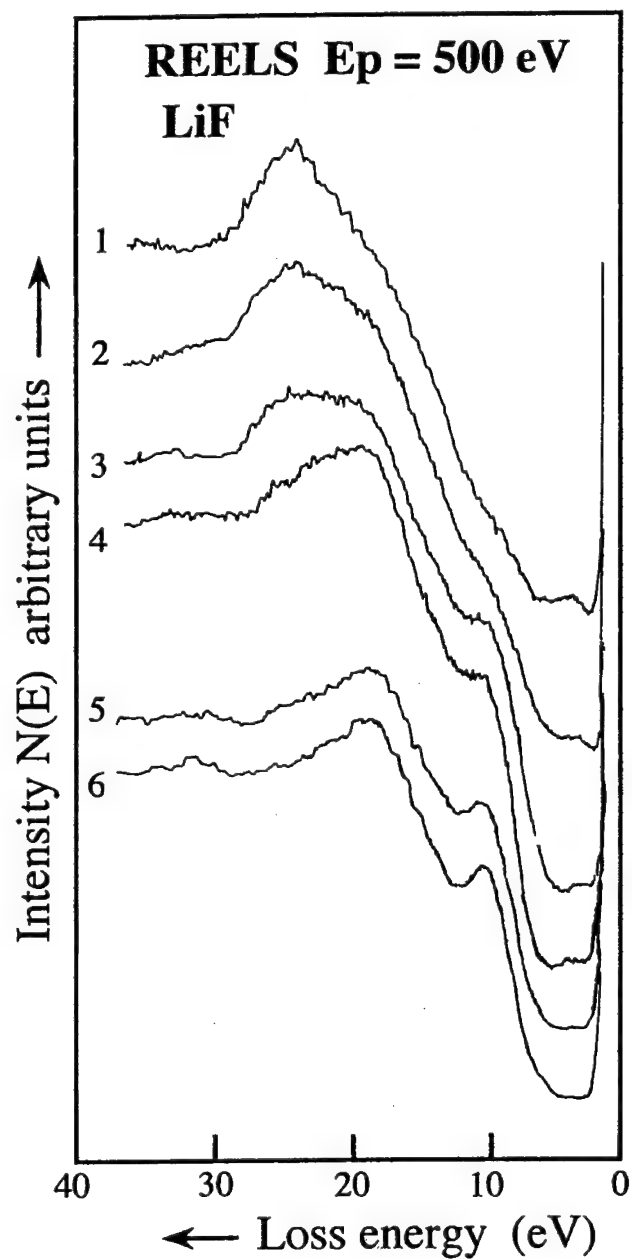


FIGURE 2 The change of the electron energy loss spectra of LiF: (1, 2, 3, 4) with increasing dose of electron irradiation; (5, 6) after vacuum annealing at 500°C.

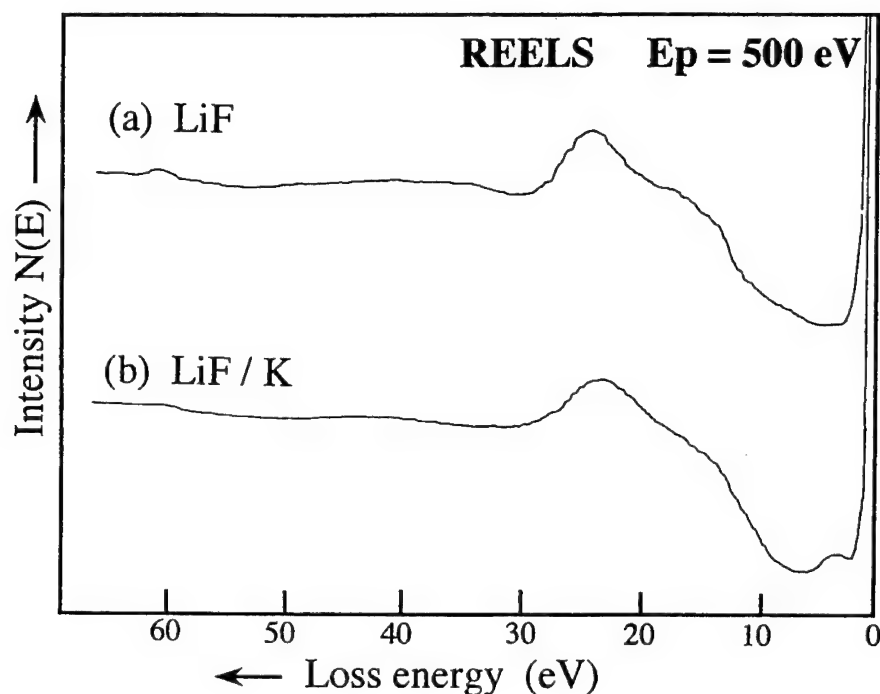


FIGURE 3 Electron energy loss spectra of pure LiF and  $K^+$  implanted LiF substrate recorded just after their introduction in the electron analyser.

$Na_3AlF_6$  films. The formation of lithium oxide has been characterized using electron energy loss spectroscopy (Figure 2) by typical losses at 18.6 and 10 eV corresponding to the excitation of volume and surface plasmons in  $Li_2O$ .<sup>8</sup>

The loss of fluorine is associated with a change in the surface potential, as deduced from the shift of the F-KLL and O-KLL Auger spectra to higher kinetic energy (Figure 1). The positive surface potential is decreased with the change in the surface composition of the material.

By using a higher energy beam (80 keV) of an electron microscope, it is possible to observe the emission of red-coloured trails of light due to the directive ejection of species at the position of the electron beam impact with the LiF surface. With some technical problems due to the fleetingness of the emission, this light has been analysed through a quartz window and attributed to the radiative relaxation of excited fluorine atoms (spectral lines near 641 nm and in the 680–700 nm range corresponding to 3s–3p transition of the neutral atom). The ejection of Li atoms may also occur, as deduced from the spectral line at 670 nm.<sup>9</sup>

It is well known that hyperthermal emission of halogen from alkali halides subjected to electron bombardment occurs along well-defined directions. The ejection of hyperthermal neutral atoms in the  $\langle 100 \rangle$  direction has been observed by Fine and Szymonski.<sup>1</sup> Negative ions of halogen species are emitted along the  $\langle 110 \rangle$  axis which corresponds to the

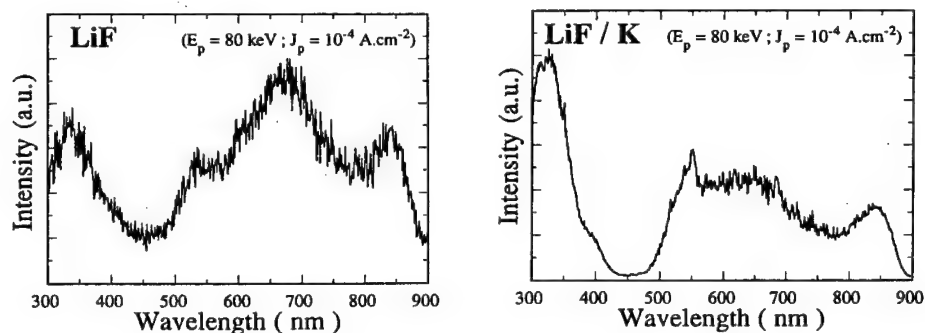


FIGURE 4 Cathodoluminescence spectra of the electron-irradiated LiF and  $K^+$ -implanted LiF samples.

geometric orientation of the H and  $V_k$  centers. This is the direction of atom transport by replacement collision sequence according to the Pooley-Hersh model.<sup>10,11</sup> In the light of the recent theories explaining the formation of F-H pairs in alkali halides,<sup>2,3</sup> the  $\langle 110 \rangle$  axis corresponds as well to the preferential direction for the off-center translational instability of the self-trapped exciton ( $V_k + e^-$ ) system which may transform into a (F-H) pair.

The structure which appears at about 4 eV in the electron energy loss spectra of LiF during electron irradiation is connected to the presence of fluorine vacancies. This loss structure is present in the spectra of the  $K^+$  implanted LiF substrate (Figure 3) and is no longer observed after heat treatment (500°C in UHV) of the samples. This treatment, which is known to decrease the number of colored centers in the material, favours the formation of lithium oxide at the surface of LiF (Figure 2).

The cathodoluminescence of the electron irradiated LiF sample at 330 nm (3.8 eV) and 400 nm (3.1 eV) may originate from the F centers (Figure 4). Other CL structures detected in the visible wavelength range at 530 nm (2.3 eV) and 670 nm (1.9 eV) are associated to  $F_3^+$  and M ( $F_2$ ) defects in agreement with previous optical emission measurements.<sup>12</sup>

### 3 THE BEHAVIOUR OF $K^+$ IMPLANTED LiF SAMPLE

The LiF sample previously implanted with potassium  $K^+$  ions displays a different behaviour. The loss of fluorine is not detected and the surface potential is not changed under electron irradiation; therefore, the implanted surface appears to be more stable than pure LiF. Because the *local* atomic or electronic excitations in pure and  $K^+$  implanted surface of LiF are expected to be nearly similar, their different behaviour against electron irradiation may be explained by non-local phenomena: a decrease in the efficiency of energy transfer mechanisms combined to the change in space-charge effects is proposed according to the experimental observations.

#### REFERENCES

1. J. Fine and M. Szymonski, *Le Vide Les Couches Minces* **S260**, 69 (1992).
2. R. T. Williams and K. S. Song, *J. Phys. Chem. Solids* **51**, 679 (1990).
3. N. Itoh and K. Tanimura, *J. Phys. Chem. Solids* **51**, 717 (1990).

4. A. Miotello, *Phys. Letters* **A103**, 279 (1984).
5. J. Cazaux, *Le Vide Les Couches Minces* **S260**, 36 (1992).
6. E. Vicario, N. Rosenberg and R. Renoud, *Conference on electrical insulation and dielectric phenomena, IEEE Annual Report N° 93 CH 3269-8*, 221 (1993).
7. A. G. Knapp, *J. Appl. Phys.* **50**, 5961 (1979).
8. C. Jardin and D. Robert, *Appl. Surface Sci.* **35**, 495 (1989).
9. A. R. Striganov and N. S. Sventitskii, *Tables of spectral lines of neutral and ionized atoms*, IFI/Plenum Press, New York, Washington, (1968).
10. D. Pooley, *Proc. Phys. Soc.* **87**, 245 (1966).
11. H. N. Hersh, *Phys. Rev.* **148**, 928 (1966).
12. J. Davenas, *Thesis N° 80-20*, UCBLyon, (1980).

## INVESTIGATION OF ZnSe FILMS GROWN ON GGG, YIG

P. KOSOBOUTSKI and P. VODOLAZSKI

*Department of Physics, University Lvivska Politechnika 12 Bandery Str., Lviv, Ukraine*

A new class of heterostructures such as semiconducting film coatings of the iron-garnet substrates is investigated on the issue of their physical properties. It is proven that unlike a world of difference in their crystal lattice parameters, heterostructures like ZnSe-GGG and ZnSe-YIG possess satisfactory mechanical properties and crystal structure.

*Key words:* ZnSe-GGG (YIG), luminescence, exciton band, adhesion.

### 1 INTRODUCTION

Heterostructures being semiconducting film coatings of iron-garnet crystals are quite promising in the development of a class of microelectronic devices that work by the new physical grounds, namely, based on interaction between magnetostatic waves and electronic subsystem within a semiconductor. Firstly, such a device can be controlled by either applying the electric field or illuminating the semiconducting film surface. Secondly, the presence of photosensitive coats gives the possibility of simultaneous memorizing the picture there.<sup>1</sup> However, the technological growth of epitaxial semiconducting films at iron garnets is rather difficult. The point is that there is a lot of discrepancy between both crystal lattice parameters, and they also differ in their thermal expansion coefficients.

### 2 EXPERIMENTAL PROCEDURE

ZnSe films were grown on gadolinium-gallium garnet (GGG) and yttrium-iron garnet (YIG) substrates via sublimation in quasi-closed volume. The garnet substrates were oriented on (110). The luminescence was excited with a He-Cd laser at a generation wavelength of  $\lambda = 441.6$  nm, and with an N<sub>2</sub> laser ( $\lambda = 337$  nm).

### 3 RESULTS AND DISCUSSION

As was mentioned above, a lot of discrepancy between the crystal lattice parameters in the heterojunctions under consideration, of  $a(\text{ZnSe}) = 0.56687$  nm and  $a(\text{YIG}) = 1.2376$  nm, is a characteristic feature there. However, if one takes into account that the parameters are related to one another about twice as large, the discrepancy does not exceed 9%. This implies that the strains in the film-substrate interface in the given class of heterosystems can be minimized and therefore the structures such as ZnSe-GGG (YIG) could be considered as stable. The ratio of the linear thermal expansion coefficients looks like being up to obtain stable heterostructures with a good adhesion of films to the substrate surface. They are as follows:  $\alpha_{\text{ZnSe}} = 7.8 \times 10^{-6} \text{ K}^{-1}$  and  $\alpha_{\text{GGG(YIG)}} = 8.13 \times 10^{-6} \text{ K}^{-1}$ . It is seen that there is some difference in their values, which would not be to decide the stability of heterostructures, since there is a possibility of fitting the value of  $\alpha$

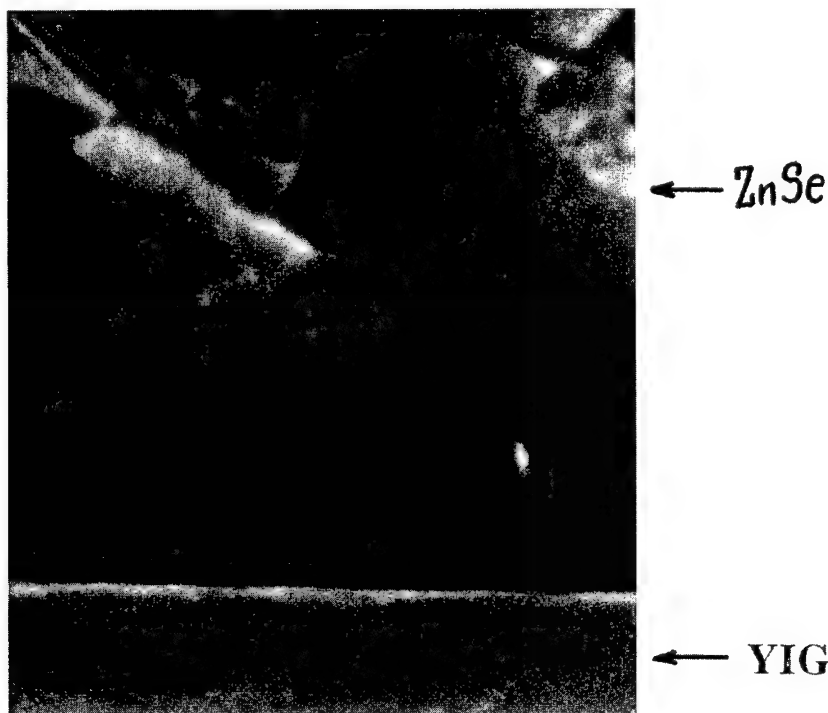


FIGURE 1 Electronic microscope picture of the cross section through ZnSe-GGG.

in a film to the bulk one in a substrate.<sup>2</sup> In Figure 1 is shown the electronic-microscope-made picture of ZnSe-GGG heterostructure interface. It is seen that the ZnSe films embody the block structure which is commonly a characteristic in such a compound. It is worthy as the electronic microscope investigations showed that the contact of the film to substrate has a block character, too. In the luminescence spectra when excited with an  $N_2$  laser at the liquid nitrogen temperature ( $T = 77$  K) there is observed a wide structureless band (curve 1 in Figure 2), which was shown by the additional studies to have a plasma character. The similar spectrum was observed from ZnSe-YIG as well. The emission bands of free and localized excitons were not observed in the emission spectra of ZnSe-YIG at the liquid helium temperature ( $T = 4.2$  K) and the low excitation levels. This could be due to the diffusion of iron atoms in the process of epitaxy, as iron atoms were found<sup>3</sup> to suppress the radiative recombination channels. The emission spectra of ZnSe-GGG under the conditions of excitation, however, show comparatively weak emission bands of localized excitons (curve 2 in Figure 2) in the region of the fundamental absorption edge. On the other hand, for both the heterostructures the exciton reflection spectra become observable at  $T = 5$  K (curve 3 in Figure 2). The bottom of the exciton band with a quantum state of  $n = 1$  lies at  $E = 2.802$  eV, which conforms to the reference data<sup>3</sup> for the cubic crystals. The fact that the extrema in the reflection curve are weak points to the strains available in the films obtained. The tests for the mechanical properties showed that the heterostructures possess satisfactory mechanical strength and adhesion. This was

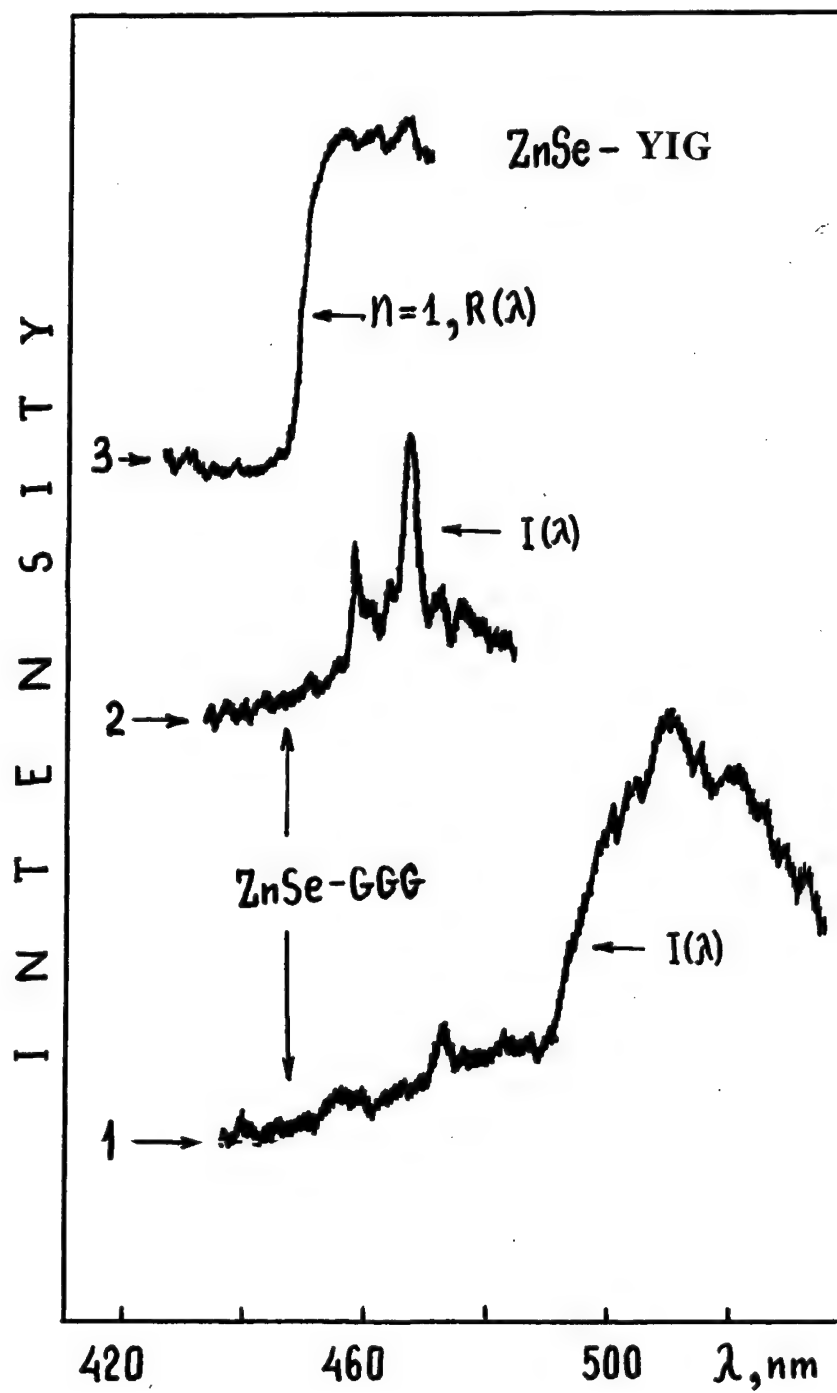


FIGURE 2 Optical spectra of ZnSe-GGG (YIG) in the region of the fundamental absorption edge.

confirmed also by the multiple thermal cycling corresponding to  $300\text{ K} \rightarrow 77\text{ K} \rightarrow 4.2\text{ K} \rightarrow 300\text{ K}$  scheme, not leading to rapidly cracked or peeled films.

#### REFERENCES

1. A. J. Koguchar, I. H. Kudraschkin, L. M. Letjk, *Zhurnal Tekhnicheskoy Fiziki* **57**, 609 (1987).
2. E. A. Nesmelo, A. G. Gusev, O. H. Ivanov *et al.*, *Optiko-Mekhaniches kaja Promyshlennost* **9**, 50 (1986).
3. M. Aven and J. S. Prener, edited by, *Physics and Chemistry of II-VI Compounds* (General Electric Research and Development Center Schenectady, New York, 1967), p. 265.



## INVESTIGATION OF THE THERMOCHEMICAL REACTION IN ZnSe CRYSTALS FROM ACTION BY INFRARED LIGHT

P. KOSOBOUTSKI, R. KIJAK and R. BIBIKOV

*Department of Physics, University Lvivska Politechnika 12 Bandery Str., Lviv, Ukraine*

In the present paper the investigation of optical properties in ZnSe single crystals from action by the infrared light radiation is provided. It is shown that laser light induced thermochemical reaction, of a certain type, harnesses a metallization effect at the sample surface.

**Key words:** ZnSe, luminescence, thermochemical reaction, IR laser light excitation.

### 1 INTRODUCTION

In the infrared (IR), which is the working range for CO<sub>2</sub> lasers, semiconducting ZnSe single crystals were shown to be one of the most promising materials in making laser-optics elements such as laser windows. This compound possesses with applicable radiational stability, and good thermal and mechanical characteristics as well.<sup>1</sup> However, it is known<sup>2,3,4</sup> that the transparency of a ZnSe crystal when exposed to IR radiation may change by the thermochemical reactions triggered there by IR light.

### 2 EXPERIMENTAL PROCEDURE

In the present paper, ZnSe single crystals grown by the Bridgeman-Stockburger method were investigated. The luminescence was excited with a He-Cd laser at a generation wavelength  $\lambda = 441.6$  nm and an output power  $P = 0.02$ – $0.03$  W. The samples were irradiated with a CO<sub>2</sub> laser ( $\lambda = 10.5$  nm,  $P = 35$  W). If necessary, the irradiance could be changed by proper focusing of the laser light beam with a KCl-made lens.

### 3 RESULTS AND DISCUSSION

#### 3.1 Luminescence From ZnSe Single Crystals

In the exciton luminescence spectra from non-irradiated ZnSe samples there are observed lines labelled  $I_1$  (exciton localized by the vacancies  $V_{Zn}$  in place of Zn atoms);  $I_2$  ( $V_{Se}$ );  $I'_1$  (Na and Li atoms in place of  $V_{Zn}$ 's).<sup>5</sup> After being irradiated for 30–60 minutes by the light at a power by two orders of magnitude smaller than the decomposition threshold power value there, the crystals showed the decreased intensities in  $I_2$  and  $I'_1$  lines, and more intense  $I_1$  line. This process can proceed on account of both the formation of new  $V_{Zn}$ 's by displacing Zn atoms to the intersite lattice space and the diffusion of Na and Li atoms away from  $V_{Zn}$  positions. It is seen in Figure 1 that the concentration of Se atoms within the area of a laser spot at the oncome sample surface is abruptly decreased, while that of Zn remains almost unchanged, and they correlate qualitatively to the previous results. Somewhat spread in the data is most likely caused by the laser beam inhomogeneity.

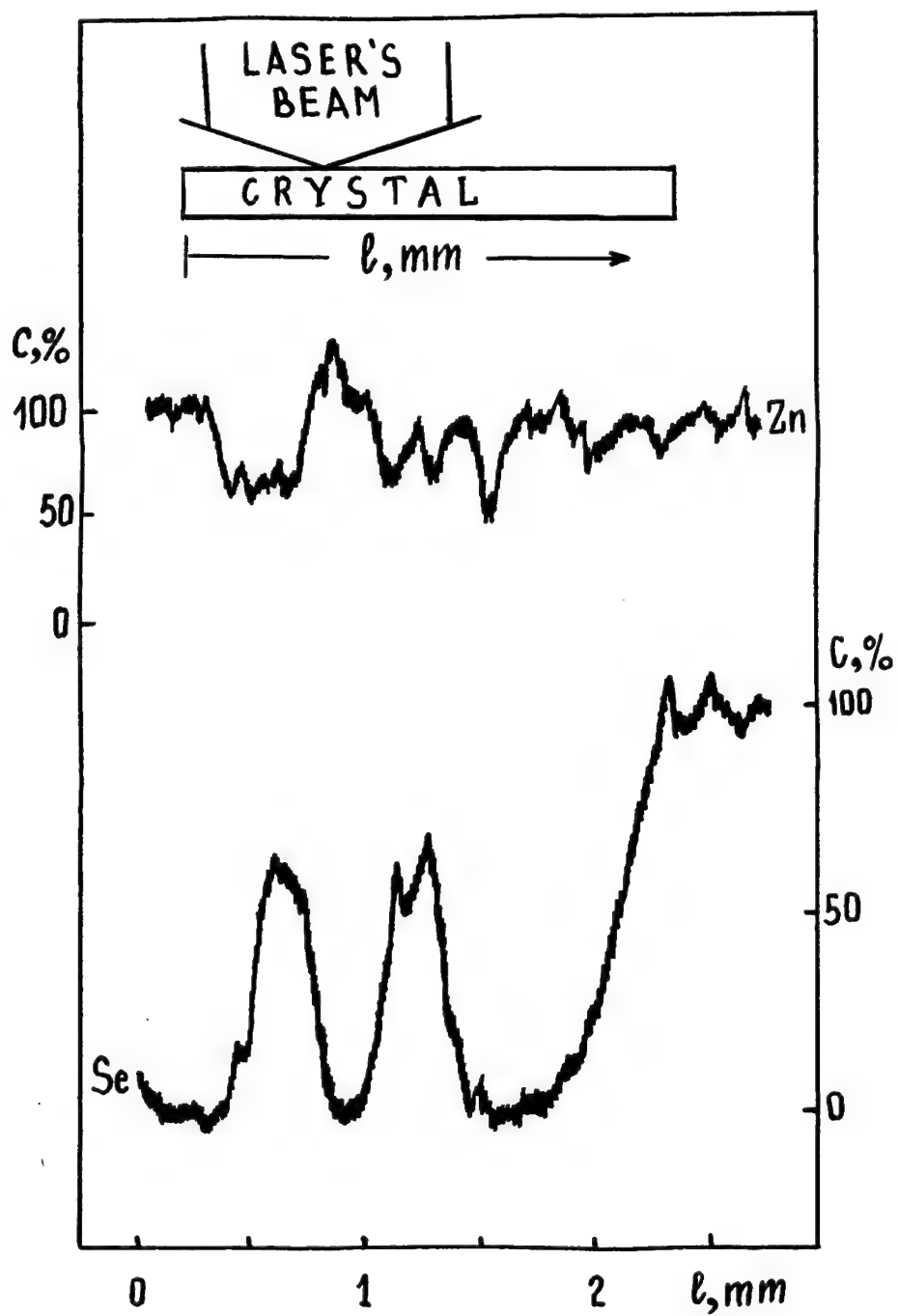


FIGURE 1 Distribution in Zn and Se concentrations at the irradiated crystal surface.

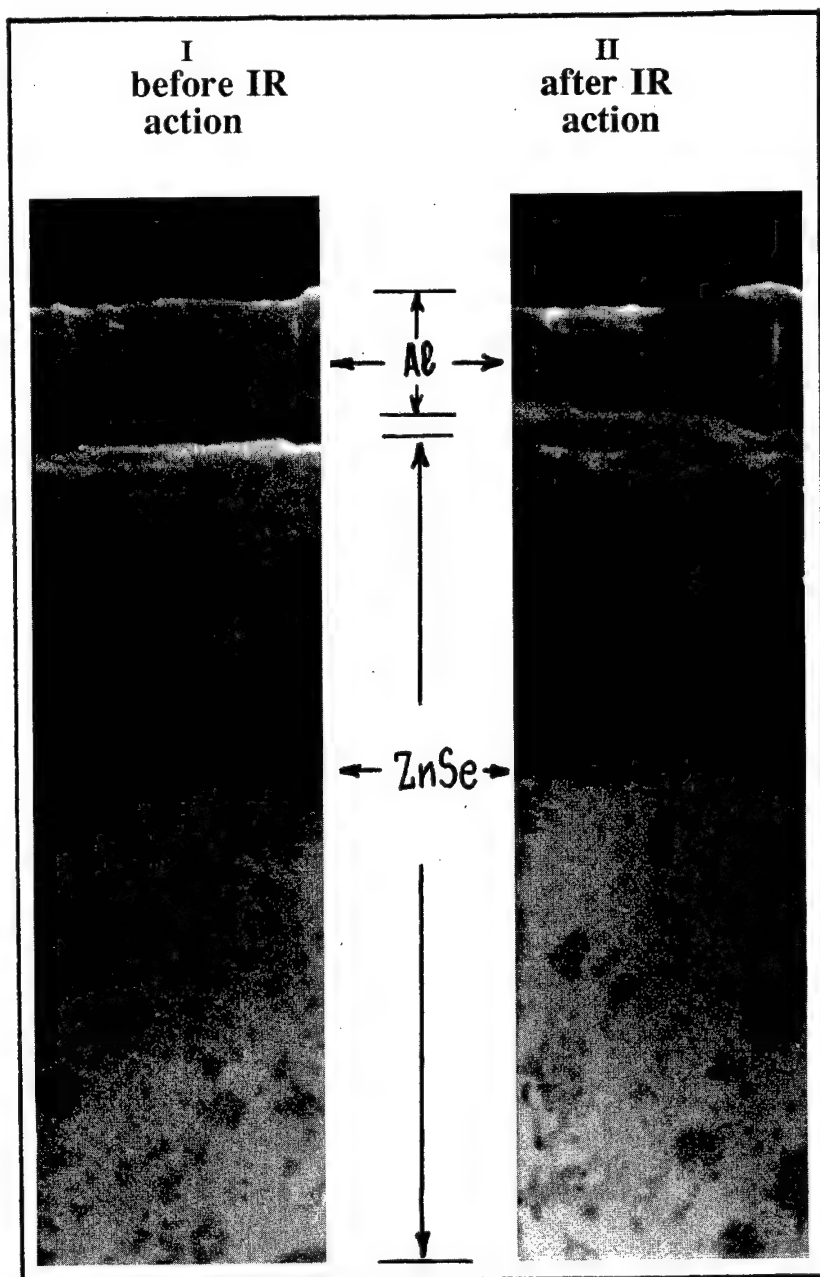


FIGURE 2 Electronic microscope picture of Al film-ZnSe surface interface: I-non-irradiated region, II-irradiated region.

### 3.2 IR Absorption Spectra of ZnSe

When exposed to more powerful radiation of a CO<sub>2</sub> laser at 4.2 K, ZnSe samples no longer show the exciton luminescence response. However, there appear new bands in the region from 700–4000 cm<sup>-1</sup> in their IR absorption spectra. These changes can be explained by the thermochemical reactions in the crystals that are triggered from the heating effect made by the continuous laser emission. We may deal here with a thermochemical reaction of the following type:<sup>2</sup>



### 3.3 X-ray Study

In order the possibility of creating ZnO films at the ZnSe surface through the oxidation of Zn atoms from action by the laser light beam be proven, the study of X-ray diagrams from irradiated ZnSe surfaces, including the determination of interplane distances  $d$  for the different  $hkl$  reflex indices has been made. The intensity correlation between the various reflexes of a laser light generated ZnO film has been settled as follows:

$$\begin{aligned} I(002) > I(103) > I(105) > I(004) > I(006) > I(104) > I(205) \approx I(124) > I(114) > \\ I(112) > I(102) > I(101) > I(100) \approx I(110) \approx I(201) \approx I(202) \approx I(203) \approx I(204) \approx \\ I(303) \approx I(123) \approx I(302) \approx I(106) \approx I(220) \approx I(200) \approx I(120) \approx I(121) > I(122). \end{aligned}$$

It follows from this sequence that reflexes from the (001) plane, i.e. I(002), I(004), and I(006), are set far left compared to those reported in the literature.<sup>6</sup> This means that the crystallites which form the ZnO film are mainly oriented perpendicular to the sample surface, that is, the (001) plane is oriented parallel to the ZnO-film surface, and the crystallites are aligned with the laser-beam propagation direction. Analysis made on the Debye diagrams showed the crystal grains not exceeding 10<sup>-3</sup> cm in size.

### 3.4 Adhesion Properties of Metal Films to Irradiated ZnSe

As was mentioned above, atomic Se is observed to sublime from the irradiated sample surface. It then could be expected that adhesion metal-film coupling properties bear a substantially close relationship to the irradiated ZnSe surface. So, two samples of the same crystal ingot, one of them annealed under vacuum at both annealing temperature and time that corresponds to the laser light induced changes in the emission spectra, were prepared, and then they were spread with Al metal at 420 K. The electronic microscope taken pictures from the faces of the samples show (Figure 2) much stronger adhesiveness of Al film to the annealed subingot. The mechanical tests of the Al spread films for their strength also indicated that the film strength is high too when the annealed sample is taken. On further heating the samples up to 780 K, the strength of the Al film on the unannealed sample decreases unlike the annealed-sample film which is not being weakened. Multiple thermal cycling made on the samples in the temperature range between 77 K and 300 K results in the partially peeled Al films at the surface of the unannealed sample, while that is now as strongly pinned to the annealed-sample surface as before.

## REFERENCES

1. H. T. Petrovski, *Izvestija AN SSSR, Ser. Fiz.* **44**, 2034 (1981).
2. P. V. Vodolazskii, B. R. Kiyak, M. G. Matsko *et al.* *Phys. Stat. Sol.* **A87**, K69 (1985).
3. N. D. Marchuk, P. V. Vodolazskii, V. V. Gonchar *et al.* *Zhurnal Prikladnoj Spektroskopii* **56**, 64 (1992).
4. V. N. Babenzov, A. Badulaeva, A. I. Vlasenko *et al.* *Fiz. Tekhn. Polupr.* **27**, 1611 (1993).
5. S. Satoh, K. Igaki, *Jap. J. Appl. Phys.* **20**, 1889 (1981).
6. L. I. Mirkin, *Spravochnik po Rentgenovskomu Analizu Polikristallov* (Gosizdat fiz.-mat. lit., Moscow, 1961), pp. 559.

## **11 NANOMATERIALS**

## EFFECTS OF RESONANCE ON LOW-FREQUENCY RAMAN SCATTERING FROM SEMICONDUCTOR NANOCRYSTALS

L. SAVIOT, B. CHAMPAGNON, E. DUVAL and A. I. EKIMOV\*

*Laboratoire de Physico-Chimie des Matériaux Luminescents URA-CNRS 442; Université  
Claude Bernard Lyon I43, Bd du 11 novembre 1918 69622 Villeurbanne Cedex France;*

*\*A. F. Joffe Physico-Technical Institute 194021 St Petersburg Russia*

An investigation of Raman scattering in CdSe nanocrystals embedded in oxide glass matrix under resonant excitation has been accomplished. First we observe the dependence of both the longitudinal optical phonon and the low frequency scattering energies with the excitation wavelength which is explained in terms of size selective excitation. A peculiar attention is given to the behaviour of low-frequency spectra and selection rules due to resonance effects are reported. Most of the first harmonics of the different predicted vibration modes have been observed and a qualitative attempt has been made to link the observed modes with the excited electronic levels.

**Key words:** II–VI semiconductor, quantum confinement, resonant Raman scattering, low-frequency Raman scattering, size selective excitation.

### 1 INTRODUCTION

The interest in large optical non-linearities and short response time as well as a fundamental point of view in the physics of confined systems are the origin of the large amount of studies concerning semiconductor quantum dots.<sup>1</sup> The electron-longitudinal optical (LO) phonon coupling has been often discussed and a lot of experimental work on CdSe nanoparticles is available<sup>2</sup> but little interest was devoted to the spectral dependence of Raman scattering. We investigated the position of the LO line with varying sizes and with excitation wavelengths between the absorption edge and the first maximum of the absorption spectra. Low-frequency Raman scattering, was measured for excitation above absorption edge to investigate acoustic vibrations. These acoustic modes of the particles are theoretically well known,<sup>3</sup> so we could link them with the electronic excited levels through resonance effects.

### 2 RESULTS AND DISCUSSION

When dealing with resonance effects, it is first necessary to know the absorption spectra of the samples. They are plotted in Figure 1. Two kinds of samples was used. The first set was provided by A. I. Ekimov and are CdSe samples with radii of the particles varying from 18 Å to 38 Å embedded in oxide glass matrix. The other sample (RG 630 1G) was provided by Schott Glasswerke. Its composition is nearly  $\text{CdS}_{0.4}\text{Se}_{0.6}$  and the radius of the particles is close to 40 Å. Absorption spectra and all other experiments reported in this paper were obtained at room temperature. All the mean radii were measured by small angle x-ray scattering. In the following, the notations and theory to describe these spectra are taken from Efros and Rodina.<sup>4</sup>

The Raman measurements were done under excitation with Argon, Krypton and Helium-Neon laser which allowed nine different wavelengths from blue to red. A five

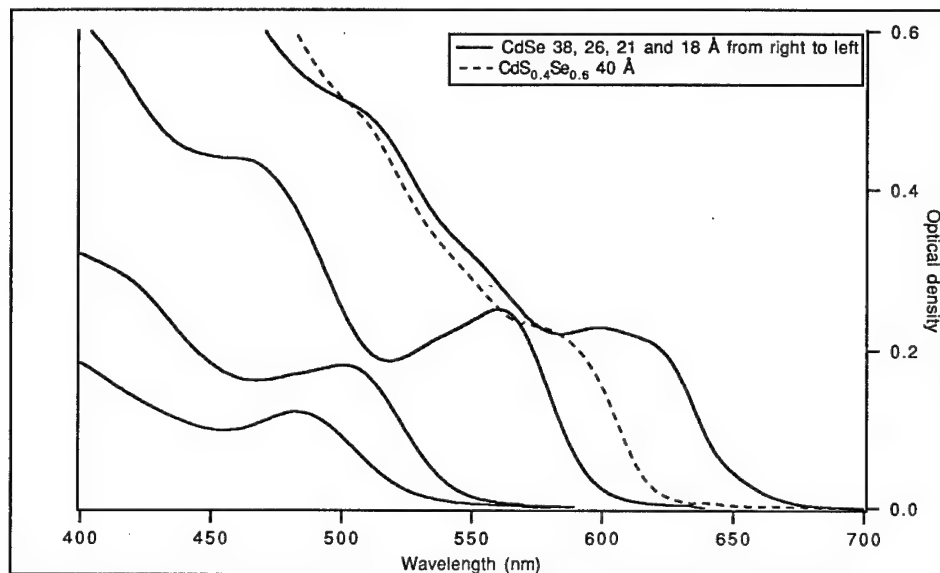


FIGURE 1 Absorption spectra of the different samples. Vertical lines show positions of Argon and Krypton laser lines.

grating spectrometer Dilor Z40 was used, and we recorded the Stokes and anti-Stokes parts of the signal at the same time for all spectra for better accuracy in peak positions.

A first set of experiments was made on Ekimov's samples with the excitation varying from the band edge to the first maxima of the absorption spectra corresponding to the  $1S_{3/2}-1S_e$  transition. The LO phonon line and three low-frequency lines were observed. A narrow low-frequency line, both excitation and sample independent, is attributed to Brillouin zone edge TA phonon. This line can be seen when the detected polarization of light is parallel to the incident one. For a given sample, the positions of the three other lines are excitation dependant. This effect was interpreted by assuming that, even at room temperature, the absorption edge is partly due to the size distribution inhomogeneous broadening. When the excitation moves from the first absorption peak to the absorption edge, the selected size varies from the sample mean size (as measured by SAXS) to larger sizes. The dependence of the position of the first transition on the radii of the particles is known from,<sup>1</sup> so we know which size is excited. Thus we know from<sup>2</sup> the wave vector of the LO-phonons who contribute to the scattering:  $k = \Pi/a$ , where  $a$  is the radius of the particle. The LO phonon dispersion curve allows to predict the position of the LO peak. The result are shown in Figure 2. The peak position is plotted as a function of  $\Pi/a$ , and it has been fitted by a parabola which is a good approximation for the long-wavelength limit. The result of the fit is in good agreement with the dispersion curve.<sup>5</sup> We did not observe size excitation above the  $1S_{3/2}-1S_e$  transition because of the overlap between the different absorption peaks.

For the low-frequency scattering, in the long-wavelength approximation and for spherical particles, several acoustical modes are allowed from a group theory point of view.<sup>3</sup> Their energy dependence follow the law:  $E = \frac{Sv_l}{2a}$  where  $a$  is the particle radius and  $v_l$  is the longitudinal sound speed. The different values of  $S$  are given in Table I for CdSe nanocrystals.



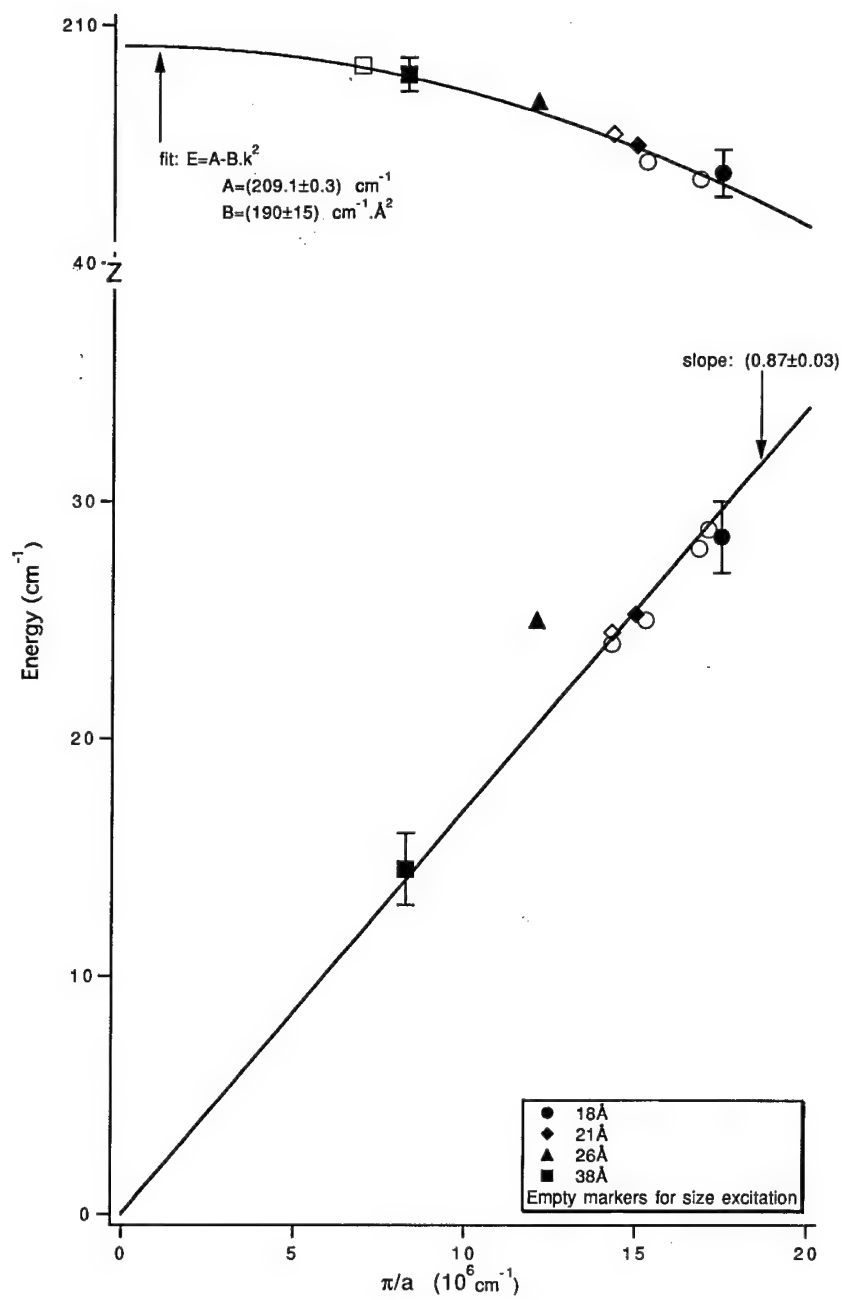


FIGURE 2 Peak positions of optical and acoustical Raman peak as a function of  $\pi/a$ . Empty markers are used when excited size is different from the mean size of the sample. The solid lines are fitting curves with the models described in the text.

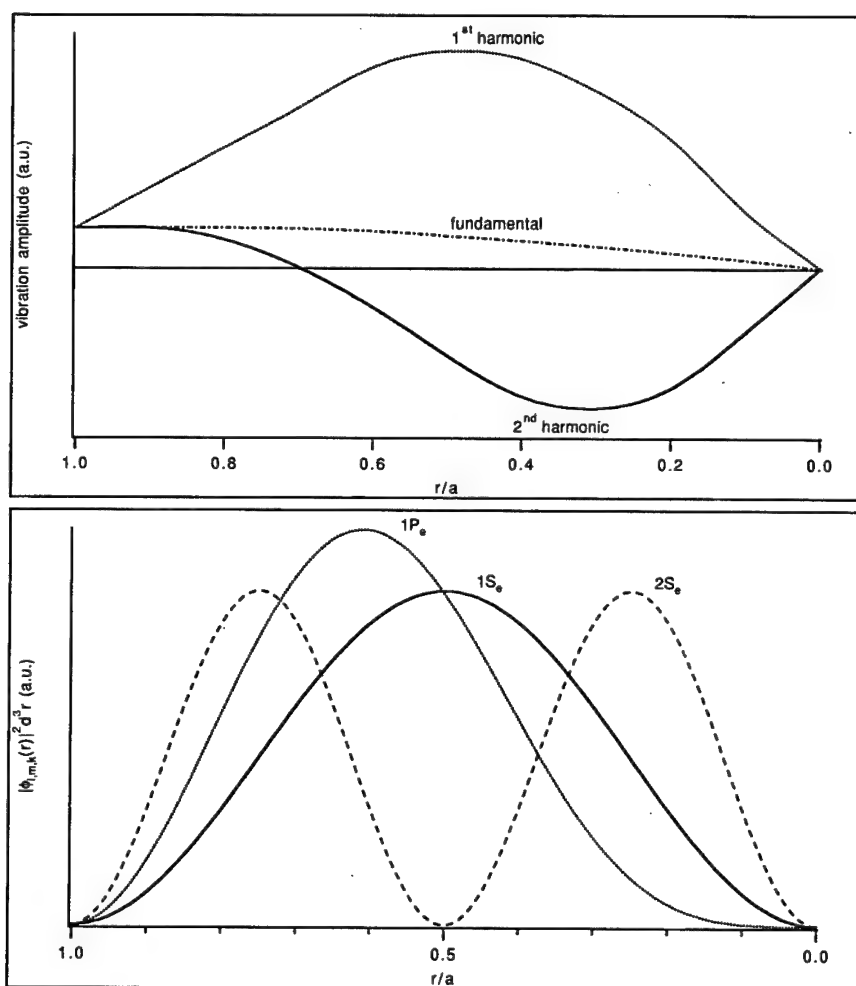


FIGURE 3 Vibration amplitude of the ellipsoidal fundamental and first two harmonics modes as a function of the distance from the centre of the particle (upper plot). The second plot represents the probability to find the electron at distance  $r$  from the centre of the particle for  $1S_e$ ,  $1P_e$  and  $2S_e$  levels.

Table I

mode	fundamental	1st harmonic	2nd harmonic
spherical	0.91	1.96	...
ellipsoidal	0.35	0.65	1.1

The scattering by spherical modes is polarized: it is observed when the scattered and incident polarizations of light are not crossed. The scattering by ellipsoidal modes is unpolarized.

The lowest frequency peak is plotted in Figure 2 as a function of size. The depolarization ratio of this peak is close to 0.5 and its position is well fitted with  $S \approx 0.9$ . Thus it seems to be the superposition of the fundamental of the spherical mode and the first and second harmonics of the ellipsoidal modes. A second polarized line was found and is fitted with  $S \approx 1.5$ . This line arises from the fundamental and first harmonic of the spherical mode. All these results show the importance of inner modes in resonant Raman scattering.

When exciting further into the absorption band, different modes are observed. This kind of experiment was made with the CdSe sample whose radius is 38 Å. When exciting with the Krypton 530.9 nm and the Argon 514.5 nm laser lines an unpolarized peak is seen which corresponds to  $S \approx 0.6$ , and a small polarized part with  $S \approx 0.9$ . These modes are the first harmonic of the ellipsoidal mode and the fundamental spherical mode. With the 476.5 nm Argon laser line, only the fundamental spherical mode is seen. The Argon 488 nm laser line reveals the fundamental spherical mode and the first harmonic of the ellipsoidal mode. For excitation near the band edge, the modes have been described above. To explain this behaviour, we have to compare the shapes of the electron and hole presence probability for the resonant levels and the acoustical vibration amplitudes inside the particle. Figure 3 shows these curves for the three first electronic levels and the first harmonics of the ellipsoidal mode. The coupling is expected to be important if the electron is located near the points where the vibration amplitude is important. For example, few coupling is expected with the fundamental ellipsoidal mode who has a maximum near the surface where the electronic wave functions are zero. No scattering from this mode has been seen. Of course, the hole wave function should be taken into account to say that no scattering from this mode is possible. On the other hand, a great coupling is expected between the first harmonic of the ellipsoidal mode and the  $1S_e$  and  $1P_e$  levels, the three associated curves having a maximum near the same position. To make this argument more quantitative, the real resonant states should be known with more precision and excited with a dye laser for example.

Another example of the importance of the excitation laser line is found in the RG630 sample case. For CdSe samples, no signal (LO or low-frequency) was found when exciting in the gap. For RG630, a huge polarized signal corresponding to the fundamental spherical mode was found when exciting with the Krypton 647 and 676 nm laser line, while the LO peak was weak (647 nm) or absent (676 nm). The excitation seems to be resonant with levels other than those seen previously. Low temperature luminescence experiments reveal a peak at  $450 \text{ cm}^{-1}$  with the 676 nm excitation. This peak is caused by defects in the particles. At room temperature, the red lines of the krypton laser are resonant with this level. The defects are probably surface defects which would explain their strong coupling with the fundamental spherical mode which has a maximum amplitude at the surface. For excitation inside the absorption band, the same kind of spectra as for CdSe are obtained.

### 3 CONCLUSION

Resonant Raman scattering seems to be a very powerful tool to study vibrations properties in  $\text{CdS}_x\text{Se}_{1-x}$  quantum dots. First, it is possible to link the position of the LO peak with the dispersion curve of bulk crystal. Second, different acoustical modes have been seen in the same particle when varying the excitation wavelength into the absorption structure, these modes having different coupling with the different electron-hole pair states. A strong coupling with defects states is also possible.

## REFERENCES

1. A. I. Ekimov, F. Hache, M. C. Schanne-Klein, D. Ricard, C. Flytzanis, I. A. Kudryavtsev, T. V Yazeva, A. V. Rodina and Al. L. Efros *JOSA* **B10**, 100 (1993).
2. see for example M. C. Klein, F. Hache, D. Ricard and C. Flytzanis, *Phys. Rev.* **B42**, 11123 (1990).
3. E. Duval, *Phys. Rev.* **B46**, 5795 (1992).
4. Al. L. Efros and A. V. Rodina, *Solid State Commun.* **72**, 645 (1989).
5. R. Purlis and I. Yakimavichus, *Izvestia Vusov USSR (Physica)* **N3**, 98 (1987).

## NANOCRYSTALLINE COPPER DOPED ZINC OXIDE GAS SENSORS

ALAN V. CHADWICK, ANNETTE HARSCH, NIGEL V. RUSSELL, KIM F. TSE,  
ADAM R. WHITHAM and ALAN WILSON

*Centre for Materials Research, Chemical Laboratory, University of Kent,  
Canterbury CT2 7NH, UK*

Samples of nanocrystalline Cu doped ZnO have been prepared and characterised by several techniques including chemical analysis, X-ray powder diffraction and X-Ray absorption spectra (EXAFS). The particle sizes are typically less than 100 Å on the largest diameter. The diffraction results show that lightly doped samples, less than 10 mole per cent Cu, are single phase with the ZnO crystal structure. The EXAFS results indicate that although the Zn<sup>2+</sup> ions occupy normal cation sites the Cu<sup>2+</sup> ions are in highly disordered sites, suggesting that there is possible surface aggregation. Gas sensing experiments show a good response to low ppm concentrations of toluene vapour.

*Key words:*- Nanocrystals, doped zinc oxide, EXAFS, gas sensing.

### 1 INTRODUCTION

Nanophase materials, systems in which the particle size is the order of nanometres, are the subject of intense current research activity.<sup>1-4</sup> The interest arises from the fact that the physical and chemical behaviour of these materials can be very different from their normal, larger dimensioned parents. Examples of properties that are altered include the electrical, magnetic, optical and mechanical characteristics and some applications of nanostructured materials include improved catalysts, malleable ceramics, harder metals, and ferrofluids. The origin of these properties is believed to be related to the presence of large area, disordered interfaces that may constitute up to 50% by volume of the sample. However, the physical understanding of the modification of these properties and sample characterisation considerably lags behind the synthetic chemistry of these materials. Our particular interest is the potentially enhanced gas-sensing capabilities of nanocrystalline semiconducting metal oxides; advantages enhanced by the low temperature fabrication techniques and high proportion of grain boundaries.

In recent work<sup>5</sup> we have prepared gas sensors from nanocrystalline zinc oxide (ZnO) and characterised the material by X-ray powder diffraction (XRPD), transmission electron microscopy (TEM) and extended X-ray absorption fine structure (EXAFS). Crystals of ZnO were produced with the hexagonal wurtzite structure with typical dimensions of approximately 50 Å in the 100 direction and 30 Å in the 002 direction. The Zn K-edge EXAFS indicated reduced coordination numbers beyond the first shell, consistent with the particle size, i.e. the first cation shell contained ~ 8 Zn ions compared to 12 in the bulk material. We are now extending these studies to cation doped metal oxides with the aim of altering the electrical, and hence gas sensing, properties and we are using the same range of characterisation techniques. In this contribution we will focus on the synthesis and properties of copper (Cu) doped ZnO.

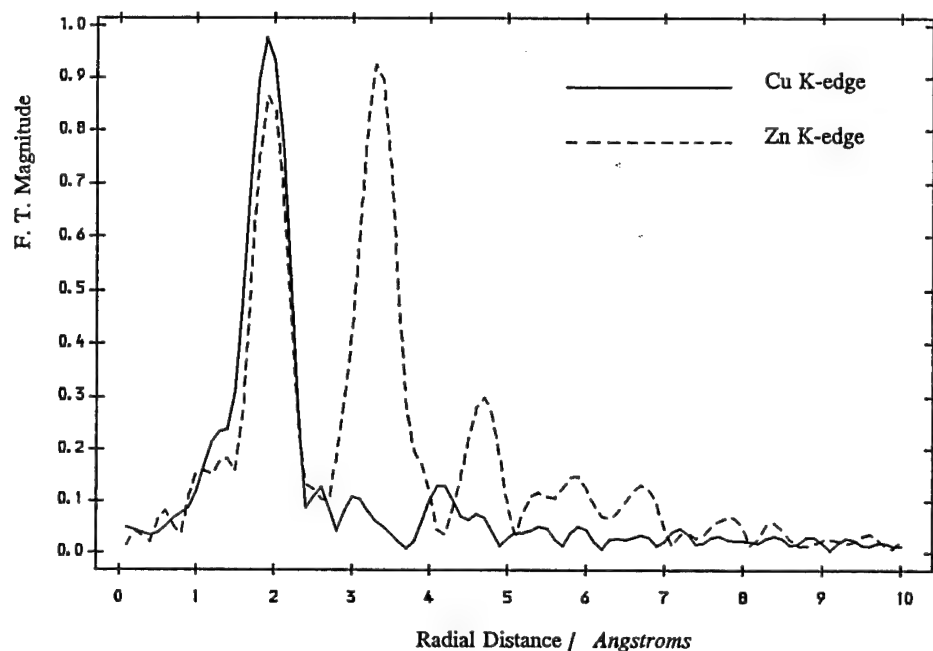


FIGURE 1 Fourier transforms of the EXAFS of 3 mole per cent Cu doped nanocrystalline ZnO; Zn K-edge(---) and Cu K-edge(\_\_\_\_\_).

## 2 EXPERIMENTAL

### 2.1 Materials

Samples of nanocrystalline ZnO can be prepared by reacting the basic chlorides with *n*-butylamine.<sup>5,6</sup> The basic chloride,  $\beta$ -Zn(OH)Cl is prepared by slow evaporation of a solution of ZnO(0.5 g) in 15 ml of 11 M aqueous ZnCl<sub>2</sub> solution at 80°C. We have found<sup>7</sup> that by adding other metal chlorides (e.g. copper and nickel chloride) to the ZnCl<sub>2</sub> in this first stage will yield ZnO samples that are appropriately cation doped. The level of doping in the final oxide is similar to that in the ZnCl<sub>2</sub> solution, for example a 5 mole per cent addition of CuCl<sub>2</sub> yielded ZnO that was 3 mole per cent Cu doped (as determined by atomic absorption spectroscopy).

### 2.2 XRPD

XRPD patterns were collected to test the phase purity and the particle sizes of the crystals. Samples of nominally 5 and 10 mole per cent Cu doped ZnO showed only peaks corresponding to ZnO. The peaks were considerably broadened and an analysis of the widths using the Scherrer formula indicated that the nanocrystals were asymmetric with dimensions  $\sim 80$  Å in the 100 direction and  $\sim 50$  Å in the 002 direction for both doping levels.

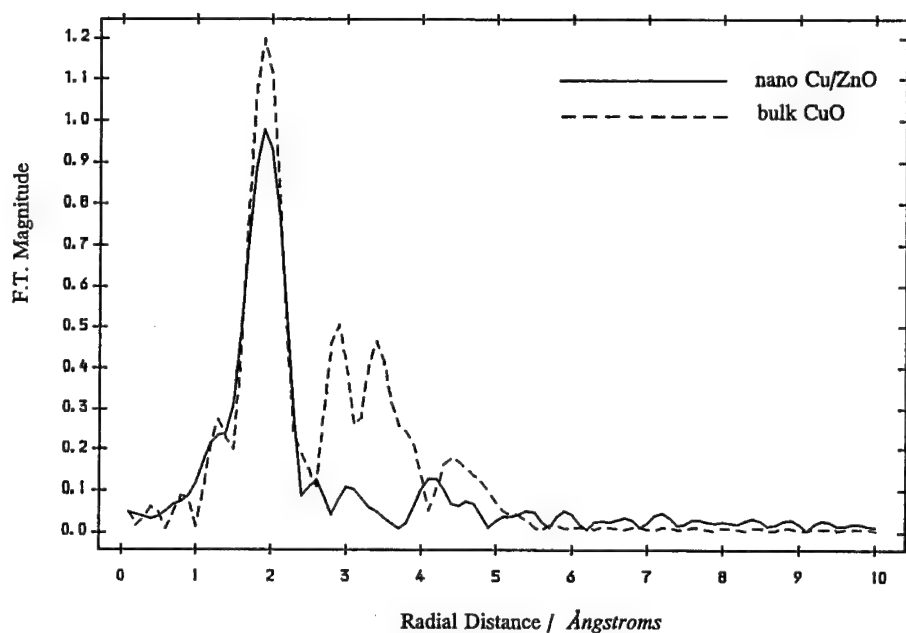


FIGURE 2 The Fourier transforms of Cu K-edge EXAFS; bulk CuO (---) and nanocrystalline Cu doped ZnO (—).

### 2.3 EXAFS

Zn and Cu K-edge EXAFS data were collected on station 7.1 at the EPSRC Daresbury Synchrotron Radiation Source (SRS) using transmission mode at room temperature. The radiation was monochromated by a Si(111) two crystal order-sorting monochromator to give rejection of harmonic components. Spectra were recorded up to 1000 eV beyond the absorption edge (i.e. to  $k = 16 \text{ \AA}^{-1}$ ). The samples were prepared by pressing the powdered samples with a diluent (boron nitride or polythene). The data reduction and analysis were performed with the Daresbury suite of EXAFS programmer,<sup>8</sup> EXCALIB, EXBACK and EXCURV92. Bulk ZnO and CuO were used as model compounds. The quantitative fitting of the data utilised the phase shifts calculated and the non-linear least-squares fitting routines within EXCURV92.

### 2.4 Gas Sensing

Sensors were fabricated by a solvent evaporation method onto alumina substrates fitted with gold electrodes and a platinum heater (Rosemount Ltd, Bognor Regis, UK). These were mounted in a testing rig consisting of either cylinder gases, the concentrations of which could be controlled using mass flow controllers, or a toluene permeation system where a steady flow of air over a toluene permeation vial maintained in a water bath at 30°C could be blended with variable flows of clean air which, after suitable calibration, could provide a range of toluene concentrations. All control and data acquisition functions were handled by a PC with suitable interfaces.

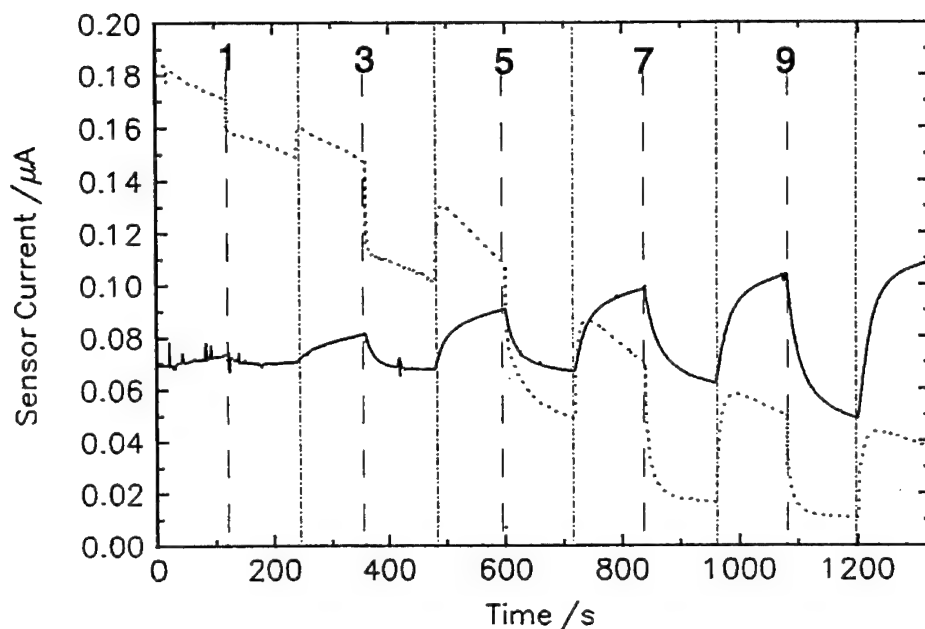


FIGURE 3 Response of nanocrystalline 0.14 mole per cent Cu doped ZnO sensor to toluene. The solid line is the response at 200°C and the dotted line the response at 400°C. The vertical dashed line represents the input of test gas, the numbers being the ppm of toluene in air. The vertical chain lines represent the input of clean air.

### 3 RESULTS AND DISCUSSION

The structural results for a 3 mole per cent Cu doped sample will be discussed in detail as they are representative of all samples with nominal dopings up to 10 mole per cent Cu. The Fourier transform of the Zn K-edge EXAFS is plotted in Figure 1 and it is similar to the corresponding plot<sup>5</sup> for nanocrystalline, pure ZnO. There are distinguishable peaks out to at least 8 Å at the same radial distances observed in bulk ZnO, however the intensities of all but the first peak are considerably reduced. The best fit model indicates the first two peaks are due to 4 O atoms (1.96 Å) and 10.1 Zn atoms (3.23 Å). For pure, bulk ZnO the EXAFS data agree well<sup>5</sup> with the diffraction data with 4 O atoms (1.96 Å) and 12 Zn atoms (3.24 Å). The reduction in the Zn-Zn coordination number in the present sample is consistent with the size of the nanocrystals.

The Fourier transform of the Cu K-edge EXAFS results for the 3 mole per cent Cu doped ZnO is shown in Figures 1 and 2. In contrast to the Zn EXAFS there are no major peaks beyond the first peak. The best fit model indicates this peak is due to 3.9 O atoms (1.97 Å). For comparison the Cu K-edge EXAFS for pure, bulk CuO is also plotted in Figure 2 and the best fit model for these data is 4 O atoms (1.95 Å), 2 O atoms (2.79 Å), 4 Cu atoms (2.92 Å) and 4 Cu atoms (3.11 Å); parameters which are close to the diffraction data.<sup>9</sup>

The striking feature of Figures 1 and 2 is the presence of only one peak in the Cu EXAFS of the nanocrystals. The fit of this peak to ~ 4 O atoms at 1.97 Å is consistent with Cu present as Cu<sup>2+</sup>, as is the absence of the distinctive pre-edge feature from Cu<sup>+</sup> in the raw EXAFS<sup>7</sup>. The absence of peaks due to Cu-cation shells is not due to particle size



as the two Cu peaks (at 2.92 and 3.11 Å in bulk CuO) are only slightly reduced in intensity in the EXAFS of 60 Å diameter nanocrystals of CuO.<sup>7</sup> Possible explanations<sup>10</sup> of reduced peak intensity in the EXAFS Fourier transform are atoms in disordered sites or at surface regions. Currently we favour the latter explanation, which is supported by parallel studies<sup>11</sup> of Ni doped nanocrystalline ZnO where the Ni K-edge EXAFS exhibits a distinct peak due to a shell of cations.

The response of a 0.14 mole per cent Cu doped ZnO nanocrystalline sample to low levels of toluene in air is shown in Figure 3. The sensor was subjected to two minute pulses of polluted air followed by two minute pulses of clean air. The toluene concentration was at levels of 1, 3, 5, 7 and 9 ppm. It can be seen that at 200°C the response increases almost linearly with toluene concentration but the response time (i.e. the time for the current to reach equilibrium values) is slow, around 60 s. At 400°C the response is much faster although there is evidence of saturation at the higher concentrations; the responses at 7 and 9 ppm toluene are almost the same magnitude. The effect of dopant concentration on response and the optimisation of the temperature is currently under investigation.

#### 4 CONCLUSIONS

We have shown that nanocrystalline ZnO can be prepared with addition of Cu<sup>2+</sup> ions up to a concentration around 10 mole per cent and that these dopant ions are in highly disordered sites, probably in the surface regions of the nanocrystals.

#### ACKNOWLEDGEMENTS

The authors are grateful to Dr. R. H. Jones (University of Keele) and Dr. G. Sankar (Royal Institution) for assistance with the XRD studies and to Daresbury staff for assistance with the EXAFS.

#### REFERENCES

1. R. W. Siegel, *Physics Today*, p. 64 (October 1993).
2. H. Gleiter, *Advanced Materials*, **4**, 474 (1992).
3. M. Nastasi, D. M. Parkin and H. Gleiter, eds, '*Mechanical Properties and Deformation Behaviour of Materials having Ultra-fine Microstructures*', NATO-ASI Series E, Vol 233 (Kluwer, Dordrecht, 1993).
4. S. Komarneni, J. C. Parker and G. J. Thomas, eds, '*Nanophase and Nanocomposite Materials*', MRS Conference Proceedings, Vol. 86 (1993).
5. A. V. Chadwick, N. V. Russell, A. R. Whitham and A. Wilson, *Sensors and Actuators B*, **18-19**, 99 (1994).
6. O. Garacía-Martínez, R. M. Rojas, Vila, E. and Martín de Vidales, J. L., *Solid State Ionics*, **63-65**, 442 (1993).
7. A. R. Whitham, *M. Sc. thesis*, University of Kent, 1993.
8. C. Morrel, J. T. M. Baines, J. C. Campbell, G. P. Diakun, B. R. Dobson, G. N. Greaves, and S. S. Hasnain, *EXAFS Users' Manual*, Daresbury Laboratory, Warrington WA4 4AD, U. K., (1986).
9. S. Asbrink and L. J. Lorrby, *Acta Cryst. B*, **26**, 8 (1970).
10. A. V. Chadwick, *Solid State Ionics*, **63-65**, 721 (1993).
11. N. V. Russell, A. V. Chadwick and A. Wilson, *Nucl. Instr. and Methods B*, (in press).

## CLUSTERING IN NaCl:Pb

K. POLAK, M. NIKL and K. NITSCH

*Institute of Physics, Czech Academy of Sciences, Cukrovarnicka 10, 162 00 Prague 6*

Absorption and emission spectra of impurity clusters and precipitates in NaCl:Pb have been measured. The results from emission kinetics measurements reveal a complicated behaviour in the 330 nm band usually ascribed to PbCl<sub>2</sub>-like phase. The band with a maximum at 380 nm appears in the emission spectrum of this crystal after fast quenching from 500°C to RT. The corresponding lifetime is close to the value of isolated lead centres. We suggest that it belongs to small lead clusters with NaCl structure.

*Key words:* alkali halides, precipitates, absorption, luminescence, emission kinetics.

### 1 INTRODUCTION

The formation of a foreign phase in doped alkali halide crystals was an unwanted phenomenon for a long time. The presence of aggregates was usually an obstacle in the precise investigation of isolated impurity optical properties. The NaCl crystal is a matrix with a very strong inclination to formation of aggregates and precipitates. At present the interest turns much more to the study of optical properties of small foreign phase inclusions usually called micro- or nanocrystals.

The published emission spectra of NaCl:Pb crystals with a low concentration of lead (a few tens ppm) consists of two main bands peaking at 310 and 380 nm, respectively. The first one is attributed to isolated lead-vacancy dipoles (the simplest defect centre of divalent impurity in alkali halide crystals). The second one has been ascribed to Pb<sup>2+</sup> small clusters with some doubts about their size (R. Capelletti *et al.*<sup>1</sup> ascribed the 380 nm emission to lead dimers, P. Aceituno *et al.*<sup>2</sup> assigned it to isolated lead ions perturbed by some other divalent impurity, F. Cusso *et al.*<sup>3</sup> ascribed it to the second JT minima on the APES of the <sup>3</sup>T<sub>1u</sub> level etc.).

We have given our attention to NaCl crystal doped with divalent lead as some previous results indicated the formation of PbCl<sub>2</sub> - like phase in it.<sup>4,5</sup> The purpose of this work is to provide an additional insight in the origin of the 380 nm emission and allow us to give an answer on the question whether small precipitates emit in the same region as well.

### 2 EXPERIMENTAL

NaCl crystals with different concentrations of lead ( $0.5 \times 10^{-3}$ ,  $1 \times 10^{-3}$  and  $20 \times 10^{-3}$  mol/mol) have been grown in our technological laboratory either by the Stockbarger/Bridgman method (the first one) or by the Kyropoulos method in an argon protective atmosphere (the other two). All the crystals were stored at room temperature for a long time. The last two as received crystals are milky as a result of large precipitates. The polycrystalline PbCl<sub>2</sub> layer was prepared by evaporation of a small piece of PbCl<sub>2</sub> crystal on a NaCl substrate.

Absorption spectra at different temperatures were obtained with a spectrometer Specord M40 of Zeiss Jena. Luminescence spectra and emission kinetics were measured at low temperatures with a modified Edinburgh spectrofluorometer model 199.

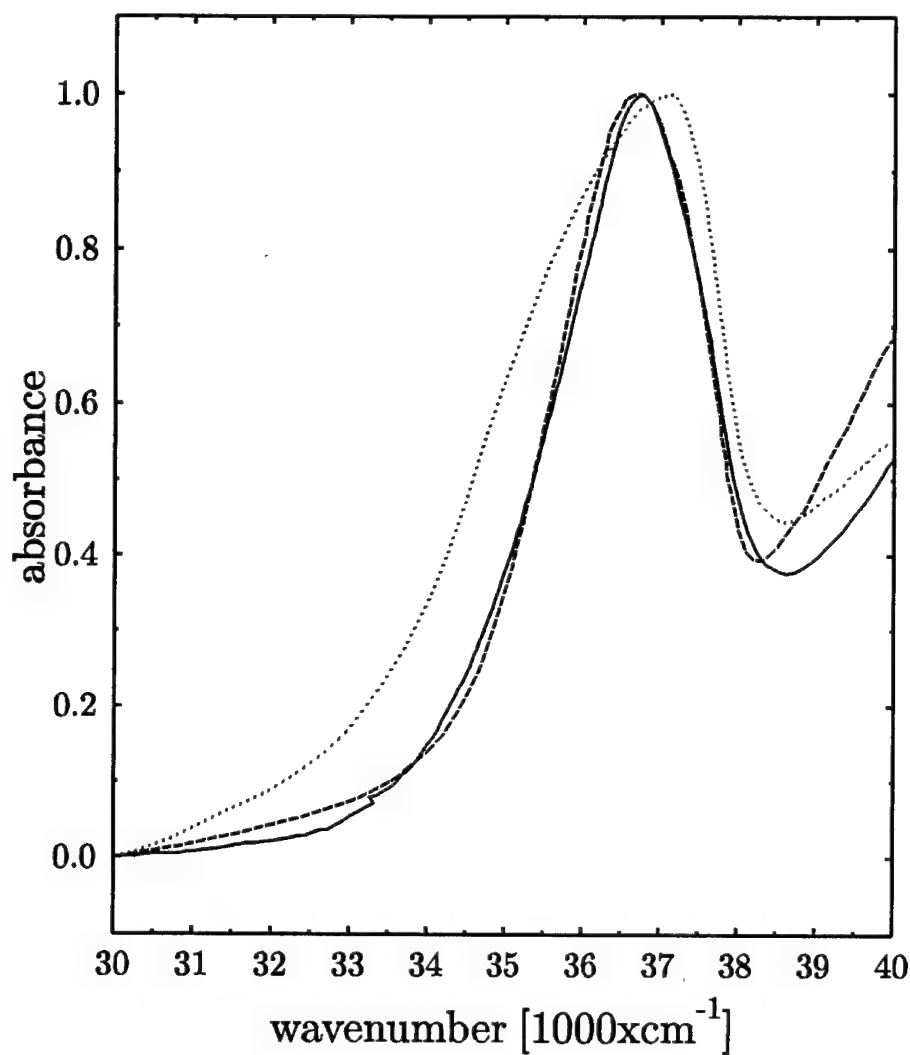


FIGURE 1 Absorption spectra of stored NaCl:Pb (0.05 mol%)-solid line, NaCl:Pb (0.1 mol%)-dotted line, PbCl<sub>2</sub> film on NaCl crystal-dashed line in A band spectral region.

The samples from the crystals were cleaved. The annealing was performed in a furnace using a closed evacuated ampoule allowing the fast quenching to room temperature.

### 3 RESULTS AND DISCUSSION

The absorption of as-received and long stored NaCl:Pb crystals (both lower concentration investigated by us) shows the already known absorption in A-band region. The band shape at RT is asymmetric and its course is very similar to the absorption of a PbCl<sub>2</sub> thin film

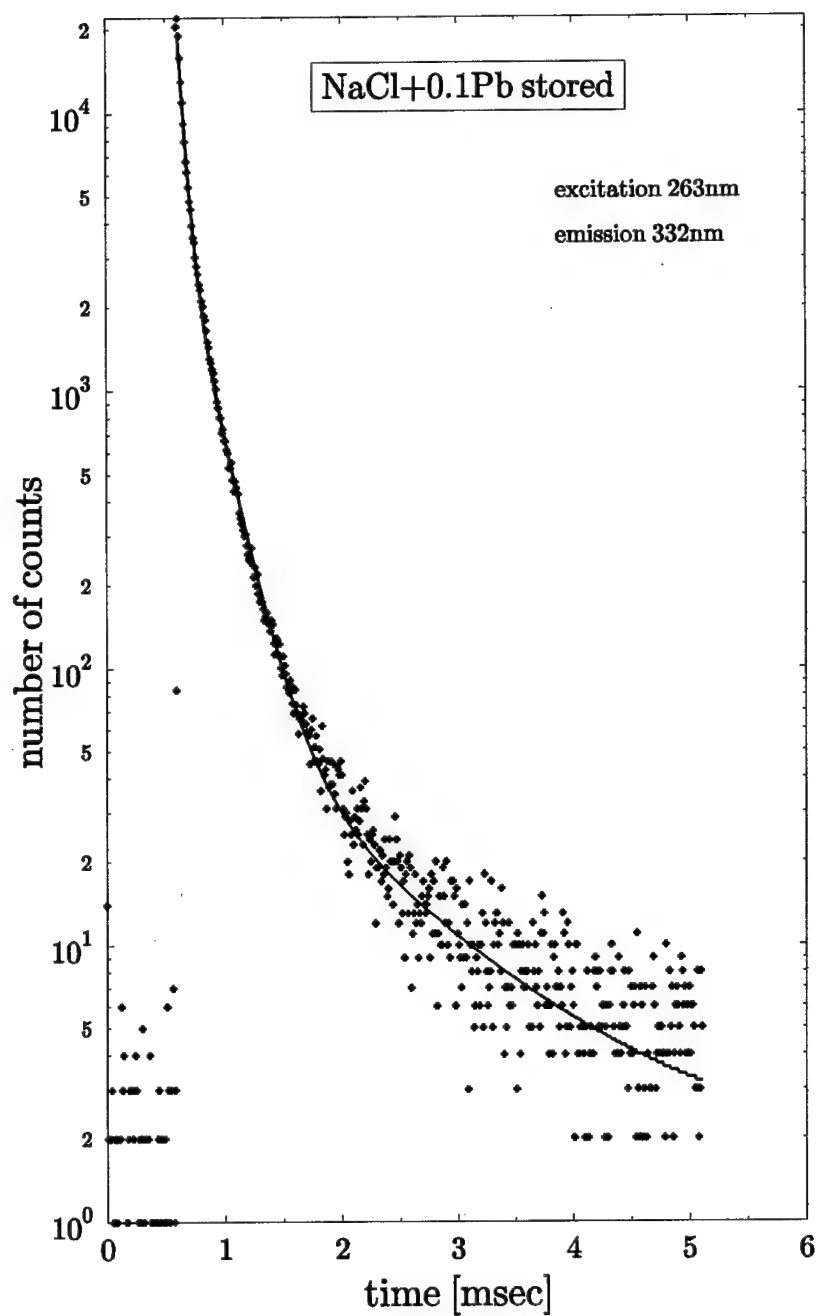


FIGURE 2 Decay of 332 nm emission of stored NaCl:Pb (0.1 mol%). The solid line is the best fit by a sum of three gaussians with  $\tau_1 = 56 \mu\text{sec}$ ,  $\tau_2 = 217 \mu\text{sec}$  and  $\tau_3 = 1.1 \text{ msec}$ .

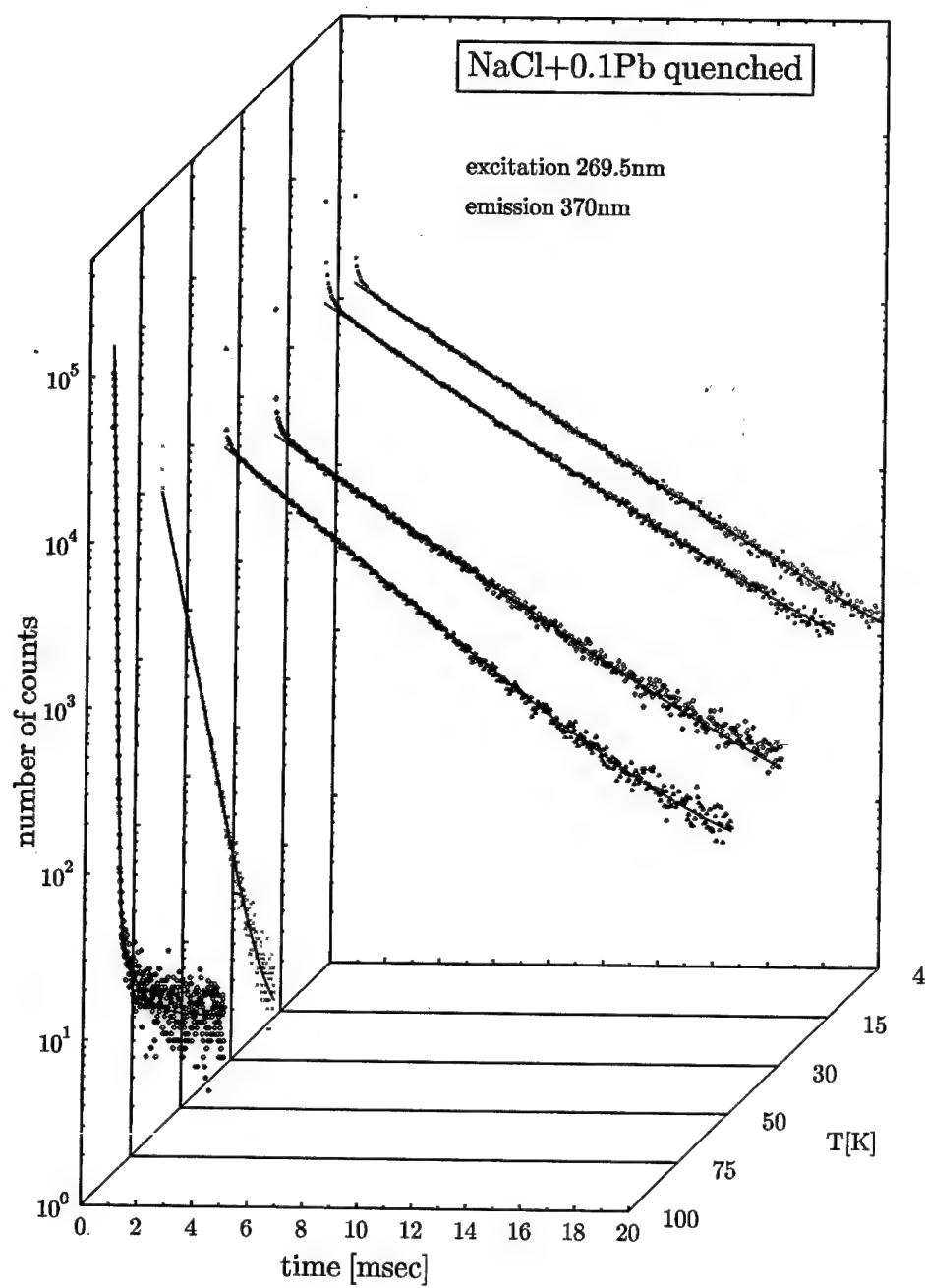


FIGURE 3 Temperature dependence of the decay curve of the 370 nm emission for quenched NaCl:Pb (0.1 mol%).

(Figure 1). By the decomposition of the absorption spectrum belonging to NaCl:Pb (0.05 mol%) we have found three components around the spectral position of A band (Table I).

Table I

Gaussian components of the absorption in A band region of longtime stored NaCl:Pb (0.05 mol%) crystal (RT)

Peak position [1000 cm <sup>-1</sup> ]	Halfwidth [cm <sup>-1</sup> ]
36.57	990
35.02	700
37.25	665
33.90	930

The A band is followed by fast increasing absorption on the high energy side. This is due to the existence of large precipitates in the crystals. By the comparison with the published absorption spectra for 390Å and 460Å radius of PbCl<sub>2</sub> spheres<sup>6</sup> we can estimate the size of our aggregates to similar values i.e. some tens of nanometers. In such large aggregates the behaviour of an exciton will be close to that in a bulk crystal. Therefore, we can expect optical properties similar to those of the Frenkel exciton in a PbCl<sub>2</sub> crystal.<sup>7</sup> This is true for the steady state luminescence spectra where two main emission bands peaking at 330 and 410 nm were observed. The kinetics of the 330 nm emission is much more complicated than for pure bulk PbCl<sub>2</sub> crystal (Figure 2). We have found three components in the mentioned emission with the lifetimes equal to 57 μsec, 217 μsec and 1.1 msec. As the slowest component is only a small part of the integrated intensity we assume that it comes from some number of isolated lead centres existing even in the stored crystals. The faster components could be connected with small microcrystals of PbCl<sub>2</sub> – like phase where the size has yet the influence on the decay characteristics.

After the crystal quenching the emission spectrum changes considerably. We have observed two main bands peaking at 312 and 378 nm with the second one dominating. There are two other weak bands which spectral position coincide with the mentioned bands of PbCl<sub>2</sub> bulk crystal observed at LHeT. The emission band peaking at 378 nm persists with relatively high intensity up to room temperature. The corresponding kinetics can be well described by a single exponential with  $\tau \cong 4$  msec at LHeT. The temperature dependence of the decay curve up to 100 K is shown in Figure 3. The shortening of this decay starts above 50 K, but the corresponding amplitude increases. This fact is displayed by the very slow decrease of its intensity. The probable origin of this band is the presence of very small clusters of Pb<sup>2+</sup> with sodium chloride structure. The second band peaking at 312 nm at LHeT belongs probably both to these clusters and isolated dipoles consisting of divalent lead and a cation vacancy. The origin of 378 band would be the second JT minimum of the adiabatic potential energy surface of <sup>3</sup>T<sub>1u</sub> term in agreement with the results published previously.<sup>5</sup>

The annealing of the quenched crystal at 200°C for 1/2 hour enhanced the intensity of 312 nm emission and reduced the intensity of 378 nm emission. This could be explained by the creation of larger precipitates from small clusters while the concentration of isolated dipoles remains nearly constant.

We have shown some interesting properties of impurity clusters and a foreign phase arising in sodium chloride crystal with a higher concentration of divalent lead. The great variety of the observed optical properties could be connected with the fact that in the excited states of Pb<sup>2+</sup> the dynamical Jahn-Teller effect plays a significant role.

## REFERENCES

1. R. Capelletti, U. Emiliani, J. Garcia Solé, M. Manfredi, *Sol. St. Comm* **46**, 531 (1983).
2. P. Aceituno, F. Cussó, F. Jaque, F. Agulló-López, *Sol. St. Comm.* **51**, 525 (1984).
3. F. Cussó, F. Jaque, J. L. Martinez, F. Agulló-López, *Phys. Rev.* **B31**, 5437 (1985).
4. C. Zaldo, J. Garcia Sole, F. Agullo-Lopez, *J. Phys. Chem. Solids* **43**, 837 (1982).
5. C. Zaldo, J. Garcia Solé, E. Diégues, F. Agulló-López, *J. Chem. Phys.* **83**, 6197 (1985).
6. M. Fayet-Bonnel, *Phys. Stat. Sol.* **B60**, 713 (1973).
7. K. Polak, D. J. S. Birch, M. Nikl, *Phys. Stat. Sol.* **B145**, 741 (1988).
8. M. Nikl, D. J. S. Birch, K. Polak, *Phys. Stat. Sol.* **B165**, 611 (1991).

## OPTICAL STUDY OF THE PHASE SEPARATION IN ALKALI HALIDE SOLID SOLUTIONS

MASAMI INABA and SATOSHI HASHIMOTO

*Department of Physics, Kyoto University of Education, Fukakusa, Fushimi-ku,  
Kyoto 612, Japan*

Thin crystals of  $\text{Na}_{1-x}\text{K}_x\text{I}:\text{Tl}^+$  solid solutions with thicknesses of  $0.1 \sim 10 \mu\text{m}$  have been produced and their phase separation has been observed in both regions of the exciton band and  $\text{Tl}^+$  impurity band. An intermediate band of  $\text{Tl}^+$  was recognized in the absorption spectrum of  $\text{Na}_{0.5}\text{K}_{0.5}\text{I}:\text{Tl}^+$ . A precursor phenomenon was found as a temporal change of the intensity ratio of two  $\text{Tl}^+$  emission bands.

### 1 INTRODUCTION

Microscopic mechanism of the phase separation occurring in alkali halide solid solutions has not been studied at all because they become to be opaque after the phase separation. The opacity is caused by a mesoscopic multi-domain structure. In order to study the phase separation optically, thin  $\text{Na}_{1-x}\text{K}_x\text{I}$  crystals with thicknesses of  $0.1 \sim 10 \mu\text{m}$  were grown from the melt. This system having 9.3% lattice misfit is decomposed at around  $240^\circ\text{C}$  when the crystals are cooled down in the quasi-static process.<sup>1</sup>

Since the thin crystals were cooled very rapidly they can be kept in non-equilibrium solid solutions for a long time. The crystals contain about 0.1 mole %  $\text{Tl}^+$  which can be expected to be a 'micro-probe' for the phase separation when the ion substitutes for an alkali ion in the solid solutions.

### 2 EXPERIMENTAL

Details and applications of the melt-growth of thin crystals have already been reported<sup>2</sup> and are not mentioned here. The sample specimens were kept in vacuum at room temperature. When optical measurement was made, the sample was mounted on the copper holder of a conduction-type cryostat, and cooled to 11 K by a closed-cycle cryogenic refrigerator.

### 3 RESULTS AND DISCUSSION

Figure 1 shows reflection spectra of the lowest exciton of a thin  $\text{Na}_{0.5}\text{K}_{0.5}\text{I}:\text{Tl}^+$  crystal. Just after the preparation, a single exciton band can be seen on the curve a. After several days, two bands appeared at 5.61 eV and 5.80 eV, as shown on the curve b, corresponding to NaI-rich and KI-rich phases, respectively. Curves b and c were measured in the midst of and after the separation. Similar changes were also observed in the undoped samples.

A-bands of  $\text{Na}_{0.5}\text{K}_{0.5}\text{I}:\text{Tl}^+$  are indicated in Figure 2, where three steps of measurements correspond to those of Figure 1. Curve a shows a broad A-band in the solid solution. In the midst of the phase separation, three bands appeared on the curve b. The central peak decreased with increase of the outer two bands with lapse of the time. The two bands locate almost same positions of A-bands of  $\text{NaI}:\text{Tl}^+$  and  $\text{KI}:\text{Tl}^+$  from lower energy side.



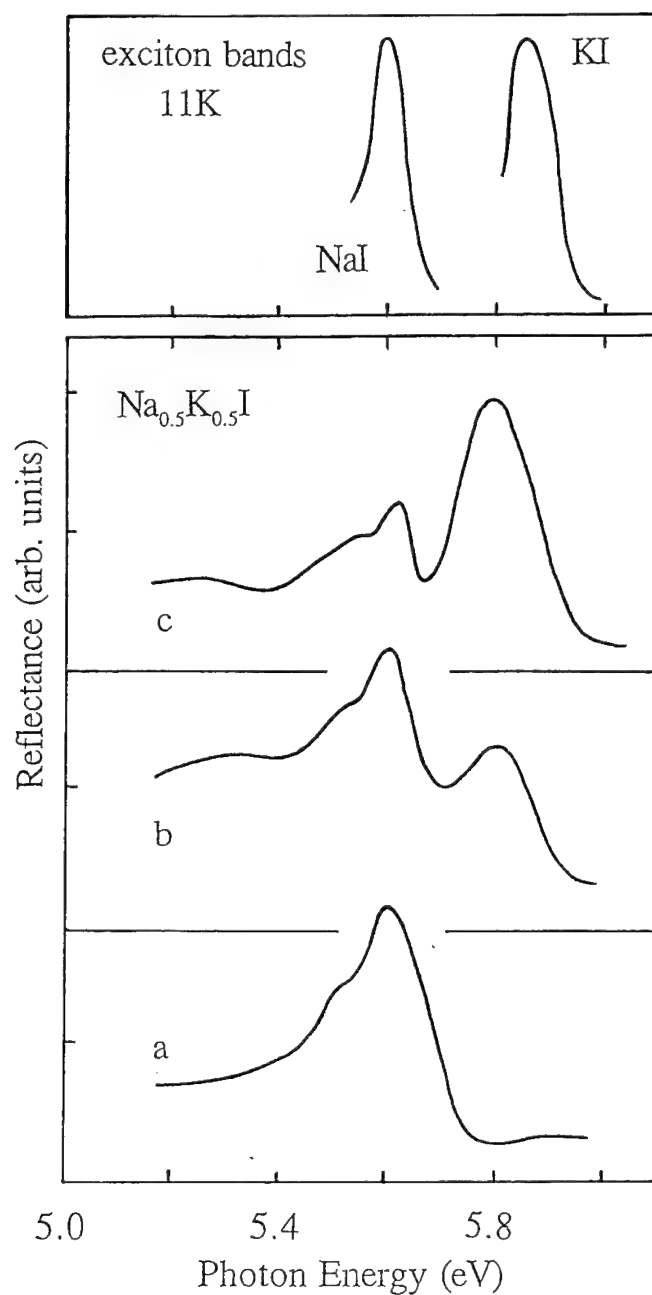


FIGURE 1 Reflection spectra of the lowest exciton of a thin  $\text{Na}_{0.5}\text{K}_{0.5}\text{I}:\text{Ti}^+$  crystal measured just after the preparation (curve a), in the midst of (curve b) and after the phase separation (curve c). Exciton bands of pure NaI and KI are also shown on the upper part of the figure.

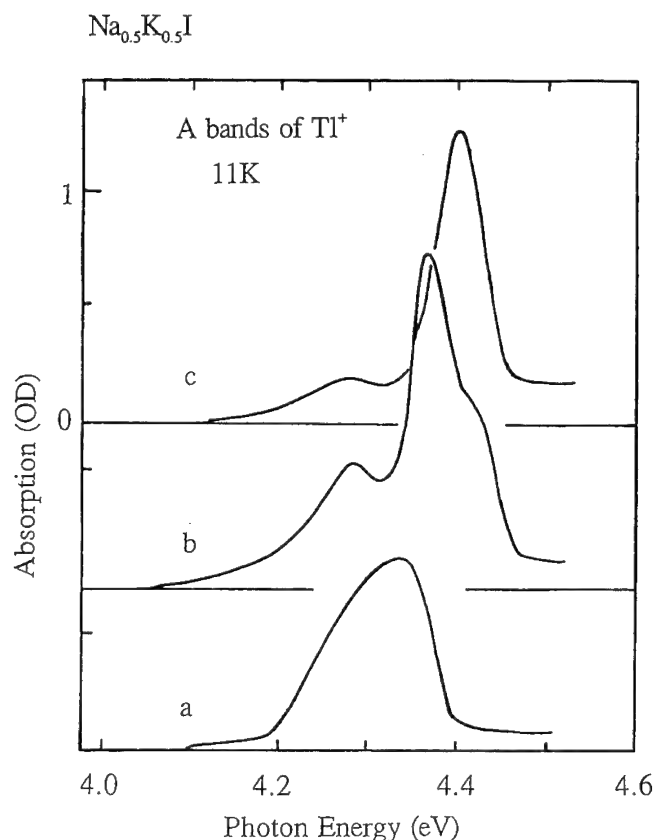


FIGURE 2 A-absorption bands of  $\text{Tl}^+$  of the thin  $\text{Na}_{0.5}\text{K}_{0.5}\text{I}:\text{Tl}^+$  crystal, where three steps of measurements are corresponded to that of Figure 1.

After the separation in curve c, a large difference in intensity between them is consistent with the fact that  $\text{Tl}^+$ -molar extinction coefficient in KI is about 10 times as large as that in NaI.

Two emission bands,  $A_T$  at higher energy and  $A_X$  at lower energy, induced by the excitation at coinciding energy with A-bands are also shown in Figure 3. The measurement steps (a, d, f) in this figure correspond to steps (a, b, c) of Figures 1 and 2. Intensity ratio  $A_X/A_T$  of the solid solution is more than 10 times larger than that of pure KI and NaI crystals. The ratio increased gradually for several days in curves b and c, and then decreased with accompanying discontinuous energy shift when the separation begins to occur in curve d.

The intermediate A-band shown in curve b of Figure 2 suggests that a specific state of  $\text{Tl}^+$  exists in the midst of the phase separation. Increase of the ratio  $A_X/A_T$  means lowering of the symmetry of ligand configuration,<sup>3</sup> and the change observed before the phase separation in curves b and c of Figure 3 is regarded as a precursor phenomenon. There are many problems which must be clarified to make clear the mechanism. We plan experiments for determination of the domain size.

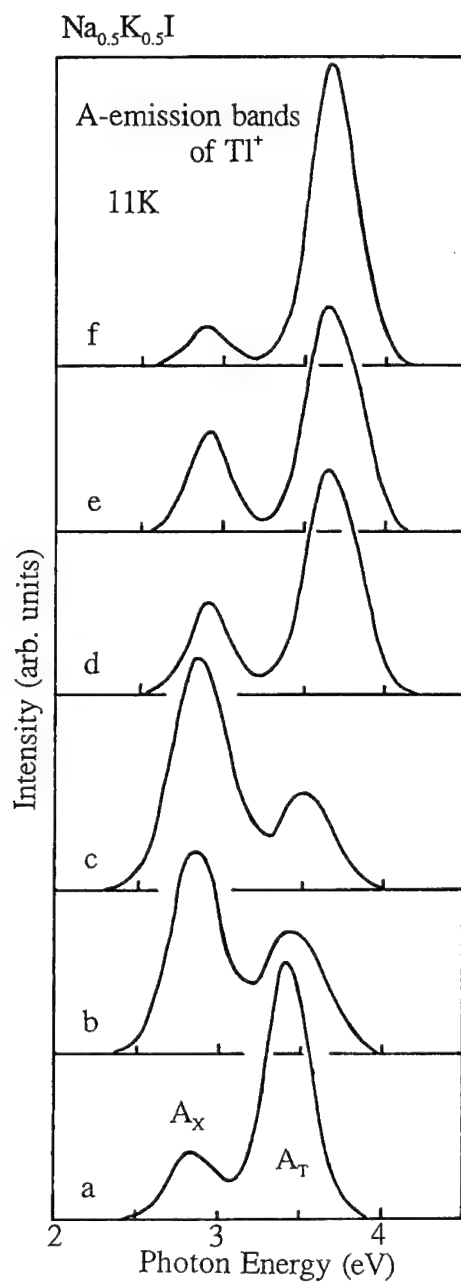


FIGURE 3 Emission spectra under excitation of A-bands of  $\text{Tl}^+$ . Measurements were done from curve a to f with the laps of time. Measurement steps (a, d, f) here are corresponded to steps (a, b, c) of Figure 1 and 2.

## REFERENCES

1. L. P. Cook and H. F. McMurdie, *Phase Diagrams for Ceramists* (The American Ceramic Society INC., 1989) 7th ed., p. 440.
2. S. Hashimoto and M. Itoh, *Jpn. J. Appl. Phys.* **27**, 726 (1988).
3. A. Fukuda, *Phys. Rev.* **B10**, 4161 (1970).

## METALLIC Na FORMATION IN NaCl CRYSTALS BY ELECTRON AND VUV PHOTON IRRADIATION

SHIGEHIRO OWAKI,\* SHIGEKO KOYAMA,\*\* MASAO TAKAHASHI,\*\*  
TOICHI OKADA,\*\* RYOUICHI SUZUKI\*\*\* and MASAO KAMADA\*\*\*\*

*\*College of Integrated Arts and Sciences, University of Osaka Prefecture. 1-1 Gakuencho, Sakai, Osaka 593, Japan; \*\*I.S.I.R., Osaka University; \*\*\*Electrotechnical Laboratory; \*\*\*\*Institute for Molecular Science, Japan*

Metallic Na was formed on crystal surfaces of NaCl with irradiation by electron beams of low energy (10–30 KeV) or photon fluxes in the VUV region and was evaluated with AES and UPS. The states of Na formed in or on NaCl crystals with irradiation of high (21 MeV) and low energy electrons and VUV photons are discussed comparing the results from different analysis methods.

*Key words:* radiation effects, metallic Na, VUV, AES.

### 1 INTRODUCTION

At ICDIM 1992, we reported that due to aggregation of F centers after dense irradiation of 21 MeV electron pulses from a linac, metallic Na particles in NaCl single crystal were formed. This was established using optical absorption and positron annihilation lifetime measurements.<sup>1</sup> However, metallic Na was not detected in the crystals by X ray photoelectron spectroscopy (XPS). We proposed that the particle size was too small and the density was too low due to a uniform distribution in the bulk.

In this paper, NaCl crystals are irradiated with electrons of low energy (30–10 KeV) or with photons in the vacuum ultraviolet (VUV) region from synchrotron radiation (SR). In both cases, metallic Na is formed on the crystal surface as determined by Auger electron spectroscopy (AES) and UV photoelectron spectroscopy (UPS). The results are compared with those using high energy electrons.

### 2 EXPERIMENTS

Sodium chloride crystals, cleaved in Ar gas, were installed in a XPS apparatus (Vacuum Generator microlab Mk3) in which a pressure of  $3 \times 10^{-9}$  Torr was maintained during electron irradiation. The cleavage surface was scanned within the region of  $2 \times 2 \mu\text{m}^2$  by a thin focused electron beam (30 KeV, 1.6  $\mu\text{A}$ ) from a high luminosity gun of LaB<sub>6</sub> for AES.

The results of AES near Na KLL peaks are shown in Figure 1 with curve fits. In Figure 1(a) obtained at the initial stage of the measurements, there is a single peak corresponding to KLL Auger line of ionic Na (peak (1) at 978 eV). In Figure 1(b) of the spectrum after the electron irradiation for 10 min., a new peak (2) appears at 4–5 eV higher energy than that of ionic Na. The kinetic energy of the new peak corresponds to that of metallic Na.<sup>2,3</sup> It is important to note that this peak was not observed in a sample irradiated with 21 MeV electrons from a linac.

With the higher current or longer irradiation time, the peak of ionic Na shifted to 981 eV and the new peak also shifted 8 eV to the higher energy side than that of ionic Na.

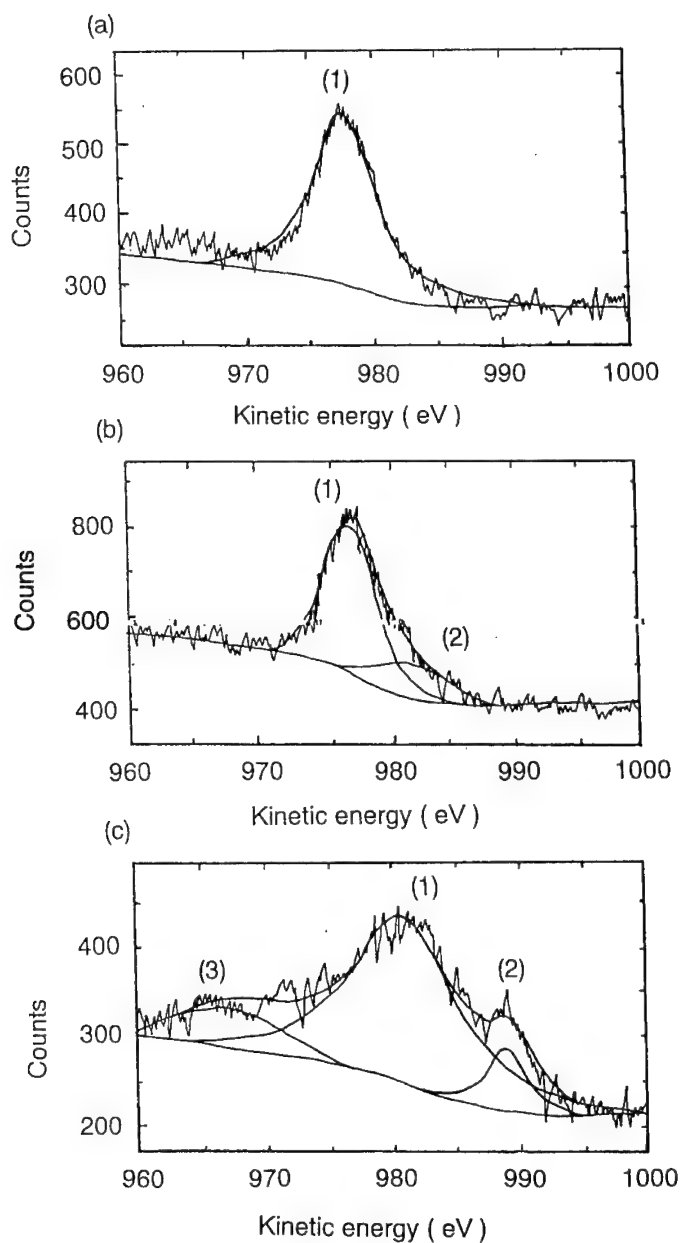


FIGURE 1 Auger electron spectra of a region near Na KLL in NaCl crystals: (a) before irradiation, (b) after irradiation of electrons of 30 KeV, and (c) after the longer irradiation. Peak (1); ionic Na, (2); metallic Na and (3); atomic Na. Smooth curves are calculated fitting curves.

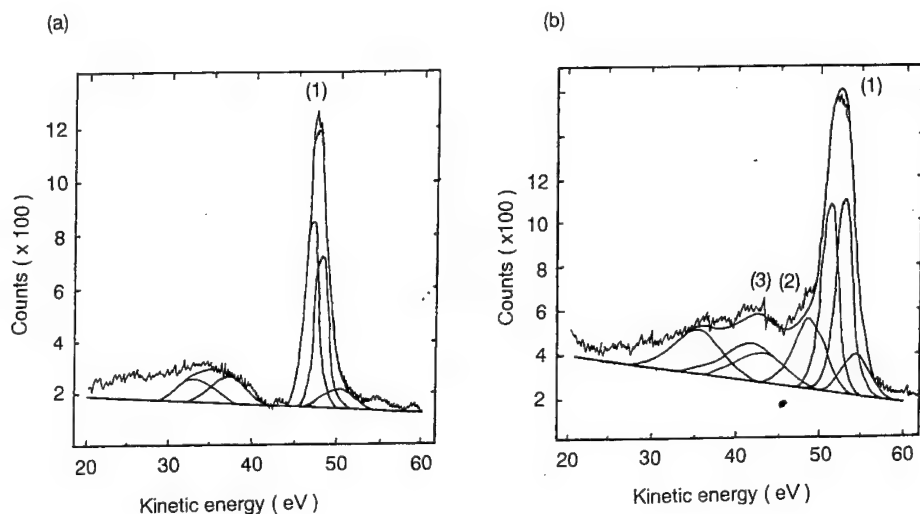


FIGURE 2 Photoelectron spectroscopy of a region of near Na 2p in NaCl powdered crystals: (a) before exposure, and (b) after exposure to VUV of SR for 30 min.. Peak (1); ionic Na, (2); metallic Na, (3); bulk plasmon loss from metallic Na. Smooth curves are calculated fitting curves.

Moreover, another broad peak (3) was observed on the lower energy side as shown in Figure 1 (c) and it seems to correspond to isolated atomic Na, because of the kinetic energy of KLL of Na vapor, 977 eV.<sup>4</sup>

As another radiation sources for metal formation on NaCl surface and an analysis method, intense photon fluxes in the VUV region of SR and UPS were used at the UVSOR facility in Institute for Molecular Science, Japan.<sup>5</sup> The irradiation was performed on powdered crystals of NaCl with a photon flux diameter of 1 mm of white light (0 order light of grating monochromator); the analyzing light was monochromatic at 100 or 130 eV at Beam Line 6A2.

The peak analysis near the Na 2p line by UPS of a sample before and after VUV irradiation for 30 min. is shown in Figure 2(a) and (b). Peak (2) in Figure 2(b) is consistent with metallic Na and peak (3), with a satellite due to plasmon loss from metallic Na (energy of bulk plasmon; 5.8 eV, energy of surface plasmon; 4.1 eV).<sup>2</sup> In the UPS vacuum system, electrons of 10 KeV were used for irradiation and the surfaces were analyzed by UPS for comparison of radiation effects between VUV photons and electrons of low energy. The former appears to be more effective than the latter, though it is difficult to compare the two flux intensities.

### 3 DISCUSSION

It is easily found from the broadening of the ionic Na KLL peak in AES that irradiation of high currents of low energy electrons damage NaCl crystal surfaces. As one of the results, formation of metallic Na was confirmed with separation of the metallic peak from the ionic peak. With further exposure to electrons, the metallic peak shift to 8 eV on the higher energy side than that of ionic Na and neutral Na (vapor state) was observed during irradiation.

The line broadening and shift of the Na 2p peak in UPS shows that the irradiation by VUV photon produces similar radiation damage to that of low energy. Exposure of NaCl to VUV may be a more effective method to create metallic Na than by electron. The observation of the bulk plasmon loss peak in a sample after VUV exposure of 30 min. means that there is metallic layer of thickness sufficient to produce the bulk plasmon. Irradiation by 21 MeV electron creates only particles of metallic Na with a size on the order of 10 nm and a bulk mole fraction less than  $10^{-3}$  estimated from the optical absorption.

Dense metal formation due to surface damage in high vacuum seems to depend on that fact that Cl ions (H center) can escape from the surface more easily than aggregation of F centers which is competitive with recombination of Frenkel pairs in the bulk.

#### REFERENCES

1. S. Owaki, S. Koyama, K. Nobugai, T. Okada, K. Inabe, and Y. Fukuda, *Proc. 12th Int. Conf. Defects in Insulating Materials* (World Scientific 1993) pp. 853.
2. A. Barrie and F. J. Street, *J. Electron Spectrosc. Relat. Phenom.*, **7**, 1 (1975).
3. C. D. Wagner, *Disc. Faraday Soc.*, **60**, 291 (1975).
4. H. Hilling, B. Cleff, W. Mehlbon and Schmitz, *Z. Physik*, **268**, 225 (1974).
5. M. Watanabe, *Nucl. Instr. Meth. Phys. Res.*, **A246**, 15 (1986).



## NANO-STRUCTURES AND QUANTUM SIZE EFFECTS IN HEAVILY IRRADIATED NaCl

D. VAINSHTEIN, H. P. DEN HARTOG, H. C. DATEMA, J. SEINEN  
and H. W. DEN HARTOG

*Solid State Physics Laboratory, University of Groningen, Nijenborg 4, 9747 AG  
Groningen, The Netherlands*

Sodium particles in heavily irradiated synthetic doped NaCl and natural rocksalt have been studied by electron spin resonance (ESR), differential scanning calorimetry (DSC) and dielectric loss measurements. For the first time we have studied quantum size effects of Na colloids in irradiated NaCl at different temperatures between 140 K and 30 K. A weak temperature dependence of the electronic susceptibility of these particles is observed, that deviates from the simple metallic behaviour and may be due to interactions in the system. The magnetic properties of sodium particles in heavily damaged NaCl (3–15 mole % metallic Na) measured by ESR below 160 K might be associated with antiferromagnetic interactions between the extremely small colloids, which suggests a transition to a spin density or charge density wave ground state; this is in agreement with the observation of an anomalous peak in the AC conductivity at about 150 K.

*Key words:* sodium particles, magnetic properties, AC conductivity.

### 1 INTRODUCTION

We have investigated doped NaCl, containing nano-precipitates of sodium, with concentrations between 0 and 15%. We report the ESR and preliminary dielectric loss studies on sodium nano-structures in heavily irradiated NaCl. The temperature dependence of the spin susceptibility of sodium particles shows a broad maximum of the ESR intensity as a function of  $T$  at about 160 K and an anomalously decreasing linewidth with increasing temperature in the same range of temperatures. This corresponds with a peak in the AC conductivity at same temperature.

### 2 RESULTS

Absorption and dispersion ESR signals of sodium particles have been measured. The  $g$ -value was found to be  $2.0012 \pm 0.0002$ . Depending on the irradiation conditions the peak to peak ESR linewidth was observed to vary between 17 Gauss and 120 Gauss at RT. The ESR linewidth of the sodium particles of 120 Gauss has been associated with presence of ultrafine sodium particle in “low”-damaged crystals (latent heat of melting of  $\text{Na} \leq 0.1 \text{ J/g}$ ). We have observed a stepwise change of the linewidth and intensity at RT as function of dose and irradiation temperature which is connected with a rapid growth of sodium precipitates and the development of fractal nano-structures. The temperature dependence of the ESR linewidth and the doubly integrated intensity (i.e.  $\chi''$ —the imaginary part of the magnetic susceptibility) of the sodium particles has been measured between 4 and 300 K. The “low”-damaged crystals, containing ultrafine colloids, show anomalous Curie paramagnetism expected for small odd particles (Figure 1a). For the first time in irradiated NaCl with  $0.15 \text{ J/g} \leq \text{latent heat of melting of Na} \leq 0.5 \text{ J/g}$  we have studied quantum size effects (QSE) of the discreteness of the electronic levels of the sodium particles, modulated slightly by inter-precipitate interactions at 160 K. Figure 1b shows a cross-over at 60 K, where for  $T \leq 60 \text{ K}$  the paramagnetic susceptibility of sodium

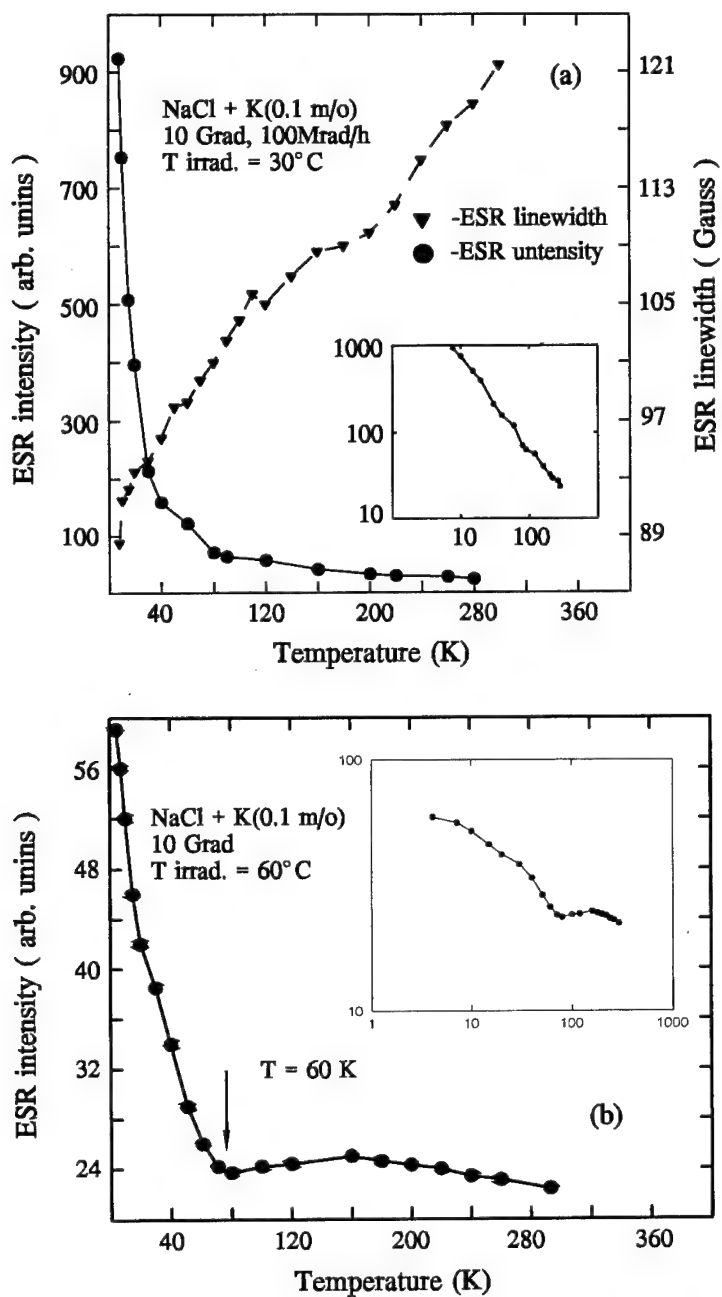


FIGURE 1 The temperature dependence of the doubly integrated intensity and ESR linewidth in K doped NaCl, (a) Curie type paramagnetism of the small odd sodium clusters, (b) the quantum size effect, i.e. the Pauli-Curie transition, is clearly present at 60 K.

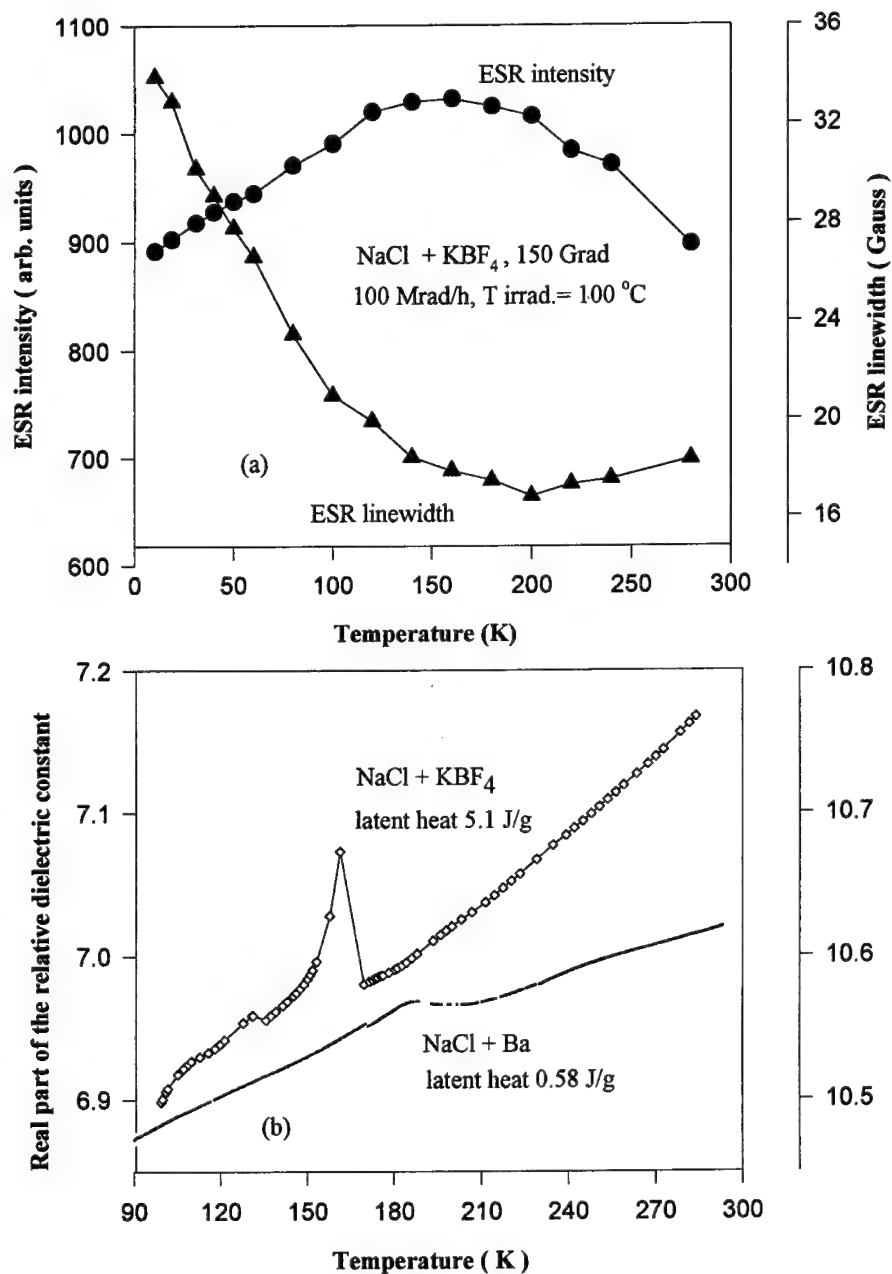


FIGURE 2 The anomalous temperature dependence of the paramagnetic susceptibility and ESR linewidth (a) and the real part of dielectric constant (b) at about 160 K. The transition at 160 K is suggested to a spin density or charge density wave ground state.

particles follows the Curie law ( $\chi''_{\text{odd}} \propto 1/T$ ,  $k_B T < \Delta$ ) and becomes quasi-Pauli ( $\chi \approx \chi_{\text{Pauli}}$ ,  $k_B T > \Delta$ ) with a weak peak at  $T \approx 160$  K for higher temperatures. We have studied QSE for many irradiated crystals at different temperatures from 140 K down to 30 K. From the cross-over temperatures, we have estimated<sup>1</sup> the average diameters ( $d$ ) and the numbers of conduction electrons ( $N$ ) of the sodium precipitates to be  $21 \text{ \AA} \leq d \leq 48 \text{ \AA}$  and  $310 \leq N \leq 1750$ , respectively. In heavily irradiated crystals (latent heat of melting of  $\text{Na} \geq 1.5$  J/g) we have found an anomalous broadening of the ESR line and increasing the spin susceptibility as a function of temperature (Figure 2a). Above 150 K the spin-susceptibility  $\chi''$  is large and about Pauli-like up to 240 K. The decreasing spin susceptibility below 150 K and the broadening of the ESR line are characteristic of a magnetic transition. Recent ESR experiments on alkali metal fullerenes for quasi-1D dimensional electronic structures<sup>2</sup> have revealed similar temperature dependence as observed for irradiated NaCl. Figure 2b shows the results of dielectric loss measurements. A sharp peak in the real part of dielectric constant was observed for  $\text{KBF}_4$  doped irradiated NaCl at 160 K, the result for a less damaged Ba doped NaCl shows a weak peak in the same temperature region.

### 3 SUMMARY

The electronic structure of the nano-precipitates in heavily irradiated crystals is the underlying reason for the anomalous magnetic and electronic properties of the sodium particles. For "low"-damaged crystals a large Curie susceptibility associated with the ultrafine sodium colloids is observed. Extensive quantum size effects of the sodium particles have been observed for irradiated NaCl with latent heat values up to 0.5 J/g. The anomalous temperature dependence of the magnetic susceptibility and ESR linewidth as well as AC conductivity are characteristic of antiferromagnetic correlations and support the idea that sodium nano-structures with extremely small parts of individual Na-precipitates are present. We suggest that these electronic structures lead to spin or charge density waves.

### ACKNOWLEDGEMENTS

We would like to thank the Dutch ministry of Economic Affairs for partly funding this project.

### REFERENCES

1. A. Kawabata, *J. Phys. Soc. Jpn.* **29**, 902 (1970).
2. O. Chauvet, G. Oszlányi, L. Forro, P. W. Stephens, M. Tegze, G. Faigel, A. Jánossy. *Phys. Rev. Letters*. **72**, 2722 (1994).

## STACKING FAULT EXCITONS IN AgBr MICROCRYSTALS WITH TWIN PLANES

A. MARCHETTI

*Imaging Research and Advanced Development Eastman Kodak Company, Rochester, NY 14652–3208 and Center for Photoinduced Charge Transfer, University of Rochester, Rochester, New York 14627*

The visible emission and excitation spectra of AgBr microcrystals containing single and parallel double twin planes has been obtained. A band at 462.28 nm (2.6813 eV) is observed in the excitation spectrum. This feature is about 2.5 meV below the indirect exciton band edge. Coincident emission features are observed. The band in the excitation spectrum of microcrystals with two parallel twin planes is often split into a doublet with splittings between 1 and 2 meV. The new band is assigned to an exciton created at a stacking fault and the splittings are thought to be due to tunnelling of the exciton between proximate twin planes.

Key words: AgBr, Stacking Fault, Exciton, Twin Plane, Low temperature Spectra

### 1 INTRODUCTION

Twin planes are a subset of defects known as stacking faults.<sup>1</sup> In cubic crystals they represent a mirroring in the layer sequence aBcAbC to aBcA'b'AcBa. Twinning in fcc, rock salt structures occurs at a (111) plane and can also be viewed as a 60° rotation of one plane with respect to another. Twin planes can have either a cationic or an anionic mirror layer. Twin planes are of pedagogical interest because they represent a symmetry breaking structure related in many ways to a surface. They are of industrial importance because they are a feature that engenders tabular or planar growth in silver halide microcrystals used in photographic films. These tabular microcrystals have a larger surface-to-volume ratio allowing more dye to be adsorbed per unit volume and hence more light absorption per unit volume.

Stacking fault excitons (SFE) have been observed in BiI<sub>3</sub> and GaSe.<sup>2–4</sup> The stacking fault excitons in BiI<sub>3</sub> appear as several sharp lines in the absorption and emission spectra just below the indirect exciton edge.<sup>2,3</sup> Stacking fault excitons are expected to exhibit a more two-dimensional nature than their more normal exciton counterparts.<sup>2–4</sup>

AgBr is an indirect band-gap semiconductor, thus its absorption spectrum is very weak in the region of the indirect band-gap energy (2.6838 eV). The excitonic properties of this material have been studied extensively by emission spectroscopy.<sup>5</sup> Excitation spectroscopy has been used to examine the absorption of AgBr in the region of the indirect band-gap.<sup>6</sup> These investigations have found that the indirect exciton absorption can be observed by monitoring either the iodide bound exciton emission (500 nm–2.48 eV) or the donor-acceptor emission (590 nm–2.10 eV), which contains a contribution from intermediate case excitons (close D-A pairs) recombination.<sup>6,7</sup>

Silver halide microcrystals, when grown in gelatin, normally have one of two regular morphologies: cubes and octahedra.<sup>8</sup> AgBr microcrystals can also be grown in a tabular morphology with (111) faces and one or more twin planes parallel to the tabular faces.<sup>8</sup> Twin planes have been observed in cryosectioned samples by transmission electron microscopy.<sup>9</sup> In those microcrystals with two parallel twin planes the spacing between twin planes is generally between 8 and 20 nm.

This report describes absorption and emission features that occur because of an exciton created at twin planes in AgBr. We have examined the excitation spectra of a number of

three-dimensional and tabular AgBr microcrystals dispersed in gelatin. A new band is found in the excitation spectrum of microcrystals containing twin planes. This feature is found in dispersions of microcrystals that have a large proportion of single twins (but no double twins) as well as those with parallel double twins. This absorption line is split into a doublet in several of the dispersions of microcrystals with two parallel twin planes. Coincident emission lines are observed.

## 2 EXPERIMENTAL

The AgBr microcrystal dispersions that were examined were made by standard techniques used for producing silver halide in gelatin dispersions for photographic films.<sup>10,11</sup> These procedures allow the production of cubic, octahedral, and tabular morphologies (with single or double twin planes) by controlling the precipitation conditions. The most important factor is the silver ion activity during nucleation and growth. All of the microcrystals produced were examined in a scanning electron microscope and were generally between 300 and 900 nm in diameter or edge length. The octahedral microcrystals were monodispersed in size with an octahedral edge length of 320 nm. Those dispersions with tabular grains that contained only single twins were 45% single twins by number count with the rest being smaller octahedral grains and < 1.5% microcrystals with double twins. The single twin microcrystals were triangular in shape with an edge length of  $330 \pm 50$  nm. The doubly twinned microcrystals were hexagonal in shape and had a mean thickness of  $47 \pm 6$  nm and an equivalent circular diameter of  $800 \pm 190$  nm.

The excitation spectra of these samples were obtained at liquid helium temperatures ( $T \approx 6$  K or 2 K) with a continually tunable dye laser. The dye laser employed coumarin 120 in a glycerol-benzylalcohol mixture with cyclooctatetrene added to reduce triplet-triplet absorption. The bandwidth of the dye laser emission was 0.12 meV. The dye was pumped by the 351/360 nm UV lines from an argon ion laser. The rest of the spectroscopic apparatus has been described previously.<sup>12</sup>

## 3 RESULTS AND DISCUSSION

Figure 1 shows the excitation and emission spectra for three dispersions of AgBr microcrystals in the region of the indirect exciton band-gap energy [ $E - g(\text{ex})$ ]. These dispersions are composed of octahedral microcrystals (O), single twin microcrystals (ST), and microcrystals with two parallel twin planes (DT). In these excitation spectra the emission is monitored at 500 nm (iodide bound exciton emission). Similar spectra were obtained when the monitoring wavelength was 600 nm (donor-acceptor emission).<sup>6</sup> Equivalent excitation spectra were obtained on other octahedral and cubic microcrystal dispersions and no evidence was found for a new band in the excitation spectra.

The new absorption feature at 2.681<sub>3</sub> eV (vacuum corrected), which is associated with microcrystals containing twin planes, is approximately 2.5 meV below the exciton band-gap energy [ $E_g(\text{ex}) - 2.6838$  eV]. The appearance of a new feature in the excitation spectrum is thought to be caused by the symmetry breaking effect of the twin plane, which allows the creation of a weakly trapped exciton in the region of a twin plane. The emission spectra for those microcrystals that contain a single twin plane have a 0-0 band at 2.680<sub>8</sub> eV, which is coincident with the absorption feature, and they have a strong TO phonon band at 2.672<sub>2</sub> eV with weaker LA and LO phonon lines at 2.669<sub>6</sub> and 2.662<sub>9</sub> eV, respectively. Several preparations of microcrystals containing single twin planes and

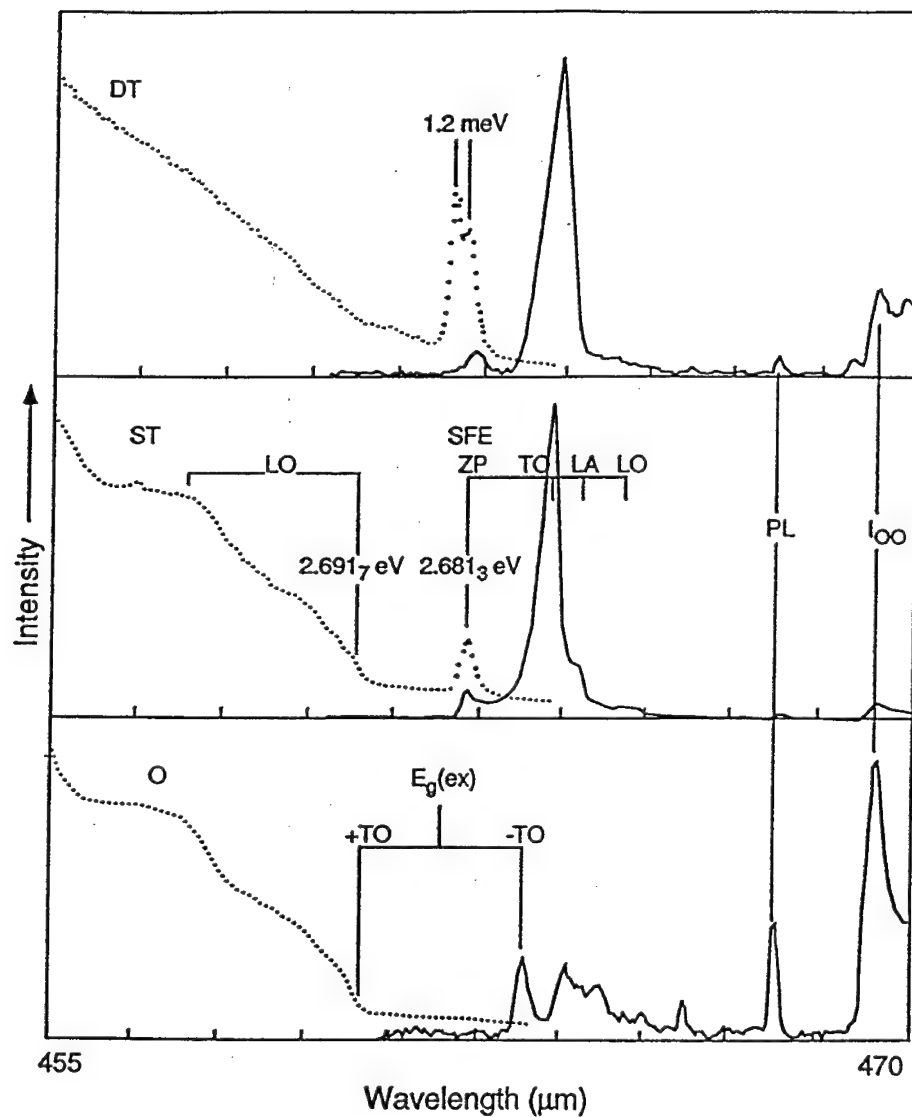


FIGURE 1 The excitation and emission spectra of double twinned (DT), single twin (ST), and octahedral (O) AgBr microcrystals at 6 K. The monitoring wavelength was 500 nm. The new feature associated with exciton localization at a twin plane is at 462.28 nm. The broad, higher energy peaks in the excitation spectra are caused by LO phonon scattering. The splitting in the excitation spectrum of the DT microcrystal is 1.2 meV. The O-O band of the iodide bound exciton ( $I_{00}$ ) and a plasma line (PL) used for calibration are indicated.

respectively. Several preparations of microcrystals containing single twin planes and double twin planes were examined. All microcrystals examined that contained twin planes exhibited the new band in the excitation spectrum.

The exciton wavefunction in AgBr is a product of valence band (L-point [ $L_4^-$ ,  $L_5^-$ ]) and

conduction band ( $\Gamma_6^+$ ) wavefunctions.<sup>13,14</sup> In the absence of exchange there are four degenerate states: two are of pure triplet character and two are of mixed singlet-triplet character. Exchange interactions split this into two doubly degenerate pairs with the pure triplets lower in energy. The exchange energy has been estimated by magneto absorption (0.33 meV) and more recently by Raman scattering (0.17 meV) and quantum beat spectroscopy (0.13 meV).<sup>13,14</sup> With absorption and emission linewidths on the order of 1.5 meV, the exchange splitting is not observed.

Some of the dispersion of microcrystals containing two parallel twin planes exhibit a doublet in their excitation spectrum. The example shown in Figure 1 has a splitting of 1.2 meV. This splitting, when observed in other double twin preparations, ranged from 1 to almost 2 meV. The average energy of the two lines (2.6814 eV) is the same as the energy of the line in the single twin preparations. A band in the emission spectrum is coincident to the lower component in the excitation spectrum. The coincident band in the emission spectrum of the DT preparation (Figure 1) broadens from 1.3 to 2.0 meV (FWHM) as the temperature was raised from 2 to 12 K. This suggests that the upper component is emissive and becomes more populated at higher temperatures. The splitting of the new feature in AgBr tabular microcrystals with double twin planes is assigned to tunneling of an exciton between wells (the excitons oscillating between two closely spaced twin planes). Estimates for the tunneling splitting of a particle in coupled square wells of several nm width and separated by  $\approx 10$  nm are on the order of a few meVs.

The fact that the stacking fault related absorption is observed in excitation spectra by monitoring either the iodide bound exciton emission at 500 nm or the D-A emission at 600 nm indicates these excitons are mobile, even at liquid helium temperatures. Using the measured trap depth (2.5 meV) and a reasonable estimate for a preexponential factor ( $10^9$ ) leads to an estimated mean trapping time of  $\approx 0.1 \mu\text{s}$ .<sup>15</sup>

A consideration of the stabilization energy of an exciton (2.5 meV) created at a twin plane suggests that twin planes are not barriers for electrons or holes at room temperature. The exciton stabilization could occur by a small change in the dielectric constant in the vicinity of the twin plane, by a small fluctuation in the potential in either the valence or conduction band or by combinations of these mechanisms. In any case, these small stabilizations should not be a barrier for electrons or holes at higher temperatures.

## REFERENCES

1. W. Bollmann, *Crystal Defects and Crystalline Interfaces* (Springer-Verlag, New York, 1970), Ch. 3.
2. M. Ichida, T. Karasawa, and T. Komatsu, *Phys. Rev.* **B47**, 1474 (1993) and references cited.
3. K. Watanabe, T. Karasawa, T. Komatsu, and Y. Kaifu, *J. Phys. Soc. Jpn.* **55**, 897 (1986).
4. Y. Sasaki and Y. Nishina, *Physica* **105B**, 45 (1981) and reference cited.
5. W. von der Osten and H. Stolz, *J. Phys. Chem. Solids* **51**, 765 (1990).
6. M. Timme, E. Schreiber, H. Stolz, and W. von der Osten, *J. Luminescence* **55**, 79 (1993).
7. A. P. Marchetti, M. S. Burberry, and J. P. Spoonhower, *Phys. Rev.* **B43**, 2378 (1991).
8. R. C. Baetzold and C. R. Berry, in *Theory of the Photographic Process*, edited by T. H. James (Macmillan Publishing Co., New York, 1977), 4th ed., Ch. 1-II.
9. D. L. Black, J. A. Timmons, and G. L. Bottger, in Papers in *The International East-West Symposium on Factors Influencing the Efficiency of Photographic Imaging*, C15 Oct. 1988.
10. C. R. Berry, in *Theory of the Photographic Process*, edited by T. H. James (Macmillan Publishing Co., New York, 1977), 4th ed., Ch. 3.
11. A. K. Tsaur *et al.*, US Patents: 5,147,771 (1992), 5,147,772 (1992), 5,147,773 (1992), 5,171,659 (1992), 5,210,013 (1993).
12. A. P. Marchetti, K. P. Johansson, and G. L. McLendon, *Phys. Rev.* **B47**, 4268 (1993).
13. M. Matsushita, *J. Phys. Soc. Jpn.* **35**, 1688 (1973).
14. W. von der Osten in *Light Scattering in Solids VI*, edited by M. Cardona and G. Guntherodt (Springer-Verlag, New York, 1991), Ch. 7.



## OPTICAL PROPERTIES OF METALLIC NANOPARTICLES SYNTHESIZED BY IMPLANTATION OF ALKALI IONS IN LiF

J. DAVENAS and C. JARDIN

*Département de Physique des Matériaux, 43 Bd du 11 Novembre, Université Cl. Bernard  
Lyon 1-UA CNRS 172, 69622 Villeurbanne Cedex, France*

The optical functions of metallic particles, resulting from the precipitation of alkali ions implanted in LiF crystals, have been calculated from optical absorption and reflectivity measurements in the photon energy range 0.4-6 eV. Optical data are analyzed in terms of local electrical field effects. The real part of the dielectric function remains positive in the whole energy spectrum, in opposition to the one calculated in the Maxwell-garnett approximation where enhanced reflection should correspond to negative values of the dielectric function. Additional resonances shown by the energy loss function are responsible for this discrepancy. An absorption peak associated to Li precipitates and a secondary peak of the plasma resonance are revealed, so as a loss structure at 5 eV due to F centres also detected in electron energy loss spectrometry (REELS). Implications for non linear optical properties are addressed.

*Key words:* optical constants, nanoparticles, alkali halides, implantation, non linear optics.

### 1 INTRODUCTION

Photons will be used in the next future to carry information instead of electrons since they allow the fast propagation of high information densities. Photoelectronic devices are now developed involving non linear optical effects. In particular the interest for optical materials exhibiting the Kerr effect grows rapidly. In such materials the refractive index is modified upon exposure to an intense radiation  $I$  according to:

$$n = n_0 + n_1 I \text{ where } n_1 \text{ is a non linear refractive index}$$

Different functions based on this effect allow optical signal processing, such as optical switching, bistability, harmonic generation... The material response has however to be rapid and absorption losses limited. Composite optical materials involving metallic or semi-conducting nanoparticles dispersed in transparent matrices have been studied for that purpose. We had studied in the past (20 years ago!) the optical properties of metallic particles induced by the precipitation of implanted ions in ionic crystals. New absorption bands, giving rise to characteristic colorations: brown for implanted  $\text{Li}^+$ , pink for  $\text{Na}^+$  and blue for  $\text{K}^+$ , in thermally annealed LiF crystals had in particular been attributed<sup>1,2</sup> to the plasma resonance of the metallic nanoparticles embedded in the host crystal. LiF is an interesting matrix (in view of harmonic generation for example) since transparent in the UV, where most optical materials exhibit absorption bands. It is in particular the case of glasses, KDP, aromatic polymers... A significant background of data is available on LiF, due to the extensive studies performed in the past on colour centres. However most of the former optical studies involved only optical absorption measurements that provides a partial analysis of the optical data since the optical functions of an absorbing medium are complex. In this case, it is necessary to perform a Kramers Kronig treatment to determine the real and imaginary parts of the optical functions, or to measure separately the optical absorption and specular reflection spectra. However the dispersion relations leads to sum extending over the whole photon energy range, which must be truncated to the

experimentally available energies. A variation law of the optical functions outside this domain must be assumed. Because of this main difficulty, we developed the second method.

## 2 OPTICAL DATA ANALYSIS

LiF crystals have been implanted with alkali ions at 170 keV and thermally annealed for 1 h. at 300°C. We discuss in this limited contribution the optical properties of potassium doped crystals, whereas the results of  $\text{Li}^+$  and  $\text{Na}^+$  implantations will be presented in a next paper. Optical absorption and specular reflection spectra have been recorded with a CARY 2300 spectrophotometer. The measured optical transmittance has been corrected from the reflection on the 2 crystal surfaces.

The real and imaginary parts of the optical index :  $n = v - j\chi$ , have been calculated from these 2 sets of measurements. We know that the light is attenuated according to the relation:

$$I = I_0 \exp(-4\pi \chi / \lambda z) = I_0 \exp(-\alpha z)$$

in which  $\alpha$  is the absorption coefficient. Introducing the experimental values of  $\alpha$  we deduce the extinction coefficient through the relation:

$$\chi = \frac{\alpha \lambda}{4\pi}$$

The usual Fresnel's relations provide the relation between the reflection coefficient and the optical index:

$$R = \frac{(1 - v)^2 + \chi^2}{(1 + v)^2 + \chi^2}$$

Since the imaginary part of the optical index  $\chi$  has been calculated and the reflection coefficient has been measured as functions of the wavelength, it is possible to obtain the refractive index  $v$  that is a solution of a second degree equation:

$$v = \left( \frac{1+R}{1-R} \right) + \sqrt{\left( \frac{1+R}{1-R} \right)^2 - (1 + \chi^2)}$$

The dielectric function:  $\varepsilon = \varepsilon_1 + j\varepsilon_2$ , is easily deduced at any given frequency from the optical index through the relations:

$$\begin{aligned} \varepsilon_1 &= v^2 - \chi^2 \\ \varepsilon_2 &= 2v\chi \end{aligned}$$

At last, the energy loss function defined by:

$$\text{Im} \left( -\frac{1}{\varepsilon(\omega)} \right) = \frac{\varepsilon_2}{\varepsilon_1^2 + \varepsilon_2^2} = \frac{2v\chi}{(v^2 + \chi^2)^2}$$

has been calculated to relate the optical study to the Electron Energy Loss results obtained on same samples<sup>3</sup>. We know that this function provides informations on the energy level structure of valence electrons. The plasmon resonances, which correspond to the poles of the function, are in particular directly evidenced.

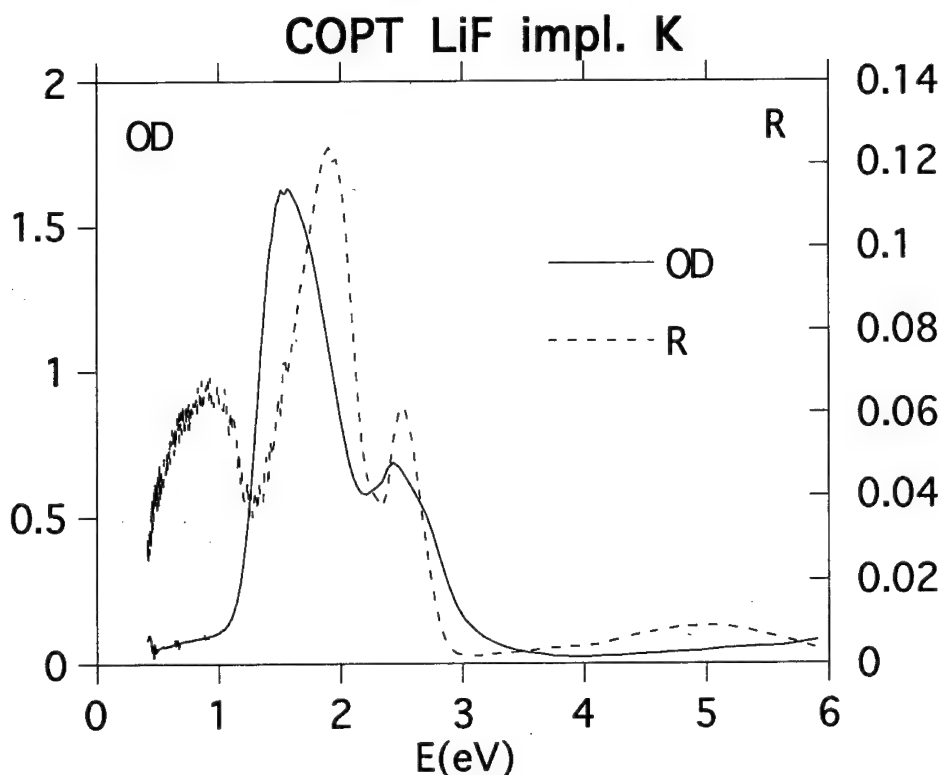


FIGURE 1 Optical absorption and specular reflectance spectra versus photon energy of a LiF crystal implanted with  $5 \cdot 10^{16} \text{ K}^+/\text{cm}^2$  at 170 keV and annealed at  $300^\circ\text{C}$  for 1 h.

### 3 DIELECTRIC RESPONSE

#### 3.1 Optical Absorption and Reflectivity

Figure 1 shows the as recorded absorption spectrum exhibiting a strong resonance at 1.5 eV, which is responsible for the blue coloration of the thermally annealed crystals, whereas a secondary resonance appears at 2.4 eV, as previously reported.<sup>1</sup> A first question is to check whether these resonances are true absorption bands by taking into account the crystal reflectivity, which is important in this domain spectral domain. However, the correction from the optical losses due to the reflections on the crystal surfaces confirms these two absorption bands, which are situated on each side of the peak of enhanced reflectivity. In early studies of aggregated metals, Marton and Lemon<sup>4</sup> made the distinction between the two resonances associated to the resonance of the optical conductivity and the plasma resonance, which are respectively the pole and the zero of the dielectric function. A second consideration is then to check the dielectric constant. Comparison has been done between a computed one and the experimental one.

#### 3.2 Dielectric Function

That singularities of the dielectric function are interpreted in the framework of a local field description. The Drude's relations provide the dielectric response of a bulk metal, which

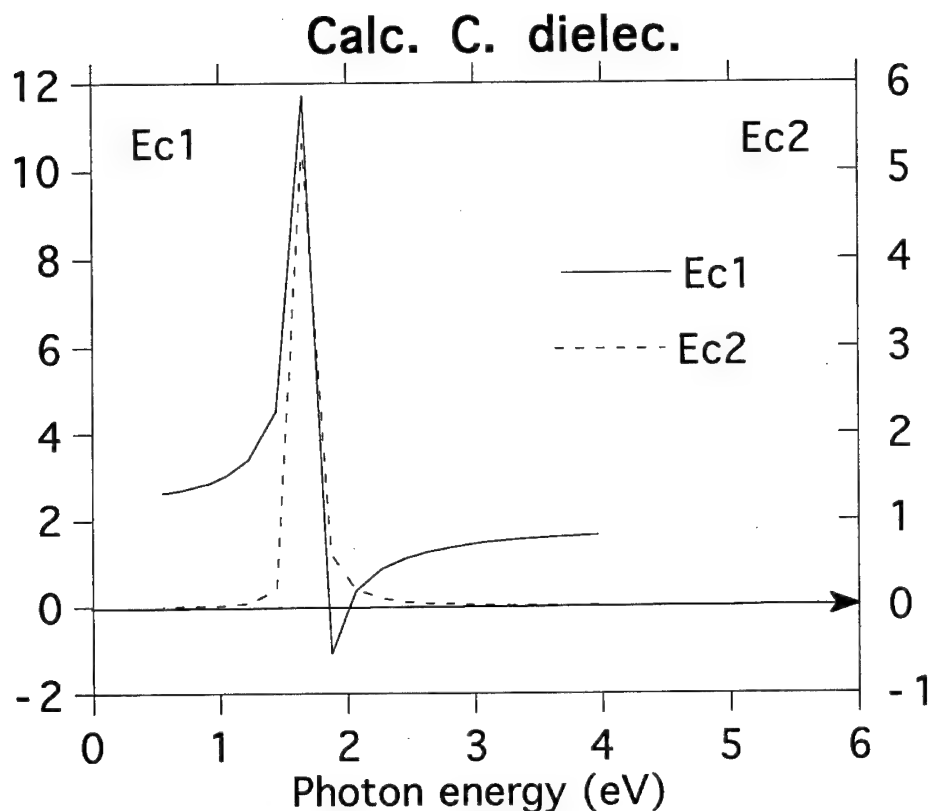


FIGURE 2 Real and imaginary parts of the dielectric constant computed from the Maxwell-Garnett theory for a 10 % fractional volume of spherical potassium spheres embedded in a LiF crystal.

shows a zero for the plasma frequency. A plasmon resonance in the energy loss function correspond to this singularity. The metal is reflecting below the plasma frequency since the dielectric function is negative and transparent at high frequencies. This behaviour is not modified when considering the metal surface if the electrical field is parallel to the surface. A polarization effect has however to be taken into account for other electrical field directions due to the charges induced at the surface. The local field is then different from the applied electrical field:

$$E_{\text{local}} = E - \frac{P}{\epsilon_0} = E - \frac{\alpha E_{\text{local}}}{\epsilon_0}$$

An effective dielectric constant is then defined by:

$$D = \epsilon E = \epsilon_0 + P$$

exhibiting two singularities, which are the zero and the pole of the function. The dielectric constant is negative in the frequency range limited by these two characteristic frequencies inducing optical reflection in this domain. These local field effects become extremely high for finely divided metal particles due to the importance of the surfaces.

In the case of spherical metallic particles dispersed in a dielectric matrix, characterized

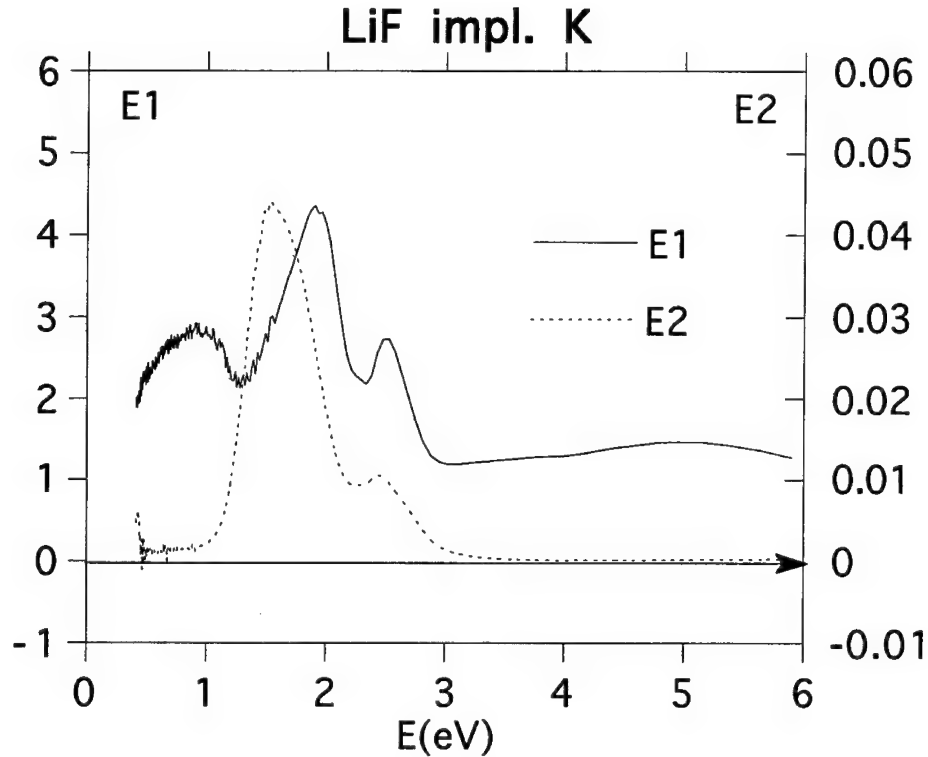


FIGURE 3 Real and imaginary parts of the dielectric constant as evaluated from spectrophotometric measurements for a LiF crystal implanted with  $5.10^{16}$  K<sup>+</sup>/cm<sup>2</sup> at 170 keV and annealed at 300°C for 1 h.

respectively by the dielectric constants  $\epsilon_m$  and  $\epsilon_i$ , the local field is connected to the applied field through the simple expression:

$$E_{\text{local}} = \frac{3\epsilon_i(\omega)}{\epsilon_m(\omega) + 2\epsilon_i(\omega)} E_0 = f_1(\omega) E_0$$

The resonance corresponding to the pole of this function means that the Kerr susceptibility  $\chi^{(3)}$ , that controls the non linear response, is exalted since proportional to  $f_1^4$ . Using the Maxwell-Garnett approximation,<sup>5</sup> we have calculated the effective dielectric constant of a composite medium  $\epsilon(\omega)$  involving potassium spherical nanoparticles embedded in a LiF matrix. Figure 2 shows the real and imaginary part of the dielectric function for a 10% volume fraction of potassium particles, for which we used the optical constants of the bulk metal. The real part of the calculated dielectric function is negative between 1.9 and 2.1 eV corresponding to the peak of enhanced reflection shown in Figure 1. The dielectric function deduced from optical and reflection measurements remains however positive over the whole spectral domain as shown by Figure 3, whereas a resonance is observed at 2.5 eV for the real and imaginary parts  $\epsilon_1$  and  $\epsilon_2$ . From the analysis of the dielectric response it results that the two absorption bands shown by the absorption spectrum of potassium nanoparticles cannot be attributed to the two singularities discussed by Marton and Lemon.

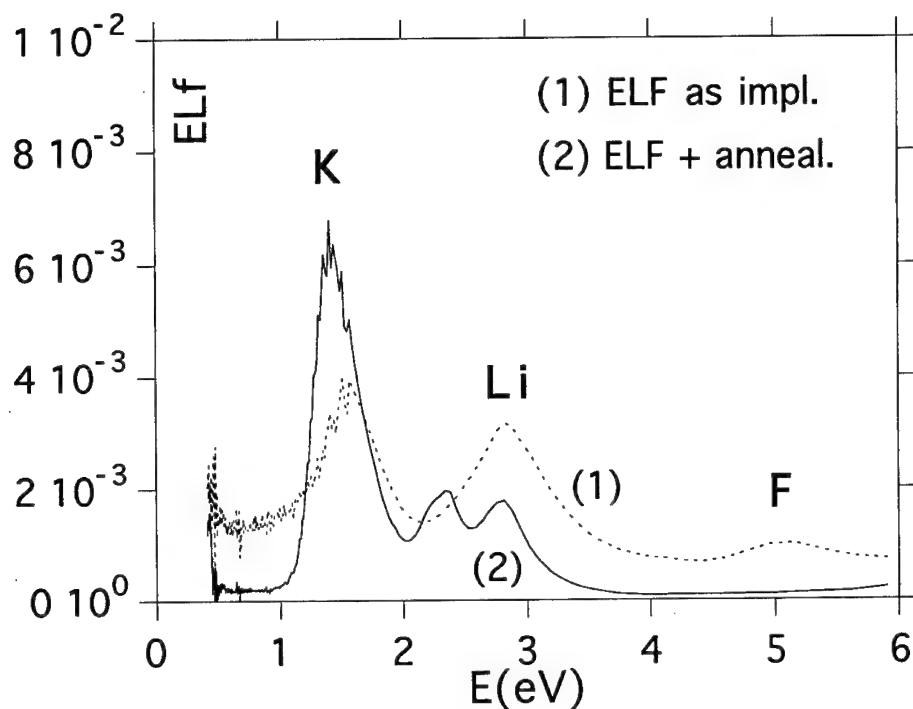


FIGURE 4 Energy Loss function deduced from spectrophotometric measurements for a LiF crystal: (1) as implanted, (2) annealed at 300°C for 1 h.

### 3.3 Energy Loss Function

The Energy Loss Function calculated from the optical measurements shows in figure 4 that a structure can be resolved with two peaks at 2.3 and 2.8 eV in addition to the main plasma resonance at 1.5 eV. The comparison with the loss spectrum of the as implanted LiF crystal indicates that the 2.8 eV peak is present before thermal annealings. According to a composite medium calculation, this contribution may be attributed to lithium precipitates. A contribution at 5 eV is observed, in accordance with the REELS spectrum discussed in another contributing paper,<sup>3</sup> which can be assigned to the F centres. The evolution of the energy Loss function upon thermal annealings shows the precipitation of the potassium metal, the partial dissolution of lithium precipitates and F centres bleaching.

## 4 CONCLUSION

The analysis of the optical data of LiF crystals implanted with potassium ions has shown the formation of metallic particles associated to the precipitation of the implanted and matrix alkali metals. Thermal annealings enables the optimization of the magnitude of the plasmon absorption and enhanced reflectivity. Third order non linear Kerr effects can be expected from the exaltation of the local field effect. The secondary absorption band at high photon energies is not connected to the zero of the dielectric function. Further

investigations involving other metals and matrices will be useful for the interpretation of this resonance.

## REFERENCES

1. J. Davenas, A. Pérez, P. Thévenard, C. Dupuy, *Phys. Stat. Solidi (a)* **19** (1973) 679.
2. J. Davenas, A. Pérez, C. Dupuy, *J. de Phys.*, sup. n° 12, 37 (1976) 531.
3. C. Jardin, P. Durupt, J. Davenas, *Rad. Eff.*, this issue.
4. J. P. Marton, J. R. Lemon, *J. Appl. Phys.*, **44** (1973) 3953.
5. J. C. Maxwell-Garnett, *Philos. Trans. Roy. Soc. Lond.*, **205** (1906) 237.

## NANOMETRIC METALLIC PARTICLES IN INSULATING MATERIALS: Bi-SiO<sub>x</sub>

C. MARTET, J. F. ROUX, M. TREILLEUX, B. CABAUD, J. C. PLENET  
and G. FUCHS

*Département de Physique des Matériaux, Unité Associée au CNRS, Université Claude  
Bernard-Lyon I, 43 Bld du 11 Novembre 1918, 69622 Villeurbanne Cedex, France*

Low Energy Cluster Beam Deposition (LECBD) has been used to synthesize cermets with controlled size nanoparticle. In the Bi-SiO<sub>x</sub> system, this technique allows the formation of Bi nanograins uniformly distributed in the SiO<sub>x</sub> insulating matrix. The size of the Bi nanograins (mean diameter about 4 nm) may be responsible of a surprising optical property of the LECBD Bi-SiO<sub>x</sub> cermets. The difference between theoretical and experimental optical behavior of LECBD cermets is assumed to be a clue of size effects inducing a metal-semiconductor transition.

### 1 INTRODUCTION

Cermets are composite materials of metals and insulators used as resistive materials<sup>1</sup> and efficient absorbers.<sup>2</sup> The ideal cermet film is composed with small metal particles presenting a narrow size distribution and uniformly distributed in the insulating material. In our laboratory, we have developed a technique named Low-Energy Cluster Beam Deposition (LECBD) which allows, for instance, the formation of ultrathin films presenting new structure and different properties<sup>3</sup> compared to films obtained by the conventional Molecular Beam Deposition (MBD). The size distribution of the supported particles roughly corresponds to that of clusters in the beam. So the LECBD technique appears to be an interesting way to synthesize cermet films with controlled size nanoparticles. In this paper, we present the first results obtained on LECBD cermet films obtained by simultaneous deposition of neutral Bi clusters and SiO<sub>x</sub> molecules. LECBD cermet films have been characterized by Transmission Electron Microscopy (TEM), optical transmission and X-ray Photoelectron Spectroscopy (XPS).

### 2 EXPERIMENTAL PROCEDURE

Bismuth clusters are generated by the gas aggregation technique in a thermal source.<sup>4</sup> The metallic vapor obtained from an heated crucible is cooled in an inert gas (Ar or He) at liquid nitrogen temperature to obtain a Bi cluster beam. The cluster size, which is controlled by the pressure and the nature of the inert gas, is measured by a time of flight mass spectrometer before deposition. In the present experiments the mean diameter of incident Bi clusters is 4 nm (850 atoms). The SiO<sub>x</sub> and Bi cluster deposition are simultaneous and the deposition rate of SiO<sub>x</sub> in comparaison with the Bi one controls the cermet composition. During deposition, the residual pressure is less than 10<sup>-4</sup> Pa. Cermets are deposited at room temperature on optically polished glass substrat and on amorphous carbon-coated grids for transmission electron microscopy (JEOL-200 CX operating at 100 kV accelerating voltage). The optical transmission has been made at normal incidence over the wavelength range  $\lambda = 200$  to 3000 nm with a Cary 2300 spectrophotometer.



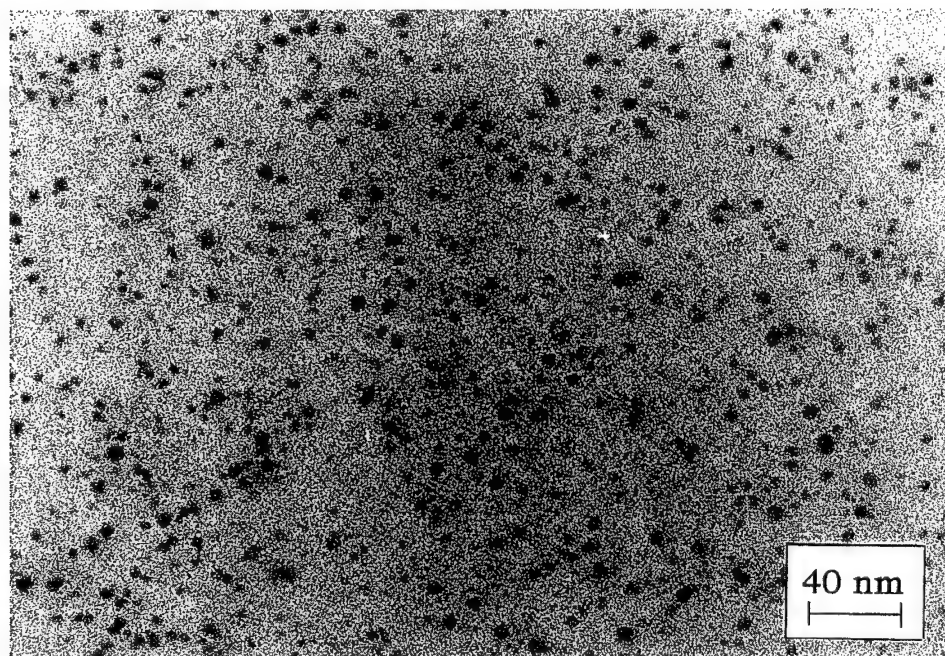


FIGURE 1 TEM micrograph showing the morphology of cermet (30 nm thickness and 1.6% Bi volumic concentration).

Chemical analysis has been performed by X-ray photoelectron spectrometry (XPS) in a UHV Nanoscan Cameca system. The XPS spectra were recorded on a MAC2 spectrometer using a Mg-K $\alpha$  radiation.

### 3 RESULT

TEM observations have been performed on 30 nm thick cermets of 1.6% Bi volumic concentration. For this concentration, the Bi nanograins are isolated as shown on Figure 1. This TEM micrograph (Figure 1) shows spherical and isolated particles homogeneously distributed on the substrate. The Bi nanograins present a narrow size distribution (3–5 nm) with a mean diameter of 4.2 nm. The size distribution of Bi inclusions is very similar to free cluster size distribution, indicating that the Bi cluster diffusion is very low. High resolution electron microscopy and dark field observations with Bi reflections show that most part of Bi grains is amorphous. Nevertheless some grains are crystallized, but not surrounded by an amorphous layer as observed for crystallized supported Bi particles.<sup>5</sup> The homogeneity in depth distribution of Bi nanograins has been shown by cross-section TEM observations on thick films.<sup>6</sup> These results confirm that LECBD is a promising technique to elaborate cermets with a given grain size distribution (corresponding to that of the cluster in the beam) in the nanometric range.

To control the composition of the metallic inclusions of LECBD cermets, XPS measurements have been carried out. We choose a 18% volumic concentration of Bi which corresponds to the percolation threshold in a three- dimensional system. XPS results are

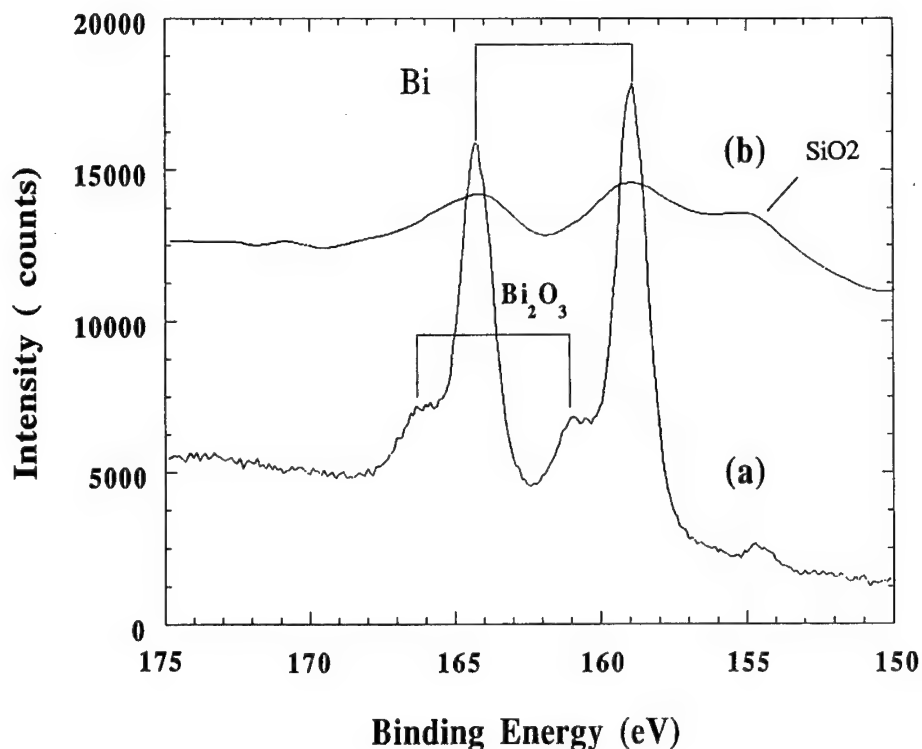


FIGURE 2 X-ray photoemission spectra of 30 nm thick Bi film (a) and LECBD cermet (b). Because of the charge accumulation effects in LECBD specimen, a charge correction determined on the 2p<sub>1/2</sub> core level transition of SiO<sub>2</sub> has been applied on spectra 2b (3 eV energy shift).

presented in Figure 2. Spectra 2a and 2b correspond respectively to a 30 nm thick Bi film and LECBD cermet. The two doublets observed on spectrum 2a correspond to the 4f<sub>5/2</sub> and 4f<sub>7/2</sub> lines of Bi and Bi<sub>2</sub>O<sub>3</sub> (surface native oxide). The comparison of this 'reference' spectrum with the LECBD cermet one shows that no Bi oxide contribution has been noticed in the LECBD cermets. The LECBD technique, contrary to other methods,<sup>7</sup> allows to elaborate Bi-SiO<sub>x</sub> unoxidized cermets. It is an appropriated method for carry out unoxidized films (for example Samarium films)<sup>11</sup> when other techniques can't.

As Bi nanograins are not oxidized in LECBD cermets, they are expected to behave as metallic particles. This assumption has been analysed using optical spectrometry. Metallic particles embedded in a matrix give an extra contribution to the effective dielectric permittivity of the medium. A theoretical model for the explanation of this phenomenon was set up by Maxwell-Garnett assuming that the particles are spherical and small with respect to the wavelength of incident light. So simulations have been completed using the calculations of Marton and Lemon<sup>8</sup> assuming that the optical constants of fine bismuth particles are the same as those for bulk bismuth. The constants *n*, *k* of bulk Bi are determined by ellipsometric measurements in a range of 200–700 nm of wavelength. The Figure 3 shows the calculated optical density versus the wavelength  $\lambda$  of the incident light

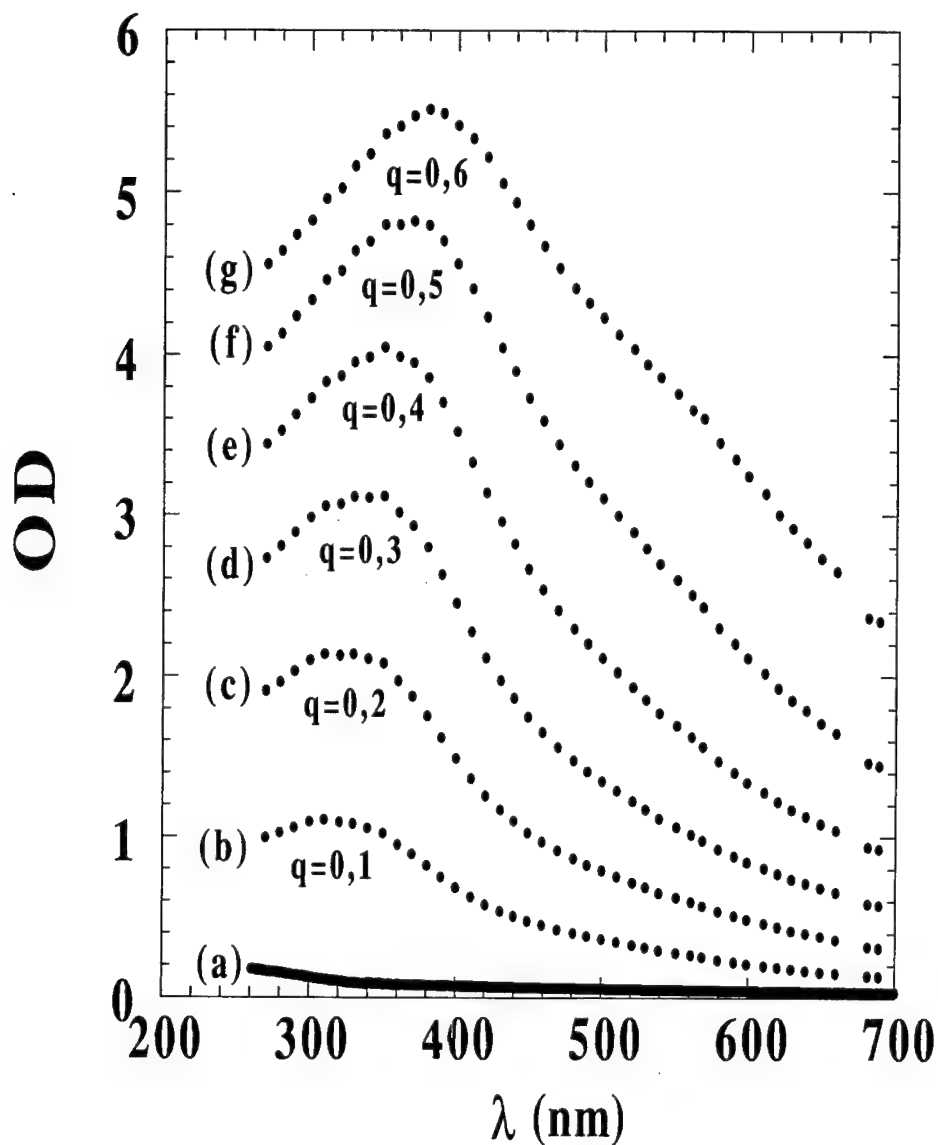


FIGURE 3 Evolution of optical density OD calculated with the Maxwell-Garnett theory versus the wavelength  $\lambda$  of the incident light, for several Bi filling factor  $q$  (The thickness for curves b-c-d-e-f-g is 20 nm). The curve (a) is the experimental spectrum of a cermet ( $q = 0.1$  and the thickness is 20 nm). The other experimental spectra with several filling factor  $q$  give also no absorption band.

for several filling factors  $q$ . The filling factor is a measure of the volume fraction of the particles in the composite. We can see on the Figure 3 an optical absorption band due to the presence of metallic particles embedded into the insulating matrix. The wavelength at maximum optical density is red shifted, as the filling factor  $q$  increased. The experimental

optical transmission measurements have been performed on LECBD cermets with several filling factors  $q$  ( $q$  lower than the percolation threshold filling factor  $q_c$ ). The absorption band predicted by the Maxwell-Garnett theory has not been observed. This can be considered as the first evidence that Bi nanograins do not behave as metallic grains. This size effects is in agreement with other experimental results obtained on thin Bi films. This size effect (or quantum size effect) is wellknown for Bi.<sup>9,10</sup> For example, Hoffman<sup>10</sup> has shown a decrease of electron concentration with film thickness:  $5.10^{18}$  electrons  $\text{cm}^{-3}$  for a 500 nm thickness  $9.10^{17}$   $\text{cm}^{-3}$  for a 20 nm Bi film thickness. This semi-metal-semiconductor transition should occur also in LECBD cermets for which size effect in 4 nm diameter Bi particles are expected to be enhanced. Raman spectroscopy studies are now in progress to confirm this assumption.

#### REFERENCES

1. B. Abeles, P. Sheng, M. D. Coutts and Y. Arie, *Adv. Phys.* **24** (1975) 407.
2. C. Sella and J. Lafait, *Appl. Surf. Scie.*, **33/34** (1988) 942.
3. G. Fuchs, P. Melinon, M. Treilleux, A. Hoareau, J. X. Hu, B. Cabaud., *Appl. Phys. Lett.* **59** (1991) 1421.
4. M Broyer, B. Cabaud, A. Hoareau, P. Melinon, D. Rayane, B. Tribollet., *Mol. Phys.* **B62** (1887) 559.
5. M. Treilleux, G. Fuchs, C. Montandon, F. Santos Aires, B. Cabaud and A. Hoareau, *Phil. Mag.* **A67** (5) (1993) 1071.
6. J. F. Roux, M. Treilleux, B. Cabaud, G. Fuchs, C. Montandon, A. Hoareau, *J. Phys. France* **4** (1994) 991.
7. Takeo Hattori, Hideki Akazawa., *Thin Solid Films*, **57**, 98 (1979) 71.
8. J. P. Marton, J. R. Lemon., *Phys. Rev.* **B4** (1971) 271.
9. M. G. Mitch, S. J. Chase, J. Fortner, R. Q. Yu, J. S. Lannin, *Phys. Rev. Lett.*, **67** (7) (1991) 875.
10. C. A. Hoffman, J. R. Meyer, F. J. Bartoli, A. Di Venere, X. J. Yi, C. L. Hou, H. C. Wang, J. B. Ketterson, *Phys. Rev.*, **B48** (15) (1993) 11431.
11. G. Fuchs, P. Melinon, M. Treilleux, J. Le Brusq., *J. Phys.*, **D26** (1993) 143.

## ELECTRONIC STRUCTURE AND OPTICAL SPECTRA OF OVERSTOICHIOMETRIC CADMIUM ATOMS IN CdI<sub>2</sub> CRYSTALS

I. BOLESTA, I. KITYK,<sup>1</sup> V. KOVALISKO and R. TURCHAK

*Department of Physics, Lviv State University, 50 Dragomanova st., Lviv, 290005, Ukraine*

The article deals with the investigation of concentration dependences of absorption, luminescence and photosensitivity impurity bands, caused by the introduction of overstoichiometric cadmium atoms (Cd<sub>i</sub>) into the lattice of strongly anisotropic CdI<sub>2</sub> layered crystal. The model, explaining concentration dependences of CdI<sub>2</sub>-Cd<sub>i</sub> spectra, suggests localization of Cd<sub>i</sub> atoms in Van-der-Waals gaps of layered crystals and their interaction with themselves and with lattice iodine atoms. The character of these interactions strongly depends on Cd<sub>i</sub> concentration (i.e. on the distance between Cd<sub>i</sub> atoms) and changes from *s*-Cd<sub>i</sub> - *p*-I (at  $N_{Cd_i} < 10^{18} \text{ cm}^{-3}$ ) to *s*-Cd<sub>i</sub> - *s*-Cd<sub>i</sub> interaction at higher concentration. The quantum-chemical simulations were carried out to confirm the proposed model.

**Key words:** nonstoichiometric atoms, concentration dependence, optical spectra, layered crystals, impurity defect.

### 1 INTRODUCTION

The characteristic properties of layered crystals are caused by the ability of impurities to localize in different crystallographic positions depending on doping method. The localization of impurity atoms at Van-der-Waals gaps of layered crystals during the crystal growth would cause the formation of system similar to intercalated one, which is created by diffusion method.<sup>1</sup> The above mentioned quasiintercalated system was achieved in the strongly anisotropic CdI<sub>2</sub> layered crystals with overstoichiometric cadmium atoms. Modified Bridgman method<sup>1</sup> was used to obtain a number of CdI<sub>2</sub>-Cd<sub>i</sub> single crystals with monitored overstoichiometric cadmium atoms concentration ( $N_{Cd_i}$ ):  $10^{-4}$ ,  $10^{-3}$ ,  $10^{-2}$ , and  $10^{-1}$  mol.% and pure (specially undoped) CdI<sub>2</sub>. The corresponding atom per volume concentrations are  $10^{16}$ ,  $10^{17}$ ,  $10^{18}$  and  $10^{19} \text{ cm}^{-3}$ , while the concentration of Cd<sub>i</sub> atoms in undoped CdI<sub>2</sub> crystals was assumed to be  $10^{15} \text{ cm}^{-3}$  ( $10^{-5}$  mol.%).

### 2 RESULTS AND DISCUSSION

The Cd<sub>i</sub> atoms give rise to complicated 383-387 nm impurity bands in absorption spectra, and additional emission band at 690 nm. The intensities of these bands increase with Cd<sub>i</sub> atoms concentration increasing till it reaches  $10^{18} \text{ cm}^{-3}$ . At higher Cd<sub>i</sub> concentration the absorption bands at 383-387 nm disappear, but a new band peaked at 800 nm is observed in spectra. Similarly to the absorption bands, the impurity luminescence band peaked at 690 nm disappears at  $N_{Cd_i} > 10^{18} \text{ cm}^{-3}$ . As a result the emission spectrum of CdI<sub>2</sub>-Cd<sub>i</sub> ( $N_{Cd_i} > 10^{18} \text{ cm}^{-3}$ ) coincides with the spectrum of undoped CdI<sub>2</sub> ( $\lambda_m = 500 \text{ nm}$  at 290 K)<sup>1</sup>.

The investigations of  $X_{14} \equiv X_{123}$  component of nonlinear susceptibility, electrooptical coefficient  $r_{41}$ , and <sup>127</sup>I NQR peak frequencies  $\nu_1$  and  $\nu_2$  of 4H-polytype CdI<sub>2</sub>-Cd<sub>i</sub> shows

<sup>1</sup> Institute of Physics, Pedagogical University, Al. Armii Krajowej 13/15, 42201 Czestochowa, Poland.

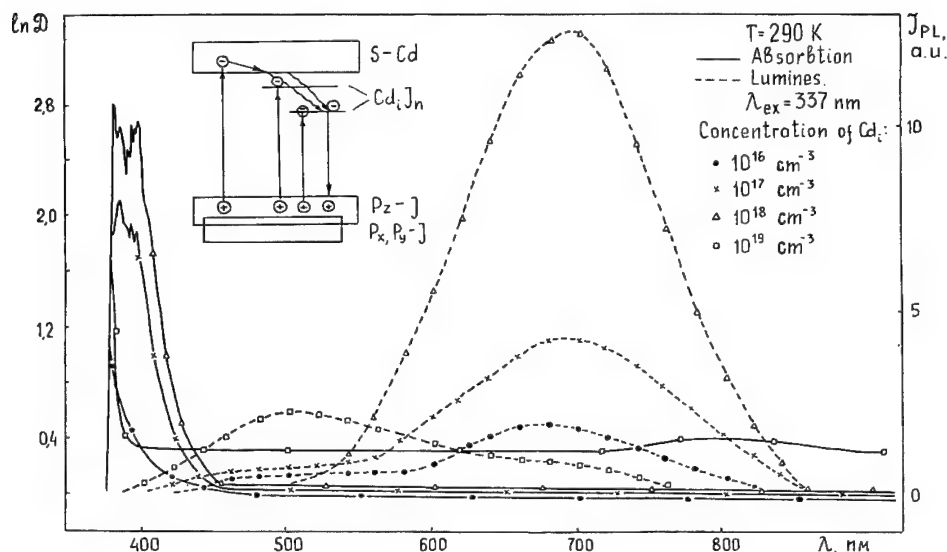


FIGURE 1 Differential absorption and luminescence spectra of  $\text{CdI}_2\text{-Cd}_i$  single crystals.

the similarity of concentration dependences of above mentioned physical parameters (Figure 2).

To explain the concentration dependence of  $\text{CdI}_2\text{-Cd}_i$  single crystals' physical properties, the following model is proposed. It suggests that  $\text{Cd}_i$  atoms built up into octahedral and/or tetrahedral holes in Van-der-Waals gaps of layered crystals and interact with themselves and with lattice iodine atoms. At  $N_{\text{Cd}_i} < 10^{18} \text{ cm}^{-3}$  the interaction of  $\text{Cd}_i$  atoms with iodine ions ( $s\text{-Cd}_i - p\text{-I}$  interaction) prevails, resulting in creation of  $[\text{Cd}_i \text{I}_n]$  complexes ( $n = 4, 6$  for tetrahedral and octahedral holes respectively). These complexes give rise to local levels in  $\text{CdI}_2$  forbidden gap band. Therefore, the observed impurity bands in absorption and luminescence spectra are attributed to electron transitions between valence band and local levels of  $[\text{Cd}_i \text{I}_n]$   $n = 4, 6$  complexes. In this model the appearance of impurity photosensitivity band is associated with the motion of holes in valence band, formed by  $p$ -orbitals of iodine (insert on Figure 1).

The formation of  $[\text{Cd}_i \text{I}_n]$  complexes leads to a redistribution of the electronic density of  $\text{CdI}_2$  and thus modifies the value of acentricity and electric field gradient of  $4\text{H-CdI}_2$  lattice. This explains the variation of nonlinear optical parameters and  $^{127}\text{I}$  peak frequencies of  $\text{CdI}_2\text{-Cd}_i$  crystals. At  $N_{\text{Cd}_i} > 10^{18} \text{ cm}^{-3}$  the  $s\text{-Cd}_i - s\text{-Cd}_i$  interaction becomes predominating, causing formation of nanoinclusions of metallic cadmium  $(\text{Cd}_i)_m$  ( $m > 2$ ) in  $\text{CdI}_2$  lattice. These nanoparticles give rise to additional absorption band at 800 nm due to light scattering, and simultaneously the changes of physical properties caused by  $[\text{Cd}_i \text{I}_n]$  complexes disappear.

The change of character of  $\text{Cd}_i$  atoms interaction due to variation of their concentration is confirmed by the calculation of  $V_{\text{sp}\sigma}$  and  $V_{\text{ss}\sigma}$  integrals, which characterize  $s\text{-Cd}_i - p\text{-I}$  and  $s\text{-Cd}_i - s\text{-Cd}_i$  interactions respectively.

The calculation of the corresponding integrals was made with taking into account the overlap and translational integrals which are calculated by the formula:

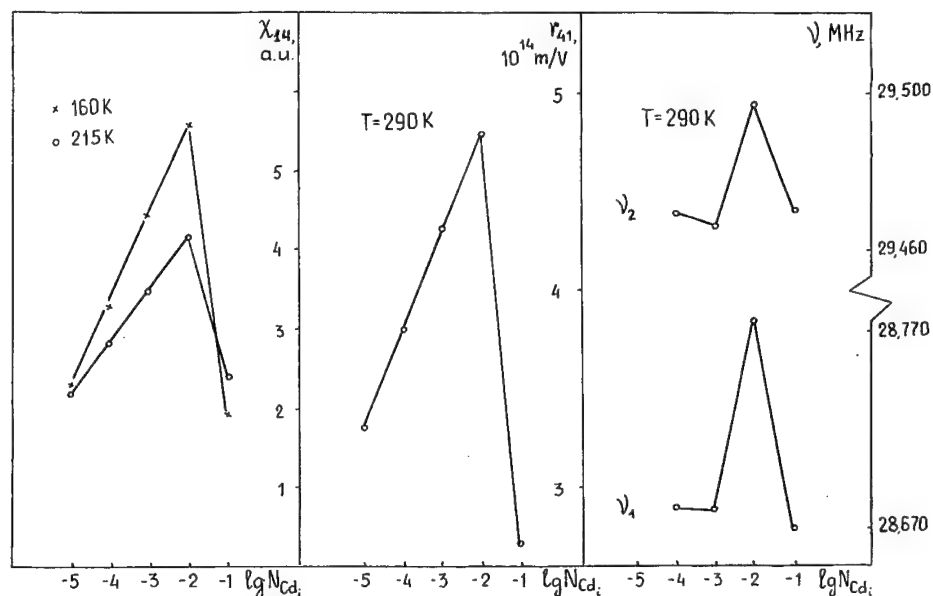


FIGURE 2 Concentration dependences of  $\chi_{14}$  component of nonlinear susceptibility tensor,  $r_{41}$  electrooptical coefficient and  $\nu_1$ ,  $\nu_2$  NQR peak frequencies of  $\text{CdI}_2\text{-CdI}$  single crystals.

$$\begin{aligned}
 V_{ss\sigma} &= \int \Psi_{s\text{Cd}_i}^* (\vec{r}_i - \vec{r}) \cdot \Psi_{s\text{Cd}_j} (\vec{r}_j - \vec{r}) d^3\vec{r} + \\
 &+ \int \Psi_{s\text{Cd}_i}^* (\vec{r}_i - \vec{r}) \cdot V_{\text{Cd}_j} (\vec{r}_i - \vec{r}) \cdot \Psi_{s\text{Cd}_j} (\vec{r}_j - \vec{r}) d^3\vec{r}; \\
 V_{sp\sigma} &= \int \Psi_{s\text{Cd}_i}^* (\vec{r}_i - \vec{r}) \cdot \Psi_{p\text{I}} (\vec{r}_j - \vec{r}) d^3\vec{r} + \\
 &+ \int \int \Psi_{s\text{Cd}_i}^* (\vec{r}_i - \vec{r}) \cdot V_{\text{Cd}_j} (\vec{r}_i - \vec{r}) \cdot \Psi_{p\text{I}} (\vec{r}_j - \vec{r}) d^3\vec{r};
 \end{aligned}$$

where

$$V_{\text{Cd}_i} (\vec{r}_i - \vec{r}) = V_{e-e}^{\text{Cd}} (\vec{r}_i - \vec{r}) + V_{e-e}^{\text{Cd}} (\vec{r}_i - \vec{r}) + V_{\text{ex}}^{\text{Cd}} (\vec{r}_i - \vec{r})$$

In the latter expression the terms  $V_{e-e}^{\text{Cd}} (\vec{r}_i - \vec{r}) = 4\pi e^2 \rho (\vec{r}_i - \vec{r})$ , and  $V_{\text{ex}}^{\text{Cd}} (\vec{r}_i - \vec{r}) = (3/8 \pi) [\rho (\vec{r}_i - \vec{r})]^{1/3}$  describe the Poisson and Slater screening, and  $V_{e-i}^{\text{Cd}}$  term describes electronic contribution into the overlap integral. To calculate  $V_{ss\sigma}$ ,  $V_{sp\sigma}$  values the summation was done up to the fifth coordinative sphere. This corresponds to the coincidence of eigenstates not less than 0.01 Ry. The concentration dependence of  $V_{ss\sigma}$  and  $V_{sp\sigma}$  obtained in such a way are presented in Figure 3. The analysis of these dependences shows that at  $N_{\text{Cd}_i} < 10^{18} \text{ cm}^{-3}$   $V_{ss\sigma} < V_{sp\sigma}$ , while in the vicinity of  $N_{\text{Cd}_i} = 10^{18} \text{ cm}^{-3}$   $V_{ss\sigma} > V_{sp\sigma}$ . The equality of  $V_{ss\sigma}$  and  $V_{sp\sigma}$  values at  $N_{\text{Cd}_i} = 3 \cdot 10^{18} \text{ cm}^{-3}$  allows to estimate the critical

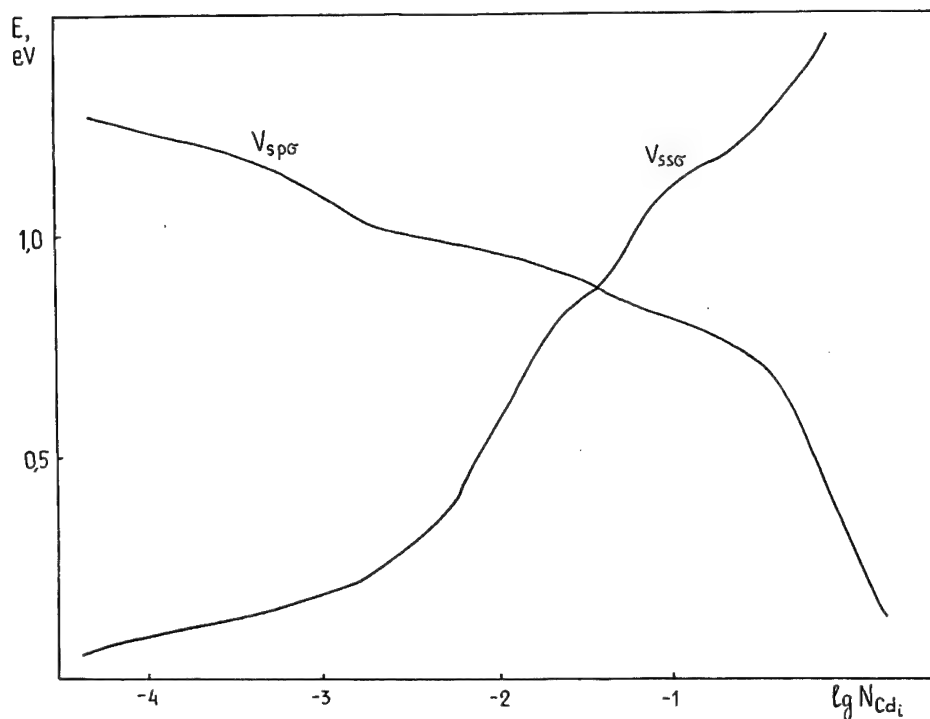


FIGURE 3 Concentration dependence of  $V_{ss\sigma}$  and  $V_{sp\sigma}$  integrals.

distance  $r_0$  at which the change of interaction mode in  $\text{CdI}_2\text{-Cd}$  lattice occurs. This distance is equal to  $\sim 70 \text{ \AA}$  and is in good agreement with the experimentally obtained values of  $r_0 = (N_{\text{Cd}_i})^{-1/3} \approx 50 \text{ \AA}$  for  $N_{\text{Cd}_i} = 10^{18} \text{ cm}^{-3}$ .

#### ACKNOWLEDGMENTS

This work was supported by the State Committee on Science and Technology of Ukraine.

#### REFERENCES

1. A. B. Lyskovich, N. K. Gloskovska, I. M. Bolesta, *Wide Gap Band Layered Crystals* (Vyscha shkola, Lviv, 1978), p. 126.



## ENHANCED RAMAN SCATTERING OF PHONONS IN $\text{CaF}_2$ AND $\text{MgO}$ CONTAINING Ca AND Li COLLOIDS

P. B. OLLETE, M. L. SANJUÁN and V. M. ORERA

*Instituto de Ciencia de Materiales de Aragón, C.S.I.C.-Universidad de Zaragoza Pza. San  
Francisco s/n, 50009 Zaragoza, Spain*

We present Raman scattering spectra of  $\text{CaF}_2$  samples with Ca colloids and  $\text{MgO}:\text{Li}$  with Li precipitates. The samples have been prepared by different thermal and irradiation treatment in order to achieve different colloid sizes. Exciting in the colloid surface-plasmon band we observe SERS of the whole density of states of  $\text{CaF}_2$  or  $\text{MgO}$  phonons, the intensity being enhanced when the excitation approaches the colloid band maximum. In order to explain the appearance of the one phonon density of states and the resonant behaviour we propose a mechanism consisting of surface plasmon and charge transfer excitation, superposed to the electromagnetic process.

*Key words:* SERS, colloids,  $\text{CaF}_2$  phonons.

### 1 INTRODUCTION

Most of the experimental work in SERS has focused on the enhancement of Raman activity of organic molecules close to or adsorbed on a metallic surface. Raman enhancement of the phonon density of states in crystals containing metallic colloids has also been reported. As far as we know, all the work in crystals refers to alkali halides containing silver or alkali metal particles<sup>1,2,3</sup>

In this article we report on the Raman enhancement of  $\text{CaF}_2$  phonons due to the presence of Ca colloids. The advantage of  $\text{CaF}_2$  with respect to alkali halides is that it has an allowed mode, which gives a good probe of the degree of activation of the other phonon modes. We also present the observation of the  $\text{MgO}$  single phonon density of states by SERS in lithium colloids.

### 2 EXPERIMENTAL DETAILS

Raman spectra were measured in a Dilor XY spectrometer with diode array detector. An  $\text{Ar}^+$  laser was used in the 2.35–2.7 eV region and a dye-laser in the 2–2.1 eV region. The laser is focused onto the sample through a 50 X objective. The laser power was typically 10–20 mW on the sample. Back scattering geometry was used in all cases.

Metallic calcium particles in  $\text{CaF}_2$  were produced using either additive coloration or irradiation techniques.<sup>4,5</sup> We have prepared several samples with different colloid sizes. Optical absorption spectra show the F band at  $\approx 380$  nm and a broad band around 550 nm due to Ca colloids. In Table I sample characteristics derived from the absorption bands are presented. S4 could not be measured because of its high defect concentration.

We also studied samples of  $\text{MgO}:\text{Li}$  where Li precipitates were produced by thermochemical reduction (courtesy of Dr. Y. Chen, ORNL, USA). These samples presented very broad optical absorption bands with maxima near 550 and 580 nm.

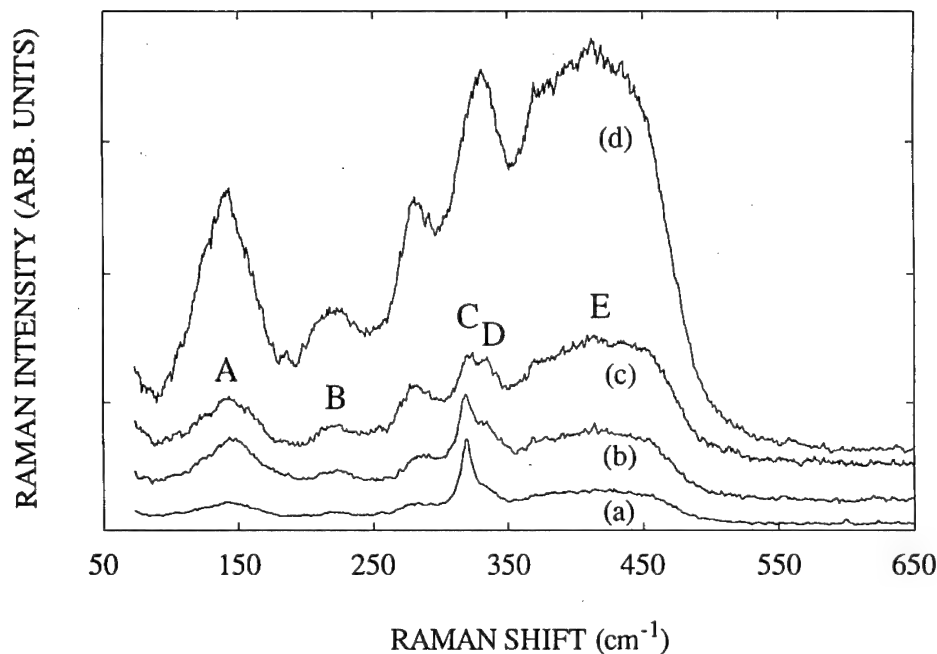


FIGURE 1 Raman spectra of S1 (a), S2 (b), S3 (c) and S4 (d) taken with  $\lambda = 528.7$  nm (2.345 eV) and  $E_i/E_s$  on (111) faces for spectra (a), (c), (d) and (100) for (b).

Table I

$r$ : mean colloid radius.  $N_p$ : number of metallic particles per unit volume.  $V_c$ : fractional colloid volume.  $I_R$ : relative intensity of the activated spectrum, in arbitrary units ( $\lambda = 528.7$  nm, band 'E',  $E_i/E_s$ ).  $S_c$ : colloid surface per unit volume.

Sample	$r(\text{nm})$	$N_p(\text{cm}^{-3})$	$V_c$	$I_R$	$S_c(\text{cm}^{-1})$
S0	12	$0.35 \times 10^{12}$	$2.7 \times 10^{-6}$	5	3.5
S1	3.5	$20 \times 10^{12}$	$3.6 \times 10^{-6}$	8	16
S2	11	$1.45 \times 10^{12}$	$8.1 \times 10^{-6}$	17.5	12
S3	25	$0.25 \times 10^{12}$	$1.7 \times 10^{-5}$	31	11

### 3 EXPERIMENTAL RESULTS AND INTERPRETATION

Raman spectra of the four  $\text{CaF}_2$  samples described above are shown in Figure 1. Since  $\text{CaF}_2$  has a unique Raman allowed mode ( $\nu_0 = 322 \text{ cm}^{-1}$ ) seen as a strong narrow peak in the spectrum of S1 and S2, all the accompanying structure is attributed to the presence of cation colloids. Though the main features are common to the spectra of all four samples the whole intensity as well as the ratio between the allowed and forbidden spectra are greatly sample dependent, being found roughly a linear correlation between the intensity of the forbidden spectrum and the colloid volume fraction.

In Figure 2 we present for sample S1 the Raman intensity vs. excitation energy of peaks labelled in Figure 1. A clear resonant behaviour towards the longer wavelengths is

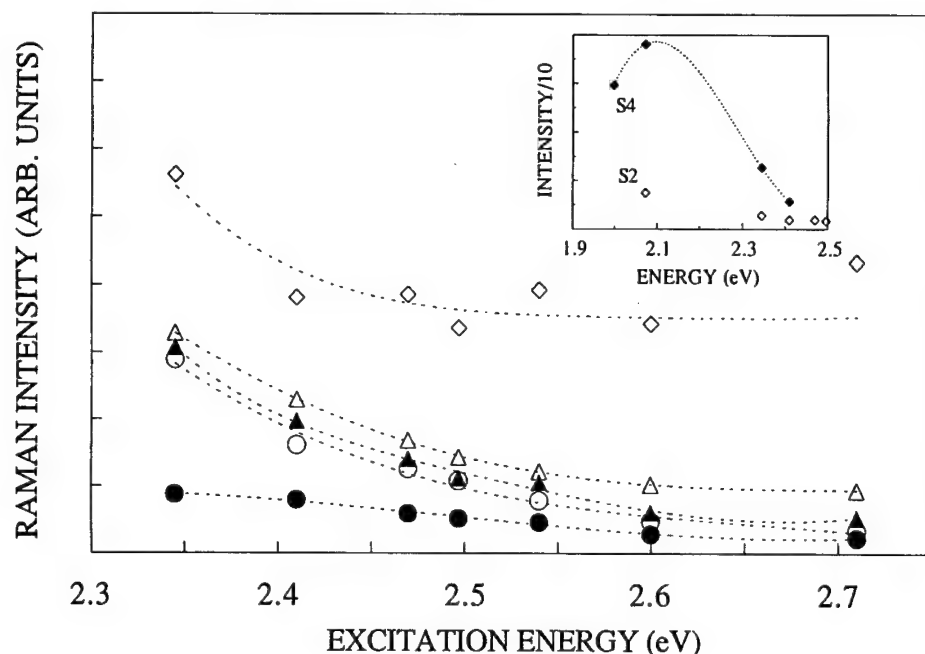


FIGURE 2 Excitation curves of peaks A ( $\circ$ ), B ( $\bullet$ ), C ( $\diamond$ ), D ( $\blacktriangle$ ) and E ( $\triangle$ ) with  $E_i/E_s$ .

seen for all the modes, except perhaps for peak B ( $\nu_0 \approx 220 \text{ cm}^{-1}$ ). Since this sample has the maximum of the colloidal band near 550 nm (2.25 eV) the intensity enhancement is ascribed to a resonance phenomenon within the colloid band, being corroborated by the measurements performed on sample S4 at energies below the colloid band maximum (see inset in Figure 2). The fact that the allowed mode shows a weaker resonant enhancement is in agreement with this interpretation: part of it is due to regions of  $\text{CaF}_2$  not perturbed by the colloids; only that part of the peak arising from regions close to the metallic particles will resonate in the SP band.

The forbidden spectrum is interpreted as due to first-order vibrations of  $\text{CaF}_2$  activated by the presence of colloids. Other possibilities are readily discarded: double phonons would extend up to much higher frequencies; local modes around vacancies or defects would not account for the high intensity observed neither for its resonant behaviour when the laser approaches the maximum of the colloid band. In Figure 3 we compare the Stokes spectrum of S2 and of a  $\text{MgO}$  sample with the one phonon density of states of  $\text{CaF}_2$ <sup>6</sup> and of  $\text{MgO}$ <sup>7</sup> respectively. Though there is a clear discrepancy in the relative intensities the position of the main features are reproduced in the experimental spectrum. Considering that the coupling of different vibrations may be different strength, the agreement is still remarkable. The fact that the major discrepancy occurs in the region of LO phonons indicates that their electron-phonon coupling is much stronger than for the rest of phonon. 'Hot phonon' non equilibrium were looked for by measuring the Stokes/Anti Stokes ratio in a  $\text{CaF}_2$  sample. The result was in agreement with the expectation for thermal equilibrium with  $kT = 300 \text{ K}$ , indicating that no anomalous phonon population exists.

There are traditionally two models that try to explain SERS results, the classical electromagnetic (EM) enhancement and charge transfer (CT) excitations. The classical EM

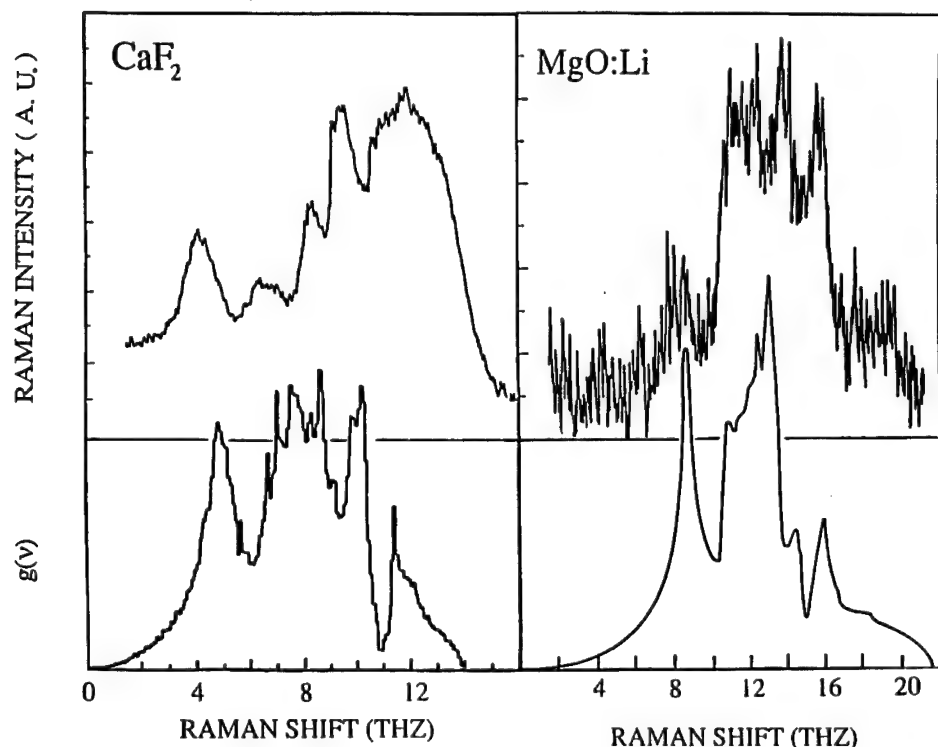


FIGURE 3 Above: Raman spectra taken with  $\lambda = 514.5$  nm of S2 with  $E_i/E_s/[100]$  and a MgO sample. Bottom: phonon density of states of  $\text{CaF}_2$  (from)<sup>6</sup> and MgO (from).<sup>7</sup>

enhancement arises from the enhancement of the electric field acting on the molecule. In this model colloid band resonance and the allowed mode dependence can be explained, but not other features observed:

- 1) within the classical EM model<sup>8</sup> and using the simple expression for molecules adsorbed on a spherical particle<sup>9</sup> enhancements for Ca and Li colloids of  $10^4$  or  $10^5$  are obtained. However, since the intensity observed will depend on the colloid density, very low for all the samples, the relative enhancement is expected to be about 10%.
- 2) the enhancement depends only on optical constants and cannot induce the selection rules breaking necessary to activate the forbidden spectrum. This can only be explained by the distortion of the host surrounding the colloid but in that case, and due to the narrowness of this region, the spectrum intensity would vary as the fractional colloid surface and not as the fractional colloid volume, as observed.
- 3) within the EM model the different proportion of the allowed mode to the rest of activated modes in different samples cannot be explained.

In order to explain the appearance of the whole density of phonons we propose the mechanism of SP+CT excitations as the most likely one, superposed to the EM process. The model consists of SP excitation followed by electron transfer from the metal to the host and de-excitation in the metal/host interface. In the host, electron-phonon interaction

takes place, as in usual Stokes or Anti Stokes processes, giving rise to single-phonon modes. The lattice distortion and loss of periodicity in the vicinity of the colloid break the  $\mathbf{k} = 0$  selection rule and account for the appearance of the whole density of states. On the other hand, EM process can explain the behaviour of the allowed mode.

P. B. Oliete thanks D. G. A. for financial support.

#### REFERENCES

1. E. Rzepka, S. Lefrant and L. Taurel 1979 *Solid State Commun.* **30**, 801.
2. H-B. Abel and F Fischer 1987 *phys. stat. sol.* **B144**, 875.
3. H-B. Abel and F Fischer 1991 *phys. stat. sol.* **B167**, 741.
4. V. M. Orera and R. Alcalá 1976 *phys. stat. sol.* **A38**, 621.
5. V. M. Orera and R. Alcalá 1976 *phys. stat. sol.* **A44**, 717.
6. M. M. Elcombe and A. W. Pryor 1970 *J. Phys. C: Solid St. Phys.* **3**, 492.
7. M. J. L. Sangster *et al.* 1970 *J. Phys. C: Solid St. Phys.* **3**, 1026.
8. J. K. Sass, H. Neff, M. Moskovita and S Holloway 1981 *J. Phys. Chem.* **85**, 621.
9. M. Kerker, D-S. Wang and H. Chew 1980 *Appl. Optics* **19**, 4159.

## TEM STUDY OF FE-CO OXIDES SYSTEM OF AMMONIA CATALYST

V. S. TEODORESCU and L. C. NISTOR

*Institute of Atomic Physics—IFTM—P.O. Box Mg-6, 76900-Bucharest, Romania*

The structure of the complex Fe-Co mixed oxides system, prepared as an industrial ammonia catalyst, is studied by TEM (transmission electron microscopy). The introduction of Co in the system create a high density of structural extended defects. Concentration of Co bigger than 10 a.% lead to the formation of a high density of precipitates which were identified as  $\text{Co}_3\text{O}_4$  in the magnetite matrix. The data in this phase identification was obtained by moiré fringe analysis.

### 1 INTRODUCTION

The unreduced state of the ammonia catalyst consists in a doped magnetite. The dopants are Al, Si, Ca and K atoms, in a total content of about 3–4% and act as structural and activity promoters.<sup>1</sup> The principal structural promoter is  $\text{Al}_2\text{O}_3$  and has the role to introduce a high density of defects in the lattice and to limit the dimensions of the magnetite grains obtained by the solidification of the melted material. The introduction of Co in the system contribute to the formation of a higher density of structural extended defects in the magnetite, even the Co atoms can substitute very easy the Fe atoms in the lattice. Lattice parameter of the  $\text{CoFe}_2\text{O}_4$  (0.8392 nm) is very close to the value of the  $\text{Fe}_3\text{O}_4$  (0.8396 nm) lattice constant and the mechanism of defect introduction is not clear.

The high complexity of the catalyst structure, with a large spectrum of lattice defects, can not be analysed only by integral method, like X-ray diffraction and magnetic measurement and need microscopic local investigation. This paper present some structural analysis results in the study of this system obtain mainly by analytical transmission electron microscopy.

### 2 EXPERIMENTAL

The samples were prepared by mixing, melting and oxidation control of the components. The fast cooling leads to the formation of a uniform bulk material with small crystallites. The TEM specimens was prepared by crushing the bulk catalyst in powder form. The Co content range was between 3 to 20 a.% and is relatively uniform in the samples, as the EDXS measurement qualitatively reveal. The observations was performed with a Jeol TEMSCAN 200-CX instrument, equipped with a Link System EDXS spectrometer.

### 3 RESULTS

At a microscopic scale the samples are not uniform from the point of view of the nature and the density of the defects. In the 3 and 5 a.% Co doped samples, two morphologies have been found. First consists in well crystallised magnetite grains (Figure 1) and the second in a low crystallised, nearly amorphous, components (Figure 2). Such low crystallised grains have always a texture. In the crystallised grains of the 5 a.% Co doped

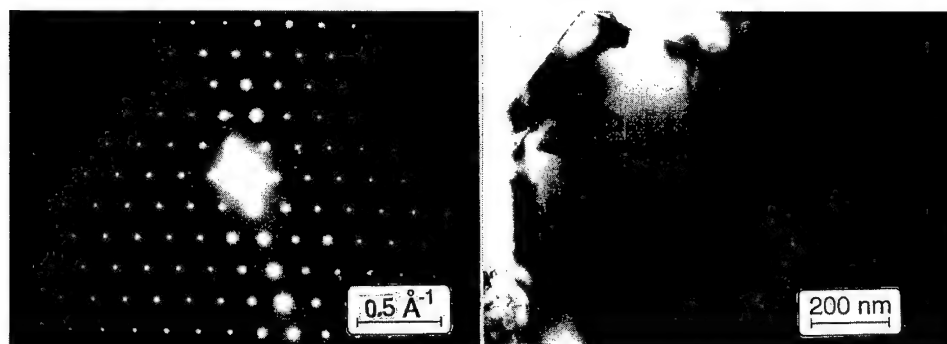


FIGURE 1 Well crystallised magnetite grain in the 3 a.% Co content catalyst, in the (110) orientation.



FIGURE 2 Low crystallised material in the catalyst with 3 a.% Co, with (100) texture.

sample, a high density of extended defects appear, and the SAED (selected area electron diffraction) images show the presence of reduced  $\text{Fe}_3\text{O}_{4-x}$  superstructure, with double lattice parameter (Figure 3).

Higher concentration of Co in the system, lead to precipitates formation and then to a sharp decreasing of the defect density in the magnetite grains. The precipitates were observed in the 10 a.% Co doped samples with dimensions in the range of 10–20 nm (Figure 4) and a density of about  $10^{22} \text{ m}^{-3}$ . The X ray diffraction spectra suggest the presence of FeO or (Co, Fe)O, but the sample is not uniform in the microscopic scale and the X-ray diffraction reveal only a average of different local structure.

The precipitates were found to be  $\text{Co}_3\text{O}_4$  coherent with the magnetite matrix, based on the parallel moiré fringes measurement determination. The moiré fringes were generated by the splitting of the 440 reflection spot of the matrix, showing a period of 4 nm (Figure 4). The possibility to have other precipitation like FeO or (Co, Fe)O is not confirmed because the calculated distances are far from the experimental one. If the concentration of the Co is bigger than 15–20 a.%, the precipitates dimensions increase to 40–60 nm in all crystallised grains and the degree of coherence with the matrix is lost.

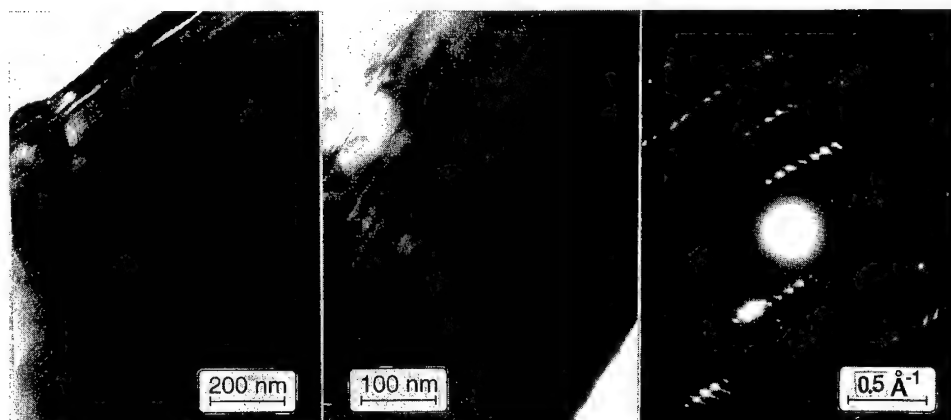


FIGURE 3 Extended defects in the lattice of the 5 a.% Co doped catalyst. The SAED image shows reflections of a double lattice nonstoichiometric structure.

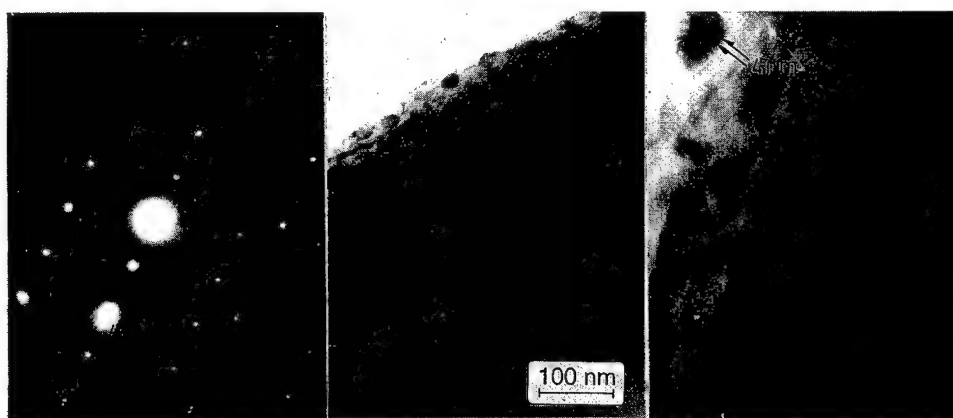


FIGURE 4 Coherent precipitation of  $\text{Co}_3\text{O}_4$  in the 10 a.% Co content catalyst grain.

#### 4 DISCUSSION

In the crystal growth process induced by the fast solidification of the melted catalyst, the magnetite monocrystalline grains can easily incorporate the Co atoms. The rest of the catalyst contains the majority of the promoter atoms and has a very low crystallinity.

This process is responsible for the non-uniformity of the bulk catalyst on the microscopic scale. The lattice of the magnetite is partially reduced and local complicated superstructures can appear with a double lattice parameter. In the TEM images, a high density of extended defects, like stacking faults and crystallographic shear planes with a superposed contrast, connected with the nonstoichiometry of the sample.



The precipitation of the  $\text{Co}_3\text{O}_4$  in the magnetite grains take place in a topotactic manner and the two lattice remain coherent for the small precipitation. The density estimation of the precipitates lead to the conclusion that the Co concentration can be bigger than the average. This observation supports the hypothesis of the Co incorporation, mainly in the well crystallised grain of the catalyst. The presence of the  $\text{CoFe}_2\text{O}_4$  structure in the system is put in to evidence by the magnetic susceptibility measurement. Because the lattice parameters of the  $\text{Fe}_3\text{O}_4$  and  $\text{CoFe}_2\text{O}_4$  are nearly equal, the diffraction data and the moiré fringes are identical with the situation of  $\text{Co}_3\text{O}_4$  precipitate in  $\text{CoFe}_2\text{O}_4$  matrix, system which is known for the spinodal decomposition.<sup>2</sup> This situation is not real, because the EDXS spectra show in all the analysed samples, a smaller concentration of Co in the catalyst grains than in the  $\text{CoFe}_2\text{O}_4$  etalon sample.

## 5 CONCLUSIONS

The introduction of Co in the magnetite prepared as ammonia catalyst, leads to the formation of a bigger density of structural defects in the crystalline lattice of the material, working in the sense of requirements for catalytic promoter. However, Co atoms are concentrated in the well crystallised catalyst grains growth in the solidification process and a nanometric coherent precipitation appear, if the average concentration of Co is bigger than 10 a. %.

## REFERENCES

1. H. Topsoe, J. A. Dumesic, M. Boudart, *J. Catal.* **28**, 477, 1973.
2. Landolt-Börnstein, Vol. 13, p. 245. ed. Springer-Verlag, Berlin, New York, 1980.

## OPTICAL NON LINEAR MEASUREMENTS IN CdS DOPED SILICA FILMS

A. OTHMANI, J. C. PLENET, E. BERNSTEIN, F. PAILLE, C. BOVIER, J. DUMAS,  
P. RIBLET,\* J. B. GRÜN,\* P. GILLIOT\* and R. LEVY\*

*Département de Physique des Matériaux, 43 Bd du 11 Nov. 1918 69622 Villeurbanne;  
\*Groupe d'Optique Non-linéaire et d'Optoélectronique,  
5 rue de l'Université 67084 Strasbourg*

Samples of CdS doped silica thin films have been prepared with weight concentrations ranging from 0.5 to 20% (CdO/SiO<sub>2</sub>). Nanocrystal structure and size distribution are determined by Transmission Electron Microscopy (TEM) and image analysis. The mean size is the same for all concentrations (4 nm) and is related to the matrix porosity. The linear absorption shows characteristic features of the excitonic level and the gap blue shift due to the quantum confinement. Non-linear optical properties are studied by Degenerate Four Waves Mixing (DFWM) to measure the third order susceptibility  $\chi^{(3)}$  which is high (typically  $10^{-7}$  esu) and depends linearly of the volume fraction of the semiconductor particles.

**Key words:** sol-gel, thin films, CdS, semiconductor nanocrystals, non-linear optics.

### 1 INTRODUCTION

Commercially available semiconductor doped silica glasses were among the first ones to be investigated for non linear optical properties related with ultrasmall and confined semiconducting particles.<sup>1–3</sup> These glasses have, however, a very complicated chemical composition. We have chosen to use the sol gel technique to prepare silica glass as this method allows to obtain ultra-pure host matrices for the nanocrystals. It is also possible to dope these sol-gel glasses with large concentrations of semiconductor. Finally, materials of good optical quality and which are not damaged by intense laser beam irradiation have been prepared.

In this paper, after a brief report of the preparation method and of the structural characterization, we will present main results of measured optical properties.

### 2 SAMPLES PREPARATION

Among the various techniques employed from sol-gel route to obtain thin films, the dip-coating method gives homogeneous samples. The solution used to prepare thin films is composed by the mixing of three components in the following ratios : 1 mole of TetraEthylOrthoSilicate (TEOS), 5 moles of H<sub>2</sub>O,  $2 \times 10^{-3}$  moles of HCl, 29 moles of Ethanol.  $5 \times 10^{-3}$  moles of cadmium is added in this solution from a methanol solution of hydrated cadmium acetate to obtain a 1% wt CdO/SiO<sub>2</sub> concentration.

The dipping system is classical and has already been described.<sup>4</sup>

The substrate—a clean microscope slide—is introduced in the solution at low speed, and after a short period of time necessary to eliminate any mechanical vibration, is withdrawn vertically at a speed adjusted between 10 and 40 mm/mn depending of the thickness desired.

It is necessary to smoothly remove liquids held in the film, eliminate the carbon compounds stored in the pores and harden the coating. Then, the sample is slowly put at

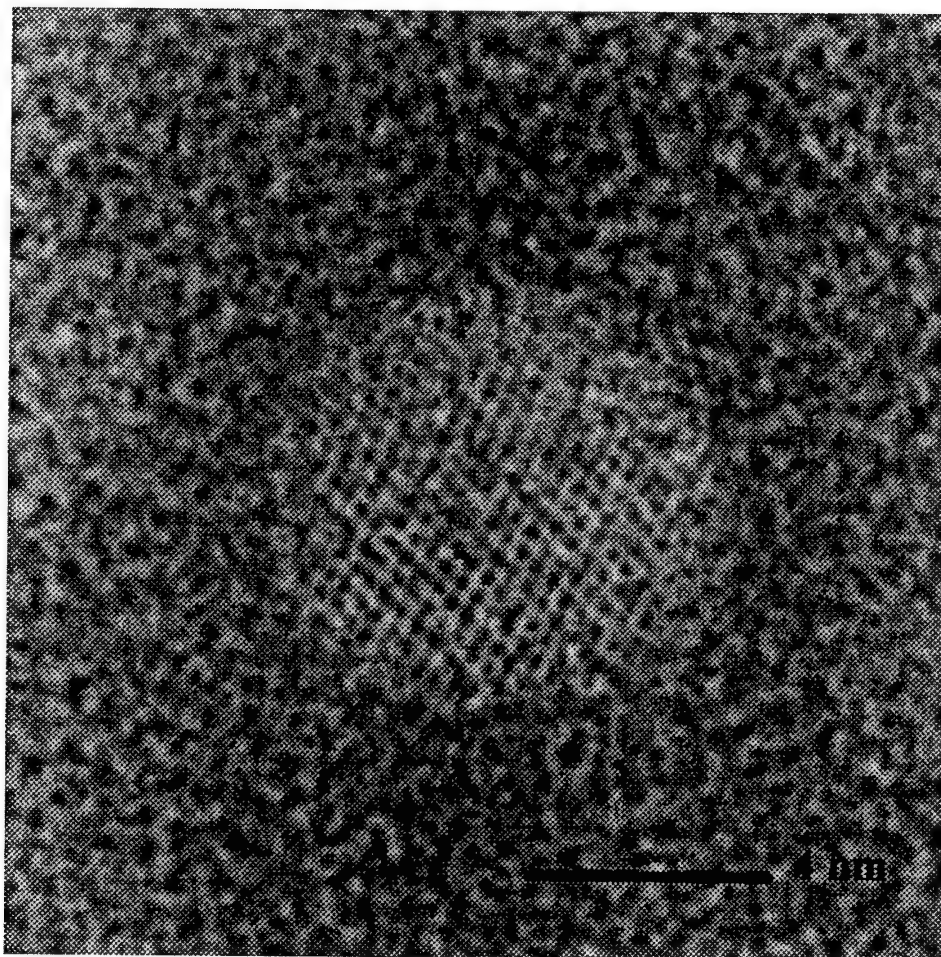


FIGURE 1 HRTEM micrograph of a CdS nanocrystal in silica thin film.

100°C, kept for 15 minutes at this temperature, and treated at 450°C in oxygen atmosphere during 5 minutes.

The coating is now submitted to a thermal treatment in H<sub>2</sub>S flow, at 200°C for 2 hours, to precipitate the CdS nanocrystals.

### 3 STRUCTURAL CHARACTERIZATION

Thin samples are obtained by grinding the silica films: electron microscopy was carried out at conventional (CTEM) and high resolution (HRTEM) with a JEOL 200CX electron microscope. CTEM was used to observe sufficiently large area of the edge of powder grains to measure size-distributions. The mean size for all concentrations studied is 4 nm and seems to be governed by the matrix porosity.<sup>5</sup>

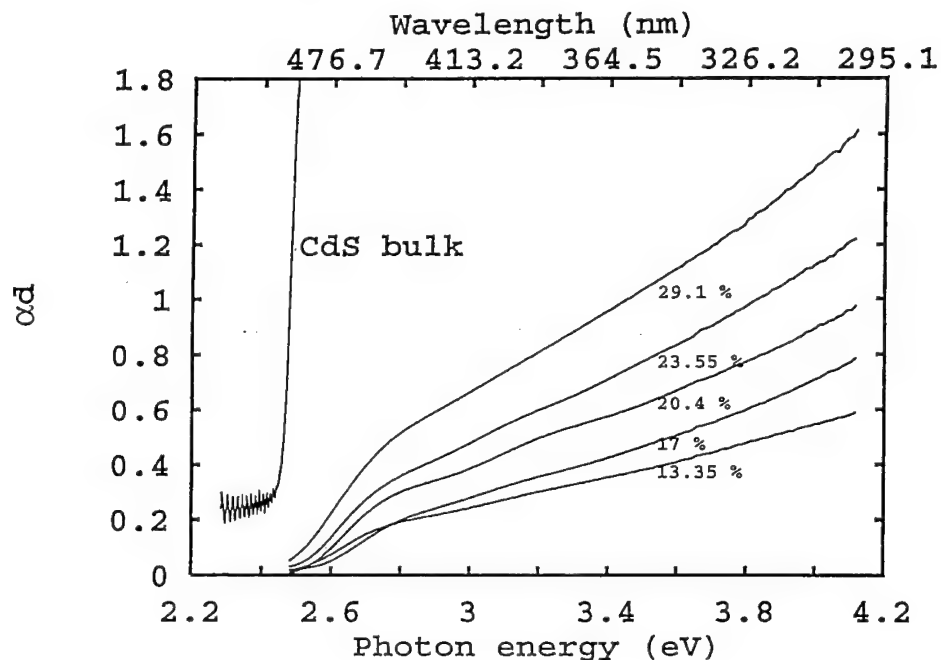


FIGURE 2 Absorption spectra at room temperature of samples with different volume fractions of CdS nanocrystallites dispersed in a sol-gel silica glass.

Figure 1 gives a typical example of a CdS nanocrystal as visualised by HRTEM. The hexagonal structure (wurtzite) of bulk CdS is observed on all the analysed nanocrystals with the same lattice constant as the bulk.

#### 4 OPTICAL PROPERTIES

The linear and non linear optical properties of CdS doped thin film glasses prepared by the sol gel method described above have been characterized as a function of the CdS concentration.

##### 4.1 Linear Optical Properties

The linear absorption spectra with different concentrations of CdS have been measured with a double beam Cary 2300 spectrophotometer at room temperature.

The different spectra obtained are summarized in Figure 2, together with the absorption spectrum of bulk CdS allowing an immediate comparison. They show an offset of absorption which is blue-shifted. The absorption spectra correspond to the electronic excitations of the quantum dots (QD) of CdS dispersed in a glass matrix, for different concentrations of the semiconductor.<sup>6</sup>

In our case QD radius is about 2 nm compared to 3 nm for Bohr excitonic radius in bulk CdS and the confinement induces a quantization of electron and hole kinetic energies

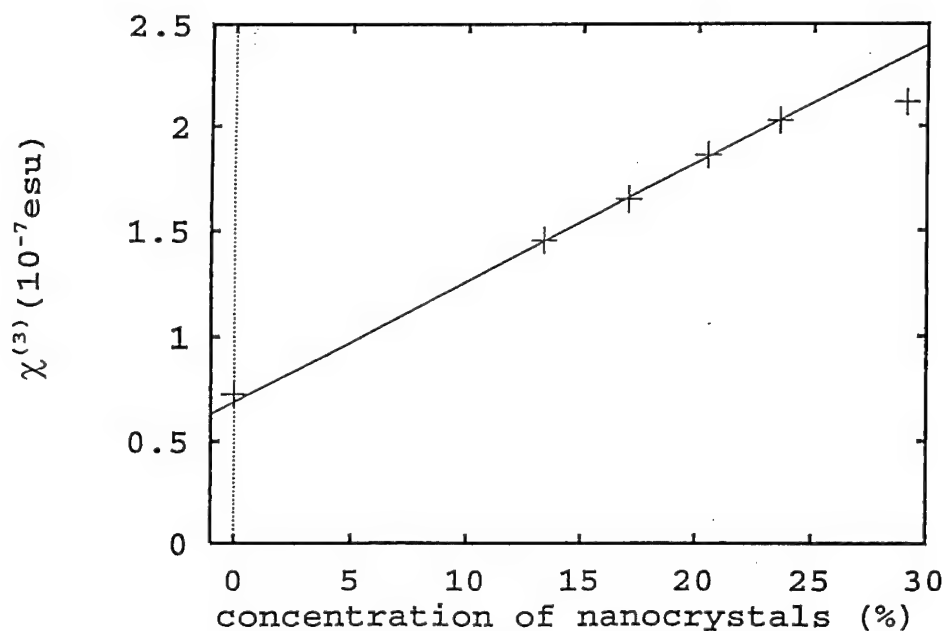


FIGURE 3 Third order non linear susceptibility  $\chi^{(3)}$  as a function of the concentration of CdS at room temperature.

and particularly of electrons because of their small effective mass ( $m^* = 0.2 m_0$ ) while quantization of hole energies can be neglected in a first approximation. The absorption due to the transition between the levels of the holes and the first level of electrons is therefore blue-shifted compared to the absorption edge of the bulk CdS as can be seen on Figure 2, the large broadening of these transition bands being mainly due to the size-dispersion of the QD.

#### 4.2 Non Linear Optical Properties

Degenerate Four Waves Mixing (DFWM) has been studied in these CdS doped silica film samples using a two beam geometrical configuration.<sup>7</sup> The light source was a tuneable dye laser with Coumarin 120 in methanol as active medium, pumped by a train of twelve third harmonic pulses of a mode-lock Nd<sup>3+</sup>:Yag laser. Single light pulses of almost Gaussian spatial intensity distribution (maximal intensity of 100 kW/cm<sup>2</sup>), of a duration of 20 ps and a spectral width of 0.3 meV are obtained and used. The beams generated in the sample by self diffraction were sent in a spectrograph through a two lenses system, and recorded by an optical multichannel analyser. The third order susceptibility  $\chi^{(3)}$  at room temperature has been determined at 440 nm from the value of the self-diffraction efficiency.<sup>7</sup> The values of  $\chi^{(3)}$  obtained are plotted in Figure 3 for the different values of the volume fraction  $f$ .  $\chi^{(3)}$  varies linearly with  $f$  as follows:

$$\chi^{(3)} = 0.55 \cdot 10^{-6} f + 0.68 \cdot 10^{-7} \text{ esu}$$

$f$  being volume fraction of CdS

This linear variation of  $\chi^{(3)}$  as a function of  $f$  supposes that the nonlinearity of the different monocrystals of the same radius (2 nm) does not vary with the concentration.

## 5 DISCUSSION

Few measurements of  $\chi^{(3)}$  were made on pure CdS nanocrystals<sup>8</sup> but mostly on CdS<sub>x</sub>Se<sub>1-x</sub> ones with different values of  $x$ . At first, commercial colored filters were studied.<sup>9</sup> It is only these last years that new methods of glass preparation have developed, like the sol-gel technique, to have a better control of the purity of samples.<sup>10</sup> In all the experiments, values of  $\chi^{(3)}$  ranging from  $10^{-9}$  to  $10^{-8}$  esu were measured in conditions of resonant excitations. It is difficult to compare the values of  $\chi^{(3)}$  obtained in such experiments because they depend on many variable parameters : the absorption of samples, the different matrices, the concentration of nanocrystals, their size<sup>11</sup> and may be the temporal regime of experiments.

## 6 CONCLUSION

By a sol-gel technique, we have prepared ultra-pure silica glass in thin film form doped with high concentrations of CdS nanocrystallites of constant mean radius. The optical properties of these CdS doped thin films have been studied as a function of the CdS volume fraction. The non-linearity of the nanocrystallites is independent of the concentration, up to the highest concentration under investigation.

## REFERENCES

1. Y. Wang, *J. Phys. Chem.* **95** (1991) 1119.
2. E. Volel, M. J. Weber and D. M. Klot, *Phys. Chem. of Glass*, 231.
3. B. Champagnon, B. Andrianasolo, A. Ramos, M. Gandais, M. Allais, J. P. Benoit, *J. of Appl. Physics* **73** (1993) 2775.
4. K. A. Cerqua, J. E. Hayden and W. C. Lacourse, *J. of Non-Crystalline Solids* **100** (1988) 471.
5. A. Othmani, J. C. Plenet, E. Bernstein, C. Bovier, J. Dumas, P. Riblet, P. Gilliot, R. Levy, J. B. Grun, *Crystal Growth* **144** (1994) 141-149.
6. A. I. Ekimov, *Phys. Scripta* **139** (1992) 217.
7. N. Bloembergen, *Non linear Optics* (New York) 1965.
8. Y. Nosaka, K. Tanaka and N. Fujii, *Appl. Phys. Lett.* **62** (1993) 1863.
9. S. M. Satiel, B. Von Wonerghem and P. M. Plentzpis, *Opt. Com* **77** (1990) 59.
10. J. Yumoto, H. Shinojima, N. Uesugi, K. Tsunetomo, H. Nasu and Y. Osaka, *Appl. Phys. Lett* **57** (1990) 2393.
11. H. Shinojima, J. Yumoto and N. Uesugi, *Appl. Phys. Lett.* **60** (1991) 298.

## **12 CARBON AND POLYMERS**

## EPR STUDY OF THE HOLE PARAMAGNETIC CENTER IN C<sub>70</sub> FULLERITE

L. S. SOCHAVA,<sup>1</sup> V. S. VIKHNIN,<sup>1</sup> Yu. S. GRUSHKO,<sup>2</sup> S. N. KOLESNIK<sup>2</sup>  
and M. V. KORNIENKO<sup>1</sup>

<sup>1</sup>A. F. Ioffe Physical-Technical Institute, 194021 St.-Petersburg, Russia; <sup>2</sup>Nuclear Physics  
Institute, 188350 Gatchina, Russia

The hole paramagnetic center ( $S = 1/2$ ,  $g = 2.0028$ ) was observed in undoped C<sub>70</sub> fullerite for the first time. It was shown that the possible model of this center is C<sub>60</sub><sup>+</sup>-hole center with charge compensation at the surface.

**Key words:** fullerite, hole center, EPR.

Up to now, EPR spectra of C<sub>70</sub> fullerite have been detected only after doping it with alkaline metals,<sup>1</sup> the doping resulted in electron transfer from a metal atom to a C<sub>70</sub> molecule. In this paper we report on the detection of an EPR signal in undoped C<sub>70</sub> fullerite.

### 1 PARAMAGNETIC HOLE CENTER IN (C<sub>70</sub>)<sub>1-x</sub>(C<sub>60</sub>)<sub>x</sub> FULLERITE

1. Polycrystalline C<sub>70</sub> powder was obtained using a standard technic. It was separated by liquid chromatography from a toluene extraction of the soots produced by arc heating of graphite at 600 Torr in helium atmosphere. The concentration of impurity C<sub>60</sub> molecules estimated from the Raman scattering spectra was about 0.5% in the purest samples.<sup>2</sup>

A single EPR line with  $g = 2.0028 \pm 0.0002$  and width (1.1–1.6) Oe was detected in C<sub>70</sub> samples. Both  $g$ -factors and the line width remain constant over the temperature range 1.8–300 K. The paramagnetic center concentration is about  $1 \cdot 10^{-5}$  spin per C<sub>70</sub> molecule.

An unexpected feature of the EPR signal is the remarkable dependence of the center concentration on the gas atmosphere. A reduction of the air pressure from normal to  $3 \cdot 10^{-3}$  Torr decreases the center concentration by half. Note that the pressure rise produces a faster change in the center concentration than the pressure decrease.

2. It has been found experimentally<sup>3</sup> that electron transfer between C<sub>60</sub> and C<sub>70</sub> molecules takes place in the solid solution (C<sub>60</sub>)<sub>1-x</sub>(C<sub>70</sub>)<sub>x</sub> and is accompanied by production of paramagnetic centers of two types and by a rise in electric conduction. Two EPR signals observed in<sup>3</sup> (a narrow one, with  $g = 2.002$  and a broad one, with  $g = 2.0034$ ) may be produced by negatively ( $\Delta g < 0$ ) and positively ( $\Delta g > 0$ ) charged fullerene molecular ions, respectively. Taking into account the  $g$ -value = 2.002 of the EPR signal in K<sub>x</sub>C<sub>70</sub><sup>1</sup> which should attributed to C<sub>70</sub><sup>-</sup>, we may assume that the charge exchange in the (C<sub>60</sub>)<sub>1-x</sub>(C<sub>70</sub>)<sub>x</sub> solid solution occurs in accordance with



This means that the narrow signal in<sup>3</sup> was produced by C<sub>70</sub><sup>-</sup> and the broad one by C<sub>60</sub><sup>+</sup>.

Suppose a similar charge transfer takes place in the case of solid solution (C<sub>70</sub>)<sub>1-x</sub>(C<sub>60</sub>)<sub>x</sub>, in accordance with (1) too. It should be pointed out that the measured  $g$ -factor ( $g = 2.0028$ ) agrees within the experimental error with the  $g$ -factor of the C<sub>60</sub><sup>+</sup> ion in the solution<sup>4</sup>(2.0030) and is close to that of the C<sub>60</sub><sup>+</sup> line arising in C<sub>60</sub> fullerite after doping



## Temperature dependence of EPR line intensity

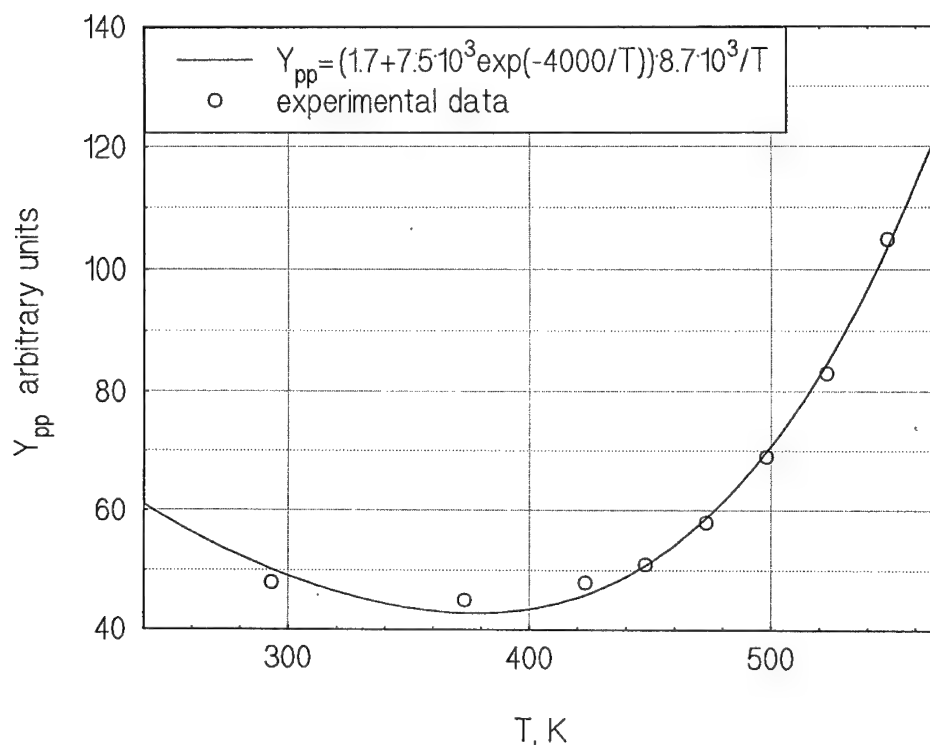


FIGURE 1 Temperature dependence of EPR line intensity. Solid curve is a result of fitting by the expression:  $Y_{pp} = (b+c \cdot \exp(-\Delta/T)) \cdot a/T$ .

with bromine<sup>5</sup> (2.0026) or iodine<sup>5</sup> (2.0038). These data support our assumption that the  $C_{60}^+$  molecular ion is responsible for the detected EPR signal.

The clear dependence of the paramagnetic center concentration on the air atmosphere suggests an essentially nonlocal charge compensation in this case. The oxygen atoms adsorbed at the sample surface are apparently acceptors<sup>6</sup> which trap extra-electrons from  $C_{70}$  molecules. As a result, the positive charge of  $C_{60}^+$  ions is compensated by the surface negative charge. Thus, only one type of paramagnetic center appears in fullerene molecules,  $C_{60}^+$ , whose line is observed in our experiments. The detected sensitivity of the spectrum intensity to air environment should be attributed to the changing conditions for charge compensation at the sample surface, which leads to a change in the  $C_{60}^+$  concentration in the sample bulk.

We may conclude that the existence of the  $C_{60}^+$  hole center is associated with long range charge compensation due to localized charge states at the surface.

## 2 UNCOMMON TEMPERATURE DEPENDENCE OF THE HOLE CENTER SPECTRUM INTENSITY

A reversible increase of the spectrum intensity was detected when a C<sub>70</sub> sample was heated above 150°C. The sample was placed in an evacuated quartz ampule (10<sup>-3</sup> Torr), inserted into the spectrometer cavity. The spectrum intensity increases doubly in the temperature range of 150–300°C, while the line width remains constant. This rise can be described by the exponent with activation energy of  $\Delta = 0.34 \pm 0.05$  eV (Figure 1).

The discussed effect can be caused by the correlation of the number of C<sub>60</sub><sup>+</sup> centers and the number of charged centers-compensators at the sample surface. The charge transfer from C<sub>60</sub> molecule to the surface center, which becomes a compensator as the result, is a transition of a pair of centers under consideration to the excited state. We believe that corresponding excitation energy is equal to 0.34 eV.

Thus the energy of 0.34 eV can be attributed to the energy of charge transfer from C<sub>60</sub> to the surface center.

This research is supported by the Russian State Program 'Fullerenes and Atomic Clusters. '(Project 'Oscillator'.)

## REFERENCES

1. K. Imaeda, K. Yakushi, H. Inokuchi *et al.*, *Sol State Commun.* **84**, 1019 (1992).
2. M. F. Limonov. *Private communication.*
3. N. Sudhakar, S. V. Sharma, L. S. Grigoryan *et al.*, *Phys. Lett.* **A170**, 235 (1992).
4. S. J. Kukolich, D. R. Huffman, *Chem. Phys. Lett.* **182**, 263 (1991).
5. N. Kinoshita, Y. Tanaka, M. Tokumoto, S. Matsumiya, *J. Phys. Soc. Jap.* **60**, 4032 (1991).
6. T. Arai, Y. Murakami, H. Suematsu *et al.*, *Sol. State Commun.* **84**, 827 (1992).

## CARBON NANOSTRUCTURES IN IMPLANTED NONCONJUGATED POLYMERS

O. YU. POSUDIEVSKY

*L. V. Pisarzhevsky Institute of Physical Chemistry of National Academy of Sciences of  
Ukraine, Prospect Nauki 31, Kiev 252039, Ukraine*

Nanosized carbon  $\pi$ -clusters have been identified in implanted nonconjugated polymers by means of small angle X-ray scattering. The consistency of obtained numerical data with results of optical absorption spectra analysis and measurements of electrical conductivity has been shown.

*Key words:* implantation, X-ray scattering nanosized  $\pi$ -clusters.

### 1 INTRODUCTION

Ion implantation into nonconjugated polymers is known as one of alternative routes for conducting polymer preparation. It is generally considered that novel electronic properties of implanted polymers—the red shift of optical absorption, increase of the bulk plasmon energy, appearance of electrical conductivity in accordance with insulator-conductor transition, and so on—result from the formation of disordered carbon network containing  $\pi$ -bonded carbon enriched zones –  $\pi$ -clusters.<sup>1–3</sup> To our knowledge, the existence of  $\pi$ -clusters has not been proven directly. Therefore, the purpose of this paper was to verify them in implanted polymers by means of small angle X-ray scattering. The consistency of obtained numerical estimates with results of optical absorption spectra analysis and measurements of electrical conductivity has been considered.

### 2 EXPERIMENTAL

Implantation of 100 keV  $\text{Ar}^+$  into 0.5 mm thick polyethylene foil and 50 keV  $\text{F}^+$  into 25  $\mu\text{m}$  thick polypropylene film has been carried out at a fluence of  $1 \cdot 10^{17}$  ions/ $\text{cm}^2$  and a beam density, to prevent the polymers from thermodestruction, about 0.2  $\mu\text{A}/\text{cm}^2$ . The pressure of residual air was about  $10^{-6}$  torr. The curves of angle dependence of X-ray scattering have been received using a small angle goniometer AMUR-1 connected with registering equipment and control unit of DRON-4 diffractometer ( $\text{CuK}_\alpha$ -irradiation, tube regime—40 keV, 30 mA). The obtained data subjected to procedures of smoothing, background subtraction, and collimation correction<sup>4</sup> are represented in Figure 1. The measurements of reflection and transmission coefficients have been performed in the range 1.3–4.0 eV with a double beam M-40 spectrophotometer. The calculated energy dependence of absorption coefficient<sup>1,3</sup> is depicted in Figure 2. A routine four point probe method has been used for determination of electrical conductivity of implanted layers.

### 3 RESULTS AND DISCUSSION

The curves of X-ray scattering in Figure 1 are similar for all studied polymers. The first peak in the range  $0.5$ – $2.0^\circ$ , displaying by pristine and implanted polymers, reflects the

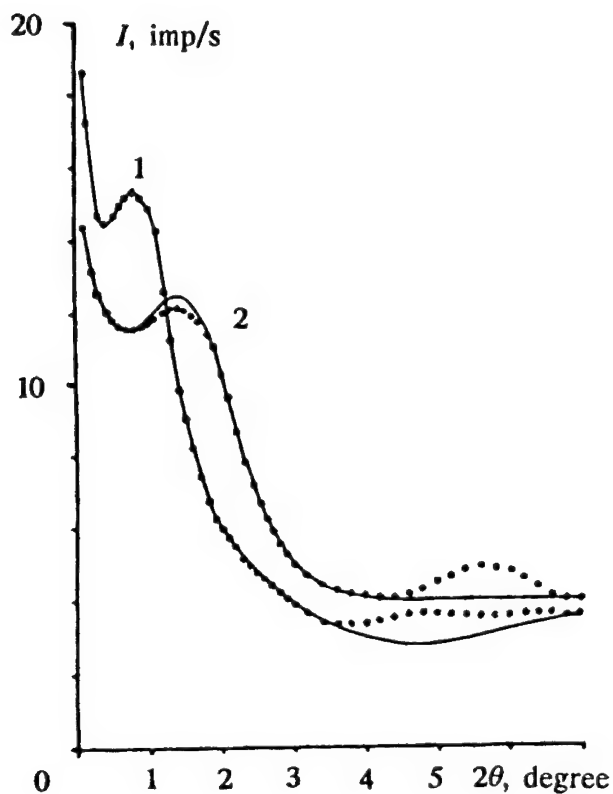


FIGURE 1 X-ray scattering in pristine (solid curve) and implanted (dotted curve) polyethylene (1) and polypropylene (2).

partial crystallinity of the samples. The position of peak maximum determines the mean distance,  $D$ , between adjacent crystalline regions (table I) separated by amorphous gaps with lower electron density. The decrease of intensity for implanted polypropylene (IPPr) provides evidence that ion bombardment modifies the morphological structure of the polymer. The absence of such changes for implanted polyethylene (IPE) is probably due to too thick PE foil, so that possible changes have not been detected by the used equipment. It should be noted that numerical estimates here will become possible when the samples with the thickness less than the projected ion range will have been studied.

It follows from Figure 1 that ion implantation leads to the appearance of the new peak in the range  $4.0-6.5^\circ$ . The peak is not so distinct as the first one, nevertheless it is reliably established. This maximum in X-ray scattering reflects the presence of regions with higher electron density in implanted polymer layer that suggests the appearance of multiple bonds between carbon atoms, i.e. formation of  $\pi$ -bonded structures— $\pi$ -clusters introduced earlier. Supposing uniform distribution of these clusters in material and interference

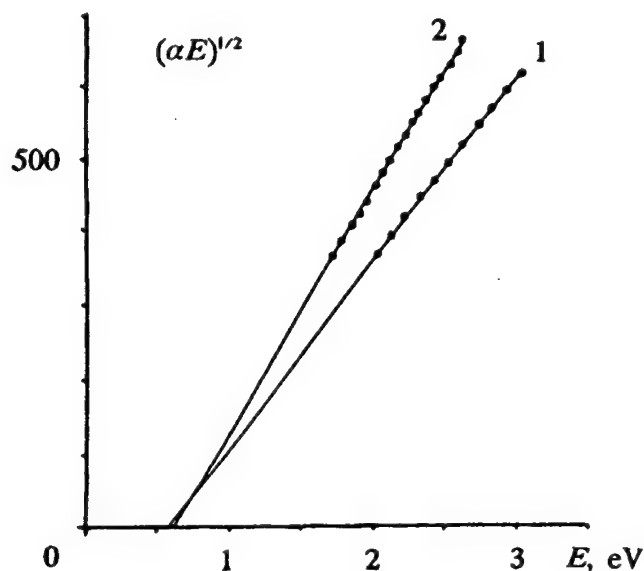


FIGURE 2 Tauc plots for implanted polyethylene (1) and polypropylene (2).

between them, one may estimate the mean distance,  $d$ , between the centers of adjacent  $\pi$ -clusters in terms of the most real approximation of liquid-like clusters arrangement:

$$\frac{4\pi \sin \theta}{\lambda} d = 7.73.$$

The results are presented in table I indicating that  $\pi$ -clusters are medium-range order structures with nanometric dimensions.

The mean size of  $\pi$ -clusters may be determined by means of optical spectroscopy using relationship between the value of optical gap,  $E_0$ , and the diameter of compact aromatic  $\pi$ -cluster,  $\delta$ .<sup>1,3</sup> In Figure 2 the energetic dependence of absorption coefficient,  $\alpha(E)$ , is represented in coordinates linearizing the Tauc equation:

$$(\alpha E)^{1/2} = B^{1/2}(E - E_0),$$

and the corresponding  $\delta$  values are inserted in table I. Comparing  $d$  and  $\delta$ , one may conclude that different experimental techniques give consistent results. The validity of approximations used for interpretation of X-ray scattering also follows as the distance between  $\pi$ -clusters boundaries,  $d - \delta$ , is much less than their diameter.

Table I shows that the size of  $\pi$ -clusters in IPPr is less than in IPE while the conductivity is one order higher. First of all, it is reasonable that  $F^+$  implantation leads to smaller  $\pi$ -clusters as the  $F^+$  mass is two times less than the  $Ar^+$  mass. The higher conductivity of IPPr is mainly due to the doping effect and the greater quantity of  $\pi$ -clusters. Really, accordingly to disordered solids theory,<sup>5</sup> the value of coefficient  $B$  is the greater the more  $\pi$ -clusters are present in polymer matrix. So, the less number of  $\pi$ -clusters

in IPE in comparison with IPPr and nearly equal their sizes lead to greater distances between cluster boundaries and accordingly less conductivity. This fact is consistent with X-ray scattering data which show that  $d-\delta$  for IPE is two times greater than that for IPPr.

TABLE I  
Structural, optical, and electrical characteristics of implanted polyethylene and polypropylene

	$2\theta$ , degree	$D$ , nm	$d$ , nm	$B$ , $\text{eV}^{-1}\text{cm}^{-1}$	$\delta$ , nm	$\sigma$ , S/cm
IPE	0.8	12.1	—	$6.7 \cdot 10^4$	1.8	$2.0 \cdot 10^{-4}$
	4.7	—	2.3			
IPPr	1.5	6.5	—	$1.1 \cdot 10^5$	1.6	$6.5 \cdot 10^{-3}$
	5.6	—	1.9			

#### 4 CONCLUSION

The high fluence ion implantation into nonconjugated polymers leads to the formation of disordered carbonaceous material which electronic properties are controlled by type of bonding between carbon atoms. The consequence of volatile polymer fragments release is appearance of unsaturated bonds, their agglomeration, and formation of  $\pi$ -clusters. The last as seen by small angle X-ray scattering, are of nanometric size. These numerical estimates are in good agreement with the data of optical absorption spectroscopy and the conductivities of studied implanted polymers.

#### REFERENCES

1. J. Davenas, X. L. Xu, G. Boiteux, and D. Sage, *Nucl. Instrum. Meth. in Phys. Res.* **B39**, 754 (1989).
2. D. Fink, K. Ibel, P. Goppelt, J. P. Biersack, L. Wong, and M. Behon. *Ibid.* **B46**, 342 (1990).
3. O. Yu. Posudievsky, I. G. Myasnikova, and A. A. Chuiko, *Poverchnost*. No. 8, 113 (1992).
4. C. G. Vonk. FFSAXS' programme for the processing of small-angle X-ray scattering data (DSM, Geleen, 1975).
5. J. Sahata, M. Yamanaha, S. Okazaki, and Y. Hayashi. *Appl. Phys.* **A48**, 295 (1989).

## COMPENSATION EFFECTS IN $C_{60}$ DOPED BY ION IMPLANTATION

P. TROUILLAS, B. RATIER and A. MOLITON

*Lepofi - Faculté des sciences-123, avenue Albert Thomas, 87060 Limoges Cedex*

We have studied electrical transport phenomena after ion implantation in sublimed  $C_{60}$  films. A n type doping exists with 30 KeV potassium ion irradiations and low fluences ( $D < 10^{15}$  ions/cm<sup>2</sup>). However degradation effects have been noted. So we have tried to discriminate doping and damage effects. Studies about the compensation phenomenon have been performed in order to prove the chemical role of the potassium atoms. An electron transfer from the alkali metal is sure; but a strong competition exists between degradation and doping phenomena. Finally, the intact  $C_{60}$  molecules are the insulator barriers,  $K_3C_{60}$  and isolated carbon atoms are the conductor phase for an heterogeneous media model.

**Key words:**  $C_{60}$ , ion implantation, doping, degradation, thermopower.

### 1 INTRODUCTION

Solid  $C_{60}$  is well known as an intrinsic insulator ( $\sigma \approx 10^{-14} \Omega^{-1} \text{cm}^{-1}$  for  $C_{60}$  films<sup>1</sup>). Energy gap separating the HOMO (highest occupied molecular orbital) band and the LUMO (lowest unoccupied molecular orbital) band is about 1.5 eV.<sup>2,3</sup> Doping of fullerene ( $C_{60}$ ) with alkali metal like potassium (K), rubidium (Rb) and cesium (Cs) leads to an electron transfer. Then  $C_{60}$  becomes a conductor with a Fermi gas containing the free electrons of the alkali atoms. Although chemical doping has been essentially used,<sup>4</sup> ion implantation is an alternative technique studied by some groups.<sup>5,6</sup> In this case the main problem is the degradation induced by the energetic ions ( $E > 30$  keV). So we try to discriminate damage and doping during implantation of the solid  $C_{60}$ . Doping reversibility and compensation effects are also discussed to prove chemical role of the potassium atoms.

### 2 EXPERIMENTAL

We have deposited thin films of sublimed  $C_{60}$  with an evaporator Edwards Auto 306. The powder of pure  $C_{60}$  (99.9%) is warmed up at around 740 K. Cleaned substrates are warmed up at around 400 K to help reorganization of the molecules. Sublimation is performed under a  $10^{-6}$  mbar vacuum. The obtained films have a thickness of about 100 nm. Ultraviolet and Raman spectra have been performed so as to control the fullerene structure.

An HVEE 400 kV accelerator was used and for the study of the doping reversibility, the implantation energy is fixed at 30 keV where chemical effects are already observed.<sup>7</sup> Current density of the ion beam is  $j = 0.2 \mu\text{A}/\text{cm}^2$ ; with this low value, local heating remains weak. Another important parameter is the fluence  $D$ ; it corresponds to concentration  $x$  of doping. First implantation has been realized with a fluence  $D = 5 \cdot 10^{14}$  ions/cm<sup>2</sup>, since at this fluence thermopower  $S$  has higher values with both samples implanted firstly with  $K^+$  or  $Br^+$ . A second ion implantation ( $Br^+$  or  $K^+$ ) thus leads to thermopowers which may be easily compared as a function of ion implantation order. Furthermore, this fluence remains low enough to prevent important sputtering of the material: thin films vanish after implantations with high fluences ( $D \geq 10^{17}$  ions/cm<sup>2</sup>).

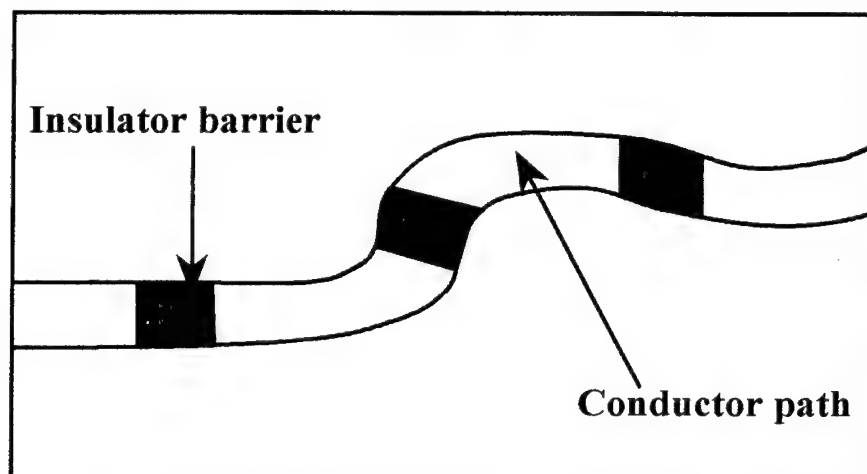


FIGURE 1 heterogeneous media model.

However, much lower fluences would not be reasonable since they would give samples with very low conductivity and thermopower measurements would lead to meaningless results.

Conductivity was measured by four-probe method. Calculation of conductivity  $\sigma$  used the thickness of the implanted zone which is calculated by the TRIM 91 program. Thermopower measurements have been performed with the method of the heating probe. Automation has been previously reported by Moliton *et al.*<sup>8</sup> Measurements of  $S$  versus temperature used another technique. Contacts have been realized with an epotecnny resin charged with silver. This method prevents the strains due to the study in a large temperature range.

### 3 COMPENSATION EFFECT IN $C_{60}$

#### 3.1 Summary About Transport Phenomena In Doped $C_{60}$

It is important, now, to remind some electrical properties of  $C_{60}$  doped by chemical doping and first results of ion implantation.

Chemical doping of  $C_{60}$  with alkali metals gives a conductor.<sup>4</sup> Electron affinity of the  $C_{60}$  molecule is quite important, and electron transfer from alkali metals is easy and performed a-n doping. On the other hand the  $C_{60}$  molecule has a large ionization potential<sup>9</sup> and p doping is difficult. Indeed, during doping process, formation of metallic grains have been observed:<sup>10</sup> the atoms of potassium bind with the  $C_{60}$  molecule in order to fill the  $t_{1u}$  state which is the lowest unoccupied molecular orbital of  $C_{60}$ .<sup>11</sup> The LUMO band corresponding to the  $t_{1u}$  state is half occupied (and becomes a conduction band) with 3 alkali atoms per  $C_{60}$  molecule: we have an electronic structure characteristic of a metal. The formation of  $K_3C_{60}$  grains arrives in the vicinity of defects zone and finally  $K_xC_{60}$  appears as a heterogeneous medium with metallic islands ( $K_3C_{60}$ ) separated by insulator phase. Such a model have been theoritically described by A.B. Kaiser.<sup>12</sup> conductor paths separated by thin barriers modelized the transport phenomena (Figure 1). In this case,



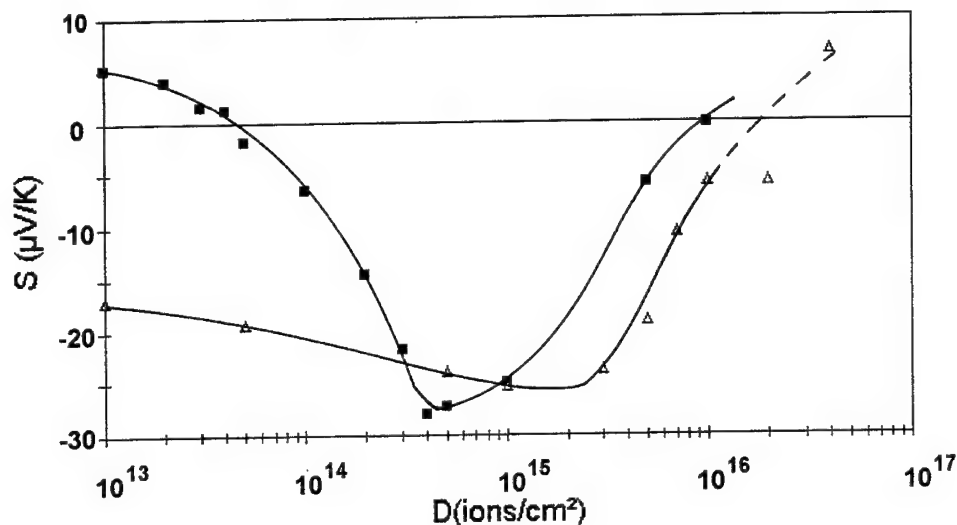


FIGURE 2 Curve  $S = f(D)$  showing the doping reversibility.

■ from p type to n type conduction.

△ from n type to p type conduction.

conductivity is thermally activated and characteristic of hopping or tunnelling, whereas thermopower is characteristic of the metallic phase (giving a non thermally activated thermopower  $S$  whose values are small:  $|S| \approx 10 \mu\text{V/K}$ ).

By ion implantation, Kastner *et al.* show formation of an amorphous carbon layer (a-C) and a buried doped C<sub>60</sub> only in the case of implantation at high temperature.<sup>6</sup> More recently we have performed another electrical study of implanted C<sub>60</sub> and the comparison with chemical doping is fine: we obtain high thermally activated conductivity and thermopower sign is negative with alkali ions and characteristic of its chemical nature: this n conduction involves electron transport just below the Fermi level. However, ion implantation with argon gives some non-negligible conductivities showing degradation effects. In fact, to confirm doping effects with chemical active ions (alkali or halogen) we propose new experiments based on the modification of the  $S$  sign versus the order of the ions implantation (first with halogen ions and then with alkali ions, or the opposite).

### 3.2 Results

At first we have realized an ion implantation of bromine (Br) at 30 keV and  $5 \cdot 10^{14}$  ions/cm<sup>2</sup>. A p type doping was then obtained with a thermopower  $S = +6 \mu\text{V/K}$ . Then successive fluences have been used for ion implantation of potassium. We observed evolution of thermopower  $S$  with the fluence of K<sup>+</sup> (Figure 2). A change of  $S$  sign occurs as soon as small fluences:  $D = 5 \cdot 10^{13}$  ions/cm<sup>2</sup>. Hence we have obtained a change in the conduction type, from p type to n type conduction. This rapid change shows effective compensation phenomenon of the initial p doping (Br<sup>+</sup> ion implantation) by potassium. Next, for the highest potassium fluences, thermopower  $S$  becomes again positive. This effect is probably due to degradations which induced usually a p type conduction<sup>13</sup> as observed with non chemically active ions (and mentioned previously with argon ions). With high implantation parameters we can destroy the C<sub>60</sub> molecules, breaking  $\pi$ -bonding or  $\sigma$ -bonding and destroy totally the C<sub>60</sub> molecules too.

Secondly we have performed an initial n doping: a first implantation of potassium at 30 keV and  $D = 5.10^{14}$  ions/cm<sup>2</sup> gives a thermopower  $S = -18$   $\mu$ V/K. Then ion implantation with bromine and successive fluences have been performed. The change of S sign occurs only at high fluences of bromine. In this case, and according to the evolution of the curve  $S = f(D)$  (Figure 2), the change of the conduction type is probably due to degradation effects and not to compensation phenomena.

### 3.3 Discussion

Briefly, we have seen that chemical role of the potassium is important and doping effect is evident. With 30 keV ion implantation and low fluences we have a n type conduction with thermopower S clearly negative. In addition, the compensation effect prove the chemical role of the potassium. As potassium is an electron donor and taking account of the electron affinity of the C<sub>60</sub> molecule, some electrons of the chemical donor (K) jump on intact C<sub>60</sub> spheres to induce a n type transport. However electrical phenomena induced by ion implantation of solid C<sub>60</sub> is not reduced to only one process.

Xenon ion implantation at 320 keV have been performed by Kalish *et al.*;<sup>5</sup> they conclude upon the total destruction of the C<sub>60</sub> molecules by the ions. No residual fragment exist after a collision between an ion and a molecule; then isolated carbon atoms are dispersed among the remaining intact C<sub>60</sub> molecules and carbon atoms behave like hopping centers between insulator medium for electrical transport.

With 30 keV ion irradiation we note also the degradation effect; for example, we notice a measurable conductivity with argon ion, amorphous carbon layer by Raman spectroscopy and a p type conduction with high fluences of K ion implantation. Destruction of the C<sub>60</sub> molecules creates free bondings which are responsible of the formation of energy states below the Fermi level and of the p type conduction as during implantation of polymers with high parameters.<sup>13</sup>

## 4 CONCLUSION

We have a strong competition between doping and damaging. With low fluences of potassium the transport phenomena are governed by two effects. Firstly, an electron transfer between alkali atoms and remaining intact molecules. It is responsible of the negative thermopower. Secondly, the destruction of C<sub>60</sub> molecules to form isolated sites with carbon atoms. This effect is important and very effective. In all cases some intact molecules stay neutral to insure the insulator phase. A heterogeneous media model can be used to explain the thermally activated conductivity and the non thermally activated thermopower.

### REFERENCES:

1. C. Wen, J. Li, K. Kitazawa, T. Aida, I. Honma, H. Komiyama, K. Yamada, *Appl. Phys. Lett.* 61, 2162 (1992).
2. M. N     Regueiro, P. Monceau, A. Rassat, P. Bernier, A. Zahab, *Nature* 354, 289 (1991).
3. K. Hoshimono, S. Fujimori, S. Fujita, S. Fujita, *J. Appl. Phys.* 32, 1070 (1993).
4. R. C. Haddon, A. F. Hebard, M. J. Rosseinsky, D. W. Murphy, S. J. Duclos, K. B. Lyons, B. Miller, J. M. Rosamilia, R. M. Fleming, A. R. Krotan, S. H. Glarum, A. V. Makhija, A. J. Muller, R. H. Eick, S. M. Zahurak, R. Tycko, G. Dabbagh & F. A. Thiel, *Nature* 350, 320 (1991).
5. R. Kalish, A. Samoiloff, A. Hoffman, Uzan-Saguy, *Phys. Rev.* B-48, 18235 (1993).
6. J. Kastner, H. Kuzmany, L. Palmethofer, P. Bauer, *N.I.M.B.* B80/81, 1456 (1993).
7. P. Trouillas, B. Ratier, A. Moliton, M. Gauneau, P. Bernier, *Phil. Mag.* B, 70, 893 (1994)

8. A. Moliton, B. Ratier, C. Moreau, G. Froyer, *J. Phys. III* **Frl** 809 (1991).
9. S. Larsson, A. Volosov, A. Rosén, *Chem. Phys. Lett.* **137**, 501 (1987).
10. P. J. Benning, D. M. Poirier, T. R. Ohno, Y. Chen, M. B. Jost, F. Stepniak, G. H. Kroll, J. H. Weaver *Phys. Rev. B* **45**, 6899 (1992).
11. R. C. Haddon, L. E. Brus, K. Raghavachari, *Chem. Phys. Lett.* **125**, 459 (1986).
12. A. B. Kaiser, *Phys. Rev. B* **40**, 2806 (1989).
13. A. Moliton, C. Moreau, B. Lucas, R. H. Friend, G. Froyer, *J. Phys. III* (September 1994) in press.

## HIGH TEMPERATURE BEHAVIOUR OF THERMOELECTRIC POWER OF IMPLANTED POLYMER FILMS

C. MOREAU, B. RATIER, A. MOLITON and B. FRANÇOIS

*LEPOFI—Faculté des Sciences, 123, avenue Albert Thomas 87060 LIMOGES CEDEX—FRANCE; \*Institut Charles Sadron (CRM-EAHP) (CNRS) 6, rue Boussingault—67083 STRASBOURG CEDEX—FRANCE*

The results of thermopower  $S$  measurements performed on implanted polyparaphenylene and polyimide films between 150 K and 450 K are presented. The implantations of Caesium or Iodine ions in polyparaphenylene with low parameters induce a sign of  $S$  characteristic to chemical nature of the implanted ions and an increase of  $|S|$  at around 350 K due to a transition from a VRH process to a polaronic conduction. With Iodine implanted sample at higher energy ( $E = 250$  keV) and low dose ( $D = 2 \times 10^{15}$  ions/cm<sup>2</sup>) a transition from p type to n type doping at 400 K is attributed to a migration of negative oxygen ions as in the case of polyimide samples implanted with Caesium and Iodine ions where a similar behaviour of  $S$  is found.

*Key words:* Thermopower, Conductivity, Implantation, Polymer.

### 1 INTRODUCTION

The transport phenomena of implanted electroactive polymers have already been studied extensively.<sup>1,2,3</sup> In particular we have proposed a band scheme which describes the evolution of electronic levels according to implantation parameters (energy  $E$  and fluence  $D$ ) and also gives a consistent explanation of the behaviours of the electrical parameters such as the conductivity  $\sigma$  and the thermoelectric power (T.E.P.)  $S$ .

From a general point of view we remind<sup>2</sup> that these characteristics vary with temperature because of the successive activations of different types of carriers located on energy levels becoming higher and higher: the curves  $\log \sigma = f(1/T)$  display linear shapes in the case of processes only thermally activated, whereas  $\log (\sigma\sqrt{T})$  is proportionnal to  $(T^{-1/4})$  for the Variable Range Hopping (V.R.H.) mechanism which is generally making responsible for the evolutions observed at low temperature.

As for the T.E.P.  $S$ , it presents either a linear evolution with reverse temperature or a straight line on a  $(S/T)$  versus  $(T^{-1/4})$  representation; in fact, this last case gives experimentally a very small evolution of  $S$  with  $T$  and is found when the effect of thermal generation of carriers is weak.<sup>4</sup> Moreover, when structural defects can give rise to a heterogeneous medium<sup>1,5</sup> the conductivity  $\sigma$  is essentially representative of transport mechanism produced by the defects (potential barrier between grains), whereas the T.E.P. rather describes the processes along conducting paths (and so in zones probably doped).

### 2 EXPERIMENTAL RESULTS AND DISCUSSION

Until now, we have only studied the evolution of  $S$  up to temperatures which do not much exceed room temperature.<sup>1,6,7</sup> In order to analyse the nature of carriers generated at higher temperatures, we have specially designed a novel automatized system for sensitive T.E.P.  $S$  and conductivity  $\sigma$  measurements which are determined by a similar method to the one we proposed elsewhere.<sup>7</sup> This experimental set-up is composed of a vacuum enclosure

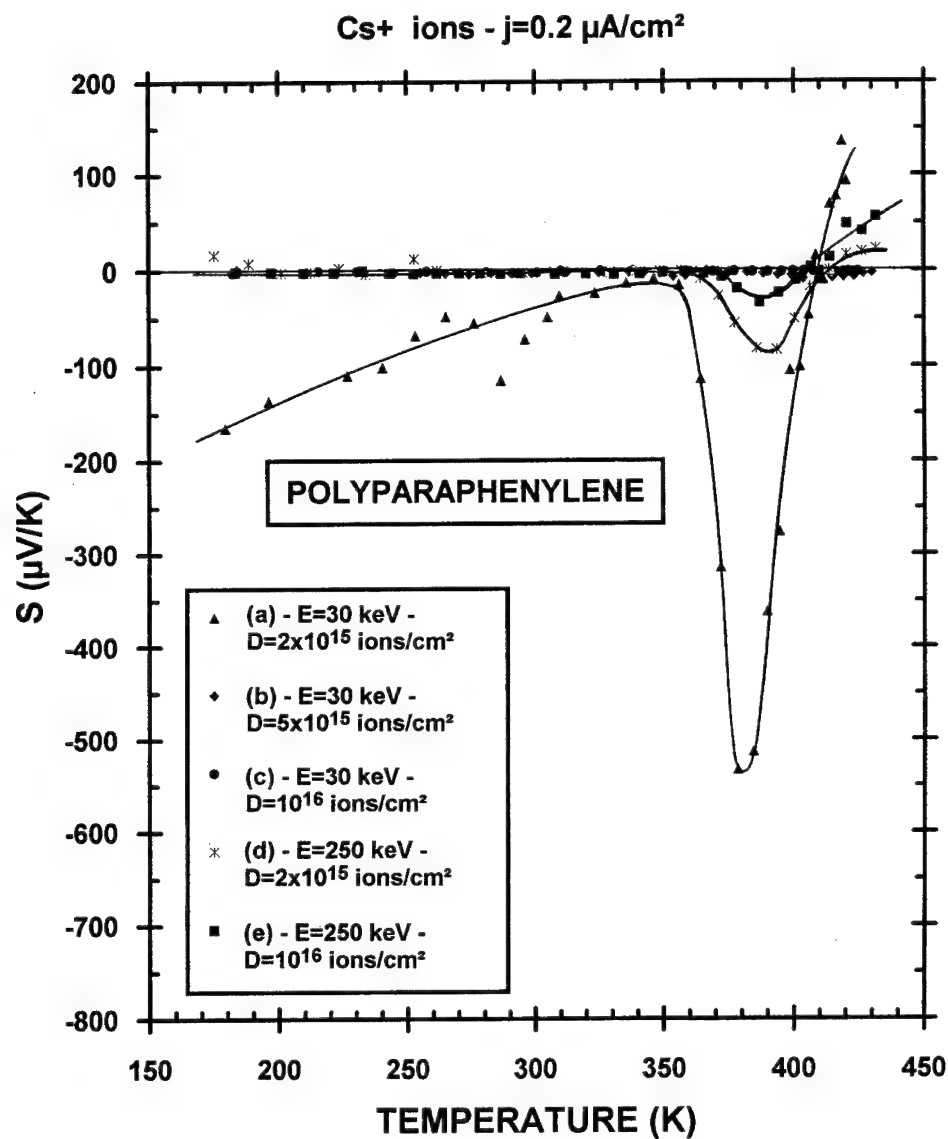


FIGURE 1 Temperature dependence of the thermoelectric power  $S$  of polyparaphenylene films implanted with Caesium ions. Results are shown for different implantation parameters.

where the samples under test are kept, several KEITHLEY instruments (electrometer, multimeter, ...), a KEITHLEY current source (only used for conductivity measurements), a power supply for sample and thermopower probes heatings, and a PC computer which completely controls all the instruments. On top of the implanted polymer film coated on glass substrate, (the resulting film thickness is  $\approx 2000 \text{ \AA}$ ) we made by thermal evaporation

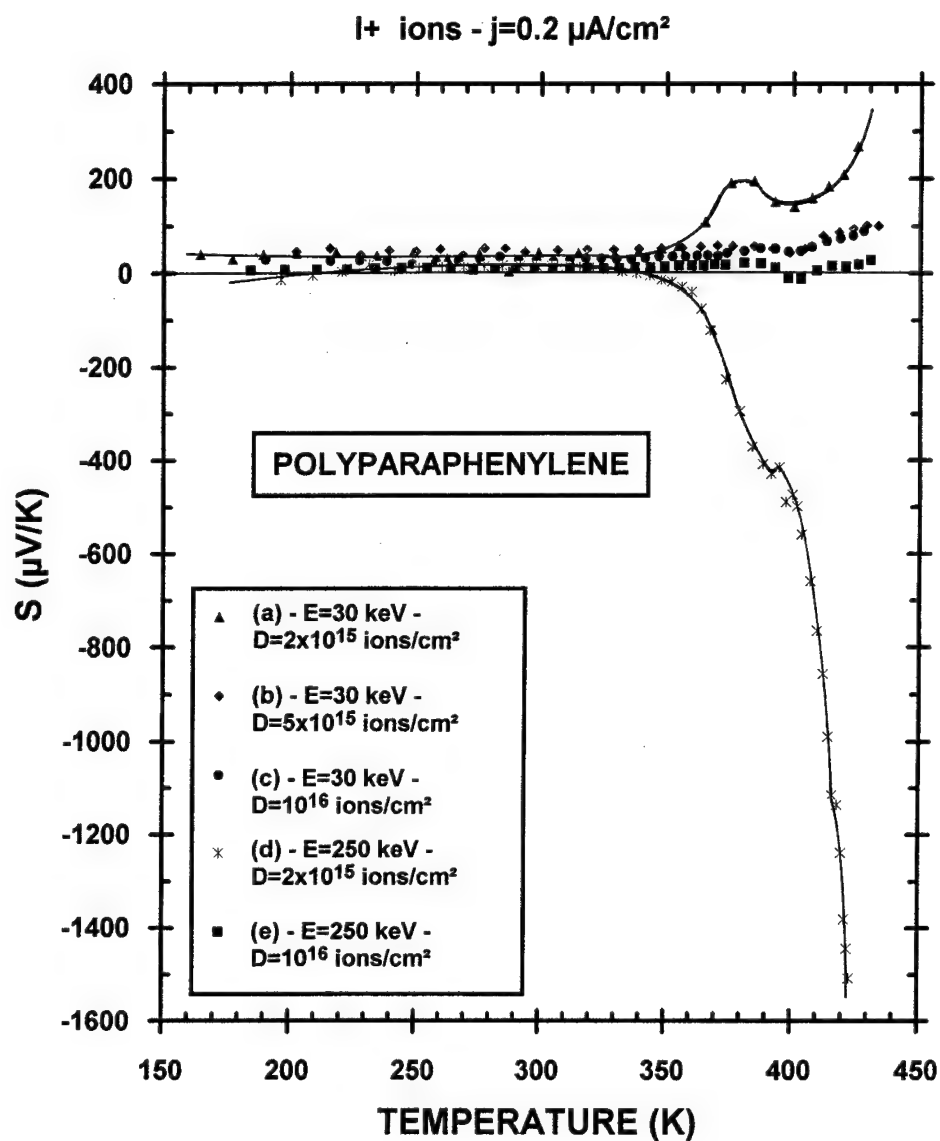


FIGURE 2 Evolution of the thermoelectric power  $S$  with the temperature for polyparaphenylene films implanted with Iodine ions by using various parameters.

of Silver two circular contact metallizations (1.5 mm in diameter) spaced by 5 mm. To determine the conductivity by the four-point probe technique, two more contacts are useful. A silver wire is glued to each contact with a silver-filled epoxy adhesive for wire bonding. In the case of T.E.P., two 1 mm silver probes (which play the same role as

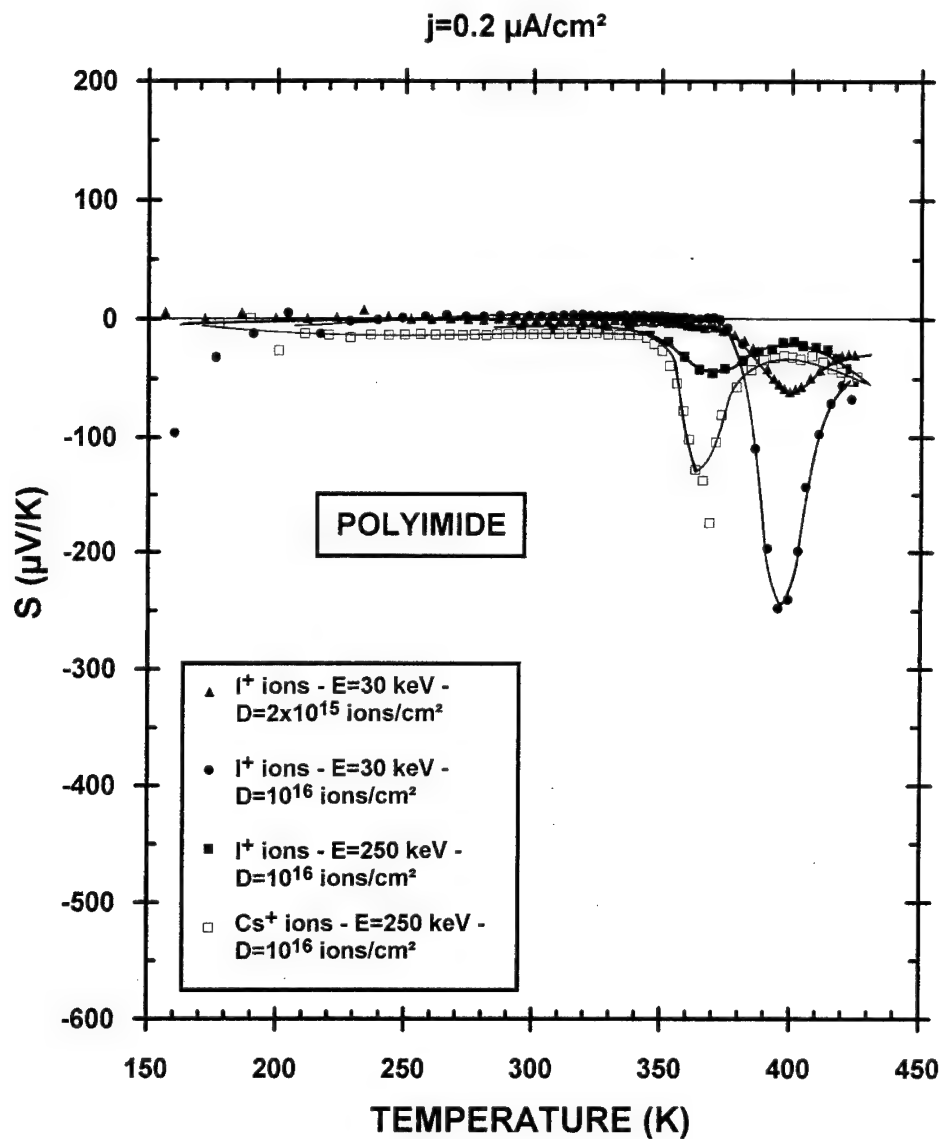


FIGURE 3 Variation with the temperature of the thermoelectric power  $S$  of polyimide films implanted with Caesium and Iodine ions. Results are shown for various implantation parameters.

tungsten electrodes used in our previous apparatus<sup>7</sup>) are pressed onto the contacts and the silver wires are wrapped round them and painted with silver dag to prevent the loss of electrical/thermal contact. After that, the sample is put inside the chamber and kept under

vacuum ( $p \approx 10^{-3}$  mbar) in order to limit the cooling down of the sample holder by the thermal conduction at highest temperatures. By plunging this chamber into a nitrogen bath we can perform the measurements from around 150 K and go up to 450 K with the help of the external power supply connected to the sample holder.

In the case of polyparaphenylene samples made by thermal depolymerization of polystyrene component included inside the copolymer PPP-PS,<sup>8,9</sup> we present in Figure 1 (implantations with Caesium ions) and in Figure 2 (implantation with Iodine ions) the evolution of  $S$  according to the temperature for various implantation parameters. All the implantations have been performed with a HVEE 400 kV accelerator by using a current density of the ion beam equal to  $0.2 \mu\text{A}/\text{cm}^2$ .

For the lowest implantation parameters ( $E = 30 \text{ keV}$ ,  $D = 2 \times 10^{15} \text{ ions}/\text{cm}^2$ ) we note that the sign of  $S$ , which is negative with Caesium (curve (a) in Figure 1) and positive with Iodine (curve (a) in Figure 2), is characteristic of the doping ( $n$  and  $p$  respectively) induced by the chemical nature of the implanted ions. Moreover and in both cases, an increase of  $|S|$  appears from 350 K. We attribute this phenomenon to a transition from a VRH type transport process (although in that case, the sign of  $S$  theoretically depends on the chemical nature of implanted ion<sup>5</sup>) to a polaronic conduction mechanism.<sup>2</sup>

Except for the implantation at  $E = 250 \text{ keV}$  and  $D = 2 \times 10^{15} \text{ ions}/\text{cm}^2$  of Iodine ions (curve (d) in Figure 2), the other implantation parameters lead to higher conductivity values, whereas the absolute value of the T.E.P. becomes in the meantime lower and lower (with not necessarily the respect of  $S$  sign with implanted ions type-; see for example Figure 1)-: with these implantation parameters, the polymer film becomes a conducting material and on its surface appears an equipotential which makes difficult the underscoring of a potential difference related to any thermal migration of any kind of carriers.

On the other hand, with an Iodine implantation at high energy ( $E = 250 \text{ keV}$ ) and with a low fluence ( $D = 2 \times 10^{15} \text{ ions}/\text{cm}^2$ ) (curve (d) in Figure 2), giving rise to the lowest conductivity  $\sigma$  ( $\sigma \approx 10^{-5} \text{ S}/\text{cm}$  in this case but much higher with the other parameters), it appears, in a surprising way *a priori*, a transition from  $p$  type to  $n$  type doping at about 400 K. We attribute this behaviour to the appearance of an ionic thermoelectric power<sup>10</sup> related to the migration of negative oxygen ions ( $\text{O}^-$ ) whose the presence we have previously noticed in the implanted layers of our polymer samples by S.I.M.S. analysis.<sup>11</sup> Moreover, this phenomenon appears clearly for the lowest conducting materials:-

- for the samples implanted with Iodine ions at  $E = 30 \text{ keV}$  and  $D = 2 \times 10^{15} \text{ ions}/\text{cm}^2$  (curve (a) in Figure 2) we obviously observe a decrease of  $S$  at about 400 K which 'limits' locally the  $S$  increase due to polaronic conduction.
- for the sample implanted with Caesium ions at  $E = 250 \text{ keV}$  and  $D = 2 \times 10^{15} \text{ ions}/\text{cm}^2$  (curve (d) in Figure 1) a decrease of  $S$  occurs but it is less marked than with Iodine because the conductivity is higher ( $\sigma = 10^{-4} \text{ S}/\text{cm}$ ). Moreover, in the case of Caesium implantations, the contribution of T.E.P. due to conduction by electronic polarons is superposed (in sign) on the component related to ion nature, what allow us to explain the huge peak noticed after implantation of Caesium ions with low parameters.

In order to reinforce our assumption about the influence of oxygen on T.E.P. behaviour, we must emphasize that as well in the case of amorphous germanium as with amorphous silicon a decrease of  $S$  at around 400 K has already been attributed to the presence of oxygen atoms.<sup>12</sup>

Nevertheless, we have studied the behaviour of  $S$  with the temperature for a non-electroactive polymer—polyimide—with the aim of demonstrating positively the validity of our last assumption (Figure 3). The conductivity of this polymer is very low



( $\sigma < 10^{-5}$  S/cm) after ion implantation with our own parameters (even if the film is 'carbonized' by damage produced with very high parameters of ion beam-; many studies have been extensively carried out by many research groups<sup>13</sup> on the properties of that kind of samples which are not yet well-defined).

In the Figure 3, first of all we notice that the sign of S can not be related to the chemical nature of the implanted ion, what is due to non-electroactive character of the polymer. Secondly, we effectively observe a strong variation of S at around 400 K which may be attributed to negative charges, i.e. in accordance with our previous assumption about a T.E.P. contribution due to negative ionic charges. A similar phenomenon seems to have also been noticed with a form of amorphous carbon.<sup>14</sup>

### 3 CONCLUSION

The high concentration of oxygen previously discovered in layers of implanted electroactive polymers leads us to attribute the anomalous behaviour of S at around 400 K for some implanted samples to the oxygen migration and therefore to an ionic P.T.E. contribution-; moreover by using lowest implantation parameters, it appears beyond 350 K the generation of polaronic charges related to doping process.

### REFERENCES

1. A. Moliton, C. Moreau, J. P. Moliton, G. Froyer, *Nucl. Inst. Meth.* **B80/81**, 1028- (1993).
2. A. Moliton, C. Moreau, B. Lucas, R. H. Friend, G. Froyer, *J. Phys. III*, **4**, 1689 (1994).
3. A. Moliton, B. Lucas, C. Moreau, R. H. Friend, B. François, *Philosophical Magazine* **B69**, 6, 1155 (1994).
4. P. Nagels, in *Hopping and Related Phenomena*, edited by H. Fritzsche and M. Pollak (World Scientific Publishing Company, 1990), pp 385, 392.
5. A. B. Kaiser, *Physical Review* **B40**, 5, 2806 (1989).
6. A. Moliton, B. Ratier, B. Guille, G. Froyer, *Mol. Cryst. Liq. Cryst.* **186**, 223 (1990).
7. A. Moliton, B. Ratier, C. Moreau, G. Froyer, *J. Phys. III* **1**, 809 (1991).
8. X.F. Zhong, B. François, *Makromol. Chem., Rapid Commun* **9**, 411 (1988).
9. X.F. Zhong, B. François, *Synthetic Metals* **29**, E35 (1989).
10. R. R. Heikes in *Thermoelectricity: Science and Engineering*, edited by R.R. Heikes and R. W. Ure, Jr (Interscience Publishers, New York, 1961), p 82.
11. B. Ratier, M. Gauneau, A. Moliton, G. Froyer, R. Chaplain, C. Le Hùe, J. P. Moliton, *J. Phys. III* **2**, 1757 (1992).
12. W. Beyer, J. Stuke, *Proceedings of the Fifth International Conference on Amorphous and Liquid Semiconductors* Garmisch-Partenkirchen, 1973, edited by J. Stuke and W. Brenig (Taylor & Francis, London, 1974), p. 251.
13. J. Davenas, *Solid State Phenomena* **30-3**, 317 (1993).
14. W. M. Daud, M. Badri, H. Mansor, *J. Appl. Phys.* **67**, 4, 1915 (1990).

## OPTICAL PROPERTIES INDUCED BY THE FORMATION OF CARBON NANOPARTICLES IN IRRADIATED POLYIMIDE

J. DAVENAS<sup>1</sup> and J. P. SALVETAT<sup>2</sup>

<sup>1</sup>*Université Cl. Bernard LYON 1-UA CNRS 172; Département de Physique des Matériaux,  
43 Bd du 11 Novembre, 69622 VILLEURBANNE CEDEX, FRANCE;* <sup>2</sup>*Service de  
Physique et Techniques Nucléaires, CEA; BP 12, 91680 BRUYÈRES LE CHÂTEL,  
FRANCE*

Ultra thin polyimide layers have been prepared by the Langmuir Blodgett method and bombarded with a beam of 170 keV Ne<sup>+</sup>. Optical absorption and specular reflectance studies have been performed in the spectral domain 2.5–6.5 eV. The energy loss function is deduced and shows the development of a new absorption band at 3 eV, which accounts for the shift of the absorption edge towards the visible in thick films. An effective medium calculation shows that this resonance can be attributed to graphitic nanoparticles dispersed in the polymeric matrix. The development of these conducting domains accounts for the transition to a conducting regime at high irradiation fluence.

*Key words:* polymer, carbon, nanoparticle, irradiation, percolation.

### 1 INTRODUCTION

Polyaromatic polymers exhibit low sensitivity to radiations. It has however been established in the last ten years that the irradiation of polymers with ion beams induces dramatic property modifications that result from the large densities of energy deposited by heavy particles in matter.<sup>1,2</sup> These polymers, which are intrinsically good insulators, show in particular a steep transition to a conducting behaviour at high irradiation doses. Electron spin resonance (ESR) indicates that high spin densities are produced in correlation with this insulator-conductor transition<sup>3</sup> for ion fluences larger than  $10^{14}$  cm<sup>-2</sup>. These new electronic properties are interpreted in terms of percolation between condensed aromatic domains resulting from the polymer degradation.<sup>4,5</sup> The dimension of such structures has been estimated to some nanometers by neutron or X ray scattering experiments.<sup>6,7</sup> No straightforward relation between the progressive increase of the optical absorption in the UV and the abrupt change of the transport properties could however be established till now. We have previously shown<sup>8</sup> that the shift of the absorption edge towards the visible, observed for increasing irradiation doses, was due to the reduction of the bandgap as the size of the carbon clusters increases. We have found that the growth of a new absorption band at 3 eV is responsible for the evolution of the optical absorption. Using an effective medium model, we show in this contribution that the 3 eV absorption band can be attributed to graphitic clusters dispersed in the polymeric matrix.

### 2 EXPERIMENTAL

100 Å thick (PMDA-ODA) polyimide layers have been obtained by the Langmuir Blodgett technique. The successive deposition of 23 monolayers on each side of a glass (suprasil) substrate allowed the production of highly ordered films, as required for the optical study. Optical data measurements have been performed using a Varian 2300

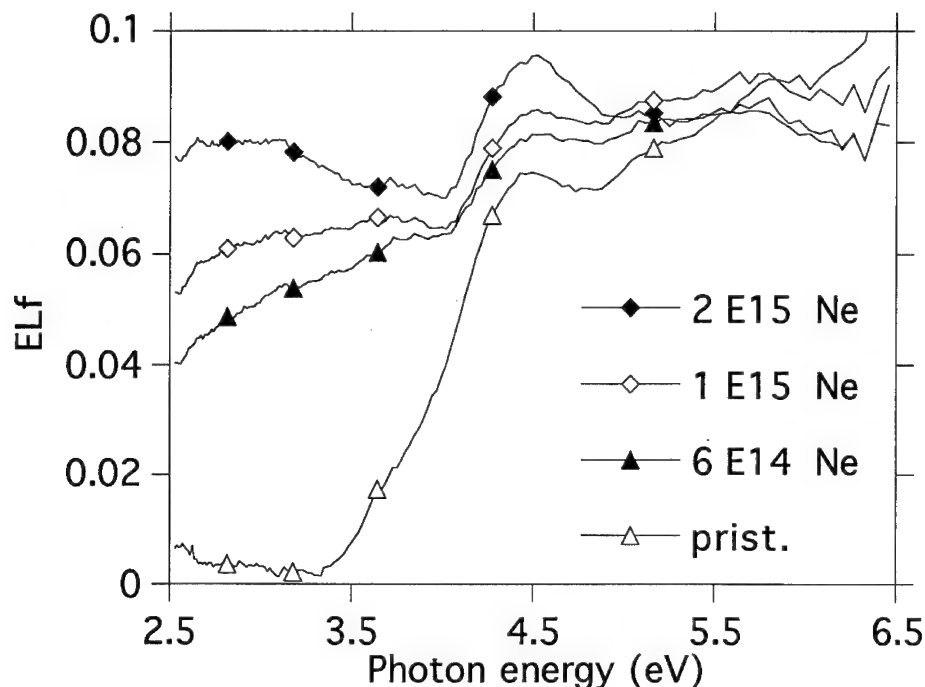


FIGURE 1 Energy loss function vs. photon energy for LB films irradiated with increasing ion fluences calculated from optical data.

spectrophotometer in the absorption and specular reflectance (VW accessory) modes. For such low thicknesses it is possible to study the  $\pi$ - $\pi^*$  transitions, which are responsible for intense absorption bands in the UV, and interferences are avoided. Ion beam irradiations have been performed using a 200 keV Balzers implantor. Current densities were of the order of some nA to avoid beam heating effects. The spectrum of pristine PI shows in particular the absorption bands assigned to charge transfer transitions in the PMDA-ODA molecule. The measured optical transmittance is corrected from the reflection on the film surface, according to the previously described method,<sup>8</sup> in order to obtain the true absorption and reflection coefficients.

### 3 OPTICAL DATA ANALYSIS

The polymer irradiation leads to the production of carbonaceous thin films exhibiting optical properties inbetween the diamond and the graphite ones. The formation of delocalized  $\pi$  states induces in particular a strong UV absorption extending far in the visible, which is responsible for the polymer darkening. The optical data are analyzed in terms of a complex optical index, where the imaginary part is the expression of the optical absorption. We have previously discussed the modification of the refractive index and extinction coefficient for photon energies below 2.5 eV, showing the transition to a

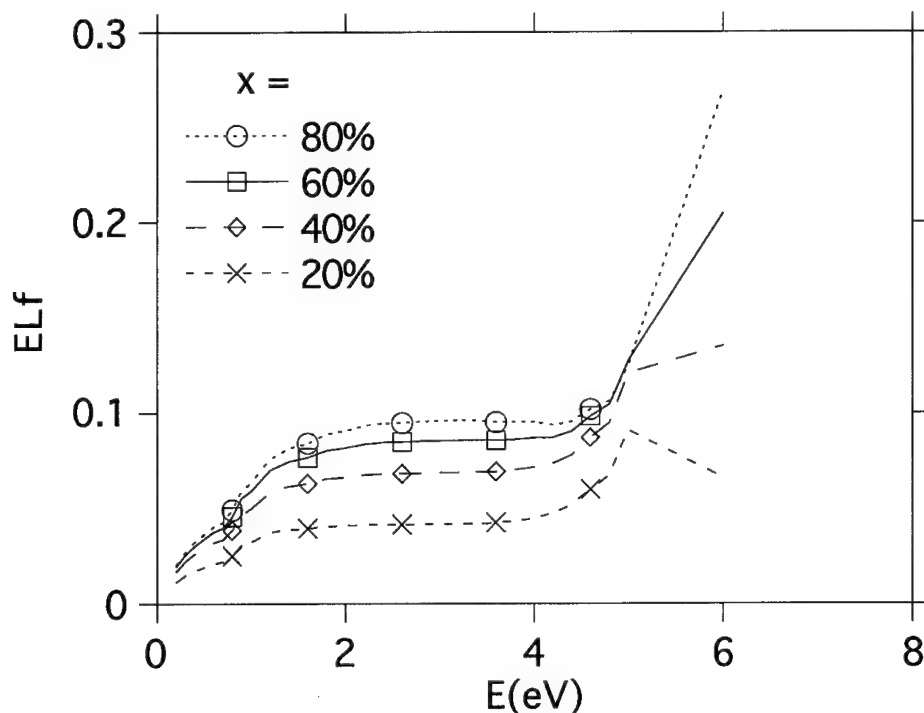


FIGURE 2 Computed energy loss function of graphitic nanoparticles dispersed in a polyimide matrix with varying filling factors.

graphite-like spectrum of the optical functions at high irradiation fluences. It is useful to introduce the loss function defined as:

$$\text{Im}\left(-\frac{1}{\varepsilon(\omega)}\right) = \frac{\varepsilon_2}{\varepsilon_1^2 + \varepsilon_2^2} = \frac{2\nu\chi}{(\nu^2 + \chi^2)^2} \quad \text{where: } \varepsilon = \varepsilon_1 + j\varepsilon_2 \text{ and } n = \nu + j\chi$$

at high photon energy, where the plasmon resonances appear for the zero of the dielectric function. It is in particular known that graphite has a sharp plasmon peak at 7 eV assigned to the collective excitations of  $\pi$  electrons and another broad peak at 27 eV, which involves  $\pi + \sigma$  electrons. We have shown in a previous study<sup>10</sup> the existence of such modes in irradiated polyimide using electron energy loss spectroscopy (EELS). Absorptions at energies under 5 eV are however not resolved since superposed to the elastic peak. Marletta has attributed the development of a step-like structure in this region to  $\pi$  electrons.<sup>11</sup> Ritsko and Bigelow<sup>12</sup> had however reported some years before the growth of a weak absorption in heavily irradiated PS and PVP, which was interpreted by the production of unsaturations on the polymer backbone.

Figure 1 shows the energy loss function calculated from optical and reflectance measurements. Two types of components are observed. One results from the intramolecular transitions, which according to Lafemina<sup>9</sup> are due to charge transfers between the PMDA and ODA groups of polyimide, giving rise to absorption peaks at 6.4,

5.9 and 4.4 eV. The computed optical absorption spectrum performed in this study on different models of molecules shows that the modification of the relative peak intensities following irradiation is probably due to a deformation of the molecule. However the most interesting feature is the appearance of a new component at 3 eV, which grows as the irradiation fluence increases. This energy loss peak becomes in particular well resolved for a fluence of  $2.10^{15}$  Ne<sup>+</sup>/cm<sup>2</sup>, which corresponds to the development of a strong ESR signal and conductivity onset. This relation suggests that the 3 eV absorption could be attributed to the graphitic clusters, which are assumed to be responsible of the transport property transition.

#### 4 OPTICAL COMPOSITE MODEL

Optical properties of nanoparticles dispersed in a dielectric can be treated using an effective medium theory, which leads to the determination of an averaged dielectric function. The Maxwell-Garnett approximation<sup>13</sup> provides a satisfactory description for dilute suspensions of metal nanoparticles dispersed in a dielectric. The position of the plasma resonance is generally correct, whereas particle size corrections are generally needed to account for the observed band width (for a general review, see for example Kreibig<sup>14</sup>). The dielectric function of the composite medium  $\varepsilon(\omega)$  can be calculated for spherical particles from the general expression:

$$\frac{\varepsilon(\omega) - \varepsilon_i(\omega)}{\varepsilon(\omega) + 2\varepsilon_i(\omega)} = x \frac{\varepsilon_m(\omega) - \varepsilon_i(\omega)}{\varepsilon_m(\omega) + 2\varepsilon_i(\omega)}$$

where  $x$  is the volume fraction (filling factor) of the material dispersed in the dielectric,  $\varepsilon_i$  and  $\varepsilon_m$  are the dielectric functions of the dielectric and of the particle material. The complex dielectric function of graphite  $\varepsilon_m$  has been calculated from the optical data published by Taft and Philipp,<sup>14</sup> whereas the refractive index of polyimide ( $n=1.78$ ) has been used for the dielectric (the charge transfer transitions of the PMDA-ODA molecule cannot be represented because of this simplification). Figure 2 shows the energy loss function calculated for various values of the filling factor  $x$ . The growth of a flat absorption band centered at 3 eV is predicted, which confirms the assignment of the observed resonance to  $\pi$ - $\pi^*$  transitions induced in graphitic inclusions. Size effects are probably responsible for the width of the absorption band, which is less satisfactory than the band position, as usually. It is however more difficult to take into account this effect for graphite than for metals, since Drude's relations are not valid in the present case and only bulk constants are available.

#### 4 CONCLUSION

A new peak at 3 eV has been revealed in the energy loss spectrum of irradiated polyimide thin films. The growth of this absorption band accounts for the reduction of the band gap previously discussed for thick films. The optical data analysis is consistent with the formation of disordered carbon layers involving an important graphitic component, which controls the electronic properties. Because of the importance of the bombardment energy in the techniques of hard carbon deposition, it would be interesting to consider the influence of the irradiation energy on the development of the 3 eV absorption band. Investigations in the deep UV would also be an attractive extension of the optical study to obtain more informations on the plasmon region.

## ACKNOWLEDGEMENT

We are pleased to thank J. M. Bureau at LCR Thomson-CSF for providing Langmuir-Blodgett films.

## REFERENCES

1. T. Venkatesan, L. Calcagno, B. S. Elman, G. Foti, *Ion beam modification of materials 2* (Elsevier, Amsterdam, 1987) Chap. 8, pp. 301, 379.
2. J. Davenas, *Solid State Phen.*, **30-31**, 317 (1993).
3. J. P. Salvétat, A. Berthault, F. Brisard, J. M. Costantini, J. Davenas, *Rad. Effects and Defects in Solids*, this issue.
4. M. L. Kaplan, S. R. Forrest, P. H. Schmidt, T. Venkatesan, *J. Appl. Phys.*, **55**, 732 (1984).
5. B. Wasserman, *Phys. Rev.* **B34**, 1926 (1986).
6. D. Fink, K. Ibel, P. Goppelt, J. P. Biersack, L. Lang, M. Behar, *Nucl. Inst. and Methods* **B46**, 342 (1990).
7. O. Y. Posudievsky, *Rad. Effects and Defects in Solids*, this issue.
8. J. Davenas, P. Thévenard, *Nucl. Inst and Methods* **B59-60**, 1249 (1991).
9. J. P. Lafemina, *J. Chem. Phys.*, **90**, 5154 (1989).
10. J. Davenas, G. Boiteux, C. Jardin, M. Gamoudi, *Mol. Liq. Cryst.*, **187**, 143 (1990).
11. G. Matletta, S. Pignataro, C. Oliveri, *Nucl. Inst and Methods* **B39**, 773 (1989).
12. J. Ritsko, R. Bigelow, *J. Chem. Phys.*, **69**, 4162 (1978).
13. J. C. Maxwell-Garnett, *Philos. Trans. Roy. Soc. Lond.*, **205**, 237 (1906).
14. U. Kreibig, *Contribution of Clusters Physics to Materials Science and Technology* (Nijhoff Pub., Dordrecht, 1986), series E-104, chap. 11, pp. 373, 421.
15. E. A. Taft, H. R. Philipp, *Phys. Rev.* **A138**, 197 (1965).

## **13 DISORDERED SYSTEMS**

## LOW-FREQUENCY EXCITATIONS IN FLUORIDE GLASS STUDIED BY NUCLEAR SPIN RELAXATION AND ELECTRICAL CONDUCTIVITY

J. DIECKHÖFER, O. KANERT, R. KÜCHLER and H. JAIN\*

*Institute of Physics, Univ. Dortmund, D-44221 Dortmund, Germany; \*Lehigh Univ., Bethlehem, PA, USA; K. L. Ngai, Naval Res. Lab., Washington DC, USA*

Nuclear spin relaxation (NSR) and electrical conductivity measurements were performed between about 1 K and room temperature in various fluoride glasses. The  $^{19}\text{F}$  NSR rates are found to exhibit a pronounced peak around 10 K which is not observed by conductivity experiments. The underlying relaxation process is interpreted by magnetic fluctuations between neighbouring  $^{19}\text{F}$  nuclear probes without accompanying charge motions. The observed NSR rates and conductivities can be described phenomenologically in the context of excitations of asymmetric double well potential (ADWP) configurations intrinsic to the glassy state.

**Key words:** Low-Frequency Excitation, Glasses, Nuclear Spin Relaxation, Conductivity.

### 1 INTRODUCTION

At low temperatures, nuclear spin relaxation (NSR) and electrical conductivity in inorganic glasses are dominated by localized low-energy excitations of disorder modes intrinsic to the glassy state of matter. Since the physical nature of the modes is largely unknown at present, they are commonly described phenomenologically by asymmetric double well potential (ADWP) configurations with appropriate distributions of the barrier height,  $V$ , and of the asymmetry parameter,  $\Delta$ . Using the model the NSR rate  $1/T_1$  is given by:<sup>2</sup>

$$\frac{1}{T_1} = C_{ADWP} \langle \omega_c^2 \rangle \int_0^{\Delta_m} \int_0^{V_m} d\Delta dV \frac{p(\Delta)g(V)}{\cosh^2(\Delta/2kT)} \frac{\tau_c}{1 + \omega^2 \tau_c^2} \quad (1)$$

Here  $C_{ADWP}$  is the concentration of ADWP's,  $\langle \omega_c^2 \rangle$  is the mean coupling strength between the nuclear probe ensemble and a single ADWP configuration,  $p(\Delta)$  and  $g(V)$  are the distribution functions of  $\Delta$  and  $V$  with upper limits  $\Delta_m$ ,  $V_m$ , and  $\tau_c$  denotes the correlation time of an ADWP transition. Above about 1–5 K, the transitions become thermally activated,<sup>2</sup> i.e.  $\tau_c = \tau_0 \cosh(\Delta/2kT) \cdot \exp(-V/kT)$ . In alkali containing oxide glasses the NSR rate  $1/T_1$  and ac conductivity were found to be related at low temperatures through the fluctuation-dissipation (F-D) theorem according to:<sup>3</sup>

$$1/T_1(\omega, T) \propto kT/\omega^2 \cdot \sigma(\omega, T) \quad (2)$$

Theoretically, the link requires a common susceptibility based on a uniform relaxation mechanism due to charge movements connected with the ADWP transitions. In the present paper we demonstrate that relation (2) does not hold for fluoride glasses. In particular,  $^{19}\text{F}$  NSR is shown to specifically detect further low-energy excitations obeying Eq.(1), which



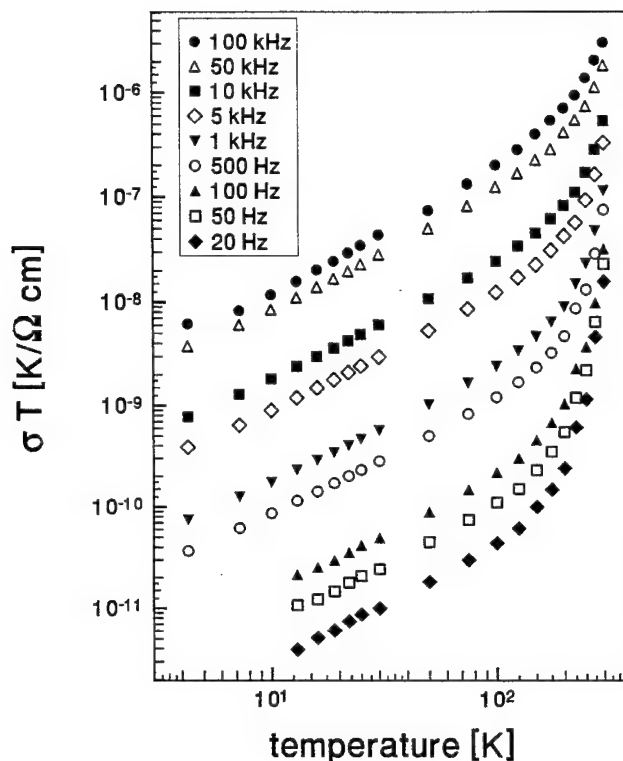


FIGURE 1 Log-log plot of conductivity  $\sigma T$  vs temperature in a ZBLAN glass of composition  $55\text{ZrF}_4\text{-}25\text{BaF}_2\text{-}4\text{LaF}_2\text{-}3\text{AlF}_3\text{-}13\text{NaF}$  (mol%) observed at different frequencies.

are not observed by conductivity experiments. Hence, the observed NSR rate has to be written as a sum of two different contributions:

$$1/T_1 = 1/T_1|_a + 1/T_1|_b \quad (3)$$

where only the first term  $1/T_1|_a$  is related to  $\sigma$  by the F-D theorem (2), i.e. the contribution is caused by the same relaxation mechanism which is responsible for  $\sigma$ .

## 2 EXPERIMENTAL RESULTS AND DISCUSSION

AC conductivity and NSR experiments using different nuclear probes ( $^{19}\text{F}$ ,  $^{23}\text{Na}$ ,  $^{27}\text{Al}$ ) were performed in fluoride glasses, with compositions listed in the figures, between about 1 K and room temperature over a wide range of frequencies. Typical results of such measurements are presented in Figures 1–4. Figures 1 and 2 show that  $\sigma T$  increases monotonically with rising temperature and frequency following approximately the power law

$$\sigma T \propto T^{1+\alpha} \cdot \omega^{2-\beta} \quad (4)$$

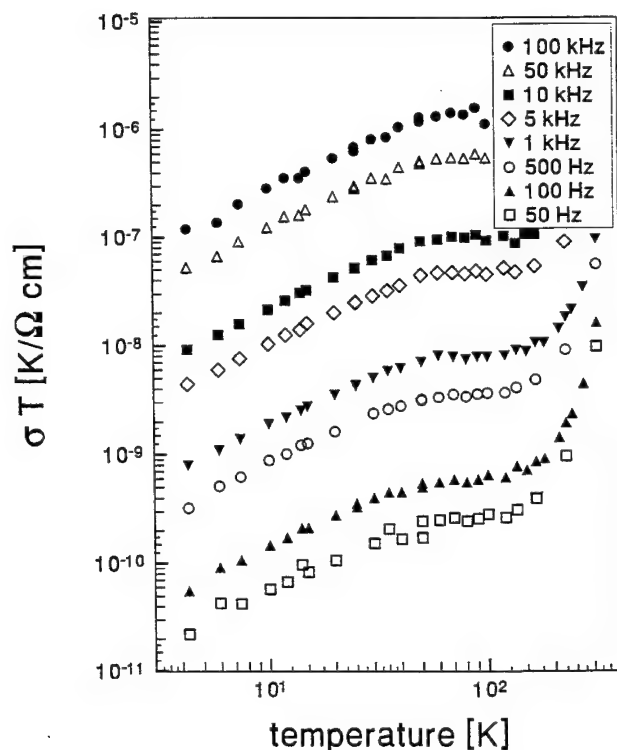


FIGURE 2 Log-log plot of  $\sigma \cdot T$  vs temperature in a CLAP glass of composition 9.5CdF<sub>4</sub>-11.5CdO-3CdCl<sub>2</sub>-6LiF-4KF-30AlF<sub>3</sub>-30PbF<sub>2</sub>-2LaF<sub>3</sub> (mol%) observed at different frequencies.

The coefficients  $\alpha$ ,  $\beta$  are listed in Table I.

Application of the F-D theorem (2) to Eq.(4) yields

$$1/T_1 \propto T^{1+\alpha} \cdot \omega^{-\beta} \quad (5)$$

which has recently been verified in various oxide glasses.<sup>3</sup> However, as demonstrated in Figures 3 and 4, strong deviations from the monotonic temperature dependence occur in fluoride glasses exhibiting a peak in the NSR rate around 20 K. Obviously, the peak is detected specifically by <sup>19</sup>F NSR, while the <sup>23</sup>Na and <sup>27</sup>Al probe nuclei observe the maximum very weakly. Therefore we conclude that only movements of fluorine atoms are responsible for the peak while other nuclear probes such as <sup>23</sup>Na or <sup>27</sup>Al do not take part in these fluctuations. The findings can be interpreted quantitatively by Eq.(3) assuming two different types of ADWP configurations in Eq.(1). The first term  $1/T_1|_a$  is found to obey Eq.(5), where the coefficients  $\alpha$ ,  $\beta$  agree with those observed by the conductivity experiments (Eq.(4), see Table I). The result points to a common relaxation mechanism connected with fluctuating charges. The second term  $1/T_1|_b$  which is caused according to the above discussion by fluctuations of the magnetic interaction between neighbouring fluorine nuclear probes can be described by Eq.(1). The related NSR rate peaks are shifted to higher temperatures with rising frequency. Evaluation of the shift by means of the condition  $\omega \cdot \langle \tau_c \rangle = 1$  leads to an Arrhenius behaviour of the mean correlation time  $\langle \tau_c \rangle$  of

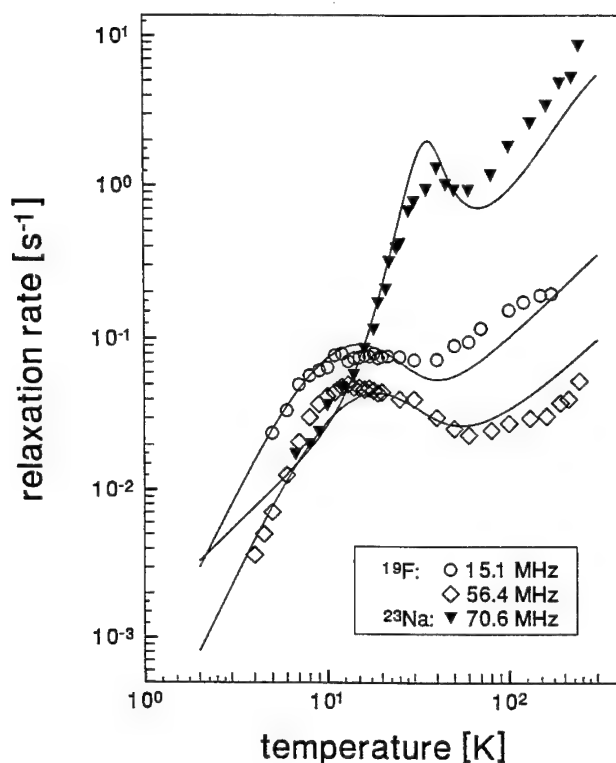


FIGURE 3 Temperature dependence of  $^{19}\text{F}$  and  $^{23}\text{Na}$  NSR rates in ZBLAN glass. Solid lines are fits to the data by means of the ADWP model.

the ADWP configurations of type (b). The resulting preexponentials  $\langle\tau_o\rangle$  and energies  $E$  are presented in Table I. Further, from the magnitude of the observed  $^{19}\text{F}$  NSR rate peak the fraction of the fluorine atoms involved in the relaxation process was estimated to be about  $10^{-3}$ – $10^{-4}$ . The solid lines in Figures (3, 4) are fits to the data by means of Eqs.(1, 2, 5) using  $g(V) \propto \text{sech}(V/V_o)$  and  $p(\Delta) \propto \Delta^\gamma$ . The relevant parameters used for the fits are listed in Table I.

TABLE I

Summary of the relevant fitting parameters related to the NSR and conductivity results shown in Figures 1–4.

glass	$\alpha$	$\beta$	nucleus	$\langle\tau_o\rangle(s)$	$E(K)$	$V_m(K)$	$\Delta_m(K)$	$\gamma$	$V_o(K)$	$\tau_o(s)$
ZBLAN	0.2	1.0	$^{19}\text{F}$	$1.93 \cdot 10^{-11}$	94	461	59	1.06	31.8	$1.1 \cdot 10^{-11}$
			$^{23}\text{Na}$	—	—	402	768	3.4	1540	$1.3 \cdot 10^{-13}$
CLAP	0.0	1.1	$^{19}\text{F}$	$2 \cdot 10^{-9}$	64	234	55.8	0.93	15.7	$5.0 \cdot 10^{-10}$
			$^{27}\text{Al}$	—	—	803	300	0.73	137	$1.01 \cdot 10^{-11}$

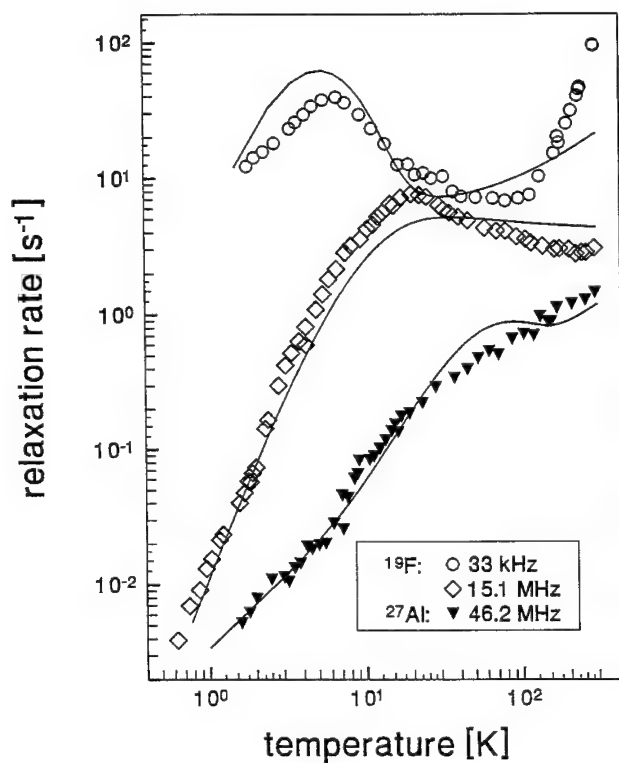


FIGURE 4 Temperature and frequency dependence of  $^{19}\text{F}$  and  $^{27}\text{Al}$  NSR rates  $1/T_1$  in CLAP glass. Solid lines are fits to the data by means of the ADWP model.

#### REFERENCES

1. M. Klinger, *J. Non-Cryst. Sol.* **150** 212 (1990).
2. O. Kanert, R. K  chler, J. Dieckh  fer, X. Lu, H. Jain, and K.L. Ngai, *J. Non-Cryst. Sol. Vol.* **172-174**, 1277 (1994).
3. O. Kanert, R. K  chler, J. Dieckh  fer, X. Lu, and H. Jain, *Phys. Rev.* **B49** 629 (1994).

## CONDUCTIVITY AND STRUCTURE RELATIONS IN POLYCRYSTALLINE $\alpha/\beta$ -LEAD FLUORIDE DOPED WITH SCANDIUM FLUORIDE

A. MEYER,\* J. TEN EICKEN,\* O. V. GLUMOV,\*\* W. GUNSSER,\* M. KARUS,\*  
and I. V. MURIN\*\*

*\*Institut für Physikalische Chemie, Universität Hamburg, Bundesstrasse 45, 20146  
Hamburg, Germany; \*\*St. Petersburg University, St. Petersburg, Russia*

A study is made of temperature and pressure dependence of impedance spectroscopy and x-ray analysis for lead fluoride doped with various concentrations of scandium fluoride for samples with mixed orthorhombic/cubic phase composition.

The conductivity is seen to increase with higher scandium concentration, higher lattice distortion of the orthorhombic phase and a higher concentration of the orthorhombic phase in the sample.

**Key words:** Impedance spectroscopy, temperature dependent x-ray studies, lead fluoride, scandium fluoride, ionic conductivity.

### 1 INTRODUCTION

Lead fluoride belongs to the class of superionic conductors. The fluorine sublattice starts melting at temperatures about 500°C, where because of the resulting high fluorine mobility a very high ionic conductivity arises.

The defect concentration, hence the properties of the material can be changed by heterovalent doping.<sup>1</sup> In this work we discuss the special case of scandium fluoride as dopant.

The so-called solid solutions of  $\text{ScF}_3$  in  $\text{PbF}_2$  have been studied by EPR, x-ray diffractometry, DTA and impedance spectroscopy.<sup>2,3,4,5</sup> These works deal with the cubic  $\beta$ -phase of the lead fluoride system. Few investigations have been performed on the orthorhombic  $\alpha$ - or a mixed  $\alpha/\beta$ -system.<sup>6,7</sup>

The thermodynamically more stable  $\beta$ -modification<sup>8</sup> changes under pressure to the  $\alpha$ -form due to the smaller unit cell volume of the orthorhombic  $\alpha$ -phase. An irreversible phase transition from the orthorhombic  $\alpha$ - to the cubic  $\beta$ -phase takes place at temperatures about 615 K.<sup>7,8</sup>

Pure  $\alpha$ - $\text{PbF}_2$  shows a lower conductivity than  $\beta$ - $\text{PbF}_2$  at temperatures below 550 K.<sup>8</sup>

We have performed temperature and pressure dependent impedance spectroscopy and x-ray studies on the mixed  $\alpha/\beta$ - $\text{PbF}_2$  system doped with  $\text{ScF}_3$  (between 0 mol% and 15 mol%).

### 2 EXPERIMENTAL

The polycrystalline material was pressed to pellets (diameter 10 mm, thickness between 1 mm and 3 mm) under pressure up to 2.5 GPa at room temperature (For synthesis see<sup>1</sup>). The pressure applied here is referred to by the pressure dependence in this work. For in situ measurements see reference.<sup>10</sup> Contacts on the pellets were done with sputtered gold. The impedance spectroscopic measurements were performed with a HEWLETT PACKARD

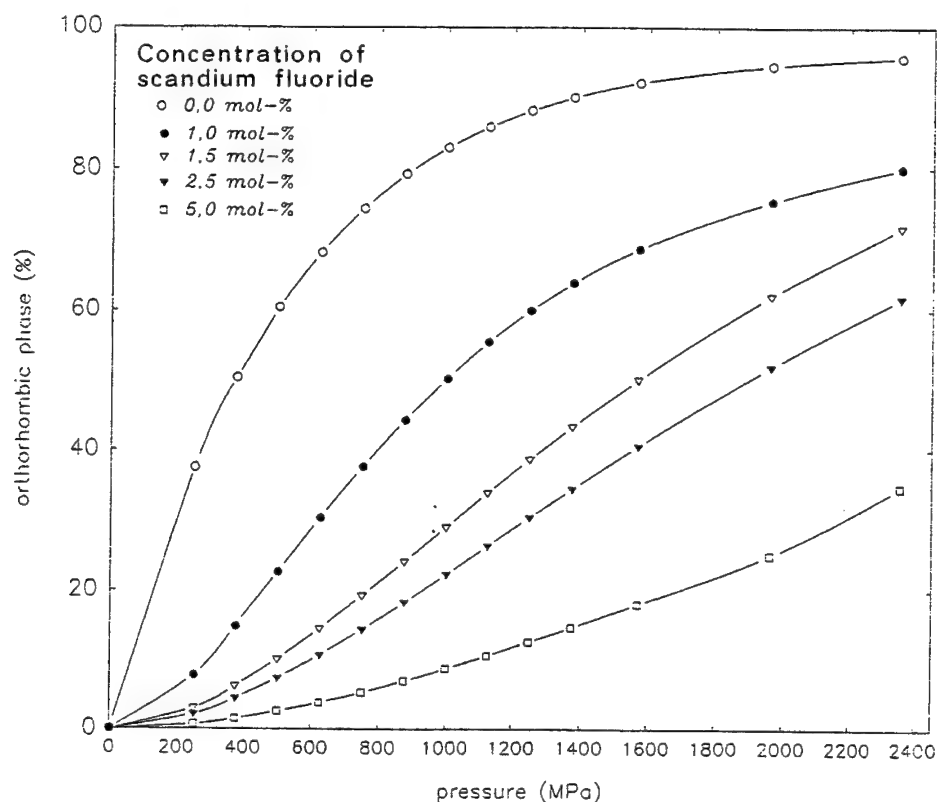


FIGURE 1 Percentage of the orthorhombic phase as a function of pressure.

HP 4284 A bridge (frequency range 20 Hz to 1 MHz) in a self-constructed, externally heated cell with automatic temperature control (typical temperature error  $\pm 2$  K), all linked to a computer. The temperature range used for this work was between 295 K and 800 K. The environment of the sample is variable from vacuum to any desired gas; helium was used for the present study. The temperature dependent x-ray analysis was performed with a PHILLIPS diffractometer type PW3710-BASIS in vacuum from 295 K to 650 K.<sup>9</sup>

### 3 RESULTS AND DISCUSSION

The intensities of the (111)-reflections of the  $\alpha$ - and the  $\beta$ -phase for pure lead fluoride as a function of pressure were measured. The decrease of the  $\beta$ -(111)-reflection corresponds with the increase of the  $\alpha$ -(111)-reflection. From these results the percentage of the orthorhombic  $\alpha$ -phase was evaluated as shown in Figure 1 for different scandium concentrations. The  $\beta$ -phase is stabilized by increasing the concentration of scandium fluoride.

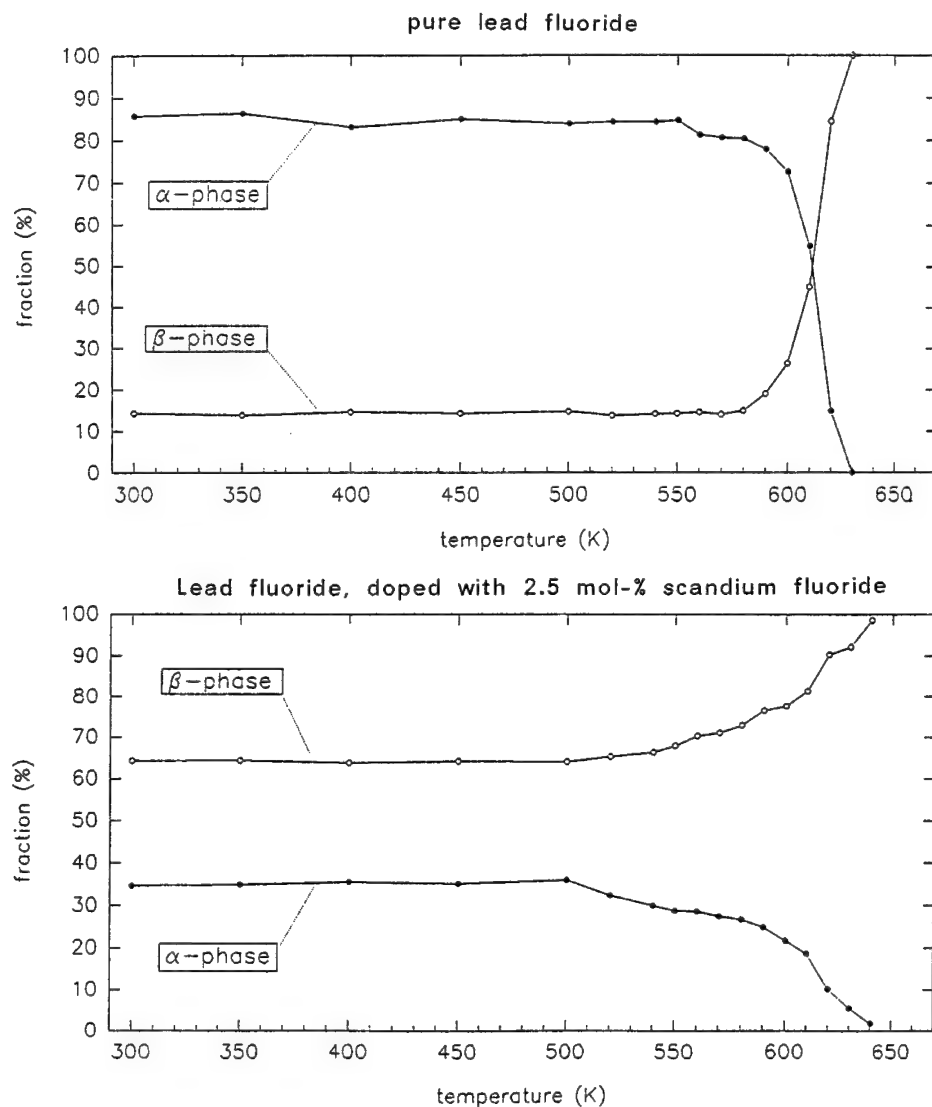


FIGURE 2 Phase percentage as a function of temperature.

The distances of the (111)-planes are constant within the applied pressure range for both phases, so the volumes of the unit cells are not changing.

Figure 2 shows the temperature dependence of  $\alpha$ - and  $\beta$ -phase percentages as a function of temperature for pure and with 2.5 mol% scandium fluoride doped lead fluoride. The phase transition starts at 500 K in the doped sample and at 550 K in the pure material. The lattice distortions of the  $\alpha$ - and the  $\beta$ -phases in the doped sample show a different

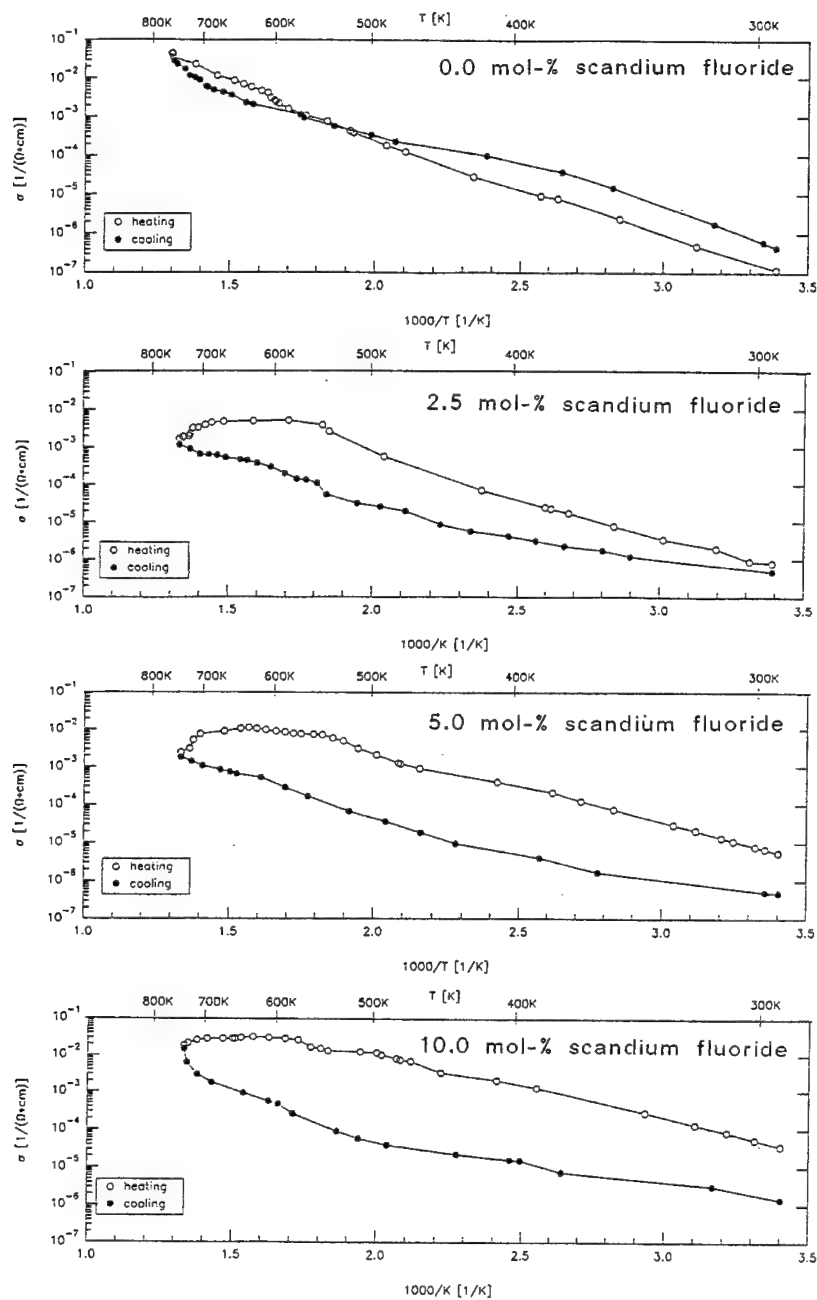


FIGURE 3 Conductivity versus temperature for various concentrations of scandium fluoride.



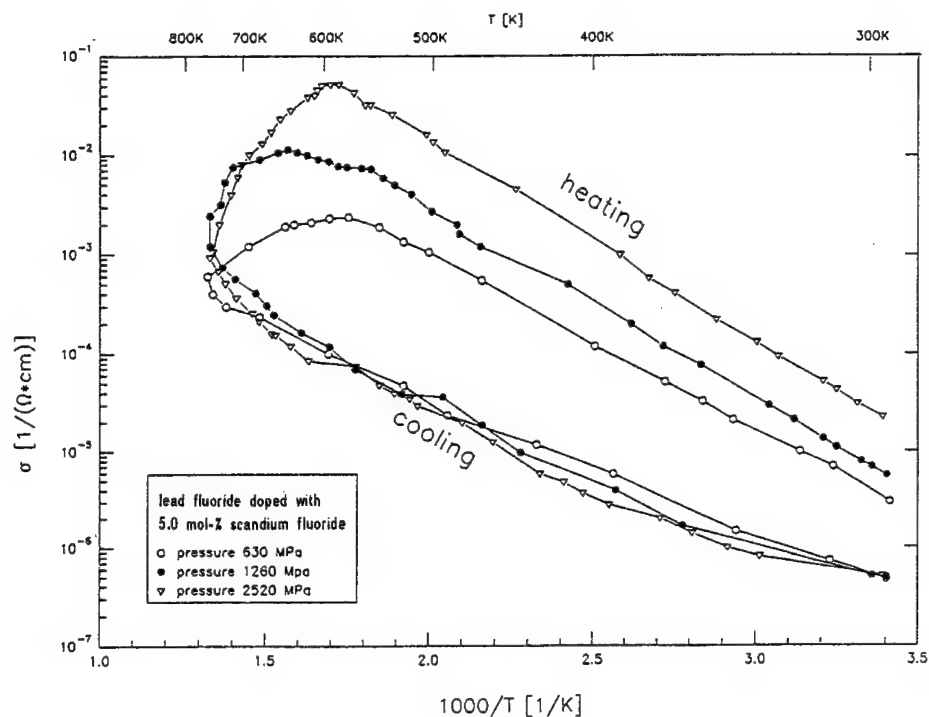


FIGURE 4 Conductivity versus temperature for various pressures.

temperature dependence. The  $\alpha$ -phase in the doped sample is more distorted than the  $\beta$ -phase and the distortion only decreases near the transition temperature. This difference is not observed for the undoped sample.

The conductivity measurements as a function of temperature and scandium fluoride concentration for the first temperature cycle are shown in Figure 3. The conductivities of the  $\alpha/\beta$ -phase mixtures in the *first heating* period are higher than in the cooling period of the then pure  $\beta$ -phase except for undoped lead fluoride. All following heating and cooling cycles show the same conductivities as the first cooling cycle. This is a result of the complete and irreversible phase transition from the orthorhombic to the cubic phase. The comparison of the conductivities for the first heating period (i.e. for the  $\alpha/\beta$ -phase mixture) as a function of scandium concentration shows a clear increase of conductivity with increasing scandium content. The same result, but with a smaller increase, was found for the cubic  $\beta$ -system (this work and ref.<sup>1</sup>). So the difference in conductivity between  $\alpha/\beta$ -mixed system and pure  $\beta$ -phase also increases with increasing scandium concentration, as Figure 3 clearly shows. Table I presents the activation energies for the dc-conductivity for an Arrhenius-like behavior for some scandium fluoride concentrations. The activation energies decrease in both systems with increasing dopant concentration, with generally smaller values for the pure  $\beta$ -system.

Table I  
Activation energies for various concentrations of scandium fluoride.

doping concentration [mol-%]	$E_{A\alpha/\beta}$ [eV]	$E_{A\text{ pure } \beta}$ [eV]
0.0	$0.507 \pm 0.002$	$0.429 \pm 0.015$
2.5	$0.472 \pm 0.013$	$0.303 \pm 0.036$
5.0	$0.403 \pm 0.004$	$0.268 \pm 0.065$
10.0	$0.376 \pm 0.002$	$0.247 \pm 0.013$

The pressure dependence of the conductivity for the sample with 5 mol% scandium fluoride is shown in Figure 4. The conductivities of the  $\alpha/\beta$ -mixed samples (heating period) are much higher than the ones of the pure samples. A higher pressure produces a higher content of  $\alpha$ -modification in the sample which results in a higher conductivity. These differences vanish after exceeding the conversion temperature to the cubic  $\beta$ -phase (cooling period). The activation energies show only a slight decrease with increasing pressure.

#### 4 CONCLUSIONS

The big difference in the conductivity behavior of undoped and scandiumfluoride doped leadfluoride in a mixed  $\alpha/\beta$ -system cannot be explained by the existence of a two phase system alone. The percentage of the  $\alpha$ -phase, the distortion of the orthorhombic lattice and the scandium fluoride concentration together have an influence on the defect concentration, which leads to the high differences in conductivity between the different systems.

#### REFERENCES

1. J. ten Eicken, *Dissertation*, Hamburg 1993.
2. J. ten Eicken, W. Gunßer, S. V. Chernov, O. V. Glumov, I. V. Murin, *Solid State Ionics* **53-56** (1992) 843.
3. J. ten Eicken, W. Gunßer, S. V. Chernov, I. V. Murin, *Ber. Bunsenges. Phys. Chem.* **96** (1992) No. 11 1723.
4. S. Palchoudhuri, G. K. Bichile, *Solid State Commun.* **5** (1988) 554.
5. O. V. Glumov, I. V. Murin, *Soviet Elektrochem.* (1979) 966.
6. J. ten Eicken, W. Gunßer, M. Karus, I. V. Murin *Solid State Ionics* (1994) in press.
7. M. Karus, *Master Thesis in Physics*, Hamburg 1993.
8. J. H. Kennedy, R. Miles, J. Hunter, *J. Electrochem. Soc.* **120** (1973) 1441.
9. A. Meyer, *Master Thesis in Chemistry*, Hamburg 1993.
10. O. V. Glumov, W. Gunsser, M. Karus, I. V. Murin (Proceedings EURODIM 1994 LYON.) Radiation Effects and defects in Solids 1995 Vol. 133-134.

## PHOTOVOLTAIC EFFECT AND ELECTRONIC TRANSITIONS IN $\text{RbAg}_4\text{I}_5$

A. BORIS,\* T. HATTORI and M. ISHIGAME

*Research Institute for Scientific Measurements, Tohoku University, 2-1-1 Katahira, Sendai 980, Japan*

A study has been made of the effect of local light irradiation and silver saturation on the contact photo-emf excitation spectrum of  $\alpha\text{-RbAg}_4\text{I}_5$  superionic crystals at room temperature. It was found that irradiation with light having energies 2.75 eV and 2.92 eV causes color centers formation in the crystals. The possible nature of the bands in the photo-emf excitation spectrum is discussed. Time dependences of the photo-emf for the main excitation bands were measured at various illumination levels. A characteristic asymmetry of the relaxation curves governed by the excitation kinetics was observed at high illumination intensities. The estimation of the photon capture cross sections for the electronic transitions gives the values of the order of magnitude of  $10^{-17}\text{cm}^2$ . The transient experiments have shown that the photocarrier lifetimes in the crystals are of the order of 1000 sec.

*Key words:* superionic conductor, photo-emf, color center.

### 1 INTRODUCTION

A lot of vacancies of mobile ions in superionic crystals results in creation of imperfection levels with high density of states in the forbidden gap of the crystals. Due to the Coulomb interaction between mobile ions and nonequilibrium holes or electrons defect processes are closely connected with the processes of electronic excitation in superionic crystals. For the same reason one would expect considerable increase of lifetime of nonequilibrium carriers in conduction or valence band and low values of their mobilities in superionic crystals. The specific features of generation of nonequilibrium carriers were exhibited in studying the spectral, illumination intensity and time dependences of the contact photo-emf of superionic  $\alpha\text{-RbAg}_4\text{I}_5$  crystals under sub-bandgap illumination ( $h\nu \leq E_g = 3.2\text{ eV}$ ).<sup>1</sup>

### 2 EXPERIMENTAL RESULTS AND DISCUSSION

Investigations were carried out on polycrystalline  $\text{RbAg}_4\text{I}_5$  samples. A finely dispersed graphite powder was used for electrode preparation. For the photo-emf measurements a Keithley Model 236 electrometer with  $> 10^{14}\Omega$  input impedance was used. A high-pressure xenon lamp and a grating spectrophotometer were used for specimen illumination. During measurements the specimens were housed in an optical thermostat. Vacuum was  $2 \times 10^{-2}$  Torr.

Figure 1 shows typical short-circuit photocurrent spectra for a nonuniformly illuminated  $\text{C} | \text{RbAg}_4\text{I}_5 | \text{C}$  cell at room temperature. The spectral dependences were obtained by decreasing the light wavelength. Curve 1 in the figure presents the result obtained by the first scanning of the wavelength and corresponds to initial  $\text{RbAg}_4\text{I}_5$  crystal prior to irradiation of the sample by light. Two peaks at 425 nm and 437 nm corresponding to energies of 2.92 eV and 2.85 eV were observed. The appearance of two wide bands with

\* Permanent Address: Institute of Solid State Physics Russian Academy of Sciences, 142432, Chernogolovka, Moscow dist., Russia

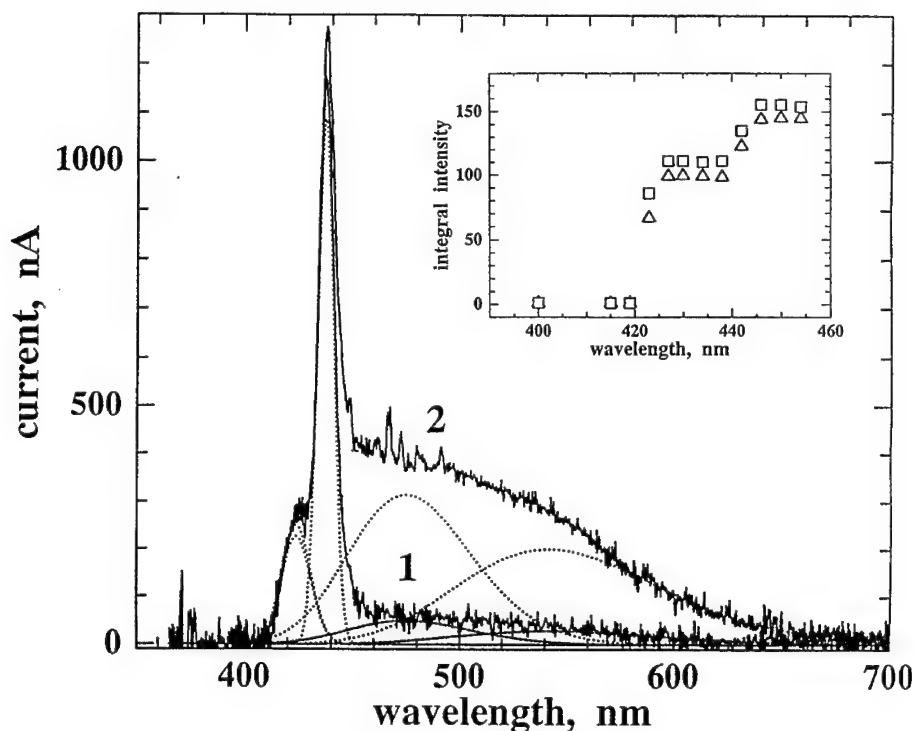


FIGURE 1 Short-circuit photocurrent of the nonuniformly illuminated C | RbAg<sub>4</sub>I<sub>5</sub> | C cell versus exciting-light wavelength obtained by decreasing the wavelength,  $T = 305$  K. (1) Spectrum of initial RbAg<sub>4</sub>I<sub>5</sub> crystal. (2) Spectrum obtained after the light irradiation ( $400 \text{ nm} < \lambda_{ex} < 455 \text{ nm}$ ). Insert: Spectral dependence of integral intensities of the bands with maxima at 475 nm (□) and 540 nm (Δ) in the short-circuit photocurrent spectra measured in sequence after the same (5 sec) exposure to light irradiation of the sample.

maxima at 475 nm (2.62 eV) and 540 nm (2.29 eV) and a peculiarity in the region 445 nm (2.75 eV) were observed in the spectral response as a result of the local light irradiation of the sample. It has been found that the irreversible transformation of the spectrum was easily produced by the irradiation with light having energies 2.75 eV and 2.92 eV (see insert Figure 1). After the irradiation short-circuit photocurrent spectrum was finally changed as shown in Figure 1 (curve 2).

The effect of addition of silver into RbAg<sub>4</sub>I<sub>5</sub> crystal and the additive coloration in iodine vapor on the photocurrent excitation spectra was investigated. A marked decrease in the relative intensity of the 2.92 eV band was observed in silver doped RbAg<sub>4</sub>I<sub>5</sub>; in some cases the band disappeared completely. By contrast, the intensity of the 2.92 eV band increased in the spectra for crystals following coloring in the iodine vapor which is associated with an increase in the concentration of silver cation vacancies in the crystal bulk. The results obtained support the model that the 2.92 eV band corresponds to the generation of nonequilibrium holes in the valence band from an imperfection level at a depth of  $\sim 0.3$  eV under the conduction band of RbAg<sub>4</sub>I<sub>5</sub> crystals. An increase in the concentration of silver cation vacancies leads to a shift down of the Fermi level position in

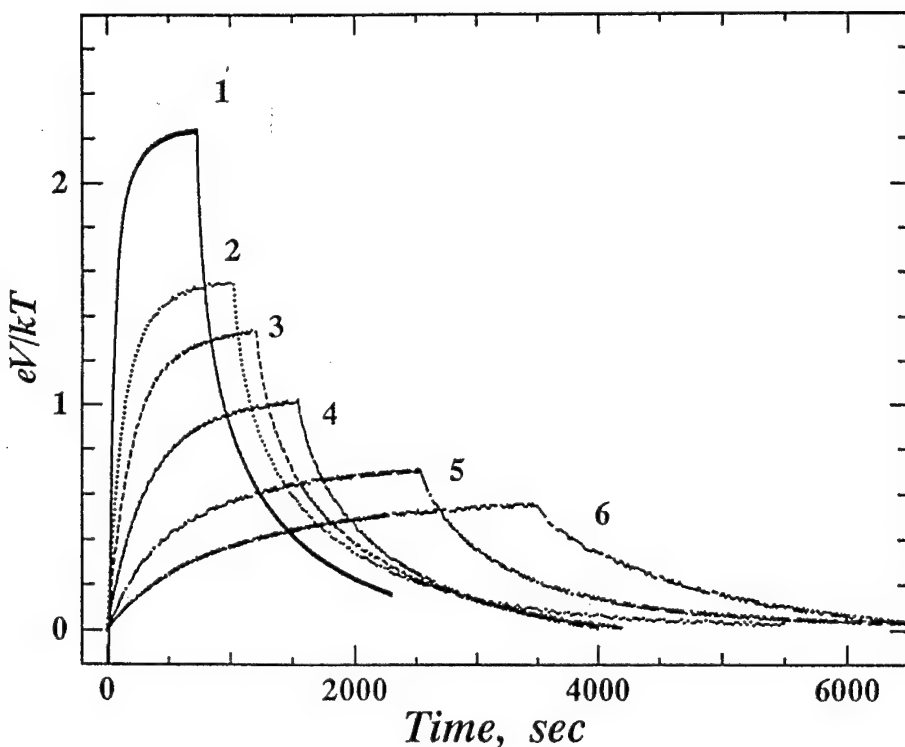


FIGURE 2 Time dependences of the barrier photo-emf for 425 nm excitation band at various illumination levels.  $I_0 = 9.2 \times 10^{14}$  photon/cm<sup>2</sup>sec,  $T = 305$  K (1)  $I_0$ ; (2)  $0.5 \times I_0$ ; (3)  $0.25 \times I_0$ ; (4)  $0.125 \times I_0$ ; (5)  $0.062 \times I_0$ ; (6)  $0.031 \times I_0$ ; (7)  $0.016 \times I_0$ .

the forbidden gap and to the corresponding change of the level occupancy. As a result an increase in the intensity of the 2.92 eV band in the photocurrent spectrum was observed in colored crystals. Hole excitation from the level to the valence band may cause iodine losses from the surface of the sample and formation of F-type electron centers involving iodine vacancies. The photoinduced bands peaked by 2.62 eV and 2.29 eV in the photocurrent spectrum are probably due to the F-type color centers created on the surface of sample as a result of the irradiation with light having energies 2.92 eV and 2.75 eV. The peculiarity observed in the photocurrent spectra at 2.75 eV corresponds to thermo-optical electronic transitions from the valence band to the level  $E_c - 0.3$  eV. The narrow intensive 2.85 eV band corresponds to the generation of nonequilibrium electrons in the conduction band from deep silver iodine impurities.

Time dependences of the barrier photo-emf for the two main excitation bands with maxima at 2.92 eV and 2.85 eV were measured at various illumination levels. The experimental relaxation curves for the 2.92 eV band are shown in Figure 2. Closely similar time dependences were measured at 2.85 eV excitation. It has been found that the relaxation law for the photo-emf during contact illumination is  $e\varphi = \frac{kT}{2} \ln[g_i W(1 - \exp(-t/\tau)) + 1]$ , where  $g_i$  is a factor of the order of  $10^{13}$  and  $W$  is

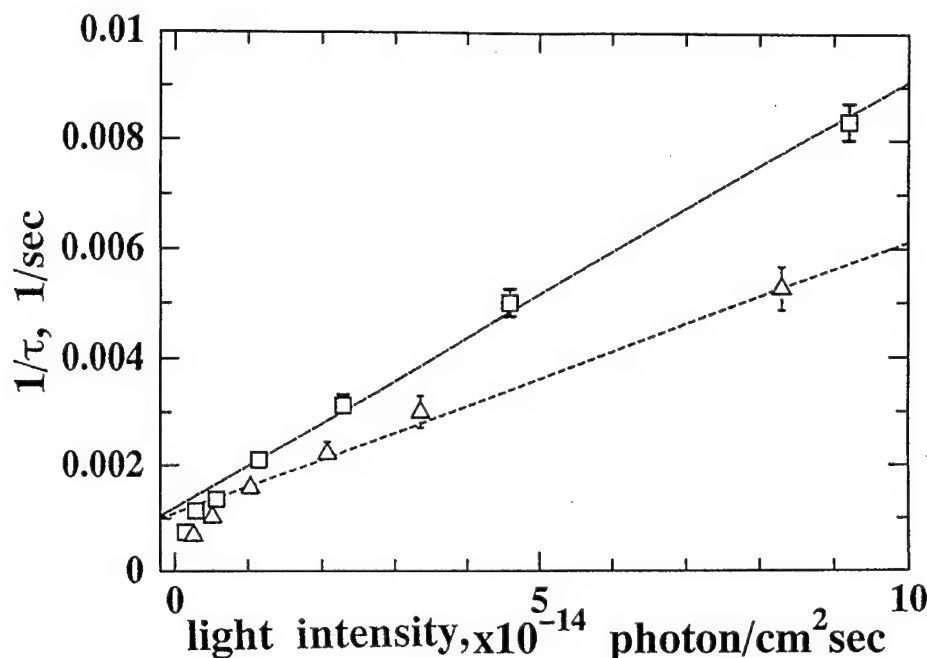


FIGURE 3 Dependence of the relaxation time constant on the illumination intensity. ( $\Delta$ )  $\lambda_{ex1} = 425$  nm (2.92 eV),  $\sigma_1 = 5.0 \pm 0.4 \times 10^{-18}$  cm<sup>2</sup>; ( $\square$ )  $\lambda_{ex2} = 437$  nm (2.85 eV),  $\sigma_2 = 7.7 \pm 0.3 \times 10^{-18}$  cm<sup>2</sup>.

the intensity of illumination in term of photon/cm<sup>2</sup>sec. An increase of the time constant  $\tau$  with decreasing illumination intensity was observed. Such behaviour is governed by the nonequilibrium excitation kinetics and allows us to determine the value of the cross section  $\sigma$  for the capture of a photon by an electron at an impurity or defect center. Under conditions in which the competing absorption processes are unimportant  $1/\tau$  is proportional to  $\sim \sigma W$  at high illumination intensities.<sup>2</sup> The estimation of the cross sections for the capture of a photon for the electronic transitions under consideration gives the values of the order of magnitude of  $10^{-17}$  cm<sup>2</sup> (Figure 3). These values look quite reasonable for the photon capture cross section at deep noncharged imperfection or impurity levels. The transient experiments have shown that the photocarrier lifetimes in the crystals are of the order of 1000 sec.

In superionic crystals diffusion of nonequilibrium carriers from the illuminated region sets in motion mobile ions in such direction as to compensate the space charge and reestablish the neutrality in the crystal. The movement of mobile ions and nonequilibrium electrons or holes comes about in the ambipolar diffusion regime and here the diffusion may spread over considerable distances, governed by the lifetime of free carriers and their mobilities. The relaxation characteristics of the barrier photo-emf depending on the position of the injection region between the contacts were tentatively measured. It has been found that behaviour of the relaxation transient characteristics at generation of nonequilibrium holes in the valence band by light having energy 2.92 eV is radically different from that of the characteristics obtained for the excitation band with

maximum 2.85 eV corresponding to the generation of nonequilibrium electrons in the conduction band. Preliminary data obtained substantiate our present conclusions and indicate that the investigations of the relaxation of the barrier photo-emf using a traveling light spot with high spatial resolution are useable as a powerful tool to determine the lifetime and mobility of carriers of electron subsystem in superionic crystals. Such a study is now in progress.

## REFERENCES

1. R. S. Bauer and B. H. Huberman, *Phys. Rev.*, **B13**, 3344 (1976).
2. S. M. Ryvkin, *Photoelectric Effects in Semiconductors* (Consultants Bureau, New York, 1964), Chap. 9, pp. 190, 198.

## EXAFS STUDIES OF DISORDER IN $\text{CdF}_2\text{-PbF}_2$ SYSTEMS

T. T. NETSHISAULU,<sup>†</sup> C. R. A. CATLOW,\* A. V. CHADWICK,<sup>‡</sup> G. N. GREAVES<sup>°</sup>  
and P. E. NGOEPE<sup>†</sup>

<sup>†</sup>*Department of Physics, University of the North, Sovenga 0727, South Africa; \*The Royal Institution, 21 Albermarle Street, London W1X 4BS, U.K.; <sup>‡</sup>Department of Chemistry, University of Kent at Canterbury, Canterbury, CT2 7NH.; <sup>°</sup>Science and Engineering Research Council, Daresbury Laboratory, Daresbury, Warrington WA4 4AD*

The local environments of Cd and Pb cations in the system  $\text{Cd}_{1-x}\text{Pb}_x\text{F}_2$  ( $x = 0.6$ ) have been measured by means of EXAFS. A comparative analysis of the Fourier transforms of the experimental data provides evidence of the Pb-F bond length being longer than the Cd-F one. Furthermore, our studies show a loss of structure around the  $\text{Pb}(\text{L}_{111})$  edge with increasing temperature. This suggests that the temperature-induced vacancies on the anion sub-lattice are preferentially located adjacent to Pb ions as previously observed in  $\text{PbSnF}_4$  mixed-metal fluorides. The results obtained accord well with our computer simulation findings.

**Key words:** EXAFS, computer simulation,  $\text{PbF}_2$ ,  $\text{CdF}_2$ ,  $\text{Cd}_{0.4}\text{Pb}_{0.6}\text{F}_2$ , vacancies.

### 1 INTRODUCTION

EXAFS measurements are carried out using a synchrotron as a source for x-ray radiation. In this study, EXAFS technique is used to elucidate the temperature dependence of the local structures of Cd and Pb cations in  $\text{CdF}_2\text{-PbF}_2$  systems. These experimental studies will be complemented by computer modelling studies.

Previous EXAFS studies on mixed-metal fluorides with very high  $\text{F}^-$  ion conductivities such as  $\text{RbBiF}_4$  and  $\text{PbSnF}_4$  successfully revealed the local structural environments of their respective cations.<sup>1–2</sup> The main features of note were the contrasts between the temperature dependence of the cation-anion amplitudes and frequencies. Furthermore,  $\text{F}^-$  vacancies were preferentially located in anion sites neighbouring cations having larger ionic radii and lower charges. This intriguing behaviour was attributed to the fact that it is easy to remove ions from sites in excess of singly charged ions (e.g. Rb in  $\text{RbBiF}_4$ ) than to remove them from sites adjacent to the more highly charged Bi ions. In the present investigation, both cations have the same charge (+2) as in  $\text{PbSnF}_4$ ,<sup>2</sup> so that no electrostatic advantage exists for the creation of  $\text{F}^-$  vacancies in anion sites adjacent to the cations with an excess of either Cd or Pb ions.

$\text{Cd}_{1-x}\text{Pb}_x\text{F}_2$  mixed crystals also possess high levels of  $\text{F}^-$  ion disorder.<sup>3</sup> Recent high temperature studies on these compounds<sup>3–5</sup> have provided strong evidence for a relatively low value of the transition temperature  $T_c$  to the fast-ion phase. However, a detailed study of their structural properties is still lacking. For these reasons it is particularly suitable for a predictive theoretical and EXAFS experimental studies on  $\text{Cd}_{0.4}\text{Pb}_{0.6}\text{F}_2$  system. This compound has been chosen since it exhibits the lowest  $T_c$  in the entire range of  $\text{Cd}_{1-x}\text{Pb}_x\text{F}_2$  mixed systems.



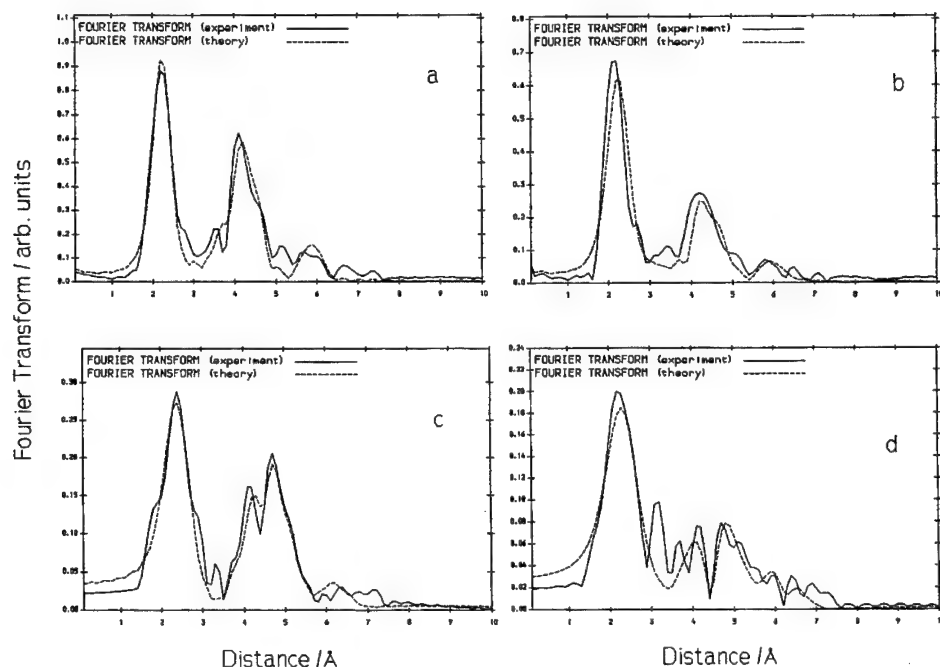


FIGURE 1 EXAFS experimental Fourier transforms for the Cd [(a) and (b)] and Pb [(c) and (d)] edges in  $\text{CdF}_2$  and  $\text{PbF}_2$  at 300 and 500 K, respectively.

## 2 EXAFS THEORY

EXAFS is a technique which yields information on the local structures of a specific kind of atom in disordered systems. In these experiments, X-ray absorption is measured as a function of an X-ray energy on the high-energy side of an absorption edge. In the single scattering approximation the oscillatory EXAFS function  $\chi(k)$  can be mathematically represented by the following equation

$$\chi(k) = \sum_j [N_j/kR_j^2] |f_j(\pi)| \exp(-2\sigma_j^2 k^2) \exp(-2R_j/\lambda) \times \sin(2kR_j + \phi_j(k)) \quad (1)$$

where EXAFS oscillation frequency arising from each shell,  $j$ , is given by  $F_j(k)$  and the amplitude of oscillations by  $A_j$ , so that

$$\chi(k) = \sum_j A_j(k) \times F_j(k) \quad (2)$$

The EXAFS data are processed using the SRS library programs EXCALIB and EXBACK and the subsequent data are analyzed by an iterative EXCURV92 package which generates theoretical spectra. The phaseshifts for a particular atom pair are obtained empirically, using appropriate model compounds with known geometries.<sup>6</sup> In this work,  $\text{CdF}_2$  and  $\text{PbF}_2$  are the model compounds.

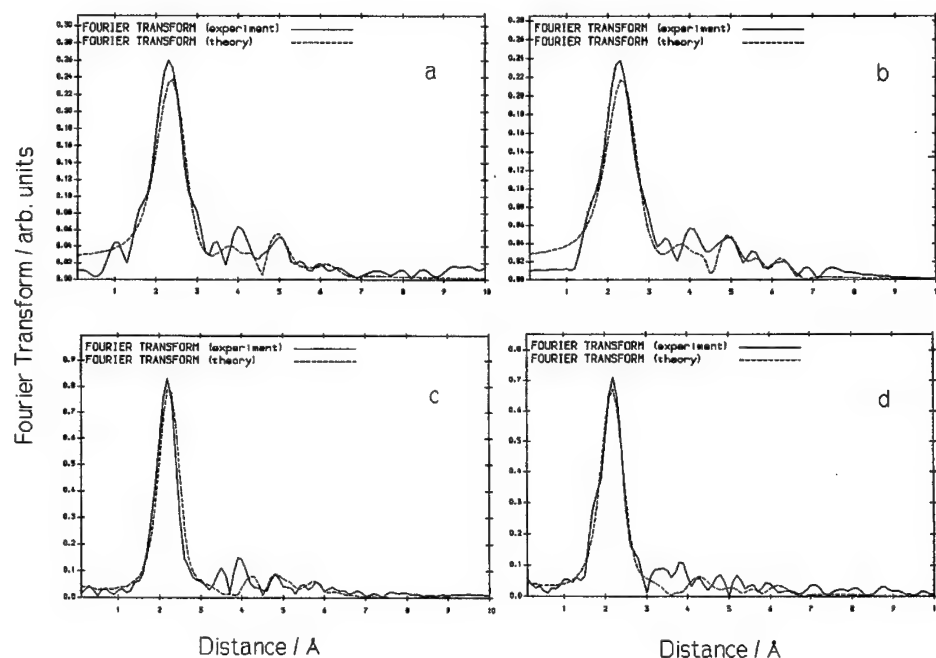


FIGURE 2 EXAFS experimental Fourier transforms for the Pb [(a) and (b)] and Cd [(c) and (d)] edges in  $\text{Cd}_{0.4}\text{Pb}_{0.6}\text{F}_2$  at 300 and 500 K, respectively.

### 3 EXPERIMENTAL DETAILS

#### 3.1 Sample Preparations

The 2:3 mixtures of  $\text{CdF}_2$  and  $\text{PbF}_2$  powders of high purity were intimately mixed and melted in quartz tubes at temperatures above 1100 K until a uniformly clear melt was obtained under high vacuum ( $10^{-6}$  torr). Crystalline  $\text{PbF}_2$  was prepared as a reference specimen in EXAFS analysis for the Pb edge in  $\text{Cd}_{0.4}\text{Pb}_{0.6}\text{F}_2$ , whilst powdered  $\text{CdF}_2$  was used for the Cd edge. X-ray diffraction patterns were collected to check that single cubic fluorite phase crystals had been prepared. These prepared specimens were finely ground ( $< 20 \mu\text{m}$ ) with a mortar and pestle and well diluted with silica and boron nitride into thin coherent pellets using a 13 mm die. After preparation the samples were mounted in an evacuable crystal heating furnace.

#### 3.2 Experimental Conditions

The EXAFS measurements of  $\text{Pb}(L_{111})$  and  $\text{Cd}(K)$  edges in  $\text{Cd}_{0.4}\text{Pb}_{0.6}\text{F}_2$  were carried out using the SERC synchrotron radiation facilities at EXAFS stations 7.1 (for the Pb edge) and 9.2 (for the Cd edge). X-ray absorption spectra for the two edges were measured at various temperatures in transmission mode using a channel-cut Si (111) monochromator to study the  $\text{Pb}(L_{111})$  edge and the Si (220) one for the Cd edge. All scans were typically 40 min. duration. During the data collection, the SRS was operated at about 2.0 GeV with a typical beam current of 150 mA.

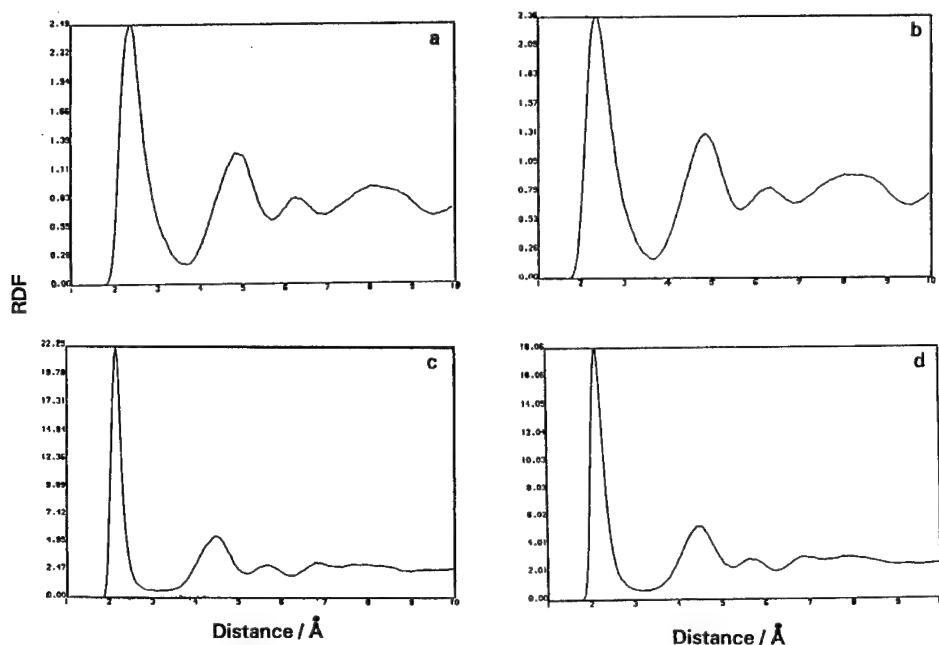


FIGURE 3 Pb-F [(a) and (b)] and Cd-F [(c) and (d)] radial distribution functions in  $\text{Cd}_{0.4}\text{Pb}_{0.6}\text{F}_2$  at 300 and 500 K, respectively.

#### 4 COMPUTER MODELLING TECHNIQUE

Molecular dynamics (MD) simulations were conducted using procedures incorporated in a FUNGUS program.<sup>7</sup> As in previous MD simulations, empirically derived rigid-ion potentials were employed. In the fluorite structure of  $\text{Cd}_{1-x}\text{Pb}_x\text{F}_2$ , Cd and Pb cations, form a fcc lattice. First Cd ions were placed on all alternate cube centers sites, forming  $\text{CdF}_2$ . Next a suitable number of Cd ions were replaced at random by Pb ions forming  $\text{Cd}_{0.4}\text{Pb}_{0.6}\text{F}_2$ . Several simulation runs were made at temperatures corresponding to those used in EXAFS measurements. Time dependent structural properties were acquired via radial distribution functions.

#### 5 RESULTS AND DISCUSSIONS

The Fourier transforms for the experimental and theoretical spectra of  $\text{CdF}_2$  and  $\text{PbF}_2$  compounds are shown in Figure 1. Both spectra clearly reveal two peaks corresponding to cation-anion (for the first shell) and cation-cation (for the second shell) radial distances. The amplitudes of their second peaks diminish with an increase in temperature. However, for the  $\text{Pb}(L_{111})$  edge, the spectrum of the second peak splits into two. Such a phenomenon is not observed on the Cd edge.

Figure 2 shows the Fourier transform plots for the  $\text{Cd}(K)$  and  $\text{Pb}(L_{111})$  edges in  $\text{Cd}_{0.4}\text{Pb}_{0.6}\text{F}_2$  at 300 and 500 K. Their Fourier transforms are different, indicating different local geometries for the two cations in  $\text{Cd}_{0.4}\text{Pb}_{0.6}\text{F}_2$ . Both RDFs contains only one well-defined peak. These results accord well with our molecular dynamics findings (Figure 3).

Hence, the level of disorder in Cd<sub>0.4</sub>Pb<sub>0.6</sub>F<sub>2</sub> is modelled satisfactorily. The peak in the Pb-F radial distance is also broader than that in the Cd-F radial distance. This suggests that the static disorder in the Pb-F coordination shell is greater than the Cd-F one. A similar result was found by Cox *et al*<sup>2</sup> for Rb-F in RbBiF<sub>4</sub>. The first peak (at 300 K) in the Cd-edge Fourier transform is almost three times greater than that of the Pb-edge. Furthermore there is a significant reduction in the amplitudes of the Pb peaks with temperature increase as compared to the Cd peaks.

In the present study, coordination numbers were kept fixed to their preset values. In Tables 1-2 we compare our EXAFS and simulation bond lengths. The two sets of results are generally in good agreement. Both methods indicate that the Cd-F radial distances are shorter than those for Pb-F. The results further indicate that the Cd-F and Pb-F distances reduce with an increase in temperature. The same behaviour was observed on the Bi and Sn edges in RbBiF<sub>4</sub> and PbSnF<sub>4</sub>, respectively.<sup>1-2</sup> Furthermore, we note that the Debye - Waller factors obtained in all our analyses are high for the Pb edge, reflecting the extensive disorder around the Pb cations in Cd<sub>0.4</sub>Pb<sub>0.6</sub>F<sub>2</sub>.

Table I  
Radial distances (RD) for the Cd edge in Cd<sub>0.4</sub>Pb<sub>0.6</sub>F<sub>2</sub> as a function of temperature.

T(K)	Atom type	Coordination number	Simulated RD (Å)	EXAFS RD (Å)	Debye-Waller factor (Å <sup>2</sup> )
300	F	8	2.192	2.287	0.024
	Pb	12	3.735	3.887	0.050
500	F	8	2.190	2.219	0.033
	Pb	12	3.769	3.924	0.063

We may summarise our observations in the following manner. Cations with large ionic radii (e.g. Pb<sup>2+</sup>) promote vacancy stabilisation in neighbouring sites. Kosacki *et al*<sup>3</sup> also observed that the ionic transport processes in Cd<sub>1-x</sub>Pb<sub>x</sub>F<sub>2</sub> are determined by the fluorine ion movement in the nearest neighbourhood of Pb ions. This is well supported by our EXAFS and simulation results. Hence, Cd<sub>0.4</sub>Pb<sub>0.6</sub>F<sub>2</sub> can serve as a better electrolyte in future microbatteries.

Table II  
Radial distances (RD) for the Pb edge in Cd<sub>0.4</sub>Pb<sub>0.6</sub>F<sub>2</sub> as a function of temperature.

T(K)	Atom type	Coordination number	Simulated RD (Å)	EXAFS RD (Å)	Debye-Waller factor (Å <sup>2</sup> )
300	F	8	2.539	2.471	0.053
	Pb	12	4.177	4.192	0.050
500	F	8	2.500	2.437	0.077
	Pb	12	4.173	4.131	0.057

## REFERENCES

1. C. R. A. Catlow, A. V. Chadwick, G. N. Greaves and L. M. Moroney, *Crys. Latt. Def. and Amorph. Mat.* **12**, 193 (1985).
2. P. A. Cox, C. R. A. Catlow, A. V. Chadwick and L. M. Moroney, To be published.
3. I. Kosacki, *Appl. Phys.* **A49**, 413 (1989).
4. I. Kosacki, K. Hibner, A. P. Litvinchuk, M. Ya. Valakh, *Phys. Stat. Sol.* **134**, 495 (1986).
5. I. Kosacki and K. Zalibowski, *Phys. Stat. Sol.* **108**, 765 (1988).
6. P. A. Lee and J. B. Pendry, *Phys. Rev.* **B11**, 2795 (1975).
7. C. R. A. Catlow, *Annu. Rev. Mater. Sci.*, **16**, 517 (1986).

## AMORPHOUS SOL-GEL DERIVED LEAD TITANATE THIN FILMS USED AS PASSIVE WAVEGUIDES

C. URLACHER,\* A. BAHTAT,\*\* J. MUGNIER,\*\* C. BOVIER\* and J. SERUGHETTI\*

*\*Department de Physique des Materiaux (U.R.A. 172); \*\*Laboratoire de Physico-Chimie des Materiaux Luminescents (U.R.A. 442)*

*Universite Claude Bernard, Lyon I 43 bld du 11 novembre 1918 69622 Villeurbanne Cedex, France*

Sol-gel derived PbO-TiO<sub>2</sub> waveguides were prepared on pyrex substrates using the dip coating technique. Heat treatments conducted at 200°C, 300°C and 400°C for one hour led to the densification of the layers and the increase of the refractive index values. The effect of water concentration in the precursor sol on the optical qualities of the waveguides is reported. Monolayer waveguides prepared with high water concentration provided the best coefficients of attenuation values (< 1 dB/cm). Preliminary study of Waveguide Raman Spectroscopy is presented.

*Key words:* Sol-Gel, PbO-TiO<sub>2</sub>, Planar waveguides.

### 1 INTRODUCTION

Thin films of the PbO-TiO<sub>2</sub> system have recently earned some great interest.<sup>1</sup> Indeed ferroelectric PbTiO<sub>3</sub> thin films and crystallized PbTiO<sub>3</sub> waveguides have already been studied by several authors.<sup>2,3,4</sup> Amorphous PbO-TiO<sub>2</sub> optical waveguides have been far less investigated. In this study the optical qualities of thin amorphous PbO-TiO<sub>2</sub> films prepared by sol-gel process, at low annealing temperatures (between 200°C and 400°C), were measured. Sol-gel method for the deposition of thin layers has many known advantages including low processing temperatures, good homogeneity, easy control of composition, deposition on large area substrates, inexpensive equipment and so on.

Single and multilayer PbO-TiO<sub>2</sub> thin films were prepared on pyrex substrates using the dip-coating technique. The thickness, the index of refraction and the optical loss evolutions as a function of annealing temperature and water / ethoxide molar ratio in the precursor sol were analysed. Refractive index and thickness were determined by m-lines spectroscopy.<sup>5</sup> A microcomputer-assisted video camera system, described below, was used to measure waveguide attenuation. Preliminary results provided by the so called Waveguide Raman Spectroscopy<sup>7</sup> (WRS) were presented.

### 2 EXPERIMENTAL

#### 2.1 Waveguides Preparation

Lead acetate trihydrate Pb(OCOCH<sub>3</sub>)<sub>2</sub> · 3H<sub>2</sub>O and titanium isopropoxide Ti(OCH(CH<sub>3</sub>)<sub>2</sub>)<sub>4</sub> were used as precursors for preparing the lead titanate sol (molar ratio Pb/Ti = 1). The lead salt solution was obtained by dissolving lead acetate trihydrate in an acetic acid solution (concentration = 700g/l). Various quantities of water were added to promote hydrolysis and condensation. To maintain a stable precursor sol, titanium isopropoxide was modified with acetylacetone<sup>1</sup> (AcacH) following the exothermic reaction:

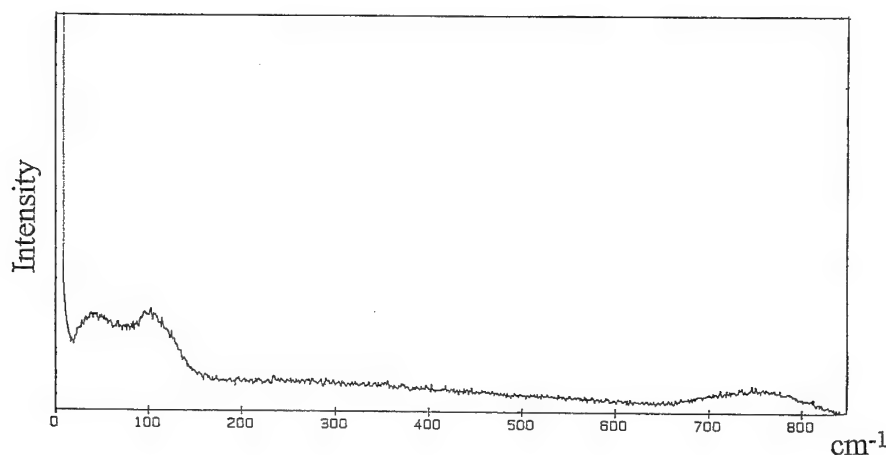
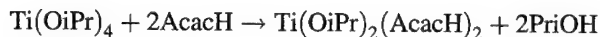


FIGURE 1 Waveguide Raman Spectroscopy spectrum of a monolayer PbO-TiO<sub>2</sub> waveguide ( $n = 10$ ) densified at 400°C for 1 hour.



Methanol was added to adjust sol viscosity. Different sol containing  $n = 3, 10$  and 20 mole of water for 6 mole of ethoxide were prepared.

Pyrex slides substrates with an area of  $75 \times 25 \text{ mm}^2$  were carefully cleaned and dip-coated into the sol with a withdrawal speed of 50 mm/min. The films were then heat treated under oxygen flow to remove solvents and organic compounds. Successive heat treatments were conducted for 1 hour at different annealing temperatures (200°C, 300°C and 400°C). High transparency monolayer and multilayer films were obtained and studied at room temperature.

## 2.2 Waveguides Characterization

**Refractive index and thickness** In the 'm-lines spectroscopy' technique two propagating modes are at least required to provide a precise determination of both refractive index and thickness of single or multilayer thin films assuming a step index waveguide structure. The incident light was polarized either parallel (TE mode) and perpendicular (TM mode) to the waveguide plane. The optical measurements were made at a wavelength of 632.8 nm. Monolayer films were monomode TE and TM so that thickness and index of refraction of those films were not determined.

**Optical loss measurements** Optical loss of the films was obtained by measuring the propagated light scattered from the waveguide as a function of the position. The light is taken to be proportional to the intensity in the waveguide at that position, thereby assuming the scattering to be uniform throughout the layer. A video camera was set to observe the light streak of the excited mode in the waveguide and the output video signal of the camera is directly sent to a microcomputer. The logarithm of the scattered intensity versus the propagation position was plotted and a linear least squares fit of the scattering points gave the average optical loss (in dB/cm).

### 3 RESULTS AND DISCUSSION

#### 3.1 Refractive Index and Thickness

Refractive index and thickness results, obtained on five-layer films by m-lines spectroscopy technique, were summed up in Table I. Those multimode films were found to support three TE modes and three TM modes after a 200°C heat treatment, whereas only two TE modes and two TM modes could be excited in films annealed at 300°C and 400°C. The Table revealed that the smaller the water quantities in the precursor sol, the thicker the films. For example, the film thickness decreased from 632 nm to 547 nm when increasing the water content from  $n = 3$  to  $n = 20$ , at the same annealing temperature (200°C). Generally, a high water concentration increased the rate of hydrolysis and induced a more densified network. This densification should affect film thickness as well as film index. However, it can be noticed that the amount of water had almost no effect on refractive indices, as already observed by Budd *et al.*,<sup>6</sup> suggesting that the rate of hydrolysis is not the main parameter for such layers elaboration. A densification of about 120 nm and a refractive index increase were also simultaneously observed when increasing the annealing temperature from 200°C to 400°C, whatever the water concentration introduced into the sol.

TABLE I

Refractive index and thickness evolution of five-layer PbO-TiO<sub>2</sub> films with annealing temperature and water of hydrolysis content in the precursor sol ( $n$  represented the mole number of water for 6 mole of ethoxy groups).

	Annealing temperature	$n = 3$	$n = 10$	$n = 20$
Thickness ( $\pm 2$ nm)	200°C	638	619	547
	300°C	539	515	444
	400°C	517	480	417
Refractive index ( $\pm 0.01$ ) (632.8 nm)	200°C	1.95	1.94	1.93
	300°C	1.96	2.05	2.01
	400°C	2.04	2.06	2.04

#### 3.2 Optical Loss Measurements

Optical coupling prism formed cracks on five-layer films, preventing light propagation by creating randomly distributed scattering centers in the waveguides. Propagation loss was then investigated at 632.8 nm on monolayers (monomode TE and TM) for the TE<sub>0</sub> excited mode and thus was assumed to be the same for multilayer films because of homogeneity between the different layers. Attenuation results were summarized in Table II. Best results were obtained for waveguides prepared with high water concentration and annealed at temperature higher than 300°C. Indeed, high rate of hydrolysis induced better particle size homogeneity. More generally, propagation loss decreased with increasing annealing temperature and subsequently with densification of the layers and the removal of the organic compounds. Discontinuities in scattered intensity were sometimes observed along the propagation direction, suggesting local inhomogeneities or defects in some waveguides. A cleaner environment (clean room) could improve the optical qualities of the waveguides.

#### 3.3 Waveguide Raman Spectroscopy

Details and advantages of WRS technique have already been described elsewhere.<sup>7</sup> Measurements of Raman spectra were conducted, from 7 cm<sup>-1</sup> up to 800 cm<sup>-1</sup>. On

monolayers prepared from various water of hydrolysis content and annealed at different temperatures. No perturbation due to the pyrex substrate was detected. The spectra obtained were quite similar whatever the water quantities in the precursor sol and the temperature of densification. A typical Raman spectrum for a waveguide heat-treated at 400°C for 1 hour is shown in figure 1. This spectrum presented two large peaks around 50 cm<sup>-1</sup> and 100 cm<sup>-1</sup> and a broad band around 750 cm<sup>-1</sup>. Nakamura *et al.* had already observed the same responses, characteristic of the amorphous state, when studying molten 99.9% PbTiO<sub>3</sub> crystalline powder.<sup>8</sup> It can then be deduced from Waveguide Raman Spectroscopy study that the layers remained in the amorphous phase with increasing the annealing temperature from 200°C to 400°C.

TABLE II

Optical loss of the TE<sub>0</sub> mode for monolayer PbO-TiO<sub>2</sub> waveguides (632.8 nm) for various annealing temperature and water content in the precursor sol.

	Annealing temperature	n = 3	n = 10	n = 20
Attenuation	200°C	6.12 ± 0.40	3.83 ± 0.34	3.44 ± 0.34
coefficient	300°C	4.53 ± 0.35	2.89 ± 0.50	0.86 ± 0.30
(dB/cm)	400°C	2.09 ± 0.45	2.43 ± 0.30	0.95 ± 0.40

#### 4 CONCLUSION

The optical qualities obtained on PbO-TiO<sub>2</sub> amorphous films at low annealing temperature (between 200°C and 400°C) make them interesting candidate for monomode or multimode passive waveguides with relatively low attenuation coefficient. Best results were observed for the films prepared with high water/ethoxy group molar ratio. Those films provided a very low attenuation coefficient (< 1 dB/cm) when densified over 300°C. More generally, thickness, refractive index and optical loss values depended on the annealing temperature and on the concentration of the water in the precursor sol. WRS study confirmed the amorphous state of the layers with increasing the temperature of densification up to 400°C, whatever the water content in the precursor sol.

#### REFERENCES

1. M. A. Aegerter, Y. Charbouillot, N. Mohallem and L. H. De Godoy, *Ultrastructure Processing of Advanced Materials*, **53**, 613-627 (1992).
2. C. R. Cho, M. S. Jang, S. Y. Jeong, Y. B. Kim, *Cryst. Res. Technol.*, **28**, 1085-1092 (1993).
3. V. E. Wood, J. R. Busch, S. D. Ramamurthi and S. L. Swartz, *J. Appl. Phys.* **71**, [9] 4557-4566 (1992).
4. C. Urlacher, E. Bernstein, J. Serughetti and J. Mugnier, submitted to Eurodim 94.
5. R. Ulrich and R. Torge, *Appl. Opt.* **12**, 2901-2908 (1973).
6. K. D. Budd, S. K. Dey and D. A. Payne, *Mat. Res. Soc. Symp. Proc.*, **73**, 711-716 (1986).
7. J. Mugnier, B. Varrel, M. Bahtat, C. Bovier and J. Serughetti, *J. Mat. Sci. Lett.*, **11**, 875-877 (1992).
8. T. Nakamura, M. Takashige, H. Terauchi, Y. Miura and W. N. Lawless, *Jap. J. of Appl. Physics*, **23**, 1265-1273 (1984).



## ULTRASONIC ATTENUATION MEASUREMENTS IN NEUTRON-IRRADIATED QUARTZ: THE INFLUENCE OF HEAT TREATMENT FOR A DOSE OF $4.7 \times 10^{19} \text{ N/CM}^2$

V. KEPPEMS and C. LAERMANS

*Katholieke Universiteit Leuven, Dept. of Physics, Celestijnenlaan 200D,  
B-3001 Leuven, Belgium*

Ultrasonic attenuation measurements are carried out for a quartz specimen irradiated with  $4.7 \times 10^{19} \text{ n/cm}^2$  and annealed at  $700^\circ\text{C}$  during 1 hour. This dose is interesting because it is situated in the 'threshold region'. The measurements are carried out as a function of temperature (0.3–20 K) for different frequencies (80–300 MHz). The data show a behaviour that is qualitatively similar to previous observations for a much lower dose, and indicate a tendency to return to the crystalline state.

*Key words:* neutron irradiated quartz, tunneling states, ultrasonics, disordered solids.

### 1 INTRODUCTION

It is well known that amorphous solids show low-temperature properties which are quite different from those of crystals.<sup>1</sup> These 'glassy anomalies' can be successfully described by the tunneling model,<sup>2</sup> which assumes the existence of low energy excitations. But the microscopic origin of these so-called tunneling states (TS) is still unclear. In order to contribute to this study, defective crystals are very interesting: defects in a mainly crystalline environment are more easy to study than the disorder of the amorphous network. In particular neutron-irradiated quartz is very attractive as a model for the glassy state, since varying the neutron dose allows continuous structural variations from the ordered crystal to the amorphous network disorder. Thermal and acoustic measurements in neutron-irradiated quartz revealed similar 'anomalies' as amorphous solids, which are explained by the presence of TS, similar in nature to those in vitreous silica, but with a lower density of states.<sup>3,4</sup>

Upon heat treatment, quartz irradiated with a neutron dose above a threshold of approximately  $6 \times 10^{19} \text{ n/cm}^2$  evolves to vitreous silica;<sup>5</sup> for doses below that threshold, irradiated quartz returns to the crystalline state. The dose separating these 2 regions is however not well defined, and should rather be seen as a 'threshold region' instead of a sharply defined threshold dose. In ref. 6, we discussed ultrasonic attenuation measurements after heat treatment at  $700^\circ\text{C}$  of a quartz sample irradiated with a dose of  $1.2 \times 10^{19} \text{ n/cm}^2$  (further referred to as K2N3). This dose is situated well below the threshold and our measurements showed indeed a tendency to return to the crystalline state, although there were still TS left. In this paper, we report the results of the study of the TS upon heat treatment extended to a higher dose of  $4.7 \times 10^{19} \text{ n/cm}^2$ , situated in (or very near) the 'threshold region'. These measurements will be discussed in the framework of the tunneling model and compared with the previous results after heat treatment for the lower dose of  $1.2 \times 10^{19} \text{ n/cm}^2$ .

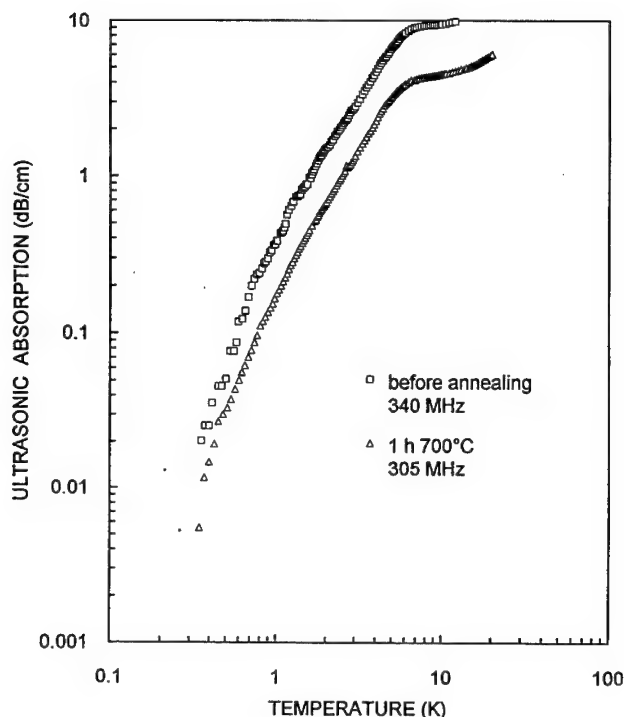


FIGURE 1 Ultrasonic attenuation in neutron irradiated quartz (dose  $4.7 \times 10^{19}$  n/cm<sup>2</sup>) before and after heat treatment at 700°C.

## 2 EXPERIMENTAL RESULTS AND DISCUSSION

An x-cut quartz sample, labeled K4N4, was irradiated up to a dose of  $4.7 \times 10^{19}$  n/cm<sup>2</sup> ( $E \geq 0.3$  MeV). The mass density of the sample was measured by a hydrostatic method:  $\rho = 2.571$  g/cm<sup>3</sup>. The sample has then been heat treated during 1 hour at 700°C. Due to this annealing, the density of the sample increased to  $\rho = 2.596$  g/cm<sup>3</sup>. After the heat treatment, the ultrasonic attenuation has been measured as a function of temperature, for different frequencies. Figure 1 shows the results at 305 MHz together with the absorption measured prior to annealing (a temperature-independent residual attenuation  $\alpha_0$  is subtracted from the measurements). As can be seen, the heat treatment causes a noticeable decrease of the attenuation, but both curves show a similar qualitative behaviour: at the lowest temperatures, a  $T^3$ -behaviour is observed, which levels off to a plateau at higher temperatures. This behaviour shows undoubtedly the presence of TS. Indeed, at very low temperatures, the tunneling model predicts a temperature-dependent absorption:<sup>7</sup>

$$\alpha = \frac{\pi^3 k^3 \bar{P} \gamma_l^2}{24 \rho^2 \hbar^4 v_l^3} \left( \frac{\gamma_l^2}{v_l^5} + \frac{2\gamma_t^2}{v_t^5} \right) T^3 \quad (1)$$

whereas at higher temperatures, the attenuation is given by:<sup>7</sup>

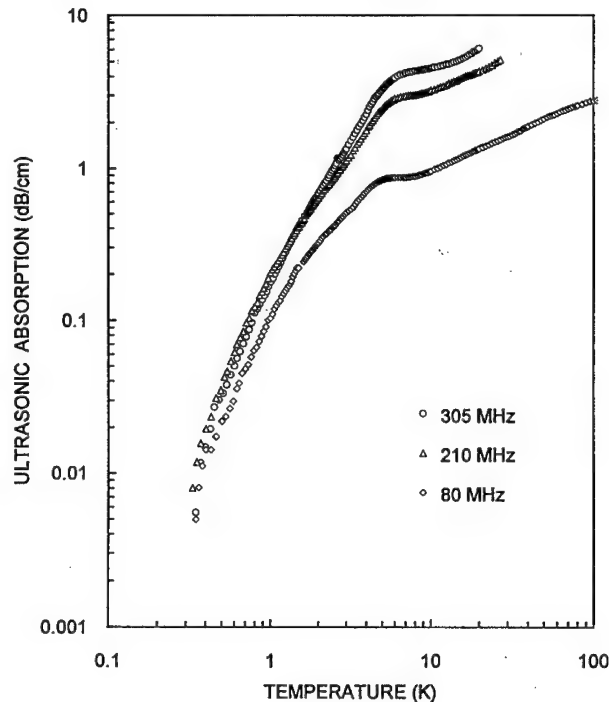


FIGURE 2 Ultrasonic attenuation in neutron irradiated quartz (dose  $4.7 \times 10^{19}$  n/cm<sup>2</sup>) after heat treatment at 700°C (1 hour) for different frequencies.

$$\alpha = \frac{\pi\omega}{2v_l} C = \frac{\pi\omega \bar{P}\gamma_l^2}{2\rho v_l^3} \quad (2)$$

which gives rise to a temperature-independent plateau. In the equations above,  $\bar{P}$  describes the density of states of the TS,  $\gamma_l$  and  $\gamma_t$  represent the coupling of the TS with respectively the longitudinal and transverse phonons. In Figure 2, the attenuation after 1 hour heat treatment at 700°C is given for 3 frequencies. It illustrates the frequency-independent attenuation of the T<sup>3</sup>-behaviour, which agrees with the predictions of the tunneling model (eq. 1). It shows also clearly that the height of the plateau increases linearly with the frequency (eq. 2).

The observed decrease of the attenuation after heat treatment indicates that the TS start to disappear. Since the plateau is proportional to the TS-parameter  $\bar{P}\gamma_l^2$  (eq. 2), a comparison of the attenuation before and after heat treatment for similar frequencies reveals that  $\bar{P}\gamma_l^2$  is reduced with about 50%. Since the shape of the curve remains unchanged upon annealing, we can assume that the coupling parameter is not drastically changed. This implies that the heat treatment will mainly affect the density of states  $\bar{P}$  of the TS. This was also the case for the lower dose K2N3.<sup>6</sup> The decrease of  $\bar{P}\gamma_l^2$  can thus be attributed to a decrease of  $\bar{P}$ , indicating a tendency to return to the crystalline state. These observations may lead to the conclusion that the sample K4N4 with a dose of  $4.7 \times 10^{19}$  n/cm<sup>2</sup> behaves like the sample K2N3 irradiated with a lower dose, i.e. like a

dose well below the threshold region. It is however interesting to note some significant differences between both samples after heat treatment: where the mass density of K2N3 returned upon annealing to the density of  $\alpha$ -quartz ( $\rho = 2.650 \text{ g/cm}^3$ ), the mass density of K4N4 increased only to  $2.596 \text{ g/cm}^3$ . Moreover, the fraction of TS left in K4N4 after heat treatment is still remarkably high, even higher than the density of states in K2N3 prior to heat treatment. Recent measurements, carried out after longer heat treatments and for higher annealing temperatures indicate no further changes in the mass density and only a slight further decrease of  $\bar{P}$  is observed. A complete return to the crystalline structure seems therefore to be rather unlikely. This can be interpreted in terms of the created disordered regions and their overlap. According to Grasse *et al.*,<sup>8</sup> high energetic neutrons create defective regions with a glassy structure and a density smaller than the crystal. For relatively low doses, they form 'islands' in the crystalline matrix. With increasing dose, these regions grow in number and tend to overlap. The disorder of these overlapping regions might then be too big to return to the crystalline structure after annealing, and the clusters will rather evolve to a-SiO<sub>2</sub>. A detailed quantitative analysis of these and additional measurements is in progress.

## REFERENCES

1. For a review, see: *Amorphous Solids: Low Temperature Properties*, edited by W. A. Phillips (Springer, Berlin, 1981).
2. P. W. Anderson, B. I. Halperin and C. M. Varma, *Philos. Mag.* **25**, 1 (1972); W. A. Phillips, *J. Low Temp. Phys.* **7**, 351 (1972).
3. C. Laermans, *Phys. Rev. Lett.* **42**, 250 (1979).
4. A. Vanelstraete and C. Laermans, *Phys. Rev.* **B42**, 5842 (1990).
5. G. Mayer and M. Lecomte, *J. Phys. Radium* **21**, 846 (1960).
6. V. Keppens, C. Laermans and A. Vanelstraete, in *Defects in insulating materials*, edited by O. Kanert and J. M. Spaeth (World Scientific, 1993), p. 899.
7. P. Doussineau *et al.*, *J. Phys. (Paris)* **41**, 1193 (1980).
8. D. Grasse, O. Kocar, H. Peisl and C. S. Moss, *Radiat. Effects* **66**, 61 (1982).

## STUDY OF THE $K_{4.2}Ti_{1.2}(PO_4)_3$ GLASS BY DIELECTRIC AND RAMAN SPECTROSCOPY

C. Z. TAN, O. KANERT and R. KÜCHLER

*Institute of Physics, University of Dortmund, D-44221 Dortmund, Germany*

The  $K_{4.2}Ti_{1.2}(PO_4)_3$  glass was used to study the interaction between dipoles and ions by dielectric and Raman spectroscopy. The activation energies for the  $K^+$  migration and dipole orientation were evaluated to be  $0.61 \pm .01$  eV and  $1.11 \pm .02$  eV, respectively. Two coordinations of Ti were identified by the Raman scattering experiment. Decrease of the Raman scattering intensity was observed under the static electric field.

**Key words:** Glass, ion migration, dipole orientation, raman spectrum.

### 1 INTRODUCTION

The response of a polar glass to an applied electric field occurs through polarization of electrons and dipoles, and through migration of charge carriers, e.g. ions and localized charge defects.<sup>1</sup> Each polarization process has a characteristic correlation time which depends on temperature. Examination of dielectric relaxation in the polar glass is shown to provide detailed information about the different correlation times. At sufficiently low temperatures, the contributions of dipole orientation and ion migration on the ac conductivity can be of the same order, which can be monitored by impedance measurement. The purpose of this work is to investigate the interaction between dipoles and ions in the  $K_{4.2}Ti_{1.2}(PO_4)_3$  glass by dielectric relaxation and in-situ measurements of Raman spectra under the applied electric field.

### 2 EXPERIMENTAL

Crystalline  $KTiOPO_4$  (KTP) is a ferroelectric and one of the best non-linear optical materials. A glass with the composition of  $K_{4.2}Ti_{1.2}(PO_4)_3$  was prepared which is similar to KTP in composition.  $TiO_2$  (Aldrich),  $K_2CO_3$  (Fluka), and  $NH_4H_2PO_4$  (Baker) were used as starting materials. The powder was mixed and then melted in a silica crucible in an electric furnace at 1623 K for 1 hour. The melt was then quenched in a nickel capsule and annealed at 623 K for 12 hours. For the impedance measurement the glass specimens were cut into thin slices and polished. Gold electrodes were sputtered onto the disc-like samples in vacuum. Dielectric measurements were performed from 0.1 to 100 kHz with a 1260 Impedance Gain-Phase Analyzer and a Chelsea Dielectric Interface. Raman scattering experiments were carried out with the T64000 spectroscopy (Jobin YVON, ISA).

### 3 RESULT AND DISCUSSION

Figure 1 shows the temperature dependence of the real part of conductivity of the glass at different frequencies. In the temperature range of 350–630 K, a frequency independent dc

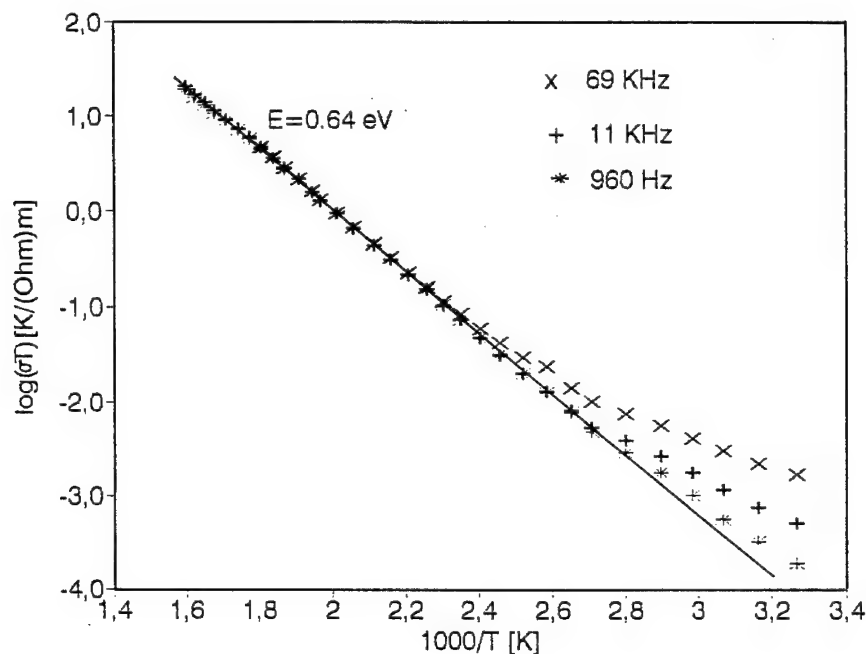


FIGURE 1  $\log(\sigma T)$  vs.  $1/T$  for the glass at different frequencies.

conductivity is observed in a restricted frequency range ( $\sim 100 - \sim 1000 \text{ Hz}$ ), indicating that the glass is a typical ionic conductor. The temperature dependence of the dc conductivity follows the Nernst-Einstein relation<sup>2</sup>

$$\sigma T = A \exp\left(-\frac{E}{kT}\right) \quad (1)$$

where  $A$  is a constant, and  $E$  is the activation energy of the mobile  $K^+$  ions. Evaluation of the data yields  $E = 0.64 \pm .005 \text{ eV}$ .

At low temperatures (from 203 K to 253 K) the conductivity is found to increase with increasing frequency. As depicted in Figure 2, the electric modulus  $M''$  exhibits a maximum which is related to the ionic jump rate  $1/\tau$  by the condition  $\omega\tau = 1$ . Evaluation of the position of the maxima leads to

$$\tau(T) = \tau_0 \exp(E/kT) \quad (2)$$

with  $E = 0.67 \pm .02 \text{ eV}$  indicating the underlying process is due to the movement of  $K^+$  ions. As shown in Figure 3, in the restricted temperature range ( $\sim 300 \text{ K} - \sim 350 \text{ K}$ ) there are two separated semicircular arcs in the  $\rho' - \rho''$  plot, corresponding to two different relaxation processes. The temperature dependence of the characteristic frequency for the two processes is illustrated in Figure 4. The smaller semicircular arc corresponds to the orientation of dipoles at low frequencies, and the other is related to the migration of  $K^+$  at high frequencies. The evaluated activation energies for dipole orientation and  $K^+$

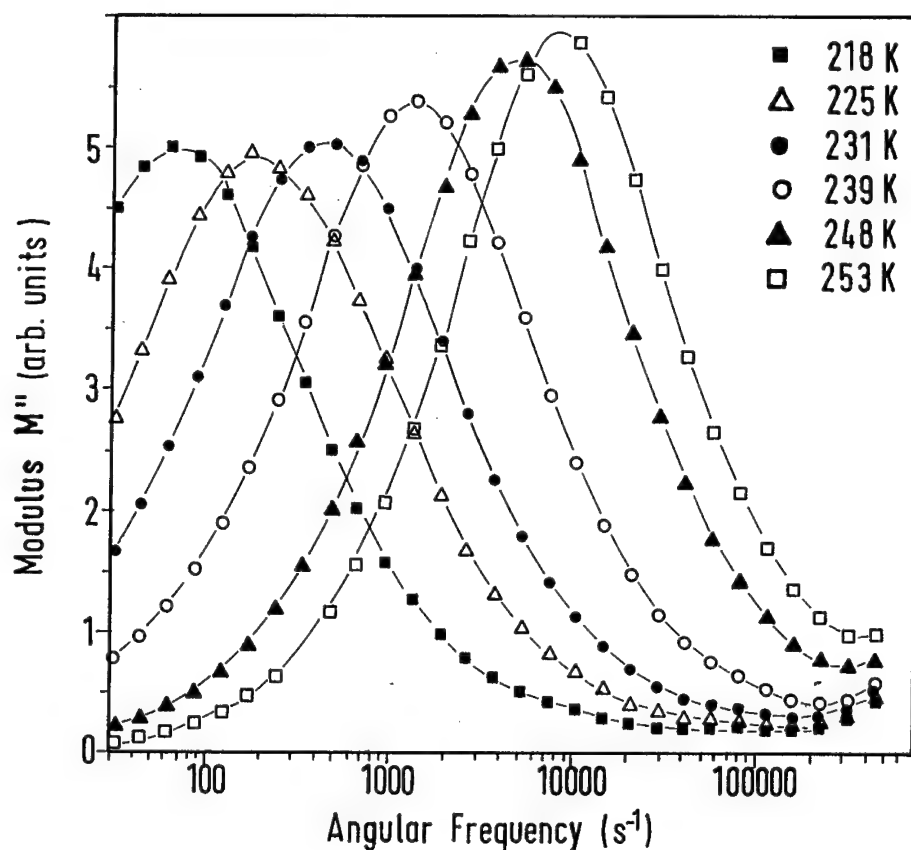


FIGURE 2 Electric modulus  $M''$  vs. angular frequency  $\omega$  at low temperatures.

migration are  $1.11 \pm .02$  and  $0.61 \pm .01$  eV, respectively. The activation energies of  $K^+$  motion evaluated by different methods are found to be in good agreement.

The glass structure and its variation in an electric field were measured by in-situ measurements of Raman spectra under the applied electric field. As shown in Figure 5, two coordinations of Ti, namely,  $TiO_4$  and  $TiO_6$  are identified, corresponding to the bands at  $927$  and  $630\text{ cm}^{-1}$ , respectively.<sup>3</sup> Decrease of intensity of the bands was observed under an external electric field. However, the positions of the bands are found to remain independent of the strength of the field.

For non-linear optical materials, the polarization vector,  $P$ , can be phenomenologically expressed by the relation of

$$P = \chi_1 E + \chi_2 E^2 + \chi_3 E^3 + \dots \quad (3)$$

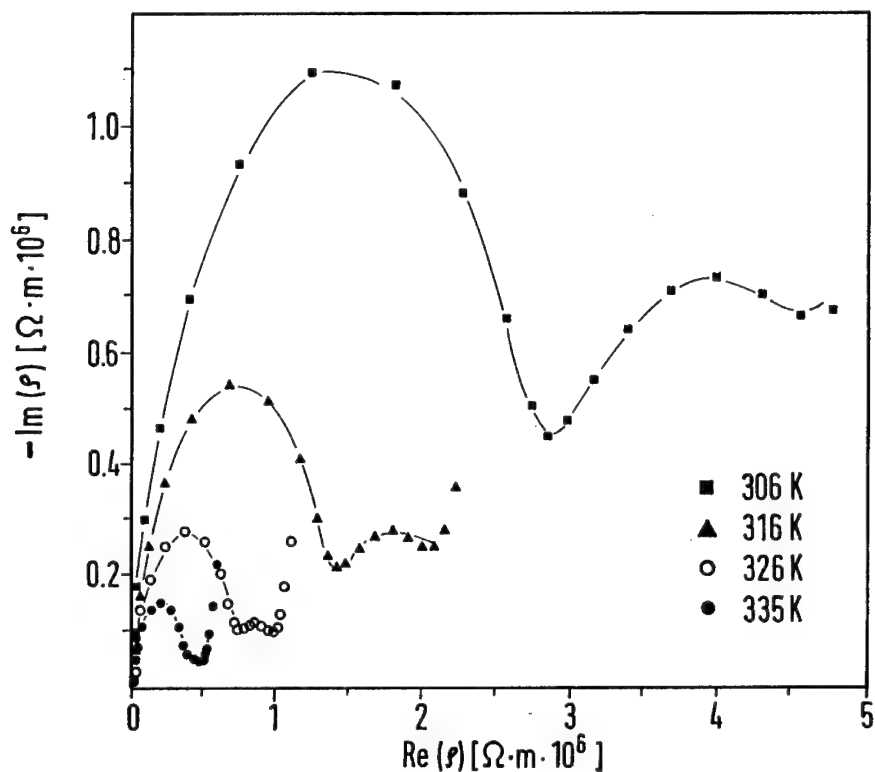


FIGURE 3  $\rho' - \rho''$  plot at different temperatures.

where  $\chi_1, \chi_2, \chi_3$  are constants, and  $E$  denotes the external electric field. For the measurements of Raman spectra under the applied dc potential, the external electric field,  $E$ , is composed of the optical electric field,  $E_{op}$  and the static field,  $E_s$ :  $E = E_{op} + E_s$ . As the Raman scattering intensity is only associated with the non-linear part of polarization, according to

$$I = c(3\chi_3 E_s E_{op}^2 + \chi_3 E_{op}^2 + \dots)^2 \quad (4)$$

where  $c$  is a proportional factor, the static field dependence of the scattering intensity under the constant optical field,  $E_{op}$ , is generally given by

$$\sqrt{\frac{I(E_s)}{I(0)}} = 1 + a_1 E_s + a_2 E_s^2 + \dots \quad (5)$$

where  $a_1, a_2$  are constants. For the  $K_{4.2}Ti_{1.2}(PO_4)_3$  glass, the evaluated parameters from Figure 5 are listed in Table I ( $E_s$  in V/m). Because of high non-linearity, this glass may be used as a good non-linear optical material.



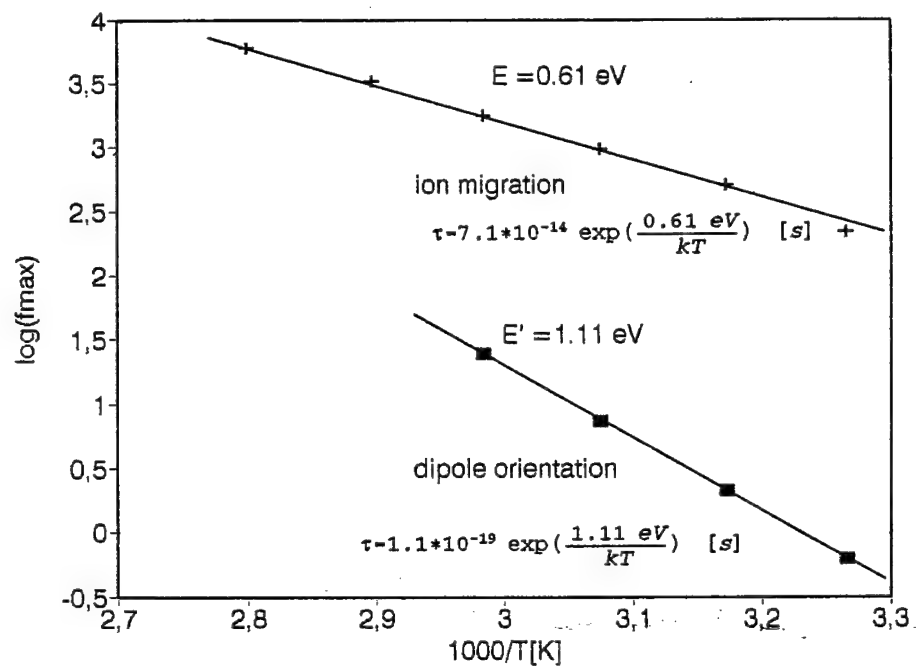


FIGURE 4  $\log(f_{\max})$  vs.  $1/T$ .  $f_{\max}$  is the frequency of maximum loss.

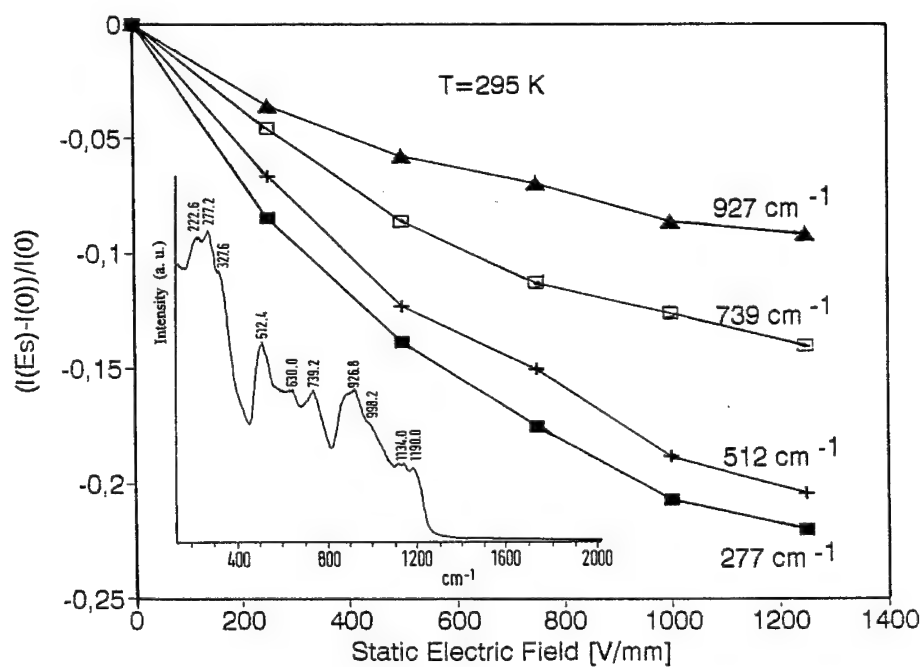


FIGURE 5 Raman spectrum of the  $K_{4.2}Ti_{1.2}(PO_4)_3$  glass and its variation in the electric field.

Table I.  
Evaluated parameters,  $a_1$  and  $a_2$  for different bands

Band	277 $\text{cm}^{-1}$	512 $\text{cm}^{-1}$	739 $\text{cm}^{-1}$	927 $\text{cm}^{-1}$
$a_1$	$-8.14 * 10^{-8}$	$-1.04 * 10^{-7}$	$-1.53 * 10^{-7}$	$-1.81 * 10^{-7}$
$a_2$	$3.76 * 10^{-14}$	$3.72 * 10^{-14}$	$5.56 * 10^{-14}$	$7.28 * 10^{-14}$

#### ACKNOWLEDGEMENTS

We would like to thank Ms. Buß for performing the Raman scattering experiments.

#### REFERENCES

1. C. Z. Tan and J. Arndt, *J. Non-Cryst. Solids* **169**, 143 (1994).
2. O. Kanert, M. Kloke, R. Küchler, S. Rückstein, *Ber. Bunsenges. Phys. Chem.* **95**, 1061 (1991).
3. Ya. S. Bobovich, *Opt. Spectr.* **13**, 274 (1962).

## LASER IRRADIATION INDUCED STRUCTURAL RELAXATION IN THE DENSIFIED $\text{SiO}_2$ GLASS AND $\text{SiO}_2$ THIN FILM

C. Z. TAN<sup>1</sup>, Z. L. WU,<sup>2</sup> and J. ARNDT<sup>3</sup>

<sup>1</sup>*Institute of Physics, University of Dortmund, D-44221 Dortmund, Germany;*

<sup>2</sup>*Department of Physics and Institute for Manufacturing, Wayne State University, Detroit, MI 48201, USA;* <sup>3</sup>*Institute of Mineralogy, Free University of Berlin, D-14195 Berlin, Germany*

Laser irradiation induced structural relaxation in the densified  $\text{SiO}_2$  glass and  $\text{SiO}_2$  thin film has been probed by collinear photothermal deflection spectroscopy (PDS). Decreasing of optical absorption with the irradiation of  $\text{Ar}^+$  laser beam was observed in the densified  $\text{SiO}_2$  glass and  $\text{SiO}_2$  thin film. The structural relaxation is associated with the reactivation and recombination of localized defects which can be well described by the proposed relaxation function of  $\Phi(t) = (1 + at)^{-b}$ . Distribution of relaxation times of the densified glass is broader than that of thin film.

**Key words:** Laser irradiation, Relaxation, Densified glass, Thin film, Spectrum,  $\text{SiO}_2$ .

### 1 INTRODUCTION

Glass can be permanently densified by high pressure and by fast neutron irradiation. The densified glass can relax the densified structure by thermal activation and optical irradiation.<sup>1–3</sup> Permanent densification of glass is associated with the creation and localization of defects, while structural relaxation of densified glass is related to the recombination of the localized defects.<sup>4</sup> The purpose of this work is to study the defect recombination process in the densified silica glass and the EBD  $\text{SiO}_2$  thin film by PDS.

### 2 EXPERIMENTAL

Photothermal deflection spectroscopy (PDS) is used to perform the in-situ measurement of laser irradiation induced structural relaxation in the densified  $\text{SiO}_2$  glass and  $\text{SiO}_2$  thin film. A bulk silica glass (Suprasil W) was compacted in the Belt apparatus at 60 Kbar and 873 K. The density of the densified  $\text{SiO}_2$  glass is  $2.4925 \text{ g/cm}^3$  (the original density is  $2.2026 \text{ g/cm}^3$ ). The  $\text{SiO}_2$  thin film is the EBD film described previously.<sup>3</sup>

The experimental setup of PDS is schematically shown in Figure 1. The sample is irradiated with a  $\text{Ar}^+$  pump laser beam working at the wavelength of 488 nm. The optical absorption inside the sample gives rise to a temperature gradient of the optically heated region and so causes a refractive index gradient. The refractive index gradient is detected by a 2 mW He-Ne prob laser beam with a wavelength of 632.8 nm. According to the theory,<sup>5</sup> the deflection angle of the prob laser beam is proportional to the absorbed optical power. The prob beam deflection is measured with a position sensitive detector.

### 3 RESULTS AND DISCUSSION

As shown in Figure 2 and Figure 3, an evolution in the photothermal signal was observed in both bulk and thin film samples. With different light powers of the pump beam, the

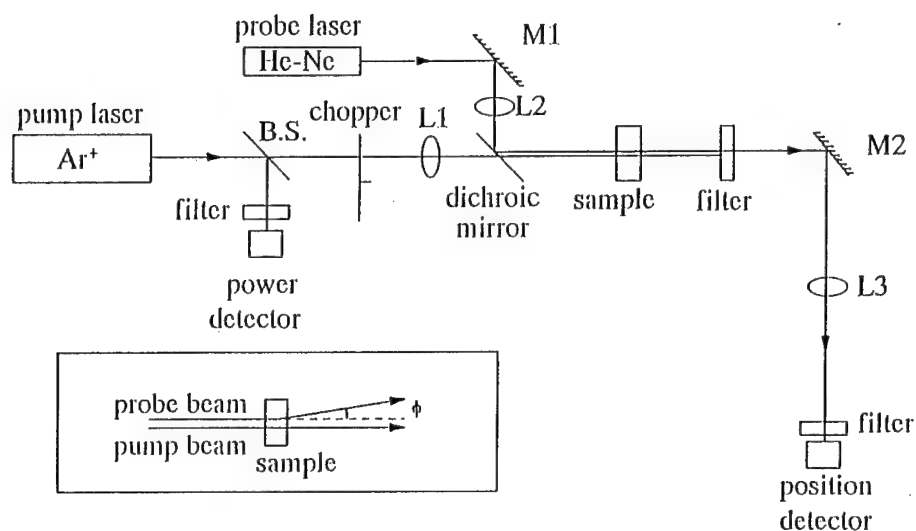


FIGURE 1 Optical depiction of experimental setup of collinear photothermal deflection spectroscopy (PDS).

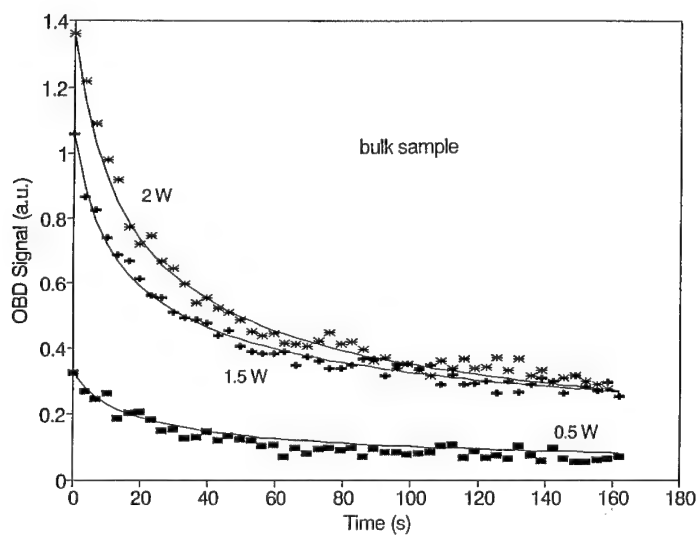


FIGURE 2 Transient absorption of the densified silica glass under the illumination with different light powers. The symbols are experimental results; curves are theoretical fittings.

optical absorption decreases with time, while for the normal SiO<sub>2</sub> glass the photothermal signal is a constant under the same condition. A rapid decrease of absorption appears during the first few minutes, then the change of absorption becomes nearly constant with time.

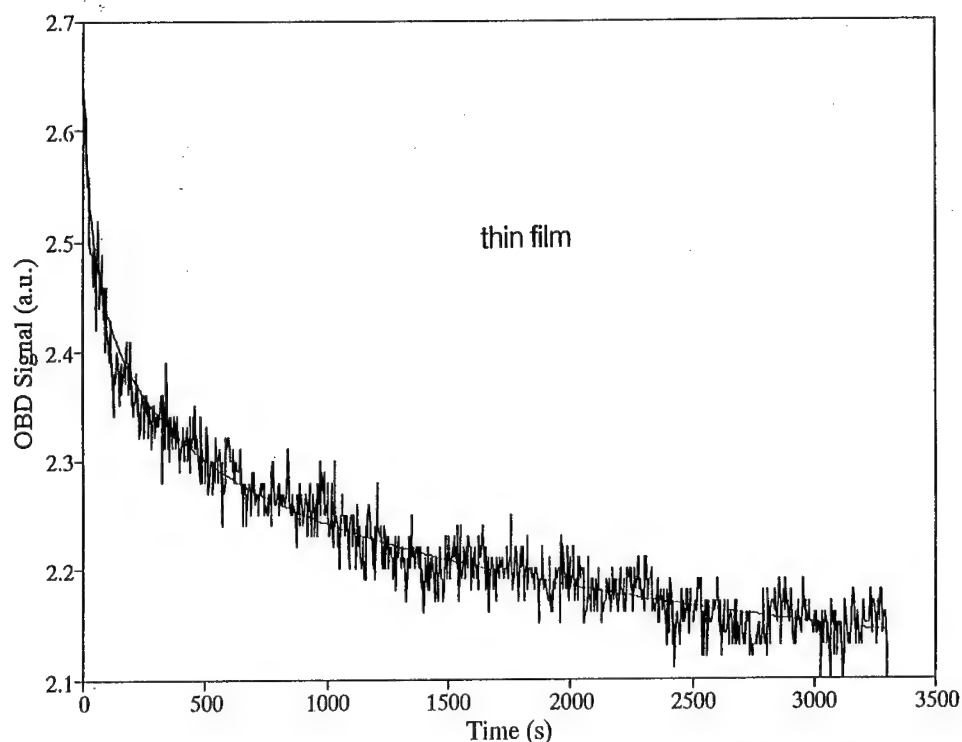


FIGURE 3 Optical absorption relaxation of the EBD  $\text{SiO}_2$  thin film. The curve is the theoretical fitting.

The localized defects in the densified glass and thin film can be activated by the laser irradiation. The defect recombination process can be described by the following differential equation:<sup>4</sup>

$$\frac{dx}{dt} = -k x^n \quad (1)$$

where  $x$  is the defect concentration,  $k$  is the rate constant, and  $n$  is the order of reaction. This equation leads to the relaxation function of

$$\Phi(t) = (1 + a t)^{-b} \quad (2)$$

where  $a = (n-1)x_0^{(n-1)}k$ , and  $b = 1/(n-1)$ . In the present investigation the relaxation function is equal to the normalized time-dependent photothermal signal.

As shown in Figure 2 and 3, laser irradiation induced structural relaxation in the densified  $\text{SiO}_2$  glass and  $\text{SiO}_2$  thin film can be well described with the proposed relaxation function. For the densified glass, the evaluated values of  $a$  and  $b$  are 0.116 and 0.516, respectively. For the thin film the evaluated  $a$  and  $b$  are 0.038 and 0.101, respectively.

Due to the disordered structure of the glass and thin film, distribution of relaxation times,  $g(\tau)$ , is characterized. It is correlated with the relaxation function  $\Phi(t)$ , according to

$$\Phi(t) = \int_0^\infty g(\tau) \exp\left(-\frac{t}{\tau}\right) d\tau \quad (3)$$

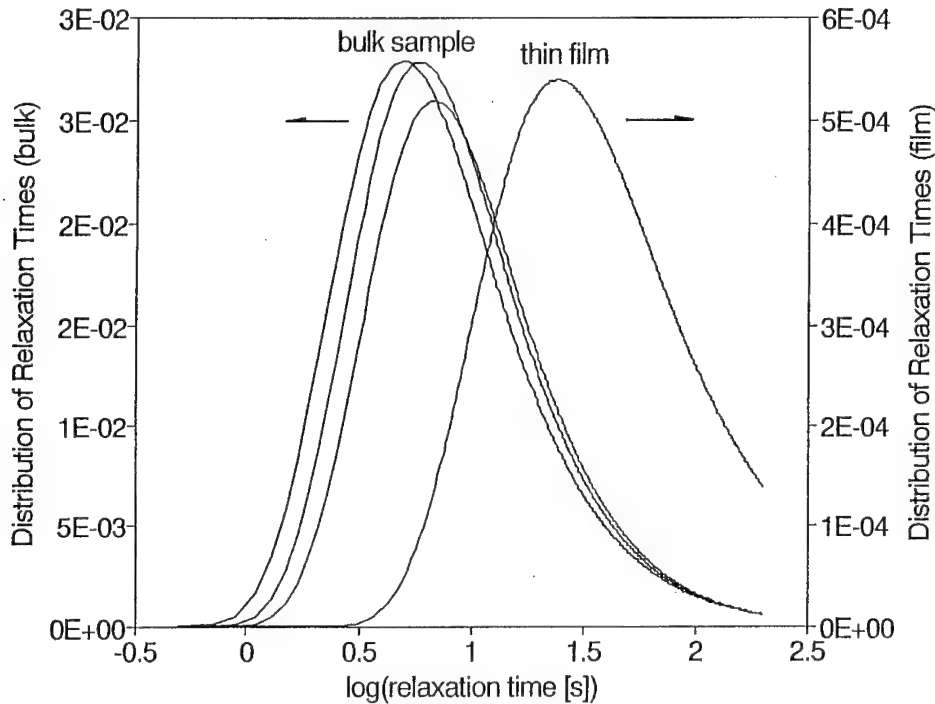


FIGURE 4 Distribution of relaxation times for the densified silica glass and the EBD SiO<sub>2</sub> thin film.

For the proposed relaxation function, an analytical solution of Eq(3) is given by

$$g(\tau) = \frac{a^{-b}}{\Gamma(b)} \tau^{-(b+1)} \exp\left(-\frac{1}{a\tau}\right) \quad (4)$$

where  $\Gamma$  denotes the Gamma function. As shown in Figure 4, the distribution of relaxation times for the EBD SiO<sub>2</sub> film is broader than that for the densified SiO<sub>2</sub> glass.

#### 4 CONCLUSIONS

Laser irradiation induced structural relaxation in the densified SiO<sub>2</sub> glass and SiO<sub>2</sub> thin film was observed by the photothermal deflection spectroscopy. It can be described with the proposed relaxation function and distribution of relaxation times.

#### REFERENCES

1. W. Hummel and J. Arndt, *J. Non-Cryst. Solids* **109**, 40 (1989).
2. C. Z. Tan and J. Arndt, *J. Non-Cryst. Solids* **169**, 143 (1994).
3. Z. L. Wu, C. Z. Tan, J. Arndt, and Z. X. Fan, *Laser-Induced Damage in Optical Materials: SPIE* **1848**, 224 (1992).
4. C. Z. Tan, Dissertation, Freie Universität Berlin (1993).
5. M. Commandre and E. Pelletier, *Appl. Opt.* **29**, 4276 (1990).

## OPTICAL BAND-GAP AND ACTIVATION ENERGY OF THIN FILMS FROM THE Se-Ag-I AND Te-Ag-I SYSTEMS

T. PETKOVA and M. MITKOVA

*Central Laboratory of Optical Storage and Processing of Information, Bulgarian Academy of Sciences, Sofia 1113, P.O. Box 95, Bulgaria*

Thin films from the systems Se-Ag-I and Te-Ag-I are investigated. The optical transmission spectra are measured and the optical band gap is estimated on their basis. The temperature relationship of the electrical conductivity is measured and the activation energy is determined. Some relationships between these parameters and the composition of the glasses are discussed.

**Key words:** optical band-gap, activation energy, chalcogenide glasses, chalco-halide glasses.

### 1 INTRODUCTION

Compared to chalcogenides and halides, glassy chalco-halide materials are a relatively less known family of glasses [1,2]. The investigation of their optical and electrical properties is interesting in view of their practical application, due to the essential role of the ionic component of the chemical bond in them. This is supposed to affect the band gap structure and the electrical properties of these glasses. We were the first to synthesize these chalcogenide-halide glasses from the systems Se-Ag-I [3] and Te-Ag-I [4]. The present investigation is a part of their general characterization.

### 2 EXPERIMENTAL

Glassy samples from the systems Se-Ag-I and Te-Ag-I are synthesized as described in [3] and [4]. Thin films 600–1000 nm thick are prepared by vacuum evaporation. The composition of the films is investigated by Auger electron spectroscopy. A good agreement between the film composition and the starting composition was found [5]. Electron microscope and X-ray investigations confirm that the films are amorphous.

The optical band-gap is determined from transmission spectra of thin films of different thicknesses with a spectrophotometer for visible and IR region.

The films for the electrical measurements are prepared as sandwich structures with two Al-electrodes. The electrical conductivity is measured in the range 292–323 K.

### 3 RESULTS AND DISCUSSION

The investigations of the spectra of the glasses from the two systems are carried out in the range 400–2000 nm. The spectral dependence of the absorption coefficient ( $\alpha$ ) is described by the formula:

$$T = (1 - R^2) \cdot \exp(-\alpha \cdot d) \quad (1)$$

where T—transmission, R—reflection, d—film thickness.

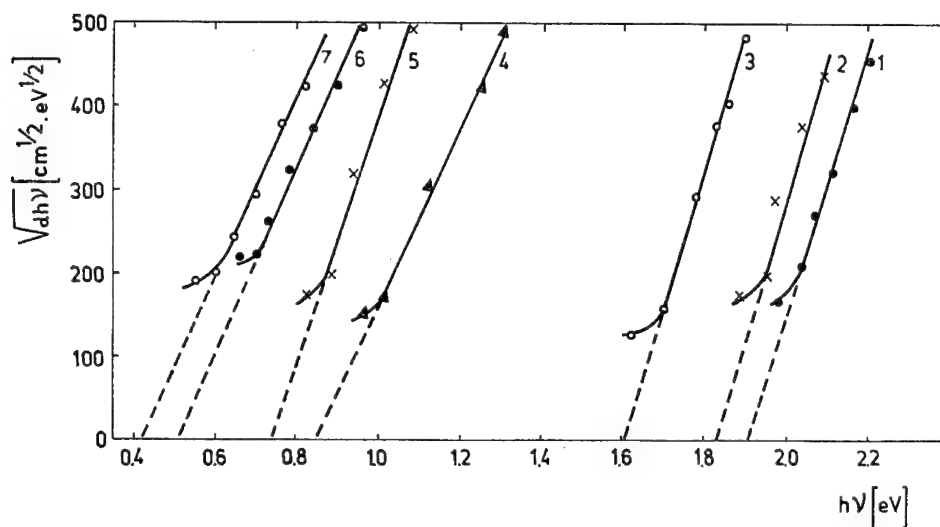


FIGURE 1 Relationships  $(\alpha h\nu)^{1/2} = f(h\nu)$  of 1-Se<sub>90</sub>Ag<sub>5</sub>I<sub>5</sub>, 2-Se<sub>80</sub>Ag<sub>10</sub>I<sub>10</sub>, 3-Se<sub>70</sub>Ag<sub>15</sub>I<sub>15</sub>, 4-Te<sub>55</sub>Ag<sub>15</sub>I<sub>30</sub>, 5-Te<sub>50</sub>Ag<sub>20</sub>I<sub>30</sub>, 6-Te<sub>60</sub>Ag<sub>20</sub>I<sub>20</sub>, 7-Te<sub>70</sub>Ag<sub>10</sub>I<sub>20</sub>.

The relationship between the absorption coefficient ( $\alpha$ ) and the optical band-gap ( $E_g^0$ ) is:

$$\alpha = B/h\nu(h\nu - E_g^0)^n \quad (2)$$

where  $n = 2$  for chalcogen-halide systems,  $b$ —parameter of the investigated substance,  $h$ —Planck's constant,  $\nu$ —frequency.

Table I  
Band gap, activation energy and conductivity at room temperature of the glasses from the systems Se-Ag-I and Te-Ag-I

Composition	$E_g^0$ (eV)	$E_a$ (eV)	$\sigma$ (S.m <sup>-1</sup> )
Se <sub>90</sub> Ag <sub>5</sub> I <sub>5</sub>	1.90	0.89	$4.5 \cdot 10^{-11}$
Se <sub>80</sub> Ag <sub>10</sub> I <sub>10</sub>	1.82	0.81	$9.5 \cdot 10^{-11}$
Se <sub>70</sub> Ag <sub>15</sub> I <sub>15</sub>	1.62	0.73	$3 \cdot 10^{-10}$
Te <sub>70</sub> Ag <sub>10</sub> I <sub>20</sub>	0.42	0.18	$6 \cdot 10^{-9}$
Te <sub>60</sub> Ag <sub>20</sub> I <sub>20</sub>	0.5	0.37	$4.5 \cdot 10^{-8}$
Te <sub>55</sub> Ag <sub>15</sub> I <sub>30</sub>	0.75	0.4	$9 \cdot 10^{-8}$
Te <sub>50</sub> Ag <sub>20</sub> I <sub>30</sub>	0.82	0.3	$9 \cdot 10^{-9}$



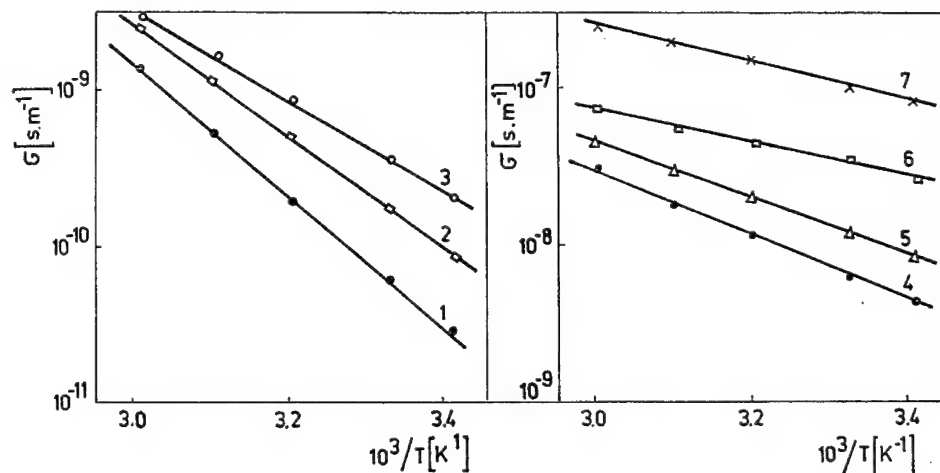


FIGURE 2 Relationship  $\sigma = f(1/T)$  of 1- $\text{Se}_{90}\text{Ag}_5\text{I}_5$ , 2- $\text{Se}_{80}\text{Ag}_{10}\text{I}_{10}$ , 3- $\text{Se}_{70}\text{Ag}_{15}\text{I}_{15}$ , 4- $\text{Te}_{55}\text{Ag}_{15}\text{I}_{30}$ , 5- $\text{Te}_{50}\text{Ag}_{20}\text{I}_{30}$ , 6- $\text{Te}_{60}\text{Ag}_{20}\text{I}_{20}$ , 7- $\text{Te}_{70}\text{Ag}_{10}\text{I}_{20}$ .

Figure 1 illustrates the relationship  $(\alpha h\nu)^{1/2} = f(h\nu)$  for some compositions from the system Se-Ag-I and Te-Ag-I. The extrapolation of straight parts of these relationships down to  $\alpha = 0$  using Tauc's procedure [6] determines the optical band-gap of the investigated samples. The results for the system Se-Ag-I show that the presence of greater quantities of silver and iodine reduces the band-gap (Table I) from 1.9 eV to 1.62 eV. The optical band-gap in the glasses from the Te-Ag-I system is 0.4–0.9 eV (Table I) and depends on composition.

The activation energy ( $E_a$ ) is determined by the relationship

$$\sigma = C \exp(-E_a/kT) \quad (3)$$

where  $\sigma$ —specific electrical conductivity,  $C$ —constant,  $T$ —temperature,  $E_a$ —activation energy,  $k$ —Boltzmann constant

Figure 2 shows the graphical relationships  $\sigma = f(1/T)$  for films with different compositions from the two systems. The smooth course of this relationship is a sign that no structural changes take place, affecting the temperature course of the specific conductivity. From the slopes of the relationships the activation energies are determined (Table I). The conductivity at room temperature is also shown on the table.

The optical band-gap depends to a large extent on the composition of the glasses. The introduction of silver and iodine in the selenium matrix increases the compositional

disorder resulting in a reduction of the optical band-gap [7]. The influence of the increase in the amount of bonds with higher ionic component is in the same direction. This is probably the reason for the decrease in the optical band-gap from 1.90 to 1.62 eV when the content of AgI in the investigated glasses is increased. The influence of AgI on the conductivity and activation energy is clearly marked in the electrical measurements. At the lower concentration  $2E_a$  is less than  $E_g^0$  and at an concentration of 15 at% AgI their values are almost equal. If we assume uniform distribution of the localized states, this results give grounds to think that at low concentrations of AgI Fermi level is closer to the valence band and with the increase in the AgI concentration it shifts to the middle of the band gap. Besides, the dependence of the conductivity on the composition shows that it is a function of the charges, activated from the existing localized states in the band gap and not on their mobility.

In the Te-Ag-I system the introduction of large quantities of iodine leads to considerable reconstruction of the glass structure and leads to the formation of Te-I bonds [4]. With the exception of the  $Te_{60}Ag_{20}I_{20}$  and  $Te_{70}Ag_{15}I_{15}$  compositions, it can be assumed that in the investigated samples the influence of the tellurium matrix on the electrical properties is commensurate with that of the other two elements, introduced in it.

The changes in the optical band gap in this system is governed by the presence of AgI, whose influence is analogous as in the previous system, and by the presence of iodine, bonded directly to the tellurium atoms, thus reducing the density of the valence alternation pairs and ionizing the chalcogenide.

This work was sponsored by Ministry of Education and Science, contract X-221.

#### REFERENCES

1. J. Lucas and J. L. Adam, *Glasstechn. Bericht*, **62**(12) 422, (1989).
2. J. Heo and D. Mackenzie, *J. Non-Cryst. Sol.* **111**, 29, (1989).
3. M. Mitkova, T. Petkova and A. Yanakiev, *Mat. Chem. Phys.*, **30**, 55, (1990).
4. T. Petkova and M. Mitkova, *Mat. Chem. Phys.*, **33**, 233, (1993).
5. T. Petkova and M. Mitkova, *Thin Solid Films*, **205**, 25, (1980).
6. L. Tauc, *Proc. Intern. Conf. Delft*, **606**, (1974).
7. M. Kastner—*Phys. Rev. Lett.* **28**, 355, (1972).

## EFFECT OF IONIC EXCHANGE UPON THE BEHAVIOR OF SODA LIME SILICATE GLASS

R. CAPELLETTI,<sup>1</sup> P. GRAU,<sup>2</sup> P. VAN HOI,<sup>3</sup> and M. SUSZYNSKA<sup>4</sup>

<sup>1</sup>*Physics Department, Parma University, 43–100 Parma, Italy;* <sup>2</sup>*Physics Faculty, M. Luther University, 06–108 Halle, Germany;* <sup>3</sup>*Institute of Physics NCSR, Nghiado, Tu liem, Hanoi, Vietnam;* <sup>4</sup>*Institute of Low Temperature and Structure Research, PAS, 50–950 Wroclaw, PO Box 937, Poland*

Thermally stimulated depolarization currents and some spectrophotometric characteristics were measured for soda lime silicate glass in as received state and after exchange with ionic silver. Both, the effectiveness of the exchange and the form of silver within the glass framework, were modified by thermal treatment of the exchanged specimens.

It has been shown that some of the bands recorded by TSDC technique are related with electrical polarization phenomena. The origin of these polarizations has been ascribed to more or less localized motion of sodium ions which in the near-surface layers of specimens became disturbed by various silver species.

*Key words:* silicate glasses, ionic exchange, depolarization currents.

### 1 INTRODUCTION

It was shown previously<sup>1</sup> that the ionic exchange of soda lime silicate glass by  $K^+$  and  $Ag^+$  ions, followed by annealing at temperatures  $T \geq 673$  K, affects the mechanical properties of these systems in a different way. It seemed reasonable to assume that in addition to the ionic radius other factors influence the magnitude of residual stresses in the exchanged specimens. Especially important seems large polarizability and diffusivity of silver ions which could result in heterogeneous distribution of the exchanging species and smaller distortions of the exchanged matrix.

In order to check this hypothesis, electric relaxation processes of these systems were studied (by exploiting the method of ionic thermocurrent, ITC), and correlated with some spectrophotometric measurements.

### 2 EXPERIMENTAL DETAILS

#### 2.1 Samples

According to the producer (Glass-Factory, Torgau, Germany), the main components of the glass-specimens (2 mm-thick plates) were: 75.25%  $SiO_2$ , 14.25%  $Na_2O$ , 6.4%  $CaO$ , and 4.5%  $MgO$ .

The ionic-exchange of samples was performed for 2 h at 673 K in a mixture of molten salts (2% of  $AgNO_3$  in 98% of  $NaNO_3$ ). Some of the exchanged samples were annealed for 2 h at 823 and 873 K in air, and some—for 2 h at 673 K in  $NaNO_3$ .

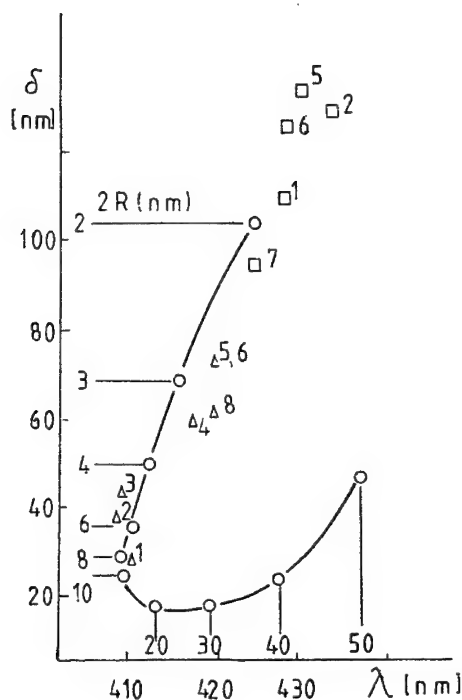


FIGURE 1 Calculated<sup>2</sup> (○) and experimental pairs of  $\delta$ - $\lambda_{\max}$  values determined for different penetration depths of silver-exchanged samples annealed at 823 (□) and 873 K (·); 2R (nm) gives the diameter of particles.

## 2.2 Measurements

Optical density (OD) measurements were performed by using a Zeiss-spectrophotometer and an electron-probe microanalyzer (EMX-SM.32); in the latter case OD was measured versus the penetration depth X.

Measurements of thermally stimulated depolarization currents (TSDC) were principally the same as in the case of ITC used for ionic crystals. Testing temperature was ranging between 140 and 620 or 420 K for measurements performed at a constant heating rate  $b \cong 0.1 \text{ K} \cdot \text{s}^{-1}$ . The polarization conditions were as follows:  $V_p = 20-500 \text{ V}$ ,  $T_p = (250), 323, 423 \text{ and } 573 \text{ K}$ ,  $t_p = 1-20 \text{ min}$ . Some measurements were also performed during the polarization phase (TSPC-1  $\Rightarrow$  TSPC-2  $\Rightarrow$  TSDC-3) with and without blocking electrodes (2 thin sheets of Teflon).

## 3 RESULTS AND DISCUSSION

### 3.1 Optical Data

About 75% of  $\text{Na}^+$  ions in the near-surface layers was replaced by  $\text{Ag}^+$  ions, part of which became reduced to atomic silver  $\text{Ag}^0$  by the  $\text{Fe}^{2+}$  ions present as contamination of the matrix. Thermal treatment of the exchanged samples results in formation of colloidal silver particles. Their diameter 2R was estimated by comparing experimental values of half-width  $\delta$  and position of the band maximum  $\lambda_{\max}$  for different penetration depths with an

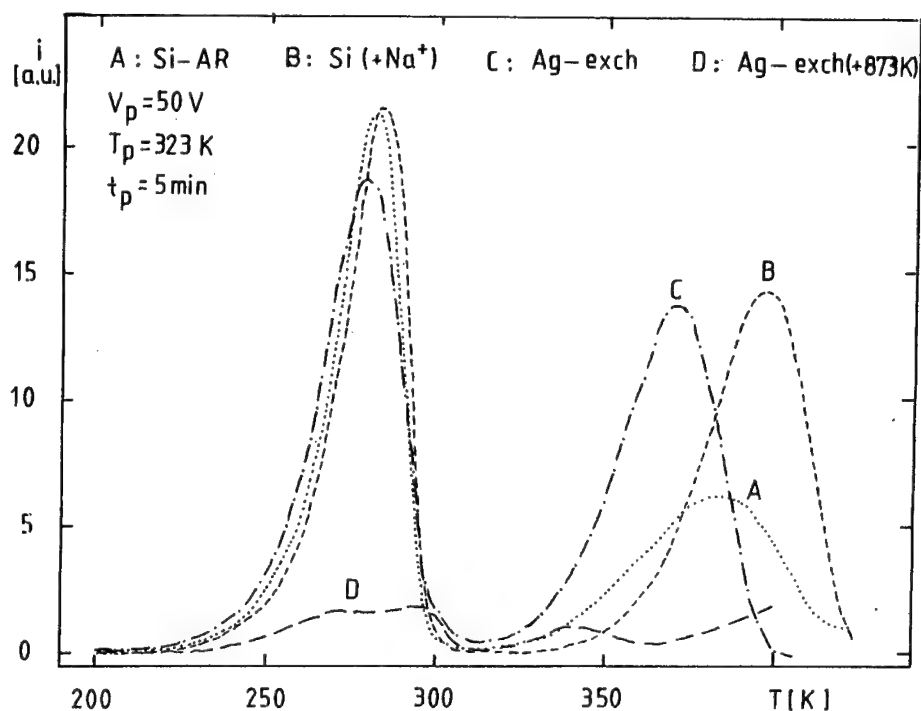


FIGURE 2 ITC-spectra detected for as received (A), chemically treated (B, C) and annealed (D) samples; B, C denote the effects of Na<sup>+</sup> and Ag<sup>+</sup>, respectively D—the effect of thermal treatment at 873 K for the C-sample.

empirical curve derived by Kreibig *et al.*<sup>2</sup> for monodispersed and size distributed systems, cf. Figure 1. It was stated that the penetration depth and the diameter of colloidal silver particles was larger for samples annealed at 873 K (8 nm, 460  $\mu$ ) than at 823 K (2 nm, 250  $\mu$ ).

### 3.2 Depolarization currents

Two main bands were detected at temperatures below those characteristic of the quartz samples, being indicative of motions of the Na<sup>+</sup> ions, see Figure 2. The shape factor is not characteristic of a first-order process, and the activation energy was equal to 0.6–0.8 eV. TSPC-measurements performed with teflon-sheets, linearity of band-magnitude with  $V_p$ , and independency on properly chosen  $T_p$  are indicative of dipolar character of the related polarizations rather than of space-charge or near-electrode phenomena.

The effect of annealing in NaNO<sub>3</sub> (increase of the magnitude of the high-T-band) confirms the correlation of these bands with the presence of Na<sup>+</sup> ions. The main effect of annealing of the exchanged samples was to reduce the magnitude of both bands, to 'split' the high-T-band, and to shift its  $T_m$  toward lower temperatures. These effects were larger for higher annealing temperatures, correlating with the optical data. Thus, the effect of thermal treatment, indirect in character, is to affect the formation of various silver species at different penetration depths. These species could be considered as effective barriers of the Na<sup>+</sup>-motion.

According to the suggestions by R. J. Charles,<sup>3</sup> the main features of the low-T-band could be considered as related with dipolar processes, where reorientation of permanent dipoles is active. The role of dipoles could be played by Na<sup>+</sup>-ions bonded with the non-bridging oxygen ions. The motion of Na<sup>+</sup>-ions can also lead to some interfacial polarizations of the Maxwell-Wagner type, where either stress-profiles or colloidal particles of silver play the role of heterogeneities in thermally and/or chemically treated soda-lime silicate glasses. Work is in progress to obtain more complete explanation of these characteristics also for samples exchanged with potassium ions.

#### ACKNOWLEDGMENTS

The authors wish to thanks Dr M. Czapelski and B. Macalik for valuable discussions, and Mrs M. Szmida for technical assistance.

#### REFERENCES

1. K. J. Berg, P. Grau, D. Nowak-Wozny, M. Petzold and M. Suszynska. *Mater. Chem. Phys.*, (1994), in print.
2. U. Kreibitz and C. V. Fragstein. *Z. Physik*, **224**, 307 (1969).
3. R. J. Charles. *J. Appl. Phys.* **32**, 1115 (1961).

## POLARIZATION AND DEPOLARIZATION IN SILICA BY MIGRATION OF ELECTRIC CHARGE CARRIERS

M. BARLAND, E. DUVAL, T. ACHIBAT and A. BOUKENTER

*Laboratoire de Physico-Chimie des Matériaux Luminescents Université Claude Bernard  
Lyon I-URA CNRS 442 Bât. 205-43 boulevard du 11 Novembre 1918  
69622 Villeurbanne Cedex (France)*

A thermally stimulated depolarization current was measured in pure silica glasses and crystalline quartz, after a linear temperature increase under applied electric field, up to 520 K. The depolarization peak at 480 K disappeared after UV illumination at room temperature. A negative depolarization current was observed in silica glasses after polarization by an electric field under UV illumination at room temperature. There exist two different types of dipoles which are electron-hole pairs, in which electron and hole are trapped on two different defects respectively.

### 1 INTRODUCTION

Intrinsic defects exist in silica. Due to the disordered structure, their concentration is higher in the glass than in crystalline quartz. They can be observed by light absorption<sup>1,2</sup> electron paramagnetic resonance if they are paramagnetic<sup>3</sup> or by other techniques. In general, their concentration increases by X-ray,  $\gamma$ -ray, neutron or electron radiations.

Several defects are electrically charged and associated in pairs or electric dipoles.<sup>4,5</sup> In consequence, an electric polarization can be created in silica under electric field when a migration of electrons or holes occurs. Such a migration can be induced by heating or excitation of electrons or holes respectively in the conduction band or in the valence band by a light beam. The measurement of depolarization current after polarization is a very sensitive method to observe the charged defects. In this paper we present the results of depolarization current measurements in silica-glass. The polarization and depolarization currents in silica-glass are compared to the ones in crystalline quartz.

### 2 EXPERIMENT

#### 2.1 Experimental Technique

The silica samples, in the form of small plates (thickness 0.5 to 1 mm) were mounted between two electrodes, a copper block and a transparent metallized quartz plate, and kept under vacuum ( $10^{-7}$  Torr). Currents were measured with a Cary 401 electrometer. Applied electric fields were about  $100 \text{ kV m}^{-1}$ . Samples were illuminated by a deuterium lamp through the transparent electrode. Samples were heated to a maximal temperature of 520 K, at a constant rate of  $0.2 \text{ K s}^{-1}$  controlled by a programmable digital temperature regulator. Different silica glass samples were tested, in particular suprasil 1 and 2 from Heraeus, and also silica obtained by sol-gel method. Furthermore, the measurements were carried out on synthetic pure crystalline quartz.

#### 2.2 Experimental Results

Figure 1 shows the thermostimulated current from room temperature to 520 K in glassy and crystalline silica, when a voltage of 100 V is applied to the sample. In the glass, a rapid

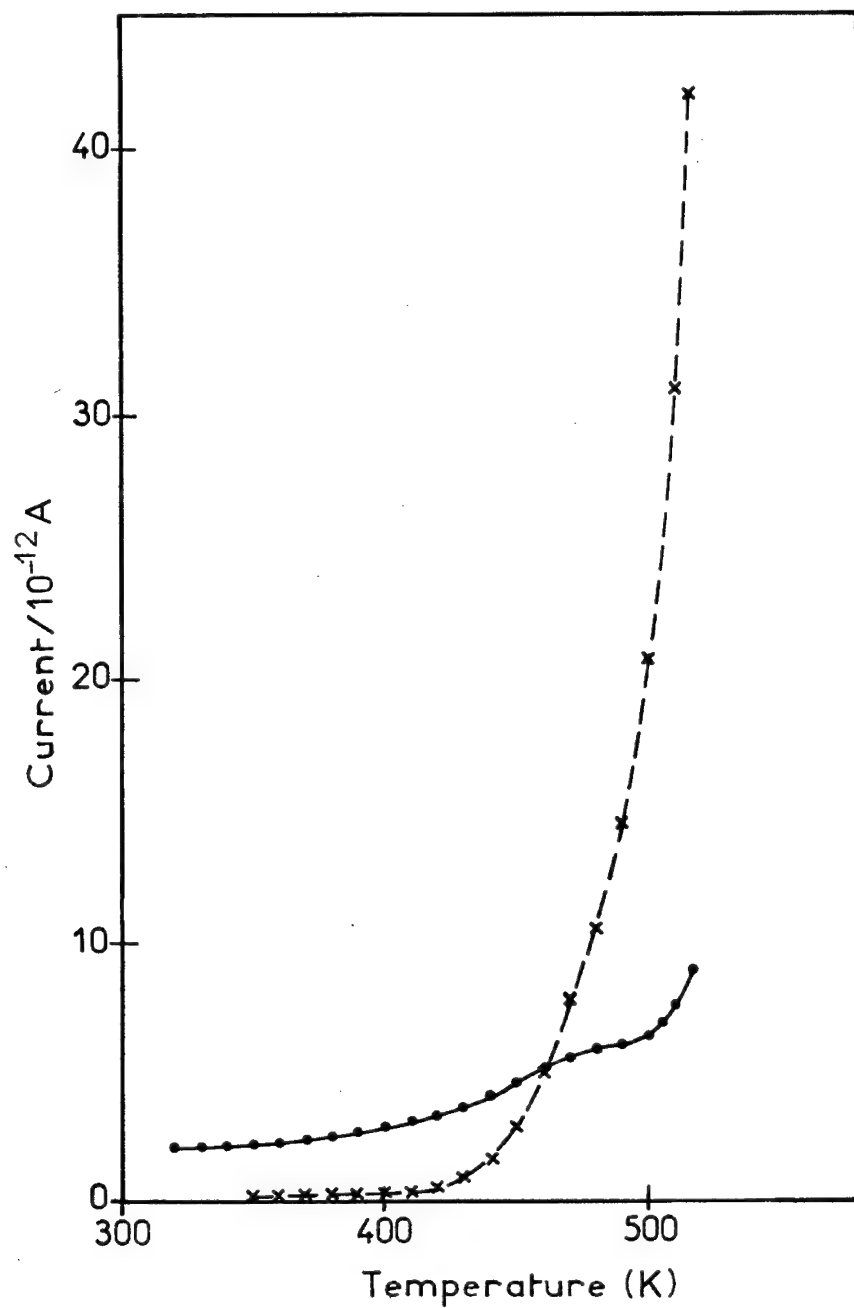


FIGURE 1 Thermostimulated electric current of silica samples : x glass sample (Suprasil 1), ● crystalline quartz. The heating rate temperature is: 0.2 K/s.



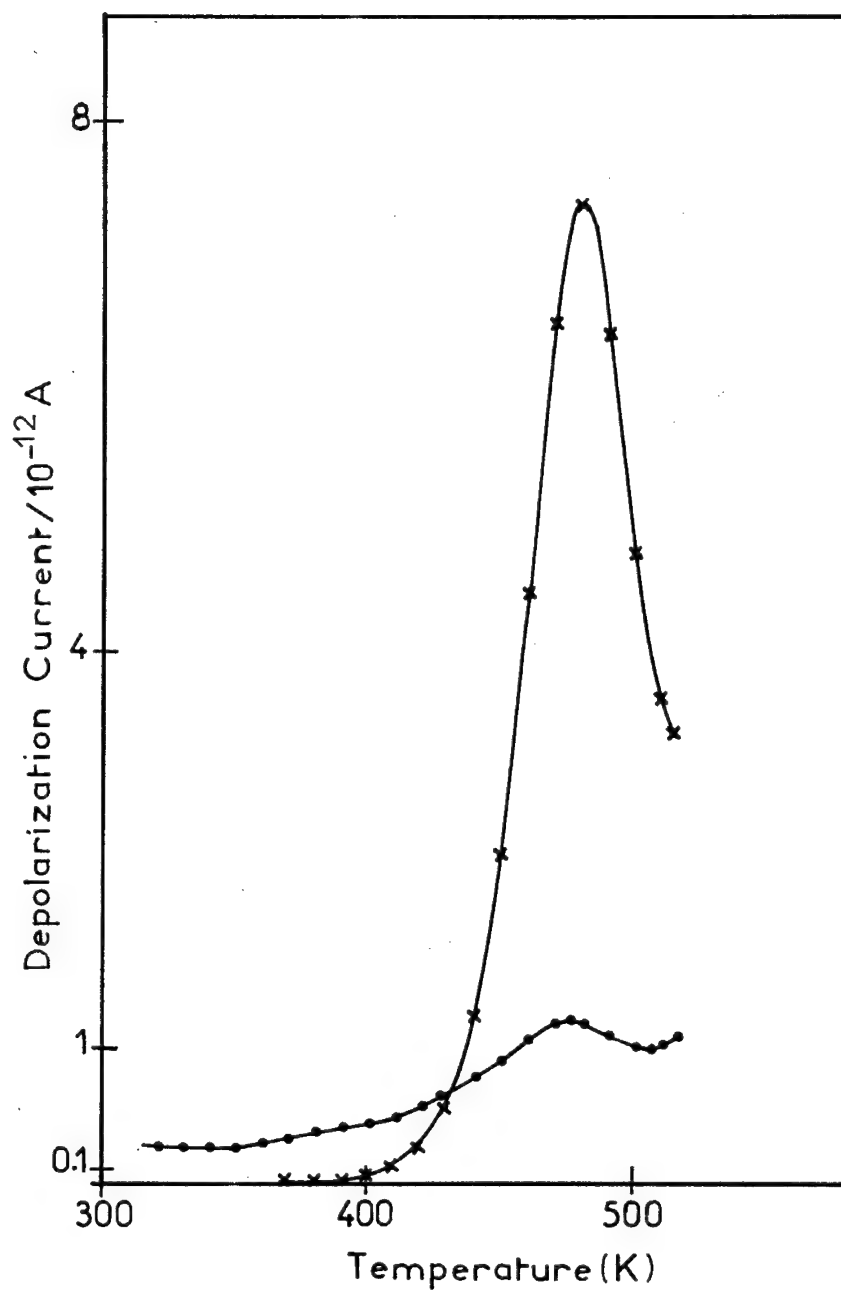


FIGURE 2 Thermostimulated depolarization current after polarization by an electric field up to  $T = 520$  K.  $\times$  glass sample,  $\bullet$  crystalline quartz. The heating rate temperature is:  $0.2$  K/s.

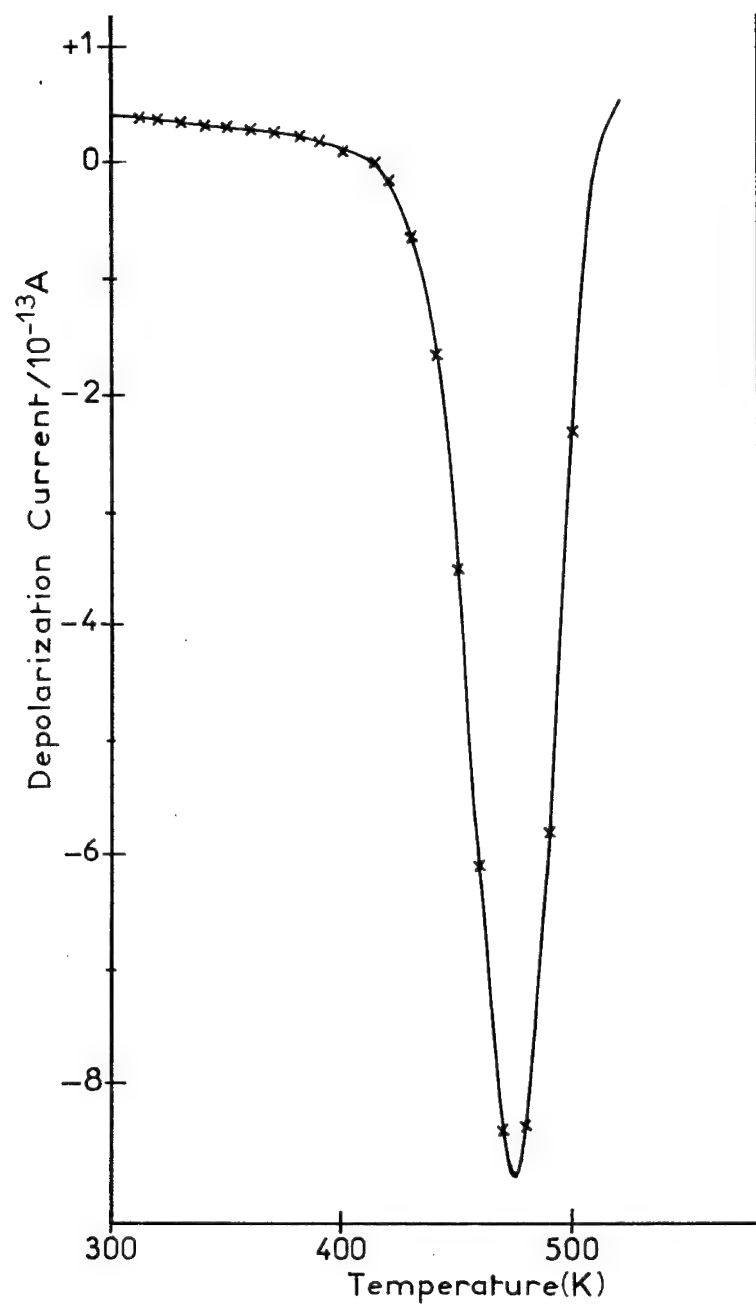


FIGURE 3 Depolarization current after polarization by an electric field under UV illumination at room temperature. The heating rate temperature constant is: 0.2 K/s.

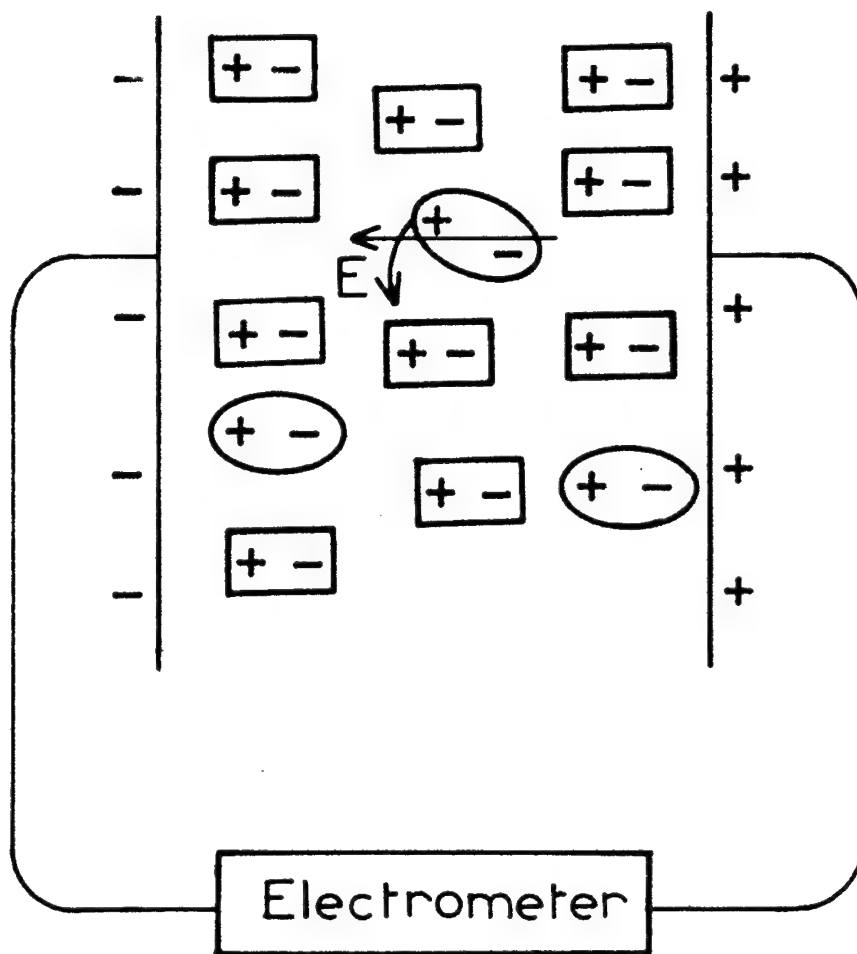


FIGURE 4 Schematic presentation of an orientation of the low-temperature dipoles ( $S_{i3}^+ - O_1^-$ ), by the local electric field  $\vec{E}$  induced by the high-temperature dipoles.

and monotonic rise appeared from a temperature of 400 K, while weaker thermally stimulated current with a shoulder at 480 K was observed in crystalline quartz.

After the temperature rise, the samples was cooled down to the room temperature, keeping applied the voltage. Before a new temperature rise, the battery voltage was removed and the electrometer directly connected to the electrodes to measure the current of depolarization. The thermostimulated depolarization currents are represented in Figure 2. A peak appears at about 480 K in glassy and crystalline quartz. The foot of another peak at higher temperature could be also observed.

After these measurements, the sample was again polarized up to 520 K and cooled under applied voltage down to the room temperature. The electrodes were short-circuited and the glass sample was UV illuminated with a deuterium lamp still at room temperature. The depolarization peak was again observed at 480 K but was greatly reduced and practically invisible after this UV illumination.

In a third experiment, the silica samples were illuminated at room temperature, with a deuterium lamp (the incident power on the sample was about 1 mW) during one hour, the battery voltage (100 V) being applied. A photoconductivity of about  $10^{-11} (\Omega\text{m})^{-1}$  was observed. The battery was removed and the electrometer was directly connected to the electrodes. During the temperature rise, a current was observed. A beautiful peak appeared at the same temperature as the one of the preceding depolarization peak, but with the same sign as the photocurrent (Figure 3). That is a priori surprising. This peak appeared also in crystalline silica with an intensity divided by about ten. Same results were obtained with other silica glasses and in particular glasses obtained by sol-gel method.

The process responsible for the depolarization peak was of the first order. The activation energy was roughly equal to 1 eV. It decreased slightly with the annealing of the glass between 1000°C and 1400°C, around the glass-transition temperature.

### 3 INTERPRETATION AND DISCUSSION

#### 3.1 *The Origin of the Depolarization Current at 480 K*

The depolarization peak at 480 K has an electron origin. It is not related to a relaxation of the lattice: no such relaxation was observed at a so low temperature, for instance by mechanical spectroscopy.<sup>6</sup> It is confirmed by the UV illumination after polarization. By UV illumination with a deuterium lamp, electrons are excited in the conduction band. It was verified that the photoconductivity was observed for a wavelength of the excitation light less than 214 nm. That corresponds to the absorption of the  $E'$  center<sup>1,3</sup> (electron trapped in the non-bonding orbital of a three-coordinated silicon atom), and consequently to an electron excitation up to the conduction band. If the polarization is produced by electron or hole migration, then it should be possible to destroy the polarization by electron excitation in the conduction band when electric field is not applied.

What is the origin of the electric dipoles? Most of the defects in silica are related to dangling bonds of oxygen and silicon, or to anomalous coordination. Using a notation close to that of Kastner,<sup>4</sup> we consider the following centers:  $S_{\text{Si}}^{\circ}$ ,  $S_{\text{Si}}^{+}$ ,  $O_1^{\circ}$ ,  $O_1^{-}$ ,  $O_3^{+}$ , where the subscript denotes the covalent coordination of silicon or oxygen and the superscript means the charge state. The  $S_{\text{Si}}^{\circ}$  center is not considered because probably, its ground state is situated in the conduction band of silica. Two different dipolar pairs can be considered:  $S_{\text{Si}}^{+}-O_1^{-}$  and  $O_3^{+}-O_1^{-}$ .

We are interested by the dipoles thermally oriented or disoriented at 480 K. In Figure 1, the polarization is visible for the crystalline silica. It is masked in glass-silica by the conduction coming from the thermal excitation of electrons or holes from shallow levels corresponding to different defects. Electron spin resonance (ESR) results inform us on the polarization process. It was shown that the  $E'$  center observed in ESR corresponds to  $S_{\text{Si}}^{\circ}$ .<sup>3</sup> The ESR signal of  $E'$  anneals away at a temperature close to 473 K.<sup>7,8</sup> Such a temperature can be compared to the temperature of depolarization current peak (Figure 2).

Considering now the extinction of the depolarization peak at 480 K by UV illumination, we observed that the photoconductivity appeared for a light wavelength shorter than 214 nm, that corresponds to the absorption of the  $S_{\text{Si}}^{\circ}$  center (5, 8 eV).<sup>1,3</sup>

From these informations, we deduce that the electric polarization or depolarization peaks at 480 K are related to the  $S_{i3}^{\circ}$  and  $S_{i3}^{+}$  centers. The phenomena observed around 480 K can be explained by a migration of these centers or an electron transfer from one center to another, with an activation energy close to 1 eV. This energy is too low for an atomic or vacancy displacement. On the other hand, it seems difficult to explain all physical phenomena, which occur around  $T = 480$  K, by a simple electron transfer. Another mechanism, that can be considered is the migration of  $S_{i3}^{+}$  or  $S_{i3}^{\circ}$  by exchange of the dangling bond between two neighbors Si without atomic movement. By pairing with a negative center as  $O_1^{-}$ ,  $S_{i3}^{+}$  will form an electric dipole which will orient under electric field, or disorient without electric field.

This mechanism can explain the other physical phenomena: decrease of the ESR signal,<sup>7,8</sup> thermoluminescence,<sup>9</sup> observed in silica samples coloured by an energetic radiation, X or  $\gamma$  rays, neutrons... From the migration of  $S_{i3}^{\circ}$  can result a recombination with a trapped hole, a decrease of the ESR signal of  $S_{i3}^{\circ}$  and a thermoluminescence in the case of radiative recombination.

Our interpretation is in agreement with recent results on the pressure effect on the thermoluminescence of quartz.<sup>10</sup> It was found that the activation energy for the thermoluminescence at 473 K decreases with the hydrostatic pressure. An hydrostatic pressure which shortens the distance between atoms would increase the activation energy for an atomic movement but certainly decreases that for a  $Si^{-}$  dangling bond migration.

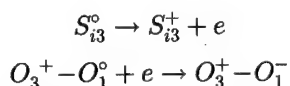
The extinction of the depolarization peak by UV illumination at room temperature without applied electric field is easily explained by the excitation of the electron of  $S_{i3}^{\circ}$  in the conduction band. The excited electron is then trapped by another  $Si^{3+}$  center. Consequently, a redistribution of the  $S_{i3}^{+}$  or  $S_{i3}^{\circ}$  centers occurs, and then a depolarization.

### 3.2 Polarization by ultraviolet illumination

Under applied electric field a photoconductivity of about  $10^{-11} (\Omega m)^{-1}$  was observed when the wavelength of the excitation light is lower than 214 nm, that corresponds to the absorption of the  $E'$  center<sup>12</sup> and consequently, to an electron excitation up to the conduction band. This electron transfer brings again a dipoles redistribution and a polarization of the sample. After removing the applied electric field, a depolarization current (opposite to the photocurrent) would be observed during a temperature rise. On the contrary, we observed a polarization current peak (same sign as the photocurrent).

Such negative depolarization peak should be explained by a heterogeneous structure of the glass. However this peak was also observed in crystalline silica, but much weaker. It means that it is not specific to the glass. As it appears in Figure 2, a depolarization peak at higher temperature than 500 K exists. Therefore two different types of dipoles exist in silica. 1) Low-temperature dipoles oriented at 480 K; 2) High-temperature dipoles oriented at higher temperature. The dipole  $O_3^{+}-O_1^{-}$  called valence alternation pair<sup>4</sup> was considered by different authors.<sup>5,11</sup> We can assume that dipoles 2) are these  $O_3^{+}-O_1^{-}$  pairs.

When electrons of  $S_{i3}^{\circ}$  centers are excited in the conduction band, there is creation and orientation under electric field, not only of  $S_{i3}^{+}-O_1^{-}$  dipole, but also of  $O_3^{+}-O_1^{-}$  pairs by the following process:



The presence of these two types of close dipolar pairs explains the negative depolarization peak after UV illumination under electric field at room temperature. When the sample is

heated up to 480 K  $S_{i3}^+-O_1^-$  dipoles are created and (or) oriented by the local electric-field induced by high-temperature  $O_3^+-O_1^-$  dipoles which were oriented by UV illumination. From Figure 4, it is clear that the dipole induced electric field has the same direction as that of the preceding applied electric field, so that it will appear a polarization current at 480 K, after UV illumination at room temperature, in agreement with the experiment. This interpretation supposes that the size of dipoles is very small and that  $S_{i3}^+-O_1^-$  dipoles are oriented between  $O_3^+-O_1^-$  dipoles.

#### 4 CONCLUSION

Two processes of electric polarization or depolarization in silica have been observed by thermal activation, and light excitation of electrons in the conduction band. The thermal depolarization at 480 K is interpreted as being due to the disorientation of  $S_{i3}^+-O_1^-$  dipoles, where  $S_{i3}^+$  is a positively charged silicon and  $O_1^-$  a negatively charged oxygen, each one with a dangling bond. The thermal orientation of these dipoles can occur by a migration of the dangling bonds of silicon without motion of atoms or vacancies. The polarization or depolarization by UV light comes from the excitation of the  $S_{i3}^0$  electrons in the conduction band and consequently, from a redistribution of the  $S_{i3}^0$  and  $S_{i3}^+$  centers. As expected, the thermostimulated electric current and the depolarization one are weaker in the quartz crystal than in the vitreous silica because there is a smaller concentration of dangling bonds in the crystal than in the glass.

It was shown that UV light excitation under electric field orient other dipoles which are assumed to be  $O_3^+-O_1^-$ . Thermal polarization or depolarization of these dipoles occur at a temperature higher than 520 K. After their orientation by UV light at room temperature, we observed the thermal orientation of the  $S_{i3}^+-O_1^-$  dipoles by the local electric field induced by the  $O_3^+-O_1^-$  dipoles.

These reversible phenomena of polarization or depolarization were clearly observed in different unirradiated silica samples: pure silica glasses obtained by fusion (suprasil) or by sol-gel method, and crystalline quartz. However for the crystal the negative thermal depolarization current after UV irradiation was much weaker. The technique of the depolarization is very sensitive for the observation of dipoles consisting of charged defects pairs. The observed effects show the possibility of optical or electric memorization in silica.

#### REFERENCES

1. C. M. Nelson and R. A. Weeks, *J. Am. Ceram. Soc.* **43** (1960) 396.
2. D. A. Pinnow, T. C. Rich, F. W. Ostermayer and M. Didomenico, *Appl. Phys. Lett.* **22** (1973) 527.
3. R. A. Weeks and C. M. Nelson, *J. Appl. Phys.* **31** (1960) 1555.
4. M. Kastner, D. Adler and H. Fritzsche, *Phys. Rev. Lett.* **37** (1976) 1504.
5. G. Lucovsky, *Phil. Mag.* **B41**, (1980) 457.
6. S. Etienne, private communication.
7. E. J. Friebele, D. L. Griscom, G. H. Sigel, *Fourth International Conference on Non-crystalline Solids*, edited by G. H. Frischat (Aedermannsdorf: Trans. Tech. Publications), p. 154.
8. P. M. Lenahan and P. V. Dressendorfer, *J. Appl. Phys.* **55** (1984) 3495.
9. S. W. S. Mc Keever, *Radiation Protection Dosimetry*, **8** (1984) 81 and referenced papers.
10. B. J. Baer and H. G. Drickamer, *Solid State Comm.* **83** (1992) 669.
11. M. Kastner, *J. Phys. C: Solid St. Phys.* **13** (1980) 3319.

## THE POLAR TRANSITION OF Li-DOPED AND Nb-DOPED $\text{KTaO}_3$ : COMPARATIVE ANALYSIS FROM HARD-PHONON RAMAN SPECTRA

P. CALVI, P. CAMAGNI, E. GIULOTTO, L. ROLLANDI

*Dipartimento di Fisica 'A. Volta', Via Bassi 6, 27100 Pavia (Italy)*

Raman investigations have been performed on  $\text{K}_{0.984}\text{Li}_{0.016}\text{TaO}_3$  and  $\text{KTa}_{0.976}\text{Nb}_{0.024}\text{O}_3$  single crystals, in order to follow the peculiarities of non-ferroelectric phonons, which may be indicative of a different evolution of microscopic order during the polar transition. Specific features in the Nb case confirm a ferroelectric behaviour, whereas in the Li-doped sample the results are in agreement with a dipole glass transition.

### 1 INTRODUCTION

$\text{KTaO}_3$  is an oxidic perovskite exhibiting an incipient ferroelectric behaviour. The system remains centrosymmetric at all temperatures, but shows a divergent dielectric susceptibility related to softening of a transverse optic mode as  $T \rightarrow 0$  K. The soft mode,  $\text{TO}_1$ , involves atomic displacements along Ta-O chains.

The presence of substitutional impurities such as Nb or Li may induce a transition to a polar phase at finite temperature, whose nature depends on the type and concentration of the specific impurity.<sup>1</sup> Nb substitutes for Ta in the ferroelectric chains and affects directly soft mode dynamics, driving a displacive polar transition at low temperature. An order-disorder contribution to the transition can arise from local Nb dynamics,<sup>2</sup> due to hopping between eight equivalent off-centre minima along  $\langle 111 \rangle$  directions. Li substitutes for K and can jump between six equivalent off-centre minima along pseudo-cubic directions; dipolar and elastic interactions between Li ions control the rise of a low temperature polar phase, provided dopant concentration is  $\geq 1\%$  mol.<sup>3</sup> There is no general agreement as to whether the polar transition at low Li or Nb concentration is towards an ordered (ferroelectric) or disordered (dipole glass) phase.

In order to characterize the phase transition in lightly doped  $\text{KTaO}_3$  we made a comparative study of the Raman response of the transverse optic phonons in  $\text{KTaO}_3\text{:Nb}$  2.4% and  $\text{KTaO}_3\text{:Li}$  1.6%. These crystals are denoted by KTN and KLT, respectively. The two systems were investigated in a temperature range covering the respective transition temperature  $T_t$ , independently defined by the onset of linear birefringence and second harmonic generation (32 K in KTN and 36.5 K in KLT).<sup>4,5</sup>

### 2 RESULTS AND DISCUSSION

Raman measurements were performed in  $x(\text{zz})y$  and  $x(\text{yz})y$  polarization geometries in zero-field cooling (ZFC) and in the presence of a poling field of 2 kV/cm applied along the z-direction during cooling (FC). Cooling between successive measurements was effected at a rate of 1 K/min. The electroded faces were (001) and (111) in KLT and KTN samples respectively. First-order spectra from hard transverse optic modes were observed and analyzed over the range from 100 K to 15 K (see for example Figure 1, 2). Figure 3 summarizes the results concerning integrated intensities vs. temperature for these lines in both samples.

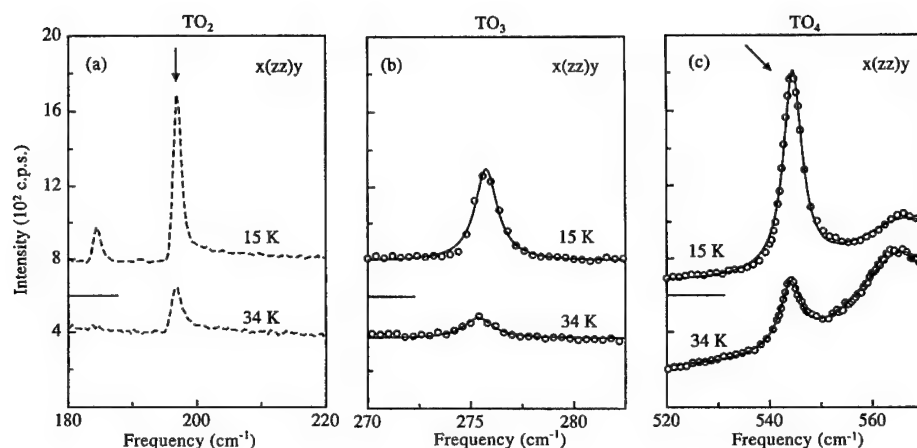


FIGURE 1 ZFC Raman spectra from  $\text{TO}_2$ ,  $\text{TO}_3$ ,  $\text{TO}_4$  hard phonons, above and below the transition temperature ( $T_i = 32 \text{ K}$ ) in  $\text{KTa}_{0.976}\text{Nb}_{0.024}\text{O}_3$ . Full lines denote Lorentzian fits to the experimental data.

We start with the analysis of the  $\text{TO}_4$  phonon line at  $545 \text{ cm}^{-1}$  which is the most intense hard-phonon Raman component and shows up with a FWHM substantially larger than instrumental resolution (set at  $1 \text{ cm}^{-1}$  and  $2 \text{ cm}^{-1}$  for KTN and KLT, respectively). Its shape is symmetric in both systems over the entire temperature range and can be fitted by a Lorentzian, provided the background from the adjacent  $\text{TO}_4 + \text{TA}$  band is subtracted. Figure 1c and 2c illustrate the results to be obtained by fitting the ZFC spectra with the sum of two Lorentzians. Temperature dependence of the intensity of this line in KTN under zero-field cooling is shown in Figure 3a. We remark: i) the onset of  $\text{TO}_4$  is a few degrees above  $T_i$  ii) a small and reproducible maximum occurs at about 2 K above the transition: this precursor effect was already observed in other perovskites with structural phase transitions, for example  $\text{KMnF}_3$ <sup>6</sup>; iii) the line strength grows critically below  $T_i$ . The same features are observed in field cooling conditions. An alternative behaviour of KLT is shown in Figure 3d. Here the line is detectable at temperatures substantially higher than  $T_i$  and its strength grows very little in ZFC, whereas it is strongly enhanced around  $T_i$  in the presence of a field. The same features are observed in  $x(yz)y$  geometry.

The  $\text{TO}_2$  line at  $198 \text{ cm}^{-1}$  shows a peculiar asymmetric shape in both systems (Figure 1a, 2a) in all experimental conditions. Evaluation of line strength was obtained by direct integration after subtracting a constant background: the results of this analysis are quite similar to the  $\text{TO}_4$  case for what concerns the evolution in different conditions, in the two compounds (Figure 3a, 3b).

$\text{TO}_3$  is the only non-polar TO phonon; its line at  $276 \text{ cm}^{-1}$  is symmetrical and can also be fitted by Lorentzian (Figure 1b, 2b). The evolution of this line is different from that of  $\text{TO}_2$  and  $\text{TO}_4$ : it is undetectable above 36 K in KTN (Figure 3a) and above 50 K in KLT (Figure 3c) and its intensity undergoes a rapid increase around the transition temperature in both systems, irrespective of cooling conditions. In the Li case, the line is only observed in  $x(yz)y$  geometry.

The critical increase of the line strength for the various TO phonons in KTN is indicative of the occurrence of a ferroelectric phase transition and is in agreement with previous second-harmonic generation and hyper-Raman experiments.<sup>7</sup> This idea is also



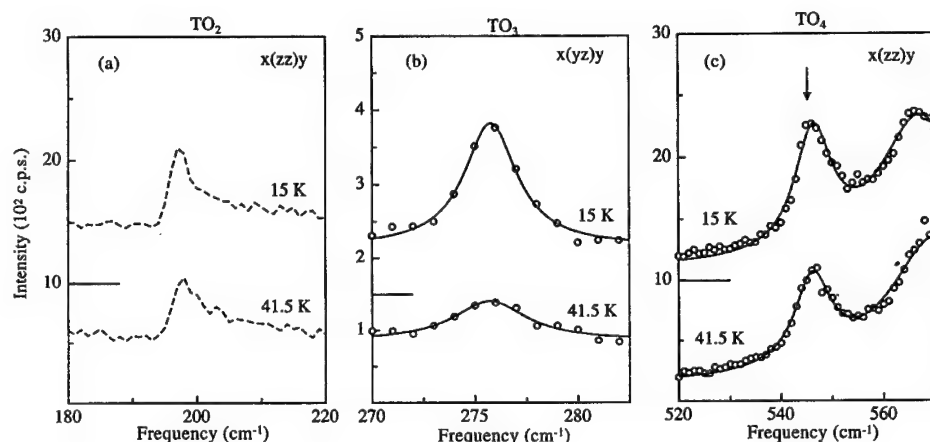


FIGURE 2 ZFC Raman spectra from  $\text{TO}_2$ ,  $\text{TO}_3$ ,  $\text{TO}_4$  hard phonons, above and below the transition temperature ( $T_t = 36.5$  K) in  $\text{K}_{0.984}\text{Li}_{0.016}\text{TaO}_3$ . Full lines denote Lorentzian fits to the experimental data.

confirmed by previous Raman analysis of the soft mode, made by the authors:<sup>4</sup> in the same sample critical frequency behaviour, growth and splitting in two symmetrical lines were observed below  $T_t$  (Figure 4a). These features were shown to be consistent with a general model, in which coupling of the soft-mode oscillators to relaxational motions rapidly vanishes below the transition temperature.

On the contrary, the results for KLT are consistent with a dipole-glass transition,<sup>5</sup> for which one reasonably expects absence of criticality and dependence on the field. The same features had been found to characterize the intensity behaviour of  $\text{TO}_1$  in previous studies.<sup>8</sup> Furthermore it is known that the soft-mode line shows a marked asymmetric broadening, extending from 30 to  $170\text{ cm}^{-1}$  even at low temperature, in zero field; this effect is strongly reduced in FC conditions. We ascribe the  $\text{TO}_1$  peculiar lineshape in KLT to scattering from phonons of the whole branch, due to breaking of wave-vector selection rules in the presence of short-range polar order.<sup>9</sup> Figure 4b illustrates recent results obtained from spectra analysis of the  $\text{TO}_1$  line at 15 K: the solid curve here represents the best fit from a model cross section, taking into account a finite polar correlation length.<sup>10</sup> From this analysis we inferred that the scale of polar order is about 2 nm at low temperature, in substantial agreement with second-harmonic results.<sup>5</sup> We remark that the special sensitivity of the  $\text{TO}_1$  lineshape to the spatial scale of polar correlation is strictly connected with the strong dispersion of the soft phonon branch, well known from neutron scattering studies.<sup>11</sup>

From the above observations we can draw conclusive remarks about the hard phonons, as follows:

i) polar order on a nanometric scale is sufficient to induce first-order Raman activity. The lack of observation of the  $\text{TO}_3$  mode in a dipole glass such as  $\text{KTaO}_3\text{:Li 1\%}$  by Toulouse *et al.*<sup>12</sup> may be due to the experimental geometry: for example we found that in KLT its intensity vanishes, for  $x(\text{zz})y$  polarization;

ii) although finite correlation effects are active even in scattering from hard phonons, we expect the observation of line broadening to be prevented by the flatness of the concerned dispersion curves.<sup>11</sup> This should explain the substantial invariance of the

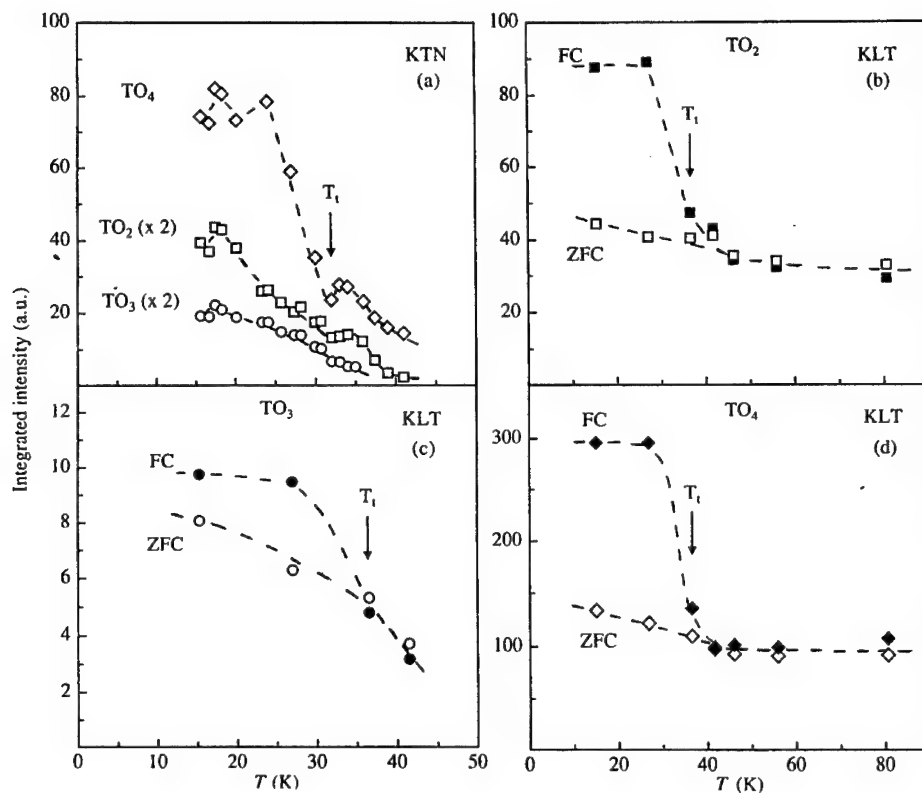


FIGURE 3 Temperature dependence of integrated intensity for different hard-phonon lines in KTN (a) and KLT (b), (c), (d). Open and black symbols denote zero-field cooling and field cooling conditions respectively. Dashed lines are guides to the eye.

lineshapes in KTN and KLT, in spite of the different scales of polar correlation in the two systems. In this view the asymmetric  $\text{TO}_2$  lineshape should not be ascribed to such effects, as proposed by DiAntonio *et al.*<sup>13</sup> from their analysis one infers a phase velocity for the  $\text{TO}_2$  branch which is too large ( $v_h \sim 100$  meV) if compared with neutron scattering results.<sup>11</sup> An alternative explanation of the  $\text{TO}_2$  lineshape, based on Fano coupling to the background, had already been advanced.<sup>14</sup>

In conclusion, the present analysis points out the different nature of pretransitional effects in KTN and KLT. In KTN first order Raman scattering is activated a few degrees above  $T_1$ , indicating that order parameter fluctuations occur on a spatial and temporal scale higher than that associated with TO vibrations. This is intrinsic to the ideal dynamics of a displacive system near its critical point.<sup>6</sup> The case of KLT is quite different: since the hopping frequency of Li ions<sup>15</sup> is much lower than the TO mode frequencies, quasi-static distortions of the host matrix are induced by off-centre impurities well above  $T_1$ , giving rise to a violation of symmetry selection rules. Therefore first order scattering from TO phonon, forbidden in the cubic of the pure crystal, is permitted.

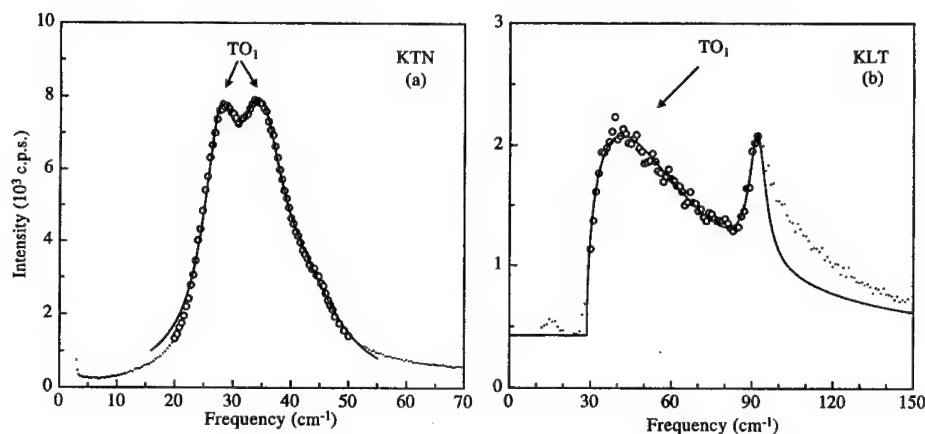


FIGURE 4 Low-frequency Raman spectra obtained at 15 K in ZFC conditions and  $x(zz)y$  geometry for KTN and KLT. Solid lines: (a) fitting to an uncoupled oscillators model of the split  $\text{TO}_1$  line plus the additional TA structure at  $45 \text{ cm}^{-1}$ ; (b) fitting to a model cross section taking into account broadening of the  $\text{TO}_1$  line from finite correlation effects, with a Lorentzian correction for the 2TA branch at  $100 \text{ cm}^{-1}$ . Fitted data are denoted by open symbols in both cases.

#### REFERENCES

1. U. T. Höchli, K. Knorr, A. Loidl, *Adv. Phys.* **39**, 405 (1990).
2. B. E. Vugmeister, T. V. Antimirova, *Phys. Stat. Sol. (B)* **157**, 183 (1990).
3. F. Borsa, U. T. Höchli, J. J. van der Klink, D. Rytz, *Phys. Rev. Lett.* **45**, 1884 (1980).
4. P. Calvi, E. Giolotto, L. Rollandi, *Procs. Eighth International Meeting on Ferroelectricity*, Gaithersburg (1993), (to be published on *Ferroelectrics*).
5. G. A. Azzini, G. P. Banfi, E. Giolotto, U. T. Höchli, *Phys. Rev.* **B43**, 7473 (1991).
6. A. D. Bruce, W. Taylor and A. F. Murray, *J. Phys.* **C13**, 483 (1980).
7. G. Kugel, H. Vogt, W. Kress, D. Rytz, *Phys. Rev.* **B30**, 985 (1984).
8. G. P. Banfi, P. Calvi, P. Camagni, E. Giolotto, G. Samoggia, *Procs. Intern. Conf. on Defects in Insulating Materials* (Nordkirchen, FRG, Aug. 1992) vol. 1, p. 660, World Scientific (1993).
9. H. Uwe, K. B. Lyons, H. L. Carter, P. A. Fleury, *Phys. Rev.* **B33**, 6436 (1986).
10. E. Giolotto, Thesis, University of Pavia, to be published.
11. C. H. Perry, R. Currat, H. Buhay, R. M. Migoni, W. G. Stirling, J. D. Axe, *Phys. Rev.* **B39**, 8666 (1989).
12. J. Toulouse, P. DiAntonio, B. E. Vugmeister, X. M. Wang, L. A. Knauss, *Phys. Rev. Lett.* **68**, 232 (1992).
13. P. DiAntonio, B. E. Vugmeister, J. Toulouse, L. A. Boatner, *Phys. Rev.* **B47**, 5629 (1993).
14. Y. Yacoby, *Z. Physik* **B31**, 275 (1978).
15. J. J. van der Klink, D. Rytz, F. Borsa, U. T. Höchli, *Phys. Rev.* **B27**, 89 (1983).

---

## **14 DISLOCATION, PLASTICITY**

## PLASTIC DEFORMATION AND DISLOCATIONS IN CERAMIC MATERIALS

JACQUES RABIER

*Laboratoire de Métallurgie Physique, U.R.A. 131 CNRS, Université de Poitiers,  
40 Avenue du Recteur Pineau, 86022 Poitiers Cedex, France*

This paper deals with the properties of dislocations in some ceramic materials. The implication of the intimate structure of dislocations revealed at the TEM level, on the macroscopic properties is discussed. Not only consequences on mechanical properties are taken into account but also consequences on physical properties. Examples are given for structural ceramics ( $\text{ZrO}_2$ ), as well as for superconducting ceramics ( $\text{YBa}_2\text{Cu}_3\text{O}_{7-\delta}$ ). In this latter class of materials it is shown that dislocations can be used to locally change the thermodynamic range of nucleation of non stoichiometric phases. Pinning of vortices by dislocations is also discussed.

### 1 INTRODUCTION

Macroscopic plastic behaviour of ceramic materials can be achieved using standard deformation techniques in the high temperature range ( $T > 0.7T_M$ ,  $T_M$ : melting temperature). Then deformation takes place usually by matter diffusion involving bulk, grain boundaries or to a less extend dislocations located within the grains.<sup>1</sup> However dislocation activity can be important as soon as stress level is increased or temperature lowered. This deformation mode can be also achieved in thin films epitaxied on substrate.

Below  $0.5 T_M$  obtaining plastic deformation in ceramic materials by dislocation motion rather than crack propagation requires that there is an hydrostatic component in the applied stress tensor. Compression under hydrostatic pressure can be used to promote this type of deformation mode to study, for example, the high stress regime reached in epilayers. This technique has been previously applied to the study of high stress plastic deformation of single crystals: semi conductors Si,<sup>2</sup> GaAs<sup>3</sup> and oxides  $\text{Al}_2\text{O}_3$ <sup>4</sup>,  $\text{MgAl}_2\text{O}_4$ .<sup>5</sup>

Dislocations in ceramics are not only controlling the plastic behaviour, they can also affect significantly the physical properties of the materials: electronic properties, thermal properties, chemical reactivity. This paper gives examples of the consequences of dislocation core structures on macroscopic behaviour: the plastic behaviour of  $\text{ZrO}_2$  single crystals below  $500^\circ\text{C}$ , the influence of dislocations on non stoichiometry and on the physical properties of the high  $T_c$  super conductor  $\text{YBa}_2\text{Cu}_3\text{O}_{7-\delta}$ .

### 2 DISLOCATION MOBILITIES AND PLASTIC DEFORMATION OF $\text{ZrO}_2$ SINGLE CRYSTALS

Single crystals of cubic  $\text{ZrO}_2$  with fluorite structure were plastically deformed at low temperature ( $250^\circ\text{C}$ – $550^\circ\text{C}$ ) at a constant strain rate of  $\dot{\epsilon} = 2 \cdot 10^{-4} \text{ s}^{-1}$  under a confining pressure of 0.4 GPa.<sup>6,7</sup> The plot of the yield stress as a function of temperature between  $250^\circ\text{C}$  and  $550^\circ\text{C}$  shows an anomaly: instead of decreasing continuously with temperature, the yield stress exhibits a peak at about  $450^\circ\text{C}$  (Figure 1). Before this anomaly the yield stress is strongly temperature dependent. Glide planes were determined from slip traces analysis on lateral surfaces, as well as at the TEM level. In the whole range of temperature investigated, glide systems are: (001)[110] for [112] and [326] compression axes and

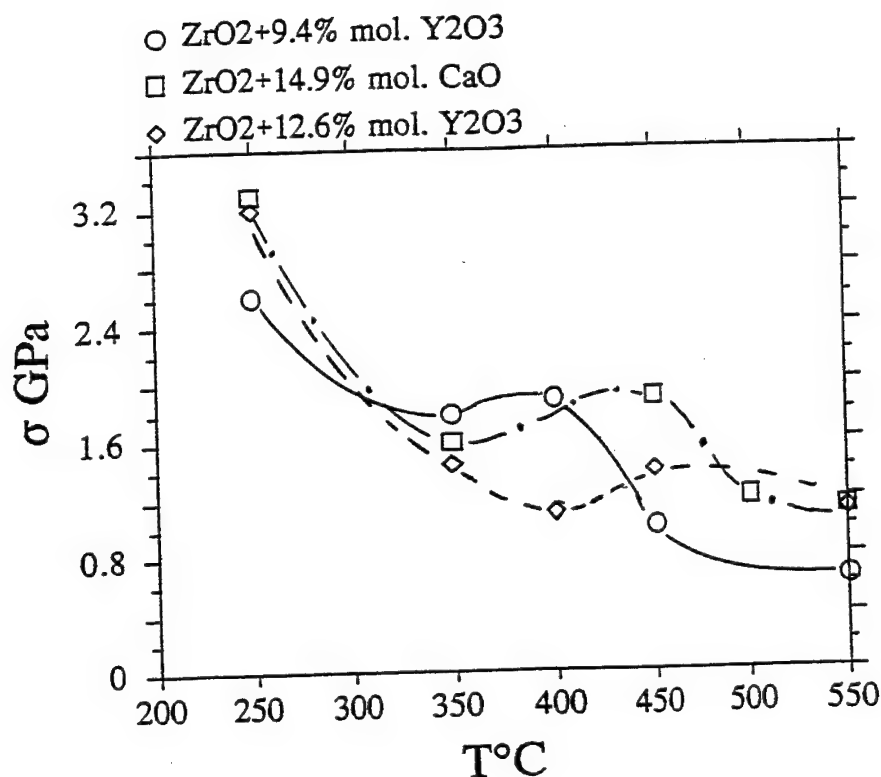


FIGURE 1 Yield stress as a function of temperature, for the [112] compression axis (single slip (001) [110]). A yield stress anomaly is evidenced for each of the compositions.

{111}⟨110⟩ for [001]. For the easy glide system (001)[110], activated in single slip for [112] and [326] compression axes, the resolved shear stress measured at 400°C is respectively 893 MPa and 593 MPa. This shows that the Schmid law is violated for this glide system. This is also true for the (111)[110] glide system.<sup>6</sup> Slip lines are always found wavy, which is consistent with the activation of cross slip.

Examples of the deformation substructure in the (001) glide plane are given here for samples deformed along [112] at 250°C (Figure 2). Glide loops of dislocations with  $a/2[110]$  Burgers vector are elongated in the screw orientation leaving behind screw dipoles. Long dipolar loops with screw character result from the local recombination of these dipoles. Pinning points are seen on the screw parts of the glide loops. At 550°C the edge components of the glide loops are longer, but the screw segments components are still very long and pinning points on the screw parts give rise to small dipoles having mostly edge character.

These TEM observations show that the characteristics of the low temperature macroscopic deformation are controlled by screw dislocation segments whose core

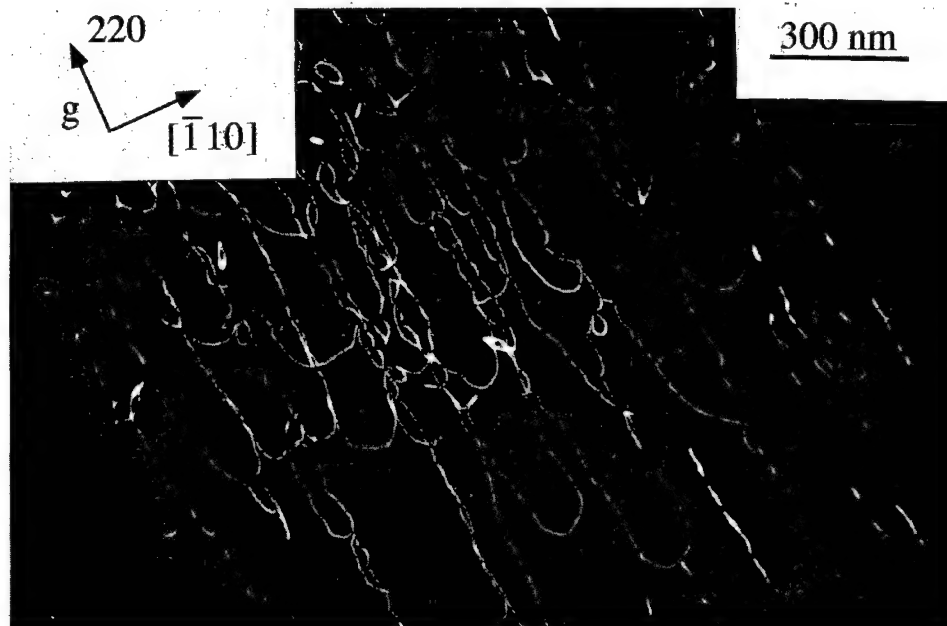


FIGURE 2  $\text{ZrO}_2$ +9.4% mol.  $\text{Y}_2\text{O}_3$  deformed at  $250^\circ\text{C}$  along  $[112]$ . The observation plane is the  $(001)$  glide plane (weak beam dark field, 3.9 g excited): long screw segment with pinning points, screw dipoles with debris.

structure can explain macroscopic properties as the violation of the Schmid law and the yield stress anomaly.

- The violation of the Schmid law together with a strong temperature dependence of the yield stress at low temperature could be explained by a BCC like dislocation mechanism: a sessile screw dislocation core.<sup>8</sup> It is likely that, since stacking fault energies are high in the fluorite structure,<sup>9</sup> the core structure could be described by a continuous distribution of Burgers vectors on several planes, yielding to a sessile configuration.
- A screw dislocation core extended on several planes can also explain the observation of cross slip. Core constriction required for cross slip can be assisted not only by thermal activation but also by interaction of mobile screw dislocations with impurities or clusters which induce in the crystal a stress field with a non spherical symmetry. Oxygen vacancy-aliovalent impurity complexes which have been characterized in this type of materials are liable to nucleate cross slip events<sup>10</sup> and the increase of the yield stress can be explained by the hardening introduced by dipole dragging. Indeed an increase of the number of dipoles is observed in the range of the stress anomaly and the yield stress increase  $\Delta\tau$  resulting from the dragging of dipoles created by double cross slip can be estimated as<sup>11</sup>:  $\Delta\tau = \mu/4\pi(1-\nu) b/y \ln(h/b)$

where  $h$  and  $y$  are respectively the dipole height and the distance between dipoles in the glide plane. Taking  $y = 80b$  and  $h = 10b$  with  $\mu = 90\text{GPa}$  yields to  $\Delta\tau = 290\text{ MPa}$

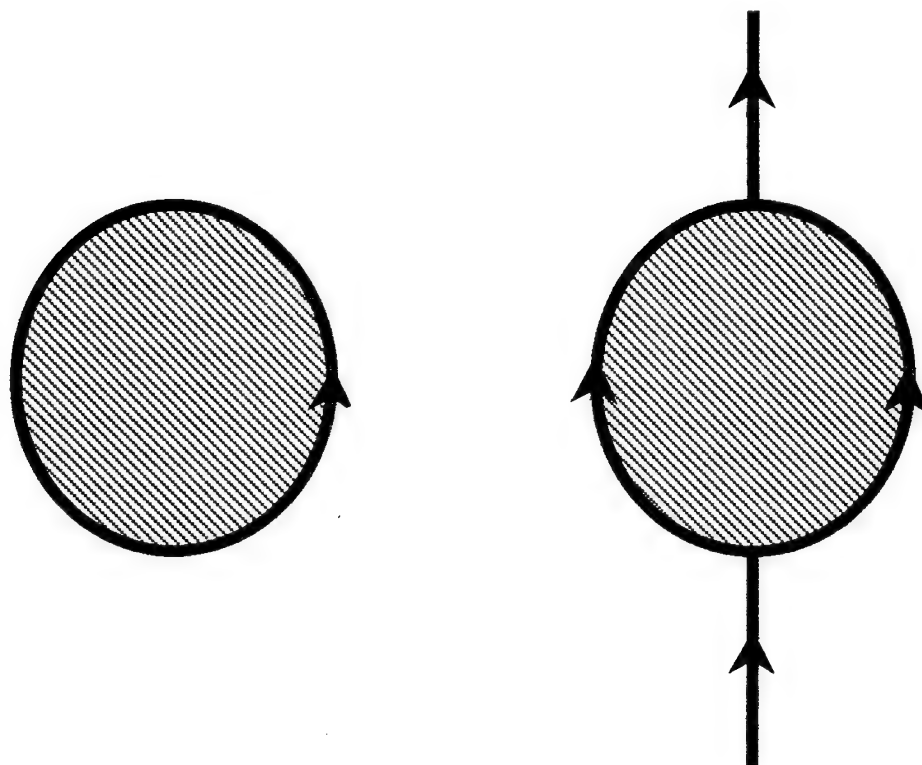


FIGURE 3 (a) Faulted dislocation loop  $1/6[031]$  corresponding to the intercalation of a CuO layer in the 123 matrix  
 (b) the same process on a pre existing dislocation  $\langle 100 \rangle$ : the dislocation is locally dissociated following the reaction:  $[010] \rightarrow 1/6[031] + 1/6[03\bar{1}]$ .

which is of the order of magnitude of the measured increase in yield stress. When temperature increases the height  $h$  covered by the dislocation in the cross slip plane increases and loops can escape by an Orowan mechanism: then the yield stress decreases when temperature increases. However atomistic core structure calculations of screw dislocation are required to get more insights into Schmid law violation and the cross slip mechanism.

### 3 DISLOCATIONS IN $\text{YBa}_2\text{Cu}_3\text{O}_{7-\delta}$

Dislocations can be introduced by plastic deformation under confining pressure at room temperature in  $\text{YBa}_2\text{Cu}_3\text{O}_{7-\delta}$  ceramic materials (123 compound). The easy glide system is  $\langle 100 \rangle (001)$  and dislocations are usually found undissociated.<sup>12</sup> The operation of such a glide system was expected from the lamellar structure of this compound. After high temperature treatments, dislocations appear widely dissociated<sup>13</sup> following the reaction:  $[010] \rightarrow 1/6[031] + 1/6[03\bar{1}]$ .

This corresponds to the insertion of an additional CuO layer on (001) into the core of the dislocations and is discussed in what follows.



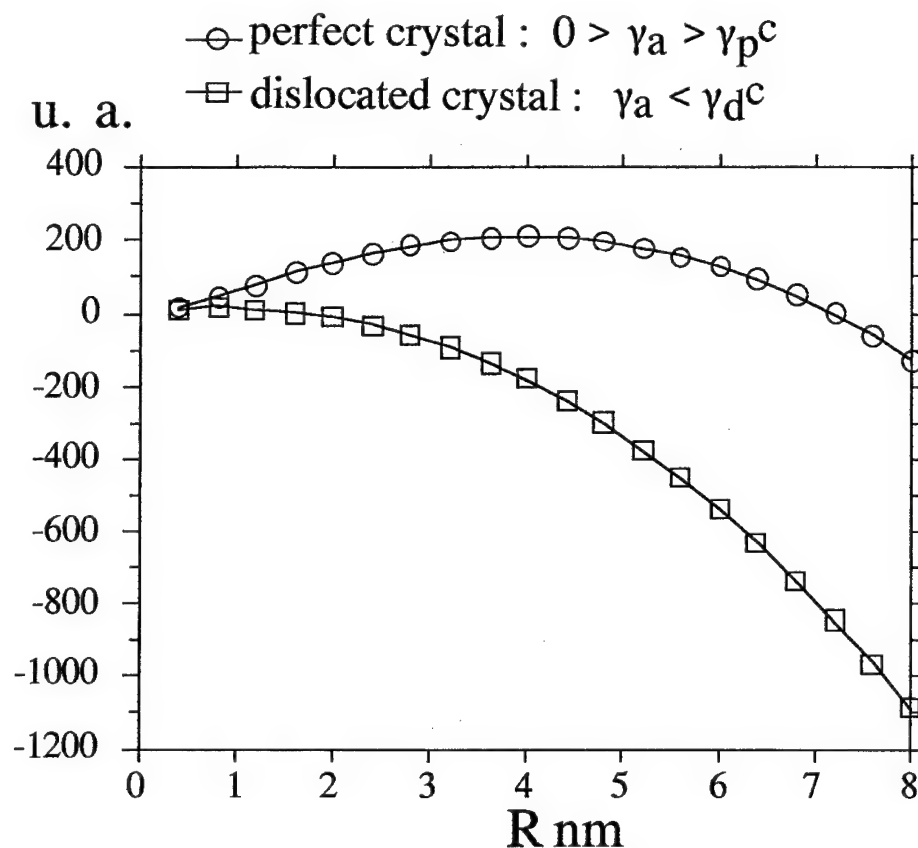


FIGURE 4 Plot of  $W(\gamma_a, R)$  in a perfect and in a dislocated crystal for an apparent stacking fault energy

$\gamma_a = 0.2 \mu b$

(a) perfect crystal:  $0 > \gamma_a > \gamma_p^c$

(b) dislocated crystal:  $\gamma_a < \gamma_d^c$

### 3.1 The Effect of Dislocations on non Stoichiometry in $YBa_2Cu_3O_{7-\delta}$

Yttrium barium copper oxides exist in various range of compositions with different CuO contents. In particular 124 compound  $YBa_2Cu_4O_8$  can be obtained by the intercalation, in the 123 matrix, of a CuO layer on (001) planes assisted by a shear  $a/2[010]$ . The periodicity of such an intercalation along the c axis yields to the formation of various compounds : 124, 127... The elementary process i.e. the intercalation of one CuO layer is associated to the formation of a so called  $1/6[031]$  'stacking fault'. This type of defect is often observed in bulk 123 as well as in thin films. An embryo of such a new phase is then limited by a dislocation loop with Burgers vector  $1/6[031]$  which erases the shear of the matrix as well as the dilatation  $c/6$  due to the additional CuO layer (cf Figure 3a).

The energy associated to the precipitation of a platelet of one atomic layer of CuO, assimilated to a disc of radius R, using isotropic elasticity, can be written as:

$$W(\gamma_a, R) = R\mu b^2/2(1-\nu) \ln(2R/r_0) + \pi R^2 \gamma_a = K_p R \ln(2R/r_0) + \pi R^2 \gamma_a$$

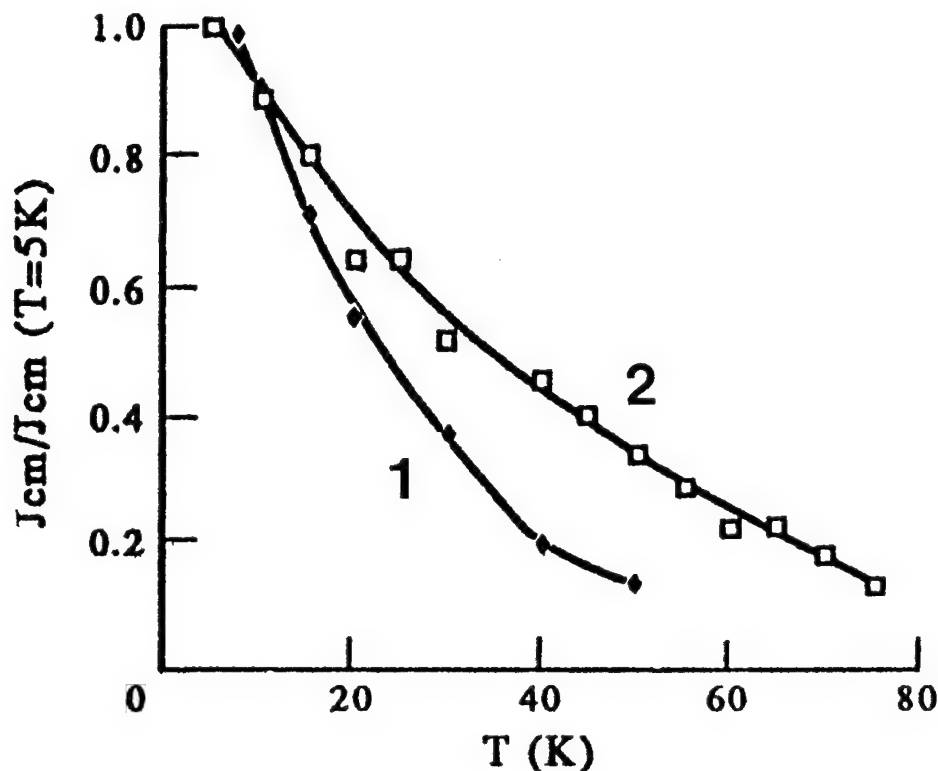
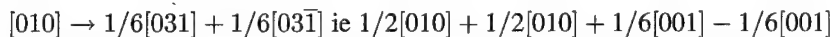


FIGURE 5 Temperature dependance of  $J_c$  for  $\text{YBa}_2\text{Cu}_3\text{O}_7$  oriented powder (from 21)  
 (1): standard powder, (2): powder with a high density of dislocations

where the first term is the strain energy of the partial dislocation loop ( $b = 1/6[031]$ ) bounding the CuO layer, the second one is the energy associated to the 'stacking fault' with surface energy  $\gamma_a$ . This apparent 'stacking fault' energy  $\gamma_a$  is the sum of the interface energy of the CuO layer with the host matrix  $\gamma_e$  and the difference in free energy per surface unit  $\Delta F = (F_2 - F_1)$  between the free energy  $F_2$  of the precipitated state and the free energy  $F_1$  of the unprecipitated state.

A critical stacking fault  $\gamma_p^c = -K_p/2\pi\epsilon_0$  can be defined, so that for  $\gamma_a < \gamma_p^c$ ,  $W(\gamma_a, R)$  is always negative: below this critical value of the apparent stacking fault energy, a CuO layer is spontaneously nucleated in a 123 matrix. For  $\gamma_p^c < \gamma_a < 0$ ,  $W(\gamma_a, R)$  is not a monotonous function of  $R$ . When  $\gamma_a$  is positive,  $W(\gamma_a, R)$  is positive whatever the values of  $R$ : then the CuO layer is unstable unless additional thermodynamic constraints are applied to the system (Figure 4).

Such a precipitation can be also promoted on pre existing dislocation with  $\langle 100 \rangle$  Burgers vectors following the dissociation reaction:



The precipitation of a platelet of one atomic layer of CuO, assimilated to a disc of radius  $R$ , leads to the replacement of a perfect dislocation segment of length  $2R$  by a dissociated one bounding a disc of stacking fault of radius  $R$  (Figure 3b). It can be shown<sup>13</sup> that, in the same way as in the preceding section, this energy can be formally written as:

$$W_d(\gamma_a, R) = K_d R \ln(2R/r_0) + \pi R^2 \gamma_a$$

Computations show that  $K_d \approx K_p/3$ . A critical stacking fault energy can be defined here again as:  $\gamma_d^c = -K_d/2\pi r_0$  with  $\gamma_d^c \approx \gamma_p^c/3$ . Then for the same thermodynamical conditions defined by the value of  $\gamma_a$  ( $\gamma_a < 0$ ), an additional CuO layer can be unstable in a perfect crystal and stable in a dislocated crystal (Figure 4). This analysis shows that pre-existing dislocations provide sites for nucleation of additional CuO layers and that high temperature treatments can convert clean dislocation cores into non stoichiometric cores as soon as CuO diffusion is efficient.

### 3.2 The Effect of Dislocations on the Pinning of Vortices in $YBa_2Cu_3O_{7-\delta}$

High  $T_c$  superconductors ceramics are characterized by very small correlation distances between superconducting carriers: 0.4 nm in the [001] direction and 3.1 nm in the perpendicular directions for  $YBa_2Cu_3O_{7-\delta}$ .<sup>14</sup> Since any defect which is associated to a disturbed part of crystal of the order of  $\xi$  can be efficient in the core pinning of flux lines, this put forward the possible influence of lattice defects, as dislocations, on superconducting properties in such materials. Furthermore dislocations have the same cylindrical symmetry as vortices and are potential defects for the pinning of fluxoids in two ways: i) strain effects: coupling of strain fields of dislocations and vortices, as well as electronic effects associated to local pressure variations in dislocation cores, ii) stoichiometry effects: stoichiometry can be locally affected at dislocation core (see above section), leading to a local change in  $T_c$  since  $T_c$  depends drastically on stoichiometry.<sup>15</sup>

Neglecting the coupling between electronic effects (see for example)<sup>16</sup> and the stress field of dislocation, the interaction energy between a dislocation and an infinitesimal length of vortex distant of  $r$  can be formally written as:<sup>19</sup>

$$E_{int} = E_s + E_i = -P_{ij}\epsilon_{ij}(r) - \epsilon_{ij}(r)\alpha_{ijkl}\epsilon_{kl}(r)$$

where  $E_s$  is the size effect due to the volume change of the vortex compared to the superconducting state and  $E_i$  is the inhomogeneity interaction due to the change in elastic constant between the vortex and the matrix ( $P_{ij}$ : dipole tensor of the vortex,  $\epsilon_{ij}(r)$ : strain induced by dislocation at  $r$ ,  $\alpha_{ijkl}$ : dielastic polarisability which contributes to the change in elastic constants).

Indeed dislocation effects on physical properties have been observed (increase of critical current ( $J_c$ )) after high temperature deformation of melt textured YBCO<sup>17</sup> and after specific processing of ceramic materials.<sup>18</sup> However in these experiments where dislocations are nucleated at high temperature, it is difficult to separate the effect of strain from the effect of non local stoichiometry. To separate these two contributions, dislocations were introduced at room temperature in ceramic material in the (001) plane<sup>20</sup> and the powder characterized before and after the treatment by magnetic measurements.<sup>21</sup> The introduction of these dislocations has no significant influence on relaxation for field parallel to the  $c$  axis. However for field in the (001) plane dislocation seem to act as efficient pinning center for vortices moving along the (001) plane: the decrease of  $J_c$  as a function of temperature is lower for dislocated powders (Figure 5).

#### 4 CONCLUSION

Extreme mechanical testing conditions can promote plasticity in ceramic materials at low temperature and high stress. Using uniaxial compression under confining pressure, plasticity by dislocation glide can be induced. This technique is useful in deriving the deformation mechanisms operating below the usual brittle-ductile transition temperature, for example in hetero-epitaxial thin films. Glide configuration of dislocations are obtained, so that intrinsic characteristics of dislocations can be derived. In this temperature range, dislocation mobilities are found to be controlled by core structure and Peierls mechanisms. Controlled deformation substructures can be used also to modify physical properties of materials. Indeed physical properties of HTc superconductors depend strongly on microstructure: grain boundaries, microcracks, local fluctuations of oxygen content, dislocations, stacking faults... Dislocations have been found to act as pinning centers. However better knowledge of pinning mechanisms and plastic deformation properties are needed in this class of materials in order to improve critical currents.

#### REFERENCES

1. T. Bretheau, J. Castaing, J. Rabier and P. Veyssière, *Adv. in Physics* **28**, 835 (1979).
2. J. Castaing, P. Veyssière, L. P. Kubin and J. Rabier, *Phil. Mag.* **A44**, 1407 (1981).
3. P. Boivin, J. Rabier, H. Garem, *Phil. Mag.* **A61**, 647 (1990).
4. J. Castaing, J. Cadoz and S. H. Kirby, *J. Amer. Ceram. Soc.* **64**, 504 (1981).
5. P. Veyssière, S. H. Kirby and J. Rabier, *J. Physique Colloq.* **41**, C6-175 (1980).
6. P. Teracher, *Thèse*, Université de Poitiers (1990).
7. P. Teracher, H. Garem and J. Rabier, *ICSMAG*, Brandon, R. Chain and A. Rosen eds (Freund Pub. Co. 1991) 217.
8. P. B. Hirsch, *Oral Communication* at 3th Int. Cong. on Crystallography, Cambridge (1960).
9. R. J. Gaboriaud, M. Boisson and J. Grilhé, *J. Phys.* **C8**, 3499 (1975).
10. N. H. Andersen, K. Clausen, M. A. Hackett, W. Hayes, M. T. Hutchings, J. E. Mac Donald and R. Osborn, *Physica* **B136**, 315 (1986).
11. S. Naka, *Thèse* Université Paris-Sud (1983).
12. J. Rabier and M. F. Denanot, *Phil. Mag.* **A65**, 427 (1992).
13. J. Rabier, P. D. Tall and M. F. Denanot, *Phil. Mag.* **A67**, 1021 (1993).
14. W. J. Gallagher, T. K. Worthington, T. R. Dinger, F. Holtzberg, D. L. Kaiser and R. L. Sandstrom, *Physica* **B148**, 221 (1987).
15. R. J. Cava, B. Batlogg, S. A. Sunshine, T. Siegrist, R. M. Fleming, K. Rabe, L. F. Schneemyer, D. W. Murphy, R. B. Van Dover, P. K. Gallagher, S. H. Glarum, S. Nakahara, R. C. Farrow, J. J. Krajewski, S. M. Zahurak, J. V. Waszczak, J. H. Marshall, P. Marsh, L. W. Rupp, W. F. Peck and E. A. Rietman, *Physica C* **153-155**, 560 (1988).
16. F. Guinea, *Europhys. Lett.* **7**, 549 (1988).
17. V. Selvamanickam, M. Mironova, S. Son and K. Salama, *Physica* **C208**, 238 (1993).
18. X. Zheng, H. Kuriyaki, K. Hirakawa, E. Tanaka and Y. Tomokito, *Jpn J. Appl. Phys.* **31**, L1236 (1992).
19. M. P. Puls, *Phil. Mag.* **A51**, 893 (1985).
20. J. Rabier and M. F. Denanot, *Rev. Phys. Appl.* **25**, 55 (1990).
21. C. Aguilon-Levillain, S. Senoussi and H. Gu, *J. Phys. Chem. Solids* **54**, 477 (1993).

## PLASTIC DEFORMATION OF $\text{CaF}_2$ SINGLE CRYSTALS

A. MUÑOZ, A. DOMINGUEZ RODRIGUEZ and J. CASTAING\*

*Dept. Física Materia Condensada & ICMSE, Apartado 1065, 41080 Sevilla (Spain)*

$\text{CaF}_2$  single crystals have been deformed in compression along various axis in order to determine their slip systems. Strong plastic anisotropy was found below 600°C. The slip planes are {100}, {111} and {110}, the CRSS increasing from the first to the last.

*Key words:* plastic anisotropy; dislocation, slip plane,  $\text{CaF}_2$ .

### 1 INTRODUCTION

There have been many studies on the plastic deformation of  $\text{UO}_2$  and cubic zirconia because of their important applications. These compounds have the crystalline structure of  $\text{CaF}_2$ . They all have the same {110} slip direction, but display contrasted behaviours as for their slip planes [1–2]. This is ascribed to the large amount of point defects related to non-stoichiometry in  $\text{UO}_2$  and to stabilising additives ( $\text{CaO}$ ,  $\text{MgO}$ , . . .) in zirconia. In order to have a basis for the understanding of the plastic behaviour of  $\text{CaF}_2$  structure crystals, we have performed mechanical test experiments on  $\text{CaF}_2$  single crystals to determine the different slip planes which can be activated between the brittle to ductile transition and the high temperature isotropic regime ( $T \sim T_M/2$ ;  $T_M = 1418^\circ\text{C}$ , melting temperature).

### 2 EXPERIMENTAL TECHNIQUES

High quality  $\text{CaF}_2$  single crystals were provided by SOREM (Pau, France). There were cut as parallelepipeds of about  $3 \times 3 \times 6 \text{ mm}^3$  size with various orientations allowing us to favour different slip systems, as depicted in the following table.

compression axis	lateral faces	{ 100 } Schmid factor	{ 110 } Schmid factor	{ 111 } Schmid factor
{001}	{110}, {110}	0.00	0.50	0.41
{115}	{552}, {110}	0.26	0.44	0.45
{113}	{332}, {110}	0.39	0.36	0.45
{112}	{111}, {110}	0.47	0.25	0.41
{011}	{111}, {211}	0.35	0.25	0.41

Compression tests were conducted at a constant strain rate of about  $1.4 \times 10^{-5} \text{ s}^{-1}$  in air, at temperatures between 20°C and 600°C. The critical resolved shear stress (CRSS) were taken at the off-set from the initial linear behaviour.

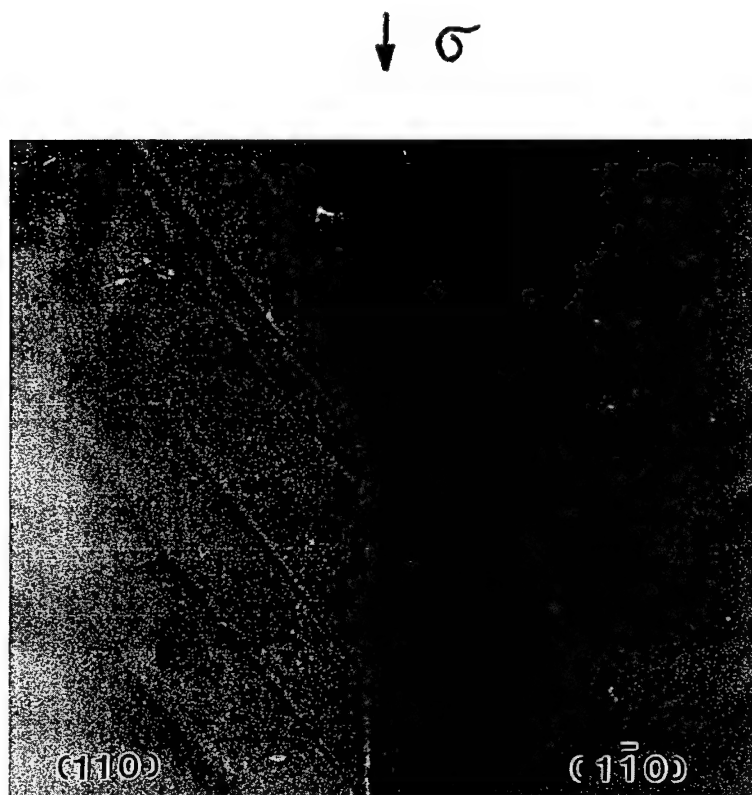


FIGURE 1 simultaneous observation of the slip lines in two orthogonal faces of a deformed specimen.  $T = 597^\circ\text{C}$ . Total strain = 0.85%. The slip lines are at an angle of about  $54^\circ 7'$  from the  $\langle 001 \rangle$  compression axis, corresponding to  $\{110\}$  slip planes.

The slip planes which were activated were deduced from the optical observations of the surface of the specimens.

### 3 RESULTS AND DISCUSSION

Specimens deformed at room temperature were generally brittle, except in some cases where  $\{100\}$  slip was activated.<sup>2</sup> This indicates that for our  $\text{CaF}_2$  crystals, the brittle to ductile temperature is around  $20^\circ\text{C}$ , well below previous results,<sup>3-6</sup> probably because we used high quality crystals.

Whatever the specimen orientations, the stress strain curves show gradual changes from the initial linear stage ("elastic" behaviour) to the plastic yielding which displays large work-hardening rates decreasing with the deformation.<sup>2</sup> The understanding of the details of the mechanisms, at all stages of the stress strain curves, is worth further investigations.

The observation of the faces of the specimens (Figure 1) allowed us to determine the slip planes which were activated, the slip direction being  $\langle 110 \rangle$ . We found the  $\{100\}$  plane at all temperatures for the stress  $\sigma$  parallel to  $\langle 113 \rangle$ ,  $\langle 112 \rangle$  and  $\langle 011 \rangle$ . For  $\sigma // \langle 115 \rangle$ ,  $\{100\}$  is activated below  $400^\circ\text{C}$  in spite of its small Schmid factor (see table) indicating that it has

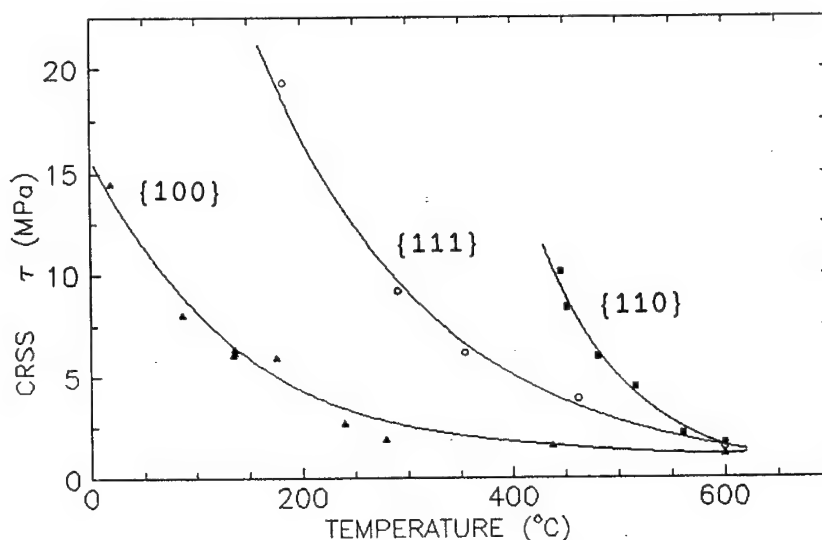


FIGURE 2 Critical resolved shear stress (CRSS) at the onset of bulk deformation, as a function of temperature for the various slip planes.

the lowest CRSS, as already found previously.<sup>3-6</sup> Above a temperature of 400°C, {111} is observed suggesting that it has a CRSS lower than the one of {110}, contrary to what has been admitted until now. For  $\sigma//\langle 001 \rangle$ , the primary slip plane {100} cannot be activated (see table); below 400°C, we observed {111} confirming that it is the secondary slip plane in high purity  $\text{CaF}_2$ . The CRSS values for the various slip planes are shown in Figure 2. At 600°C (0.52  $T_M$ ) the plasticity is isotropic, the choice of the slip plane being determined by the Schmid factor (see table).

As usual, we consider three criteria to explain plastic anisotropy: (i) dislocation elastic properties, (ii) Peierls force, (iii) electrostatic interactions during dislocation glide. Only the third one is able to explain the observations for  $\text{CaF}_2$ .<sup>1</sup> Obviously, it cannot be applied so directly to zirconia and to  $\text{UO}_2$  which do not follow the same sequence of slip planes with increasing CRSS values.

#### ACKNOWLEDGEMENTS

The work was partly supported by the PICASSO program of scientific exchanges between Spain and France.  
\*CNRS & Université EVE, Blvd Coquibus, 91025 Evry Cedex (France)

#### REFERENCES

1. A. Domínguez Rodríguez, A. H. Heuer and J. Castaing, *Rad. Effects & Def. in Solids* **119** - **121** (1991) 759.
2. A. Muñoz, A. Domínguez Rodríguez and J. Castaing, *J. Mat. Sci.* **29** (1994) 6207.
3. W. L. Phillips, *J. Amer. Ceram. Soc.* **44** (1961) 499.
4. A. G. Evans, P. L. Pratt, *Phil. Mag.* **20** (1969) 1213.
5. A. G. Evans, P. L. Pratt, *Phil. Mag.* **21** (1970) 951.
6. V. Baudinaud, Thesis, Université de Poitiers, France (1978).

## A MATERIAL SCIENCE APPROACH FOR THE EVALUATION OF THE RHEOLOGICAL STATE INTO THE EARTH'S LOWER MANTLE

F. VALLIANATOS,<sup>1</sup> K. EFTAXIAS<sup>2</sup> AND A. VASSILIKOU-DOVA<sup>2</sup>

<sup>1</sup>Technical University of Crete, Chania, 73100, Crete, Greece; <sup>2</sup>University of Athens,  
Section of Solid State Physics, Greece

In the present paper, making the crucial assumption that the rheological state of the lower mantle silicate materials controlled by creep mechanism, we study: (i) the upper and lower limits in the depth (i.e. temperature and pressure) variation of the activation volume for creep and (ii) the lower permissible isoviscous temperature profile.

The calculation indicates that: (i) the activation volume decreases by almost 50% from the top to the bottom of the lower mantle, (ii) it is impossible to maintain a rheological state in which both isoviscosity and adiabaticity can *precisely* exist, throughout the lower mantle.

*Key words:* rheology, creep, silicates, mantle, viscosity.

### 1 INTRODUCTION

The rheological parameters of the Earth's interior are critical in our understanding of the Earth's evolution and among others the viscosity is a crucial one, in any speculation of mantle's convection.<sup>1</sup>

In order to calculate the rheological parameters of the Earth's lower mantle we use a solid state physics approach, accepting that mantle must flow by solid state creep.<sup>2</sup> To estimate, the viscosity  $\eta$  at a pressure  $P$  and temperature  $T$ , the following equation (suggested by creep experiments<sup>3</sup>) is usually used:  $\eta = \eta_0^* \exp(g^{\text{act}}/kT)$ ,<sup>1</sup> where  $\eta_0^*$  is a preexponential factor,  $k$  is Boltzman's constant and  $g^{\text{act}}$  is the activation Gibbs energy.

The viscosity should depend on temperature (through the activation energy) and pressure (through the activation volume). In order to estimate the Gibbs activation energy and the activation volume we rely in a thermodynamic model termed as  $cB\Omega$ .<sup>4</sup> This model results from thermodynamical considerations that lead to a connection between  $g^{\text{act}}$  and the macroscopic properties of a solid.

It is the purpose of this paper i) to apply this model in order to estimate, the boundary values of activation volume in the Earth's Lower Mantle and ii) to estimate the lower bound of the isoviscous temperature profile and compare it with the adiabatic one.

### 2 THE $cB\Omega$ MODEL

According to the so-called  $cB\Omega$  model<sup>4</sup> the Gibbs energy  $g^{\text{act}}$  is given by:  $g^{\text{act}} = c^{\text{act}} B \Omega$ ,<sup>2</sup> where  $B$  is the isothermal bulk modulus,  $\Omega$  is the mean atomic volume and  $c^{\text{act}}$  is a factor which, for a given host lattice is *practically* temperature independent, under the well justified assumption that the 'isochoric' defect entropy does not change significantly with temperature.<sup>4</sup> The pressure variation of  $g^{\text{act}}$  has been studied,<sup>4</sup> using the value of the quantity  $\kappa^c$  defined by:  $\kappa^c = -d \ln c^{\text{act}} / dP|_T$ . They concluded that if the compressibility  $\kappa^{\text{act}} = -d \ln V^{\text{act}} / dP|_T$  of the activation volume  $V^{\text{act}}$  has a value which is, at most a few



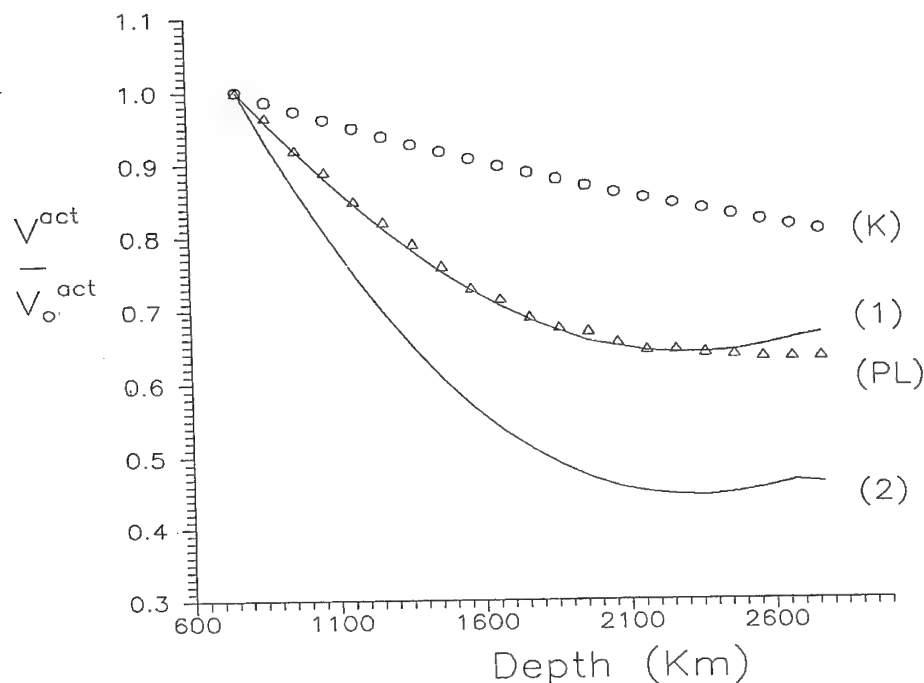


FIGURE 1 Variation of activation volume for creep with depth for various models.  $V^{\text{act}}/V_o^{\text{act}} = 1$  at 770 Km: (K) Karato (1981a, b); (PL) Poirier and Liebermann (1984). Lines (1) and (2) represent the upper (lower) boundary limits in the values of the depth variation of the activation volume obtained using  $cB\Omega$  model.

times larger than the bulk compressibility  $\kappa (= 1/B)$  then the factor is independent of pressure in pressure range  $\Delta P$  for which  $(\Delta P/B) < 0.1$ . It was also pointed out that generally  $0 \leq \kappa^c \leq \kappa$ , and at very high pressures i.e.  $(\Delta P/B) > 0.1$ , a decrease of the value of  $c^{\text{act}}$  should be considered; the maximum pressure variation of  $c^{\text{act}}$  can be estimated, when  $\kappa^c = \kappa$  and then  $c^{\text{act}}$  can be expressed by:

$$c^{\text{act}}(P) = c_o^{\text{act}} \exp\left(\int_{P_o}^P -\kappa dP\right) \quad (3)$$

where  $c^{\text{act}}(P)$  and  $c_o^{\text{act}}$  denotes the values of  $c^{\text{act}}$  at pressures  $P$  and  $P_o$  respectively.

We recall that the reliability of eq(2) has already been checked in various categories of solids and liquids and different processes.<sup>4,5,6</sup>

### 3 GEOPHYSICAL APPLICATION OF THE $cB\Omega$ MODEL

*Boundaries in the variation of the activation volume for creep within the Earth's Lower Mantle* By differentiating eq(2), in respect to pressure and recalling that  $V^{\text{act}} = dg^{\text{act}}/dP|_T$  we get:

$$V^{\text{act}} = c^{\text{act}}\Omega\left(\frac{dB}{dP}\bigg|_T - 1\right) - \kappa^c c^{\text{act}} B\Omega \quad (4)$$

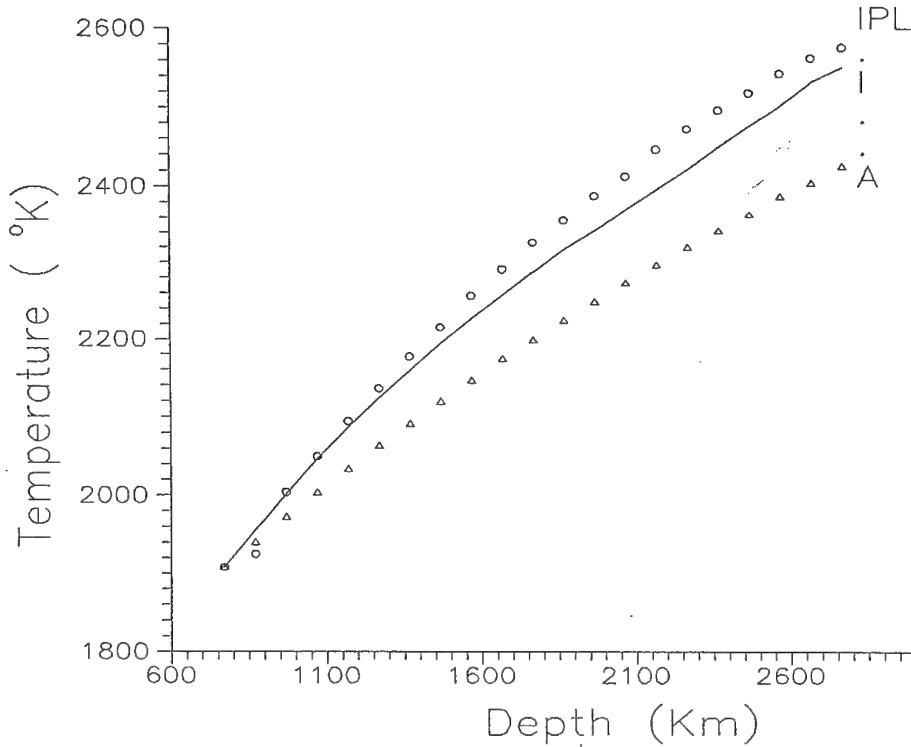


FIGURE 2 The lower permissible value of isoviscous geotherm (I) calculated from eq.(10) with  $\rho$  and B from P.R.E.M. The adiabat is taken from Brown and Shankland (1981). The curve IPL is the isoviscous geotherm calculated by Poirier and Liebermann (1984).

In order to estimate the maximum ( $V_m^{\text{act}}$ ) and the lower ( $V_1^{\text{act}}$ ) values of  $V^{\text{act}}$ , for each depth of the lower mantle we use the aforementioned constraints for  $\kappa^c$  i.e.  $0 \leq \kappa^c \leq \kappa$ . An application of eq.(4) gives, for  $\kappa^c = 0$ :

$$\frac{V_m^{\text{act}}}{V_{m0}^{\text{act}}} = \frac{\Omega \left( \frac{dB}{dP} \right)_T - 1}{\Omega_0 \left( \frac{dB}{dP} \right)_0 - 1} = \frac{\rho_0 \left( \frac{dB}{dP} \right)_T - 1}{\rho \left( \frac{dB}{dP} \right)_0 - 1} \quad (5)$$

A combination of eq(4) with eq(3) leads to an expression for  $V^{\text{act}}$ , when  $\kappa^c = \kappa$

$$\frac{V_1^{\text{act}}}{V_{10}^{\text{act}}} = \frac{\Omega \left( \frac{dB}{dP} \right)_T - 2}{\Omega_0 \left( \frac{dB}{dP} \right)_0 - 2} = \exp \left( \int_{Z_0}^Z -\kappa(z) \, dP(z) \right) \quad (6)$$

where  $\Omega$ ,  $\rho$ ,  $dB/dP$  denote the mean molecular volume, the density and the pressure derivative of bulk modulus, in a certain depth of the lower mantle, respectively; those labelled with the subscript 'o' correspond to the values at the top of the lower mantle. The values of  $\rho$  and  $dB/dP$  are deduced from the seismic velocities available at various depths when the Preliminary Reference Earth Model<sup>7</sup> is employed. Figure 1 shows the two ratios and  $V_m^{\text{act}}/V_{m0}^{\text{act}}$  versus depth in the Earth's lower mantle.

*Isoviscosity and adiabaticity in the Lower Mantle* We now proceed to the discussion of the isoviscosity of the lower mantle by applying the  $cB\Omega$  model. A combination of eqs(1) and (2) leads to an expression for the viscosity  $\eta$ :

$$\eta = \eta_0^* \exp(c^{\text{act}} B \Omega / kT) \quad (7)$$

An insertion of the definition of isoviscous temperature into eq(7) leads to:

$$T_{\text{isov}} = (B/B_0)(\rho_0/\rho)(c^{\text{act}}/c_0^{\text{act}})T_0 \quad (8)$$

In order to obtain the lower value of  $T_{\text{isov}}$  we use eq(3) for the depth variation of  $c^{\text{act}}$  (i.e.  $\frac{\kappa^c = \kappa}{z}$ ) and we get:

$$T_{1,\text{isov}} = (B/B_0)(\rho_0/\rho)T_0 \exp\left(\int_{z_0}^z -\kappa(z)dP(z)\right) \quad (9)$$

In Figure 2 we have plotted  $T_{1,\text{isov}}$  calculated from eq(9) and compared it with the adiabatic temperature  $T_{\text{ad}}$  from the lower mantle derived by Brown and Shankland.<sup>8</sup>

#### 4 DISCUSSION

The present paper deals with an application of a model from Solid State Physics to a Geophysical problem.

- a) We have apply the  $cB\Omega$  model into the estimation of the upper and lower bounds of the ratios  $V^{\text{act}}/V_0^{\text{act}}$ , versus depth in the Earth's lower mantle. It is found that the activation volume decreases by almost 50% from the top to the bottom of the lower mantle. This variation is in agreement with the results of Poirier and Liebermann<sup>9</sup> but disagree with those of Karato.<sup>10</sup> The compatibility of our results to those of Poirier and Liebermann can also be seen as follows: in order to estimate the ratio  $V^{\text{act}}/V_0^{\text{act}}$  the latter authors used an expression which connect  $\kappa^{\text{act}}$  with the bulk modulus  $B$  and the thermal Gruneisen parameter  $\gamma$ . Their expression, however can be derived in the frame of  $cB\Omega$  model as a limiting case for  $\kappa^c = 0$ .<sup>11</sup> On the other hand Karato<sup>10</sup> arbitrarily assumed that  $\kappa^{\text{act}} = \kappa$  which is valid only when  $dB/dP$  is constant, i.e. in the case of *quasi-harmonic* (QA) approximation in solids. In the case of real solids however the quantity  $dB/dP$  varies significant with pressure<sup>12</sup> and a rough estimation of the quantity  $\kappa^{\text{act}}/\kappa$  gives for olivine values of the order of 2.3 and 4 for  $\kappa^c = 0$  and  $\kappa$  respectively. The latter difference might explain why the values obtained by Karato<sup>10</sup> for the ratio  $V^{\text{act}}/V_0^{\text{act}}$ , lie outside of the range determined in the present paper.
- b) A second result, is the estimation of the lower permissible value of isoviscous temperature throughout the lower mantle. It is found that it is impossible to maintain, throughout the lower mantle, a state in which both isoviscosity and adiabaticity can exist as it was usually assumed.<sup>13</sup> This result agrees with that obtained by Poirier and Liebermann.<sup>9</sup> The latter can be shown as follows: in order to estimate  $T_{\text{isov}}$  they use the equation<sup>3</sup>:  $n = n_0 \exp(\alpha T_M/k T)$  (10) where  $n_0$  a proexponential factor,  $\alpha$  an empirical constant and  $T_m$  the melting temperature. Equation (10) is a straightforward result of the empirical law that the experimental activation enthalpy scales with melting temperature i.e  $h^{\text{act}} \approx \alpha T_M$ . Such an empirical law however has been already explained<sup>11</sup> in the frame of the  $cB\Omega$  model, which also enables the understanding of the value of the proportionality factor  $\alpha$ .

## REFERENCES

1. R. Teissieyre, *The evolving earth and its Lithospheric stresses*, (Elsevier, Amsterdam, 1993) pp. 331.
2. D. J. Stevenson and J. S. Turner. *Geophys. Space Phys.*, **8**, 145 (1979).
3. J. Weertman. *Rev. Geophys. Space Phys.*, **8**, 145 (1970).
4. P. Varotsos and K. Alexopoulos. *Thermodynamics of point defects and their relation with bulk properties*, (North Holland, Amsterdam, 1986) pp. 451.
5. F. Vallianatos and K. Eftaxias. *Acta Geophys. Polonica*, **39/2**, 233 (1991).
6. F. Vallianatos and K. Eftaxias. *Acta Geoph. Polonica*, **42**, 1 (1994).
7. A. M. Dziewonski and D. L. Anderson. *Phys. Earth Planet. Inter.*, **25**, 297 (1981).
8. J. M. Brown and T. J. Shankland. *Geophys. J. R. Astron. Soc.*, **66**, 579 (1979).
9. J. P. Poirier and R. C. Lieberman. *Phys. Earth Planet. Inter.*, **35**, 283 (1984).
10. S. Karato. *Phys. Earth Planet. Inter.*, **25**, 38 (1981).
11. F. Vallianatos and K. Eftaxias. *Phys. Earth Planet. Inter.*, **71**, 141 (1992).
12. P. Vinet, H. J. Rose, J. Ferrante and J. R. Smith. *J. Phys. Condens. Matter*, **1**, 1941 (1989).
13. T. Spohn and G. Schubert. *J. Geophys. Res.*, **87**, 4682 (1982).

## DIFFUSION-CONTROLLED TRANSITORY CREEP IN BINARY OXIDES

M. JIMÉNEZ-MELENDO, A. DOMÍNGUEZ-RODRÍGUEZ and J. CASTAING\*

*Departamento de Física de la Materia Condensada. Aptdo. 1065. 41080 Sevilla (Spain)*

*\*Laboratoire de Physique des Matériaux, CNRS-Bellevue, 92195 Meudon (France)*

Valuable information about minority point defects in binary oxides can be obtained by using fast temperature (T) and oxygen partial pressure ( $P_{O_2}$ ) changes during high temperature creep deformation. A creep transient is established after a T or  $P_{O_2}$  change, which reflects the evolution of the point defect concentration responsible for the diffusion of the slowest species to the new equilibrium value, allowing us the determination of the chemical diffusion coefficient and the migration energy of these defects.

*Key words:* creep, diffusion, oxide, point defect.

### 1 INTRODUCTION

At elevated temperatures, different physical and chemical properties of ceramic oxides are related to the point defect concentrations that they contain. In simple oxides, the thermodynamic parameters temperature T and oxygen chemical activity (oxygen partial pressure,  $P_{O_2}$ ) determine the point defect equilibria.

Different techniques (thermogravimetry, ionic and electrical conductivity, etc.) are sensitive to the majority point defects. However, observations of the minority point defects are rather difficult because of their very low concentrations. It has been shown<sup>1</sup> that, at high temperatures, the steady state strain rate  $\dot{\epsilon}$  is proportional to the diffusion coefficient of the slowest species  $D_i$  when transport of matter is the ultimate rate-controlling mechanism. If a fast T or  $P_{O_2}$  change is performed during steady state creep deformation, a transitory creep<sup>2</sup> is induced, which characterizes the evolution of the minority point defect responsible for  $D_i$  towards the new equilibrium value. Analysis of this creep transient can bring information about the formation and migration of these defects.

### 2 ANALYSIS OF CREEP TRANSIENTS

At high temperatures, the strain rate  $\dot{\epsilon}$  is usually controlled by mass transport (diffusional creep, grain boundary sliding, climb recovery creep, etc.) and can be written:

$$\dot{\epsilon} = A \cdot \sigma^n \cdot D_i$$

where A is a constant,  $\sigma$  the stress and  $D_i$  the diffusion coefficient of the slowest species. For the transition metal oxides (NiO, CoO, Cu<sub>2</sub>O, etc.) and Al<sub>2</sub>O<sub>3</sub>, the slowest moving atoms are oxygen, whereas they are cations for Y<sub>2</sub>O<sub>3</sub>-stabilized ZrO<sub>2</sub>.  $D_i$  has the form:

$$D_i = B \cdot [d] \cdot D^d$$

where B is a constant, and [d] and  $D^d$  are the concentration and the diffusion coefficient of the point defects, respectively.

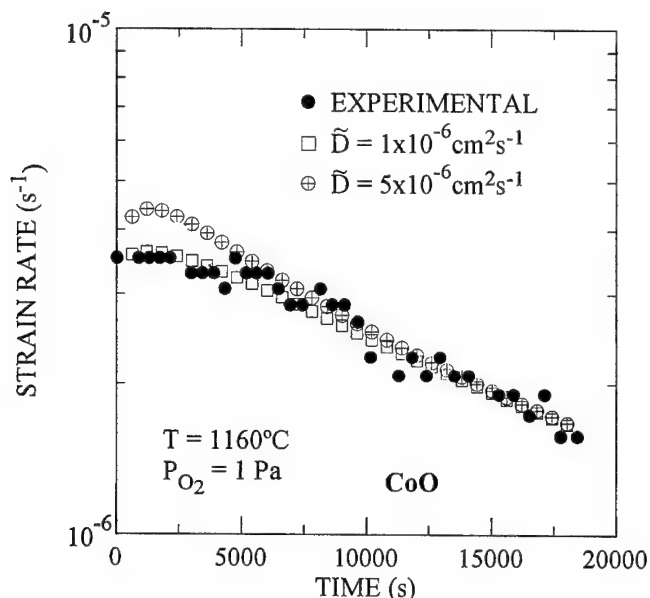


FIGURE 1 Creep transient after a temperature change plotted as  $\log \dot{\epsilon}$  vs  $t$  for a CoO single crystal. Comparison of the experiments with the calculated point for various  $\tilde{D}$ .

If a fast  $P_{O_2}$  change is performed during creep deformation, a transitory state  $\dot{\epsilon}(t)$  is established due to the evolution of  $[d]$  from an initial value ( $\dot{\epsilon}_1 \propto [d_1]$  at  $t = 0$ ) to a final one ( $\dot{\epsilon}_2 \propto [d_2]$  for  $t \geq t_{eq}$ ). The analysis<sup>3</sup> of  $\dot{\epsilon}(t)$  between  $t = 0$  and  $t = t_{eq}$  allow us to the determination of the chemical diffusion coefficient  $\tilde{D}$ , which characterizes the rate of equilibrium of the minority point defect.

The same creep transient is expected after a  $\Delta T$  change, except that the creep rate is increased by a factor  $(T_1/T_2) \cdot \exp(-\Delta H_m \Delta T / k T_1 T_2)$  immediately after the  $T$  step because of the enhancement of the point defect migration rate. The corresponding activation energy  $\Delta H_m$  can be measured from this instantaneous jump of  $\dot{\epsilon}$ .

### 3 RESULTS AND DISCUSSION

Temperature changes have been performed on  $NiO^4$  and  $CoO^5$  single and polycrystals. Figure 1 displays a transitory creep for a CoO single crystal after a  $T$  change on a strain rate  $\dot{\epsilon}$  vs time  $t$  plot, showing the sensitivity in the determination of  $\tilde{D}$ . The chemical diffusion coefficient  $\tilde{D}$  deduced from these experiments were in good agreement with those determined for cation vacancies, the majority defects in these oxides, as shown in Figure 2 for NiO single crystals.

The same behavior has been found in  $CoO^2$  and  $Cu_2O^3$  using  $P_{O_2}$  changes. These results indicate that the change of minority point defects which control the strain rate  $\dot{\epsilon}$  (oxygen vacancies for the oxides mentioned above) is controlled by the diffusion of metal vacancies from/to the surface.

No transients after  $T$  changes were found in  $Y_2O_3$ -stabilized  $ZrO_2$  and  $Al_2O_3$  single crystals, indicating that the concentration of the rate-controlling point defects are fixed by

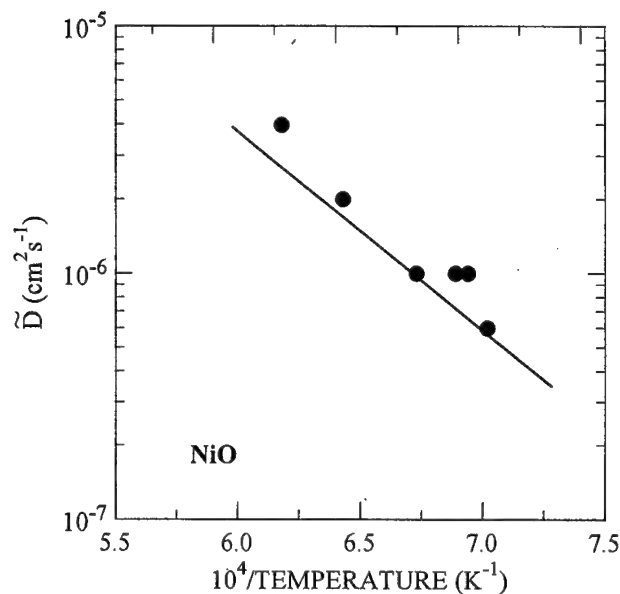


FIGURE 2 Arrhenius plot of chemical diffusion coefficients  $\tilde{D}$  for NiO deduced from transitory creep tests after T changes (black circles) and from electrical conductivity (solid line).

alloying and impurities, respectively. In these conditions, the activation energy found by standard creep experiments can be ascribed to the migration energy of minority point defects.

#### ACKNOWLEDGMENTS

The support of CICYT No. MAT/91-1196-C02 (Ministerio de Educación y Ciencia, Spain) is acknowledged.

#### REFERENCES

1. J. Castaing, C. Monty and A. Domínguez-Rodríguez, *Defects and Diff. Forum* **64/65**, 97 (1989).
2. A. Domínguez-Rodríguez, C. Monty and J. Philibert, *Phil. Mag.* **A46**, 869 (1982).
3. C. Clauss, A. Domínguez-Rodríguez and J. Castaing, *Revue Phys. Appl.* **21**, 343 (1986).
4. M. Jiménez-Melendo, A. Domínguez-Rodríguez and J. Castaing, *J. Phys. Chem. Solids* **52**, 517 (1989).
5. M. Jiménez-Melendo, C. Clauss, A. Domínguez-Rodríguez and J. Castaing, *Ceramic Trans.* vol. 24 (ed. by T. O. Mason and J. L. Routbort, *Am. Ceram. Soc.* Westerville, Ohio), pp. 131-138, 1991.
6. M. Jiménez-Melendo, A. Domínguez-Rodríguez and J. Castaing, *Third Euroceramics*, vol. 3 (ed. by P. Durán and J. F. Fernández, Faenza Edit. Ibérica, Spain), pp. 537-542, 1993.

## CREEP BEHAVIOUR OF 21 MOLE% $\text{Y}_2\text{O}_3$ -FULLY STABILIZED ZIRCONIA SINGLE CRYSTALS

D. GÓMEZ-GARCÍA, J. MARTÍNEZ-FERNÁNDEZ, A. DOMÍNGUEZ-RODRÍGUEZ,  
P. EVENO\* and J. CASTAING\*

*Dpto. de Física de la Materia Condensada—Instituto de Ciencia de Materials,  
Universidad de Sevilla—C.S.I.C. Apdo. 1065.41080—Sevilla, Spain; \*Laboratoire de  
Physique des Matériaux. C.N.R.S. Bellevue, Meudon Cedex France*

Creep tests have been performed on 21 mole% yttria fully stabilized zirconia single crystals between 1400°C and 1800°C. The mechanical parameters measured have been adjusted to a conventional creep law. The temperature dependence of the strain rate has been fitted to a conventional Arrhenius plot. From the stress exponents and activation energies found, it is concluded that there is a remarkable transition in the mechanical behaviour of this solid solution at  $T \cong 1500^\circ\text{C}$ . This behaviour is compared with one found for lower Yttria concentration single crystals, within the full stabilized field.

*Key words:* Y-FSZ, creep, activation energy.

### 1 INTRODUCTION

One of the interests for  $\text{Y}_2\text{O}_3$ -stabilized cubic zirconia (Y-FSZ) comes from its high flow stress at high temperatures.<sup>1</sup> On top of that, plastic deformation is useful because considerable basic information concerning the controlled-diffusion mechanisms can be obtained from these studies.

Several previous papers have been published on the creep mechanical properties of Y-FSZ with low Yttria concentration, like in Ref.<sup>2</sup> However, there exists a lack of corresponding information in the case of High Yttria concentration zirconia solid solutions, especially all aspects regarding their temperature dependence. This work aims at covering this matter.

### 2 EXPERIMENTAL PROCEDURE

Raw samples of 21 mole%-Y-FSZ single crystals grown by skull melting provided a Ceres Corporation; (Masachussets, U.S.A.) were oriented by means of the Laue X-ray backscattering technique and cut into parallelepipeds ( $2.0 \times 2.0 \times 4.5$  mm) in such a way that the longer axis, the loading one, was a  $\langle 112 \rangle$ -direction and the parallel faces were (110) and (111) planes. With this orientation, at the yield point, only one slip system is activated  $\{(001), [110]\}$  with a Schmidt factor of 0.47.<sup>3</sup> The samples were polished mechanically with diamond pastes of different grain sizes up to 3  $\mu\text{m}$ .

Creep tests were carried out in compression using the machine described in reference<sup>4</sup> at temperatures between 1400°C and 1800°C, with strain rates from  $2.10^{-7}\text{s}^{-1}$  to  $3.10^{-6}\text{s}^{-1}$ . In each test, different creep rates were achieved by changing either the load or the temperature. It was never changed both of them at the same time. In order to avoid indentation, silicon carbide pads were interposed between the samples and the rams. The data were recorded as strain rate versus strain.



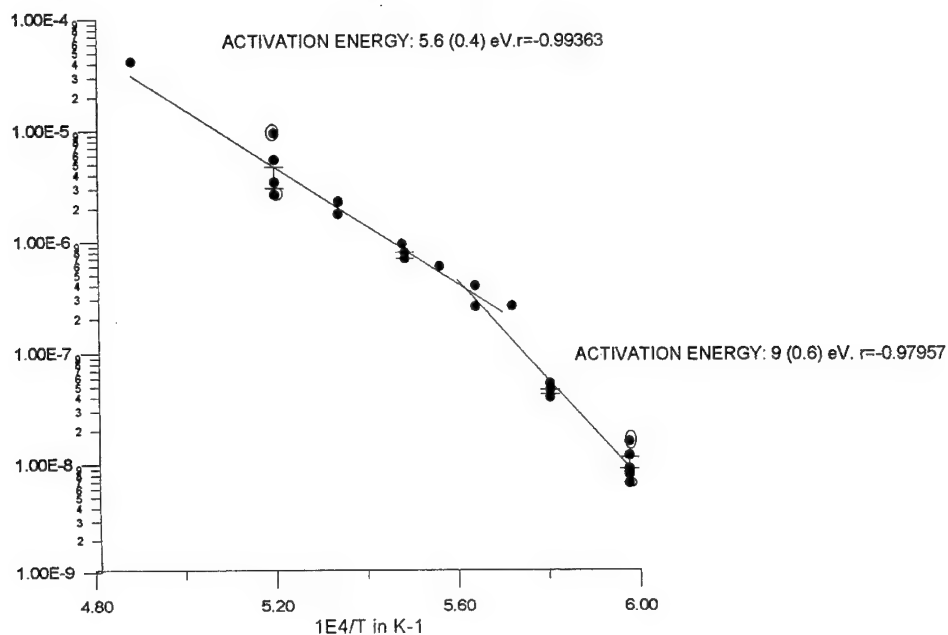


FIGURE 1 Strain rate normalized to a conventional value of 100 MPa versus the inverse of temperature.  
( $\ln \dot{\epsilon}$  vs.  $1/T$ )

### 3 RESULTS AND DISCUSSIONS

The data measured were the steady-state strain rate and the condition of working (The couple  $\sigma$ ,  $T$ ). It was admitted that the mechanical behaviour can be described by the conventional empirical law for creep in single crystals:<sup>5</sup>

$$\dot{\epsilon} = A \frac{\mu b}{kT} \left( \frac{\sigma}{\mu} \right)^n \exp \left( \frac{-Q}{kT} \right) \quad (1)$$

where  $\dot{\epsilon}$  is the strain rate,  $b$  is the Burgers vector for dislocations in YFSZ ( $b = 3.63 \text{ \AA}$ ),  $\mu$  is the shear modulus,  $n$  and  $Q$  are the empirical parameters known as the stress exponent and the activation energy, respectively, and  $A$  is an empirical constant. The rest of the symbols have their conventional meaning. The most interesting information achieved from the data measured are the parameters  $n$  and  $Q$ . They were calculated using three different ways:

$n$  and  $Q$  were calculated by means of jumps of load and temperature, respectively, during the creep tests.

On the other hand, all the stress were normalized to a conventional value (100 MPa) using the stress exponents measured, and the plot  $\ln \dot{\epsilon}$  vs.  $1/T$  was performed. (Figure 1). An additional way was performed in order to measure  $Q$ :

Creep tests were carried out in which the same load was kept all the time, and the temperature was increased progressively from 1400°C up to 1650°C in intervals of 50°C.

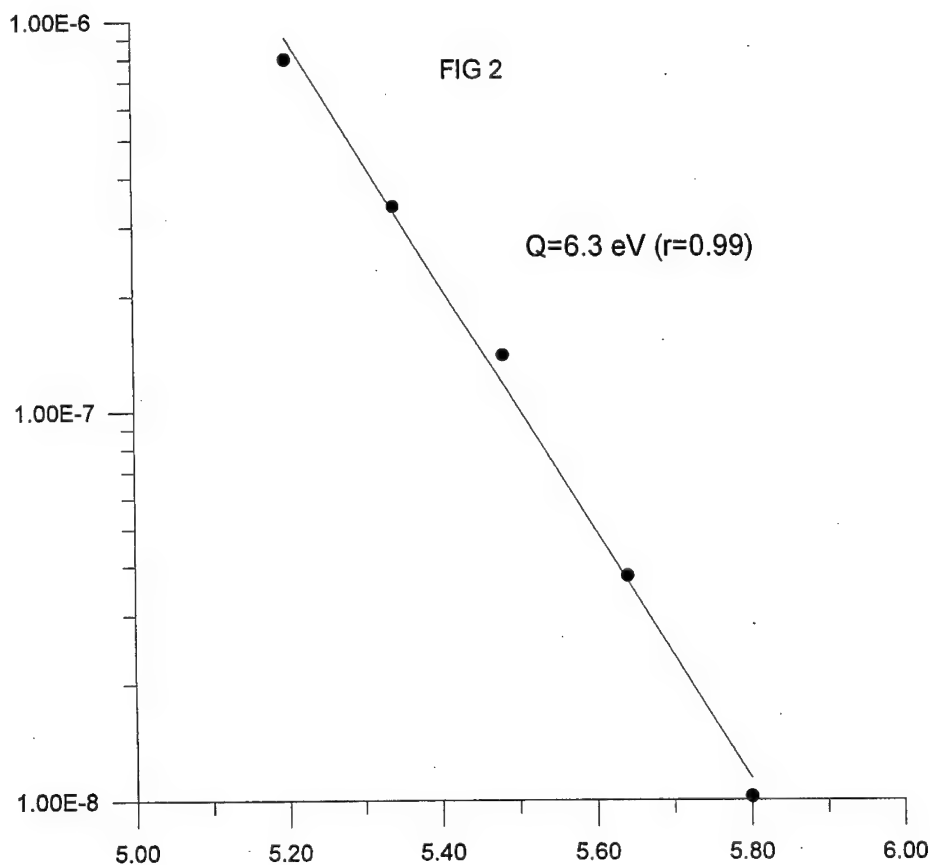


FIGURE 2.  $\ln \dot{\epsilon}$  vs.  $1/T$  for a sample in which a load was kept constant and the temperature was increased progressively from 1400°C up to 1650°C.

After each temperature rise, the system was kept long enough time deforming in order to reach the stationary state again and have an accurate measure of the strain rate. We have restricted ourselves to a short interval of temperature so that all the strain rates found were in the same ranges of values considered for the other tests. This fact prevents us from studying different deformation mechanisms. The plot recorder is shown in Figure 2.

Comparisons of the various data show a good agreement between them for  $T > 1500^\circ\text{C}$ . The activation energy at temperatures higher than  $1500^\circ\text{C}$  is  $5.5 \pm 0.4$  eV, whereas it is near 9 eV. ( $8.9 \pm 0.6$  eV) for  $T < 1500^\circ\text{C}$ . As for the stress exponents, they turn to be around 5 for  $T < 1500^\circ\text{C}$ , and decreases to 3 for  $T > 1500^\circ\text{C}$ . This qualitative behaviour has already been found for 9.4 mole%-YFSZ single crystals,<sup>2</sup> but in our case the change is more striking. On the other hand, the mechanical properties of our samples are considerable enhanced with respect to those crystals, as the strain rate diminishes two orders of magnitude for the same load and temperature.

From these results, it is clear that a different deformation mechanism controls the plastic deformation of 21 mole%-Y-FSZ single crystals in the two ranges of temperature taken into consideration. The rate controlling mechanism for  $T > 1500^{\circ}\text{C}$  is characterized by an energy which is quite similar to that found by Martínez *et al.*<sup>2</sup> in the case of 9.4 mole%-Y-FSZ for  $T > 1450^{\circ}\text{C}$ . This fact may indicate that a similar deformation mechanism must work in the two materials, no matter the composition.

Up to this point, it is not possible to conclude which plastic deformation mechanisms are involved, because the transition must be studied by means of other techniques, like TEM, which is in progress in the present time.

Table I  
Creep-law parameters determined by incremental changes during deformation

Interval of temperature	Stress exponent (n)	Activation energy (Q) in eV
1400–1500°C	$5.4 \pm 0.4(5)$	$8 \pm 1(6)$
1500–1800°C	$2.8 \pm 0.2(3)$	$5.7 \pm 0.5(13)$

In parenthesis, we have written the number of determination considered to calculate the mean value of the parameters shown.

#### 4 CONCLUSIONS

Creep tests done in 21 mole%-Y-FSZ allowed us to say that the deformation mechanisms controlling the deformation are rather different, as it can be seen from the values measured for the activation energy, between  $T > 1500^{\circ}\text{C}$  and  $T < 1500^{\circ}\text{C}$ . Comparisons with similar tests made for lower Yttria concentration Y-FSZ have been done, pointing out the main coincidences between the two materials.

#### ACKNOWLEDGEMENTS

We would like to acknowledge the technical support during the creep tests given by B. Pellicier, (C.N.R.S.-Bellevue) as well as the financial support given by the C.I.C.Y.T. MAT91-1196-CO2-01), and la Acción Integrada Hispano-Francesa nº H.F. 35B.

#### REFERENCES

1. A. Domínguez-Rodríguez, K. P. D. Lagerlof, and A. H. Heuer, *J. Am. Ceram. Soc.*, **69** (3) 281–84 (1986).
2. J. Martínez Fernández, M. Jiménez Melendo, A. Domínguez-Rodríguez, A. H. Heuer, *J. Am. Ceram. Soc.*, **73** (8), 2452–56 (1990).
3. A. Domínguez-Rodríguez, D. S. Cheong, A. H. Heuer, *Phil. Mag. A*, **64**, 4, 923–29 (1991).
4. H. Gervais, B. Pellicier and J. Castaing, *Rev. Int. Hautes Temp. Refract.* **15**, 43 (1978).
5. J. P. Poirier. 'Creep in Crystals'. Cambridge University Press, 1985.

## MICROSCOPICAL STUDIES OF DISLOCATIONS AND PLASTICITY IN DEFORMED IONIC CRYSTALS

M. V. NAZAROV and T. A. NAZAROVA

*Technical University of Moldova, 277012, Kishinev, Moldova*

The combination of scanning electron microscopy (SEM), cathodoluminescence (CL) and scanning optical microscopy (SOM) with a computer-controlled signal detection system is promising in the study of deformed ionic crystals. The present experiments were designed to unite many image processing methods in scanning microscopies and to clarify the structure of the deformed regions around the indentation.

*Key words:* microscopy, cathodoluminescence, microindentation, MgO, LiF, KCl.

### 1 INTRODUCTION

Deformation zones in indented crystals have been studied rather thoroughly both theoretically and experimentally.<sup>1–5</sup> However, the exact interpretation of the physical phenomena in different zones of indentation stage is still open to discussion. For example, the origin of the luminescence from the indented zone is not well understood and has been a subject of controversy over the last decade. Using a combination of SEM and SOM techniques, new experimental information about CL emission and other phenomena in the different zones of ionic crystals can be obtained.

### 2 EXPERIMENTAL

The crystals KCl, LiF and MgO having the NaCl lattice and progressively increasing hardness ( $10^2$ ,  $10^3$ ,  $8 \times 10^3$  MPa) were investigated with a 'JSM-50A' SEM having an additional multi-functional attachment in the form of optical laserscan and computer with digitizing peripherals. The samples were deformed by the Vickers diamond pyramid within the wide range of indenter load from 0.5 N to 5 N. The temperature of the indentation was changed from 77 K to 800 K. Thus, the microhardness values of the investigated crystals were still more changed giving us the possibility to observe their influence on the feature of the deformed region on a same crystal. He-Ne laser served as a source of coherent light in SOM. Scanning was realized with a fixed beam and shifting specimen in X and Y coordinates. The laser and SEM mode scans could be synchronized and the image is digitized and features of interest on the image may be selected and measured using a computer and specific programmes. Different SEM modes of this technique have been used to investigate deformed zones in indented ionic crystals: secondary electrons, cathodoluminescence, electron beam induced current, electron beam induced voltage, and also both polarized and transmitted light modes in SOM including Y-modulation. Recent advances in computer graphic technology have made possible the visualization of three dimensional (3D) data through various modeling and reconstruction techniques.

### 3 RESULTS AND DISCUSSION

The destruction zones near the indentation, intensely damaged regions and the heavily-work-hardened zones were revealed and measured. The temperature displacement of the destruction region appearance was established.

We have distinguished two types of the CL and transmission pictures. Type '1' is characterized by the decreasing of the luminescence area and the transparency. In other cases the indentation crater became dark and the transparency zone is a bit larger than the indentation dimension and does not repeat its form (type '2'). Type '1' is characteristic for comparatively soft specimen, type '2' is for hard ones. Moreover, it is not important how type '1' or type '2' has been achieved: either by transition from soft KCl to hard MgO in the row KCl-LiF-MgO at room temperature or by changing the temperature of the indentation on a same crystal.

However the temperature range, where the range of the CL and transmission images takes place, is higher when the crystal is harder at room temperature. So, for LiF, which has an intermediate hardness among the investigated crystals, this conversion is observed in the temperature range (77–293 K), while for the hardest MgO such a transition was discovered in a higher temperature region (293–800 K). The transition point for the softest KCl was not achieved in the studied temperature range. Perhaps it could be found in a range lower than 77 K.

The dependence of CL emission on indentation conditions (temperature and load) was demonstrated. A temperature rise leads to a visible reduction of dislocations or annihilation of anion vacancies when annealed to 800 K. An increase of load results in an increased concentration of point defects and an increase of luminescence intensity.

The presence of CL emission in the UV range has been found in the indentation craters. Five peaks for MgO crystals were observed in the short wave-length band and the dependence of their intensity on coordinates in the deformation zone was demonstrated. The difference in CL spectra apparently is consistent with the formation of different types of luminescence centers generated by gliding screw and edge dislocations. Spatial distribution of several types of defects has been sorted out and visualized in 3-D computer graphics.

### 4 CONCLUSION

A model of plastic deformation based on the dislocation loops gliding during indentation was proposed. It is concluded that such defects as F-centers are mainly responsible for the CL emission; the microindentation process in ionic crystals is mainly governed by dislocation plasticity. The correlation between cathodoluminescent, electric, optical and plastic properties of deformed crystals was established.

The techniques of complex nondestructive microscopic investigation provide a useful tools to understanding the feature of plastic deformation.

### REFERENCES

1. C. Ballesteros, J. Llopis, J. Piqueras, *J. Appl. Phys.* **53**, 3206 (1982).
2. L. Brown, M. Khan, M. Chaudhri, *Phil. Mag.* **A57**, 187 (1988).
3. M. Chaudhri, J. Hagan, J. Wells, *J. Mat. Sci.* **15**, 1189 (1980).
4. J. Llopis, C. Ballesteros, J. Piqueras, A. Remon, R. Gonzalez, *Phys. Stat. Sol. A* **78**, 679 (1983).
5. W. O'Connell, B. Henderson, J. Bolton, *Sol. Stat. Com.* **38**, 283 (1981).

---

## **15   TRANSPORT PHENOMENA**

## ATOMIC TRANSPORT OF OXYGEN IN NONSTOICHIOMETRIC OXIDES

J. L. ROUTBORT and G. W. TOMLINS

*Argonne National Laboratory, Argonne, IL 60439 USA*

Atomic transport of oxygen in nonstoichiometric oxides is an extremely important topic that overlaps science and technology. In many cases, diffusion of oxygen controls sintering, grain growth, and creep. High oxygen diffusivity is critical for efficient operation of many fuel cells. Additionally, oxygen diffusivities are an essential ingredient in any point defect model. Secondary ion mass spectrometry (SIMS) is the most accurate modern technique for measuring oxygen tracer diffusion. This paper will briefly review the principles and applications of SIMS for the measurement of oxygen transport. Case studies will be taken from recent work on ZnO and selected high-temperature superconductors.

### 1 INTRODUCTION

The atomic transport of oxygen is an extremely important technological and scientific problem that is best illustrated by the perovskite-structured high-temperature superconductors. These compounds, whether they are La-Sr-Cu-O, Y-Ba-Cu-O, or Bi-Sr-Ca-Cu, all deviate from stoichiometry by the formation of oxygen ion vacancies that are in equilibrium with oxygen partial pressure ( $P_{O_2}$ ) and temperature. From a technological standpoint, stoichiometry is important because the superconducting transition temperature is very sensitive to stoichiometry. The time and temperature required for complete oxygenation is determined by oxygen diffusion kinetics, generally chemical diffusion that can be related to tracer diffusion via the thermodynamic factor. Oxygen vacancies and interstitials are the minority defects in many nonstoichiometric ionically bonded oxides, e.g., NiO, CoO, MnO, etc. Therefore, technologically important processes such as sintering and grain growth in these materials are controlled by oxygen diffusion. Furthermore, no defect model can be complete without an understanding of both the minority and majority defects.

Early measurements of oxygen diffusion were made by exchange techniques (see, for example, Ref. 1), which presented many difficulties in use and interpretation. This technique usually involves the measurement by a mass spectrometer of the amount of  $^{18}\text{O}$  exchanged for  $^{16}\text{O}$  in a sample in a reaction chamber, and as such is an integral technique in which the boundary conditions are poorly defined. For the last two decades, a powerful technique, dynamic secondary ion mass spectrometry (SIMS) has been available (see, for example, Ref. 2). SIMS has allowed quite accurate and relatively rapid direct depth profiling of an  $^{18}\text{O}$  concentration profile setup by a diffusion anneal in quite small samples. In fact, oxygen diffusion in the  $a$ -,  $b$ -, and  $c$ -direction of  $1 \times 1 \times 0.1$  mm single crystals of  $\text{YBa}_2\text{Cu}_3\text{O}_{7-\delta}$  have been measured.<sup>3</sup> The theoretical depth resolution of SIMS is of the order of a lattice parameter.

This paper will discuss the SIMS technique and its application to a variety of oxides. In particular, recent results for single-crystal ZnO will be presented and compared to older results obtained using exchange techniques, proton activation, and SIMS. Recent results on all of the high-temperature superconductors will be presented, with particular emphasis on the relationship between the anisotropy of oxygen diffusion and crystal structure.

## 2 SIMS TECHNIQUE

This article is written for scientists interested in diffusion rather than for SIMS specialists. Details may be found in the book by Benninghoven, *et al.*<sup>4</sup> or the article by Lodding.<sup>5</sup> The vast majority of our diffusion profiles have been measured with the Cameca model IMS 3f or 5f and hence, our discussion will be restricted to this instrument. Samples are polished and subjected to a prediffusion anneal in normal oxygen at the temperature and  $P_{O_2}$  of the diffusion anneal. Samples are then encapsulated in quartz capsules, evacuated and backfilled with 95%  $^{18}O$  to the required pressure, and subjected to a diffusion anneal. After annealing, the  $^{18}O$  diffusion profiles are measured by SIMS.

The SIMS process includes<sup>6</sup> bombardment of the sample surface by a focused beam of primary ions, which sputter secondary particles from the outermost layers of the sample; mass-spectrometric separation of the ionized secondary species (atoms, molecules, clusters) according to their mass-to-charge ratios; and collection of the separated secondary ions as quantifiable mass spectra (usually  $^{16}O$  and  $^{18}O$ ) by depth profiling or line scanning, or as images of the sample surface. In the former mode, depth profiling, the beam is continually rastered over a fixed area on the sample, and a set of counts of the various masses of interest is obtained. The latter mode, line scanning, is used when the penetration depth is greater than  $\approx 10 \mu m$ . In a line scan, a taper of an appropriate angle is cut into the surface of the sample annealed in  $^{18}O$ . The surface is scanned in steps of a predetermined length.

The depth of the crater eroded during a spot scan is determined by a profilometer, and the depth of each channel is calculated on the assumption that the material sputtering rate is constant with time. The depth of each step scan is determined from geometry of the wedge measured with a profilometer. The penetration plot (concentration corrected for 0.02% natural  $^{18}O$  background) versus depth is fitted to the solution to the diffusion equation, with the appropriate boundary conditions, to calculate an oxygen diffusivity.

## 3 ZINC OXIDE

ZnO is the major constituent of a technologically important class of devices known as varistors. Polycrystalline ZnO containing many additives is used in these non-ohmic devices which have a resistance that is nonlinear with applied voltage and therefore are used as protectors against voltage surges. While the utility of a varistor relies on its grain-boundary properties and the effects of many additives, a complete understanding of the defect chemistry of the device relies on both grain-boundary and bulk properties. The tracer diffusion of oxygen is an important ingredient in this picture. Figure 1 indicates the status of oxygen tracer diffusion studies in ZnO single crystals. The discrepancies are alarming.

The first measurements were made by a gaseous exchange technique.<sup>7</sup> An extremely high preexponential factor ( $6.5 \times 10^{11} \text{ cm}^2/\text{s}$ ) and a high activation energy (7.2 eV/atom) were reported. A similar technique was used by Hoffman and Lauder, who reported a preexponential of  $1.05 \times 10^3 \text{ cm}^2/\text{s}$  and an activation energy of 4.2 eV/atom.<sup>8</sup> The exchange technique is subject to many drawbacks and does not directly measure a concentration profile. In addition, recent experiments in our laboratory have shown that evaporation of ZnO during a diffusion anneal at  $\geq 1000^\circ\text{C}$  is a significant problem. Robin *et al.*<sup>9</sup> used a proton activation technique in which a sample was annealed in  $^{18}O$ . This was followed by activation of the  $^{18}O$  by protons in an  $^{18}O(p, \alpha)^{15}N$  reaction. The penetration plot was constructed by measuring the corresponding  $\alpha$ -particle spectrum. The resulting preexponential was  $1.2 \times 10^{-10}$  and the activation energy was 1.28 eV/atom. Finally in 1980, Sockel *et al.*<sup>10</sup> used a SIMS technique to obtain depth profiles and hence oxygen



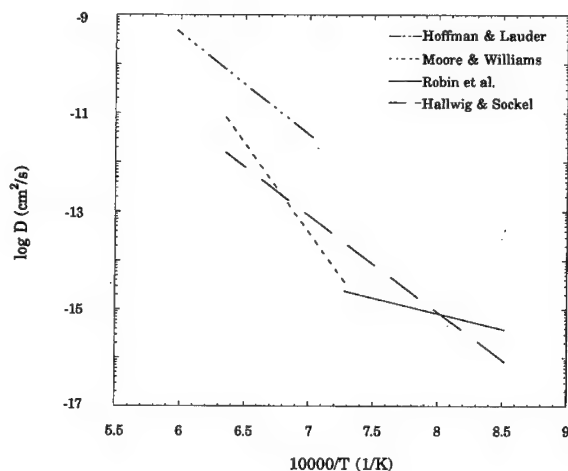


FIGURE 1 Arrhenius plot of oxygen diffusivity in ZnO.

diffusivities. These authors evidently accounted for evaporation, but the details were sketchy and no preexponential factor was quoted; the activation energy was close to that obtained by Hoffman and Lauder.<sup>8</sup> Therefore, as part of an investigation into point defects in ZnO, we are measuring  $^{18}\text{O}$  diffusion.

In our first experiments, a small ZnO single crystal was annealed at 1100 and 1200°C in a quartz capsule backfilled with  $^{18}\text{O}$ . Weight-loss measurements indicated that evaporation, as expected, was significant. The penetration profiles could be fitted to a solution of the diffusion equation, which considered a moving boundary,  $Vt$ , where  $V$  was the experimentally determined evaporation rate in cm/s and  $t$  was the time of the diffusion anneal. However, the diffusivity,  $D$ , was very sensitive to the choice of  $V$ , which could depend on the crystal orientation and would therefore be difficult to measure.

For these reasons, a series of experiments have been undertaken to limit evaporation by using a container with a tight-fitting top made from polycrystalline ZnO annealed for a

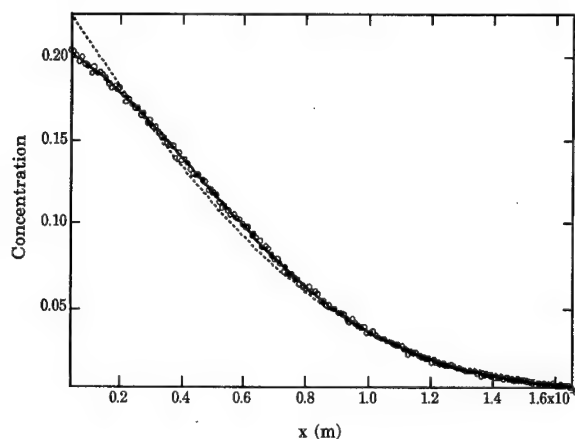


FIGURE 2 Penetration plot measured for  $\alpha$ -direction of ZnO annealed 115.7 h at 1040°C. Open circles are experimental data; dotted line is a fit to a single complementary error function solution; solid line is a fit for the changing surface concentration solution.

long time in  $^{18}\text{O}$ . Initial measurements indicate that this is an effective means to reduce evaporation. A profile measured after a diffusion anneal in the  $a$ -direction for 115.7 hr at  $1040^\circ\text{C}$  is shown in Figure 2. The shape of the penetration plot indicates that the boundary condition of an infinite source of  $^{18}\text{O}$  that leads to a  $C = C_o \operatorname{erfc}(x/2\sqrt{Dt})$  solution to the diffusion equation is not valid, as shown by the dotted line. In this solution,  $C$  is the concentration of  $^{18}\text{O}$ ,  $C_o$  is the surface concentration,  $x$  is the depth,  $t$  is the time of anneal, and  $D$  is the diffusivity. We believe that the  $^{16}\text{O}$  in the ZnO container was not fully exchanged by  $^{18}\text{O}$ . Therefore, we have used a solution of the diffusion equation that accounts for the changing surface concentration.

$$C = C_o \operatorname{erfc}(x/2\sqrt{Dt}) - kt^{1/2} \left( \exp(-x^2/4Dt) - \frac{x\sqrt{\pi}}{2\sqrt{Dt}} \operatorname{erfc}(x/2\sqrt{Dt}) \right),$$

in which it is assumed that the surface concentration changes by diffusion as  $C(0, t) = C_o - kt^{1/2}$  where  $k$  is a constant. This solution is shown as the solid line in Figure 2 and yields a  $D = 4.8 \times 10^{-15} \text{ cm}^2/\text{s}$ , quite close to the value reported at the same temperature by Sockel *et al.*<sup>10</sup> Further experiments are in progress to explore whether this procedure will lead to the correct oxygen diffusivity in ZnO.

#### 4 HIGH-TEMPERATURE SUPERCONDUCTORS

Diffusion of oxygen in high-temperature superconductors is scientifically and technologically important. The critical transition temperatures are very sensitive to the stoichiometry, which in turn is controlled by oxygen diffusion. The field of oxygen mobility in the high-temperature perovskite-structure cuprate superconductors is vast. Recent reviews of all aspects of oxygen diffusion are available.<sup>11,12</sup> In this report, we will merely illustrate the technique and the importance of oxygen diffusion measurements, using some results from high-temperature superconductors.

An Arrhenius plot of the oxygen diffusion coefficient measured in polycrystalline  $\text{YBa}_2\text{Cu}_3\text{O}_{7-\delta}$  (1 : 2 : 3) at  $P_{\text{O}_2} = 10^5 \text{ Pa}$  is presented in Figure 3.<sup>13,14</sup> These data represent diffusion in the  $ab$ -plane. The highly anisotropic diffusion between diffusion along the  $c$ -axis and in the  $ab$ -plane leads to complications in the data analysis,<sup>3,13</sup> but the agreement between the two sets of experiments performed on different ceramic samples is considered to be quite reasonable, as is the reproducibility at a given temperature. The activation energy for diffusion in the  $ab$ -plane is 0.97 eV/atom.<sup>13</sup>

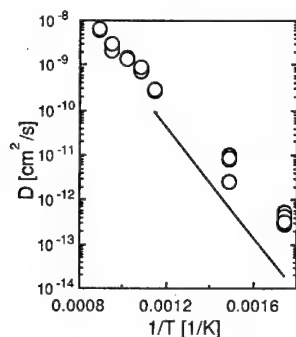


FIGURE 3 Arrhenius plot of oxygen diffusivity in polycrystalline 1:2:3 at  $P_{\text{O}_2} = 10^5 \text{ Pa}$ . Points are taken from Rothman *et al.*,<sup>13</sup> while solid line is from Sabras *et al.*<sup>14</sup>

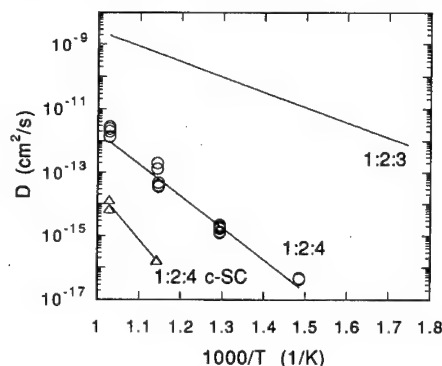


FIGURE 4 Arrhenius plot of oxygen diffusion data measured for polycrystalline 1:2:4 (circles) and c-axis crystals (triangles) compared to polycrystalline 1:2:3.<sup>17</sup>

The results obtained from oxygen diffusion studies shown (Figure 3), combined with results measured in single crystals of 1 : 2 : 3,<sup>3,15,16</sup> have led to the suggestion that diffusion in the *ab*-plane of 1 : 2 : 3 is controlled by the motion of a modified interstitial, while diffusion along the *c*-axis takes place via an oxygen vacancy mechanism.<sup>3</sup> Support of these suggested mechanisms was obtained from oxygen diffusion experiments on a structural variant of  $\text{YBa}_2\text{Cu}_3\text{O}_{7-\delta}$ , 1 : 2 : 4.<sup>17</sup> The results are shown as an Arrhenius plot (Figure 4). Diffusion in *ab*-plane 1 : 2 : 4 is much slower than *ab*-diffusion in 1 : 2 : 3 and is characterized by an activation energy of 2.08 eV/atom and a higher preexponential. The results were interpreted as suggesting that diffusion in the *ab*-plane of 1 : 2 : 4 occurs via a vacancy mechanism. The fact that diffusion along the *c*-axis is slower, with a higher activation energy than oxygen diffusion in the *ab*-plane, is a consequence of the structure and of the high energy of formation of oxygen vacancies occupying non-CuO-planes.<sup>17</sup>

The situation is similar in the two Bi-Sr-Ca-Cu-O superconductors in which oxygen diffusivity has been measured, i.e., 2201 and 2212, as may be seen from Figure 5. Oxygen diffusion is highly anisotropic, with diffusion in the polycrystalline 2212 being considerably faster and having a lower activation energy (0.93 eV/atom) than diffusion along the *c*-direction of a 2212 single crystal characterized by a much higher preexponential and a higher activation energy (2.20 eV/atom).<sup>18</sup> The oxygen diffusion

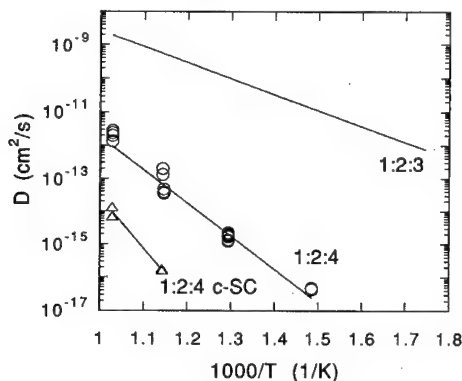


FIGURE 5 Arrhenius plot showing oxygen diffusion in *c*-direction in  $\text{Bi}_2\text{Sr}_2\text{CaCu}_2\text{O}_x$  (triangles) and  $\text{Bi}_2\text{Sr}_2\text{CuO}_x$  (circles) compared to diffusion in polycrystalline  $\text{Bi}_2\text{Sr}_2\text{CaCu}_2\text{O}_x$  (solid line).<sup>18,19</sup>

coefficient in polycrystalline 2201 is almost identical to that in polycrystalline 2201,<sup>19</sup> and diffusion in the *c*-direction is a factor of  $\approx 4$  slower than in the 2212 (Figure 5). Therefore it is clear that in all of the superconductors, diffusion in the *ab*-plane and in the *c*-direction occurs by different mechanisms.

## 5 SUMMARY

We have reviewed how SIMS is used to measure the tracer diffusion of oxygen in oxides. The results have been illustrated by two contemporary problems: ZnO, used by the electronic industry as varistors, and high-temperature superconductors. Measurements of oxygen diffusion and their incorporation into point-defect models will continue to play an important role in the development of most ceramic oxides. For example, an electrode for a solid oxide fuel cell must have a high oxygen diffusivity as well as a high ionic conductivity. Recent efforts have concentrated on nonstoichiometric perovskite-structure oxides and have not only identified potential materials, but have increased our understanding of the relationships between selective doping and oxygen diffusivity.<sup>20</sup>

## ACKNOWLEDGMENTS

Work supported by the U.S. Department of Energy (DOE), Basic Energy Sciences-Materials Sciences, and the Argonne Division of Educational Programs with funding from DOE, under Contract W-31-109-Eng-38. JLR is pleased to acknowledge Dr. S. J. Rothman as a partner in all of the superconductor investigations.

## REFERENCES

1. W. D. Kingery, J. Pappis, M. E. Doty and D. C. Hill, *J. Am. Ceram. Soc.* **42**, 393 (1959).
2. R. J. Chater, S. Carter, J. A. Kilner and B. C. H. Steele, *Solid State Ionics* **53-56**, 859 (1992).
3. S. J. Rothman, J. L. Routbort, U. Welp and J. E. Baker, *Phys. Rev.* **B44**, 2326 (1991).
4. A. Benninghoven, F. G. Rüdenauer and H. W. Werner, *Secondary Ion Mass Spectrometry* (Wiley-Interscience, New York, NY, 1987).
5. A. Lodding, in *Inorganic Mass Spectrometry*, eds. F. Adams, R. Gijbels and R. van Grieken, (Wiley, New York, NY, 1987).
6. J. Rothman, J. L. Routbort, J. E. Baker, L. J. Nowicki, K. C. Goretti, L. J. Thompson and J. N. Mundy, *Diffusion Analysis and Applications* (The Minerals, Metals & Materials Society, Warrendale, PA, 1989).
7. W. J. Moore and E. L. Williams, *Crystal Imperfections and the Chemical Reactivity of Solids* (The Faraday Society, Aberdeen, Scotland, 1959).
8. Hoffmann, J. W. and J. Lauder, *Trans. of the Faraday Soc.* **66**, 2346 (1970).
9. R. Robin, A. R. Cooper and A. H. Heuer, *J. Appl. Phys.* **44**, 3770 (1973).
10. H. G. Sockel, D. Hallwig and R. Schachtner, *Mater. Sci. and Engr.* **42**, 59 (1980).
11. Y. M. Baikov, E. K. Shalkova and T. A. Ushakova, *SPCT* **6**, 449 (1993).
12. J. L. Routbort and S. J. Rothman, *J. Appl. Phys.* **76**, 5615 (1994).
13. S. J. Rothman, J. L. Routbort and J. E. Baker, *Phys. Rev.* **B40**, 8852 (1989).
14. J. Sabras, C. Colin, J. Ayache, C. Monty, R. Maury and A. Fert, *Coll. de Phys.* **51**, C1 (1990).
15. S. I. Bredikhin, G. S. Emel'chenko, V. S. Shechtman, A. A. Zhokhov, S. Carter, R. J. Carter, J. A. Kilner and B. C. H. Steele, *Physica C* **286** (1991).
16. S. Tsukui, T. Yamamoto, M. Adachi, T. Oka, Y. Shono, K. Kawabata, N. Fukoka, A. Yanase, Y. Yoshioka and F. Tojo, *Defect and Diffusion Forum* **1123** (1993).
17. J. L. Routbort, S. J. Rothman, J. N. Mundy, J. E. Baker, B. Dabrowski and R. K. Williams, *Phys. Rev.* **B48**, 7505 (1993).
18. M. Runde, J. L. Routbort, S. J. Rothman, K. C. Goretti, J. N. Mundy, X. Xu and J. E. Baker, *Phys. Rev.* **B45**, 7375 (1992).
19. M. Runde, J. L. Routbort, J. N. Mundy, S. J. Rothman, C. L. Wiley and X. Xu, *Phys. Rev.* **B46**, 3142 (1992).
20. S. Carter, A. Selcuk, R. J. Chater, J. Kajda, J. A. Kilner and B. C. H. Steele, *Solid State Ionics* **53-56**, 597 (1992).

## DEFECT INTERACTIONS, STATISTICAL THERMODYNAMIC AND ELECTRONIC TRANSPORT IN IONIC NONSTOICHIOMETRIC OXIDES

R. TETOT and G. BOUREAU\*

CNRS-URA 446. Laboratoire des Composés Non-Stoechiométriques, Bât 415, Université  
Paris-Sud, 91405 ORSAY Cedex, France; \*Laboratoire de Chimie Physique, Université  
Pierre et Marie Curie, 11 rue Pierre et Marie Curie, 75321 Paris Cedex 05, France

In this paper, we discuss the effects of the defect interactions on the thermodynamic properties and electronic transport of nonstoichiometric oxides. We first show that two limited thermodynamic behaviours can be distinguished depending on whether the oxide has a metallic type electronic conduction or a hopping electronic conduction. In the first case, the interactions are expected to be short ranged because of the screening of the conduction electrons, while they are Coulombic in the second case. This paper is limited to this last case, exemplified mainly by  $M_{1-x}O$  ( $M = Co, Mn, \dots$ ) cubic oxides.

Next, we analyse the two approximated methods usually used in this field, the ideal mass action law method and the Debye Hückel theory, and we show that they are both insufficient to accurately describe these compounds. We finally show by means of Monte Carlo simulations that a simple model in which point defects interact through a unique dielectric constant allows us to render an account of the main features of the thermodynamic and electronic transport properties of these oxides.

**Key words:** nonstoichiometry, binary metal oxides, defect structure, Monte Carlo simulations, Statistical Thermodynamics.

### 1 INTRODUCTION

The most important thermodynamic functions for nonstoichiometric oxides (NSO) are  $\Delta G(O_2)$  and  $\Delta H(O_2)$ , respectively the molar free energy and enthalpy of mixing of oxygen. As a matter of fact, these quantities can generally be experimentally determined as functions of both composition and temperature.<sup>1</sup>  $\Delta G(O_2)$  is determined from the measurement of the equilibrium oxygen partial pressure  $PO_2$  with which it is related through the relation:

$$\Delta G(O_2) = RT \log PO_2$$

$\Delta H(O_2)$  can be determined either by differentiation of  $\Delta G(O_2)/T$  with respect to inverse temperature at constant composition:

$$\Delta H O_2 = \partial(\Delta G(O_2)/T) / \partial(1/T)$$

or directly by high temperature microcalorimetry.

At thermodynamic equilibrium, the nonstoichiometry is generated by the presence of atomic point defects (we do not consider here extended defects as shear planes in  $WO_3$  for example). These defects have a charge balanced by the presence of electronic defects of opposite charge. Two extreme behaviours may then be considered: either the electronic defects are immersed in a large conduction band ( $TiO$ ,  $VO$ , solid solutions of oxygen in transition metals, . .) or, they are localized on the cations which then change their valence ( $CoO$ ,  $MnO$ ,  $FeO$ ,  $CeO_2$ ,  $UO_2$ , . .).

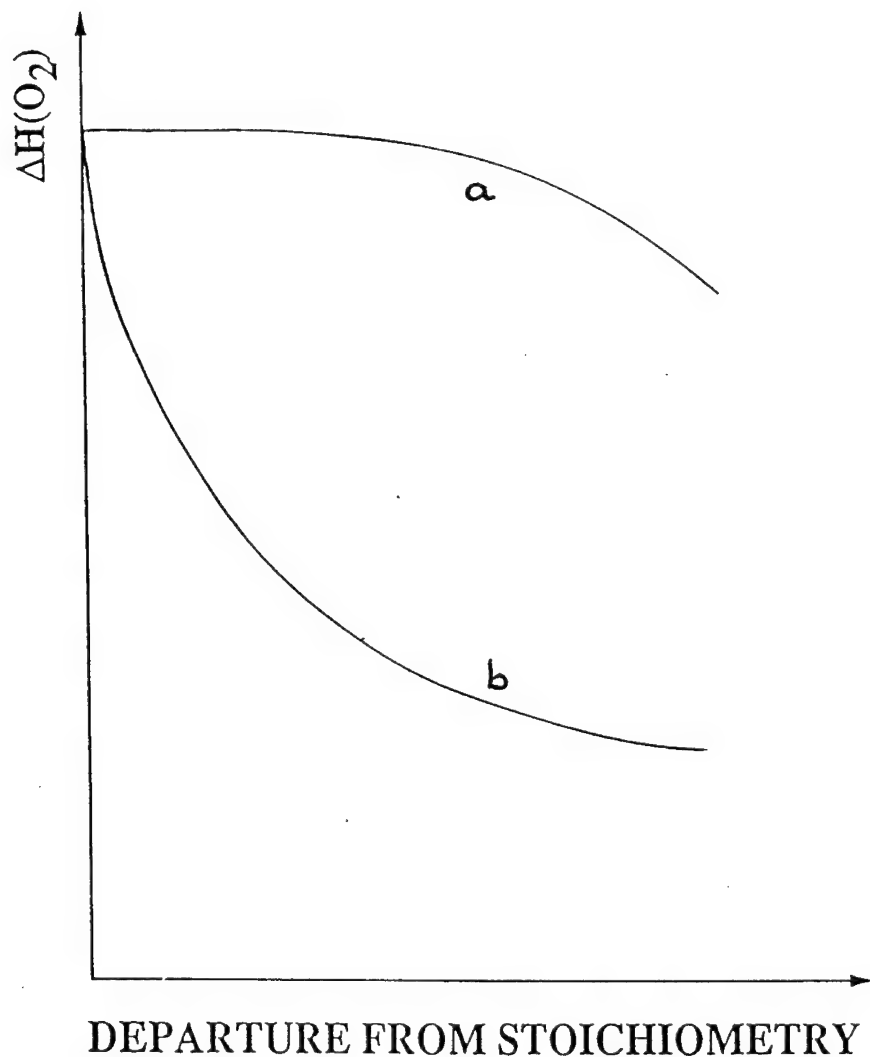


FIGURE 1 Schematic variations of  $\Delta H(O_2)$  vs. departure from stoichiometry

a) metallic system

b) ionic system.

In the first case, due to the screening of conduction electrons, the interactions between atomic defects are limited to short range. One can often assume that, at least to first neighbours, the interactions are much greater than  $kT$  (blocking site scheme).  $\Delta H(O_2)$  is then constant for small  $x$  and then increases when more distant interactions are acting (see Figure 1a). This behaviour is observed particularly in solid solutions of oxygen in transition metals.<sup>2,3</sup>

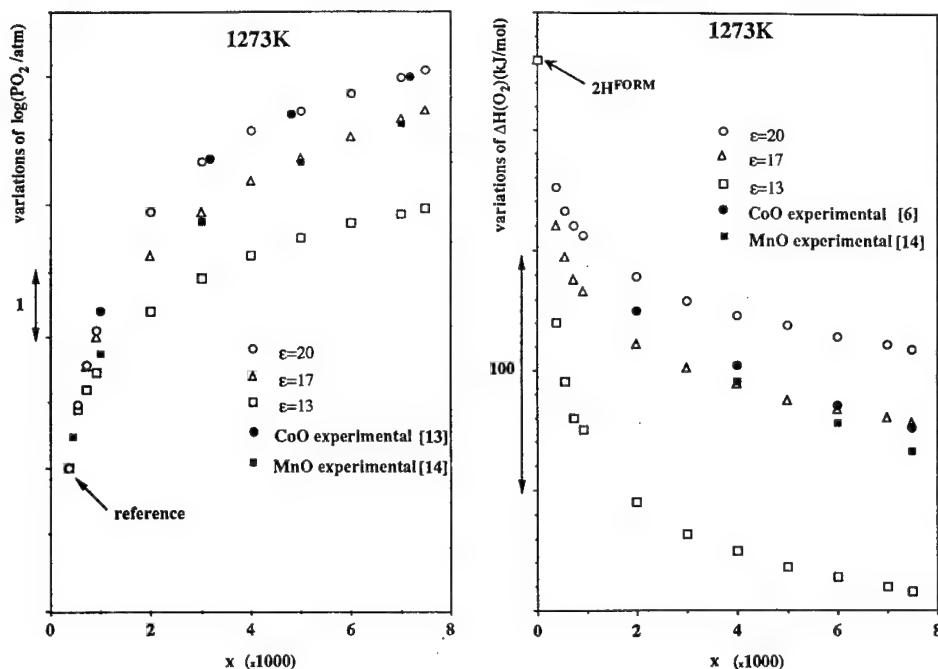


FIGURE 2 The oxygen pressure and the partial molar enthalpy of oxygen as functions of the departure from stoichiometry and the dielectric constant.

In the second case, one has principally to handle long range Coulomb interactions between two types of defects (atomic and electronic) of opposite charges. Let us note that the dielectric constant is small ( $\epsilon \cong 13$  at room temperature for CoO).<sup>4</sup> For small value of  $x$ , the Debye-Hückel theory<sup>5</sup> shows that the first significant correction of the total energy according to the ideal solution is proportional to  $x^{3/2}$ .  $\Delta H(O_2)$  therefore varies as  $x^{1/2}$  (see Figure 1b). This is what is observed for a number of partially ionic oxides (see reference 1, 6 and references therein). Only this case will be considered in the following.

The direct conclusion of this rapid analysis is that, in partially ionic oxides, the interactions have an important effect even and particularly for small ranges of nonstoichiometry.

## 2 APPROXIMATED METHODS

Two analytical methods are usually used for the study of the nonstoichiometry and related properties in ionic oxides, the ideal mass action law (IMAL) method developed by Kofstad<sup>7</sup> and the Debye-Hückel (DH) theory.<sup>5</sup> From the foregoing, it seems that the DH model is well adapted for this purpose. Unfortunately, this method has to be confined to very small departures from stoichiometry ( $< 1 \times 10^{-3}$  in CoO).<sup>8</sup>

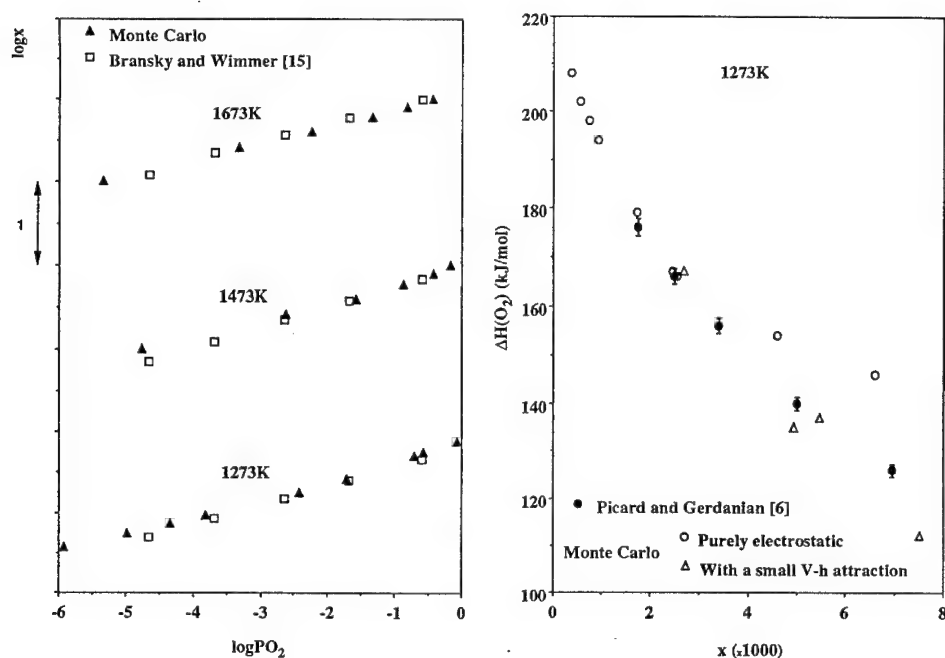


FIGURE 3  $\log x$  as function of  $\log PO_2$  and the partial molar enthalpy of oxygen as a function of the departure from stoichiometry for  $Co_{1-x}O$ .

The IMAL method is actually the most often used. In this formalism, several varieties of defects are simultaneously considered and are assumed non interactive and randomly distributed, one type of defect being predominant in a particular  $PO_2$  range. Some of these defects are complex ones, made of the association of elementary point defects. In the case of  $M_{1-x}O$  cubic oxides, metal vacancies in different states of ionization are usually invoked. Thus, a single ionized vacancy,  $V'$ , is made of a vacancy with two minus charges,  $V''$ , with an electronic hole,  $h'$ , in its immediate vicinity, and may be represented by the cluster  $\{V'', h'\}$ . In the same way, a neutral vacancy,  $V^x$ , may be represented by  $\{V'', 2h'\}$ . This clustering is a way to partly take into account the attraction between vacancies and free holes of opposite charges. On the contrary, repulsive interactions between vacancies on one hand and free holes on the other hand are ignored. Some authors consider in addition the existence of vacancy clusters such as the so-called 4 : 1 cluster predicted by theoretical calculations.<sup>9</sup> In fact, there is much evidence against the existence of these clusters at least in the vicinity of stoichiometry.<sup>10</sup> The reliability of the IMAL formalism has been investigated very recently.<sup>11</sup> It has been shown that its range of application is limited to the case where the interactions are not too large, therefore  $\epsilon$  not too small (typically  $\epsilon > 17$ ) and for moderate departures from stoichiometry i.e. neither too small nor too large. As a matter of fact, close to the stoichiometry there are not enough charged defects to screen the interactions and too far, the interaction between vacancies begin to play a noticeable role.



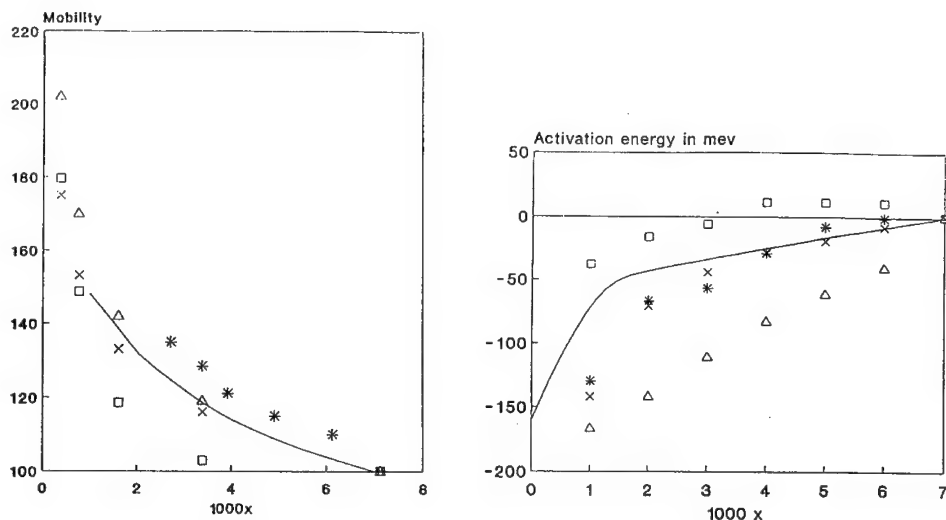


FIGURE 4 Comparison of calculations with experimental determination of the electronic mobility and the activation energy as functions of the departure from stoichiometry for  $\text{Co}_{1-x}\text{O}$ .

\*:reference 17, x :reference 18, □:reference 19, Δ:reference 20,  
— :calculations.

As a conclusion, neither of these two approximated methods is really satisfactory. The only way to rigorously handle Coulomb interactions is to perform Monte Carlo simulations. This is the subject of the next section.

### 3 MONTE CARLO SIMULATIONS

#### 3.1 Thermodynamic

The numerical methods used in our calculations have been described in detail elsewhere<sup>12</sup> and therefore, are not reported here. The important point is that we only consider elementary interactive point defects: metal vacancies with two minus charges and electron holes localized on cations. Within a nonstoichiometry range sufficiently small, say  $x \leq 5 \times 10^{-3}$ , Coulomb interactions strongly prevail, whereas for greater departures short range interactions have to be added to take into account covalent effects. The dielectric constant  $\epsilon$  is taken as an adjustable parameter for a given oxide.

In the Figure 2 are reported the dependence of  $\log P_{\text{O}_2}$  and  $\Delta H(\text{O}_2)$  on  $x$  calculated in a pure electrostatic model with various values of  $\epsilon$ . Let us note that our results are known within a constant and that only the variations of these quantities are significant. We have also reported some experimental data related to CoO and MnO. Qualitatively, one can see that the experimental behaviour of these oxides is well reproduced with our model,  $\epsilon = 20$  corresponding to CoO and  $\epsilon = 17$  to MnO. However it can be shown that the agreement is less good for  $\Delta H(\text{O}_2)$  than for  $\log P_{\text{O}_2}$ . The reason is that  $\Delta H(\text{O}_2)$  is more sensitive to short range interactions which have to be added to improve the model. This is illustrated in the Figure 3 which shows results on CoO. Here, a short range attraction of  $-2.5 \text{ kJ mol}^{-1}$  between vacancies and holes first neighbours has been added in the calculations. The

agreement is now very satisfactory for both the thermodynamic functions.

### 3.2 Electrical Conductivity

The interaction parameters evaluated from the previous thermodynamic analysis have been used to study the electronic conductivity of CoO in a frame of a simple hopping model.<sup>16</sup> Our model assumes that electronic holes are trapped in potential wells, the height of which is the sum of two terms: one which is unknown but composition and temperature independent, and another one which is equal to the opposite of the interaction seen by the trapped hole. This interaction is of course different for every polaronic site. In this way, even before performing any calculation, it may be easily understood that the strong increase of electrostatic interactions as the departure from stoichiometry increases causes both a decrease of the hole mobility and an increase of the related activation energy. As it will be seen further, these features are in agreement with experiments. The electrical conductivity is calculated by Monte Carlo simulations from the relation:

$$\sigma = \lambda \sum_{N_h} (12 - L) \exp(E_{\text{int}}/RT)$$

The sum runs over the number of holes.  $L$  is the number of cations sites surrounding a hole and already occupied by a hole (therefore not accessible to a new hole).  $E_{\text{int}}$  is the interaction energy on the polaronic site. The coefficient  $\lambda$  takes the form:

$$\lambda = C/T \times \exp(-E/RT)$$

where  $C$  and  $E$  are constants. At a given temperature, the composition dependence of the mobility is caused by the variation of the factor:

$$f = \sum_{N_h} (12 - L) \exp(E_{\text{int}}/RT)$$

The activation energy has been evaluated by using the Arrhenius law. The results of the calculations, compared with some experimental data are reported in Figure 4 in arbitrary units. Our calculations providing only relative values, we have to use a reference value. We have chosen at  $x = 7 \times 10^{-3}$ , the value 100 for the mobility and 0 for the activation energy. In spite of the scattering of experimental results, the trend is unambiguous: the mobility strongly decreases while the activation increases as  $x$  increases, which is perfectly rendered by our model.

## 4 DISCUSSION AND CONCLUSION

In  $M_{1-x}O$  cubic oxides ( $M = \text{Co}, \text{Mn}, \dots$ ) (as also in  $\text{CeO}_{2-x}$ <sup>21</sup>), the nonstoichiometry and related properties can be explained by considering a very simple point defect model. The key point is to accurately handle the interactions. Only Monte Carlo simulations allows that satisfactorily. As far as small departures from stoichiometry are concerned, these interactions are essentially Coulombic. As and when the departure increases, short range interactions have to be added: first, attractive between atomic and electronic defects and then repulsive between atomic defects.

The only disadvantage of the Monte Carlo method is its heaviness. For this reason, it is useful to return to the already mentioned approximated methods which are, on the contrary, very simple to use. This is all the more interesting because exact results are now

available.

As already reported, the IMAL formalism has been analyzed recently.<sup>8,11</sup> Conceptually, the taking into account of several types of vacancies, which is the basic idea of the method, can be justified by the observation of the radial distribution functions calculated by Monte Carlo.<sup>12</sup> As a matter of fact, the clustering between vacancies and holes at first and second neighbours appears to be quite preponderant over more distant neighbours. We have also shown clearly that the mass action constants must be evaluated by considering both enthalpic and entropic contributions, which is generally omitted in a number of works and leads to erroneous results. Unfortunately, the IMAL formalism fails when the dielectric constant of the compound is too low, which prevents its use for a study of MnO for example. It also fails for very small departures from stoichiometry, which is not practically a serious drawback as experiments are generally not available in this range where impurities play an essential role. More serious is the fact that the formalism fails also for departures greater than, say  $7 \times 10^{-3}$ , because it is impossible to introduce vacancy-vacancy interactions (otherwise to consider vacancy clusters).

Contrary to the IMAL method, the DH theory is appropriate to the study of small departures from stoichiometry. Unfortunately, its applicability is reduced to very small concentrations of charges. The physical reason is that the ratio  $l_D/a$ , where  $l_D$  is the Debye length (representing the order of magnitude of the radius of the ionic cloud around a particular ion) and  $a$  the mean separation between two ions must be much greater than 1. Then, this ratio is equal to 1 for  $x = 4 \times 10^{-3}$  in  $\text{Co}_{1-x}\text{O}$ .<sup>8</sup> Nevertheless, contrary to the case of liquid electrolyte, in defective solids, the method seems to work and is often used beyond this physical limit. However, let us note that the values of the slope  $n_x = (\partial \log x / \partial \log \text{PO}_2)^{-1}$  calculated by this method are rather different from the ones obtained by Monte Carlo.<sup>8</sup> Moreover, this method also does not allow the introduction of short range order interactions.

To conclude, one can say that a suitable analytical method aimed at supplying heavy Monte Carlo calculations is not yet available. One direction may be adapt the cluster variation method (CVM)<sup>22</sup> used in the case of short range interactions<sup>23</sup> to long range Coulomb interactions.

## REFERENCES

1. R. Tétot, C. Picard, G. Boureau and P. Gerdanian, *Advances in Ceramics* Vol. 23 (1987).
2. G. Boureau and P. Gerdanian, *J. Phys. Chem. Solids* **45**, 141 (1984).
3. R. Tétot, C. Picard, G. Boureau and P. Gerdanian, *J. Chem. Phys.* **69**, 326 (1978).
4. K. V. Rao and A. Smakula, *J. Appl. Phys.* **36**, 2031 (1965).
5. J. O'M. Bockris and A. K. N. Reddy, *Modern Electrochemistry*. (Plenum Press, New York, 1970).
6. C. Picard and P. Gerdanian, *J. Phys. Chem. Solids* **50**, 383 (1989).
7. P. Kofstad, *Non Stoichiometry, Diffusion and Electrical Conductivity in Binary Oxides* (Wiley-Interscience, New York, 1972).
8. R. Tétot, B. Nacer and G. Boureau, *J. Phys. Chem. Solids*, **55**, 617 (1994).
9. S. M. Tomlinson, C. R. A. Catlow and J. H. Harding, *J. Phys. Chem. Solids* **51**, 477 (1990).
10. D. Schuster, R. Dieckmann and W. Schweika, *Ber Bunsenges. Phys. Chem.* **93**, 1347 (1989).
11. R. Tétot and G. Boureau, *J. Phys. Chem. Solids* **55**, 357 (1994).
12. R. Tétot, B. Nacer and G. Boureau, *J. Phys. Chem. Solids* **54**, 517 (1993).
13. U. Hölshner and H. Schmalzried, *Z. Physik Chem. Neue Folge* **139**, 69 (1984).
14. C. Picard and P. Gerdanian, *J. Sol. St. Chem.* **11**, 190 (1974).
15. I. Bransky and J. M. Wimmer, *J. Phys. Chem. Solids* **33**, 801 (1972).
16. G. Boureau, O. Masmoudi and R. Tétot, *Solid State Comm.* **87** 417 (1993).
17. B. Fisher and D. S. Tannhauser, *J. Chem. Phys.* **44**, 1663 (1966).
18. N. G. Error and J. B. Wagner, *J. Phys. Chem. Solids* **29**, 1597 (1968).
19. F. Morin and R. Dieckmann, *z. fur Phys. Chem. N. F.* **129**, 219 (1982).

20. G. Petot-Ervas, P. Ochin and B. Sossa, *Solid States Ionics* **12**, 277 (1984).
21. G. Boureau, O. Masmoudi and R. Tétot, *Solid State Comm.* **79**, 299 (1991).
22. R. Kikuchi, *Phys. Rev.* **B81**, 988 (1951).
23. R. Tétot, C. Giaconia, A. Finel and G. Boureau, *Phys. Rev.* **B48**, 10090 (1993).

## DEFECT PARAMETERS FOR RUBIDIUM CHLORIDE FROM IONIC CONDUCTIVITY MEASUREMENTS

PATRICK W. M. JACOBS and MARCIA L. VERNON

*Department of Chemistry, University of Western Ontario, London, Ontario N6A 5B7  
Canada*

The ionic conductivity of well-annealed crystals of rubidium chloride and of RbCl doped with  $\text{Sr}^{2+}$  or  $\text{S}^{2-}$  ions has been measured, using an automated system, over a wide range of temperature, generally from 960 K until precipitation occurred. Conductivity data were analyzed using a multiparameter non-linear least squares fitting program. The defect model used allowed for the possibility of Frenkel defects on both cation and anion sublattices and the association of cation vacancies with divalent cations and of anion vacancies with divalent anions. Data for the individual crystals were analyzed separately and a consistent set of defect parameters were obtained.

### 1 INTRODUCTION

Previous studies<sup>1,2</sup> of the ionic conductivity of NaCl and KCl have revealed the necessity of including anion Frenkel defects in the defect model for KCl in order to obtain an accurate representation of transport data. Though the possibility of contributions from Frenkel defects to ionic transport in NaCl<sup>1</sup> was investigated, such contributions appear to be too small to have noticeable effects. Theoretical calculations of Arrhenius energies for NaCl, KCl and RbCl<sup>3,4</sup> show (i) that, while Schottky defects are the majority defects in NaCl and KCl, contributions from Frenkel defects should be significant, at least in KCl; (ii) that in RbCl a much stronger contribution from interstitials to transport processes is to be expected. Analysis of these new data for RbCl will show that interstitials make an even bigger contribution in RbCl than in KCl.

### 2 EXPERIMENTAL AND RESULTS

New features of the experimental procedure will be described in greater detail elsewhere.<sup>4</sup> Suffice it to say here that the crystals were grown from zone-refined RbCl which had a residual divalent cation impurity concentration of 1.3–1.9 ppm. Nine cleaves in all were measured and analyzed, three each of pure RbCl,  $\text{RbCl}:\text{Sr}^{2+}$  and  $\text{RbCl}:\text{S}^{2-}$ . The concentration of  $\text{Sr}^{2+}$  was measured by ion chromatography; that of  $\text{S}^{2-}$  was determined during the computer fitting procedure. Crystals were mounted in a specially-designed double cell<sup>5</sup> and conductivities measured with a B905 Wayne-Kerr Autobalance bridge using a pre-set  $T$ - $\sigma$  sequence controlled by a PC. The furnace temperature was regulated by a Watlow 945 digital controller connected to the PC.

Arrhenius plots  $\sigma(T)$  are shown in Figure 1 for three pure RbCl crystals. The continuous curvature observed contrasts with the classical behaviour of NaCl and is indicative of more than one transport mechanism. Figure 2 shows the ratio of the conductivities of a  $\text{RbCl}:\text{Sr}^{2+}$  crystal ( $\sigma$ ) and a pure RbCl crystal ( $\sigma_0$ ) at the same  $T$ . The initial rise in  $\sigma/\sigma_0$  is due to the decreasing concentration of intrinsic defects with fall in  $T$ ; the maximum and subsequent decrease in  $\sigma/\sigma_0$  are due to association.

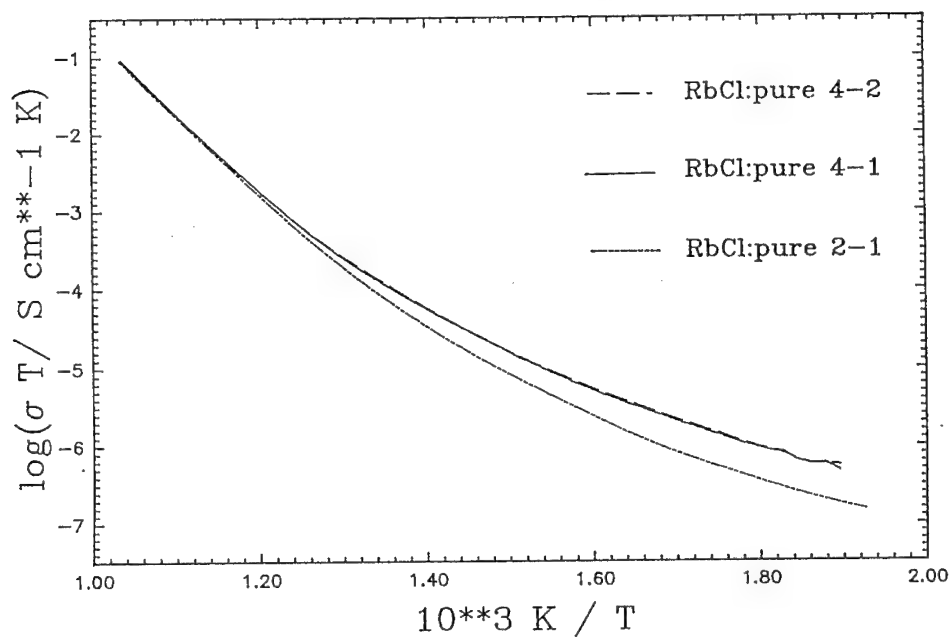


FIGURE 1 Arrhenius plots of the conductivity of three pure RbCl crystals.

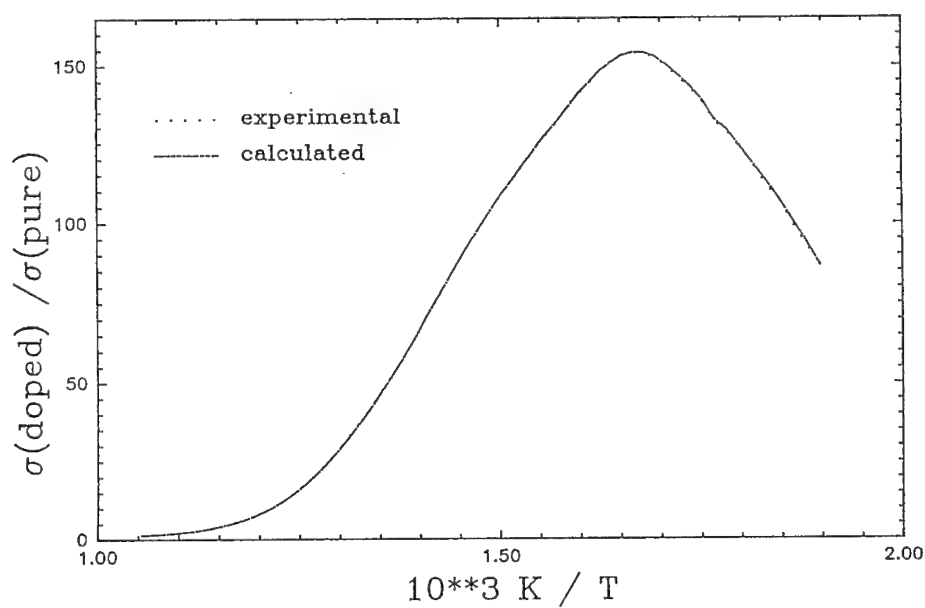


FIGURE 2 Temperature dependence of the ratio of the conductivity of a RbCl crystal containing 45.4 ppm of  $\text{Sr}^{2+}$  to that of a pure RbCl crystal containing 1.3 ppm residual divalent cation impurity. Points show experimental data and the dash-dot line the results of computer fitting.

Table I

Defect parameters for RbCl from analysis of ionic inductivity measurements, k = association,  $\Delta$  indicates a migration parameter, c = cation, a = anion, v = vacancy, i = interstitial, S = Schottky, F = Frenkel

$h_s$	$s_s$	$\Delta h_{cv}$	$\Delta s_{cv}$	$\Delta h_{av}$	$\Delta s_{av}$	$h_{Fc}$	$s_{Fc}$	$\Delta h_{ci}$
2.52	8.87	0.661	1.910	0.720	2.920	3.457	7.40	0.208
$\Delta s_{ci}$	$h_{Fa}$	$s_{Fa}$	$\Delta h_{ai}$	$\Delta s_{ai}$	$h_{ck}$	$s_{ck}$	$h_{ak}$	$s_{ak}$
5.60	3.484	9.55	0.188	6.72	-0.592	-2.85	-0.872	-3.05

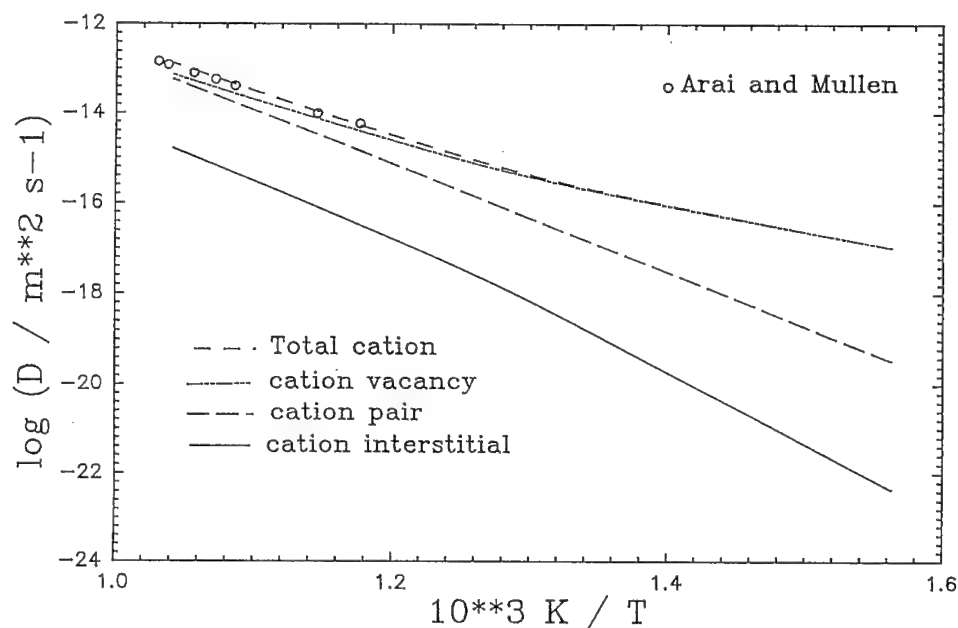


FIGURE 3 Arrhenius plots of Rb diffusion in pure RbCl.  $\circ$  Show the experimental results of Arai and Mullen<sup>6</sup> and the four lines the calculated total D, and contributions to D from vacancies, interstitials, and cation jumps into vacancy pairs.

### 3 DISCUSSION

The defect model included the possibility of Frenkel defects on both sub-lattices in addition to Schottky defects. The calculated conductivity<sup>5</sup> was compared with the measured conductivity at each temperature and the defect parameters varied systematically using a non-linear least squares code until the residual sum of squares was minimized. The procedure followed involved fitting the data for the set of three cation-doped crystals first, then those for the set of anion-doped crystals, and finally those for the pure crystals. This procedure was repeated iteratively until constant values were obtained for each sample. The values within each set were averaged and finally the averages for the three sets: cation-doped, anion-doped and pure crystals were calculated. Within each set  $\sigma$  is insensitive to

certain parameters and initially these were held constant, but eventually all parameters had been allowed to vary. Initial choices for the energies were the results of pair-potential calculations, and for the entropies the values that had been obtained previously for KCl. Although it was found necessary to include cation Frenkel defects in the model, the fitting was insensitive to small variations in their values and this was taken to imply that cation interstitials are present only in low concentration. Final defect parameters are given in Table I. As a test of the predictive value of these parameters we calculated the diffusion coefficients  $D$  of Rb and Cl as functions of  $T$  and compared the results with experimental measurements of  $D$ . That for Rb is shown in Figure 3, which gives also the individual contributions from cation vacancies, vacancy pairs and cation interstitials, the latter being about 1% of the pair contribution. The agreement of the calculated  $D$  with experiment is excellent; that for Cl diffusion in RbCl is not quite as good but still quite satisfactory.

#### ACKNOWLEDGEMENT

We thank NSERC for a Research Grant (to PWMJ).

#### REFERENCES

1. I. E. Hooton and P. W. M. Jacobs, *Can. J. Chem.* **66**, 830 (1988).
2. L. Acuña and P. W. M. Jacobs, *J. Phys. Chem. Solids*, **41**, 595 (1980).
3. P. W. M. Jacobs, *J. Chem. Soc. Faraday Trans. 2* **85**, 415 (1989).
4. P. W. M. Jacobs and M. L. Vernon, to be published.
5. I. E. Hooton and P. W. M. Jacobs, *J. Phys. Chem. Solids* **51**, 1207 (1990).
6. G. Arai and J. G. Mullen, *Phys. Rev.*, **143**, 663 (1966).



## TRANSPORT PROCESSES IN FLUORIDE CRYSTALS UNDER HIGH PRESSURE

I. V. MURIN,\* O. V. GLUMOV,\* W. GUNSSER,\*\* M. KARUS\*\*

\*St. Petersburg University, St. Petersburg, Russia; \*\*Institut für Physikalische Chemie,  
 Universität Hamburg, Bundesstrasse 45, 20146 Hamburg, Germany

The effect of hydrostatic pressure on the ionic conductivities in  $\beta\text{-PbF}_2$   $\beta\text{-Pb}_{1-x}\text{M}^m\text{F}_{2+(m-2)x}$  (where  $\text{M}^m = \text{Na}^+$ ,  $\text{Cd}^{+2}$ ,  $\text{Tb}^{+3}$ ,  $\text{U}^{+4}$ ),  $\text{LaF}_3$  and  $\text{La}_{1-x}\text{Ca}_x\text{F}_{3-x}$  has been investigated in the temperature range between 300 K and 700 K for pressures up to 0.25 GPa (for  $\beta\text{-PbF}_2$ ) and 0.8 GPa (for  $\text{LaF}_3$ ). The activation volumes of defect formation and migration, impurity defect segregation and dissociation were determined from the effect of pressure on the conductivity. Keyes' treatment based on the strain energy Zener model in Grüneisen approximation was used to estimate theoretical values of activation volumes.

**Key words:** superionic conductors, fluorides, high pressure technique, activation volumes.

### 1 INTRODUCTION

Fluoride crystals based on fluorite- and tysonite matrixes are very perspective classes of superionic conductors with predominant anionic conductivity.<sup>1</sup>

The study of superionic conductors under high pressure is one of the most powerful approaches for elucidation of ionic processes and electrophysical properties of materials with high ionic conductivity. The investigation of the high hydrostatic pressure dependence on the ionic conductivity gives direct information about the elastic volume relaxation associated with the formation of point defects (Schottky and Frenkel type) and more complicated lattice defects (clusters)  $\Delta V_f$  and the lattice relaxation accompanying the diffusive motion of these defects  $\Delta V_m$ .<sup>1-3</sup> Since the Gibbs free energy for the conduction process can be expressed as  $\Delta G = V\delta P - S\delta T$ , a characteristic activation volume can be obtained from the pressure dependence of  $\Delta G$ :

$$\Delta V = (\delta \Delta G / \delta P)_T \quad (1)$$

Employing the Arrhenius-type equation for the ionic conductivity on the basis of reaction rate theory,

$$\sigma = (Ne^2 a^2 \nu / kT) \exp(-\Delta G / kT) \quad (2)$$

we obtain the activation volume

$$\Delta V = -kT(\delta \ln \sigma / \delta P)_T + kT(\delta \ln Ne^2 a^2 \nu / \delta P)_T \quad (3)$$

where  $N$  is the number of ions per unit volume,  $e$  is their electronic charge,  $\nu$  is the vibrational (or attempt) frequency of the mobile species and  $a$  is the jump distance.

The first term is obtained directly from the measured pressure dependence of the conductivity. The second term, which is usually small compared with the first one, can be evaluated indirectly from the compressibility and the pressure dependence of the elastic constants. In the extrinsic region, where defects are not being produced in significant quantities, only the activation volume of defect motion is observed, so that  $\Delta V = \Delta V_m$ . In the intrinsic region where defects are both created and moved,  $\Delta V = \Delta V_f / 2 + \Delta V_m$ .

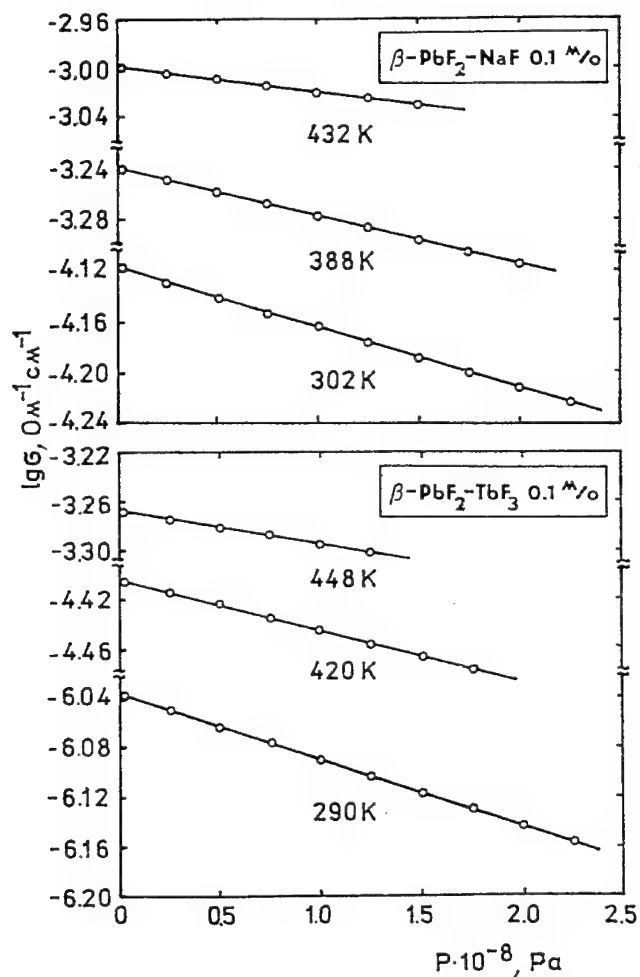


FIGURE 1 Pressure dependence of conductivity for  $\beta$ -PbF<sub>2</sub>-NaF and  $\beta$ -PbF<sub>2</sub>-TbF<sub>3</sub>.

## 2 EXPERIMENTAL

Fluoride crystals  $\beta$ -PbF<sub>2</sub>,  $\beta$ -Pb<sub>1-x</sub>M<sup>m</sup>F<sub>2+(m-2)x</sub> (where M<sup>m</sup> = Na<sup>+</sup>, Cd<sup>+2</sup>, Tb<sup>+3</sup>, U<sup>+4</sup>), LaF<sub>3</sub> and La<sub>1-x</sub>Ca<sub>x</sub>F<sub>3-x</sub> were grown by Stockbarger-Bridgeman technique. A hydrostatic pressure environment was built using an externally heated 1.0 GPa (10 kbar) pressure apparatus with a pressure cell, which used silicon oil as the pressure transmitting medium. The pressure was determined using a calibrated manganin gauge. Complex impedance measurements were performed in the frequency range between 100 Hz and 200 kHz. The electrical contacts to the samples were made with graphite on platinum (or silver) buttons. Two samples (pure and doped) were measured simultaneously in a specially constructed sample holder.

### 3 RESULTS AND DISCUSSION

The typical experimental data for the pressure dependence of the conductivity data of  $\beta$ -PbF<sub>2</sub>, doped with NaF and TbF<sub>3</sub> are shown in Figure 1. At each temperature,  $\sigma$  decreases as  $P$  increases and at constant  $T$ ,  $\lg \sigma$  decreases linearly with pressure. The pressure was restricted ( $\sim 0.2$  GPa) with respect to the  $\beta$ - to  $\alpha$ -PbF<sub>2</sub> phase transition.<sup>4</sup> The measured  $\Delta V$  and the calculated activation volumes  $\Delta V_{\text{calc}}$  for the investigated single crystals are summarized in Table I. The most important feature of the results in Table I is the fact that the value of the activation volume of the defect formation is larger than the activation volume of defect migration. For  $\beta$ -PbF<sub>2</sub> we found  $\Delta V_f \simeq 3\Delta V_m$ . We could not estimate  $\Delta V_f$  for LaF<sub>3</sub>, because the temperature in the pressure apparatus was limited to 400°C. The formation volume  $\Delta V_f$  can be especially useful in determining the type of disordering. For Schottky disordering the ratio should be:  $\Delta V_f/\Delta V_{\text{molar}} > 1$ , for Frenkel disordering:  $\Delta V_f/\Delta V_{\text{molar}} < 1$ . In the case of PbF<sub>2</sub> we obtained the additional information that Frenkel defects are predominant in this crystal. The small values of activation volumes of defect migration in LaF<sub>3</sub> conforms that LaF<sub>3</sub>-matrixes are very good superionic conductors. Keyes' treatment based on the strain energy Zener model in Grüneisen approximation  $\Delta V_{\text{calc}} = 2(\gamma - 1/3)\chi\Delta H/(1 + 2\beta(\gamma - 1/3)T)$ , where  $\gamma = \beta/\chi c_v$  ( $\beta$ —thermal expansion coefficient,  $c_v$ —specific heat,  $\chi$ —isothermal compressibility,  $\Delta H$ —activation energy of the corresponding processes of defect formation and migration, obtained from analysis of electroconductivity data) can be used for theoretical estimation of activation volumes.<sup>5</sup> We compared (Table I) the experimentally determined activation volumes with those calculated using the Zener model. The results of this comparison are satisfactory in the sense that  $\Delta V$  is proportional to  $\Delta V_{\text{calc}}$ . It is suggested that the difference between measured and calculated values could be due to the temperature dependence of the compressibility. Taking into account the temperature dependence of  $\chi$ , it should be possible to reduce the occurring differences.

Table I  
Activation volumes  $\Delta V$  and  $\Delta V_{\text{calc}}$

Compound	Process	T (K)	$\Delta H$ (eV)	$\Delta V$ (cm <sup>3</sup> /mol)	$\Delta V_{\text{calc}}$ (cm <sup>3</sup> /mol)	$\Delta V/V_{\text{calc}}$
$\beta$ -PbF <sub>2</sub>	Frenkel defect formation	300–530	1.04	4.6	4.9	0.9
	Fluorine vacancy migration	340–500	0.22	1.4	1.1	1.3
	Fluorine interst. migration	325–435	0.33	2.4	1.7	1.4
	Dissociation Na <sup>+</sup> – V <sub>F</sub>	273–340	0.24	2.0	1.2	1.7
	Dissociation Tb <sup>3+</sup> – F <sub>i</sub>	273–325	0.34	2.2	1.7	1.3
$\beta$ -PbF <sub>2</sub> - CdF <sub>2</sub> (34 mol%)	Defect migration	285–335	0.36	1.1	1.7	0.65
$\beta$ -PbF <sub>2</sub> - UF <sub>4</sub> (15 mol%)	Defect migration	300–450	0.34	1.7	1.7	1.0
LaF <sub>3</sub>	Defect migration	465–670	0.30	1.8	1.6	1.1
LaF <sub>3</sub> - CaF <sub>2</sub>	Defect segregation	273–325	0.48	2.8	2.4	1.2
(1.2mol%)	Dissociation Ca <sup>2+</sup> – V <sub>F</sub>	325–465	0.43	2.2	2.1	1.05
	Defect migration	465–670	0.31	1.9	1.6	1.2

## REFERENCES

1. I. V. Murin, *Izv. Sibirskogo Otdelenija nauk SSSR, ser. chim. nauk, Nr.1*, **53** (1984).
2. I. V. Murin and W. Gunsser, *Solid State Ionics* **53-56**, 837 (1992).
3. G. A. Samara, *Sol. Stat. Phys, Advance and research and applications* (H. Ehrenreich, D. Fumbull, Orlando, USA, AP, 1984, pp. 454).
4. W. Klement Jr., Lewis H. Cohen, *J. Electrochem. Soc.*, **126**, 1403 (1979).
5. R. W. Keyes, in: *Solids under pressure*, W. Paul and D. M. Warschauer, Eds. (McGraw-Hill, NY, 1963), chapt. 4.

## TRANSPORT PHENOMENA IN ALKALI HALIDE MIXED CRYSTALS

FRANÇOIS BÉNIÈRE, VISSAMSETTI HARI BABU, MICHELLE BÉNIÈRE and  
KOTHAKOTA V. REDDY

*Groupe Matière Condensée et Matériaux (URA 804) Université de Rennes—F35042  
RENNES (France)*

We have investigated the enhancement effect on the transport phenomena in solid solutions relative to the pure end members. Only single crystals and measurements carried out in the middle of the intrinsic range have been considered. The enhancement effect for both the self and heterodiffusion coefficients reaches a factor of about 2 around the middle composition. The diffusion data are analysed in terms of vacancies. The correlation effects have been accounted for by making use of Manning's equations for vacancy diffusion in random alloys via unbound free vacancies. We conclude that the major part of the enhancement originates from an increase of the vacancy concentration relative to the pure end members.

*Key words:* Mass transport, mixed crystals, diffusion, ionic crystals.

### 1 INTRODUCTION

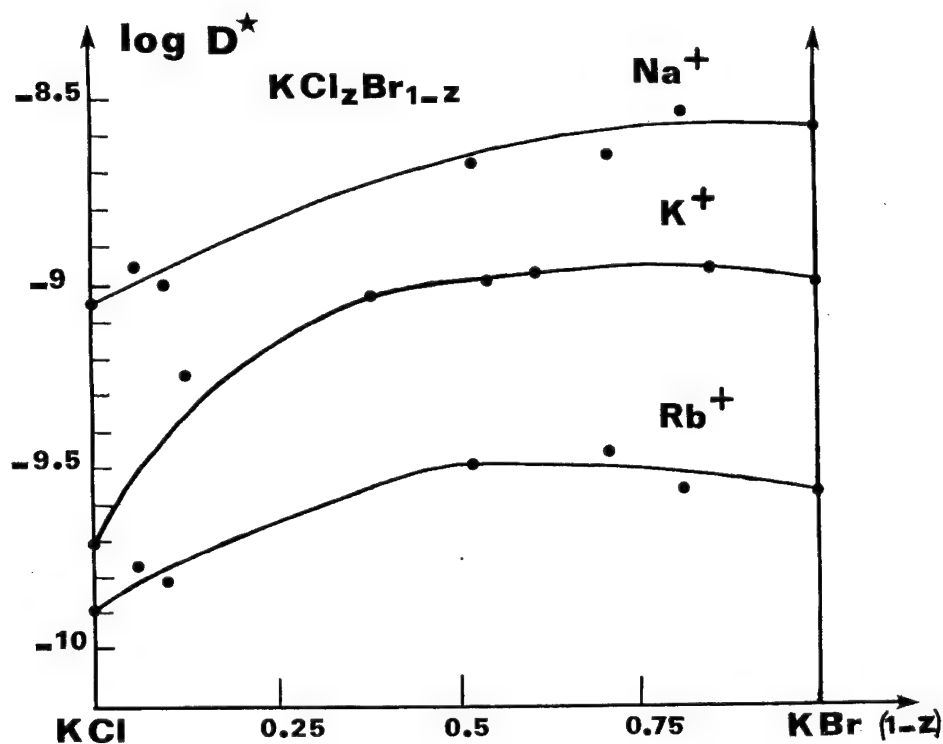
We present a self consistent analysis of a complete set of atomic diffusion data in monocrystalline alkali halide mixed crystals. In order to obtain intrinsic data that can be interpreted in terms of purely thermodynamic point defects, we have selected some combinations of alkali halides that give solid solutions in the full concentration range and for which exist radioactive tracers for the three constituent ions. These conditions have enabled the measurements of the self-diffusion coefficients of the three ions as a function of the composition for at least one given temperature. New measurements of the heterodiffusion coefficients of  $\text{Na}^+$  and  $\text{Rb}^+$  in  $\text{KCl}_z\text{Br}_{1-z}$  are combined with previous data for the self-diffusion coefficients of the three host ions constitutive of the solid solutions:  $\text{KCl}_z\text{Br}_{1-z}$  [1],  $\text{K}_z\text{Rb}_{1-z}\text{Cl}$  [2] and  $\text{K}_z\text{Rb}_{1-z}\text{I}$  [3].

### 2 ANALYSIS OF EXPERIMENTAL DATA

A detailed account of the experimental results is being published in a complete report [4]. As an example, the composition dependence on the self-diffusion coefficients of the cation as well as on the diffusion of  $\text{Na}^+$  and  $\text{Rb}^+$  in  $\text{KCl}_z\text{Br}_{1-z}$  mixed crystals is shown as  $\log(D^*)$ -vs- $(1-z)$  on Figure 1. The choice of the logarithmic scale better emphasizes the influence of the composition whatever the magnitude of  $D^*$ . We first notice that there IS an enhancement effect of the mass transport in the solid solution. The effect is maximum around the middle composition where it reaches a factor of about 2 as compared to the weighted average in the two end compositions. It is therefore MUCH LESS important than usually reported from the conductivity data in non-crystalline samples [5]. Self and heterodiffusion via vacancies in the fcc lattice are both expressed by the general equation:

$$D^* = 4a^2 f \omega x \quad (1)$$

with  $a$ : the anion-cation separation distance in the NaCl structure,  $f$ : the correlation factor,  $\omega$ : the jump frequency, and  $x$ : the mole fraction of vacancies.

FIGURE 1 Self and heterodiffusion coefficients in  $\text{KCl}_2\text{Br}_{1-z}$  at  $650^\circ\text{C}$ .

We have used for the correlation factor the expressions proposed by Manning [6] in random alloys. In this model, the vacancy has no preference for one type of atom over another. When both tracer diffusion coefficients  $D_A^*$  and  $D_B^*$  can be measured in the solid solution  $A_zB_{1-z}$ , the corresponding correlation factors are then given by the unequivocal equations:

$$f_A = f_0 \left[ 1 - \frac{2N_B(D_A^* - D_B^*)}{M_0(N_A D_A^* + N_B D_B^*)} \right] \quad (2)$$

$$f_B = f_0 \left[ 1 + \frac{2N_A(D_A^* - D_B^*)}{M_0(N_A D_A^* + N_B D_B^*)} \right] \quad (3)$$

where  $f_0 = 0.78$  and  $M_0 = 2f_0(1 - f_0)^{-1} = 7.15$  in the vacancy mechanism in the fcc lattice, while  $N_A$  and  $N_B$  are the mole fractions of A and B atoms, respectively.

At the limit  $N_B \rightarrow 0$ , equations (2) and (3) take the limiting forms:  $f_A = f_0$  and

$$f_B = f_0 \left[ 1 + 2 \frac{(D_A^* - D_B^*)}{M_0 D_A^*} \right] \quad (4)$$

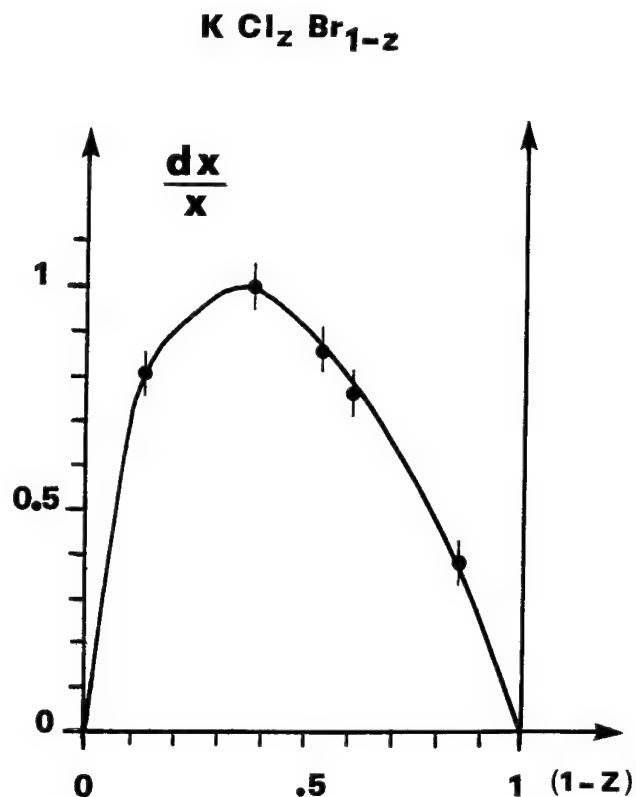


FIGURE 2 Relative excess mole fraction of vacancies in  $\text{KCl}_z\text{Br}_{1-z}$ .

which is a very useful expression for heterodiffusion at infinite dilution, as long as  $D_A^*$  and  $D_B^*$  are not too different in magnitude.

Originally, these expressions involved several assumptions and were believed to be restricted to concentrated alloys. The computer simulation [7] of diffusion in binary alloys gave a first serious indication that Manning's relation could be used with more confidence. Simultaneously, Lidiard [8] gave a careful analysis of Manning's equations. He showed that under certain assumptions the theory of non equilibrium thermodynamics led to the same relations. As another important new result, those analytical relations were proved also to apply at both dilute limits of binary alloys [9] when applied to the random alloy model.

The self-diffusion data in the monoatomic sublattice are first considered:  $\text{K}^+$  in  $\text{KCl}_z\text{Br}_{1-z}$ . It was proved [3] that the major cause for the enhancement effect of the transport properties is due to the increase in the Schottky defect concentration. The correlation factor in eq.(1) has the fixed value  $f = 0.78$ . The relative excess vacancy concentration is thus derived from eq.(1). The jump frequency  $\omega_{\text{K}^+}$  is fairly well known at both ends of the diagramme:  $z = 1$  or pure KCl; [10] and  $z = 0$  or pure KBr [11] and the

absolute value  $x$  of the cation vacancy mole fraction is finally determined as a function of the composition  $z$ .

The anion diffusion coefficients of  $\text{Cl}^-$  and  $\text{Br}^-$  in the mixed anion sublattice are then analysed. The anion vacancy mole fraction in the intrinsic range is obviously equal to the cation vacancy mole fraction. The correlation factors  $f_{\text{Cl}^-}$  and  $f_{\text{Br}^-}$  are calculated from eqs.(2) and (3). The jump frequencies of exchange of the vacancy with  $\text{Cl}^-$  and with  $\text{Br}^-$  are then derived from eq.(1).

Lastly, the heterodiffusion coefficients of  $\text{Na}^+$  and  $\text{Rb}^+$  are decomposed in order to obtain the jump frequencies of foreign ions for comparison. The correlation factor is given the limiting form of eq.(4). Finally, one gets the jump frequencies of exchange of the vacancy with  $\text{Na}^+$  and  $\text{Rb}^+$  in  $\text{KClBr}_{1-z}$  as a function of  $z$  from eq.(1).

The relative excess vacancy concentration in the solid solution as compared to the weighted average  $\bar{x} = z \times x_{\text{KCl}} + (1 - z)x_{\text{KBr}}$ , namely  $(x - \bar{x})/\bar{x}$  is shown in Figure 2. Similar diagrammes are obtained in  $\text{K}_z\text{Rb}_{(1-z)}\text{Cl}$  and  $\text{K}_z\text{Rb}_{(1-z)}\text{I}$ . [4].

### 3 CONCLUSION

There is a clear enhancement of the diffusivity in mixed alkali halides. This effect is evident on the self-diffusion coefficients in both sublattices as well as on the heterodiffusion coefficient of foreign alkali cations. The order of magnitude of this effect in the intrinsic range reaches a maximum of about a factor 2 in the systems:  $\text{KCl-KBr}$ ,  $\text{KI-RbI}$  and  $\text{KCl-RbCl}$  where the measurements refer to single crystals. The Nernst-Einstein relation demands that the enhancement of the ionic conductivity should be of the same amount. It must be noted on the contrary that much larger effects have been reported on the ionic conductivity of other mixtures of alkali halides [5] and of other ionic solids [12]. However, some of those results concern low temperature data (below the intrinsic/extrinsic transition temperature) and pressed pellets instead of single crystals. One cannot exclude that a part of the enhancement is of extrinsic or intergranular nature.

Making use of Manning's equations to account for the correlation effects, we have shown that it is possible to develop a self-consistent analysis of the whole set of hetero-and self-diffusion coefficients and found that the major part of the enhancement is directly related to the parallel increase in the free vacancy concentration relative to the pure end members.

### REFERENCES

1. F. Bénére and V. Hari Babu, *Cryst. Latt. Def. and Amorph. Mat.*, **15**, 263 (1987).
2. R. Lindström, *J. Phys. C, Solid State Phys.*, **6**, 197 (1973).
3. L. Bonpunt, N. B. Chanh, G. Comberton, Y. Haget and F. Bénére, *Radiation Effects*, **75**, 33 (1983).
4. F. Bénére, M. Bénére, V. Hari Babu and K. V. Reddy, *J. Phys. Chem. Solids*, **55**, 595 (1994).
5. P. Manoravi and K. Shahi, *J. Phys. Chem. Solids*, **52**, 527 (1991).
6. J. R. Manning, *Phys. Rev.*, **4**, 1111 (1971).
7. G. E. Murch and S. J. Rothman, *Phil. Mag.*, **A43**, 229 (1981).
8. A. B. Lidiard, *Acta Metall.*, **34**, 1487 (1986).
9. A. R. Allnatt and A. B. Lidiard, *Acta Metall.*, **35**, 1555 (1987).
10. M. Bénére, M. Chemla and F. Bénére, *J. Phys. Chem. Solids*, **37**, 525 (1976).
11. N. Brown and P. W. M. Jacobs, *J. de Physique*, **34 C9**, 437 (1973).
12. D. B. Sirdeshmukh and K. Srinivas, *J. of Materials Science*, **21**, 4117 (1986).



## LOCAL STRUCTURE AND OXYGEN TRANSPORT IN TRANSITION METAL DOPED YSZ

N. NICOLOSO, J. MAIER, F. K. KOSCHNICK\* and J. M. SPAETH\*

*Max-Planck-Institut für Festkörperforschung, Heisenbergstr., 70569 Stuttgart, F.R.G;*

*\*University of Paderborn, Fachbereich Physik, Warburger Str. 100, 33098  
Paderborn, F.R.G.*

The chemical diffusion of oxygen and the structure of the electronic defects in undoped and transition metal doped YSZ single crystals have been investigated by a contactless relaxation technique and magneto-optical resonance (MCD(A))-studies. The local structure and the transport properties of YSZ (9.5 mol%  $\text{Y}_2\text{O}_3$ ) are inter-related by the actual defect distribution of 7- and 6-fold coordinated Zr-defects with trigonal symmetry which mainly originate from Zr d- conduction band tail states and act as electron traps.

The strong interaction between the ionic and electronic transport properties can be quantitatively explained by a modified ambipolar transport model. Experimentally, the diffusion behaviour of oxygen can be precisely followed by the optical relaxation technique.

**Key words:** Fast Ion Conductors, Transport Properties, Chemical Diffusion, Magnetic Resonance, Optical Absorption.

### 1 INTRODUCTION

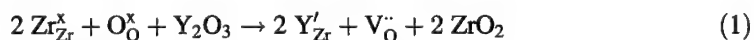
#### 1.1 Exchange Kinetics of Solid Oxide Ion Conductors

Within the class of high temperature materials, the ternary compound  $\text{Zr}_{1-x}\text{Y}_x\text{O}_{2-x/2}$ ;  $x \simeq 0.16$  (YSZ) is considered a prototype fast oxide ion conductor with important applications ( $\lambda$ - probe in cars, membrane in solid oxide fuel cells, etc.). Despite of its technological importance, the kinetics of the oxygen exchange is poorly understood. At high temperature this quantity should be mainly controlled by the bulk diffusion and, hence, should simply depend on the chemical diffusion coefficient of oxygen,  $\tilde{D}$ .<sup>1</sup> However, the experimental  $\tilde{D}$ -values strongly deviate from the expected ones. In the following we present

- i)  $\tilde{D}$ -values of transition metal doped YSZ crystals obtained by a contactless measuring technique ('Optical Absorption Relaxation')[1a] and
- ii) an improved theoretical analysis of the chemical diffusion in oxides in the presence of redox-active impurities, here transition metal ions[1b].

#### 1.2 Structural Analysis of Defects in YSZ

Due to the substitution reaction



rather high oxygen vacancy defect concentrations ( $[\text{V}_{\text{O}}^{\bullet\bullet}] \gg 1\%$ ) are achieved in yttria doped zirconia. However, the fast oxygen transport in this material does not only depend

<sup>1</sup> according to the classical ambipolar diffusion theory  $\tilde{D}$  should correspond in this case to the self diffusion coefficient of the respective electronic minority charge carrier,  $D_e$  (reducing) or  $D_h$  (oxidizing conditions).

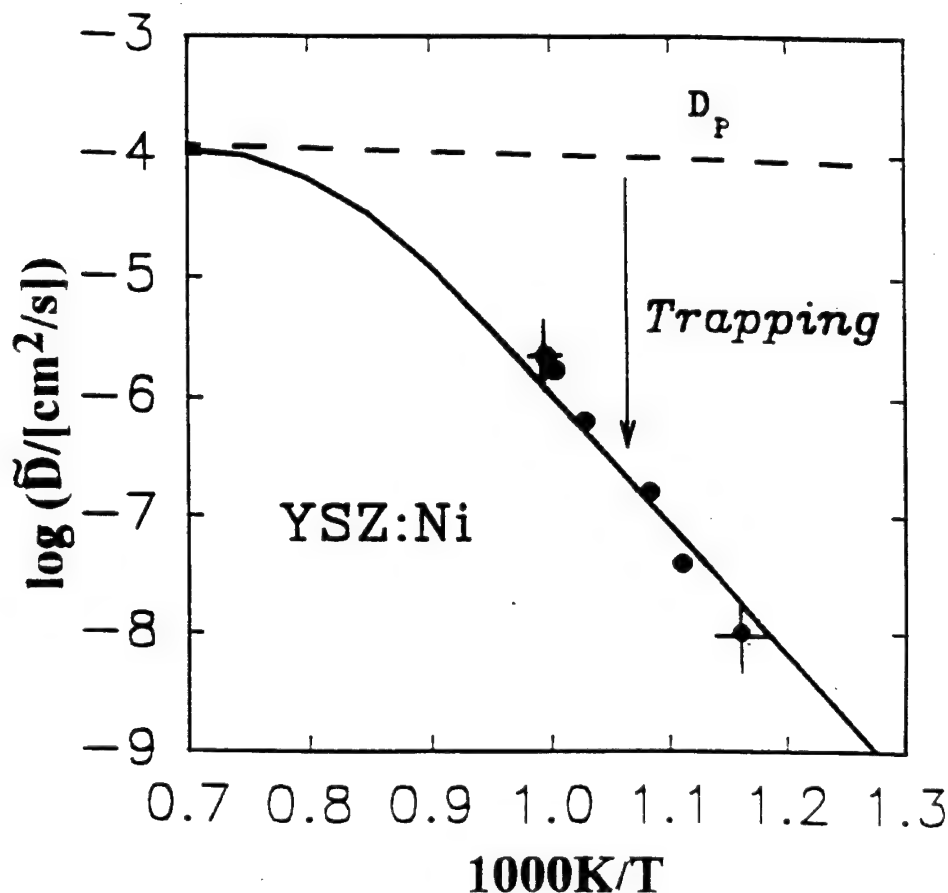


FIGURE 1 (a) Experimental and calculated  $\tilde{D}$ -values (full and dashed lines) of transition metal doped YSZ ( $\approx 0.1$  wt%) as a function of temperature at  $p_{O_2} \approx 10^3$  (Ni) and  $10^{-10}$  Pa (Ti, Nb and Co).

on the *number* of defects but also on their *arrangement* in the lattice. The vacancies may be distributed randomly, trapped by electrostatic forces, e.g., as dopant cation-vacancy pair  $Y'_{Zr} V_{O^{\bullet}}$ , or ordered by thermodynamic (long range) ordering. In the latter cases the transport properties will be appreciably modified by changes in the carrier mobility and the concentration of the mobile defects; an effect which is most clearly seen in the non-monotonic increase of the conductivity with the nominal vacancy concentration (a maximum occurs at  $\approx 4\%$ ).

Concerning the local structure, the introduction of oxygen vacancies into the cubic crystal structure of YSZ on the one hand causes local distortions, i.e., fluctuations of the  $M \dots O$  bondlength. Consequently, band-tailing at the conduction and valence band edges should be discernible just as in non-crystalline solids. On the other hand, the average coordination number of the metal atoms has to decrease with increasing oxygen vacancy content favouring 7- and 6-fold coordinated Zr-defects,  $ZrO_7 V_{O^{\bullet}}$  and  $ZrO_6 (V_{O^{\bullet}})_2$ . The distribution of  $ZrO_8$  structure units with 0, 1 and 2 oxygen vacancy defects has been studied by site selective spectroscopies (Raman, PAC, ...) using rare earth ions or isotopes

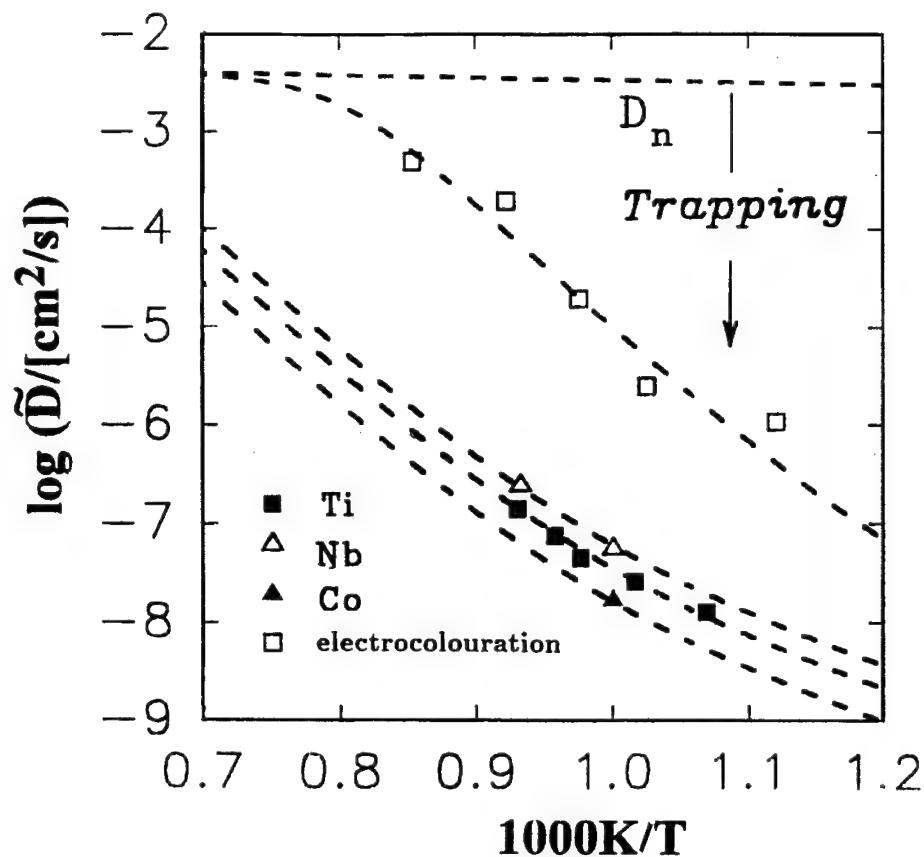


FIGURE 1 (b)

such as  $^{111}\text{Cd}$  as markers[2, 3, 4]. However, the clearest information about these defects arises from combined optical absorption and ESR-studies on irradiated and thermo-chemically reduced YSZ [5, 6, 7, 8].

In order to obtain further information about the structure of these defects, multiple resonance methods (ENDOR and MCD(A)) have been applied to  $\text{H}_2$ -reduced single crystals (1300 K/24 h) or x-ray irradiated crystals at LHeT. For further details of these experiments and the determination of the chemical diffusion coefficient of oxygen the reader is referred to [1, 9].

## 2 RESULTS AND DISCUSSION

### 2.1 Chemical Diffusion of Oxygen in YSZ

Under high oxygen partial pressures (oxid. conditions) the concentration of oxygen vacancies ( $\text{V}_{\text{O}}^{\bullet}$ ) and free holes ( $\text{h}^{\bullet}$ ) is determined by the variables  $T$ ,  $P_{\text{O}_2}$  and  $m$  (temperature, oxygen partial pressure and doping content) via the mass action law for the oxygen incorporation reaction

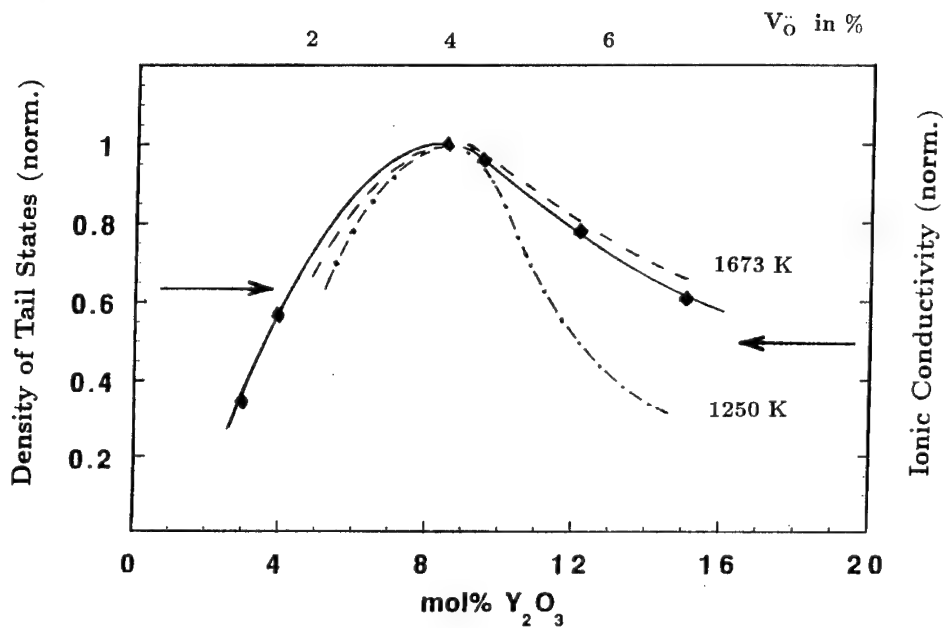
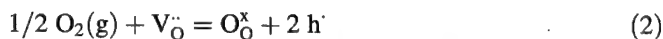


FIGURE 2 Comparison of the normalized density of tail states with the normalized conductivity of yttria doped zirconia.



and the condition of local electroneutrality. Internal valence changes due to the trapping of electronic carriers- by transition metal impurities or by intrinsic defects- are caused by ionization reactions. For example, in the case of Ni-doped YSZ (Ni-content  $\ll$  Y-content)



Hence, a quantity such as the optical absorbance of these impurity defects can be used as a probe of the local chemical potential of oxygen during re-equilibration. According to eq. 3 internal source and sink terms influence the chemical diffusion process requiring a correction of the classical ambipolar transport model:<sup>2</sup>

$$\tilde{D} = t_{\text{h,e}} D_{\text{V}} + t_{\text{V}} D_{\text{h,e}}$$

where  $t_{\text{h,e}}$  and  $t_{\text{V}}$  denote the transference numbers of the electronic charge carriers and vacancies;  $D_{\text{V}}$  and  $D_{\text{h,e}}$  represent the corresponding diffusion coefficients. A decrease of the diffusion by the trapping of free carriers can be quantitatively explained by introducing a correction factor  $\chi$  representing the differential fraction of free electronic carriers<sup>16</sup>:

$$\tilde{D} = t_{\text{h,e}} D_{\text{V}} + \chi t_{\text{V}} D_{\text{h,e}} \quad (4)$$

or

<sup>2</sup> for YSZ this reduces to  $\tilde{D} \simeq D_{\text{h,e}}$ , since  $t_{\text{h,e}} \ll t_{\text{V}} \simeq 1$  and  $D_{\text{h,e}} \geq D_{\text{V}}$ .)

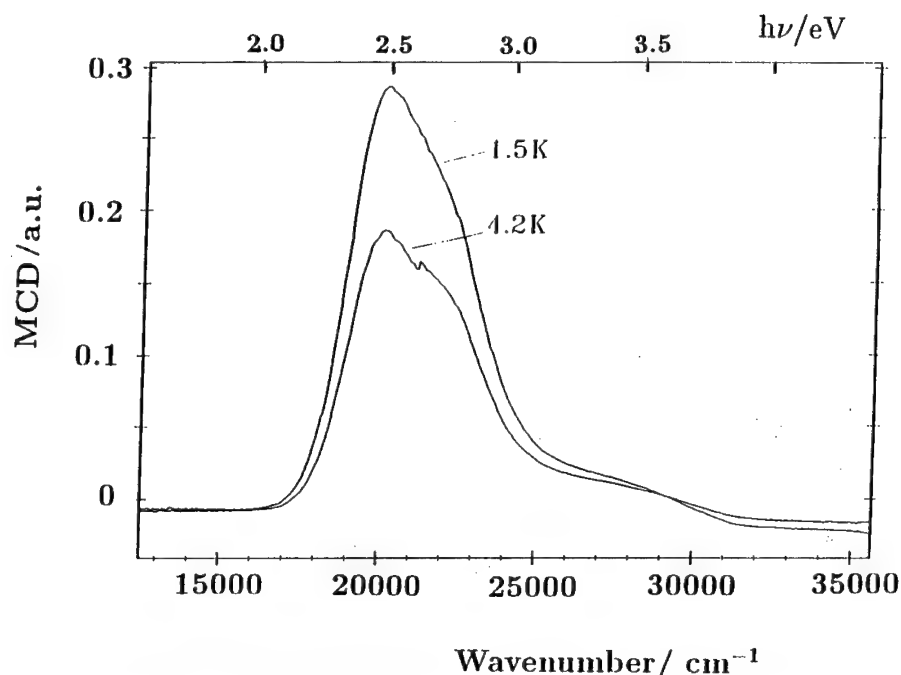


FIGURE 3 Temperature dependence of the MCD(A)-signal of  $H_2$ -reduced yttria stabilized zirconia (9.5 mol%  $Y_2O_3$ ) single crystals.

$$\tilde{D} \simeq \chi D_{h,e} \quad (5)$$

in case of fast ion conductors.

As discussed more detailed in ref [1],  $\chi$  can be evaluated from defect chemical relations and is given by

$$\chi(T, p_{O_2}, Y, m) = \left( 1 + \frac{mK_2}{K_2 + K_1^{1/2} p_{O_2}^{1/4} Y^{1/2}} \right)^{-1} \quad (6)$$

where  $K_1$  and  $K_2$  are the mass action constants of the above reactions (eqs. 2 and 3),  $Y = 1/2$  of the yttria content and  $m$  the total impurity content (here Ni-doping level).

Experimentally, the diffusion of oxygen in YSZ is monitored by following the change in the normalized optical absorption of  $Ni_{Zr}''$  after a sudden  $p_{O_2}$  change ('Optical Absorption Relaxation'). Figure 1 a-b displays the temperature dependence of  $\tilde{D}$  obtained in transition metal doped YSZ in the oxidized (Ni) or reduced case (Ti-, Nb- and Co). The solid and dashed lines represent the  $\tilde{D}$ -behaviour according to eqs. 5 and 6 (and their equivalents in the case of reduction). Since the ionization equilibrium (eq. 3) shifts to the right hand side with temperature, hole (electron) trapping is not dominant at high temperature and the absolute value of  $\tilde{D}$  approaches  $D_h$  and  $D_e$ , respectively.

In an analogous manner the strong scatter in the literature values for the chemical diffusion coefficient of oxygen can be analyzed and attributed to the neglect of trapping

effects (impurity and possibly even self trapping, especially in reduced YSZ). Although nominally pure materials, the drastic differences in the literature  $\bar{D}$ -values very likely arise from the unintentional doping of the YSZ which -according to our model- typically ranges from about 50 ppm to 500 ppm.

## 2.2 Structure of Defects and Electrical Transport in YSZ

As has been shown in ref. [10], the density of band tail states and the concentration of oxygen vacancy defects are intimately connected. Furthermore, the close correspondence between the electronic structure of the system, especially the band tailing part, and the transport properties can be nicely demonstrated by comparing the normalized density of tail states with the normalized conductivity -see Figure 2.

As regards the structure of the electronic defects in YSZ, our first MCD(A) result of H<sub>2</sub>-reduced YSZ (1300 K /48 h), see Figure 3, essentially agree with the models proposed by refs. [7, 6], although there exist some inconsistencies (more than two types of paramagnetic defects with  $S = 1/2$  and  $g$ -values  $\leq 2$  can be inferred from Figure 3). Deconvolution of the signal leads to 3 gaussian bands with energies of  $\approx 2.5$ , 2.8 and 3.3 eV. The temperature dependence of the MCD(A) proves that the bands originate from a paramagnetic ground state, i.e. arise from paramagnetic defects- see, e.g., ref. [11]. The latter band coincides with one of the optical bands of the 10 K spectrum [8]) which suggests that this feature arises from the 6-fold coordinated Zr<sup>3+</sup>-defect. Similarly, the second MCD(A)-band at  $\approx 2.8$  eV can be tentatively attributed to the 7-fold coordinated Zr<sup>3+</sup>-center. Whether the third MCD(A)-band at about 2.5 eV arises from an impurity center ( $n d^1$  (Ti, Hf ?) or  $n f^1$ -state (Ce ?)) or a 7-fold coordinated Zr<sup>3+</sup>-defect with lower than trigonal symmetry can not be decided yet; further magnetic resonance studies with O<sup>17</sup>-exchanged samples and Ce-doped single crystals, as well as an improved chemical analysis are in progress.

## 2.3 Summary and Conclusions

In the fast oxide ion conductor YSZ the local structure and the transport properties are interrelated by the actual defect distribution of 7- and 6-fold coordinated Zr-defects which mainly originate from Zr d- (band tail) states and act as pre-formed traps for electrons (on reduction these defects are further stabilized by the lattice polarization energy forming 111-axialsymmetric electron centers).

The strong interaction between the ionic and electronic transport properties can be quantitatively explained by a modified ambipolar transport model. Experimentally, the diffusion behaviour of oxygen may be precisely followed by an optical relaxation technique.

Besides providing a clear and elegant analysis of the chemical diffusion in fast ion and mixed conducting oxides, the modified ambipolar diffusion approach allows a simple quantification of an electron transport influenced by reaction coupling between free and trapped electronic carriers and can be extended to other wide band gap materials such as nitrides and carbides when the relevant defect chemical parameters (see eqs. 2 and 3) will be available.

## REFERENCES

1. (a) T. Bieger, H. Yugami, N. Nicoloso, J. Maier and R. Waser, in: *Solid State Ionics* **72**, 41, 1994; (b): J. Maier, *J. Amer. Ceram. Soc.* **76**, 1223 (1993); *ibid* **76**, 1212, 1218, 1228.

2. H. Yugami *et al.*, *Phys. Rev.* **B44**, 9214, 1991; H. Yugami, S. Matusuo and M. Ishigame, *Solid States Ionics* **53-56**, 1264, 1992.
3. H. T. Su *et al.*, *J. Am. Ceram. Soc.*, **11**, 3215, 1993.
4. R. I. Merino and V. M. Orera, *Solid State Commun.* **89**, 435, 1993.
5. R. Ben-Michael, D. S. Tannhauser, and J. Genossar, *Phys. Rev.* **B43**, 7395, 1991.
6. V. M. Orera *et al.*, *Phys. Rev.* **B42**, 9782, 1990.
7. C. B. Azzoni and A. Paleari, *Phys. Rev.* **B44**, 6858, 1991.
8. N. Nicoloso, Habilitationsschrift, Universität-6h Kassel, 1994.
9. N. Nicoloso, F. Koschnick, J. Maier, and J. M. Spaeth, to be published.
10. N. Nicoloso, B. Leibold and H. -U. Habermeier, in *Laser Ablation of Electronic Materials*, E. Fogarassy and S. Lazare, Eds., Elsevier Science Publ., 1992, p. 385 ff.
11. J. M. Spaeth, J. R. Niklas, and R. H. Bartram, *Structural Analysis of Point Defects in Solids*, Springer Series in Solid State Sciences 43, Springer Verlag, Berlin, 1992.

## ANOMALOUS POINT DEFECT FORMATION AND PHASE TRANSITIONS: THE SIGNIFICANCE OF A CUBE ROOT LAW

N. HAINOVSKY<sup>1,2</sup> and J. MAIER<sup>1</sup>

<sup>1</sup>Max-Planck-Institut für Festkörperforschung, Heisenbergstraße 1, 70569 Stuttgart, Germany; <sup>2</sup>Institute for Solid State Chemistry, Derzhavina 18, 630091 Novosibirsk, Russia

Here we discuss a phenomenological approach for the understanding of the anomalous point defect formation in ionic crystals prior to the phase transition as well as the prediction of the phase transition temperatures. Quantitative agreement was achieved using a simple cube root law for the defect-defect interaction potential. This approach was applied to materials (AgCl, AgBr, AgI, PbF<sub>2</sub>) with different structures (rock salt, fluorite, wurtzite), different types of disorder (Frenkel and anti-Frenkel) and different types of phase transition (solid-liquid and solid-solid, first and second order). The computed defect-defect interaction leads to a quantitative description of the conductivity anomalies and to the prediction of a phase instability at a temperature which is very close to the actual transition point.

**Key words:** defect-defect interaction, phase transition, thermodynamics, ionic conductivity.

### 1 INTRODUCTION

For many ionic crystals the dilute defect chemical approach fails when the temperature approaches the phase transition point. This anomalous defect generation is easily observed in conductivity experiments, as performed on silver halides and PbF<sub>2</sub>.<sup>1-4</sup> Several attempts have been undertaken to explain this by using either an ad-hoc approach to describe the defect interaction (linear model,  $\mu_{int} \sim c$ ) or within traditional electrochemical theory<sup>5</sup> (Debye-Hückel,  $\mu_{int} \sim c^{1/2}$ ). Some qualitative aspects of the defect behavior in the pre-phase transition region may be understood by these models. However, a satisfactory quantitative agreement has not yet been achieved.

### 2 CUBE-ROOT-MODEL AND PREMELTING ANOMALY

In general, all former models as well as the model to be discussed are formulated in a mean-field approximation in which the equilibrium defect concentration  $c$  may be written as

$$c = \exp\left(-\frac{\Delta F + \mu_{int}(c)}{kT}\right)$$

where  $\Delta F$  denotes the standard formation energy for  $c \rightarrow 0$ , i.e. the first formation value. Here we show that the conductivity enhancement prior to the phase transition temperature can be quantitatively described by cube-root-law for the excess chemical potential:  $\mu_{int} = -Jc^{1/3} = kT \ln f$ ,  $J$  and  $f$  being a defect-defect interaction constant and the activity coefficient. This finding indicates the approximate validity of the mean field approach in which the effective potential in the defect site varies with the defect-defect distance ( $\sim c^{-1/3}$ ) and may be microscopically explained in the framework of a Mott-Littleton



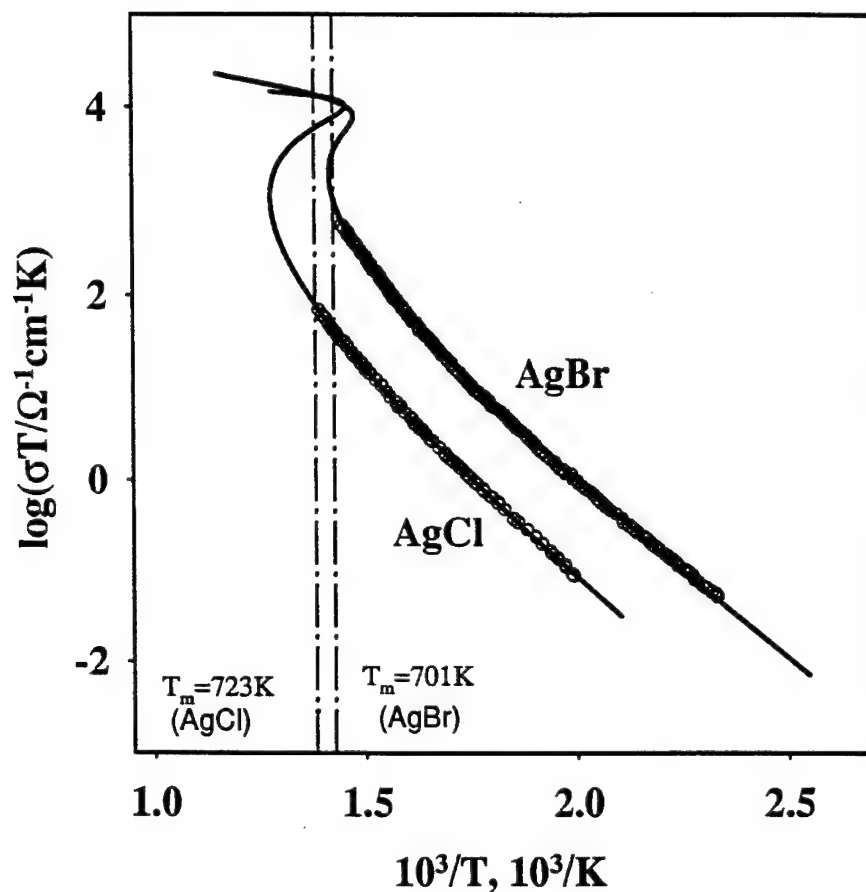


FIGURE 1 Temperature dependence of conductivity for the rock salt structure materials AgCl and AgBr. Points represent experimental data: AgCl<sup>1</sup>, AgBr<sup>2</sup>. Solid lines show the result of fitting with the cube root dependence. Vertical dash lines indicate the experimental melting temperatures.

approximation.<sup>6</sup> Thus the defective solid may be understood – in an effective sense – in terms of superposition of a perfect lattice and the defect sublattice. It is important to emphasize that the same cube root dependence of the excess chemical potential has been found for concentrated liquid electrolytes<sup>7</sup> in a rather wide range of concentration.

We used a non-linear fitting procedure to treat conductivity data and to extract the defect-defect interaction parameter  $J$  as well as the standard defect formation free energy  $\Delta F$ . Figures 1–3 show the quantitative agreement of the cube root dependence and experimental data for AgCl, AgBr, AgI and PbF<sub>2</sub>.

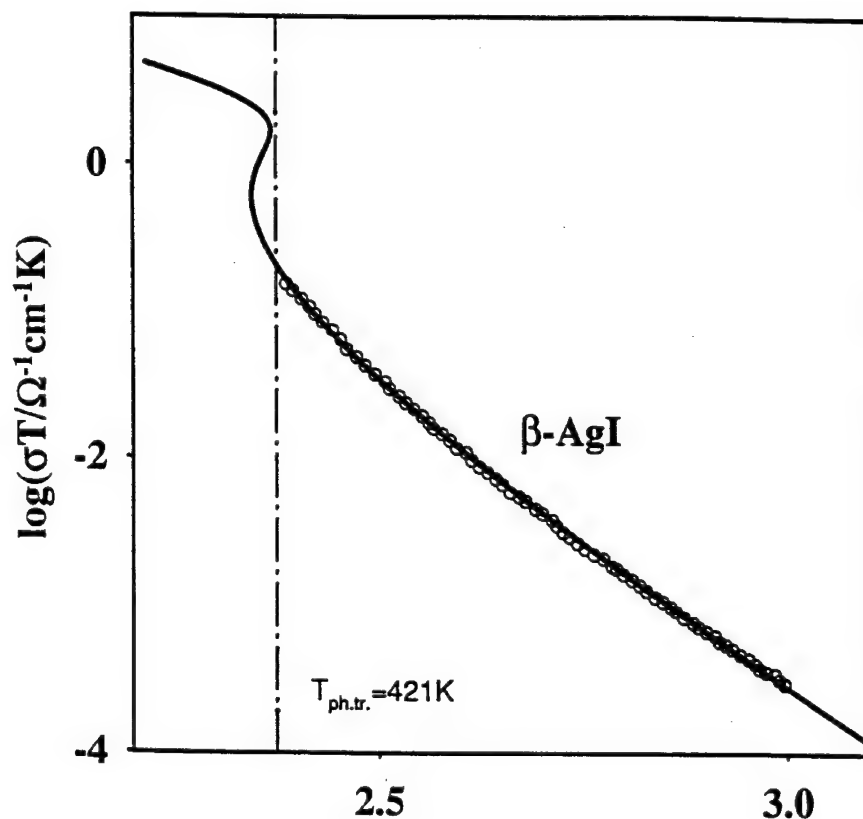


FIGURE 2 Temperature dependence of conductivity for  $\beta$ -AgI (wurtzite). Points represent experimental data.<sup>3</sup> The solid line shows the result of fitting with the cube root dependence. The vertical dashed line indicates the experimental temperature of the superionic phase transition.

### 3 CUB-ROOT-MODEL AND PHASE TRANSITIONS

The appearance of the excess chemical potential  $\mu_{int}(c)$  in the equation of state leads to the total free energy of the crystal as follows

$$F = F_{perfect} + c \cdot \Delta F - 3/4 J \cdot c^{4/3} - kT \ln W$$

where  $k \ln W$  denotes the conventional configuration entropy of the defects at random distribution. This equation has either one or three solutions corresponding to one minimum or to two minima separated by a maximum. For different values of  $\Delta F$  and  $J$  different types of temperature dependencies may be observed.

The first type, when only one solution exists over the whole temperature range, shows a smooth increase of the defect concentration compared to the Arrhenius law. Finally, the

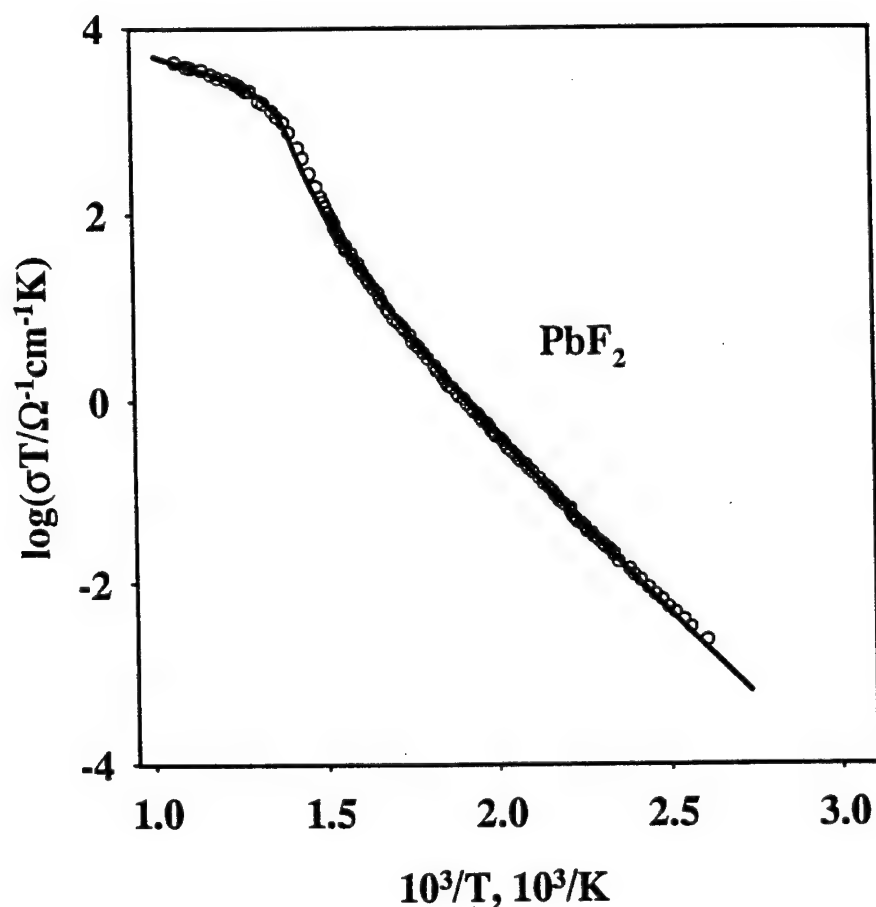


FIGURE 3 Temperature dependence of conductivity for  $\text{PbF}_2$  (fluorite). Points represent experimental data.<sup>4</sup> The solid line shows the result of fitting with the cube root dependence.

concentration reaches a saturation limit value. The conductivity of  $\text{PbF}_2$  illustrates a behavior of this kind (Figure 3). The same set of energetic parameters also allows to describe the specific heat anomaly in  $\text{PbF}_2$ .<sup>8</sup>

The second type displays the evolution of a second minimum of the free energy at high concentrations. At sufficiently high temperatures the second minimum corresponding to a highly disordered state, becomes the absolute minimum and an abrupt transition from a low to a high disordered state can occur. The melting transition of  $\text{AgCl}$ ,  $\text{AgBr}$  and the superionic phase transition of  $\text{AgI}$  are examples of such a first order transition.

In all these cases ( $\text{AgCl}$ ,  $\text{AgBr}$ ,  $\text{AgI}$  and  $\text{PbF}_2$ ) the  $J$  parameters used to describe the conductivity anomalies predict the correct phase transition temperature quite accurately ( $\pm 3\%$ ).

#### 4 CONCLUSIONS

The main content of the paper is twofold:

1. The conductivity anomalies observed for many ionic conductors prior to the order-disorder phase transition could be quantitatively described for the first time for AgCl, AgBr, AgI and PbF<sub>2</sub>.
2. For these materials the same very simple formalism leads to the prediction of the transition temperature. This is partly surprising for two reasons:
  - a) We used a simple cube root law with only one parameter. In view of the complexity of the problem a more detailed analysis is necessary. The situation seems to be somehow analogous to the situation in concentrated liquid electrolytes where also a cube root law is approximately valid.
  - b) Concerning the phase transition temperature, no information about the high temperature phase has been used. This means: i) the same effect, which leads to the conductivity anomaly, stabilizes the high temperature phase; and ii) the difference between the free energy of the hypothetical disordered high temperature phase which exhibits the structure of the LT-phase, and the free energy of the real HT-phase is insignificant. This has to be proven by further calculations. In this context the empirical rules connecting defect properties and melting points provide additional support.

#### REFERENCES

1. J. K. Aboague, R. S. Friauf, *Phys. Rev.* **B11**(4), 1654 (1975).
2. R. S. Friauf, in *Fast Ion Transport in Solids*, eds. Vashishta, Mundy and Shenoy, (Elsevier North Holland, inc), p. 181.
3. R. J. Cava, E. A. Rietman, *Phys. Rev.* **B30** (12), 6896 (1984).
4. A. Azimi, V. M. Carr, A. V. Chadwick, F. G. Kirkwood, R. Saghaian, *J. Phys. Chem. Solids* **45** (1), 23 (1984).
5. see for example, R. S. Friauf, *J. Phys. (Paris)*, **38** (1977), *ibidem* **41** C6, 97 (1980).
6. N. F. Mott, M. J. Littleton, *Trans. Faraday Soc.* **34**, 485 (1938).
7. see for example A. Münster, *Statistical Thermodynamics, Volume II*, (Springer-Verlag, Berlin, 1974), p. 783 and ref. herein.
8. N. Hainovsky and J. Maier, *Phys. Rev. B* to be published.

## INTRINSIC ELECTRON TRAPS AND ELECTRONIC CONDUCTION IN YSZ

R. I. MERINO and V. M. ORERA

*Instituto de Ciencia de Materiales de Aragón. C.S.I.C.-Universidad de Zaragoza  
Pza. San Francisco s/n, 50009 Zaragoza, Spain*

In the following paper we report the results of a study, by means of impedance spectroscopy, of the conducting properties of thermochemically blackened Yttria Stabilized Zirconia (YSZ) samples, previously investigated by means of optical and paramagnetic resonance spectroscopies. The work focuses on the relation between the characterized electron traps and the semiconducting properties of YSZ. On the light of the results we propose a level diagram for the electrons that accounts for the optical properties of the defects as well as for the electronic conduction of thermochemically reduced samples. This conduction would take place through a band of defects situated about 1.3 eV below the conduction band.

*Key words:* Reduced Stabilized-Zirconia, Electronic Conduction, Electron Traps, Impedance Spectroscopy.

### 1 INTRODUCTION

Zirconia stabilized in the fluorite cubic structure possesses a big amount of structural oxygen vacancies, which are responsible for the ionic conducting properties in a wide range of oxygen partial pressures. In reducing environments the material becomes colored due to the trapping of the electrons left behind by the outgoing oxygen ions and the electronic conduction grows.<sup>1</sup> In many of its applications this onset of the electronic conduction is unwanted and its understanding is of importance.

Different kinds of traps for electrons have been studied by means of optical and paramagnetic spectroscopic techniques.<sup>2</sup> Upon reduction the T-defects are formed first (electrons trapped at a  $Zr^{3+}$  surrounded by two oxygen vacancies along a cube diagonal). Stronger reduction produces a severe darkening due to the appearance of a strong absorption band with maximum at about 480 nm and which has been assigned<sup>2</sup> to heptacoordinated  $Zr^{3+}$  (C-defects), although in this case we have very little experimental information. The results that we present in the following address to the question of identifying the electron traps that take part in the electronic conduction of the material.

### 2 EXPERIMENTAL RESULTS

We have used samples of YSZ with 16 mol%  $Y_2O_3$  (CERES Corp., USA) thermochemically reduced at 1400°C (named TCR1400) and characterized spectroscopically as reported elsewhere.<sup>2</sup> The impedance measurements were performed on samples of a typical size of  $25\text{ mm}^2 \times 0.2\text{ mm}$  with painted silver paste electrodes. They were performed with a HP4192A and a Schlumberger 1260 impedance analyzers in the 5Hz to 10 MHz frequency range, and under argon atmosphere. The reduced samples presented the strong absorption band reported in ref. 2 as well as the trigonal EPR signal. We estimate the number of injected electrons to be  $3 \times 10^{19}\text{ cm}^{-3}$  trapped in T-defects and  $1.5 \times 10^{20}\text{ cm}^{-3}$  in C. Since the number of C-traps for this crystal is estimated to be<sup>2</sup> of about 2%, we have less injected electrons than available electron traps.

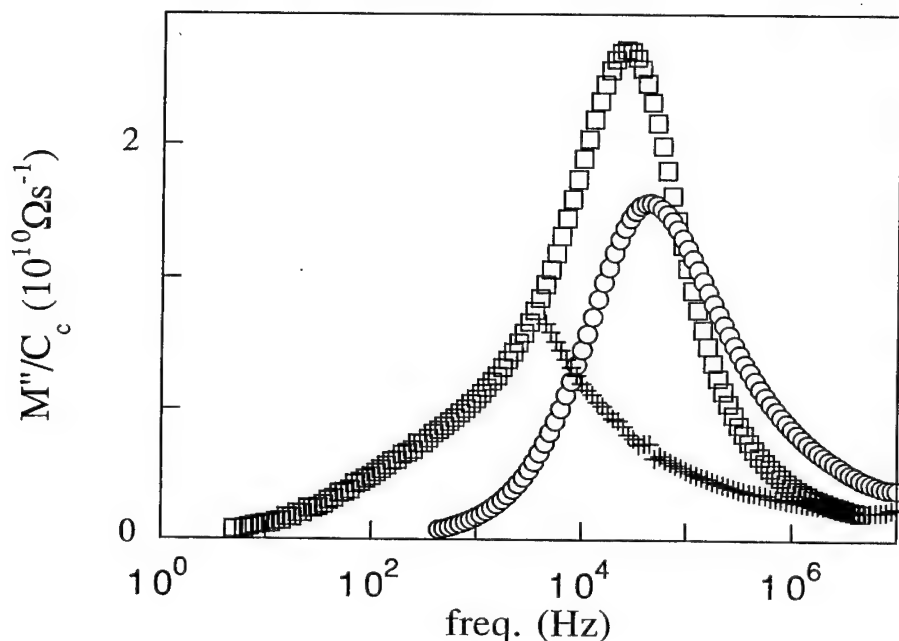


FIGURE 1 Imaginary part of the complex modulus (divided by the capacitance of the empty holder) versus frequency of a thermochemically reduced sample:  $\square$  after reduction measured at 270°C, + after a partial reoxidation at 420°C (measured at 270°C), and  $\circ$  reoxidized sample measured at 415°C.

The impedance diagrams have been measured at low temperatures to enhance the contribution of the electronic conduction as well as to prevent the reoxidation of the crystal during the measurements. They show a semicircle in the high frequency range assigned to the bulk properties of the material, with a much resistive one at low frequencies. The latter is associated to the region of the crystal adjacent to the surfaces and that are being oxidized during the measurements. To analyze the arcs we have chosen the complex modulus representation to prevent its overlapping.

In Figure 1 we plot the imaginary part of the complex modulus versus frequency in the reduced and reoxidized samples (only T-defects left). The different shapes and broadening of the relaxation peaks in reduced and reoxidized samples allow to conclude that there are different transport mechanisms taking place in each case. The high frequency capacitance (100 KHz) of the sample does not change with reoxidation, being equal to 18 pF (being 0.65 pF the capacitance of the empty cell). The temperature dependence is presented in Figure 2. In both cases the conductivity data have been fitted to an expression of the form

$$\sigma T = A \exp(-E/kT) \quad (1)$$

with  $A = 1 \times 10^7 \text{ K}/\Omega\text{cm}$  and  $E = 1.37 \text{ eV}$  for the oxidized sample, and  $A = 1.13 \times 10^7 \text{ K}/\Omega\text{cm}$  and  $E = 1.1 \text{ eV}$  for the reduced one. We see a conductivity greater by two orders of magnitude for the strongly reduced sample, that must be associated with the presence of the C-defects. The change in the concentration of oxygen vacancies can not account for this big increase in conductivity, that we have thus associated to electronic conduction. In this case, the activation energy in expression<sup>1</sup>

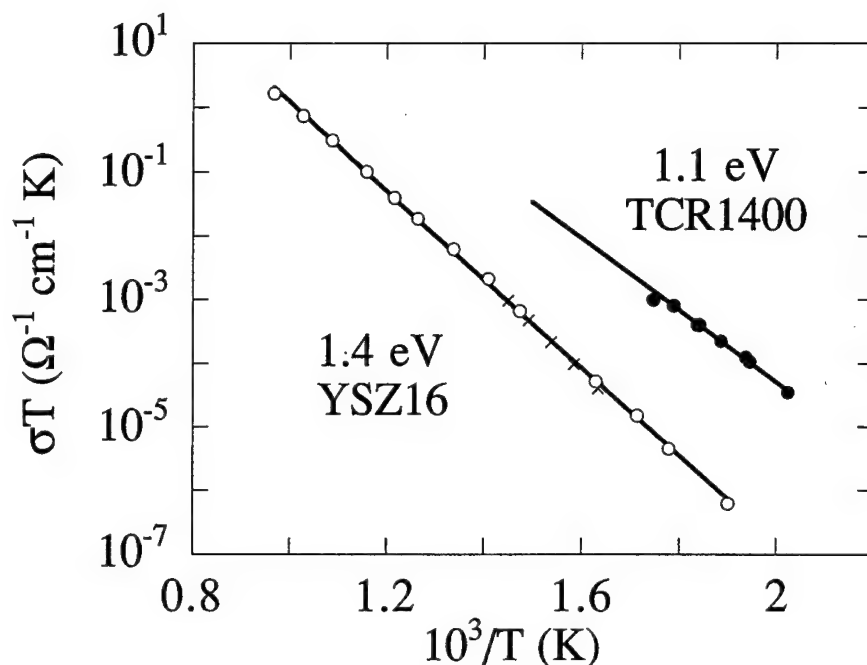


FIGURE 2 Semilogarithmic plot of the conductivity as a function of  $1/T$ . ● thermochemically reduced sample, × partially reoxidized (C-defects bleached), and ○ untreated sample.

comprises the contributions of the activation enthalpy for the freeing of electrons from the C-traps ( $\Delta H_e$ ) and the activation for the mobility ( $E_{\mu e}$ ), that according to ref. 1 we assume very small. Thus we have,  $\Delta H_e = 1.1 \text{ eV}$ .

### 3 DISCUSSION

On the light of these results we can tentatively locate the ground state level of the C-defect inside the band diagram presented in reference 2. This is shown in Figure 3. As shown by cluster calculations by Sobolev *et al.*<sup>3</sup> the states of the bottom of the conduction band (Zr(3d) mixed with O(2p)) relax in the proximity of an oxygen vacancy, creating empty electronic states into the gap. Being so, and since the material presents a high degree of disorder these states may form a band of defects through which the electrons can move. The existence of such a band, which may account for the low electron mobility of stabilized zirconia underlies in many studies concerning the electronic transport of YSZ.<sup>1</sup>

When the material starts to reduce, the electrons trap at the deepest traps (T-defects), whose ground states locate at about 2 eV below the defect conduction band. As the reduction goes on further, the shallower C-traps are filled, whose ground level lies at about 1.1 eV below the 'narrow' conduction band. Photons of 2.6 eV will promote these electrons into the excited state of the C-defect, close to or into the conduction band, so that this absorption band can act as a charge transfer band.

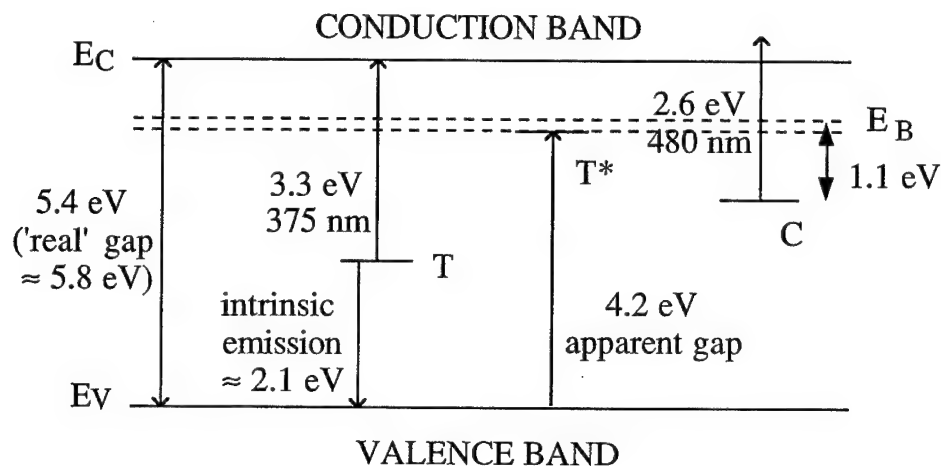


FIGURE 3 Energy level diagram in which C and T-defects have been located. The arrows show the observed optical transitions and  $E_B$  indicates the 'narrow' band of defects.

In conclusion we have ended up with the identification of two intrinsic electron traps, which are related to the electrons trapped in 4d orbitals of  $Zr^{3+}$  ions perturbed by oxygen vacancies. We show that the shallower C-defect determines the low temperature electronic conductivity of moderately reduced YSZ. We postulate the existence of a conduction band at about 1.3 eV below the 'true' conduction band consisting of perturbed 4d orbitals of  $Zr^{4+}$  ions perturbed by oxygen vacancies and  $Y^{3+}$ .

#### REFERENCES

1. M. Levy, J. Fouletier and M. Kleitz. *J. Electrochem. Soc.* **135**, 2867 (1989).
2. V. M. Orera, R. I. Merino, Y. Chen, R. Cases and P. J. Alonso. *Phys. Rev.* **B42**, 9782 (1990).
3. A. B. Sobolev, A. N. Varaskin, O. A. Keda and A. P. Kaimenov. *Phys. Stat. Sol.* **B162**, 165 (1990).



## HIGH TEMPERATURE ANNEALING EFFECTS ON THE A.C. CONDUCTIVITY OF SWEPT SYNTHETIC QUARTZ

P. CAMPONE, M. MAGLIOCCO, G. SPINOLO and A. VEDDA

*Dipartimento di Fisica- Università di Milano; Via Celoria 16-I 20133 Milano, Italy*

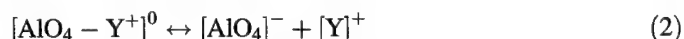
The effect of prolonged annealing treatments at elevated temperatures (900–1700 K) on the a.c. ionic conductivity of Sawyer PQ 'hydrogen swept' quartz has been investigated by impedance spectroscopy measurements. Transient and irreversible effects have been observed during the annealings: specifically, a monotonic enhancement of the conductivity is detected in the 900–1300 K temperature range, while at higher annealing temperatures an opposite effect is evidenced. The experimental results can be interpreted in the frame of a phenomenological model featuring two equilibrium reactions; an indirect role of hydrogen impurity in the ionic transport dynamics is evidenced, also by means of infrared spectroscopy measurements.

*Key words:* quartz—conductivity—impedance spectroscopy—infrared spectroscopy.

### 1 INTRODUCTION

The conductivity of crystalline quartz above room temperature is of ionic origin: the charge carriers have been identified as alkali ions, e.g.  $\text{Na}^+$  or  $\text{Li}^+$ ,<sup>1</sup> commonly present in trace concentrations in the  $\text{SiO}_2$  lattice. In as grown crystals, alkalis  $[\text{M}^+]$  act as charge compensators of aluminium impurities substitutional for silicon, giving rise to the  $[\text{AlO}_4-\text{M}^+]^0$  centers; at high temperatures, thermal dissociation of these centers takes place, and the alkali ions become free to migrate in open channels existing along the z-crystallographic axis: in fact, this conductivity is characterized by a large anisotropy, being more than two orders of magnitude lower when measured with the electric field parallel to the x-axis with respect to the z-axis orientation.<sup>1</sup>

At first, ionic conductivity measurements on  $\text{SiO}_2$  have been interpreted in the frame of a very simple model only involving the  $[\text{AlO}_4-\text{M}^+]^0$  dissociation and subsequent ion hopping in the crystalline matrix: however, the comparison between the behaviour of synthetic and natural samples in the alpha phase ( $T < 846$  K) led to hypothesize that the presence of additional unassociated aluminium ions could influence the dissociation reaction, leading to conductivity curves somehow sample-dependent.<sup>1</sup> Further studies<sup>2</sup> put in evidence that the transport process can be satisfactorily interpreted by means of a phenomenological model ('double equilibrium model'), involving two dissociation reactions concerning the aluminium impurity:



where the term Y represented an unidentified species, not necessarily participating to the transport process.

In this paper we present results concerning the effect of prolonged thermal treatments at high temperatures (900–1700 K) on synthetic 'hydrogen swept' quartz: by these measurements, we have evidenced that transient and irreversible conductivity effects occur during the annealings, which can be interpreted in the frame of the above mentioned

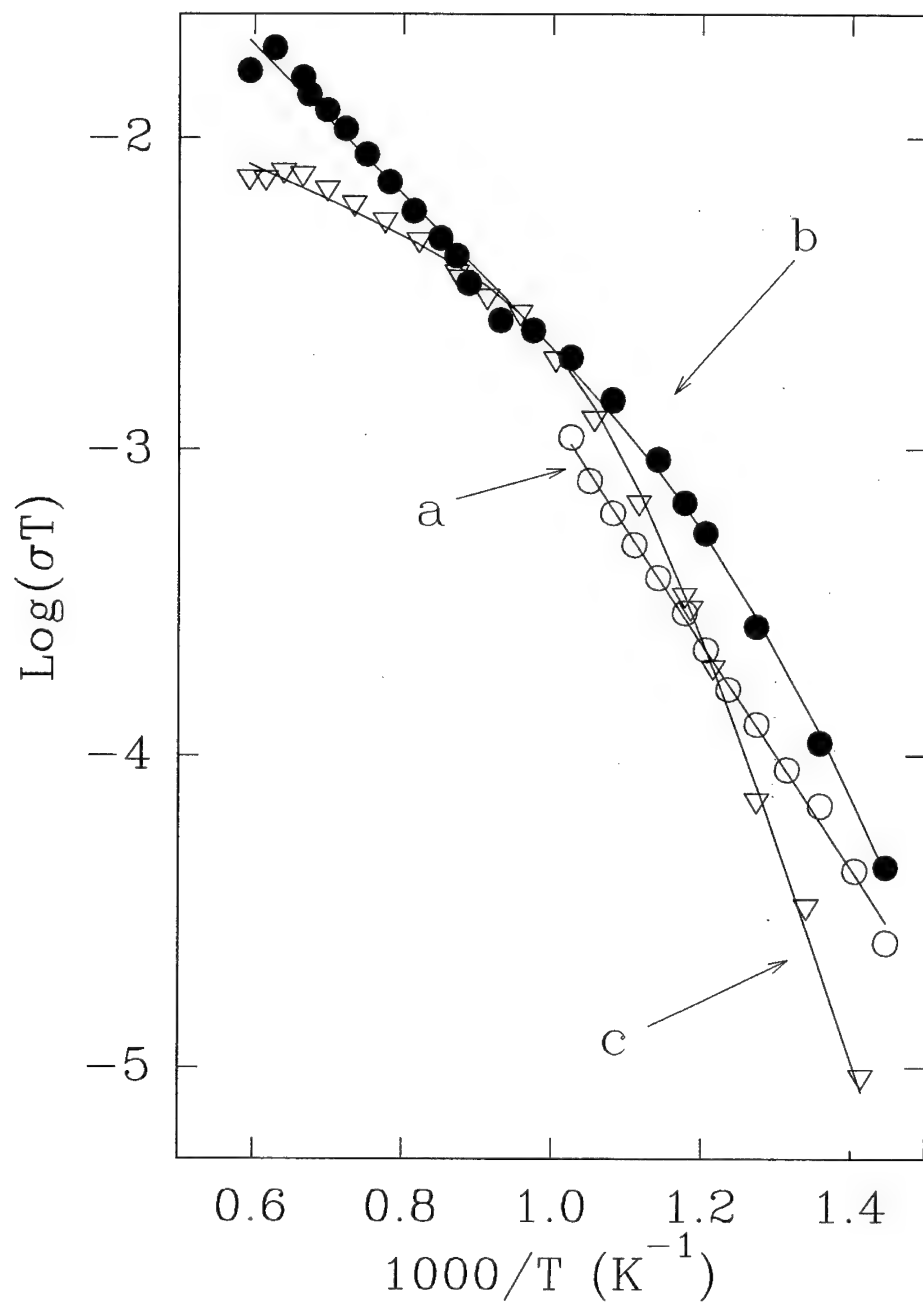


FIGURE 1 Arrhenius plot of the conductivity of Sawyer PQ swept quartz: curve a), untreated crystal; curve b), after an annealing of 10 hours at 1000 K; curve c), after an annealing of 10 hours at 1700 K.

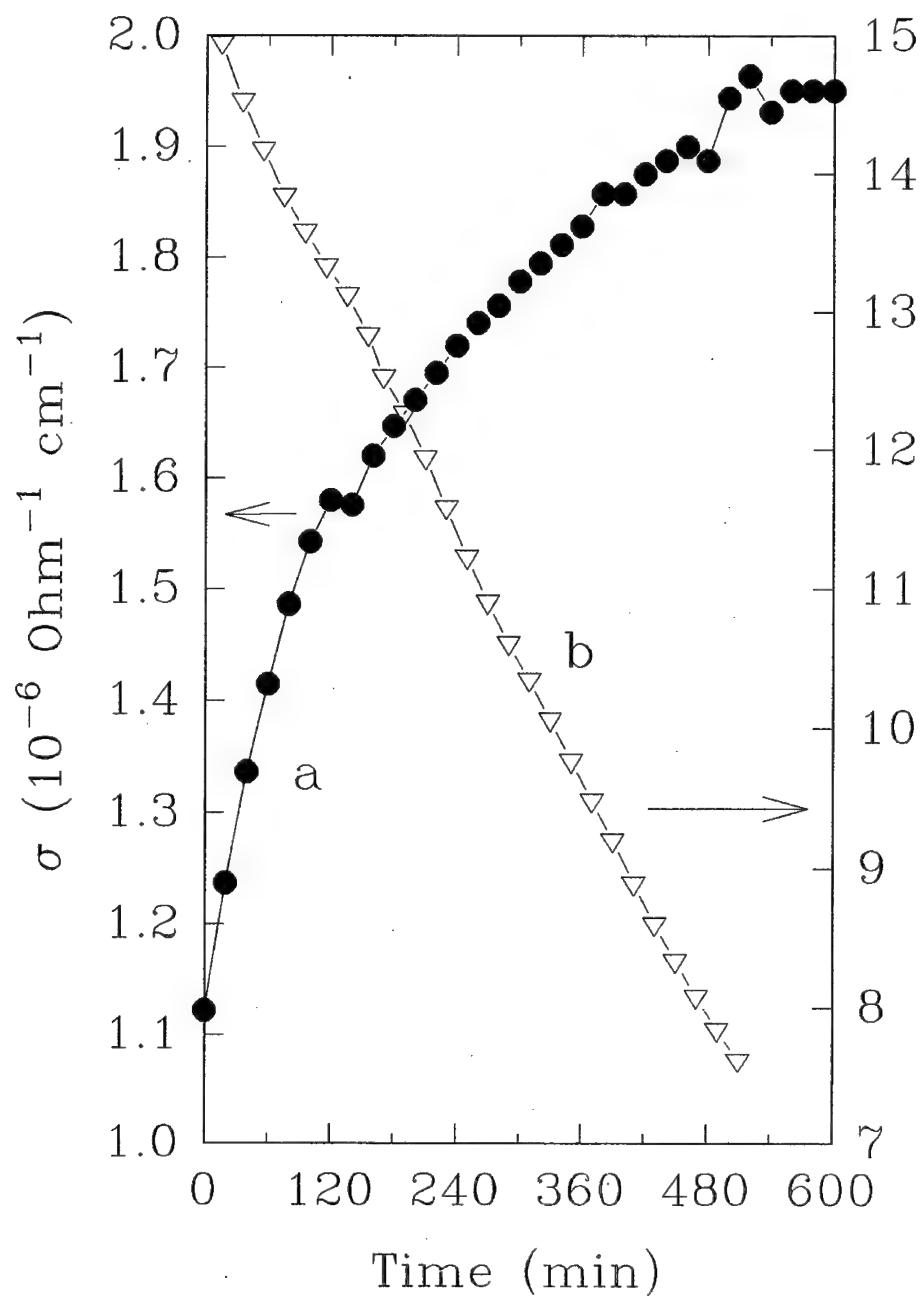


FIGURE 2 Variation of conductivity versus time of Sawyer PQ swept quartz during annealing treatments at fixed temperature: a), 1000 K; b), 1700 K.

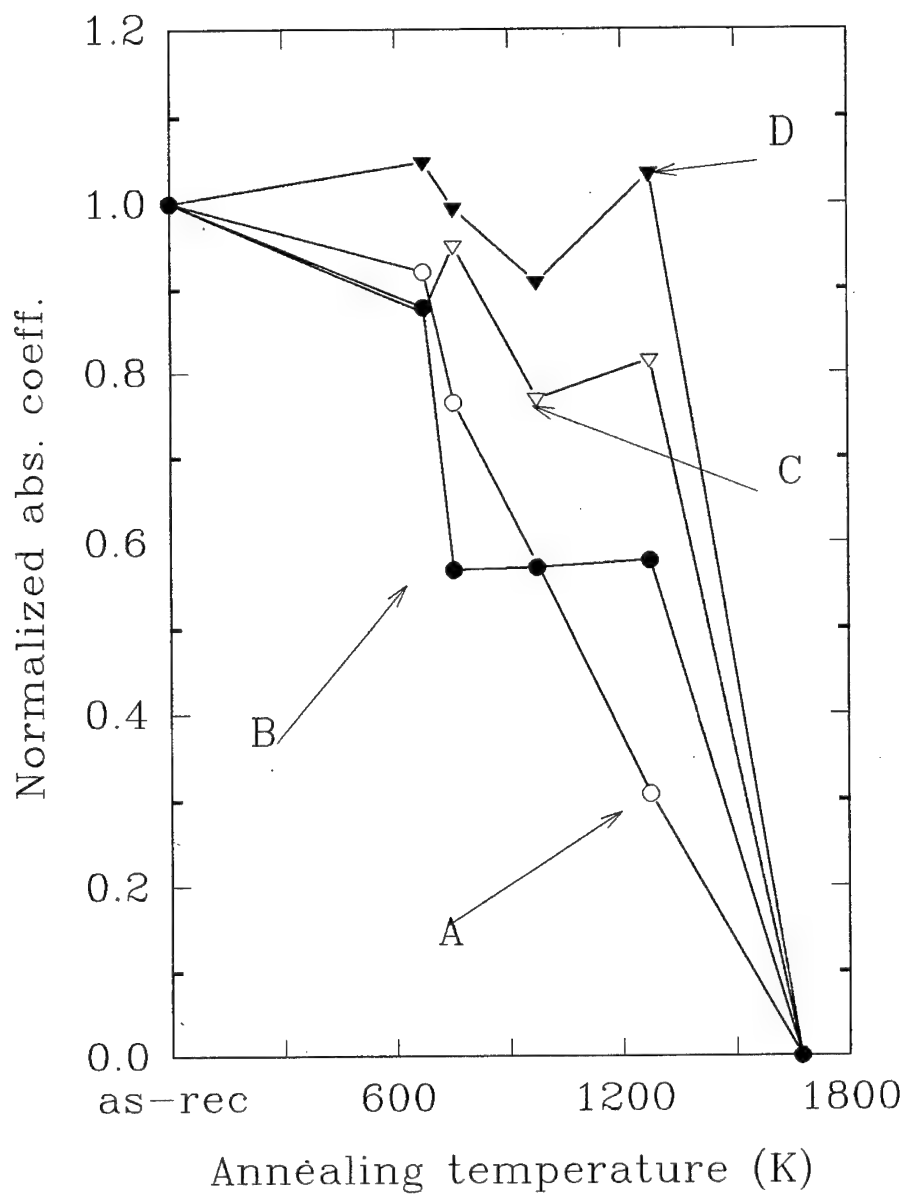


FIGURE 3 Absorption coefficient versus annealing temperature of different OH bands in Sawyer PQ swept quartz. A), 3367  $\text{cm}^{-1}$ ; B), 3400  $\text{cm}^{-1}$ ; C), 3435  $\text{cm}^{-1}$ ; D), 3585  $\text{cm}^{-1}$ .

model. Moreover, contemporary infrared spectroscopy measurements on the same samples have allowed to identify the Y species as the hydrogen impurity.

## 2 EXPERIMENTAL METHODS

We have studied Sawyer PQ-swept quartz, produced by Sawyer Research Products, Eastlake, Ohio; this type of quartz has an aluminium concentration of approximately 1 to 3 ppm; the sweeping process consists in an electrodiffusion at high temperature performed in air, having the effect to produce the conversion of the majority of the  $[\text{AlO}_4\text{-M}^+]^0$  centers present in the as grown material into  $[\text{AlO}_4\text{-H}^+]^0$  centers.

The samples studied were in the form of cylinders (diameter of 10 mm and thickness of 5 mm), with the axis parallel to the optical axis of the crystal; the samples in the measurement condenser have been heated with a tungsten mesh kept under vacuum, a Pt/Pt-Rh thermocouple allowed to measure the temperature of the sample with a precision of 1 K. The annealing treatments, lasting up to ten hours, have been performed in the same furnace used for the electrical measurements but with no electric field applied at the electrodes.

The electrical measurements have been carried on with a AC bridge (HP4284a) operating in a frequency range of 20 Hz–1 MHz, and with 1 V test signal voltage applied along the z-axis direction.

The optical measurements have been carried on at 80 K with a double beam spectrophotometer (Cary 2300 model) in the wavenumber range 3250–3600  $\text{cm}^{-1}$ .

## 3 RESULTS AND DISCUSSION

In Figure 1 we show conductivity data of Sawyer PQ swept quartz: curve a) pertains to an untreated crystal, while curves b) and c) have been obtained after an annealing of 10 hours at 1000 K and 1700 K, respectively. The comparison between these three curves shows that the thermal treatments produce irreversible effects on the conductivity process; the difference between these curves is the result of transient and opposite phenomena occurring in two different temperature ranges. Specifically, at a fixed temperature in the 800–1400 K interval, the conductivity is seen to increase as a function of time, as curve a) of Figure 2 shows. On the contrary, in the 1450–1700 K region, the opposite effect is evidenced, as shown in the same figure, curve c). Since the existence of such transient effects it is convenient to point out that in curves a) and b) of Figure 1 are plotted the values obtained immediately after thermalization of the sample was completed, but the conductivity was still slowly changing. Differently, the  $\sigma T$  versus  $1/T$  plot of curve c), after the annealing at 1700 K, did not show any time dependence.

We will first focus on the transient effect occurring in the lower temperature range. As already evidenced,<sup>2</sup> the ionic conductivity in this interval is markedly influenced by the presence of additional aluminium associated to a second and unknown species, the  $[\text{AlO}_4\text{-Y}^+]^0$  center; this center gives rise to a dissociation reaction interacting with that of the  $[\text{AlO}_4\text{-M}^+]^0$  defect. The observed conductivity enhancement upon heating treatments can be accounted for in the frame of the 'double equilibrium' phenomenological model by considering a progressive lowering of the concentration of the Y ions. In the following, a simple mathematical demonstration is presented.

Equations (1) and (2) can be written as:

$$\frac{[\text{AlO}_4]^- [\text{M}]^+}{[\text{AlO}_4 - \text{M}^+]^0} = K_1(T) = \exp(-E_D^M/k_B T) \quad (3)$$

$$\frac{[\text{AlO}_4]^- [\text{Y}]^+}{[\text{AlO}_4 - \text{Y}^+]^0} = K_2(T) = \exp(-E_D^Y/k_B T) \quad (4)$$

where  $E_D^M$ ,  $E_D^Y$  are the dissociation energies of the  $[\text{AlO}_4 - \text{M}^+]^0$  and of the  $[\text{AlO}_4 - \text{Y}^+]^0$  centers, respectively;  $k_B$  is the Boltzmann constant.

Let us name:

- $Y^*$  = molar fraction of dissociated ions of species Y;
- $A^*$  = molar fraction of aluminum ions dissociated from reaction (4);
- $A_0$  = initial molar fraction of  $[\text{AlO}_4 - \text{Y}^+]^0$  centers
- $M^*$  = molar fraction of alkali ions dissociated from reaction (3);

Under the hypothesis that, during a thermal annealing at a fixed temperature,  $Y^*$  is not constant, it will follow that at any time  $Y^* \neq A^*$ . Reaction (4) can be written as:

$$(M^* + A^*)Y^* = (A_0 - A^*)K_2 \quad (5)$$

where we have considered, as  $[\text{Al}-\text{O}_4]^-$ ,  $M^* + A^*$ , the sum of dissociated Aluminium centers from both reactions (3) and (4).

We can obtain:

$$M^* = [(A_0 - A^*)K_2/Y^*] - A^* \quad (6)$$

At a first approximation we can consider that  $A$  is constant and we can calculate:

$$dM^*/dt \div -(dY^*/dt)/(Y^*)^2 \quad (7)$$

Thus, if thermal treatments cause a lowering of the concentration of the Y species, we must expect an enhancement of dissociated alkali ions, and consequently an enhancement of the conductivity.

Interesting considerations can be done about the nature of the Y ions: actually, different experimental results allow to conclude that it can be identified as the hydrogen impurity, and thus that the  $[\text{AlO}_4 - \text{Y}^+]^0$  defect is the  $[\text{AlO}_4 - \text{H}^+]^0$  center. i) First of all, the conductivity values of hydrogen swept samples are much lower than those of as grown samples, but the temperature dependence is the same;<sup>(2)</sup> this confirms that alkali ions can be identified as the charge carriers in both cases. ii) Recent experiments have however shown that the transient irreversible effects are much stronger in swept, hydrogen rich, samples than in as grown samples, showing that hydrogen can have an indirect role in the conduction mechanism.<sup>(3)</sup> iii) Finally, we have monitored the I.R. absorption spectra of swept samples after thermal treatments at different temperatures: in Figure 3 are shown the intensities of four OH bands (peaking at 3367  $\text{cm}^{-1}$ , 3400  $\text{cm}^{-1}$ , 3435  $\text{cm}^{-1}$  and 3585  $\text{cm}^{-1}$ ) as a function of annealing temperature. The 3367  $\text{cm}^{-1}$  band is specifically associated to  $[\text{AlO}_4 - \text{H}^+]^0$  stretching vibration, while the others are assigned to as-grown OH.<sup>(4)</sup> all the bands, and particularly the structure peaking at 3367  $\text{cm}^{-1}$ , are weakened by successive thermal treatments, in accordance with the hypothesis that the  $[\text{AlO}_4 - \text{Y}^+]^0$  center can be identified as  $[\text{AlO}_4 - \text{H}^+]^0$ . Both the conductivity enhancement and the weakening of the  $[\text{AlO}_4 - \text{H}^+]^0$  band are irreversible effects: it can be supposed that the

hydrogen impurity becomes steadily trapped at different sites, or that it undergoes desorption from the sample.

Finally, we shall consider the opposite transient effect occurring at  $T > 1400$  K, shown in Figure 2, curve b: the resistivity of the sample increases by approximately a factor of two during the 10 hours thermal treatment at 1700 K. Also this phenomenon has an irreversible character, as evidenced by a  $\sigma T$  vs  $1/T$  measurement performed after the annealing (Figure 1, curve c): our possible interpretation is the occurrence, at high temperature, of effects of desorption or segregation of the alkali ions charge carriers, already experienced by hydrogen ions in a lower temperature range.

#### REFERENCES

1. H. Jain and A. S. Nowick, *J. Appl. Phys.* **53**, 477 and 485 (1982).
2. A. Cascella, M. Magliocco, G. Spinolo, A. Vedda, *Proc. XII Intl. Conf. on Defects in insulating materials* (editors O. Kanert and J. M. Spaeth), World Scientific Publishing 1993.
3. P. Campone, *Undergraduate Thesis*, Milan University, (1993).
4. H. G Lipson and A. Kahan, *J. Appl. Phys.* **58**, 963 (1985).

## DIFFUSION OF $^{18}\text{O}$ IN $\text{Cr}_2\text{O}_3$ : BULK AND SCALES AND RELATION WITH OXIDATION KINETICS

S. C. TSAI, A. M. HUNTZ, C. DOLIN\* and C. MONTY\*

*Laboratoire de Métallurgie Structurale, CNRS URA 1107, Bat 413, Université Paris XI-Orsay, 91405 Orsay, France; \*Laboratoire de Physique des Matériaux, CNRS, Bellevue, F-92190 Meudon Cedex, France*

The lattice and grain boundary diffusion coefficients of  $^{18}\text{O}$  (at 0.1 atm) were determined at  $900^\circ\text{C}$  in bulk  $\text{Cr}_2\text{O}_3$ , and in  $\text{Cr}_2\text{O}_3$  scales developed on a  $\text{Ni}_{70}\text{Cr}_{30}$  alloy. The diffusion profiles were established by SIMS and analyzed considering two domains, the first one relative to apparent diffusion and the second to grain boundary diffusion. With such an analysis and taking a  $f$  value = 0.0006, modified from a ridge model, the oxygen lattice diffusion coefficients determined in  $\text{Cr}_2\text{O}_3$  scales are then in very good agreement with those in bulk  $\text{Cr}_2\text{O}_3$ . With some assumptions, our diffusion data lead to a parabolic oxidation constant equal to the experimental one. The scale growth is ensured by counter-current diffusion of oxygen and chromium, mainly by grain boundary diffusion.

*Key words:*  $^{18}\text{O}$  diffusion, bulk  $\text{Cr}_2\text{O}_3$ ,  $\text{Cr}_2\text{O}_3$  scales, ridge model.

### 1 INTRODUCTION

$\text{Cr}_2\text{O}_3$  scale is frequently used as a barrier to protect metallic alloys at high temperatures. As a consequence, the transport properties of  $\text{Cr}_2\text{O}_3$  are of considerable interest. In the literature, it appears that the more recent values of oxygen and chromium diffusion coefficients determined in single crystals<sup>1,2</sup> are some orders of magnitude smaller than the previous data obtained on polycrystalline materials or on scales. To clarify this difference, the authors<sup>3</sup> have suggested that, in the case of  $\text{Cr}_2\text{O}_3$  scales, the diffusion coefficient determined in the first part of the profiles does not correspond to a lattice diffusion, but to an apparent one. The objective of this study is to determine and compare oxygen diffusion coefficient ( $D_L$  and  $D_{gb}$ ) in single crystals, polycrystals and in  $\text{Cr}_2\text{O}_3$  scales at  $900^\circ\text{C}$ . Secondly, oxidation of a  $\text{Ni}_{70}\text{Cr}_{30}$  alloy is studied in different oxygen atmospheres to determine the oxidation constant,  $k_c$ . This value is compared with that calculated from the diffusion data in order to justify growth mechanism of  $\text{Cr}_2\text{O}_3$  scales.

### 2 EXPERIMENTS

All diffusion experiment conditions are given in Table I. The diffusion was studied by means of  $^{16}\text{O}$ – $^{18}\text{O}$  exchange at 0.1 atm oxygen, and the concentration profiles were analyzed by SIMS, using a 10 keV  $\text{Cs}^+$  ion source. For the oxidation kinetic tests of the  $\text{Ni}_{70}\text{Cr}_{30}$  alloy at  $900^\circ\text{C}$ , the following atmospheres of oxygen were used: 0.25 atm, 1 atm, 2 atm.

### 3 RESULTS AND DISCUSSION

**3.1.1 Single crystal** Our  $D_L$  values ( $\approx 10^{-17}\text{cm}^2/\text{s}$ ) (Table II) are in good agreement with that evaluated from Hagel work ( $\approx 3 \times 10^{-18}\text{cm}^2/\text{s}$ ),<sup>4</sup> but greater than that



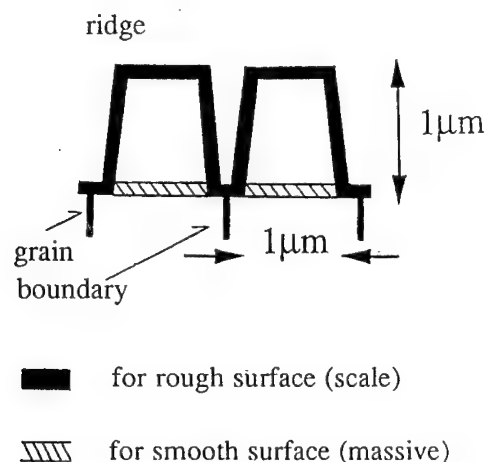


FIGURE 1 the ridge model (black) and the smooth surface model (hatched).

extrapolated from Sabioni work ( $\approx 10^{-19} \text{ cm}^2/\text{s}$ )<sup>2</sup>, though our study was performed on the same single crystal. There is possibly two reasons to explain the difference. Firstly, the value extrapolated from Sabioni work is obtained on the basis of only two points, which may lead to a great uncertainty. Secondly, Sabioni worked in a lower oxygen atmosphere than in this study. As it is further shown by the oxidation kinetics,  $\text{Cr}_2\text{O}_3$  scales behave as a p-type conductor, so in this case the possible point defect is  $\text{O}_i''$ . Then, in the  $p\text{O}_2$  range  $10^{-10}$ – $10^{-1}$  atm,<sup>2</sup> the diffusion coefficient would increase by a factor of about 30, according to  $[\text{O}_i'']$  variation with  $(p\text{O}_2)^{1/6}$ . With this consideration, the oxygen lattice self-diffusion coefficient extrapolated from Sabioni work at  $900^\circ\text{C}$  and at  $p\text{O}_2 = 0.1$  atm would be  $3 \times 10^{-18} \text{ cm}^2/\text{s}$ , i.e. a value close to our experimental values.

Table I  
Experimental conditions for each sample (working temperature =  $900^\circ\text{C}$ )

sample	material	experimental condition	*
1	single c.	pre-annealing + $\text{O}_2^{18}$ 0.1 atm, 1h	A
2	single c.	pre-annealing + $\text{O}_2^{18}$ 0.1 atm, 1h	A
3	single c.	pre-annealing + $\text{O}_2^{18}$ 0.1 atm, 5h	A
4	bulk polyc.	pre-annealing + $\text{O}_2^{18}$ 0.1 atm, 1h	A
5	bulk polyc.	pre-annealing + $\text{O}_2^{18}$ 0.1 atm, 5h	A
6	scale	$\text{O}_2^{16}$ 1atm, 15h + $\text{O}_2^{18}$ 0.1 atm, 1h	B
7	scale	$\text{O}_2^{16}$ 1atm, 165h + cooling ( $-240^\circ\text{C/h}$ ) + $\text{O}_2^{18}$ 0.1 atm, 1h	B
8	scale	$\text{O}_2^{16}$ 1atm, 165h + cooling ( $-40^\circ\text{C/h}$ ) + $\text{O}_2^{18}$ 0.1 atm, 1h	B
9	scale	$\text{O}_2^{16}$ 1atm, 15h + $\text{O}_2^{18}$ 0.1 atm, 5h	B

\*polishing – A: polished up to  $3 \mu\text{m}$  diamond; B: polished up to 1200 SiC

**3.1.2 Bulk polycrystalline  $\text{Cr}_2\text{O}_3$**  Taking into account the average grain size,  $\Phi \approx 9 \mu\text{m}$  and the grain boundary width,  $\delta = 1 \text{ nm}$ ,  $f (= 3\delta/\Phi)$ , fraction of sites associated with grain boundaries,<sup>5</sup> is equal to 0.00034. With this  $f$  value and diffusion equations mentioned in,<sup>3</sup> the oxygen lattice ( $D_L$ ) and grain boundary ( $D_{gb}$ ) diffusion coefficients were determined

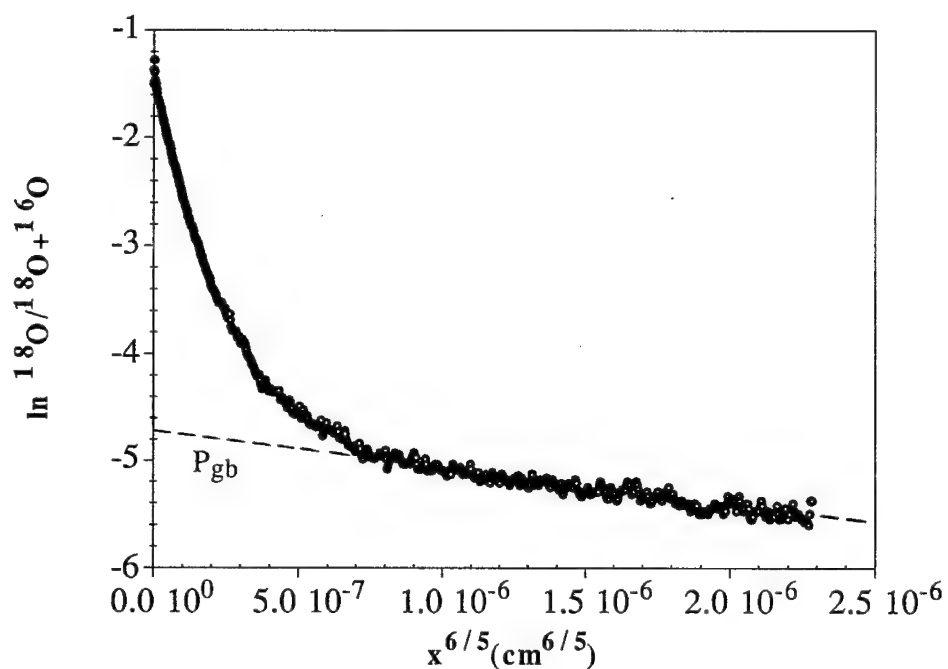


FIGURE 2  $^{18}\text{O}$  concentration profile plot against  $x^{6/5}$  (sample No. 5).

(Table III). It is shown that  $D_L$  values determined in this case are close to those in single crystals and do not depend on the diffusion time.

Table II  
 $D_L$  in single crystal,  
 $T_{\text{diff}} = 900^\circ\text{C}$ ,  $p\text{O}_2 = 0.1$  atm

sample	$D_L(\text{cm}^2/\text{s})$
1	$8.8 \times 10^{-18}$
2	$1.2 \times 10^{-17}$
3	$1.3 \times 10^{-17}$

Table III  
 $D_{\text{app}}$ ,  $D_L$  and  $D_{\text{gb}}$  determined in bulk polycrystals,  
 $T_{\text{diff}} = 900^\circ\text{C}$ ,  $p\text{O}_2 = 0.1$  atm and  $f = 0.00034$

sample	$D_{\text{app}}(\text{cm}^2/\text{s})$	$D_L(\text{cm}^2/\text{s})$	$D_{\text{gb}}(\text{cm}^2/\text{s})$
4	$1.5 \times 10^{-16}$	$7.4 \times 10^{-18}$	$4.3 \times 10^{-13}$
5	$6.0 \times 10^{-17}$	$8.1 \times 10^{-18}$	$1.6 \times 10^{-13}$

3.1.2 *In  $\text{Cr}_2\text{O}_3$  scales* Taking a value  $f = 0.003$  ( $\Phi \approx 1 \mu\text{m}$ ), the lattice and grain boundary diffusion coefficients of oxygen were determined (Table IV). Some remarks can be made:

Table IV  
 $D_{app}$ ,  $D_L$ ,  $D_{gb}$  determined in  $Cr_2O_3$  scale,  $T_{diff} = 900^\circ C$  and  $pO_2 = 0.1$  atm

sample	$D_{app}(cm^2/s)$	$D_L(cm^2/s)$ $f = 0.003$	$D_{gb}(cm^2/s)$ $f = 0.003$	$D_L(cm^2/s)$ $f = 0.0006$	$D_{gb}(cm^2/s)$ $f = 0.0006$
6	$1.0 \times 10^{-15}$	$8.3 \times 10^{-19}$	$3.3 \times 10^{-13}$	$2.0 \times 10^{-17}$	$1.6 \times 10^{-12}$
7	$1.6 \times 10^{-15}$	$3.4 \times 10^{-19}$	$5.3 \times 10^{-13}$	$8.4 \times 10^{-18}$	$2.7 \times 10^{-12}$
8	$1.2 \times 10^{-15}$	$2.6 \times 10^{-19}$	$4.0 \times 10^{-13}$	$8.9 \times 10^{-18}$	$2.9 \times 10^{-12}$
9	$2.9 \times 10^{-15}$	$4.0 \times 10^{-20}$	$4.3 \times 10^{-13}$	$5.1 \times 10^{-18}$	$4.8 \times 10^{-12}$

- (i) As  $D_L$  values determined in  $Cr_2O_3$  scales differ from those determined on bulk  $Cr_2O_3$  (compare with Tables II, III), a ridge model is proposed which modifies the  $f$  value due to the surface roughness of  $Cr_2O_3$  scales: as the average surface roughness ( $R_a$ ) is about  $1 \mu m$  (the same value as  $\Phi$ ). The ridge model is schematized in Figure 1.

Considering every ridge as a cylinder of  $1 \mu m$  diameter ( $\Phi$ ) and also  $1 \mu m$  height ( $R_a$ ). The area for lattice diffusion in case of a smooth surface ( $A_s$ ) is  $\pi(0.5)^2 = 0.25\pi \mu m^2$ . For the ridge model, this area ( $A_r$ ) is  $[\pi(0.5)^2 + 2\pi(0.5) \cdot 1] = 1.25\pi \mu m^2$ . So,  $A_r$  is about 5 times greater than  $A_s$ . As a consequence, the  $f$  value for  $Cr_2O_3$  scales becomes equal to 0.0006. The new  $D_L$  and  $D_{gb}$  values are shown in Table 4. It appears that the  $D_L$  values are in very good agreement with those in single crystal and massive polycrystals. The  $D_{gb}$  values are greater than those determined in bulk polycrystals (compare Tables III and IV), but they are in good agreement with  $D_{gb}(\approx 10^{-12} cm^2 s^{-1})$  obtained in  $Cr_2O_3$  scales by Graham *et al.* at  $900^\circ C$ .<sup>6</sup> It is believed that there may be more faster diffusion paths in the  $Cr_2O_3$  scales than in bulk polycrystals.

- (ii) In spite of the various heat treatments performed to develop the  $Cr_2O_3$  scale (No. 6–8) and in spite of the different diffusion times for  $^{18}O$  (No. 6 and 9), close values of  $D_{app}$ ,  $D_L$  and  $D_{gb}$  were obtained for all samples. It is concluded that there is no effect of cooling rate, of oxidation time and of diffusion time on the diffusion coefficient values, contrarily to the results of Lobnig *et al.* who obtained a variation of the anionic diffusion coefficients in  $Cr_2O_3$  scales with the diffusion time.<sup>7</sup>

**3.1.4 Oxidation kinetic tests** All the kinetic curves obey a parabolic law. The  $k_p$  values ( $g^2 cm^{-4} s^{-1}$ ), defined as  $(\Delta m/s)^2 = k_p t$ , are given in Table V with  $k_c$  values ( $cm^2 s^{-1}$ ) calculated by  $k_c = (M_{Cr2O3}/3 M_O \rho_{Cr2O3})^2 k_p$ . A p-type conductivity behavior is observed in our  $Cr_2O_3$  scales as the higher the  $pO_2$  the greater  $k_p$ . As a consequence, the main point defects can be either oxygen interstitial ( $O_i''$ ) or chromium vacancy ( $V_{Cr}'''$ ), or both. From the classical equation for an oxide  $M_a O_b$ ,  $k_c$  can be expressed by:

Table V  
 $k_p$  and  $k_c$  determined on the alloy  $Ni_{70}Cr_{30}$   
 in different oxygen pressures at  $900^\circ C$

$pO_2$	0.25 atm	1 atm	2 atm
$k_p$ ( $g^2 cm^{-4} s^{-1}$ )	$1.4 \times 10^{-13}$	$2.4 \times 10^{-13}$	$6.4 \times 10^{-13}$
$k_c$ ( $cm^2 s^{-1}$ )	$5.2 \times 10^{-14}$	$8.9 \times 10^{-14}$	$2.4 \times 10^{-13}$

$$K_c = \int [D_{anion} + (b/a)D_{cation}] d \ln pO_2$$

Writing  $D = D^\circ (pO_2)^n$  for each species ( $D^\circ$  being the diffusion coefficient at  $pO_2 = 1$  atm)

$$k_c = \int D_O^\circ (pO_2)^{1/6} d \ln pO_2 + 3/2 \int D_{Cr}^\circ (pO_2)^{3/16} d \ln pO_2$$

$$= 6D_O^\circ (pO_2^{\text{ext}})^{1/6} + 8D_{Cr}^\circ (pO_2^{\text{ext}})^{3/16}$$

Assuming that  $Cr_2O_3$  scale growth is ensured by counter-current of oxygen and chromium<sup>8,9</sup> and that  $D_O \approx D_{Cr}$  at 0.1 atm, we can obtain  $k_c \approx 14 D_O$  (0.1 atm)

Taking the average value of  $D_L$ ,  $D_{gb}$ ,  $D_{app}$ , the oxidation constant was calculated assuming various mechanisms (lattice, grain boundary or both) for the scale growth (Table VI). It clearly appears, by comparison of calculated and experimental values of  $k_c$ , that the scale growth proceeds by counter-current diffusion of oxygen and chromium by both the lattice and the grain boundary, the main phenomenon being grain boundary diffusion.

Table VI  
 $k_c$  calculated from diffusion data at 900°C and  $pO_2 = 0.1$  atm, (assuming  $D_O \approx D_{Cr}$ ), experimental  $k_c = 4.4 \times 10^{-14}$  cm<sup>2</sup>/s

Diffusion mechanism	Lattice diffusion	Grain boundary diffusion	Both mechanism
$D_O$ (cm <sup>2</sup> s <sup>-1</sup> )	$1.7 \times 10^{-17}$	$2.8 \times 10^{-12}$	$1.7 \times 10^{-15}$
$k_c$ (cm <sup>2</sup> s <sup>-1</sup> )	$2.4 \times 10^{-17}$	$3.9 \times 10^{-11}$	$2.4 \times 10^{-14}$

#### 4 CONCLUSION

1. In case of massive polycrystals and  $Cr_2O_3$  scale, the penetration profiles are analyzed considering two domains, the first one relative to apparent diffusion and the second to grain boundary diffusion.
2. Considering the roughness of the  $Cr_2O_3$  scales, a ridge model is proposed to modify the  $f$  value, fraction of sites associated with the grain boundaries.
3. In case of  $Cr_2O_3$  scales, with the modified  $f$  value = 0.0006 and our profile analysis, the so-determined oxygen  $D_L$  values are in good agreement with those determined in single crystals and bulk polycrystals, but oxygen  $D_{gb}$  values are slightly greater than those in bulk polycrystals.
4. By comparing the experimental oxidation constant with those calculated from the diffusion data, it appears that the scale growth must be ensured by counter-current diffusion of chromium and oxygen, mainly by grain boundary diffusion.

#### REFERENCES.

1. A. C. S. Sabioni, B. Lesage, A. M. Huntz, J. C. Pivin and C. Monty, *Phil Mag.* **A66**, n°3 333-350 (1992).
2. A. C. S. Sabioni, A. M. Huntz, F. Millot and C. Monty, *Phil Mag.* **A66**, n°3 351-360 (1992).
3. A. M. Huntz and S. C. Tsai, *Mat. Sci. Letter* **13**, 821-825 (1994).
4. W. C. Hagel, *J. AM. Ceram Sci* **48**, 70 (1965).
5. J. Philibert, 'atom movements, diffusion and mass transport in solids', Les édition de Physique (1991).
6. M. J. Graham, J. I. Elridge, D. F. Mitchell and R. J. Hussey, *Materials Science Forum 'The Reactive*

- Element on High Temperature Oxidation-after fifty years'* **43** 207-242, Trans. Tech. Publication, Switzerland (1989).
7. R. E. Lobnig, H. P. Schmidt, K. Hennesen and H. J. Grabke, *Oxid. Met.* **37**, n° 1/2 81-93 (1992).
  8. P. Kofstad and K. P. Lillerud, *J. Electrochem. Soc.* **127**, 2410 (1980).
  9. K. P. Lillerud and P. Kofstad, *J. Electrochem. Soc.* **127**, 2397 (1980).

## INFLUENCE OF YTTRIUM ON TRANSPORT PROPERTIES OF $\alpha$ ALUMINA SCALES DEVELOPED ON YTTRIUM IMPLANTED $\beta$ NiAl

J. BALMAIN, M. K. LOUDJANI and A. M. HUNTZ

*Laboratoire de Métallurgie Structurale, CNRS URA 1107, bât. 413, Université Paris XI  
Orsay, 91405 Orsay, France*

The influence of yttrium doping on the ionic and electronic conductivities of  $\alpha$  alumina developed on a  $\beta$  NiAl alloy by oxidation at 1100°C was investigated by electrochemical measurements, in order to point out the possible effect of this element on the transport properties of alumina scales. It appears that the yttrium influence is small. It slightly reduces the ionic transport number at low oxygen pressure and increases it at high  $pO_2$ : the alumina scale behaves as an ionic conductor near the substrate-oxide interface and progressively becomes a mixed conductor or an electronic conductor near the outer oxide-gas interface. The ionic-electronic transition is sharper for undoped scales.

*Key words:* Alumina, yttrium,  $\beta$ -NiAl, transport, electrochemical method.

### 1 INTRODUCTION

It is often suggested, in order to justify the influence of yttrium doping on the oxidation kinetics of alumina former alloys, that such an element modifies the transport properties of the scale.<sup>1,2</sup> Recently, self diffusion in bulk undoped or yttrium doped  $\alpha$  aluminas was studied<sup>3</sup> and it was shown that yttrium doping slightly increases the lattice and sub-boundary diffusion but decreases the grain boundary diffusion, a diffusion mechanism which is preponderant during the growth of alumina scales. But, it also appears that diffusion phenomena in bulk oxides can differ from diffusion in scales of the same nature. For instance, for chromia, scales are assumed to grow by preponderant cationic diffusion while anionic diffusion predominates over cationic diffusion in bulk chromia.<sup>4</sup> Thus, it is important to characterize the transport properties directly in the scale. This is the objective of this work on alumina scales developed by oxidation of a  $\beta$  NiAl alloy using an electrochemical method.

### 2 MATERIAL AND EXPERIMENTAL PROCEDURE

The  $\beta$  NiAl alloy was implanted with yttrium (150 keV,  $10^{16}$  at.cm<sup>-2</sup>, at CSNSM, Orsay) and it was always verified that a gaussian distribution of yttrium was obtained according to LSS theory. Afterwards samples were oxidized at 1100°C in pure oxygen. Then, using an apparatus and a procedure previously developed in our laboratory,<sup>5</sup> electrochemical measurements on the alumina scales were performed in  $pO_2$  varying between  $10^{-10}$  and 1 atm. (obtained with CO, CO<sub>2</sub>, Ar and O<sub>2</sub> gas). The plot of the variation of  $V_o$ , the potential difference between the two interfaces of the scale at  $I = 0$ , versus  $pO_2$  allows to determine the variation of the ionic transport number  $t_i = \frac{\sigma_i}{\sigma}$  with the oxygen pressure according to the equation:  $V_o = \frac{1}{4F} \int_1^2 t_i d\mu$ . The plot of the curves  $V = f(I)$  for various  $pO_2$  allows to determine the variation of  $\sigma$  with the oxygen pressure according to the equation:  $\frac{1}{\sigma} = \frac{S}{Z_{ox}} \frac{dV}{dI}$  with  $Z_{ox}$  the oxide thickness and  $S$  the platinum electrode surface.<sup>5</sup>

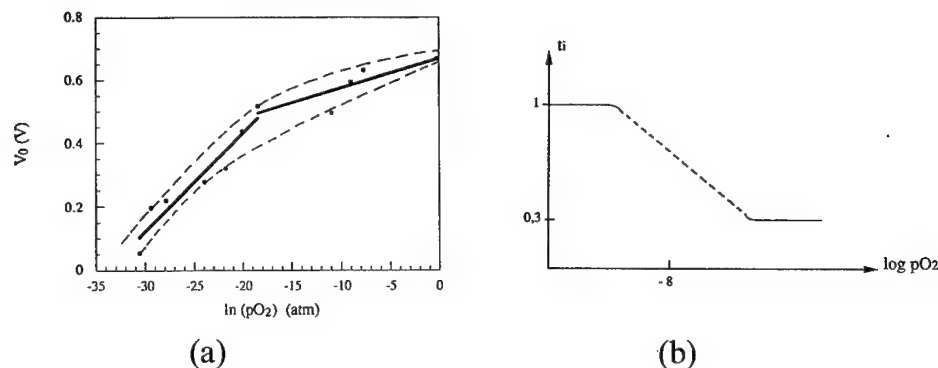


FIGURE 1 (a) and 1(b) Variations of  $V_0$  and  $t_i$  with  $pO_2$ .

### 3 RESULTS

Examples will be given mainly with yttrium doped  $\beta$  NiAl samples (for the results obtained with the undoped NiAl alloy, see<sup>6</sup>). Figures 1a and b are respectively relative to the variation of  $V_0$  with the oxygen pressure and the deduced variation of  $t_i$  with  $pO_2$ , i.e. in the Y-doped alumina scale thickness from the inner interface to the outer one. It appears that  $t_i$  progressively varies from a value near 1 at the inner interface to a value near 0.3 at the outer interface. From one sample to another slight variations are observed (see Figure 3). The variation of  $t_i$  in the undoped alumina scale was sharper (see Figure 3).

Figures 2a and b are respectively relative to the curves  $V = f(I)$  obtained at different oxygen pressures and the deduced variation of the electric conductivity  $\sigma$  versus  $pO_2$ . With the results obtained from Figure 1b for  $t_i$ , it has been possible to plot, on Figure 2b, the evolutions of  $\sigma_i$  and  $\sigma_e$  near the inner and the outer interfaces respectively. Again, it is observed that the evolution of  $\sigma$  is sharper in the case of the undoped alumina scale.

So, it appears that, for Y-doped alumina scales, ionic conductivity dominates for low oxygen chemical potentials, i.e. near the inner interface of the scale, and electronic conductivity is the major phenomenon for high oxygen chemical potential. Compared to undoped scales, the electronic behaviour is less marked (see Figure 3).

### 4 DISCUSSION

The comparison of the results concerning the variation of the ionic transport number with the oxygen pressure for several undoped (sample a) or Y-doped samples (b and c) is shown in Figure 3.

The scatter in these results could be due to the fact that the NiAl substrate grain size is large ( $\Phi \sim 2$  mm). Consequently, according to the orientation of the grains in a sample and to epitaxial relations between the substrate and the oxide grains, variations in the transport properties could be observed.

In the Y-doped scales, the yttrium profiles were determined by SIMS. Yttrium is mainly localized in the middle of the scale. Its concentration near the interfaces metal/oxide and

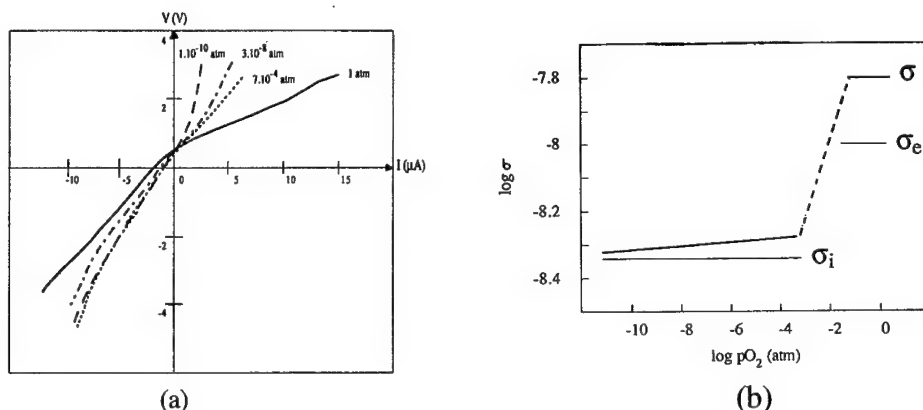


FIGURE 2 (a) and 2(b) V-I curves and variation of the conductivity with the  $pO_2$ .

oxide/gas is negligible. It was not possible by this technique to determine if yttrium was preferentially localized along alumina grain boundaries or not. Such a preferential localization is probable if it is referred to results obtained in bulk aluminas.<sup>7</sup>

According to Kröger,<sup>8</sup> it appears that the yttrium effect on the ionic transport number of alumina depends on the oxygen pressure: at low  $pO_2$ , undoped alumina behaves as an ionic conductor when Y-doped alumina behaves as an electronic conductor, and inversely at high  $pO_2$ .

Thus, in the case of our doped scales, near the inner interface, yttrium is either present (sample b) and it decreases the ionic transport number from  $\sim 1$  to  $\sim 0.5$ , or is not present in the inner part of the scale (sample c) and does not modify the ionic character of the alumina scale. Near the outer interface, the same analysis can be made: in sample b, yttrium is not present and the alumina scale keeps its electronic character, and in sample c yttrium must be somewhat present and a slight increase of  $t_i$  is observed. In the middle of the scale, zone where the yttrium content is maximum, a slight increase of  $t_i$  is observed compared to the undoped scale. In all cases, the alumina scales behave as an ionic conductor near the substrate-oxide interface and progressively becomes a mixed conductor (when doped) or an electronic conductor (when undoped) near the outer oxide-gas interface. The ionic-electronic transition is sharper for undoped scales.

Nevertheless yttrium effect on the transport properties is small and the beneficial effect of such an element on the oxidation resistance of alumina former alloys is probably related to other effects due to the presence of active elements (effect on the mechanical properties or on the segregation phenomena...). This is in agreement with the results recently obtained on the oxygen self diffusion in undoped or doped bulk aluminas<sup>3</sup> which indicate that yttrium doping has a small influence.

#### REFERENCES

1. A. M. Huntz, 'The role of active elements in the oxidation behavior of high temperature metals and alloys', Ed. E. Lang, Elsevier Applied Science, pp. 81, 109 (1988).
2. J. Jedlinski, Ed. J. Nowotny, *Solid State Phenomena*, vol 21/22, Trans Tech Publications, pp. 335, 390 (1992).



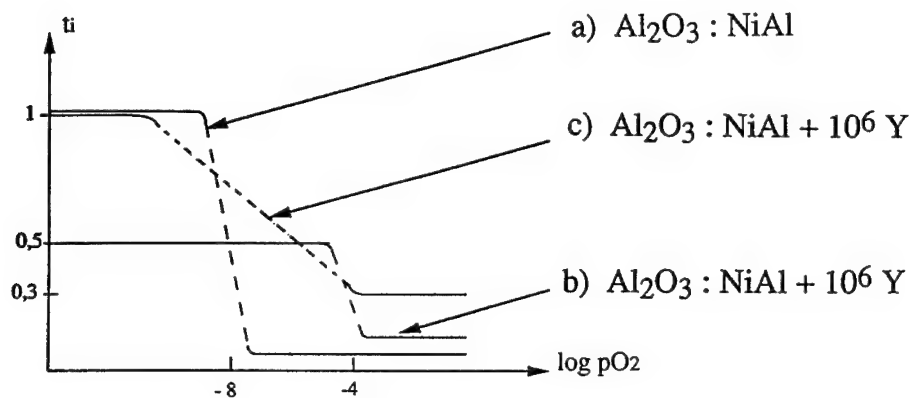


FIGURE 3 Variation of  $t_i$  with  $pO_2$  for doped and undoped samples.

3. M. Le Gall, A. M. Huntz, B. Lesage, C. Monty, G. Bernardini, *J. Mat. Sci.*, (1994).
4. A. C. S. Sabioni, A. M. Huntz, J. Philibert, B. Lesage, C. Monty, *J. Mat. Sci.*, **27**, 4782 (1992).
5. D. Nicolas-Chaubet, A. M. Huntz, F. Millot, *J. Mat. Sci.*, **26**, 6113 (1991).
6. D. Nicolas-Chaubet, A. M. Huntz, F. Millot, *J. Mat. Sci.*, **26**, 6119 (1991).
7. D. Bouchet, F. Dupeau, S. Lartigue-Konirek, *Micros. Microanal. Microstruct.*, **4**, 561 (1993).
8. M. M. El-Aiat, F. A. Kröger, *J. Am. Ceram. Soc.*, **65**, 6 280 (1982).

## EFFECTIVE DIFFUSION COEFFICIENT AND DIFFUSION-CONTROLLED REACTIONS IN INSULATING SOLIDS WITH DEFECTS

YU. H. KALNIN and P. ZAPOL

*Department of Theoretical Physics, University of Latvia, 19 Rainis bulv., Riga, LV-1050,  
 Latvia*

The expressions for effective diffusion coefficient are obtained in the mean field approximation for two-phase system for spatial dimensions of 1, 2 and 3. The existence of potential barrier for diffusion on the phase boundary was taken into account via the boundary conditions. Obtained formulae could be applied in the theory of diffusion-controlled reactions and for interpreting the experimental data on defect diffusion in two-phase media.

*Key words:* diffusion.

### 1 INTRODUCTION

The effective diffusion coefficient is derived in the present work for the case of different concentrations of diffusing particles in the matrix and inclusions (two-phase system). At the boundary between matrix and inclusions therein the concentration ratio was considered not equal to the unity, but is approximately equal to the ratio of the equilibrium particle concentrations. It gives one possibility to consider problems with different potential profiles for diffusion in the matrix and inclusions. The exact expressions for the EDC are derived in mean field approximation for one-dimensional diffusion and are generalized to for spatial dimensions of 2 and 3.

### 2 ONE-DIMENSIONAL DIFFUSION

Let us determine the effective diffusion coefficient (EDC)  $D_{\text{eff}}$  in the 1D case, supposing that the regions with diffusion coefficients  $D_1$  and  $D_2$  are placed periodically. Thus, we have the diffusion problem with the diffusion coefficient  $D(x) = D(x + L)$ , where  $L$  is the periodicity length. To determine  $D_{\text{eff}}$ , the eigenvalue problem should be solved

$$\frac{d}{dx}D(x)\frac{d}{dx}\psi_k(x) = -E_k\psi_k(x), \quad (1)$$

where  $k$  is the wave vector. Similarly to the Kronig-Penny model, the 1D diffusion in the absence of reflection by inclusions is considered in (1).

The function  $\psi$  can be represented in the regions I-III as

$$\psi_i(x) = \alpha_i e^{ik_i x} + \beta_i e^{-ik_i x}, \quad (2)$$

where  $k_i = \sqrt{E_k/D_i}$ , for  $i = 1, 2, 3$ . To obtain  $\alpha_1, \dots, \beta_3$  we use the following boundary conditions for concentrations in the points  $x_1, x_2$

$$\psi_I(x_1) = \kappa\psi_{II}(x_1), \quad \psi_{II}(x_2) = 1/\kappa\psi_{III}(x_2), \quad (3)$$

as well as periodicity of  $\psi$  and continuity of first derivative. Here  $\kappa$  accounts the difference of diffusion potentials in matrix and inclusions. Substituting eq.(2) into eq.(3), the condition of the non-trivial solution existence is received and vanishing  $x_1$ ,  $x_2$  and  $x_3$  in such a way that  $x_1/L = 1/2(1 - \phi)$ ,  $x_2 - x_1/L = \phi$  and  $x_3 - x_2/L = 1/2(1 - \phi)$ , we arrive at the expression for the EDC

$$D_{\text{eff}} = \frac{D_1 D_2}{D_2(1 - \phi)^2 + D_1 \phi^2 + (D_2/\kappa + \kappa D_1)\phi(1 - \phi)}. \quad (4)$$

This approximation means coarse graining averaging when the length of averaging is much greater than the periodicity length. Let us consider some special cases.

1. For  $\kappa = 1$  the expression for the EDC has the form:

$$D_{\text{eff}} = \frac{1}{D_2} \phi + \frac{1}{D_1} (1 - \phi). \quad (5)$$

This result coincides with that in the Maxwell-Garnett approximation.<sup>2</sup>

2. For  $\phi \ll 1$  from eq.(4) we obtain

$$D_{\text{eff}} = \frac{D_1}{1 + (1/\kappa + \kappa D_1/D_2 - 2)\phi}. \quad (6)$$

If  $\kappa \rightarrow 0$  (particles are trapped by inclusions) or  $\kappa \rightarrow \infty$  (particles are reflected from inclusions) then  $D_{\text{eff}} \rightarrow 0$ .

### 3 MEAN-FIELD APPROXIMATION

The expression for the EDC (4) could be also obtained in the mean field approximation. Let us consider the whole periodical 1D system as consisting of three regions. Two of them, I and II, are the same as in the previous model, i.e. the matrix and the inclusion with DCs  $D_1$ ,  $D_2$  and particle concentrations  $C_1$ ,  $C_2$ , respectively. These two regions are embedded into the third region, acting as an effective medium with the concentration  $C_{\text{eff}}$  and DC  $D_{\text{eff}}$ . The flow of particles through the system is assumed to be stationary. Solving the diffusion equation in the stationary case we have the solutions for all regions:

$$C_{\text{eff}} = -gx$$

$$C_i = \alpha_i + \beta_i, \quad i = 1, 2, 3 \quad (7)$$

The relation between concentrations on the boundaries is (the boundaries are denoted as  $x_1$ ,  $x_2$ ,  $x_3$ ,  $x_4$ )

$$C_1|_{x=x_2} = \kappa C_2|_{x=x_2}, \quad C_2|_{x=x_3} = 1/\kappa C_3|_{x=x_3} \quad (8)$$

$$C_1|_{x=x_1} = \eta^{-1} C_{\text{eff}} = x_1,$$

The most convenient way to obtain  $\eta$  is to use conservation law for the particle number. It means that the integrals over region  $x_1 - x_4$  of  $C_{\text{eff}}$  and  $C_1 - C_4$  should be equal.

Substituting eq.(7) into conditions (8) and demanding the continuity of flow in each point  $x$  one can easily obtain

$$D_{\text{eff}} = \frac{D_1 D_2}{\eta(D_2(1 - \phi) + \kappa D_1 \phi)}, \quad (9)$$

where  $\phi = (x_3 - x_2)/(x_4 - x_1)$ . Then the expression for  $\eta$  is derived

$$\eta = \frac{D_2(1 - \phi) + D_1\phi + (1/\kappa - 1)(D_2 - \kappa D_1)\phi(1 - \phi)}{D_2(1 - \phi) + \kappa D_1\phi}. \quad (10)$$

Finally, using  $\eta$  from (10) in eq.(9) we arrive at  $D_{\text{eff}}$  exactly coinciding with eq.(4). In principle, this approach can be easily generalized for spatial dimensions of 2 and 3.

Assuming that a ratio between mean concentrations is the same as for concentrations at the boundary, for  $\langle C_{\text{eff}} \rangle$  we have

$$\langle C_{\text{eff}} \rangle = \langle C_1 \rangle(1 - \phi) + \langle C_2 \rangle\phi = \eta \langle C_1 \rangle. \quad (11)$$

Using  $\langle C_1 \rangle = \kappa \langle C_2 \rangle$ ,  $\eta$  could be easily derived as  $\eta = 1 - \phi + \phi/\kappa$ . Substituting  $\eta$  into eq.(9), generalized for any dimension  $d$  we arrive at the expression for the EDC

$$D_{\text{eff}} = \frac{D_1}{1 - \phi + \phi/\kappa} \left[ 1 + \frac{d\phi(D_2 - \kappa D_1)}{(d - 1)D_2 + \kappa D_1 - (D_2 - \kappa D_1)\phi} \right]. \quad (12)$$

The expressions derived could be used for interpreting of experimental data on diffusion of point defects in inhomogeneous media<sup>3</sup> and in the theory of diffusion-controlled reactions.

#### 4 ACKNOWLEDGEMENT

This work is partly supported by International Science Foundation (grant LB 2000).

#### REFERENCES

1. T. Miyuzawa, T. Izuyama. *Phys. Rev.* **A36**, 5791 (1987).
2. J. C. Maxwell. *A Treatise on Electricity and Magnetism*, v.1, (Reprint: Dover: New York, 1954), Chap. 9.
3. G. M. Loubriel, T. A. Green, N. H. Tok, R. F. Haglund. *J. Vac. Sci. Technol.* **B5**, 1514 (1987).

## FAST DIFFUSION OF THE OFF-CENTER IMPURITIES $\text{Cu}^+$ AND $\text{Li}^+$ IN THE KCl LATTICE

F. DESPA and V. TOPA

*Institute of Physics and Technology of Materials, Magurele—Bucharest, M.G.-7, 76900,  
Romania*

In this work, we perform a study of the off-center effect on the diffusion coefficient and we propose a new mechanism for fast diffusion. The model assumes that the equilibrium positions of the cationic impurities are noncentral and that the diffusion proceeds by hopping across the potential barrier along the nonlinear paths with the highest probability [1]. The nonlinear paths between two consecutive positions characterize even the self-diffusion and furthermore, in the off-center diffusion this path is appropriate. The main results is that the off-center position considerably enhances the diffusion. The theoretical diffusion coefficients have been obtained by modeling the potential barrier. Changes of the configuration entropy and the vibration spectra due to the presence of the noncentral impurity are included in the model. We emphasize the good agreement of the model with the experimental data for  $\text{KCl}:\text{Cu}^+$  and show that if the impurity is placed close to the central site, the appropriate diffusion coefficient is close to that for the cationic self-diffusion. We proceeded in the  $\text{Li}^+$  cation case as in the case of  $\text{Cu}^+$  cation.

*Key words:* diffusion, off-center impurities.

### 1 INTRODUCTION

Extensive studies of ionic conductivity and self-diffusion generally accept that the Frenkel disorder is the type of point-like defects in silver halides while the Schottky disorder prevails in alkali halides with a NaCl-type structure [2]. Thus, in crystals with a NaCl-type structure, there are only substitutional impurities. The existence of interstitial ionic impurities is improbable in these crystals. Also, it is well-known that the diffusion coefficients of the  $\text{Cu}^+$  cation in the NaCl and KCl lattices [3] exceed by three or four orders of magnitude the corresponding self-diffusion coefficients in the intrinsic temperature regions [4]. In this paper [3], no explanation is given for the great difference between the impurity diffusion coefficient and the self-diffusion coefficient. Nevertheless, we can say that for some cationic impurities in alkali halide crystals the nature of ionic defect migration is not yet understood. For example, the large diffusion coefficient for  $\text{Cu}^+$  suggests interstitial diffusion so  $\text{Cu}^+$  may be interstitial instead of substitutional. In this case, optical transitions would be allowed without coupling of the lattice vibrations since we would have no inversion symmetry. But this interpretation seems unlikely. Comparison of the  $\text{Cu}^+$  band in NaCl and in the three potassium halides shows that we deal with analogues centers, and the temperature dependence of the  $\text{Cu}^+$  band in NaCl supports Seitz's model. On the other hand, it is known that some small-size ions ( $\text{Cu}^+$ ,  $\text{Ag}^+$ ,  $\text{Li}^+$ ,  $\text{Na}^+$ ,  $\text{F}^-$ ) are placed off-center in some host lattice, a fact that might throw some light on their diffusion mechanism. In this work, we perform a study of the off-center effect on the diffusion coefficient and we propose a new mechanism for fast diffusion.

### 2 THE DIFFUSION COEFFICIENT ON NONCENTRAL MONOVALENT IMPURITIES RESULTS

The diffusion coefficient of cationic monovalent impurities at high temperatures is given by the vacancy-diffusion mechanism as [2]:

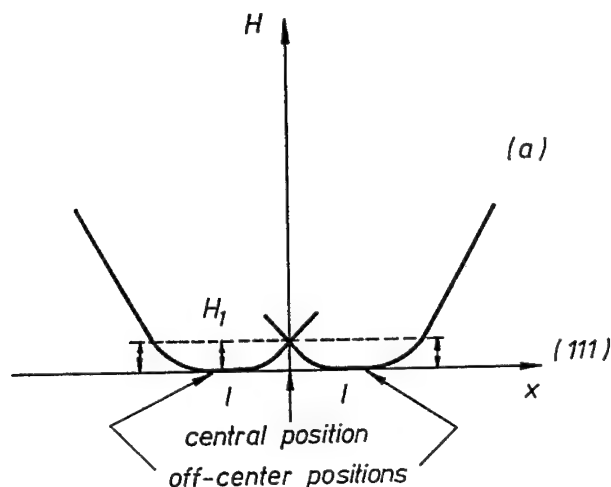


FIGURE 1(a) The potential wells of the off-center impurity on  $(111)$  direction given led to Wilson and his co-workers [5]:

$$D_+ = 2fd^2\nu_+ \exp(-\Delta G_s/2kT - \Delta G_m/kT), \quad (1)$$

Obviously, all these parameters have different values for the noncentral case. It is obvious that the impurity ion will jump from one off-center position to another. These two positions are separated by the potential barrier ( $H_o$ ). The idea of modeling the potential barrier for the specific situation in crystals is based on the possibility of operating upon  $H_o$ . This possibility must take into account the particularities of the either such off-center

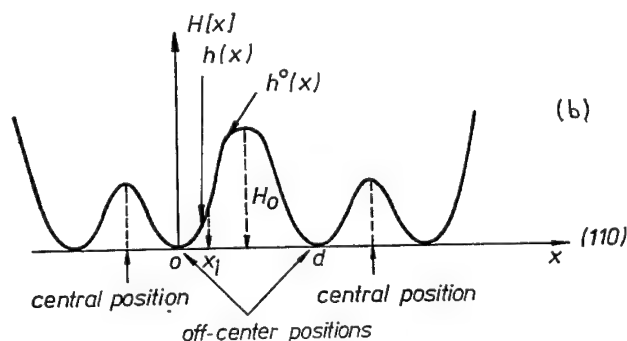


FIGURE 1(b) The shape of potential curve on the jump direction as that given in [9] is shown together with the  $[0, d/2]$  part

given by  $h(x) = \sqrt{\frac{a(l, H_l)x^3}{d(l)-x}}$  for  $x \in [0, x_i]$  and  $h^o(x) = -\frac{H_o}{2} [\cos \frac{2\pi x}{d(l)} - 1]$  for

$x \in [x_i, d/2]$   $d(l) = \sqrt{2} \cdot c - 2 \cdot \rho \cdot \cos(\alpha)$ . The extension to the domain  $[o, d]$  is done by symmetry.

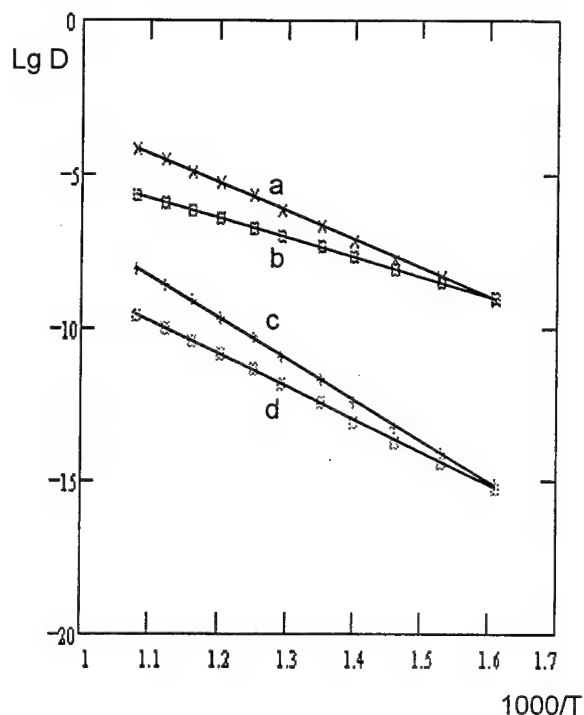


FIGURE 2 The logarithm of the diffusion coefficient for  $\text{Cu}^+$  in KCl lattice. a—the experimental curve [3]; b—the theoretical curve with  $\text{Cu}^+$  placed in off-center position ( $l = 1.36 \cdot 10^{-10} \text{ m}$ ,  $H_1 = 0.21 \text{ eV}$ ); c—the theoretical curve with  $\text{Cu}^+$  placed in on-center position; d—the experimental curve for  $\text{K}^+$  [4].

impurity:  $l$ —the off-center displacement of the impurity and,  $H_1$ —the potential difference between the central and off-center positions. Wilson *et al.* [5] took the off-center potential in the  $(111)$  direction to be a simple well potential (see Figure 1a). We consider that, on the  $(110)$  direction (the jump direction), this off-center potential may be described by  $h(x)$  for the proximity of the equilibrium position (see the Figure 1b) as a projection of Wilson's potential. By this projection we found the parameter  $a = a(l, H_1)$  obliging the graphic of the function  $h(x)$  to cross the point  $(a \cos \alpha - H_1 \cos(\pi/2 - \alpha), \rho \cos(\pi/2 - \alpha) + H_1 \cos \alpha)$ . The parameter  $\alpha$  is the angle between  $(111)$  direction and  $(110)$  direction. Generally, the potential barrier which opposes the impurity migration has a height given by the cosine-type curve ( $H_o$ ) (see  $h^o(x)$  in the Figure 1b). Smoothly joining the functions  $h(x)$  and  $h^o(x)$  one obtains the potential barrier  $H_o$ . One knows that the potential barrier which opposes the jump of the impurity from one equilibrium position to another is tight-bonded to the interactions of this impurity with the ions of the lattice. We consider that, in the above determination of the potential barrier value, one should take into account this condition through the  $l$  and  $H_1$  parameters which are the result of the delicate balance of the interaction energy created by the substitution of the host ion with the impurity. The final form of the diffusion coefficient (eq.1) is:

$$D_+ = 2fd^2\nu_+ \exp\left(\frac{\Delta S_{\text{config}}}{k} + \frac{\Delta S_s}{2k}\right) \exp\left[-\frac{1}{kT}\left(\frac{\Delta H_s}{2} + \frac{1}{2}h\nu_+ + 3kT \ln\left(\frac{h\nu_+}{kT}\right) + H_o - e\Delta\Phi\right)\right],$$

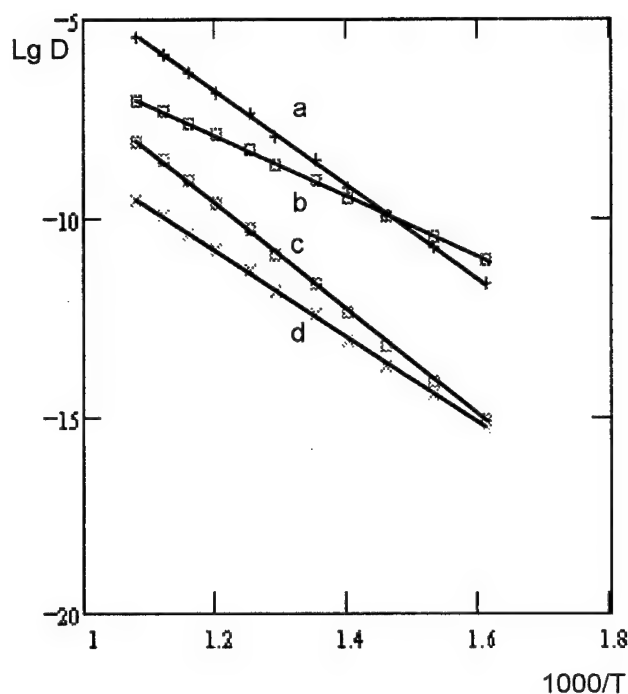


FIGURE 3 The logarithm of the diffusion coefficient for  $\text{Li}^+$  in KCl lattice. a—the theoretical curve with  $\text{Li}^+$  placed in off-center position ( $l = 1.16 \cdot 10^{-10}$  m,  $H_1 = 0.11$  eV); b—the experimental curve [11]; c—the theoretical curve with  $\text{Li}^+$  placed in on-center position; d—the experimental curve for  $\text{K}^+$  [4].

where we taken into account of the increase of the local Helmholtz phononic free energy of the impurity environment as a consequence of the vacancy occupation, the contribution to the change of the environment entropy due to the eight specific equiprobable positions of the off-center along the  $\langle 111 \rangle$  directions:  $\Delta S_{\text{config}} = k \ln \Omega = k \ln 8 \approx 2.0794 k$  and the decrease of the potential barrier  $H_o$  due to the electrostatic interaction with the vacancy which there is in the proximity of the impurity at the previous moment of the jump ( $e\Delta\Phi$ ). The  $d$  is the length of the jump,  $\nu_+$  is the vibrational frequency of the impurity and  $\Delta H_s$ ,  $\Delta S_s$  represent enthalpy and entropy of the Schottky defect formation. To obtain a good correlation between theoretical (last eq.) and experimental estimates of the diffusion coefficient of  $\text{Cu}^+$  [3], we made the assumption that  $H_1$  increases in value when  $l$  increases ( $l$  values found in the literature [6, 7, 8]). This assumption is equivalent to the 'deep off-center' hypothesis [9]. The values of  $H_o$  obtained in this way are close to those obtained by Meng and his co-workers [10] using the Buckingham potential. The logarithm of the diffusion coefficient versus temperature obtained by the present model is given in Figure 2. For a better understanding of the effect of the noncentral configuration on the diffusion coefficient let suppose that the  $\text{Cu}^+$  ion occupies a normal substitutional site. With this in mind, last eq. remains valid, but the parameters  $H_o$ ,  $d$  and  $\Delta\Phi$  should be estimated by using the smallest value for  $l$  ( $l \rightarrow 0$ ). In this case, we give up the configurational term of the entropy. It is not surprising that the diffusion coefficient computed in this way is closer to the cationic self-diffusion (see Figure 2). Now, we can conclude that the diffusion



coefficient of impurities depend strongly on the displacement of impurities from the central position. The major difference between the impurity diffusion coefficient and the self-diffusion arises from the privileged off-center position. The same method was used to find the diffusion coefficient of  $\text{Li}^+$  in the KCl lattice. We emphasize the good agreement of the model with the experimental data [11].

#### ACKNOWLEDGMENTS

The authors are indebted to dr. M. Apostol for useful discussions.

#### REFERENCES

1. Catlow C. R. A & co., *J. Phys.* **C12**, 451, (1979).
2. Beniere F., *Physics of Electrolytes*, (Hladik J. ed., Academic Press, London, 1972), pp. 203.
3. Haneda K. & co., *J. Phys. Soc. Jpn.* **25**, 643, (1968).
4. Beniere F. and S. K. Sen, *Phil. Mag.* **A64**, 1167, (1991).
5. Wilson W. D. & co., *Phys. Rev.*, **161**, 888, (1967).
6. Wilson W. D. & co., *Phys. Rev.*, **184**, 844 (1969).
7. Siu Li M. & co., *Phys. Rev. B*, **7**, 4677, (1973).
8. Sitting R., *Phys. Stat. Sol.*, **34**, K189, (1969).
9. Holland U., Luty F., *Phys. Rev.* **B19**, 4298, (1979).
10. Meng J. & co., *Phys. Rev.* **B38**, 10083, (1988).
11. Hanson R. C., *Bull. AM. Phys. Soc.*, ser.II, **13**, 902, (1968).

## INTERNAL REDUCTION OF POLYCRYSTALLINE Cr-DOPED ALUMINA

M. BACKHAUS-RICOULT and A. PEYROT

*Laboratoire de Physique des Matériaux, CNRS, 1 Pl A. Briand, 92195 Meudon, France*

Chromium precipitates generated by controlled internal reduction of  $(\text{Al,Cr})_2\text{O}_3$  polycrystals are used as indicator for the occurrence of DIGM (diffusion-induced grain boundary migration) in this material. Asymmetric precipitate-free zones limited at one side by a grain boundary are observed inside the reduction scale. This observation is ascribed to diffusion induced migration of the grain boundaries, defect relaxation in the oxygen potential gradient being the driving force.

*Key words:* DIGM, internal reduction, ruby, alumina.

### 1 INTRODUCTION

Upon exposure of a polycrystalline oxide to an oxygen activity different from its equilibrium activity, defect relaxation takes place. Normally, this relaxation is faster along grain boundaries than in the bulk. Under such conditions, the grain boundaries close to the outer surface can migrate, leaving in the overswept zones an oxide material with defect concentrations close to the new equilibrium values, while in front of the migrating boundary the defect concentrations remain unchanged. This process is generally known as 'diffusion induced grain boundary migration', DIGM, when referring to solute diffusion into a matrix.<sup>1,2</sup> In the past several attempts were made to demonstrate the occurrence of DIGM in oxides, but only few results were reported.<sup>6</sup> For instance, diffusion induced recrystallisation of oxide surfaces was reportedly identified<sup>3</sup> and denied<sup>4</sup> for the same experimental conditions.

In the present work, small chromium precipitates formed during internal reduction of chromium-doped alumina are used as indicators of boundary migration. It is then possible to study the dependence of grain boundary motion on applied oxygen potential gradient, temperature and crystal orientation.

### 2 INTERNAL REDUCTION OF $(\text{Al,Cr})_2\text{O}_3$

Upon the exposure of chromium-doped alumina to sufficiently low oxygen partial pressure, a dispersion of metallic chromium forms inside the alumina matrix, as a reduction scale growing from the outer surface into the bulk of the sample. The outer surface and the reaction front act as sink and source for the point defect fluxes across the scale: At the outer surface, gaseous oxygen is liberated, while metallic chromium is formed at the reaction front, see.<sup>5</sup>

The same reaction mechanism can be applied to the grain boundaries, the only differences being that metal nucleation is heterogeneous and easier stress relaxation can occur. As a consequence, metal precipitates in the grain boundaries have larger average size than in the bulk. Since oxygen diffusion along the grain boundaries is faster than bulk diffusion of the defects considered, the 'grain boundary reaction front' penetrates much faster into the sample. Diffusion leakage from the grain boundaries into the volume must be considered.

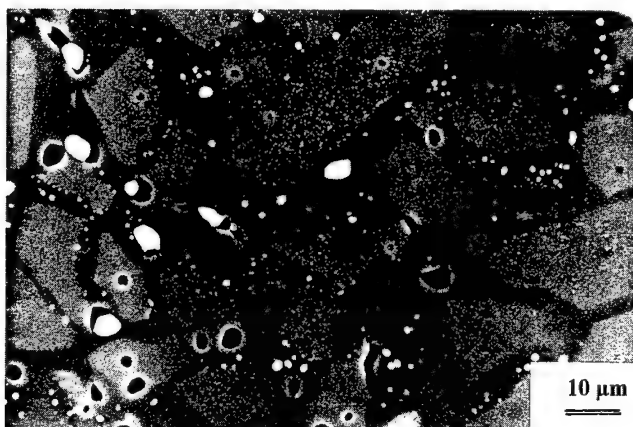


FIGURE 1 Polished cross section of a  $(\text{Al,Cr})_2\text{O}_3$  sample with 3cat% chromium after being reduced at 1873 K for 100 h in an  $\text{Al}/\text{Al}_2\text{O}_3$  buffer. White spots of the SEM image correspond to metallic chromium, while the darker regions inbetween the dark-grey grains are the chromium depleted regions which are overswept by the migrating boundary.

### 3 EXPERIMENTS

Homogeneous  $(\text{Al,Cr})_2\text{O}_3$  polycrystals with 3, 6 and 10 cat% chromium (grain size 10–50  $\mu\text{m}$ , density 97–99%) are cut and equilibrated in air at the reaction temperature for at least 250 h, to establish defined defect concentrations everywhere inside the sample and to stabilise the microstructure and avoid recrystallisation and grain growth during the reduction anneals. Their surface is then mirror-polished. TEM lattice plane imaging of several grain boundaries and triple junctions shows that no amorphous film is present between the  $\alpha$ -alumina grains.

Reduction experiments are then performed in closed reaction chambers, at temperatures between 1673 K and 1973 K, for 1 h to 100 h. The equilibrium oxygen activity is set by metal/oxide buffers, alumina/aluminium and titanium oxide/titanium. All reacted samples are cross-sectioned normal to their outer surface and characterized by optical, scanning electron and transmission electron microscopy.

### 4 EXPERIMENTAL RESULTS

Upon reduction, the crystal surface turns from pink to black, indicating the presence of metallic chromium. Polished cross sections reveal the presence of a reduction scale, the growth kinetics of which obey a parabolic rate law, see.<sup>5</sup>

At the same time, grains of pure alumina form on the surface of the initially polished sample, regardless of buffer used, Figure 1. Their size is not homogeneous and tends to increase with reaction time.

Below the initial surface, TEM observations show Cr-metal precipitates (bcc chromium containing less than 2% aluminium) regularly distributed inside the grains. Their size ranges from a few nanometers to several hundred nanometers. Details on distribution, morphology and orientation of these precipitates are reported in.<sup>5</sup>

Large chromium precipitates, up to one micron in size, are detected in the grain boundaries and at triple junctions, Figure 2. Close to grain boundaries a precipitate-free



FIGURE 2(a) TEM image of a grain boundary area next to the outer surface of a reduced sample of  $(\text{Al}, \text{Cr})_2\text{O}_3$  showing the migration distance of the boundary by the chromium precipitate depletion in this zone. ( $1 \mu\text{m} = 1 \text{ cm}$ )

zone of variable width is observed, which contains only few larger precipitates and is completely depleted in chromium (Figure 2). In all cases, the grain boundary limits the depleted zone at one side (SEM on chemically etched bulk specimens or TEM). The locus of the discontinuity in chromium concentration in the grain can be identified as the original grain boundary position.

## 5 DISCUSSION

The region depleted in chromium precipitates, which forms asymmetrically at the grain boundaries, is interpreted as the result of the oversweeping motion of the grain boundary during reduction. Despite variations from one boundary to the next, general tendencies can be identified about grain boundary motion: Close to the outer surface, it is very slow, increases to a maximum velocity value of about  $2 \cdot 10^{-9} \text{ cm/s}$  in deeper zones and progressively slows down to zero at the reduction front. The direction of migration of the grain boundary does not appear related to the size and shape of the grains. However, cross-sectional observations by TEM indicate that the migration of the boundary is more

### Cr - concentration profile in the matrix

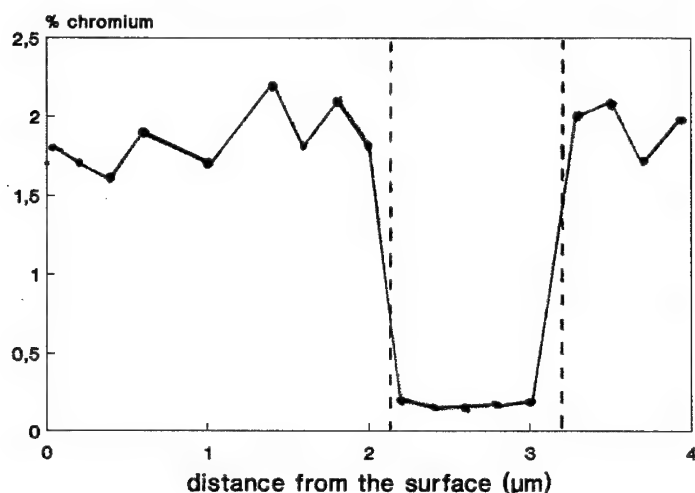


FIGURE 2(b) Concentration profile across the grain boundary.

important when the c-axis of the grains are perpendicular to each other. This indicates that diffusional transport perpendicular to the grain boundary plane and local gradients at the boundary are critical parameters for the observed grain boundary migration, which cannot be explained in terms of elastic strain fields or precipitate recrystallisation.

#### REFERENCES

1. C. A. Handwerker, in 'Diffusion phenomena in thin films', ed. Gupta, Noyes Publishers, pp. 187-230 (1988).
2. A. H. King; *Int. Mat. Reviews* **32**, 173-189 (1987).
3. T. A. Parthasarathy and P. G. Shewmon, *Acta metall* **32**, 29-33 (1984).
4. T. Pfeiffer, H. Schmalzried and M. Martin, *Scripta Met.* **18**, 383-386 (1984).
5. M. Backhaus-Ricoult, A. Peyrot and S. Hagège, *J. Am. Ceram. Soc.* **77**, 423-430 (1994).
6. H. Y. Lee, S. J. L. Kong, D. Y. Yoon; *Acta Met. Mat* **41**, 2497 (1993).

## THE SECOND-ORDER ELASTIC CONSTANTS OF AgBr FROM 20°C TO 400°C

L. S. CAIN\* and GANG HU\*\*

*\*Davidson College, Department of Physics Davidson, NC 28036 USA; \*\*3700 Chimney  
Ridge, #210 Durham, NC 27713 USA*

The second-order elastic constants of AgBr have been measured from 20°C to 400°C. Over this range,  $C'_{11}$  decreased by 50%,  $C'$  decreased by 86%,  $C_{44}$  decreased by 23%,  $C_{11}$  decreased by 61%,  $C_{12}$  decreased by 43%, and  $B_s$  decreased by 51%. The decreases in the elastic constants are linear, as expected, until approximately 200°C, whereupon they all begin to decrease more rapidly than linearly. The variations from linearity range from 4% to 31% at 400°C. This anomalous behaviour near the melting point is similar to other silver halide physical properties and may be attributed to the unusually high defect concentration. Similar elastic constant changes are seen in superionic conductors near the superionic transition, indicating that the silver halides may be starting the transition to a superionic state when the halide sublattice melts and the transition is frustrated.

*Key words:* Elastic constants, silver halides, AgBr.

### 1 INTRODUCTION

Many properties of the silver halides such as thermal expansion<sup>1</sup> and ionic conductivity<sup>2</sup> show anomalous increases near the melting point. These increases have been explained in terms of a temperature dependent Gibbs free energy of Frenkel defect formation which allows a larger than normal number of defects near the melting point. Anomalous changes in the elastic properties of these materials might also be expected, since elastic constants provide valuable information about interatomic forces and lattice defects. Previous measurements of the elastic constants of AgCl and AgBr have indicated anomalous decreases in elastic constants near the melting point.<sup>3,4</sup> We would like to report measurements of the second-order elastic constants of AgBr from 20°C to 400°C. These measurements were undertaken partly because of concerns about the bonding technique used in the previous AgBr study where the surface of the crystal was melted to attach the transducer.

### 2 EXPERIMENTAL PROCEDURE

The single crystal used was grown by Charles Childs at the University of North Carolina-Chapel Hill. The crystal had a (110) axis. Measurements were made using the Mc Skimin Pulse-Superposition technique.<sup>5</sup> Ultrasonic waves were generated by 10 MHz X- and Y-cut quartz transducers attached to the crystals with Sonotemp (Echo Ultrasound, Inc). The crystals were heated in a furnace in a helium atmosphere. The elastic constants were determined by multiplying the density of the sample (6.476 g/cm<sup>3</sup> at room temperature) by the square of the appropriate sound wave velocity. The thermal expansion values used to correct for the temperature dependence of the density and path length in the crystal were taken from Ref. 1.

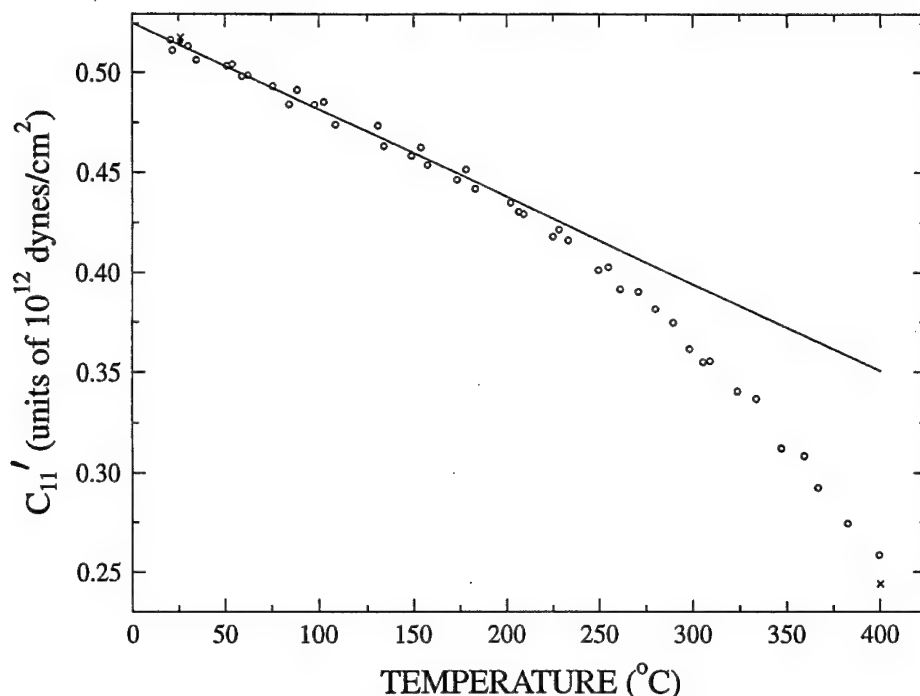


FIGURE 1 The longitudinal elastic constant  $C'_{11}$  versus temperature. o, present measurements; x, from Ref. 4 and • from Ref. 6. The solid line is a least-squares fit to the data below 200°C.

### 3 EXPERIMENTAL RESULTS

The silver halides have the face-centered cubic structure. They thus have three independent second-order elastic constants:  $C_{11}$ ,  $C_{12}$  and  $C_{44}$ . These can all be determined from the velocities of the pure sound waves propagated in the (110) direction. Several measurements were made of each elastic constant. These measurements were combined to produce a best set of elastic constants, which are shown in Table I.

The longitudinal elastic constant  $C_{11}$  decreased by 61%, the longitudinal constant  $C'_{11} = (C_{11} + C_{12} + 2C_{44})/2$  decreased by 50%, the constant  $C_{12}$  decreased by 43%, the shear constant  $C_{44}$  decreased by 23%, the shear constant  $C' = (C_{11} - C_{12})/2$  decreased by 86%, and the bulk modulus  $B_s = (C_{11} + 2C_{12})/3$  decreased by 51% over the temperature range. The decreases in the elastic constants are linear, as expected, until approximately 200°C, whereupon all the constants begin to decrease more rapidly than linearly. Figure 1 shows the constant  $C'_{11}$  versus temperature. This figure is representative of the anomalous changes in all the elastic constants. The data below 200°C for each elastic constant was fit by a least squares method to determine the temperature derivative of the elastic constant. These values were in good agreement with previous room temperature and high temperature measurements on AgBr.<sup>4,6</sup> The fitted lines also allowed the determination of the anomalous variation of the elastic constants from linearity at 400°C:  $C_{11}$  decreased by 28.2%,  $C'_{11}$  by 26.2%,  $C_{44}$  by 4.3%,  $C'$  by 11.4%,  $C_{12}$  by 31% and  $B_s$  by 30% below the expected linearity. These changes are similar to, but smaller than, the changes in AgBr

measured previously,<sup>4</sup> thus indicating some effect due to the bonding procedure used in the previous measurements.

Table I  
The second-order elastic constants of AgBr in units of  $10^{12}$  dyn/cm<sup>2</sup>.

Temperature (°C)	C <sub>11</sub>	C <sub>12</sub>	C <sub>44</sub>	C' <sub>11</sub>	C'	B <sub>s</sub>
20	0.560	0.326	0.0722	0.515	0.1172	0.404
50	0.543	0.322	0.0712	0.504	0.1106	0.396
100	0.510	0.314	0.0694	0.481	0.0977	0.379
150	0.475	0.308	0.0675	0.459	0.0837	0.363
200	0.440	0.298	0.0656	0.435	0.0712	0.345
250	0.396	0.283	0.0634	0.403	0.0567	0.321
300	0.342	0.256	0.0610	0.360	0.0430	0.285
350	0.282	0.224	0.0585	0.312	0.0293	0.243
400	0.219	0.187	0.0557	0.259	0.0163	0.197

#### 4 DISCUSSION

These measurements of the second-order elastic constants of AgBr show that the behaviour of the elastic constants becomes anomalous near the melting point. Just as for the other physical properties, this anomalous behaviour may be attributed to the unusually high defect concentration near the melting point. Previous results for the elastic constants of AgCl showed similar, but smaller, changes.<sup>3</sup> The larger changes in AgBr are expected due to the larger number of defects in AgBr near the melting point. Similar changes in elastic constants are seen in superionic conductors near the transition into the superionic state: large decreases in C<sub>11</sub> and C', but only small changes in C<sub>44</sub>.<sup>7,8</sup> This may indicate that the silver halides are just starting the transition to the superionic state when the halide sublattice melts and the transition is frustrated.

#### REFERENCES

1. B. R. Lawn, *Acta Crystallogr.* **16**, 29 (1963).
2. J. K. Aboagye and R. J. Friauf, *Phys. Rev.* **B11**, 1654 (1975).
3. L. S. Cain and C. Hughes, in *Proceedings of the XII International Conference on Defects in Insulating Materials*, edited by O. Kanert and J.-M. Spaeth, (World Scientific, 1993) Volume 1, pp. 508-510.
4. D. S. Tannhauser, L. J. Bruner, and A. W. Lawson, *Phys. Rev.* **102**, 1276 (1956).
5. H. J. McSkimin, *J. Acous. Soc. Am.* **33**, 12 (1961).
6. K. F. Loje and D. E. Schuele, *J. Phys. Chem. Solids* **31**, 2051 (1970).
7. C. R. A. Catlow, J. D. Comins, F. A. Germano, R. T. Harley, and W. Hayes, *J. Phys.* **C11**, 3197 (1978).
8. J. D. Comins, P. E. Ngoepe, and C. R. A. Catlow, *J. Chem. Soc. Faraday Trans.* **86**, 1183 (1990).



## SCHOTTKY BARRIERS IN SUPERIONIC CRYSTALS

S. BREDIKHIN, T. HATTORI\* and M. ISHIGAME\*

*Institute of Solid State Physics, 142432, Chernogolovka, Russia; \*Research Institute for Scientific Measurements, 2-1-1 Katahira, Sendai 980, Japan*

The phenomena of Schottky barrier creation in  $\text{RbAg}_4\text{I}_5$  are studied. Luminescence with high spatial resolution is used as a tool for investigation of the process on the blocking electrode-solid electrolyte boundary. The profile of the distribution of electronic centers near the contact region is measured. The presence of electrons and ions in the depletion region at the interface between the  $\text{RbAg}_4\text{I}_5$  and the graphite electrode is established and interpreted within the framework of the modified Schottky model. The kinetics of the creation of Schottky barriers is measured and described by taking into account the presence of self-trapped electrons and mobile silver ions in  $\text{RbAg}_4\text{I}_5$ . It is shown that the small value of the self-trapped electron diffusion coefficient ( $D_{st} \approx 1 \times 10^{-8} \text{ cm}^2/\text{sec}$ ) limit the kinetics of the process of creation of Schottky barriers.

**Key words:** Schottky barrier, self-trapped electrons, ambipolar diffusion.

### 1 INTRODUCTION

Superionic conductor heterojunction research is a new and important area of research of solid state ionics. One form of heterojunction considered here, namely, the metal-superionic conductor Schottky barrier junction, is most important for solid electrolytes. The situation before contact between electronic conductor and  $\alpha\text{-RbAg}_4\text{I}_5$  is the same as for nonsuperionic phase of  $\text{RbAg}_4\text{I}_5$ . The Fermi level for electrons in  $\alpha\text{-RbAg}_4\text{I}_5$  ( $\Phi_{SE}$ ) is above the Fermi level for electrons in graphite ( $\Phi_C$ ) by the amount of  $(\Phi_C - \Phi_{SE})$ . After the contact, a redistribution of charge occurs. To create the diffusion potential the self-trapped electrons together with ions come from the extent near contact region. In accordance with this the creation of near contact depletion region can be described by the process of one dimensional diffusion of self-trapped electrons and surrounding silver ions to the boundary from the bulk. For electrical neutrality, the change of the concentration of silver ions is the same as the change of the concentration of electrons. Due to this the small concentration of electrons determines the extent and time dependence of formation of the depletion region.

With the aim of studying of kinetics of creation of Schottky barriers, the photoluminescence was measured at 13 K as a function of time at room temperature. The photoluminescence studies were made in near electrode region with high spatial resolution. By means of an optical system, the light beam was focused of an area of  $150 \times 100 \mu\text{m}^2$ . The luminescence was analyzed with a double grating monochromator and detected by a photomultiplier. In accordance with the results obtained in<sup>1,2</sup> the emission bands at  $\lambda_{pl1} = 387 \text{ nm}$  and  $\lambda_{pl1.1} = 397 \text{ nm}$  may be attributed to the centers involving silver vacancies and the emission bands at  $\lambda_{pl2} = 437 \text{ nm}$  and  $\lambda_{pl4} = 462 \text{ nm}$  are associated with centers whose composition involve interstitial silver. To get information about the mechanism and time dependence of Schottky barrier formation the photoluminescence spectra were measured with high spatial resolution in near contact region of  $\text{RbAg}_4\text{I}_5$ .

For this experiment the graphite was deposited on the end-face of the sample with 8 mm length and  $3 \times 4 \text{ mm}^2$  cross-section. Figure 1 shows the photoluminescence spectra after an elapse of 65 hours from graphite deposition which are measured at different distances from the contact. From Figure 1, it is seen that the intensity of the luminescence bands at

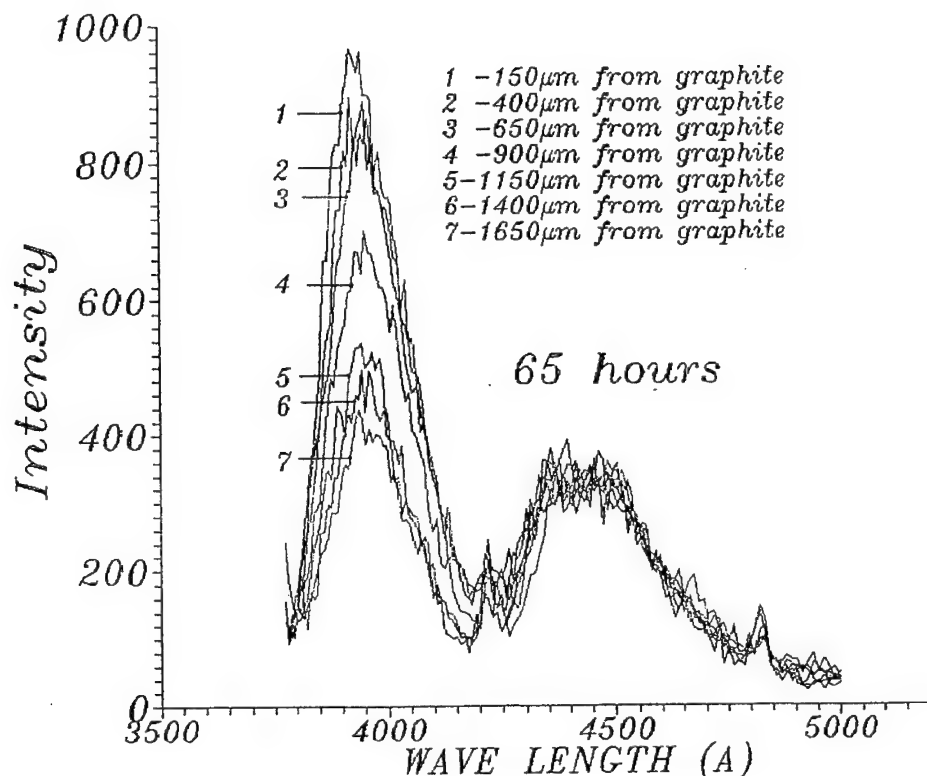


FIGURE 1 Photoluminescence spectra after an elapse of 65 hours from electronic conductor deposition as measured on a distance 150  $\mu\text{m}$  (curve-1), 400  $\mu\text{m}$  (curve-2), 650  $\mu\text{m}$  (curve-3), 900  $\mu\text{m}$  (curve-4), 1150  $\mu\text{m}$  (curve-5), 1400  $\mu\text{m}$  (curve-6) and 1650  $\mu\text{m}$  (curve-7) from the contact.

$\lambda_{p11} = 387 \text{ nm}$  and  $\lambda_{p11.1} = 397 \text{ nm}$  increases in the near contact region. The intensity of these luminescence bands decreases as a function of distance from the contact and in a distance 1650  $\mu\text{m}$  the photoluminescence spectrum looks like the spectrum from primary sample. In our previous study<sup>1</sup> it has been shown that the photoluminescence in the spectral region 3800–4150 Å is associated with luminescence centers whose composition involve silver vacancies and the integral intensity in this spectral region is proportional to the lack of silver. In accordance with this the integral intensity in spectral region 3800–4150 Å at some distance from contact is proportional to the lack of silver (or to the concentration of silver vacancies at this distance). Dependence on the distance from the contact gives the profile of relative concentration of silver vacancies in the  $\text{RbAg}_4\text{I}_5$  sample after graphite deposition. Figure 2 shows the experimental result of the distance dependence of the relative concentration of silver vacancies in the  $\text{RbAg}_4\text{I}_5$  sample after an elapse of 65 hours from graphite deposition at temperature 295 K and fitting of analytical curve to the experimental data. To get a value of the diffusion coefficient of self-trapped electrons and surrounding them silver ions, the calculated curve for solution of the diffusion equation is fitted to the experimental data by using the  $D$  as fitting parameter. For this procedure the value of self-trapped electron diffusion coefficient is obtained to be  $D_e = 0.96 \times 10^{-8} \text{ cm}^2/\text{sec}$  at temperature 295 K.

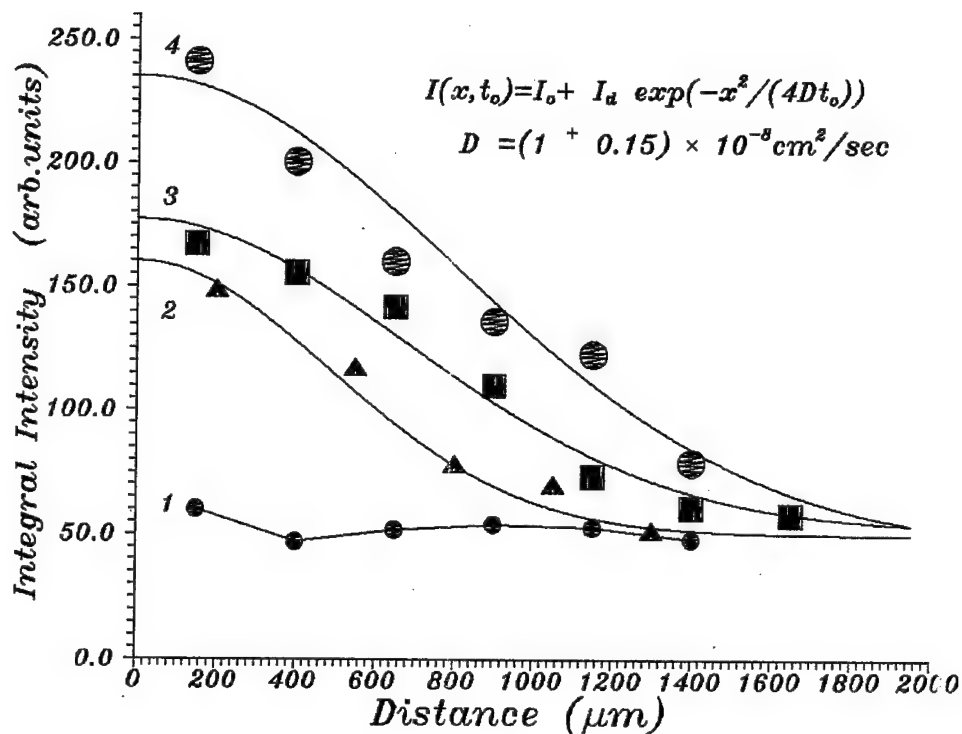


FIGURE 2 Relative concentration of silver vacancies as a function of distance from contact as measured after elapses of 27 hours, 65 hours and 102 hours from graphite deposition and fitting of analytical solution of one dimensional diffusion equation to the data (curve-2, curve-3 and curve-4). Curve-1 shows the relative concentration of silver vacancies after an elapse of 6 hours from graphite deposition.

To get information about the kinetics of the creation of Schottky barrier and near-electrode depletion region in  $\alpha$ -RbAg<sub>4</sub>I<sub>5</sub> the measurements of the distribution of the photoluminescence bands intensity in near contact region were done as a function of time from graphite deposition. Figure 2 shows the experimental result of the distance dependences of the relative concentrations of silver vacancies after elapses of 6 hours, 27 hours, 65 hours and 102 hours from graphite deposition (curve-1, 2, 3 and 4, respectively). The fitting of the calculated curve to experimental data gives the value of diffusion coefficient of  $D_e = (1 \pm 0.2) \times 10^{-8} \text{ cm}^2/\text{sec}$  to the process of one dimensional diffusion of self-trapped electrons in  $\alpha$ -RbAg<sub>4</sub>I<sub>5</sub> at 295 K (Figure 2). The calculation of diffusion coefficient from concentration profile was carried out by using Fick's second law. This value is in a good agreement with a value of self-trapped electron diffusion coefficient  $D_e = (1.7 \pm 0.7) \times 10^{-8} \text{ cm}^2/\text{sec}$  measured in our previous.<sup>1</sup>

In accordance with this the creation of Schottky barrier and of the depletion near contact region in  $\alpha$ -RbAg<sub>4</sub>I<sub>5</sub> takes place due to the diffusion of self-trapped electrons from solid electrolyte into graphite. A redistribution of charge and diffusion takes place until the Fermi levels in both materials are at the same position. The value of potential barrier is due to the difference in the values of work functions for electrons in graphite and RbAg<sub>4</sub>I<sub>5</sub>, but the properties of the barrier are determined by the presence of mobile silver ions. Really,

there is no distributed charge in near contact region of  $\alpha$ -RbAg<sub>4</sub>I<sub>5</sub>, since the charge of ionized donors are screened by the redistribution of mobile silver ions. And on the solid electrolyte side the charge appears as a surface charge. Due to this in  $\alpha$ -RbAg<sub>4</sub>I<sub>5</sub> the barrier capacitance ( $C_{sup} \simeq 10^{-5} F$ ) is much more higher than in semiconductors and in nonsuperionic phase of RbAg<sub>4</sub>I<sub>5</sub>. In this case it needs much more big amount of electrons for formation of diffusion potential ( $V_d \simeq 0.25 V$ )

$$Q_{sup} \simeq V_d \times C_{sup} \simeq 2.5 \times 10^{-6} q/cm^2 \simeq 2 \times 10^{13} e/cm^2 \quad (1)$$

For a real sample, the deposition of an electronic conductor on the surface of  $\alpha$ -RbAg<sub>4</sub>I<sub>5</sub> will change the properties of the sample drastically. For the formation of the diffusion potential it needs about  $10^{13}$  electrons per  $cm^2$  to diffuse from the bulk to the boundary and enter the electronic conductor. At the same time, the electronic conductivity of  $\alpha$ -RbAg<sub>4</sub>I<sub>5</sub> is small ( $\sigma_e \simeq 3 \times 10^{-9} (ohm \times cm)^{-1}$ ) and the concentration of mobile electrons is small ( $n_{st} \sim 10^{15} \div 10^{16} cm^{-3}$ ), too. In accordance with this if the thickness of the sample  $L_{sample}$  is small, of the order of  $Q_{sup}/n_{st}$  ( $L_{sample} \leq 0.1$  mm), then it needs approximately all mobile electrons to diffuse from the bulk to the boundary for formation of the diffusion potential. In this case the deposition of electronic conductor leads to the depletion of sample by mobile electrons and ions and to shift of the position of Fermi level.<sup>2</sup>

To describe this phenomenon let us consider the process of screening of ionized donors in  $\alpha$ -RbAg<sub>4</sub>I<sub>5</sub>. As pointed out earlier, the charge of the ionized donors is screened by ions leaving from positions surrounding donor together with the electrons from this donor. But this is the same as a transformation of the structure of donor centers and the same as a decrease of the concentration of donors in the sample. Due to this the new position of Fermi level ( $\mu$ ) and the value of work function ( $\Phi_{SE}$ ) depend on the sample size  $L_{sample}$  and on the value of diffusion potential ( $V_d$ ). At the same time the value of the diffusion potential depends on the value of the work function of RbAg<sub>4</sub>I<sub>5</sub>.

In a simple approach when the sample depletion and the decrease of the concentration of donors in the sample is small  $\frac{V_d C_{sup}}{e L_{sample}} \ll N_D^0$ . Then, the correction to the value of diffusion potential ( $V_d$ ) and to the position of the Fermi level ( $\mu$ ) is small, too. Really, from the simple calculations, it follows that the new value of the position of the Fermi level is

$$\mu = \mu_0 + \frac{\kappa T}{2} \left( \frac{V_d^0 C_{sup}}{e L_{sample} N_D^0} \right) - \frac{\kappa T}{2} \left( \frac{V_d^0 C_{sup}^2 (e V_d^0 + \kappa T)}{e (e L_{sample} N_D^0)^2} \right), \quad (2)$$

where the quantities  $\frac{\kappa T}{2} \left( \frac{V_d^0 C_{sup}}{e L_{sample} N_D^0} \right)$  is of the same order of magnitude as the correction of the concentration of donors, and  $\frac{\kappa T}{2} \left( \frac{V_d^0 C_{sup}^2 (e V_d^0 + \kappa T)}{e (e L_{sample} N_D^0)^2} \right)$  is a second-order correction. Thus

the first-order correction gives the shift of the position of Fermi level in RbAg<sub>4</sub>I<sub>5</sub> sample after the deposition of an electronic conductor. It is seen that the shift of the Fermi level and the sample depletion are proportional to the value of the diffusion potential and are inversely proportional to the thickness of the sample.

## 2 CONCLUSION

New phenomena of formation of extent ( $\sim 0.1$ – $1$  mm) depletion near contact region in RbAg<sub>4</sub>I<sub>5</sub> are discovered and investigated. It is found that the blocking electrode deposition on the surface of the sample leads to the transformation of concentration and of structure of

luminescence centers and to the decrease of the concentration of mobile silver ions and electrons in parallel in near surface region. If the extent of the sample is smaller than the extent of depletion region in  $\text{RbAg}_4\text{I}_5$  ( $\sim 1$  mm) then the deposition of electronic conductor leads to the depletion of sample by mobile electrons and ions and to shift of the position of Fermi level. It is shown that the small concentration of electrons determine the extent and time dependence of formation of depletion region. The value of self-trapped electron diffusion coefficient is obtained to be  $D_e = (1 \pm 0.2) \times 10^{-8} \text{cm}^2/\text{sec}$ .

## REFERENCES

1. S. Bredikhin, T. Hattori and M. Ishigame, *Solid State Ionics* **67**, 311, (1994).
2. S. Bredikhin, T. Hattori and M. Ishigame, *Physical Review* **B50**, (1994).

## ELECTRICAL CONDUCTIVITY OF A $\alpha$ -LiIO<sub>3</sub>:Cr<sup>3+</sup> SINGLE CRYSTAL

R. L. MOREIRA,<sup>1</sup> P. BOURSON,<sup>1,4</sup> C. ROSSO,<sup>2</sup> C. GALEZ,<sup>2</sup>  
A. RIGHI<sup>1</sup> and J. M. CRETTEZ<sup>3</sup>

<sup>1</sup>University of Minas Gerais, ICEx, CP702 30161 Belo Horizonte—Brazil; <sup>2</sup>Equipe de Recherche sur la Ferroélectricité et l'Optique Non-linéaire, ESIA-Université de Savoie, 41 avenue de la Plaine BP806 74016 Annecy cedex France; <sup>3</sup>Laboratoire de Physique, URA CNRS 1796, BP138, 21004 Dijon France; <sup>4</sup>Permanent address: Laboratory MOPS (CLOES) University of Metz-SUPELEC 2 rue Edouard Belin 57078 Metz Cedex 3 France, Email: bourson@esemetz.esemetz.fr

This paper reports the behaviour of electrical conductivity of a Chromium doped  $\alpha$ -LiIO<sub>3</sub> crystal perpendicular to c-axis from room temperature up to the melting point. Our results indicate that the sample does not break out through the sequence of phase transitions, contrary to a pure crystal. Indeed, it has been possible to measure the electrical conductivity in the  $\alpha$ ,  $\gamma$  and  $\beta$  phases. A phase-sequence scheme is then proposed and compared with other published results.

**Key words:** lithium iodate, chromium, electrical conductivity, phase transition.

### 1 INTRODUCTION

The non-centrosymmetrical crystal of  $\alpha$ -LiIO<sub>3</sub> attracts attention mainly on account of its piezoelectric and non-linear optical properties, in particular for the optical harmonic generation where this crystal is a reference. Moreover, it could exhibit enhanced photorefractive effect when doped with transition metals. Therefore the growth of pure and chromium doped  $\alpha$ -LiIO<sub>3</sub> single crystals has been developed. The possibility of growing Cr<sup>3+</sup> doped crystals with a good quality allows the analysis of their electrical properties and especially the instability of the electrical behaviour due to the presence of Cr<sup>3+</sup> ions in the lattice. Results presented are restricted to the particular behaviour of the  $\sigma_{11}$  conductivity (perpendicular to c-axis) when cycling temperature and up to the melting point.

### 2 EXPERIMENTS

Crystals were grown by slow isothermal evaporation of an aqueous solution of  $\alpha$ -LiIO<sub>3</sub> doped with 0.01%mol Cr(NO<sub>3</sub>)<sub>3</sub>. The electrical conductivity was measured using a small alternative electric field (1 kHz, 35 mV.cm<sup>-1</sup> rms) in order to minimise the influence of space charge barriers<sup>1</sup> and with a heating rate of 1°C.min<sup>-1</sup>. Such experimental conditions with a sample grown at pH = 2 (more often used in non-linear optics) and without DC field component were chosen to avoid electrolysis and damage of the crystal.<sup>2</sup> This frequency has been chosen because it is intermediate between the low frequency range where phenomena are mainly governed by space charges<sup>3</sup> and the high frequency range where the conductivity is sensitive to the growth conditions by way of structure defects and hydrogen impurities.<sup>4</sup>

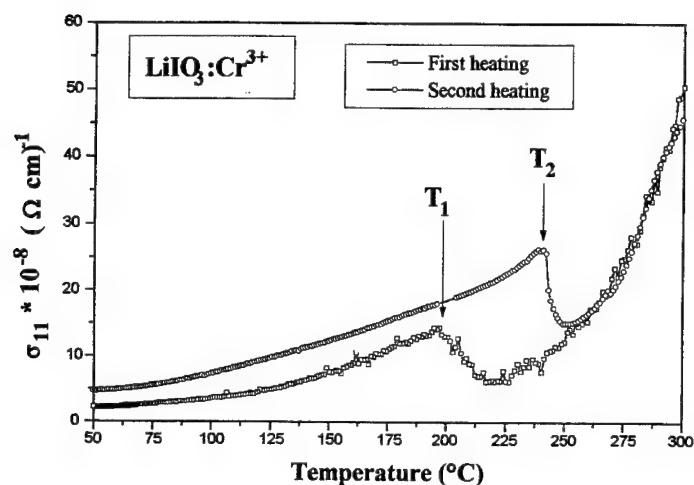


FIGURE 1  $\sigma_{11}$  temperature dependence during first and second heating for a  $\text{Cr}^{3+}$  doped  $\alpha\text{-LiIO}_3$  single crystal.

### 3 RESULTS

During the first heating (Figure 1),  $\sigma_{11}$  exhibits a first anomaly at  $T_1 = 200^\circ\text{C}$  corresponding to the occurrence of the  $\gamma$  phase, then increases regularly up to  $310^\circ\text{C}$ , a temperature at which a pure crystal is already broken by a destructive transition. In order to check the appearance of the sample, the temperature was lowered to room temperature. As the crystal was not damaged, we decided to perform a second heating under the same operating conditions up to the breaking of the sample. At low temperature, the value of  $\sigma_{11}$  was slightly higher than during the first heating and the first anomaly was found at  $T_2 = 240^\circ\text{C}$ . Such a phenomenon has already been observed by DTA measurements.<sup>5</sup> However, as the temperature was raised, it has been possible to measure accurately the conductivity of the sample up to the melting point that is up to  $394^\circ\text{C}$  (Figure 2), enabling to observe a drastic jump of two decades between  $357$  and  $363^\circ\text{C}$ .

### 4 DISCUSSION

This experiment shows that incorporation of  $\text{Cr}^{3+}$  ions in the lattice of  $\alpha\text{-LiIO}_3$  could prevent the crystal from breaking at the irreversible transition. This behaviour has been observed with only one crystal which was the most pink coloured crystal denoting undoubtedly the presence of  $\text{Cr}^{3+}$  impurities. As compared with DTA and X-ray transition schemes of  $\alpha\text{-LiIO}_3$  single crystal and polycrystalline samples given by M. Czank *et al.*,<sup>6</sup>

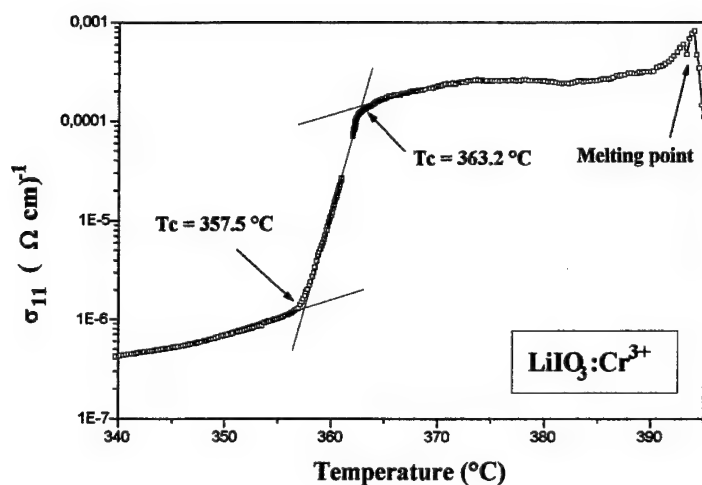
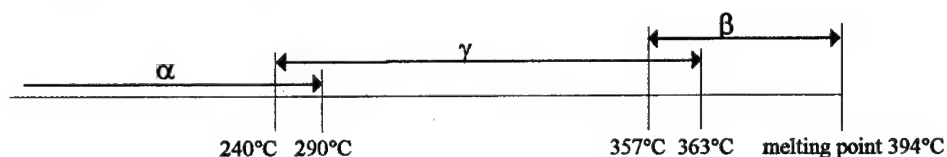


FIGURE 2 Conductivity behaviour beyond  $\gamma \rightarrow \beta$  transition temperature up to melting point.

we can conclude that the  $\text{Cr}^{3+}$  impurities enlarge the temperature range of existence of the  $\gamma$  phase and shift the temperature of occurrence of  $\beta\text{-LiIO}_3$  towards higher values. Indeed for a pure single crystal the  $\beta$  phase appears at low temperature and the internal strains through  $\gamma \rightarrow \beta$  transition are so large that the sample is destroyed at the macroscopic level. When the  $\beta$  phase appears at a higher temperature, which looks like the behaviour of polycrystalline samples, the  $\text{Cr}^{3+}$  doped crystal undergoes a non destructive transition. So we suggest the following phase transition scheme for the  $\alpha\text{-LiIO}_3:\text{Cr}^{3+}$  crystal:



The observation of pure  $\alpha\text{-LiIO}_3$  crystalline plates during heating revealed that after transformation into the  $\beta$ -phase, the sample was puffed and crumbly in consistency, with an ordering of separate blocks leading to a column-like appearance.<sup>7</sup> Indeed when the cracking of the sample occurs, the conductivity drops to zero. Such a phenomenon is not observed in  $\alpha\text{-LiIO}_3:\text{Cr}^{3+}$  so that the drastic jump of the conductivity at 357°C is



obviously due to an increase of lithium mobility but cannot be easily related to structural features. The present results must be confirmed by conductivity measurements along c-axis, direct observation and by other experimental technics.

## REFERENCES

1. A. A. Blistanov, V. V. Geras'kin, N. S. Kozlova, E. V. Makarevskaya, O. G. Portnov *Sov. Phys. Crystallogr.* **32**(5), 703 (1987).
2. L. I. Isaenko, I. F. Kanaev, V. K. Malinovskii *Sov. Phys. Solid State* **30**(2), 199 (1988).
3. A. D. Zhang, S. F. Zhao, A. Y. Xie, Z. Y. Xu, *Chin. Phys.* **1**(4), 923 (1981).
4. V. V. Vorob'ev, E. P. Lokshin, E. V. Charnaya *Sov. Phys. Solid State* **34**(3), 478 (1992).
5. H. Arend, M. Remoissenet, W. Staehlin, *Mat. Res. Bull.* **7**, 869 (1972).
6. M. Czank, H. Schulz, H. G. Wiedemann, *Z. Kristallogr.* **143**, 99 (1976).
7. J. M. Cretiez, E. Coquet, B. Michaux, J. Pannetier, J. Bouillot, P. Orlans, A. Nonat, J. C. Mutin, *Physica* **144b**, 277 (1987).

## A RENEWED APPROACH OF HOPPING CONDUCTION IN AMORPHOUS MATERIALS

R. ONGARO and M. GAROUM

LEMI Bât 721 43 Bld du 11 Novembre 1918 69622 VILLEURBANNE cedex

A novel approach is proposed to describe hopping conductivity in a band of uniformly distributed localized levels. The basic equations are taken in full forms and their respective involvements are discussed. Ultimately, a first step approach of conductivity is derived, with hopping distance expressed by a plausible empirical function.

*Key words:* Amorphous materials; hopping conduction.

### 1 INTRODUCTION

The approach concerns hopping conduction in a uniformly distributed impurity band, located anywhere relative to Fermi energy  $E_F$ . It is a first step in a treatment to be extended later to the renowned Mott and Davis<sup>1</sup> and Cohen-Fritzsche-Ovshinski<sup>2</sup> models, and to a number of presently available models displaying a variety of distributions of localized states. Our approach is to be contrasted with the preceding ones on essentially two points (1) Fermi-Dirac statistics is used consistently to describe the electronic populations of the levels as a whole, where in earlier work the Boltzmann approximation was substituted. It is known<sup>3,4</sup> that model's parameters cannot then be derived properly from a division, into linear components, of conductivity versus reciprocal temperature curves. (2) Constraints imposed by the principle of detailed balancing are carefully analysed at thermal equilibrium, in conjunction with the assumption of wave functions overlap. For the remainder, the probability of transition from a localized level at energy  $E$  to a near level at energy  $E'$  is written as the product  $f(E)[1 - f(E')]$ , in accordance with the Miller and Abrahams' approach.<sup>5</sup> Also, hopping conductivity is deduced from the electrons diffusion parameter  $D$  through Einstein's relation.<sup>1</sup>

### 2 MODEL AND CALCULATION

The involved transitions, into a band of uniformly distributed localized levels in thermal equilibrium with the extended states, are sketched in Figure 1. An electron can hop from a level  $\varepsilon_1$  to a level  $\varepsilon_2$  at a distance  $R_{\varepsilon_1\varepsilon_2}$ , and conversely an electron can hop from  $\varepsilon_2$  to  $\varepsilon_1$  distant of  $R_{\varepsilon_1\varepsilon_2}$ . The differential diffusion coefficients, for a transition from  $\varepsilon_i$  to  $\varepsilon_j$ , is written as:<sup>1</sup>

$$d^2D_{\varepsilon_i\varepsilon_j} = R_{\varepsilon_i\varepsilon_j}^2 d\varepsilon_i d\varepsilon_j \quad (1)$$

and  $d\varepsilon_i d\varepsilon_j$  is the related hopping rate. Therefore:

$$d^2D_{\varepsilon_i\varepsilon_j} = \nu_{\varepsilon_i\varepsilon_j} N R_{\varepsilon_i\varepsilon_j}^2 \exp(-2\alpha R_{\varepsilon_i\varepsilon_j}) f(\varepsilon_i)[1 - f(\varepsilon_j)] d\varepsilon_i d\varepsilon_j \quad (2)$$

$N$  is the density of sites per unit energy,  $\nu_{\varepsilon_i\varepsilon_j}$  is a frequency factor, and  $\exp(-2\alpha R_{\varepsilon_i\varepsilon_j})$  is the range of wave function attenuation. Hence,  $D$  is derived through a double integration, first over  $\varepsilon_2$  and then over  $\varepsilon_1$  (see Figure 1).

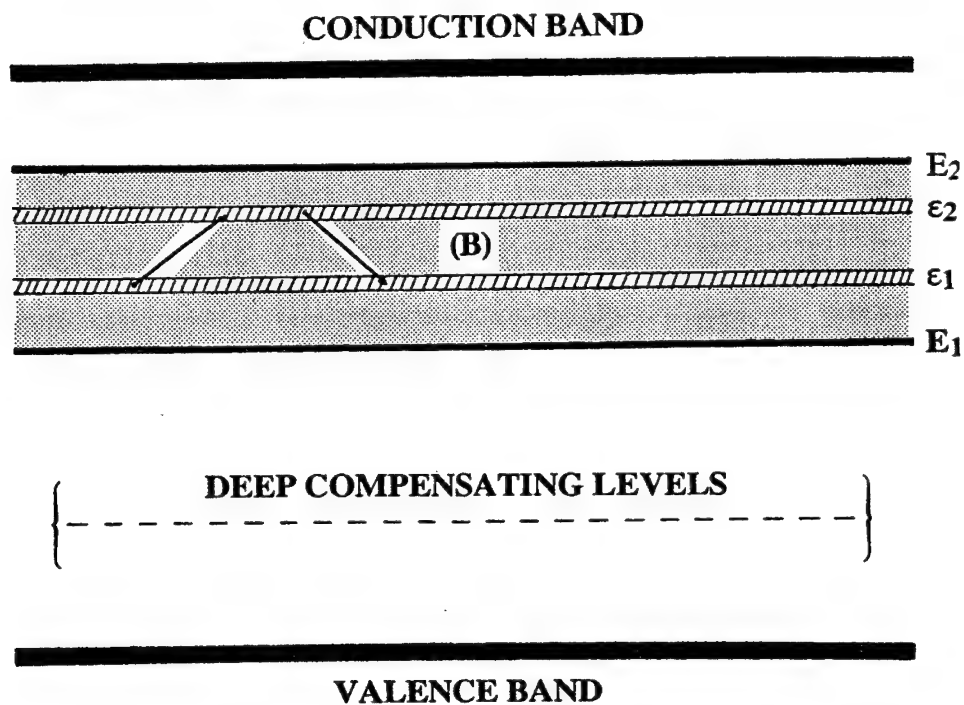


FIGURE 1 Schematic diagram of hopping processes within a band of localized states.

### 2.1 Detailed Balance Involvements

Hopping distances can, in principle, be deduced from equations (2) on applying the principle of detailed balance, which gives readily for transitions  $(\epsilon_1, \epsilon_2)$ :

$$2\alpha(R_{\epsilon_1\epsilon_2} - R_{\epsilon_2\epsilon_1}) = \frac{\epsilon_2 - \epsilon_1}{kT} + \ln \frac{\nu_{\epsilon_1\epsilon_2}}{\nu_{\epsilon_2\epsilon_1}} \quad (3)$$

Being aware that wave functions overlap implies that  $\exp(-2\alpha R) \rightarrow 1$  as  $N$  increases to a maximum admissible value  $N_m$ , and consequently that hopping would proceed through nearest neighbours ( $R_{\epsilon_i\epsilon_j} \rightarrow R_m = N_m^{-1/3}$ ) it turns out that

$$\nu_{\epsilon_i\epsilon_j} = \nu_0 \exp\left(\beta \frac{\epsilon_i - \epsilon_j}{kT}\right) \quad (4a)$$

$$\nu_{\epsilon_j\epsilon_i} = \nu_0 \exp\left[-(1 - \beta) \frac{\epsilon_i - \epsilon_j}{kT}\right] \quad (4b)$$

$\beta$  is an unspecified parameter which value can reasonably be taken in the range  $0 \leq \beta \leq 1$ . The frequency factors are then exponentially dependent on the energy difference  $\nu_i - \nu_j$ , and hopping distances are equal for any two reverse transitions.

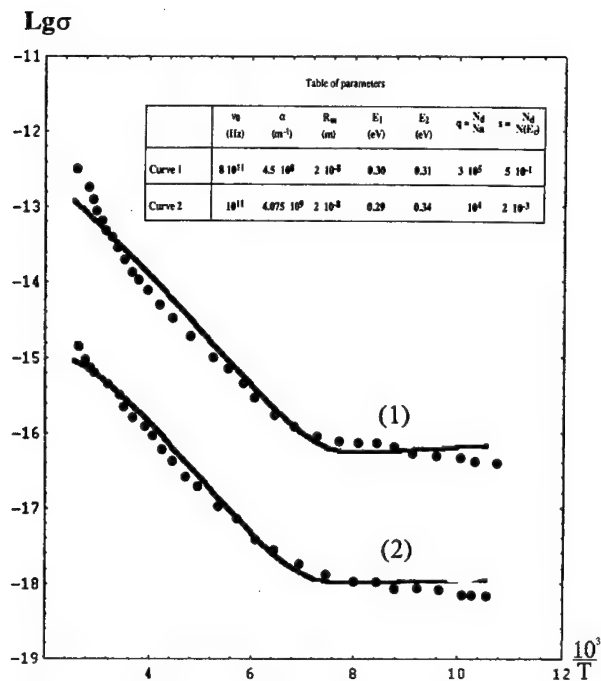


FIGURE 2 Example of application of the theory to data by Sidek *et al.*<sup>6</sup> on Samarium glasses.

## 2.2 Conductivity Derivation

Integration of equations (2) needs a knowledge of  $R\varepsilon_i\varepsilon_j$ , which in turn implies an appropriate modelling of microscopic processes. In a first step, the simplest procedure is to typify these processes by means of an empirical function  $F(\varepsilon_i - \varepsilon_j, N, T)$ . In the present development, with  $\beta = 1/2$ ,  $F$  is taken as

$$F = F_m \left[ 1 - \frac{T_0}{T} \left( \frac{N_0}{N} \right)^{1/3} \right] = (-2\alpha R_m + \ln \nu_0) \left[ 1 - \frac{T_0}{T} \left( \frac{N_0}{N} \right)^{1/3} \right] \quad (5a)$$

$$\text{so that} \quad 2\alpha R = \ln \nu_0 - F > 0 \quad (5b)$$

In this way, the hopping distance  $R$  is a linear function of  $N^{-1/3}$ ,<sup>1</sup> and  $R$  increases with decreasing  $T$ .

From that, the double integration of equation (2) yields readily

$$\sigma = e^2 \nu_0 N \alpha^{-2} k T c^2 e^{-c} [\tan^{-1} \exp X_2 - \tan^{-1} \exp X_1]^2 \quad (6)$$

$$\text{with } c = 2\alpha R_m + \frac{T_0}{T} \left( \frac{N_0}{N} \right)^{1/3} (\ln \nu_0 - 2\alpha R_m); X_1 = (E_1 - E_F)/2kT; X_2 = (E_2 - E_F)/2kT.$$

In this equation  $E_F$  is derived from the complete equation of neutrality, resulting from Fermi-Dirac statistics, and applied to all transitions between localized and free states.

Moreover, compensation is introduced in order to shift  $E_F$  as desired.

Figure 2 shows an illustrative example of fitting with our model of data by Sidek *et al.*<sup>6</sup> about d.c. conductivity in glasses containing rare-earth ions (full circles). The authors relate tentatively the behaviour of the observed conductivity  $\sigma(T^{-1})$  to a double hopping mechanism, on the observation that curves can be split into two linear components in an Arrhenius plot. The low temperature part is then attributed to small-polaron conduction in a narrow band, while the high temperature part is assigned to multiphonon-assisted hopping. Full lines drawn in the figure, with the parameter values given in the caption, show that our first approach can also work.

### 3 CONCLUSION

The present model of hopping conduction within a band of gap states brings an opportunity of interpreting  $\log \sigma$  vs  $T^{-1}$  curves, without having recourse to the usual graphical splitting of an Arrhenius plot into linear parts. It is only a first step towards a much more involved calculation, where the energy variation in hopping events is accounted for. As such however, the model is able to fit experimental data conveniently, as shown in Figure 2.

### BIBLIOGRAPHY

1. N. F. Mott E. A. Davis *Electronic processes in non-crystalline materials* (Clarendon Press-Oxford, 1971).
2. M. H. Cohen H. Fritzche S. R. Ovshinski *Phys. Rev. Lett.* **22**, 1065 (1969).
3. J. S. Blakemore Semiconductor statistics. *International series of monographs on semiconductors*. (Pergamon Press, 1962).
4. R. Ongaro A. Pillonnet *Rev. Phys. Appl. (France)* **25**, 209 (1990).
5. A. Miller E. Abrahams *Phys. Rev.* **120**, 745 (1960).
6. H. A. A. Sidek, I. T. Collier R. N. Hampton G. A. Saunders B. Bridge *Philos. Mag* **B59** 221 (1989).

---

## **16 SUPERCONDUCTIVITY**

## TRANSPORT PROPERTIES AND DEFECT CHEMISTRY OF HIGH- $T_c$ -SUPERCONDUCTORS

M. QUILTIZ and J. MAIER

*Max-Planck-Institut für Festkörperforschung, Heisenbergstrasse 1 D-70569 Stuttgart  
(Germany)*

We discuss novel electrochemical data on  $\text{Bi}_2\text{Sr}_2\text{CaCu}_2\text{O}_{8+\delta}$  (BSCCO) at high temperature, where equilibrium with the oxygen containing neighboring phase is established. Measurements of the electronic conductivity as a function of oxygen partial pressure and temperature convey information about the defect chemistry. Careful investigation of the electrochemical polarization on glass-sealed cells allows the determination of the ionic conductivity. The investigation of the instationary response of the electrochemical polarization measurements enables us to determine the chemical diffusion coefficients.

The defect chemistry can be understood by an anti-frenkel disorder of the oxygen sublattice. In  $\text{Bi}_2\text{Sr}_2\text{CaCu}_2\text{O}_{8+\delta}$  interactions between ionic and electronic charge carriers are important. The results are summarized in the framework of simple defect models which are discussed in the context of former results on  $(\text{La}, \text{Sr})_2\text{CuO}_{4+\delta}$  and  $\text{YBa}_2\text{Cu}_3\text{O}_{6+\delta}$ .<sup>1-5</sup>

*Key words:* defect chemistry, HTSc, oxygen transport, chem. diffusion.

### 1 INTRODUCTION

It is now well accepted that the properties of superconducting compounds are connected to their nonstoichiometry and thus to the charge carrier concentrations of the electronic and ionic species.<sup>1</sup> Due to this, the investigation of the defect chemistry and the kinetics of oxygen incorporation in  $\text{Bi}_2\text{Sr}_2\text{CaCu}_2\text{O}_{8+\delta}$  as in  $(\text{La}, \text{Sr})_2\text{CuO}_{4+\delta}$  and  $\text{YBa}_2\text{Cu}_3\text{O}_{6+\delta}$  leads to the development of defect models.<sup>1,2,5</sup> Thermodynamic and kinetic investigations of high temperature superconductors at high temperatures are very important for several reasons: First, processing conditions are determined by high temperature defect chemistry and high temperature diffusion and reaction kinetics. In addition partial equilibrium concerning the ionic and electronic defects is established at the usual preparation temperatures and, since the ionic defect structure is partly frozen-in after the preparation, the electronic charge carrier concentration in the superconducting state is largely influenced by the high temperature defect structure.

### 2 EXPERIMENTAL

The preparation of conventional ceramics, of oriented ceramics and of single crystals has already been given elsewhere.<sup>6</sup> The electrochemical methods has been described in ref.<sup>3,5</sup> Further details of the method will be described.<sup>7</sup>

### 3 RESULTS AND DISCUSSION

$\text{Bi}_2\text{Sr}_2\text{CaCu}_2\text{O}_{8+\delta}$  as  $\text{La}_2\text{CuO}_4$  and  $\text{YBa}_2\text{Cu}_3\text{O}_{6+\delta}$  becomes superconducting at elevated oxygen partial pressures. The variation range in oxygen stoichiometry is narrow ( $0 < \delta < 0.35$ ) compared to  $\text{YBa}_2\text{Cu}_3\text{O}_{6+\delta}$ . According to the occurrence of p-conduction

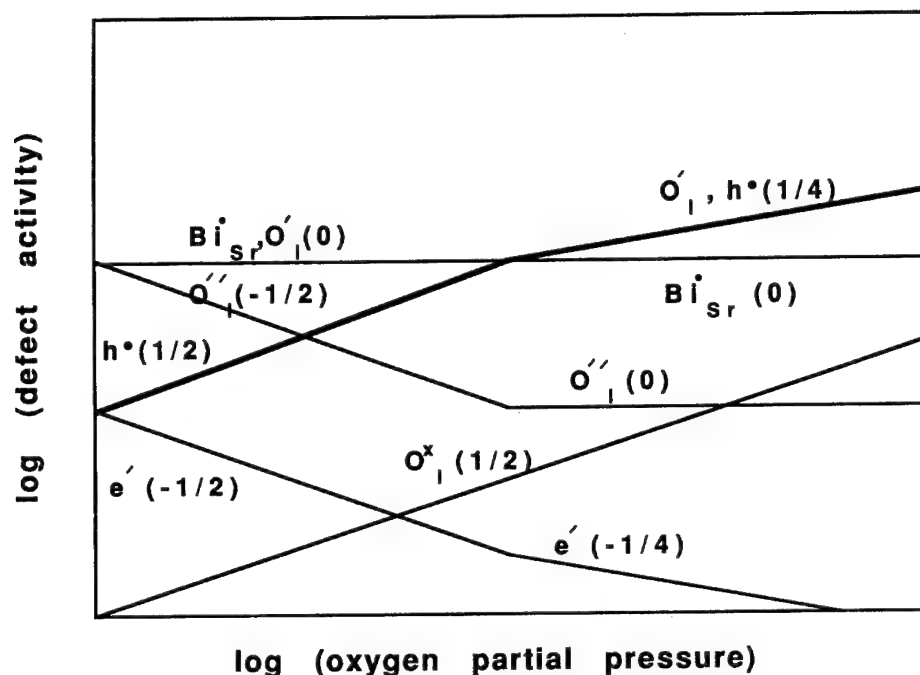
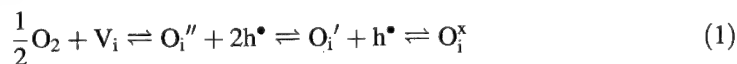


FIGURE 1 Modeled development of the defect concentrations in  $\text{Bi}_2\text{Sr}_2\text{CaCu}_2\text{O}_{8+\delta}$  with assumed Bi-excess ( $\text{Bi}_{\text{Sr}}^\circ$ ).<sup>5</sup>

in this compound we consider all extra oxygen ( $\delta > 0$ ) as interstitial oxygen. The following incorporation reaction is derived from the partial pressure dependence of the electronic conductivity:



With increasing oxygen partial pressure the p-conductivity follows a  $p\text{O}_2^{1/2}$  power law. As discussed in<sup>1,2,5</sup> in detail these results can be understood as follows. A majority of the holes are trapped at the oxygen interstitials forming large concentrations of monovalent and neutral defects. For moderate oxygen partial pressures, the activity of  $\text{O}_i'$  is roughly constant due to internal disorder giving rise to a slope of 1/2 (Figure 1). At larger  $p\text{O}_2^{1/2}$  values the slope is flattening. At higher defect-electron concentrations the electroneutrality condition reads  $[\text{O}_i'] = [\text{h}^\bullet]$  and  $\sigma \propto p\text{O}_2^{1/4}$  is predicted. The internal disorder mentioned above is due to anti-Frenkel and/or anti-site ( $\text{Bi}_{\text{Sr}}^\circ$ ) disorder. The latter possibility is supported by the similar ionic radii of Bi and Sr, high preparation temperatures and the coexistence of Bi-excess with Sr-deficit which is in line with the chemical analysis.<sup>8</sup>

At even higher oxygen partial pressures the slope is flattening to  $\sigma \propto p\text{O}_2^N$  with  $N$  nearly 0. Different explanations may be considered: The increased trapping of holes at Bi according to the reaction



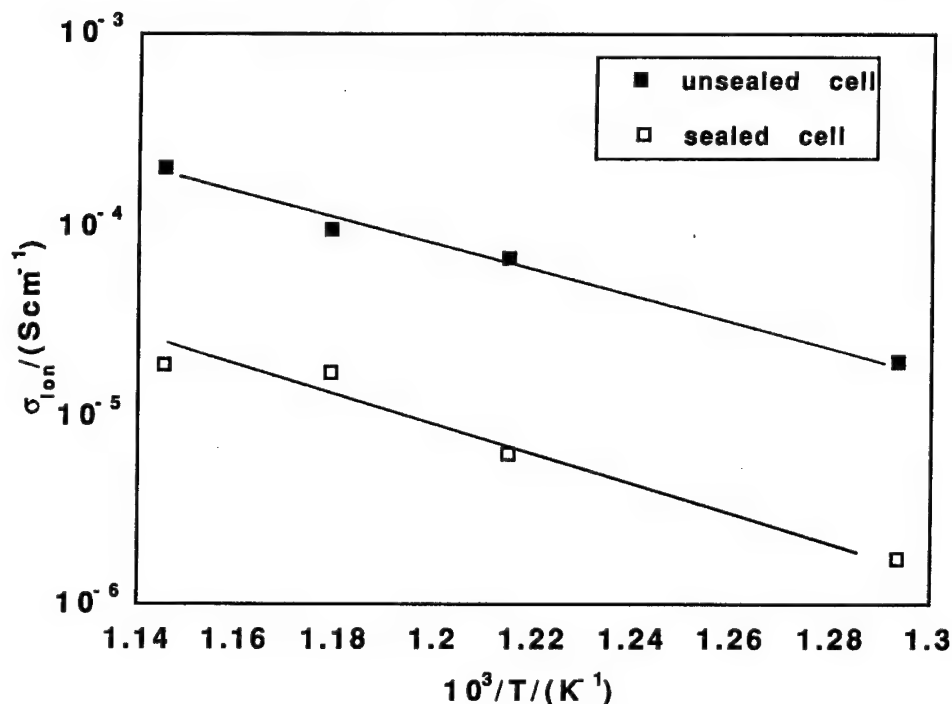


FIGURE 2 Ionic conductivity of  $\text{Bi}_2\text{Sr}_2\text{CaCu}_2\text{O}_{8+\delta}$ , unsealed cell (upper line) and glass-sealed cell (lower line).



and activity changes due to degeneracy effects and saturation phenomena may cause the same effect.

For the ionic conductivity of our carefully encapsulated  $\text{Bi}_2\text{Sr}_2\text{CaCu}_2\text{O}_{8+\delta}$  we found the values shown in Figure 2 activated with 1.33 eV resp. 1.25 eV. The values for the glass-sealed cell Pt,  $\text{O}_2/\text{YSZ}/\text{Bi}_2\text{Sr}_2\text{CaCu}_2\text{O}_{8+\delta}/\text{YSZ}/\text{Pt}$ ,  $\text{O}_2$  were found to be an order of magnitude lower than those for the unsealed cell. This is due to the interference of oxygen at the lateral parts of the sample. Chemical diffusion coefficients have been derived from electrochemical polarization shown in Figure 3. The anisotropy of the chemical diffusion coefficient in  $\text{Bi}_2\text{Sr}_2\text{CaCu}_2\text{O}_{8+\delta}$  is even larger than in  $\text{YBa}_2\text{Cu}_3\text{O}_{6+\delta}$ . The chemical oxygen diffusion parallel to the conduction plane is activated with 0.24 eV. In the perpendicular direction a value of 1.9 eV has been found, which is close to the value found in ref.<sup>9</sup> and confirmed by measurements on single crystals.<sup>7</sup>

It can be concluded that electrochemical experiments allow elegant measurements of ionic and electronic transport properties and far-reaching statements about the defect chemistry. The defect chemical situation turns out to be very similar to  $\text{YBa}_2\text{Cu}_3\text{O}_{6+\delta}$  and also, but to a lesser degree, to  $(\text{La}, \text{Sr})_2\text{CuO}_{4+\delta}$  where ionic-electronic interactions are not that distinct.

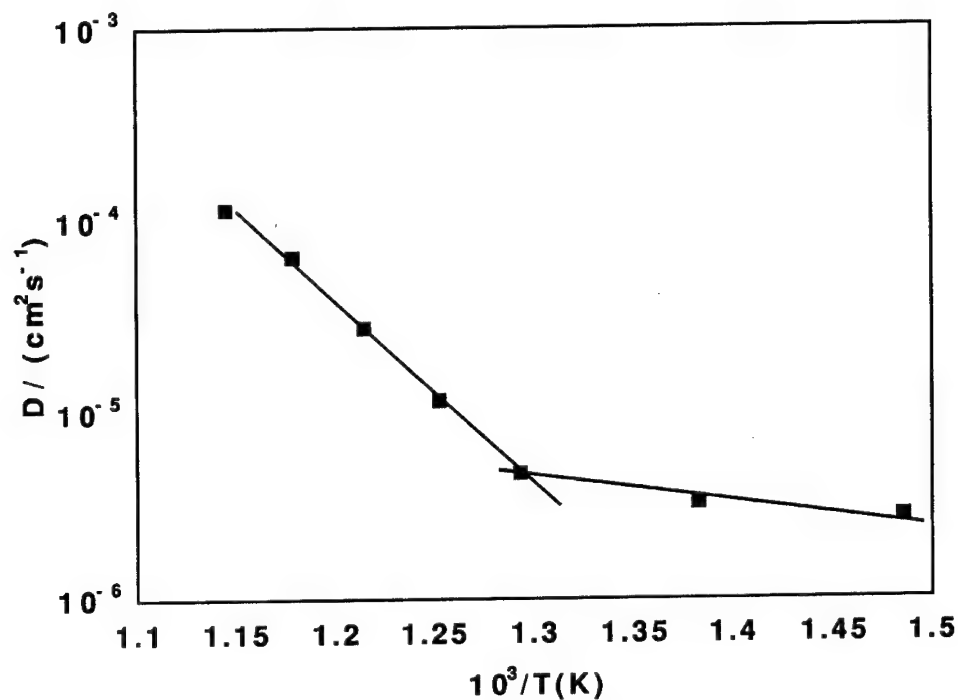


FIGURE 3 Chemical diffusion coefficients from electrochemical polarization.

#### REFERENCES

1. J. Maier, H. L. Tuller, *Phys. Rev.* **B47**, 13 (1993) 8105.
2. J. Maier, G. Pfundtner, *Adv. Mat.*, **30**, 6 (1991) 292.
3. J. Maier, P. Murugaraj, G. Pfundtner, W. Sitte, *Ber. Bunsenges. Phys. Chem.*, **93** (1989) 1350.
4. E. J. Opila, H. L. Tuller, B. J. Wuensch, J. Maier, *J. Am. Cer. Soc.*, **76** (9) (1993) 2363.
5. M. Quilitz, G. Pfundtner, J. Maier, *Proc. Int. Conf. Mat. Asp. of Superconductors*, Eds. J. Etourneau *et al.* (1993) 151.
6. P. Murugaraj, J. Maier, A. Rabenau, *Sol. St. Commun.*, **66** (1988) 735.
7. M. Quilitz, J. Maier, in preparation.
8. P. Majewski, H. L. Su, B. Hettich, *Adv. Mat.*, **4**, 7/8 (1992) 508.
9. M. Runde, J. L. Routbort, S. J. Rothman, K. C. Goretta, J. N. Mundy, X. Xu, J. E. Baker, *Phys. Rev.* **B45**, 13 (1992) 7375.

## LASER-HEATING AND PHONON MODES IN $\text{YBa}_2\text{Cu}_3\text{O}_x$

L. GASPAROV

*Institute of Solid State Physics, Russian Academy of Sciences, 142432, Chernogolovka,  
Moscow district, Russia*

The influence of temperature and pump power on phonon modes in  $\text{YBa}_2\text{Cu}_3\text{O}_x$  was investigated. The Raman spectra of the  $\text{YBa}_2\text{Cu}_3\text{O}_{6.4}$  single crystal measured after laser-heating (488 nm,  $P \leq 2.5 \text{ mWt}/\mu\text{m}^2$ ) show a decrease of linewidth and frequency of  $A_g$  apex oxygen mode. The experimental results can be explained as an ordering of chain-oxygen vacancies.

**Key words:** High temperature superconductors, Raman scattering, laser-heating, ordering.

### 1 INTRODUCTION

The oxygen content in  $\text{YBa}_2\text{Cu}_3\text{O}_x$  is very important for the superconductivity of these crystals. The increase of  $x$  from 6 to 7 transforms semiconductors into superconductors. The variation of  $x$  is mainly connected with the filling of the chain oxygen positions in the primitive cell.<sup>1</sup> While chain oxygens vibrations are Raman forbidden the  $A_g$  apex oxygen mode is very sensitive to a presence or absence of chain oxygens.<sup>2</sup> Therefore Raman Scattering can be a probe for investigation of the oxygen sublattice in  $\text{YBa}_2\text{Cu}_3\text{O}_x$ .

### 2 EXPERIMENTAL DETAILS

The experiments were carried out on single crystals of  $\text{YBa}_2\text{Cu}_3\text{O}_x$  ( $x = 6.9, 6.4$ ). All the crystals were grown by a flux method without further treatment.<sup>3</sup> Single crystals with  $x = 6.9$  and  $x = 6.4$  show the superconducting transitions at  $T_c = 90 \text{ K}$   $\Delta T_c = 1 \text{ K}$  and  $T_c = 40 \text{ K}$  with  $\Delta T_c = 10 \text{ K}$  respectively.

Oxygen concentration was estimated by the Raman shift of  $A_g$  apex oxygen mode. This line dominates in the  $zz$ -polarization spectra and its frequency very sensitive to the oxygen concentration.<sup>2</sup>

All the crystals had the shape of rectangular plates  $2 \times 2 \times 0.2 \text{ mm}$  in size with a specular basis plane. All experiments were carried out with freshly cleaved surfaces.

Raman spectra were obtained by using a 488 nm  $\text{Ar}^+$  laser line, a 'Microdila-28' spectrometer with a microscope and a 524-element intensified solid-state array detector system. High-temperature measurements were carried out by using 'Linkham TH 600' furnace.

The laser heating was produced by the radiation of  $\text{Ar}^+$  laser. The temperature at the moment of laser-heating does not exceed 550 K ( $\sim 2.5 \text{ mWt}/\mu\text{m}^2$ ) as it was calculated from the Stokes/antiStokes ratio. Such temperature from one hand does not destroy the sample surface and from the other hand it can affect the oxygen sublattice in  $\text{YBa}_2\text{Cu}_3\text{O}_x$ .<sup>4,5</sup>

A pump power at the laser-heating has been varied from 1 up to  $2.5 \text{ mWt}/\mu\text{m}^2$ . Raman measurements before and after laser-heating have been made with  $0.5 \text{ mWt}/\mu\text{m}^2$  pump power.

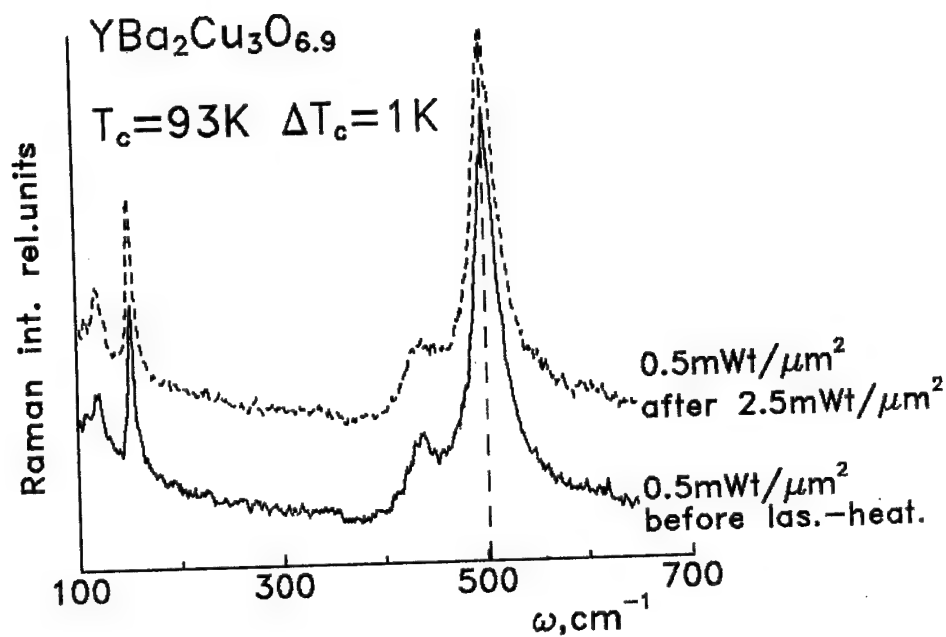


FIGURE 1 Raman spectra before (1) and after (2) laser-heating  $\sim 2.5 \text{ mWt}/\mu\text{m}^2$  in the YBa<sub>2</sub>Cu<sub>3</sub>O<sub>6.9</sub> single crystal.

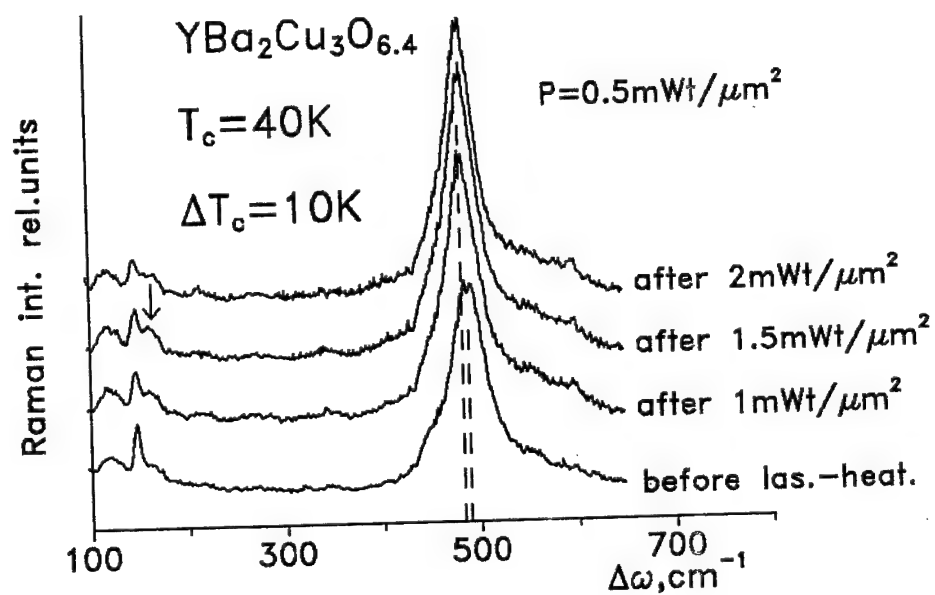


FIGURE 2 Raman spectra of the YBa<sub>2</sub>Cu<sub>3</sub>O<sub>6.4</sub> single crystal ( $P = 0.5 \text{ mWt}/\mu\text{m}^2$ ) measured after laser-heating with different pump power.

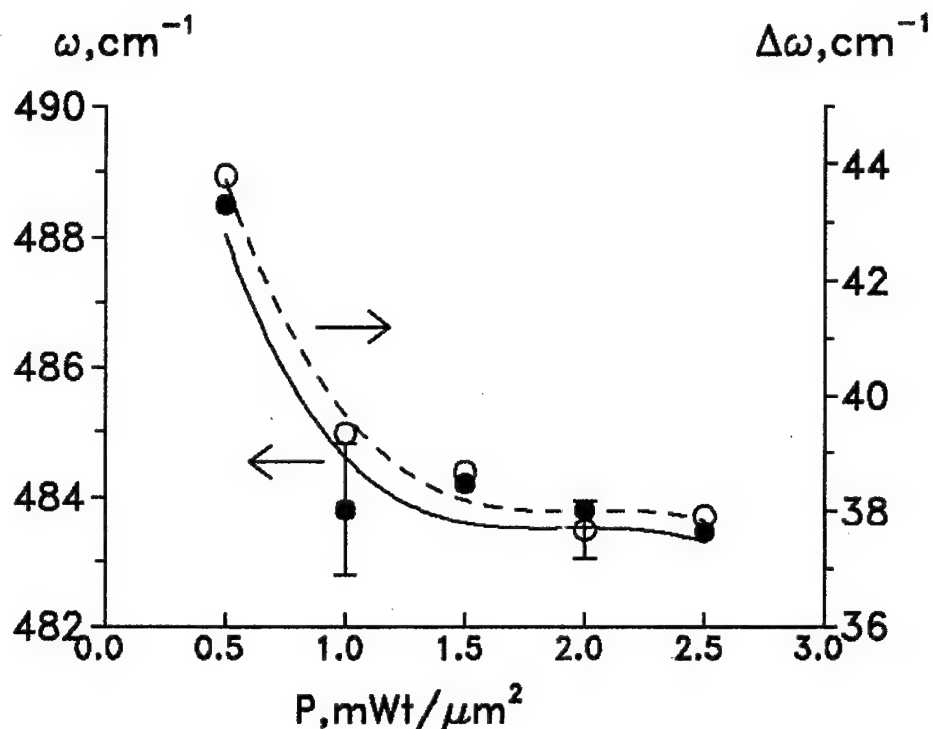


FIGURE 3 A dependence of linewidth (open circles) and frequency (filled circles) of  $A_g$  apex oxygen mode in spectra measured after laser-heating on the pump power at the laser-heating. Solid and dashed lines are only guide for eyes.

The Raman spectra for  $\text{YBa}_2\text{Cu}_3\text{O}_x$  crystals measured before and after laser-heating were compared.

### 3 RESULTS AND DISCUSSION

In the  $\text{YBa}_2\text{Cu}_3\text{O}_{6.9}$  single crystal no changes of the frequencies and linewidths of phonon modes were detected in spectra measured after laser-heating (Figure 1).

In the  $\text{YBa}_2\text{Cu}_3\text{O}_{6.4}$  single crystal a decrease of linewidth (full width on half maximum) and frequency of  $A_g$  apex oxygen mode were observed in spectra measured after laser-heating. In addition a new line has appeared in the region of  $\sim 160 \text{ cm}^{-1}$  (Figures 2, 3). The frequencies and linewidths of the lines were determined with the approximation of Lorentzian.

The experiment with the heating of the  $\text{YBa}_2\text{Cu}_3\text{O}_{6.4}$  single crystal in the furnace shows no changes of the frequencies and linewidths of phonon modes in spectra measured after heating (Figure 4). The temperature in the furnace was 550 K. This is the same temperature as it was at the laser-heating.

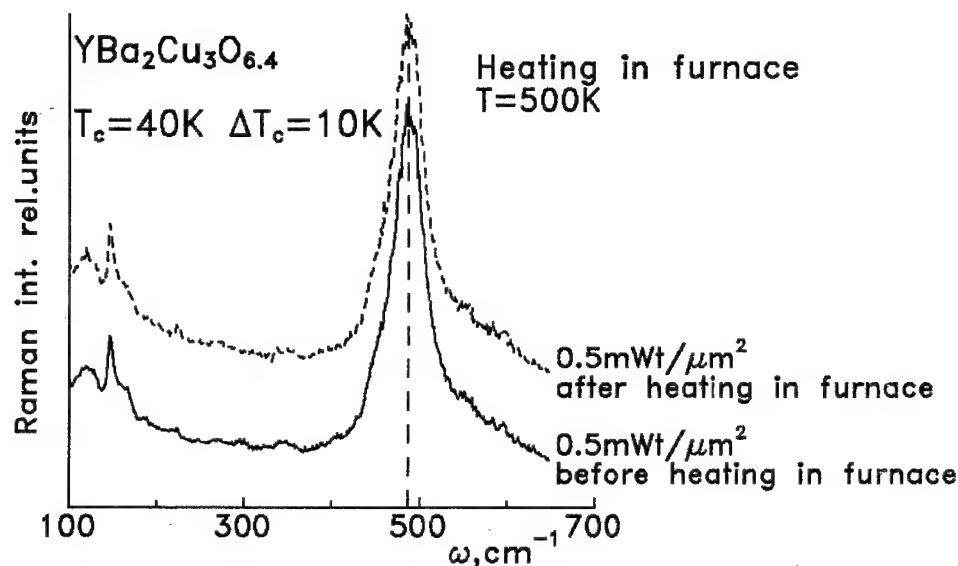


FIGURE 4 Raman spectra of the  $\text{YBa}_2\text{Cu}_3\text{O}_{6.4}$  single crystal measured before (solid line) and after (dashed line) heating in furnace ( $T = 550 \text{ K}$ ).

The laser-heating can differ from the heating in furnace only in small size of heating area (laser spot  $\sim 2 \mu\text{m}$ ). Therefore all changes in Raman spectra can be caused by the temperature gradients and hence by the stresses which is caused by the temperature gradients.

The  $x = 6.4$  single crystal has demonstrated a wide superconducting transition indicating a disorder in oxygen sublattice.<sup>1</sup> Hence the decrease of linewidth of the  $A_g$  apex oxygen mode can be explained by the ordering of the chain oxygen vacancies (the chain oxygens are easily affected in Y-Ba-Cu).<sup>6</sup> The decrease of frequency of  $A_g$  apex oxygen mode indicates a decrease of oxygen concentration in the excited volume because the frequency of this mode goes down with decrease of the oxygen concentration.<sup>2</sup> The appearance of new line ( $\sim 10 \text{ cm}^{-1}$ ) indicates an appearance of the new ordered phase. Therefore all this changes can be explained by ordering of chain oxygen vacancies possibly forming  $x = 6.35$  phase.<sup>7</sup>

#### REFERENCES

1. J. D. Jorgensen *et al.*, *Phys. Rev.*, Vol. **B36**, 1987, p. 3608.
2. R. M. Macfarlane, H. J. Rosen, E. M. Engler, R. D. Jacowitz, V. Y. Lee, *Phys. Rev.* **B38**, 284 (1987).

3. L. V. Gasparov, G. A. Emel'chenko, V. D. Kulakovskii, O. V. Misochko, V. B. Timofeev, E. I. Rashba, *J. Opt. Soc. Am.* **B6** 440 (1989).
4. K. F. McCarty, J. C. Hamilton, R. N. Shelton, D. S. Ginley, *Phys. Rev.* **B38**, 2914 (1988).
5. L. V. Gasparov, V. D. Kulakovskii, V. B. Timofeev, E. Ya. Sherman. *Sov. Phys. JETP* **73**, 929 (1991).
6. R. J. Cava, A. W. Hewat, E. A. Hewat, B. Batlogg, M. Marezio, K. M. Rabe, J. J. Krajewski, W. F. Peck Jr., L. W. Rupp Jr., *Physica* Vol. **C165**, 1990, p. 419.
7. R. Sountag, D. Hohlwein, T. Brückel, G. Collin, *Phys. Rev. Lett* **66**, 1497 (1991).

## THE $\text{YBa}_2\text{Cu}_3\text{O}_z$ PHASE DIAGRAM

C. PICARD,<sup>a</sup> P. GERDANIAN,<sup>a</sup> A. H. MOUDDEN<sup>b</sup> and M. G. BLANCHIN<sup>c</sup>

<sup>a</sup>Laboratoire des Composés Non-Stoechiométriques (URA CNRS 446), Bât.415, Université Paris Sud, 91405 Orsay Cédex, France; <sup>b</sup>Laboratoire Léon Brillouin, CE-Saclay, 91191 Gif sur Yvette Cédex, France; <sup>c</sup>Département de Physique des Matériaux (URA CNRS 172), Université Claude Bernard, 69622 Villeurbanne Cédex, France

Determinations of the T-O and OI-OII phase boundaries by electrical transport property measurements are reported. These results are coherent with those of a preliminary neutron diffraction experiment and an electron diffraction study.

**Key words:** YBC—Phase diagram—Oxygen ordering—Electrical transport—Neutron diffraction—Electron diffraction.

Many studies have been devoted to the theoretical determination of the T-z phase diagram of  $\text{YBa}_2\text{Cu}_3\text{O}_z$ <sup>1</sup> which shows three phases important to super-conductivity: the high temperature orthorhombic (OI) and tetragonal (T) phases and the low-temperature double-cell orthorhombic phase (OII). The large amount of theoretical results contrasts markedly with the lack of experimental measurements which were limited until recently to the determination of the T-O phase boundary in a temperature range between 800 and 1000 K.

We report, here, on indirect determination of the T-O and OI-OII phase boundaries obtained from electrical transport property measurements.

The samples are thin sheets consisting of 0.1 mm thick, dense, large-grained oxide with mean grain-size  $\approx 15 \mu\text{m}$  and  $d/d_h \approx 0.90$ ; they are prepared by sintering a Rhône-Poulenc precursor.<sup>2,3</sup>

Measurements were carried out at constant composition z by means of an experimental device previously described.<sup>2</sup>

The T-O phase boundary was determined from the T-variation of the electrical resistance, R, at constant oxygen composition, z. In Figure 1, a typical  $(\partial \ln R / \partial T)_z$  (T)-curve is shown. A kink is observed which corresponds to the T-O phase transition. Indeed, it is well known that R is coupled to the order-disorder phenomenon which occurs at the T-O transition and a singularity is expected for  $R(T)_z$  at this point. Our results are reported in Figure 2. For  $T \geq 750 \text{ K}$ , the T-O phase boundary was determined by the isobar method already used by previous authors.<sup>4</sup>

For  $z \geq 6.40$ ,  $\ln R(T)_z$  presents only one singularity at the T-O transition, contrary to the Seebeck coefficient,  $S(T)_z$ , which exhibits a second kink at lower temperature, see Figure 1. This second kink likely corresponds to a phase transition. Plotting the temperature of this second kink,  $T_i$ , versus composition may help to identify this unknown phase transition. This  $T_i(z)$ -curve is reminiscent of the calculated T-z phase diagrams<sup>5</sup> which suggests that the  $T_i(z)$ -curve is likely to be the OI-OII phase boundary.

In order to confirm this conjecture, we carried out neutron scattering experiments on the g43 triple axis spectrometer at Saclay's Orphee reactor. Since the order parameter of the O-T phase transition, described by the difference in the probability of the x and y site occupancies of the oxygen in the deficient layer, can only be reached in detailed studies of the structure, we chose to follow the O-T transition through the evolution of the orthorhombicity  $(a-b)/(a+b)$  which is evident in the evolution of the lineshape of particular reflections. To achieve a good momentum transfer resolution, we used a small incident neutron energy (4.5 meV) selected from the cold source with a (2 0 0) PG



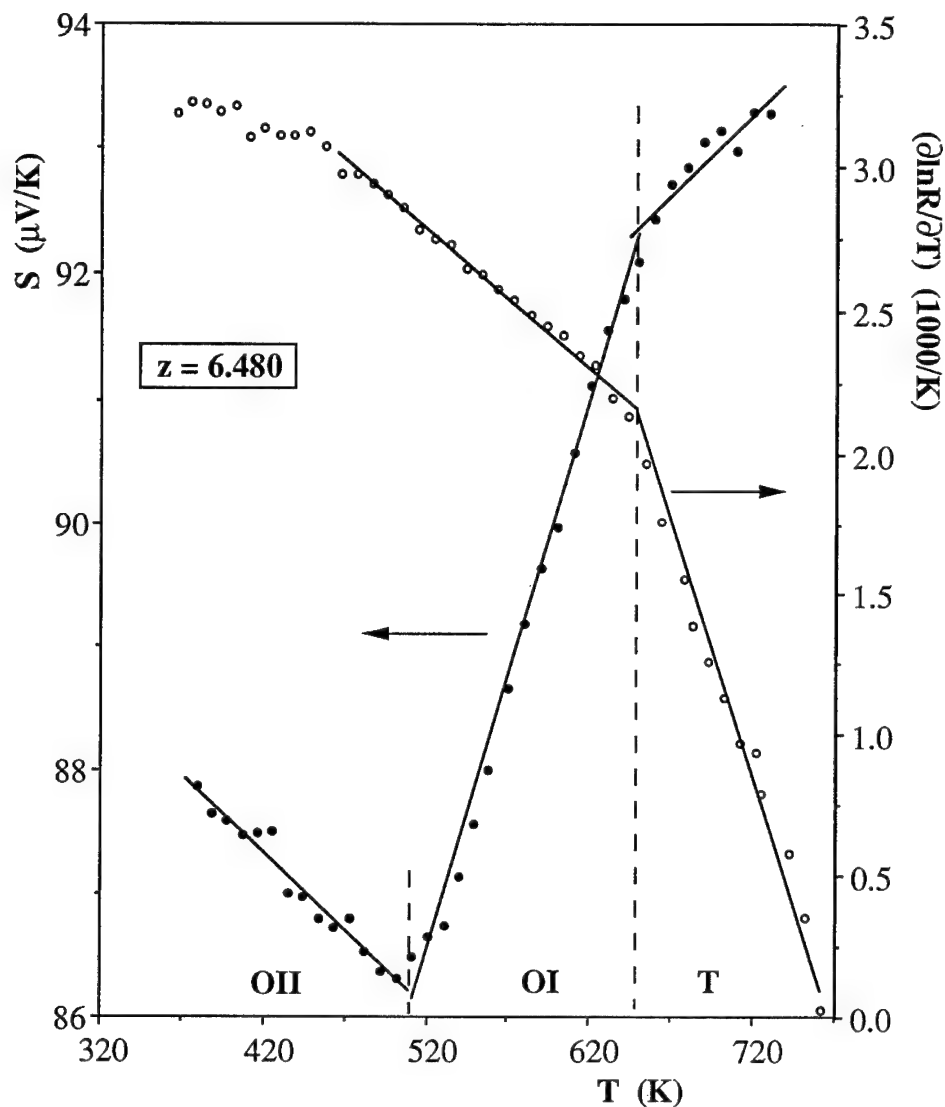


FIGURE 1  $S$  and  $(\partial \ln R / \partial T)$  versus  $T$  at constant composition  $z = 6.48$ . The lines are guides for the eye.

monochromator, 30 min collimations, (2 0 0) PG analyzer and an appropriate filter, to remove higher order contaminations, were used. The sample, about 15 g, is a porous fine-grained oxide,  $d/d_{th} \approx 0.70$ , mean-grain size  $\approx 2 \mu\text{m}$ , prepared from the previous Rhône-Poulenc precursor and in the shape of  $25 \times 10 \times 1 \text{ mm}^3$  sheets. The measurements were effected on increasing and decreasing temperature at constant composition  $z$ .

We present the results obtained for  $z = 6.48$ . We studied the temperature evolution of the Bragg angle scan across the reciprocal lattice points (0 0 1), (1 0 0), (1 0 3) and (1 1 0).

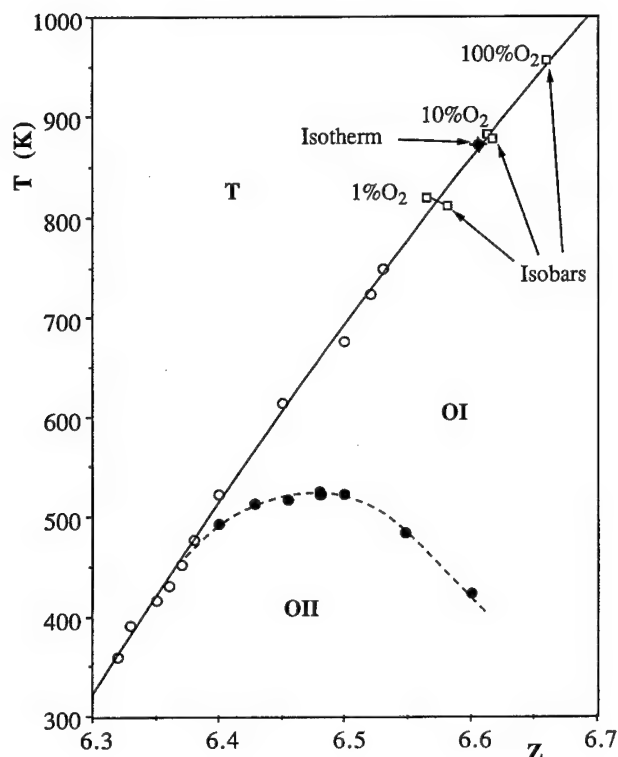


FIGURE 2  $T(z)$ —diagram from our electrical transport measurements. o,  $\square$ ,  $\blacklozenge$ : T-O limit;  $\bullet$ :  $T_I$  vs  $z$ . The curves are guides for the eye.

The data points were analysed using gaussian lineshapes represented by the solid curve in Figure 3 for (1 0 3) and (1 1 0) reflections. The results clearly show that while the profile of the (1 1 0) reflection remains unchanged, the half width of the half maximum of the (1 0 3) reflection, reported in Figure 4, decreases continuously as the temperature approaches 620 K above which it remains constant as determined by the instrumental resolution. We conclude that the orthorhombic to tetragonal phase transition occurs at about 630 K, in good agreement with electrical transport results.

When we examine carefully the variation of this (1 0 3) HWHM between 290 and 630 K, we can clearly distinguish two regions of slow, below 480 K and rapid variation between 480 and 630 K. Such a result is also obtained with (1 0 0) HWHM. We observe that this qualitative difference in the change rate of the orthorhombicity coincides with a slight change of the thermal expansion of the  $c$  lattice parameter. It also coincides with the temperature at which an anomaly appears in the electrical thermopower as described above. We believe that a phase transition from an orthorhombic to another orthorhombic phase takes place at about 480 K for this composition  $z = 6.48$ . We failed to see any evidence for superlattice peaks of the kind  $(1/2, k, 1)$  characteristic of an orthorhombic II phase. We think that other types of chain ordering are possible; thus further investigations are needed.

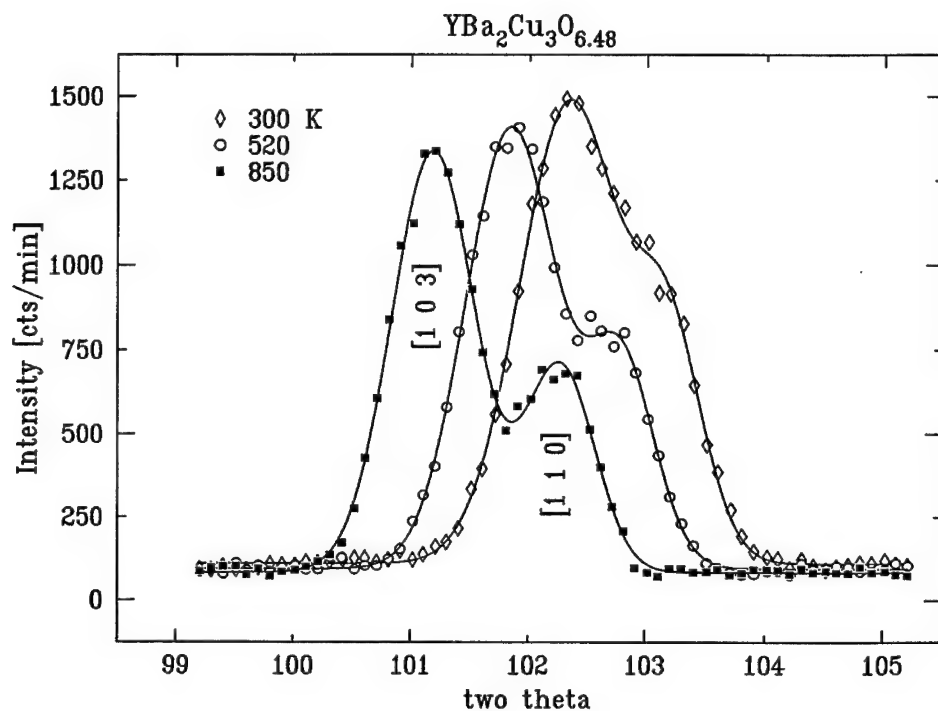


FIGURE 3 Bragg angle scan across the reciprocal lattice points (1 0 3) and (1 1 0) at three temperatures for  $z = 6.48$ . Solid curves are obtained by using gaussian lineshapes.

Moreover, electron diffraction studies using a transmission electron microscope operated at 200 kV were achieved on the dense samples prepared at room temperature in equilibrium with respect to the chain-plane oxygen rearrangement.<sup>3</sup> Illumination has been kept as low as possible and very short exposure times according to our previous results have been chosen in order to avoid any irradiation damage of our specimens. Several diffraction patterns have thus been obtained under these conditions from different flakes of the same specimen having a given composition  $z$  in the range  $7 \geq z \geq 6.3$ . Such patterns obtained along the [001] or the [010] axis enable one to identify the OI, OII or other structures, as reported previously.<sup>6</sup>

Series of diffraction experiments both at room temperature or below room temperature have led to the same conclusion that in such specimens, only two phases (as defined by thermodynamics) can be clearly identified, which correspond to the OI and OII structures respectively. The OI phase is stable in the composition range  $z \geq 6.9$  corresponding to the first plateau of  $T_c$ . The second plateau around the composition  $z = 6.55$  corresponds to the existence of OII as a single phase. In the intermediate regions i.e. for compositions  $6.5 < z < 6.8$  and  $6.3 < z < 6.5$ , all the superstructures experimentally observed are consistent with existence of more or less short-range ordered domains of OII phase consisting of rather long Cu-O chains: the order within the chains and their preferred orientation along the  $b$  direction are maintained so that the orthorhombicity is kept, as

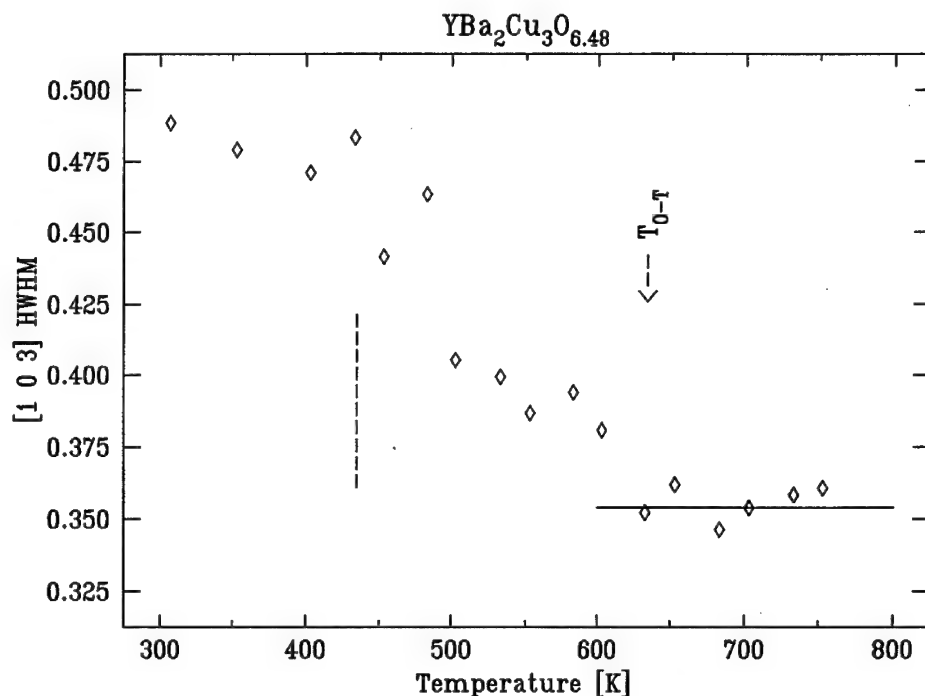


FIGURE 4 The half width of the half maximum (HWHM) of the (1 0 3) reflection versus temperature.

revealed by twinning. Diffraction patterns suggest that the  $z = 6.7$  compounds contain genuine OII phase consisting of small domains twinned at a fine scale. For compositions  $z = 6.8$ , the OI phase appears to be very disordered with respect to the periodic alternance of the Cu-O chains in the chain planes, and nuclei of incipient OII order are formed locally. On the other hand, short-range domains of the OII phase are found in the region of low values of  $T_c$  and  $z$ , whereas the tetragonal phase is obviously stable for  $z \leq 6.3$ . To date, the diffraction patterns in the present work do not provide any clear evidence for existence of any OIII phase at room temperature.

#### REFERENCES

1. See, e.g., D. de Fontaine, L. T. Wille and S. C. Moss, *Phys. Rev.*, **B36**, 5709 (1987).
2. P. Gerdanian, C. Picard and B. Touzelin, *Physica C***182**, 11 (1991).
3. C. Picard and P. Gerdanian, *Physica*, **196**, 11 (1991).
4. See, e.g., A. T. Fiory, M. Gurvitch, R. J. Cava and G. P. Espinosa, *Phys. Rev.*, **B36**, 7262 (1987).
5. E. Salomons, D. de Fontaine, *Phys. Rev.*, **B42**, 10152 (1990).
6. Y. Yan, M. G. Blanchin, C. Picard and P. Gerdanian, *J. Mat. Chem.*, **3**, 603 (1993).

## DENSITY OF ELECTRON STATES NEAR SURFACES OF LAYERED COPPER OXIDES

S. A. PROSANDEYEV and I. M. TENNENBOUM

*Department of Physics, Rostov State University, 5 Ul. Zorge, Rostov on Don 344104,  
Russia*

The electron structure of the semi infinite  $\text{CuO}_2$  layer has been calculated to understand peculiarities of the layered oxides surfaces. All computations have been performed by means of the Green function method along with the simple tight-binding model. Fourier transforms of the Green functions were derived analytically. The potential at the atoms nearest to the boundary was directed to infinity. This formal maneuver led to dividing the ideal  $\text{CuO}_2$  layer into two semi infinite layers. The density of states near the surface has been obtained by integrating the imaginary part of the diagonal element of the Green function over the wave vector. It has been shown that the charge on the surface Cu atoms is greater than on the bulk one. Changes of the density of states via the energy and the distance from the surface have been obtained.

*Key words:* surface; superconductors; the Green function method; electron states.

Layered copper oxides are known to have the property of high temperature superconductivity. By virtue of this fact, they attract much attention. There are many indications of the surface, intergranular and interface influence on properties of copper oxides. That is why the problem of the adequate description of the surface is of great importance. In this work we give the results of the electron band structure calculations for the surface of copper oxides. Computations have been carried out by the Green function method.

All the layered copper oxides have the  $\text{CuO}_2$  plane which is believed to be the decisive element for the existence of the high temperature superconductivity. To understand the electronic structure of the copper oxide surface we have investigated the band structure of the semi infinite  $\text{CuO}_2$  layer. The edge of this layer was formed of the Cu and O atoms lying along the (100) direction (see the Figure 1). The layer was divided into columns parallel to the edge, and each column was broken down into cells. One unit cell included one Cu atom and two O atoms.

The partial density of states on the  $i$ -th atom of the  $n$ -th column can be calculated using the expression

$$N_{ni} = -\pi^{-1} \lambda \text{Im} \int G_{ni}(k_x, \epsilon) dk_x \quad (1)$$

where  $\lambda = a/2\pi$ ,  $a$  is the lattice parameter,  $G_{ni} \equiv G_{ni,ni}$  is the diagonal element of the Green function which can be obtained from the Dyson equation

$$G = g + g V G \quad (2)$$

Here  $V$  is the perturbation potential,  $g$  is the Green function of the ideal  $\text{CuO}_2$  layer.

To make the semi infinite layer from the infinite one we supposed the potential at the boundary oxygen atoms to go to infinity. This formal maneuver has been already used in the investigation of the atomic vacancy in Si.<sup>1</sup> Indeed, the infinite potential at an atomic site means that all the electronic states of this site are eliminated from the basis. Thus, we can think that there is no an atom in this site at all. In the case under consideration, the formation of the column of the oxygen vacancies in the  $\text{CuO}_2$  layer leads to the breaking of

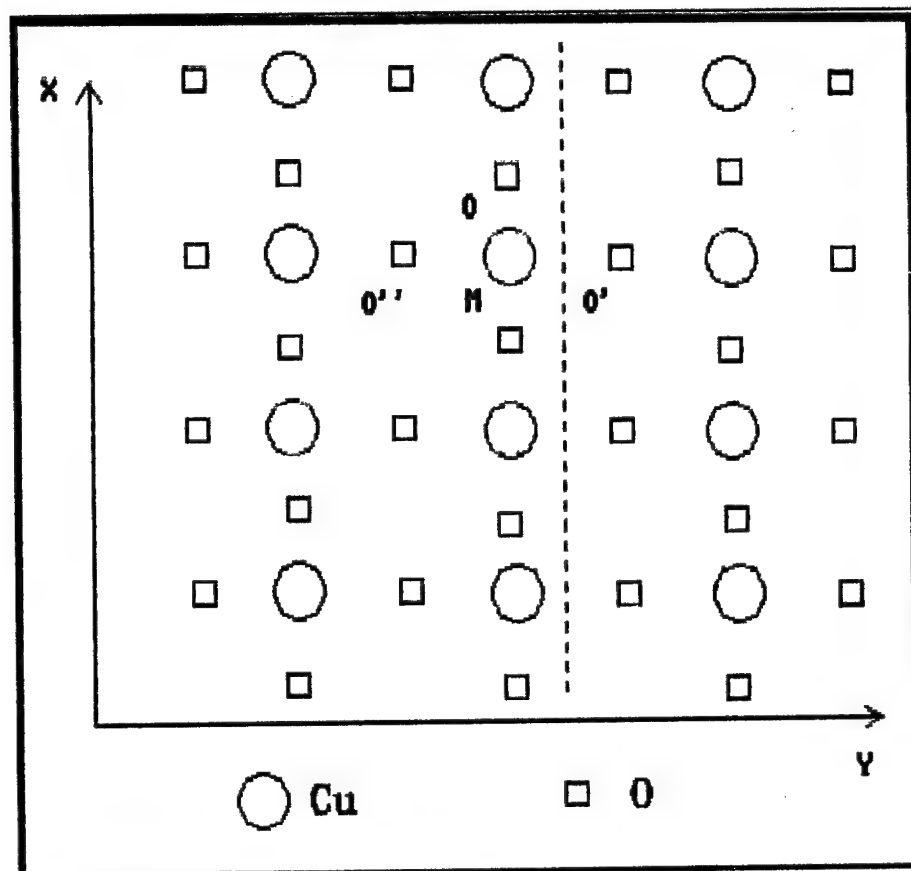


FIGURE 1 The  $\text{CuO}_2$  layer. The dashed line indicates the boundary of the semi infinite  $\text{CuO}_2$  layer.

the Cu-O bonds along the chain and, as the consequence, to partitioning the  $\text{CuO}_2$  layer into two semi infinite layers.

To obtain the Green function  $g$  we have employed the simple tight-binding model with only inclusion the nearest neighbors interactions. In this case, it is easy to obtain the analytical expressions for  $g$ . Methods for deriving such integrals have been already illustrated by us in.<sup>2,3</sup>

The density of states for the bulk Cu atoms is shown in the Figure 2. We used the value of the hopping integral between nearest Cu and O sites  $t = -1.85$  eV and supposed the energies of the Cu and O levels to be equal. One can see that at  $\varepsilon = 3.7$  eV the density of states has a singularity. It is known that in the superconductive phase the Fermi energy lies anywhere near this singularity.

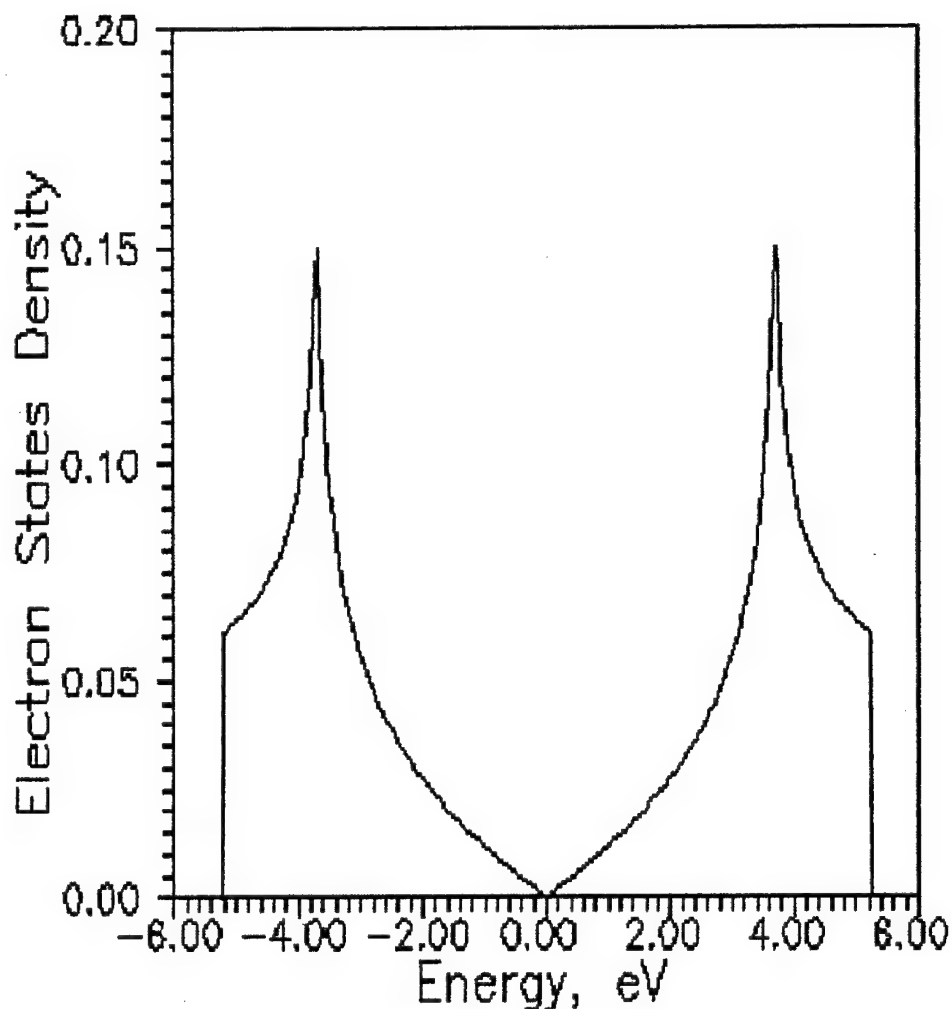


FIGURE 2 The density of the bulk Cu states.

The change of the density of states near the surface Cu columns is shown in the Figure 3. As can be seen, this change has the negative sign above the Fermi energy. Thus the charge on the surface Cu columns is greater than on the bulk one. On the next columns the charge turn to the value of a bulk Cu column.

The breaking of the chemical bonds at the surface and difference in the charge could lead to the antiferromagnetic ordering of spins and, as the consequence, to the dielectrization of the surface layer. We are going to consider this possibility in the separate paper.

This work was supported by the National Scientific Program on HTSC within the project N 92068.

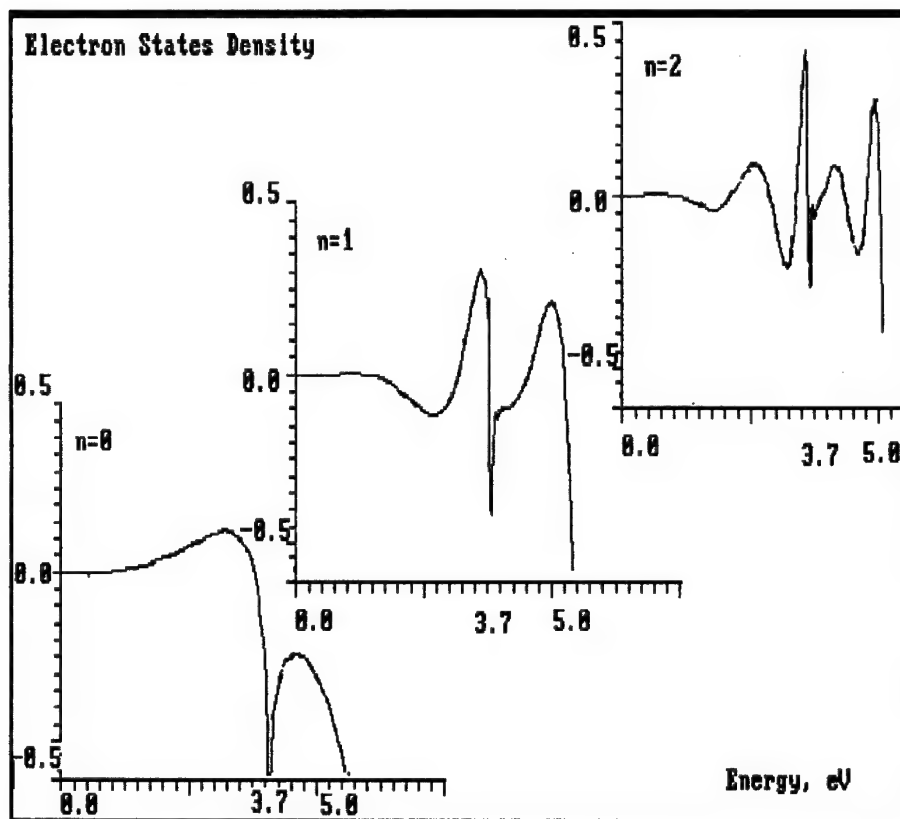


FIGURE 3 The change of the Cu electron states density at the first ( $n = 0$ ), second ( $n = 1$ ) and third ( $n = 2$ ) columns near the boundary of the CuO<sub>2</sub> semi infinite layer.

#### REFERENCES

1. J. Bernholc and S. T. Pantelides, *Phys. Rev.* **18**, 1780 (1978).
2. S. A. Prosandeev and N. M. Teslenko, *Phys. Stat. Sol. (8)* **177**, 165 (1993).
3. S. A. Prosandeev and I. M. Tennenboum, *Phys. Stat. Sol (8)* **183**, 513 (1994).



## INCREASING OF $T_c$ IN THE NEW HTSC $\text{HgBa}_2\text{CuO}_{4+\delta}$ PROMOTED BY DEFECTS

YU. N. MYASOEDOV, R. V. LUTCIV, I. V. KITKY, V. N. DAVYDOV,  
YA. V. BOYKO

*Dept. of Physics Lviv State University, Lviv, UA-290005, Ukraine*

X-ray powder diffraction of the new high- $T_c$  superconducting phase  $(\text{Hg}_{1-x}\text{Cu}_x)\text{Ba}_2\text{CuO}_{4+\delta}$ , where  $x = 0.17$  with the onset superconducting transition at 125 K was used to define coordinates, isotropic thermal parameters of the atoms and for interatomic distances calculation. For the first time in the Hg-based cuprate superconductors was observed the occurrence of the optical second harmonic generation (SHG) of YAG-Nd laser, which gives evidence for the appearance the asymmetric electronic density, correlated with an increase of superconducting transition temperature. It is assumed that the increase of  $T_c$  associated with the formation of two  $(\text{CuO}_2)$  layers in the average unit cell at the substitution of the part atoms Cu for Hg and the partial occupancy of the  $(1/2\ 0\ 0)$  sites by oxygen atoms.

**Key words:** Superconductor, substitution, second harmonic generation, magnetic susceptibility.

### 1 INTRODUCTION

The structure Hg-1201 with one  $\text{CuO}_2$  layer per lattice unit cell<sup>1</sup> is similar to the Tl-1201 with  $T_c < 10$  K, but the phase transition temperature is greater (84–96 K). Smaller spacing between  $\text{CuO}_2$  planes in the Hg-1201 could lead to better superconducting properties. In the  $\text{HgBa}_2\text{CuO}_{4+\delta}$  superconductor one could consider two types of defects. First one is caused by oxygen presence in  $(1/2\ 1/2\ 0)$  site. The second is connected with partial substitution of Hg by Cu atoms.

### 2 SYNTHESIS AND X-RAY ANALYSIS

Samples of nominal composition  $\text{HgBa}_2\text{CuO}_{4+\delta}$  were prepared by solid-state reaction at 800°C, 5 h from stoichiometric powders of HgO (99% purity), BaO (97%) and CuO (99%). After the annealing in flowing  $\text{O}_2$  at 350°C material was identified by X-ray method. For defects creation and additional doping by oxygen, samples were reannealing at 600°C for 2.5 h in a flow of oxygen. While heating from 435 to 600°C sample mass decreases at 12% as the result of losing Hg.

All structure calculations were performed using complex programmes CSD.<sup>2</sup> Starting model for  $\text{HgBa}_2\text{CuO}_{4+\delta}$  was chosen according to<sup>1</sup> (space group  $P4/mmm$ ). Thermal parameters and sites occupations differ from the model  $\text{HgBa}_2\text{CuO}_{4+\delta}$ .<sup>1</sup> Structural parameters of superconducting phase with content by X-ray method as  $(\text{Hg}_{0.89}\text{Cu}_{0.11})\text{Ba}_2\text{CuO}_{4+\delta}$  (annealing at 350°C) and  $(\text{Hg}_{0.83}\text{Cu}_{0.17})\text{Ba}_2\text{CuO}_{4+\delta}$  (reannealing at 600°C) shown in the Table I. Lattice parameters, refined using full profile data for these phases are:  $a = b = 3.87457(4)\text{Å}$ ,  $c = 9.5148(1)$  ( $\rho = 6.8533(2)\text{ g/cm}^3$ ,  $R_{\text{in}} = 4.65\%$ ,  $R_{\text{pr}} = 10.16\%$ ) and  $a = b = 3.8760(2)\text{Å}$ ,  $c = 9.5189(9)\text{Å}$  ( $\rho = 7.0003(2)\text{ g/cm}^3$ ,  $R_{\text{in}} = 9.5\%$ ,  $R_{\text{pr}} = 13.94\%$ ), respectively.

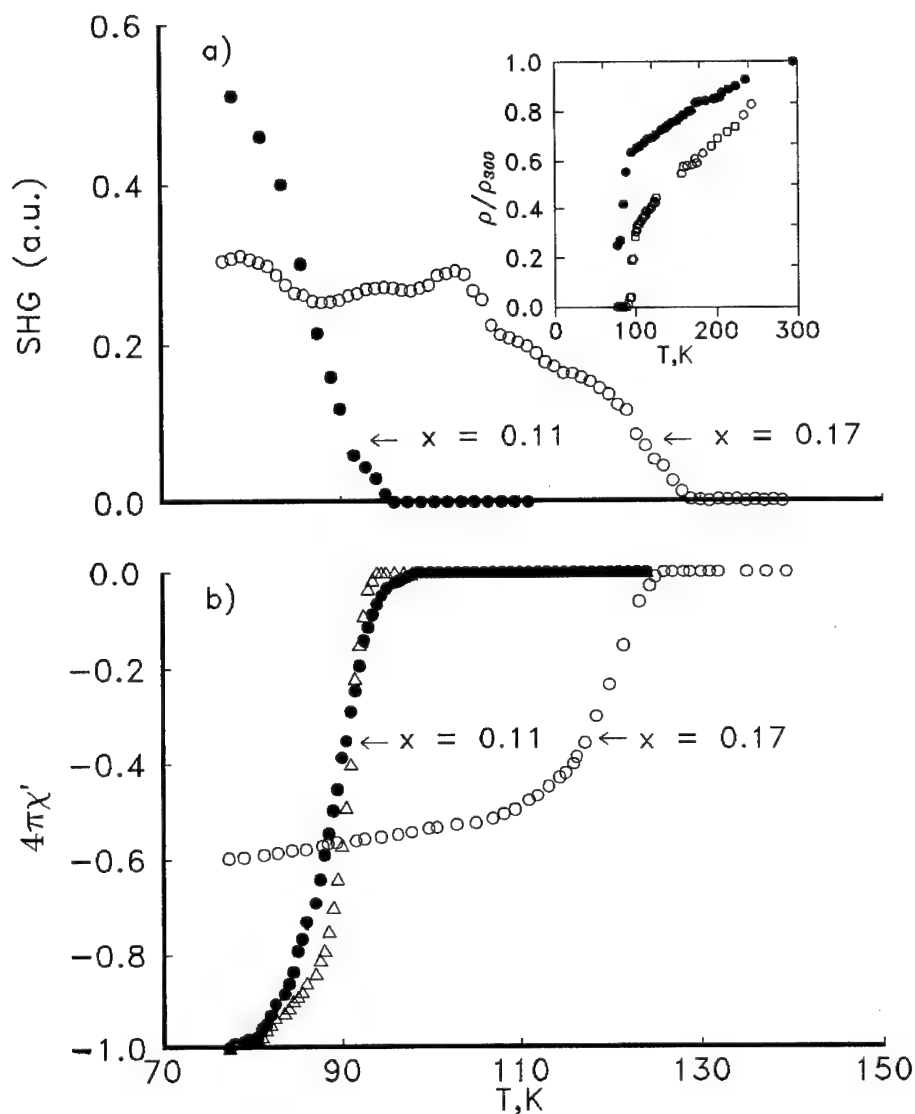


FIGURE 1 Temperature dependence SHG (a) and AC- magnetic susceptibilities (b) for Hg-1201:Δ-after the syntheses, ●-after the annealing in flowing  $O_2$  at 350°C (8h). ○-after the reannealing in flowing  $O_2$  at 600°C (2h).

### 3 SECOND HARMONIC GENERATION

In Figure 1 a, b are depicted the temperature dependences of second harmonic generation and magnetic susceptibility respectively for the different kinds of  $(Hg_{1-x}Cu_x)Ba_2CuO_{4+\delta}$  superconductors. It is necessary to account that the beginning of the SHG is shifted

towards the resistivity or magnetical susceptibility behaviors from 8 to 12 K in the high temperature region. This indicates that the SHG 'feels' the approach of the superconducting transitions, or shows the presence of the asymmetric modulation. Comparing the temperature dependences of the magnetic susceptibilities and resistivity one can see the very similar behavior.

TABLE I  
Coordinates of atoms in the  $(\text{Hg}_{1-x}\text{Cu}_x)\text{Ba}_2\text{CuO}_{4+\delta}$ .

ATOM ( $x = 0.11$ )	N	x/a	y/b	z/c ( $x = 0.17$ )	N	x/a	y/b	z/c
Hg	1*	0	0	0	1**	0	0	0
Ba	2	1/2	1/2	0.2966(1)	2	1/2	1/2	0.2937(6)
Cu	1	0	0	1/2	1	0	0	1/2
O(1)	2	1/2	0	1/2	2**	1/2	0	1/2
O(2)	2	0	0	0.209(1)	2	0	0	0.220(8)
O(3)	1*	1/2	1/2	0	2**	1/2	0	0

Sites occupations \* Hg: 0.89(1)Hg+0.11(1)Cu; 0(3): 0.12(4)0

\*\*Hg: 0.83(1)Hg+0.17(1)Cu; 0(1): 0.78(9)0; 0(3): 0.24(9)0

Interatomic distances \*Hg-O(3): 2.740 Å, \*\*Hg-O(3): 1.9376 Å

#### 4 DISCUSSION

The refine structure of the  $(\text{Hg}_{1-x}\text{Cu}_x)\text{Ba}_2\text{CuO}_{4+\delta}$  ( $x = 0.17$ ) is differed from model<sup>1</sup> and the compound with  $x = 0.11$ . Here large part of atoms Hg are substituted by atoms Cu. This leads to introduction of additional oxygen into Hg-plane in (1/2 0 0) position and to increase of the average oxidation degree of copper and as a result holes concentration becomes enough for the appearance of the superconductivity. As a results, Hg- plane become partially like a Cu- plane and quasi-two-layer structure is formed. We suppose that the asymmetric modulation is caused by the super conducting pairing which according to<sup>3</sup> appears nearby the Van Hove singularities splitted due to the band Jahn-Teller cooperative effect. The former is closely related with the occurrence of the phonon anharmonicity. If in the case of  $\text{YBa}_2\text{Cu}_3\text{O}_{6+\delta}$  the super structure modulation can be caused by the defective oxygen planes, in the case of  $(\text{Hg}_{1-x}\text{Cu}_x)\text{-1201}$  (with  $T_c = 96\text{--}125$  K) coordination of the another cations depends on the oxygen parameters  $\delta$ . Besides it can be caused by the another kinds of the defects, for example by the substitution of the Hg by Cu or by the Hg vacancies.

#### ACKNOWLEDGEMENTS

We thank the support of the SKNT Ukraine (Project 'Mercury').

#### REFERENCES

1. S. N. Putilin, E. V. Antipov, O. Chmaissem and M. Marezio. *Nature* (London) 362 (1993) 226.
2. Akselrud L. G., et al. *Abstr. on Twelfth European Crystal. Meeting Coll. V.3* (1985) 155.
3. R. S. Markiewicz, *J. Phys. Chem. Solids*. **52** N11/12 (1991) 1363.

## LARGE LOCAL DISTORTIONS INTRODUCED BY DEFECTS IN $\text{YBa}_2\text{Cu}_3\text{O}_7$ SUPERCONDUCTORS: AN X-RAY-ABSORPTION STUDY

FRANK BRIDGES,<sup>1</sup> G. G. LI,<sup>1</sup> C. H. BOOTH,<sup>1</sup> J. B. BOYCE<sup>2</sup> and T. CLAESON<sup>3</sup>

<sup>1</sup>Physics Department, University of California, Santa Cruz, CA 95064; <sup>2</sup>Xerox Palo Alto Research Center, Palo Alto, CA 94304; <sup>3</sup>Physics Department, Chalmers University of Technology, S-41296 Gothenburg, Sweden

Substituting metallic or rare-earth atoms or removing O in the superconductor  $\text{YBa}_2\text{Cu}_3\text{O}_7$  usually has a strong effect on the superconducting properties. We have made extensive XAFS studies on Co, Fe, Ni, Zn, Gd, and Pr substituted materials including some thin film samples. In nearly all cases, significant distortions are found. Although the lattice constant change is small ( $< 0.05 \text{ \AA}$ ) the local distortions can be significant larger ( $\sim 0.1$  to  $0.3 \text{ \AA}$ ). The observed large local distortions of the lattice together with a change in the charge distribution at a site indicate that the interior of the unit cell is easily distorted. The correlation of a strong  $T_c$  suppression with large local distortions suggests that distortions of the nearby layers must play a significant role in models for superconductivity in high  $T_c$  materials.

**Key words:** local structure, superconductivity, XAFS,  $\text{YBa}_2\text{Cu}_3\text{O}_7$

Since the discovery of high  $T_c$  materials there has been a tremendous effort to understand why these materials are superconducting. A large number of models have been considered—extending the standard phonon coupling model, polarization models, 2-D models that consider only the  $\text{CuO}_2$  planes and ignore other parts of the unit cell, the RVB model etc. However no obvious candidate has emerged, and constraints on the theory imposed by experimental results are clearly needed.

The substitution of other metal atoms for the constituent elements in high-temperature superconductors, such as  $\text{YBa}_2\text{Cu}_3\text{O}_7$ , is an important means of probing the parameters essential to superconductivity. Substitutions of Co, Fe, Ni, and Zn for some of the Cu in YBCO suppress  $T_c$  significantly at relatively low concentrations ( $\sim 5\%$ ). On the other hand, replacing Y with rare-earth elements or Ba with alkaline earths usually does not affect  $T_c$  very much (with some exceptions, for example, Pr). The local structures about the impurity atoms must be known before these effects can be fully understood. In this paper we summarize the results of our X-ray Absorption Fine Structure (XAFS) [1,2] investigations of the local structure in substituted YBCO [3–7], with an eye towards determining whether local structure should place constraints on models for superconductivity.

The XAFS technique [1,2] utilizes the interference effect of the incoming and outgoing photoelectron waves near the absorbing atoms excited by incident x-rays. Thus XAFS contains information about the distances to and the number of the neighbouring atoms from the point of view of a central absorbing atomic species (selected by scanning over the appropriate x-ray energy) and can therefore determine the average local structure of different elements separately. The combination of the information from different types of absorbing atoms gives a more constrained result for the local structure than diffraction experiments. Furthermore, XAFS analysis does not make use of long-range translational symmetry positions. Consequently, XAFS offers an advantage in studying the near-neighbor local structure in complicated materials, such as pure and metal doped YBCO.

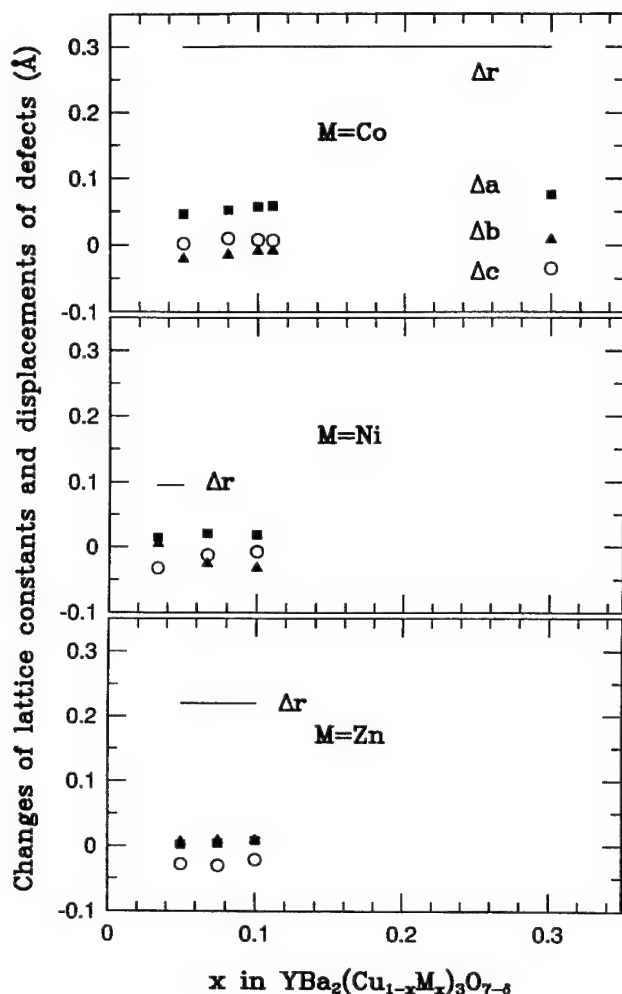


FIGURE 1 Changes of the lattice constants relative to pure YBCO and the displacements,  $\Delta r$ , of the substituted atom, M (M = Co, Ni, and Zn), as a function of the dopant concentration,  $x$ , for  $\text{YBa}_2(\text{Cu}_{1-x}\text{M}_x)_3\text{O}_{7-\delta}$ . Lattice constants are from Ref. 9 for pure YBCO and YBCO:Ni, and Ref. 5-6 for YBCO:Co and YBCO:Zn. In YBCO:Co,  $\frac{1}{2} \sim \frac{2}{3}$  of the Co(1) is displaced in the ab-plane [5]. In YBCO:Ni and YBCO:Zn, Ni(2) and Zn(2) are shifted along the c-axis [4,6].

We have studied in detail, the local structure about Cu and substituted atoms in YBCO:Co [3,5], YBCO:Fe [3,5], YBCO:Ni [4], YBCO:Zn [6], and YBCO:Pr [7], as well as the Cu and Y environments in O-deficient YBCO [8]. We find that there are large local distortions within the unit cell. Usually the impurity atom on the Cu site and the nearby Ba atoms move significantly, about 0.1 to 0.3 Å in many cases. In contrast, the size of the unit cell as determined in diffraction experiments, does not change very much, with typical changes often only a few hundredths of an angstrom.

Our XAFS results [3-6] for the local displacements of the substituted 3d-metal atoms relative to the corresponding Cu site are summarized in Figure 1, together with the changes

of the lattice constants relative to the undoped YBCO obtained from diffraction studies (the lattice constants for pure and the Ni doped YBCO are from Ref. 9 and others are from Ref. 5–6). The selected pair distances are listed in Table I, from which the Cu and the substituted atom positions relative to Y and Ba can be determined. In YBCO:Co [3,5] (YBCO:Fe is similar), Co is in the Cu(1) (chain copper) layer but about  $\frac{1}{2} \sim \frac{2}{3}$  of the Co atoms are displaced from the Cu(1) site in the ab-plane by about  $0.30 \pm 0.06 \text{ \AA}$ , depending on the thermal treatment and doping concentration; the average Co(1)-Ba distance increases by  $0.07\text{--}0.10 \text{ \AA}$  and the Cu(2)-O(4) (planar copper—axial oxygen) distance increases by about  $0.14 \text{ \AA}$ , which indicates that Ba moves towards the  $\text{CuO}_2$  while O(4) away from it, very similar to the changes in the O-deficient pure YBCO. Results for samples with thermal treatment are not plotted. In YBCO:Ni [4], Ni is found on both copper sites. Ni(1) is roughly at the ordinary Cu(1) site, however the Ni(2)-Ba distance is  $0.05 \text{ \AA}$  shorter while the Ni(2)-Y distance  $0.06 \text{ \AA}$  longer than the corresponding distances from Cu(2), which suggests that the Ni(2) atom is shifted along the c-axis by about  $0.095 \pm 0.04 \text{ \AA}$ . In YBCO:Zn [6], the Zn(2)-Ba distance has decreased by  $0.13 \text{ \AA}$  while the Zn(2)-Y distance has lengthened by a similar amount. This indicates that the Zn is displaced along the c-axis by approximately  $0.22 \pm 0.04 \text{ \AA}$ . However, some of this distortion might be a displacement of the Ba and/or Y atoms. In contrast to these large displacements about the dopant atom, the local structure about the remaining Cu atoms remains almost unchanged, even at 10% Zn. This indicates that these large displacements are localized to a few unit cells about the substituted atom. This seems also true for some other high  $T_c$  materials. For example, in Sr doped  $\text{Ti}_2\text{Ba}_2\text{CuO}_y$  [10], Sr is at a distorted Ba site with a displacement of  $0.14 \text{ \AA}$  along the c-axis (towards the  $\text{CuO}_2$  plane) while the Cu-Ba distance does not change much ( $< 0.03 \text{ \AA}$ ).

Table I  
Selected pair distances (in  $\text{\AA}$ , with the estimated uncertainty of  $0.02 \text{ \AA}$ ) obtained from XAFS studies [3–6, 8]

Pairs	$\text{YBa}_2\text{Cu}_3\text{O}_7$ M = Cu	$\text{YBa}_2\text{Cu}_3\text{O}_6$ M = Cu	YBCO:Co M = Co	YBCO:Ni M = Ni	YBCO:Zn M = Zn
M(1)-Ba	3.47	3.57	3.57	3.49	
M(2)-Ba	3.39	3.36		3.33	3.25
M(2)-Y	3.20	3.18		3.26	3.33

For the O-deficient samples, it is well known from diffraction results [11] and XAFS [8] that the Ba moves  $0.1 \text{ \AA}$  when O(1) (chain oxygen) is removed to make  $\text{YBa}_2\text{Cu}_3\text{O}_6$ . These results again indicate that Ba is easily displaced, but in this case it is likely a uniform displacement of Ba throughout the  $\text{YBa}_2\text{Cu}_3\text{O}_6$  material. However, the larger thermal factor [11], which peaks at  $O_{6.38}$  in that study, suggests that in the partially de-oxygenated samples, the Ba position depends on the local O environment. The XAFS results for partially substituted samples shows that the range of the distortion is small—a few unit cells.

Rare earth substitutions onto the Y site in YBCO are fundamentally different than metallic substitutions in that they generally have a much smaller effect on the superconducting properties. One exception is YBCO:Pr, but even in that material  $T_c$  does not go to zero until the concentration of Pr is greater than 50%. Interestingly, we also find short range disorder or distortion in the YBCO:Pr samples—the O environment about the Pr is distorted, but the Cu and Y K-edge XAFS measurements show little distortion (see Table II, Cu results not shown) [7], even at 50% Pr concentrations. This result is in contrast to Gd substitution which shows essentially no local disorder of the planar oxygens [12]. The disorder in the planar oxygen environment around the Pr is consistent

with a hybridization of  $\text{Pr}^{3+}$ -O,  $\text{Pr}^{4+}$ -O, and  $\text{Pr}^{3+}$ -O( $\underline{L}$ ) bonds, where  $\underline{L}$  indicates a ligand hole. Such a hybridization should localize holes in the planes and keep Cooper pairs from forming.

Table II

Y and Pr K-edge fit results to  $\text{Y}_{1-x}\text{Pr}_x\text{Ba}_2\text{Cu}_3\text{O}_7$ .  $R$  is the bond length,  $n\text{brs}$  is the total number of bonds, with the total Y-O bonds normalized to the pure ( $x = 0$ ) sample and the total Pr-O bonds constrained to 8.

x	Y-O		Pr - O <sub>short</sub>		Pr - O <sub>long</sub>	
	R(Å)	nbrs	R(Å)	nbrs	R(Å)	nbrs
0.0	2.41	8.0				
0.3	2.41	7.8	2.25	1.7	2.43	6.3
0.5	2.41	7.6	2.29	2.7	2.43	5.3
1.0			2.27	2.9	2.45	5.1

For each of the systems outlined above, the charge distribution has been changed by substituting or removing an atom in the YBCO crystal. This redistribution results in a large distortion of the atoms within the neighbouring unit cells but with little change in the size of the unit cell or any distortion in more distant unit cells. Consequently, electronic charge (including holes) in the  $\text{CuO}_2$  layer should couple strongly to the nearby displaced atoms (such as Ba, O(4), Zn(2), etc.) with any distortion confined to a few neighbouring unit cells. This suggests that there may be a strong coupling of holes in the  $\text{CuO}_2$  layer to a band of high- $k$  (near the Brillouin boundary) optical phonons that involves the motion of the Ba and O(4) atoms; however the coupling between these atoms and adjacent unit cells appears to be weaker. Whether or not this coupling is a major component of the pair coupling that leads to superconductivity is not certain, but clearly it cannot be ignored. In some cases, the large distortions may also lead to a localization of charge, which would decrease the number of free carriers, and therefore reduce  $T_c$ . On a more practical level, these structural results indicate that local stoichiometry may be very important for high quality bulk and thin film materials.

The experiments were performed at the Stanford Synchrotron Radiation Laboratory. The work of Bridges, Li, and Booth is supported in part by NSF grants DMR-90-04325 and DMR-92-05204.

## REFERENCES

1. T. M. Hayes and J. B. Boyce, in *Solid State Physics*, edited by H. Ehrenreich, F. Seitz, and D. Turnbull (Academic, New York, 1982), Vol. 37, p. 173.
2. E. A. Stern and S. M. Heald, in *Handbook on Synchrotron Radiation*, edited by E. E. Koch (North-Holland, New York, 1983), Vol. 1, p. 955.
3. F. Bridges, J. B. Boyce, T. Claeson, T. H. Geballe, and J. M. Tarascon, *Phys. Rev.* **B39**, 11603 (1989).
4. F. Bridges, J. B. Boyce, T. Claeson, T. H. Geballe, and J. M. Tarascon, *Phys. Rev.* **B42**, 2137 (1990).
5. G. G. Li, F. Bridges, J. Boyce, and W. C. H. Jointer, *Phys. Rev.* **B47**, 12110 (1993).
6. F. Bridges, G. G. Li, J. Boyce, and T. Claeson, *Phys. Rev.* **B48**, 1266 (1993).
7. C. H. Booth, F. Bridges, J. B. Boyce, T. Claeson, Z. X. Zhao, and P. Cervantes, *Phys. Rev.* **B49**, 3432 (1994).
8. J. B. Boyce, F. Bridges, T. Claeson, and M. Nygren, *Phys. Rev.* **B39**, 6555 (1989).
9. J. M. Tarascon, P. Barboux, P. F. Miceli, L. H. Greene, G. W. Hull, M. Eibschutz, and S. A. Sunshine, *Phys. Rev.* **B37**, 7458 (1988).
10. G. G. Li, J. Mustre de Leon, S. D. Conradson, and M. A. Subramanian, *Physica* **C219**, 371 (1994); G. G. Li, F. Bridges, J. B. Boyce, T. Claeson, to be published in *Phys. Rev. B*.
11. J. D. Jorgensen, B. W. Veal, A. P. Paulikas, L. J. Nowicki, G. W. Crabtree, H. Claus, and W. K. Kwok, *Phys. Rev.* **B41**, 1863 (1990).
12. J. B. Boyce, F. Bridges, T. Claeson, R. S. Howland and T. H. Geballe, *Phys. Rev.* **B36**, 5251 (1987).

## AUTHOR INDEX

### Proceedings of The Seventh Europhysical Conference on Defects in Insulating Materials

#### Volumes 134-137

- Achibat, T. 1417  
Agullo-Lopez, F. 1047  
Akiyama, N. 345  
Alcala, R. 521, 627, 655, 661  
Aldana, M. 299  
Aleksandrovt, V. V. 1237, 1241  
Allen, A. M. T. 437, 1205  
Alonso, P. J. 661, 677  
Alyoshin, V. A. 321  
Ambrosi, L. 741  
Andreeta, J. P. 209  
Andreeta, M. R. B. 209  
Antoniv, I. 967  
Antsigin, I. N. 303, 1131  
Apostol, E. 361  
Aramburu, J. A. 185, 189  
Armagan, G. 911  
Arndt, J. 1405  
Aubay, E. 223  
auf der Horst, C. 995  
Auffray, E. 835, 841  
Austin, J. C. 385  
Auzel, F. 975  
Averback, R. S. 1079  
Avtukh, A. S. 729  
Awano, T. 389, 457  
Azzoni, C. B. 485
- Babayan, A. K. 1167  
Babu, V. H. 1481  
Backens, M. 337  
Backhaus-Ricoult, M. 1531  
Bahtat, A. 647, 1391  
Bahtat, M. 647  
Balanat, E. 1193, 1197  
Baldacchini, G. 421, 513  
Baldochi, S. L. 513  
Ball, R. G. J. 161  
Balmain, J. 1517  
Baltog, I. 783  
Banhatti, R. D. 157  
Barboux, P. 31  
Barland, M. 1417  
Barram, P. S. 57  
Barriuso, M. T. 185, 189
- Basun, S. A. 525, 535, 567  
Baticle, B. 587  
Batygov, S. Kh. 809  
Baudry, J. 539  
Bausa, L. E. 681  
Becker, J. 847  
Bellenoue, P. 431  
Belsky, A. N. 243, 881, 1055  
Beneventi, P. 213, 287, 293, 379  
Bénière, M. 1481  
Bénière, F. 171, 1481  
Benivegna, G. 205  
Bennebroek, M. T. 79  
Bennewitz, R. 1245  
Beranger, M. 1171  
Bernstein, E. 1025, 1335  
Berthault, A. 1177  
Bettinelli, M. 741  
Betzler, K. 1029  
Beuneu, F. 1085  
Bibikov, R. 1265  
Bill, H. 619, 751, 979  
Binet, L. 223  
Birkholz, A. 165  
Bitar, L. 681  
Blak, A. R. 117, 315  
Blanchin, M. G. 1563  
Blanco, M. A. 47, 197, 201  
Boatner, L. A. 803  
Bodenschatz, N. 755  
Bolesta, I. 65, 559, 1321  
Bolis, L. 485  
Booth, C. H. 1577  
Boris, A. 457, 1379  
Bosi, L. 461  
Bouajaj, A. 745  
Bouazaoui, M. 647  
Bouffard, S. 1197  
Bougrine, E. 819  
Bouillot, J. 1021  
Boukenter, A. 1417  
Boulon, G. 509, 571, 575, 579  
Boureau, G. 179, 1465  
Bourson, P. 1545  
Boutinaud, P. 979



- Bouttet, D. 867  
 Bouwen, A. 489  
 Bovier, C. 1335, 1391  
 Boyce, J. B. 1577  
 Bracco, R. 735  
 Bravo, D. 261, 689, 1153  
 Bredikhin, S. 457, 1097, 1539  
 Brenier, A. 509, 571, 575, 579  
 Brenier, R. 1171, 1189, 1217  
 Briat, B. 1009  
 Bridges, F. 1577  
 Brisard, F. 1177  
 Bryknar, Z. 447  
 Bukun, N. G. 1001  
 Bungenstock, R. 465  
 Bunin, M. A. 75  
 Bunuel, M. A. 521  
 Burdick, G. W. 539  
 Bursian, V. 325  
  
 Cabaud, B. 1315  
 Cabrera, J. M. 989  
 Cai, Y. 583  
 Cain, L. S. 329, 1535  
 Calvi, P. 1425  
 Camagni, P. 485, 1425  
 Campagnoli, C. G. 485  
 Campone, P. 1503  
 Canut, B. 1013, 1017, 1171, 1189, 1217  
 Capelletti, R. 213, 287, 293, 379  
 Capmany, J. 681  
 Carniato, S. 179  
 Carvalho, J. F. 209  
 Casalboni, M. 417, 513, 725  
 Cases, R. 521, 627, 655  
 Cassimi, A. 1197  
 Castaing, J. 1439, 1449, 1453  
 Castrignano, T. 725  
 Catlow, C. R. A. 57, 107, 111, 1385  
 Caurant, D. 613  
 Chadwick, A. V. 91, 219, 1277, 1385  
 Chambon, B. 895  
 Chaminade, J. P. 635, 895  
 Champagnon, B. 1271  
 Chen, L. F. 405  
 Cheng, N. 697  
 Chernov, S. 773, 831  
 Chernov, V. 493  
 Claeson, T. 1577  
 Comins, J. D. 111, 437, 1193, 1205  
 Corish, J. 171  
 Cormier, G. 741  
 Corradi, G. 219  
 Costa Neto, M. A. 453  
 Costantini, J.-M. 1177  
 Courrol, L. C. 579  
 Cremona, M. 421, 513, 1073  
 Crettez, J. M. 1545  
 Cruickshank, K. 219  
 Cruz, C. M. G. S. 357  
 d'Auria, G. 425  
  
 da Silva, M. F. 1047  
 Dafinei, I. 361, 835, 841  
 Dance, J. M. 517  
 Dankert, O. 667  
 Darra, M. 379  
 Datema, H. C. 667, 921, 1299  
 Davenas, J. 1177, 1183, 1255, 1307, 1361  
 de Haas, J. T. M. 819  
 de Lima, J. F. 147, 607  
 de Lima, C. J. 209  
 De Simoné, M. 485  
 De Souza, S. S. 117  
 Demoncy, N. 613  
 den Hartog, H. P. 1299  
 den Hartog, H. W. 667, 921, 1299  
 Despa, F. 1525  
 Devitsin, E. G. 853  
 Di Bartolo, B. 911  
 Diaz, F. 1153  
 Diaz, M. P. 1211  
 Didyk, R. 967  
 Dieckhofer, J. 1367  
 Dieguez, E. 1047  
 Dimofte, C. 783  
 do N Souza, D. 607  
 do Pinho Mauricio, M. H. 1073  
 Dolin, C. 1511  
 Dominguez-Rodriguez, A. 1439, 1449, 1453  
 Donnerberg, H. 165  
 Doorhyee, E. 1197  
 Dorenbos, P. 809, 819, 823, 827  
 Doualan, J. L. 971, 1197  
 Drain, D. 895  
 Dudkevich, V. P. 321  
 Dufour, C. 1197  
 Dujardin, C. 867  
 Dumas, J. 1335  
 Drupt, P. 1255  
 Duval, E. 1271, 1417  
  
 Eachus, R. S. 599  
 Eftaxias, K. 1443  
 Eglitis, R. I. 83  
 Ehrhart, P. 1079  
 Eicken, J. T. 1373  
 Ekimov, A. I. 11  
 Endrst, R. 1251  
 Evans, B. D. 329  
 Eveno, P. 1453  
  
 Fabeni, P. 787  
 Fabris, J. L. 353  
 Feofilov, S. P. 567  
 Ferrari, M. 741, 745  
 Fieschi, R. 379  
 Finke, B. 905  
 Fischer, C. 697, 995  
 Flerov, A. V. 239, 371  
 Flerov, V. I. 239, 371  
 Flerov, S. I. 371  
 Florea, C. 1085

- Florez, M. 47, 193  
Fouassier, C. 895  
Fowler, W. B. 379  
Francisco, E. 123, 193, 197, 201  
Franco, R. 123  
Francois, B. 1355  
Frankenstein, L. 847  
Frens, A. M. 79  
Fricke, M. 337  
Frorip, A. 873  
Fuchs, G. 1189, 1315  
Furetta, C. 631, 1127  
Furgala, Y. 65, 559
- Gacon, J. C. 539  
Gaewdang, T. 635, 895  
Gainotti, A. 379  
Galez, C. 1017, 1545  
Gallagher, H. G. 953, 957  
Gallo, D. 461  
Garapon, C. 539  
Garapyn, I. 967  
Garcia Sole, J. 681, 685  
Garcia, A. 635, 895  
Garoum, M. 1549  
Gasparov, L. 1557  
Gather, B. 1029  
Gavartin, J. L. 107  
Gavrilov, V. V. 773, 831  
Gea, L. 1171  
Gegusin, I. I. 75  
Gektin, A. V. 411, 1055, 1107  
Gellermann, W. 917  
Georgescu, S. 933  
Gerdanian, P. 1563  
Gesland, J. Y. 975  
Gevorkyan, V. A. 243, 1167  
Giliberti, C. 421  
Gilliot, P. 1335  
Giulotto, E. 1425  
Glasbeek, M. 453  
Glukhov, R. A. 813  
Glumov, O. V. 1373, 1477  
Glynn, T. J. 933  
Godlewski, M. 711  
Gogoll, S. 1061  
Gomes, L. 579  
Gomez-Garcia, D. 1453  
Goovaerts, E. 1067, 1101  
Gorbunov, S. V. 767, 1131  
Gourier, D. 223, 431, 613  
Grabmaier, B. C. 899  
Grammatikakis, J. 247  
Grandin, J. P. 1197  
Grannec, J. 517, 635  
Grassano, U. M. 333, 417, 421, 513, 725  
Grau, P. 1413  
Graziani, M. 1127  
Greaves, G. N. 1385  
Greten, G. 693  
Grinberg, M. 1051
- Groh, D. J. 127  
Grone, A. 283  
Grun, J. B. 1335  
Grushko, Yu. S. 1341  
Gu, H. E. 349  
Gudel, H. U. 593  
Guglielmi, M. 31  
Gunsser, W. 1373, 1477  
Gunther, C. 1245  
Gurioli, M. 787  
Gustin, E. 489  
Guy, S. 563
- Hainovsky, N. 1493  
Hamri, A. 1009  
Han, T. P. J. 715, 953, 957, 961  
Hangleiter, TH. 499  
Happek, U. 341  
Harding, J. 179  
Harsch, A. 1277  
Hartung, S. 929  
Harutunyan, V. V. 243, 1167  
Hashimoto, S. 1289  
Hattori, T. 1097, 1379, 1539  
Haut, C. 233  
Hayashi, T. 793  
Heber, J. 755  
Henderson, B. 715, 721, 943, 953, 957, 961  
Hernandes, A. C. 209, 353  
Hizhnyakov, V. 375  
Hofmann, D. M. 641  
Holliday, K. 721  
Horowitz, Y. S. 1091  
Hosono, H. 1043, 1221  
Hourdequin, E. 1193  
Hu, Gang. 1535  
Huber, G. 929  
Huntington, J. E. 161  
Huntz, A. M. 1511
- Ibarra, A. 939  
Ibragimov, K. 1163  
Ignozza, F. 417  
Ilmer, M. 899  
Inaba, M. 1289  
Inoue, Y. 721, 943  
Ishigame, M. 1097, 1379, 1539  
Ivanov, N. P. 1107
- Jaaniso, R. 751  
Jaaskelainen, T. 209  
Jackson, R. A. 161  
Jacobs, P. W. M. 87, 107, 1473  
Jacquier, B. 563, 635, 895  
Jahnke, A. 899  
Jain, H. 1367  
Janowicz, M. 1051  
Jardin, C. 1255, 1307  
Jaskoski, W. 1051  
Jastrabik, L. 325  
Jimenez de Castro, M. 273

- Jimenez-Melendo, M. 1449  
 Johansen, H. 1061  
 Joubert, M. F. 563  
  
 Kalder, K. 375  
 Kalinov, V. 425  
 Kalnin, Yu. H. 1521  
 Kalogeras, J. M. 257  
 Kamada, M. 1295  
 Kamenskikh, I. A. 889  
 Kaminskii, A. A. 681, 689, 725  
 Kamshilin, A. A. 209  
 Kanert, O. 277, 337, 1367, 1399  
 Kaplyanskii, A. A. 567  
 Kapphan, S. 229, 283, 337, 353, 693, 697, 995  
 Kvapil, J. 867  
 Karus, M. 1373, 1477  
 Katsika, V. 247  
 Katzir, A. 799  
 Kawamura, K. 1221  
 Kawazoe, H. 1043  
 Keppens, V. 1395  
 Ketolainen, P. 395, 401  
 Khaidukov, N. M. 827, 853  
 Kijak, R. 1265  
 Kink, R. 873  
 Kip, D. 1033  
 Kirikova, N. Yu. 853  
 Kirm, M. 873  
 Kityk, I. I. 65, 1321  
 Klimenko, V. E. 853  
 Klimov, S. 1055  
 Kodama, N. 721, 943  
 Koepke, Cz. 1051  
 Kolesnik, S. N. 1341  
 Komar, V. K. 1107  
 Konakova, A. 447  
 Konate, A. 971  
 Kornienko, M. V. 1341  
 Korrovits, V. 375  
 Kortov, V. S. 1149  
 Korzhik, M. V. 819, 823  
 Koschnick, F. K. 499, 1485  
 Kosoboutski, P. 1261, 1265  
 Kotomin, E. A. 83, 87, 1119  
 Kovacs, L. 213, 287, 293  
 Kovaleva, N. 457, 1097  
 Kovalisko, V. 1321  
 Koyama, S. 1295  
 Kozlov, V. A. 853  
 Kral, J. 447  
 Krätzig, E. 983, 1033  
 Krausz, E. 513  
 Kristianpoller, N. 311, 799  
 Kruzhlov, A. V. 69, 303, 1131, 1143  
 Kuchler, R. 277, 337, 1367, 1399  
 Kudrjavitseva, I. 1163  
 Kudyakov, S. V. 767, 1131  
 Kuleshov, N. V. 729  
 Kulis, P. 481, 865  
 Kuusmann, I. 847  
  
 Kuznetsov, A. Yu. 69, 1143  
 Kuzovkov, V. N. 133, 137, 1119  
  
 Laermans, C. 1395  
 Lahoz, F. 661  
 Laredo, E. 299  
 Lavin, V. 603  
 Leblans, M. 39, 489  
 Lecoq, P. 835, 841  
 Lee, D. R. 961  
 Lefrant, S. 437, 783, 1193, 1205  
 Lempicki, A. 803  
 Leshchuk, R. Ye. 553  
 Levy, R. 1335  
 Li, G. G. 1577  
 Li, M. S. 229  
 Linares, C. 563  
 Lopez, F. J. 261, 689, 1153  
 Loudjani, M. K. 233, 1517  
 Luana, V. 47, 123, 193  
 Luci, A. 513, 725  
 Lupei, A. 947  
 Lupei, V. 705, 925, 929, 933, 947  
 Lushchik, Ch. 761, 873  
 Lushchik, A. 761, 873, 1163  
 Lutci, R. V. 1573  
 Luty, F. 367, 465  
  
 Macfarlane, P. 721  
 Madacsi, D. P. 153  
 Madej, C. 571, 575, 579  
 Magliocco, M. 1503  
 Magro, C. 735  
 Mahajna, S. 1091  
 Maier, J. 1485, 1493, 1553  
 Makhov, V. 847  
 Makhov, V. N. 853, 1167  
 Malghani, M. S. 101  
 Marasca, C. 333  
 Marchetti, A. 1303  
 Marco de Lucas, M. C. 517, 593  
 Mares, J. A. 867  
 Margerie, J. 971, 1197  
 Marsman, M. 823  
 Martelli, S. 1073  
 Martet, C. 1315  
 Martin, I. R. 603, 627  
 Martin, A. 261, 689  
 Martin, P. 1055  
 Martin Pendas, A. 123  
 Martin, M. J. 1153  
 Martinez-Fernandez, J. 1453  
 Martini, M. 631  
 Martins, E. 513  
 Martinson, I. 873  
 Maslov, V. A. 1143  
 Matsunami, N. 1221  
 Matsuyama, T. 389  
 Matthias, E. 1061, 1245  
 McClure, D. S. 525  
 McClure, G. D. 715

# AUTHOR INDEX

v

- Meddeb, J. 1013  
 Meftah, A. 1189, 1217  
 Meichenin, D. 975  
 Merino, R. I. 671, 1499  
 Mersch, F. 1039  
 Messina, A. 205  
 Messous, M. 895  
 Meyer, A. 1373  
 Meyer, B. K. 641  
 Michel-Calendini, F. 175  
 Mihokova, E. 877  
 Mihut, L. 783  
 Mikhailik, V. B. 95, 779  
 Mikhailin, V. V. 243, 881  
 Mikhailov, V. P. 729  
 Minkov, B. I. 729  
 Mitkova, M. 1409  
 Mitroaica, Gh. 361  
 Moine, B. 827, 867  
 Moliton, A. 1349, 1355  
 Mollmann, K. 917  
 Monakhov, A. V. 1149  
 Moncorgé, R. 681  
 Monnier, A. 751, 979  
 Montagna, M. 745  
 Monteil, A. 745  
 Montecali, R. M. 421, 425, 513, 1073  
 Monty, C. 1511  
 Morato, S. P. 513  
 Moreau, C. 1355  
 Moreno, M. 185, 189, 517, 593  
 Moretti, P. 1013, 1017, 1021, 1189, 1217  
 Mori, Y. 443  
 Moriera, R. L. 1545  
 Morlotti, R. 735  
 Morrison, G. 91  
 Mortier, M. 975  
 Morton-Blake, D. A. 171  
 Moudden, A. H. 1563  
 Mugnier, J. 647, 1021, 1025, 1391  
 Muller, M. 353  
 Mungan, C. E. 341  
 Munoz Santiuste, J. E. 685  
 Munoz, A. 1439  
 Munro, I. H. 889  
 Muramatsu, S. 443  
 Murch, G. E. 1  
 Murin, I. V. 1373, 1477  
 Murti, Y. V. G. S. 157  
 Myasoedov, Yu. N. 1573  
 Mysovsky, S. 493  
 Nagirnyi, V. 375, 877  
 Nagli, L. 799  
 Nagornaya, L. L. 477  
 Nakagawa, H. 367  
 Nakahara, F. 345  
 Nascimento, O. R. 619  
 Nascimento, A. E. do. 147  
 Nazarov, M. V. 307, 865, 1457  
 Nazarova, T. A. 307, 865, 1457  
 Netshisaulu, T. T. 111, 1385  
 Neukum, J. 755  
 Ngoepe, P. E. 111, 1385  
 Nguyen, T. P. 437  
 Nicoloso, N. 1485  
 Nikl, M. 787, 867, 877, 1283  
 Nishii, J. 1043  
 Nistor, L. C. 1331  
 Nistor, S. V. 1067, 1101  
 Nitsch, K. 787, 1283  
 Nosenko, A. E. 251, 553  
 Nunes, R. A. 1073  
 Nunez, P. 603  
 Obyden, S. K. 865  
 Ogorodnikov, I. N. 69, 1143  
 Ohkura, H. 345, 443  
 Okada, T. 1295  
 Okuno, E. 1211  
 Oliete, P. B. 677, 1325  
 Oliveira, L. 229, 357, 619  
 Olm, M. T. 599  
 Ongaro, R. 1549  
 Orera, V. M. 671, 677, 1325, 1499  
 Oster, L. 311  
 Ostertag, M. 899  
 Osvet, A. 1137  
 Othmani, A. 1335  
 Otte, M. 547  
 Ould Salem, S. 1013, 1189, 1217  
 Overhof, H. 547  
 Owaki, S. 1295  
 Padlyak, B. V. 553  
 Paille, F. 1335  
 Paladino, E. 205  
 Pandey, R. 127  
 Pankrath, R. 693  
 Papathanassiou, A. N. 247  
 Pariselle, M. A. 437, 1193  
 Parisot, S. 233  
 Parker, S. C. 57  
 Patnaik, B. K. 385  
 Paul, M. 219  
 Paumier, E. 1197  
 Pawlik, Th. 465, 499, 547  
 Pazzi, G. P. 787, 877  
 Pedrini, C. 509, 571, 575, 579, 619, 827, 867, 1055  
 Peka, P. 447  
 Pendas, A. M. 193, 197, 201  
 Pereira, L. 641  
 Pereira, E. 641  
 Peter, A. 213  
 Petkova, T. 1409  
 Peyrot, A. 1531  
 Pham-Thi, M. 613  
 Picard, C. 1563  
 Pitaval, M. 1217  
 Piters, T. M. 1211  
 Planelles, J. 1051  
 Plavina, I. 623  
 Plenet, J. C. 1315  
 Polak, K. 787, 1283

- Ponnambalam, M. J. 141  
 Popov, A. I. 83, 623, 1079  
 Posudievsky, O. Yu. 1345  
 Potemski, M. 509  
 Pouchard, M. 635  
 Price, K. J. 385  
 Prieto, C. 593  
 Prij, J. 1111  
 Prokofiev, V. V. 209  
 Prosandeyev, S. A. 75, 1569  
 Prosposito, P. 417  
 Protin, L. 1197  
 Pueyo, L. 47, 123, 197  
 Pung, L. 1163  
 Purton, J. 57  
  
 Qi Feng, Xi. 697  
 Quilitz, M. 1553  
  
 Rabier, J. 1431  
 Raerinne, P. 395  
 Rafiuddin, R. 91  
 Raksany, K. 153  
 Ramaz, F. 1009  
 Ramos, S. M. M. 1013, 1017, 1171, 1189, 1217  
 Ramstein, B. 1193  
 Ratier, B. 1349, 1355  
 Rebouta, L. 1047  
 Recio, J. M. 123, 127, 193, 197, 201  
 Reddy, K. V. 1481  
 Reichert, A. 1029  
 Reichling, M. 1061, 1245  
 Reyher, H.-J. 1039  
 Riblet, P. 1335  
 Righi, A. 1545  
 Riley, M. 513  
 Rodnyi, P. A. 95, 779  
 Rodriguez, V. D. 603, 627, 939  
 Rodriguez-Mendoza, U. R. 603, 939  
 Rodriguez, F. 517, 587, 593  
 Rogalev, B. 493  
 Rogulis, U. 471, 859  
 Rollandi, L. 1425  
 Rosso, C. 1017, 1545  
 Rousseau, M. 975  
 Routbort, J. L. 1459  
 Roux, J. F. 1315  
 Rubinina, N. 1029  
 Runne, M. 847  
 Ruschke, J. 1039  
 Russell, N. V. 1277  
 Ruza, E. 471  
 Rybka, V. 1251  
 Rycerz, Z. A. 107  
 Ryskin, N. N. 809  
 Rzepka, E. 1205  
  
 Salvetat, J. P. 1177, 1361  
 Sanipoli, C. 631, 1127  
 Sanjuan, M. L. 1325  
 Santos, M. T. 1047  
 Saparin, G. V. 865  
  
 Sarnbeek, A. V. 1079  
 Savikhin, F. 761  
 Saviot, L. 1271  
 Scacco, A. 333, 421, 631, 1127  
 Scavarda do Carmo, L. C. 1073  
 Schaart, D. R. 827  
 Schlarb, U. 1029  
 Schmidt, J. 79  
 Schneegans, M. 835, 841  
 Schnieper, M. 751  
 Schoemaker, D. 489, 1067, 1101  
 Schroder, A. 847  
 Schulz, H.-J. 447  
 Scott, M. A. 957  
 Seinen, J. 921, 1299  
 Seo, H. J. 715  
 Serebryanny, V. Ya. 411  
 Serughetti, J. 1025, 1391  
 Shaw, D. A. 889  
 Shcherbitsky, V. G. 729  
 Sherlock, R. 933  
 Shevchuk, V. N. 251  
 Shiran, N. V. 411, 1107  
 Shluger, A. L. 107, 1227  
 Shlyakhturov, V. V. 1107  
 Shmilevich, A. 799  
 Shpak, A. 421  
 Shulgin, B. V. 767  
 Sievers, A. J. 341  
 Sildos, I. 1137  
 Silfsten, P. 401  
 Silins, A. R. 7  
 Silva, M. A. P. 357  
 Siu-Li, M. 353, 357  
 Sitters, R. 453  
 Smith, D. Y. 101  
 Smutny, F. 325  
 Soares, J. C. 1047  
 Sobolev, A. B. 51, 69  
 Sochava, L. 325  
 Sochava, L. S. 1341  
 Solé, R. 1153  
 Somaiah, K. 631  
 Somma, F. 1073  
 Song, K. S. 405, 583  
 Soppe, W. J. 1111  
 Soppe, W. 1119  
 Sotero, A. P. 1073  
 Spaeth, J.-M. 465, 471, 499, 547, 1485  
 Spinolo, G. 1503  
 Springis, M. 481, 859  
 Stadler, W. 641  
 Stashans, A. 87  
 Stenzel, E. 1061  
 Stolovich, A. 375, 877  
 Suarez, N. 701  
 Suchocki, A. 509  
 Sunta, C. M. 1211  
 Surma, M. 711  
 Suszynska, M. 1413  
 Suzuki, R. 1295  
 Sviridov, E. V. 321

## AUTHOR INDEX

vii

- Svorcik, V. 1251  
Swanson, M. L. 385  
Swiatek, K. 543  
Symikov, P. 325
- Takahashi, M. 1295  
Takeuchi, H. 721  
Tale, A. 623  
Tale, I. 471, 477, 481, 859  
Tale, V. 477  
Tan, C. Z. 1399, 1405  
Tanase, T. 361  
Tavares, C. J. M. 453  
Tennenbaum, I. M. 75, 1569  
Teodorescu, V. S. 1331  
Tetot, R. 1465  
Thery, J. 431  
Thevenard, P. 1013, 1017, 1171, 1189, 1217  
Thien, B. V. 1183  
Tiseanu, C. 947  
Tomlins, G. W. 1459  
Topa, V. 361, 1525  
Toulemonde, M. 1189, 1197, 1217  
Toyoda, K. 793  
Treilleux, M. 1189, 1315  
Trepakov, V. 325  
Tressaud, A. 517  
Trinkler, L. E. 671, 1159  
Trinkler, M. F. 1159  
Trokss, J. 859  
Trouillas, P. 1349  
Trzesniak, P. 147  
Tsai, S. C. 1511  
Tse, K. F. 1277  
Tsuboi, T. 349  
Tsujibayashi, T. 793  
Turchak, R. 1321
- Ugozzoli, F. 213  
Ukshe, A. E. 1001  
Umisedo, N. K. 1211  
Urlacher, C. 1025, 1391  
Uvarova, T. V. 853
- Vainshtein, D. 667, 921, 1299  
Vajda, P. 1085  
Valerio, M. E. G. 147, 607  
Valiente, R. 587  
Vallianatos, F. 1443  
van den Bernt, M. 921  
van Eijk, C. W. E. 809, 819, 823, 827  
Van Hoi, P. 1413  
Varrel, B. 895  
Vasil'chenko, E. 761  
Vasil'ev, A. N. 813, 881, 889  
Vassilikou-Dova, A. 257, 1443  
Vassilikou-Dova, A. B. 247  
Vedda, A. 1503  
Veispals, A. 859  
Velasco, V. R. 1241  
Velgosh, S. 65
- Veluri, K. 171  
Verdaguer, M. 593  
Vergara, I. 685  
Vernon, M. L. 1473  
Verweij, J. W. M. 867  
Viana, B. 431  
Vianna, C. 315  
Vieira Jr, N. D. 513  
Vikhnin, V. 325  
Vikhnin, V. S. 337, 1341  
Vila, R. 273  
Villacampa, B. 655, 661  
Visocekas, R. 265  
Visser, R. 827  
Vivien, D. 431  
Voda, M. 261  
Vodolazski, P. 1261  
Voigt, P. 229, 995  
Volk, T. 1029  
Voloshinovskii, A. S. 95, 779  
von der Osten, W. 341
- Wang, G. 953  
Watterich, A. 277  
Weber, M. J. 23  
Wegener, J. 277  
Wenseleers, W. 489  
West, A. R. 219  
Whitham, A. R. 1277  
Williams, R. T. 1227, 1245  
Wilson, R. M. 1227, 1245  
Wilson, A. 1277  
Wisniewski, D. 803  
Wohlecke, M. 1029  
Wojtowicz, A. J. 803  
Wong, W. C. 525  
Wright, K. V. 57  
Wu, Z. L. 1405
- Yakovlev, V. Yu. 767  
Yakovlev, N. L. 1237, 1241  
Yamaga, M. 721, 943  
Yamanaka, H. 1043  
Yeritsian, G. N. 243  
Yoshimura, E. M. 1211  
Yosida, T. 943  
Yossian, D. 1091
- Zaiser, M. 1119  
Zakharchenko, I. N. 321  
Zakrzewski, A. J. 79, 145  
Zaldo, C. 1153  
Zapol, P. 1521  
Zazubovich, S. 375  
Zema, N. 333  
Zepelin, V. 877  
Zhao, J. 995  
Zhavoronkov, N. I. 729  
Zimmerer, G. 847  
Zinin, E. I. 1055  
Zink, A. 265

## Notes for Contributors

### TYPESCRIPTS

*Submissions:* Papers should be typed on good quality paper with double spacing and wide (3 cm) margins, using one side only, and submitted in duplicate to the Editor in Chief or to the appropriate Regional Editor:

**J. P. Biersack**, Editor in Chief, Hahn-Meitner-Institut, Glienickerstrasse 100, 14109 Berlin, Germany

**N. Itoh**, Department of Physics, Faculty Of Science, Nagoya University, Furo-cho, Chikusa-ku, Nagoya 464, Japan

**H. Kronmüller**, Max-Planck-Institut für Metallforschung, Institut für Physik, Heisenbergstrasse 1, 70569 Stuttgart 80, Germany

**M. A. Kumakhov**, Russian Research Center, Moscow 123182, Russia

**N. Tolk**, Department of Physics and Astronomy, Vanderbilt University, P.O.Box 1807-B, Nashville, Tennessee 37325, USA

The editors and publisher cannot be responsible for correcting English grammar, spelling, and idiom. Authors should ensure before submission that papers are correct in style and language.

*Abstracts, key words, running heads:* Each paper requires an abstract of 100-150 words summarizing the significant coverage and findings. Abstracts should be accompanied by up to six key words which between them characterize the contents of the paper. These will be used for indexing and data retrieval purposes. Please also provide an abbreviation of the paper's title (no more than 35 characters) for use as a running head.

*Terms of Acceptance:* Submission of a manuscript is taken to imply that the paper represents original work not previously published, is not being considered elsewhere for publication, and if accepted for publication will not be published elsewhere in the same form, in any language, without the consent of the publisher. It is also assured that the author has obtained all necessary permissions to include in the paper items such as quotations, reprinted figures, results of government-sponsored research, etc. It is a condition of acceptance for publication that the publisher acquires copyright of the paper throughout the world.

### FIGURES

All figures should be numbered with consecutive arabic numbers, have descriptive captions, and be mentioned in the text. Keep figures separate from the text, but indicate an approximate position for each in the margin.

*Preparation:* Figures submitted must be of high enough standard for direct reproduction. Line drawings should be prepared in black (India) ink on white paper or tracing cloth, with all lettering and symbols included. Alternatively, good sharp photoprints ("glossies") are acceptable. Photographs intended for halftone reproduction must be good glossy original prints, of maximum contrast.

Clearly label each figure with the authors' names and figure number, indicating "top" where this is not obvious. Redrawing or retouching of unusable figures will be charged to authors.

*Size:* Figures should be planned so that they reduce to a 12.5 cm column width. The *preferred* width of submitted line drawings is 22 to 25 cm with capital lettering 4 mm high, for reduction by one-half. Photographs for halftone reproduction should be approximately twice the desired size.

*Captions:* A list of figure captions, with relevant figure numbers, should be typed on a separate sheet and included with the typescript.

### COLOR PLATES

Whenever the use of color plates is an integral part of the research, the journal will publish color illustrations without charge to the authors.

### EQUATIONS AND FORMULAE (MATHEMATICAL)

Whenever possible, mathematical equations should be typewritten, with subscripts and superscripts clearly shown. It is helpful to identify unusual or ambiguous symbols in the margin when they first occur. To simplify typesetting, please use: (1) the "exp" form of complex exponential functions; (2) fractional exponents instead of root signs; and (3) the solidus (/) to simplify fractions—e.g.  $\exp x^a$

*Marking:* The printer will set mathematical symbols in italics, except for obvious groups like sin and log. Any symbols which are to be left in roman (upright) type should be encircled in pencil in the typescript; bold symbols should be underlined with a wavy line.

## EQUATIONS AND FORMULAE (CHEMICAL)

Ring formulae, and other complex chemical matter, are extremely difficult to typeset. Please therefore, supply reproducible artwork for equations containing such chemistry. Long reaction sequences should be designated as "Schemes" and treated like figures: i.e. keep artwork separate from the text, indicate in the margin an appropriate position, and supply a separate list of scheme captions. Where necessary, individual chemical formulae can be identified with bold arabic numbers. Chemical equations referred to in the text should be indicated with arabic numbers set over to the right in parentheses.

**Marking:** Where chemistry is straightforward and can be set (e.g. single-line formulae), please help the typesetter by distinguishing between e.g., double bonds and equal signs, and single bonds and hyphens, where there is ambiguity. The printer finds it difficult to identify which symbols should be set in roman (upright), italic, or bold type, especially where the paper contains both mathematics and chemistry. Therefore, please help the printer as much as possible by adding marginal notes in pencil.

## TABLES

Number tables consecutively with roman numerals, and give each a clear descriptive caption at the top. Avoid the use of vertical rules in tables.

## UNITS

Metric units are preferred. Acceptable abbreviations of units are given in the *Style Manual* of the American Institute of Physics and similar publications.

## REFERENCES AND NOTES

References and notes are indicated in the text by consecutive superior arabic numbers. The full list should be collected and typed at the end of the paper in numerical order. Listed references should be complete in all details but excluding article titles in journals. Authors' initials should precede their names: journal title abbreviations should conform to *Physical Abstracts*. Examples:

1. A. B. Smith and C. D. Jones, *J. Appl. Phys.* **34**, 296 (1965).
2. R. B. Brown, *Molecular Spectroscopy* (Gordon and Breach, New York, 1970), 3rd ed., Chap. 6, pp. 95, 106.

## TEXT HEADINGS

Set first-level headings in the text over to the left, type all in capitals (upper-case); begin the text on the following line. Second-level headings should be typed in small (lower-case) letters with all main words capitalized. Underline the heading and start the text on the next line. For third-level headings, only the first letter should be a capital. Underline, then run on the text after three typewriter spaces.

### FIRST LEVEL HEADING

### Second-Level Text Headings

Third-level headings. With text run on.

## PROOFS

Authors will receive proofs (including figures) by airmail for correction, which must be returned to the printer within 48 hours of receipt. Please ensure that a full postal address is given on the first page of the manuscript, so the proofs are not delayed in the post. Author's alterations in excess of 10% of the original composition will be charged to authors.

## REPRINTS

The senior author of each paper will receive 25 complimentary reprints. Additional reprints may be ordered by completing the appropriate form sent with proofs.

## PAGE CHARGES

There are no page charges to individuals or to institutions.

## A FINAL NOTE

Typescripts which do not conform to the required standards of preparation for submission outlined here will be returned to authors for correction before review.



*(Continued from inside front cover)*

© 1995 by OPA (Overseas Publishers Association) Amsterdam BV. Published under license by Gordon and Breach Science Publishers SA, a member of The Gordon and Breach Publishing Group. All rights reserved.

Except as permitted under national laws or under the Photocopy License described below, no part of this publication may be reproduced or transmitted in any form or by any means, electronic, mechanical, photocopying or otherwise or stored in a retrieval system of any nature, without the advance written permission of the Publisher.

#### ORDERING INFORMATION

Four issues per volume. 1996 Volumes: 137-139

Orders may be placed with your usual supplier or with International Publishers Distributor at one of the addresses shown below. Journal subscriptions are sold on a per volume basis only; single issues of the current volume are not available separately. Claims for nonreceipt of issues will be honored free of charge if made within three months of publication of the issue. Subscriptions are available for microform editions; details will be furnished upon request.

All issues are dispatched by airmail throughout the world.

#### SUBSCRIPTION RATES

Base list subscription price per volume: ECU 283.00 (US\$368.00). \* This price is available only to individuals whose library subscribes to the journal OR who warrant that the journal is for their own use and provide a home address for mailing. Orders must be sent directly to the Publisher and payment must be made by personal check or credit card.

Separate rates apply to academic and corporate/government institutions, and may also include photocopy license and postage and handling charges.

\*ECU (European Currency Unit) is the worldwide base list currency rate; payment can be made by draft drawn on ECU currency in the amount shown or in local currency at the current conversion rate. The US Dollar rate is based upon the ECU rate and applies to North American subscribers only. Subscribers from other territories should contact their agents or the Publisher. All prices are subject to change without notice.

**Publication Schedule Information:** To ensure your collection is up-to-date, please call the following number for information about the latest issue published: USA (201) 643-7500 – Dial extension 290 – Enter the ISSN followed by # key. Note: If you have a rotary phone, please call our Customer Service at the numbers listed below.

*Orders and enquiries should be placed through International Publishers Distributor at one of the addresses below:*

Postfach, 4004 Basel  
Switzerland  
Telephone: (41-61) 261-01-38  
Fax: (41-61) 261-01-73

820 Town Center Drive  
Langhorne, PA 19047 USA  
Telephone: (215) 750-2642  
Fax: (215) 750-6343

Kent Ridge, PO Box 1180  
Singapore 911106  
Republic of Singapore  
Telephone: 741-6933  
Fax: 741-6922

Yohan Western Publications Distribution Agency  
3-14-9, Okubo, Shinjuku-ku  
Tokyo 169, Japan  
Telephone: (03) 3208-0186  
Fax: (03) 3208-5308

#### LICENSE TO PHOTOCOPY

This publication and each of the articles contained herein are protected by copyright. If the subscription price paid by the subscriber includes a fee for a photocopy license, then the subscriber is permitted to make multiple photocopies of single articles for the internal study or research purposes of the subscriber. The Photocopy License is not available to individuals or to certain other subscribers. The Photocopy License does not permit copying for any other purpose, such as copying for distribution to any third party (whether by sale, loan, gift or otherwise); as agent (express or implied) of any third party; for purposes of advertising or promotion; or to create collective or derivative works. All requests for permission to copy beyond the scope of the Photocopy License must be made to the Publisher. No copyright licensing organization in any territory has authority to grant such permission on the Publisher's behalf. Any unauthorized reproduction, transmission or storage may result in civil or criminal liability.

#### RIGHTS AND PERMISSIONS / REPRINTS OF INDIVIDUAL ARTICLES

Permission to reproduce and/or translate material contained in this journal must be obtained in writing from the Publisher. Copies of individual articles may be obtained from SCAN, the Publisher's own document delivery service. For either service, please write or fax to: International Publishers Distributor at one of the addresses listed above.

#### VOLUNTARY PAGE CHARGES

The United States National Science Foundation has extended the allowance of page charge funds for payments to journals regardless of the Publisher's commercial status. Previously this was reserved for only nonprofit society-sponsored journals. Voluntary page charge payments are now accepted for this journal, and authors may elect to pay any amount up to a maximum of \$25.00 per page. Payments will be refunded in the form of a voucher at 100% value of total payment. This voucher can be used by the author or the author's university library for any product or service offered by the Publisher, and thereby can be used to supplement library funding.

#### NEGATIVE PAGE CHARGES

The principal author of each article will receive a voucher for his contribution in the amount of ECU 15.00 (US \$20.00, Yen 3,000), which can also be used to purchase the Publisher's products directly or through university libraries, thereby reducing costs of publications to those authors supporting the journal.

Distributed by International Publishers Distributor.  
Printed in Malaysia.

DECEMBER 1995